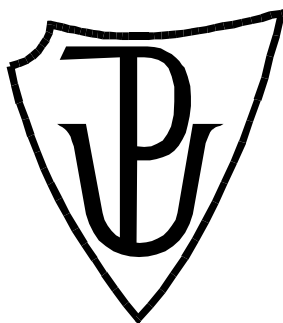


PALACKÝ UNIVERSITY OLOMOUČ

Faculty of Science

Department of Physical Chemistry



**Modeling of Small Molecules Interactions with
Biomembranes**

Ph.D. THESIS

Author: **Mgr. Markéta Paloncýová**

Study programme: Chemistry

Study field: Physical Chemistry

Study form: Daily

Supervisor: **Prof. RNDr. Michal Otyepka, Ph.D.**

Consultant: **Doc. RNDr. Karel Berka, Ph.D.**

Date of submission: 2016/07/29

Declaration of the author

I declare that I have worked out this thesis by myself using the cited references. Neither the thesis nor any of its part was previously used for obtaining any academic degree.

Olomouc, July 2016

Markéta Paloncýová

Bibliografická identifikace:

Jméno a příjmení autora	Mgr. Markéta Paloncýová
Název práce	Modelování interakcí malých molekul s biomembránami
Typ práce	Dizertační
Pracoviště	Katedra fyzikální chemie
Vedoucí práce	Prof. RNDr. Michal Otyepka, Ph.D.
Rok obhajoby práce	2016
Klíčová slova	Membrána, léčiva, permeabilita, cytochrom P450, molekulová dynamika
Počet stran	46
Počet příloh	14
Jazyk	Anglický
Abstrakt	<p>Interakce malých molekul s membránami hrají významnou roli při vstřebávání a distribuci léčiv v našem těle. V předložené práci jsem se soustředila na teoretické metody používané pro pochopení interakcí léčiv s biomembránami z pohledu termodynamiky i kinetiky při permeaci léčiv přes membrány. Dále jsem se věnovala významu chování léčiv v membránách v souvislosti s interakcemi léčiv s biotransformačními enzymy, které jsou kotvené v membránách. V úvodu popisuji nezbytné biologické základy týkající se struktury a funkce membrán a jejich interakcí s léčivy, a dále pak teoretické základy molekulově-dynamických (MD) simulací. Detailně popisuji pokročilé metody MD, tzv. biased MD methods, poskytující profily volné energie prostupu látek přes membránu. Získaný profil volné energie je základem pro odhad partičního koeficientu léčiva v membráně a společně s difúzním koeficientem i jeho permeability přes membránu. Z pohledu metodologie MD simulací ukazují, že kombinace silového pole Slipids pro membránu a GAFF s parciálními náboji získanými RESP výpočtem pro léčiva poskytují dobré výsledky výpočtu partičního koeficientu v dobré shodě s experimentem. Na druhou stranu, MD simulace jsou časově velmi náročné a pro analýzu velkého množství léčiv doporučuji využít nástroj COSMOmic. Jeho pole působnosti ovšem sahá pouze do oblasti kapalných membrán, jelikož nedokáže dobře popsat gelovou fázi. Amfifilní molekuly se v kapalných membránách vyskytují zejména blízko polárních hlav lipidů, zatímco lipofilní molekuly se nacházejí v hydrofobním jádře membrány. Substráty a metabolity izoforem enzymu cytochromu P450 (CYP) se vyskytují ve stejné hloubce v membráně jako vstupní a výstupní kanály CYP. Nakonec prezentuji pokročilou metodiku pro výpočet profilu volné energie při průchodu léčiva velmi flexibilními a nejasně definovanými tunely enzymů, kterou jsem použila pro identifikaci preferovaného kanálu izoformy CYP3A4. Předložená práce tak pokrývá současný stav poznání v oblasti interakcí léčiv s membránami, ukazuje dosažený pokrok a také nástin budoucího vývoje.</p>

Bibliographical identification:

Author's first name and surname	Mgr. Markéta Paloncýová
Title	Modeling of Small Molecules Interactions with Biomembranes
Type of thesis	Disertation
Department	Department of Physical Chemistry
Supervisor	Prof. RNDr. Michal Otyepka, Ph.D.
The year of presentation	2016
Keywords	Membrane, drug, permeability, cytochrome P450, molecular dynamics
Number of pages	46
Number of appendices	14
Language	English
Abstract	<p>The interactions of small molecules with lipid membranes play a major role in drug administration and distribution in human body. Within framework of my Ph.D. thesis I focused on theoretical methods, which can be used for understanding of drug-membrane interactions in terms of distribution of the drugs in the membranes, the thermodynamics and kinetics corresponding to the permeation process. Further, I discuss the impact of drug-membrane interactions with respect to interactions of drugs with membrane-anchored enzymes, involved in drug biotransformation. I provide the basic biological background of membrane and drug-membrane interactions as well as the theoretical background of molecular dynamics (MD) simulations. I describe in details biased methods for drug-membrane interaction studies and the impact and use of potential of mean force (PMF). PMF is the Holy Grail of the estimation of partitioning of drug in the membrane and with diffusion coefficient it provides also the permeability coefficients through the membrane. From MD simulations methodological point of view I showed that drug parameterized with RESP partial charges for GAFF force field and Slipids force field for membrane lipids provide PMFs in a good agreement with experimental data. On the other hand, biased MD simulations are time demanding and for the high throughput PMF screening on fluid membranes I recommend the use of a semi-continuous tool COSMOmic. Its usage is however limited, as it is only designed for fluid membranes and it is unable to describe the gel phase. Further I observed that the amphiphilic drugs tend to accumulate close to the polar head groups region in the fluid membranes, while the lipophilic drugs concentrate in the membrane hydrophobic core. I also observed that the positions of substrates and metabolites of cytochrome P450 (CYP) enzymes in the membrane correspond to the positions of CYP's access and egress channels. And finally I set up the methodology for calculation of PMF of a drug permeating through a highly flexible enzyme channels and used it for identification of a preferred egress channel of CYP3A4 isoform. The presented thesis covers a wide area of the field of drug-membrane interactions, shows current advances and provides also some useful outlook for further development.</p>

Acknowledgement

It is my pleasure to thank to my supervisor Prof. Michal Otyepka and the whole team of the Department of Physical Chemistry for inspiring comments, questions, suggestions, confidence in me and a congenial atmosphere in the team.

Outline

OUTLINE	1
1. ABSTRACT	2
2. ABSTRAKT	3
3. INTRODUCTION	4
4. REVIEW	5
4.1 BIOLOGICAL BACKGROUND	5
4.1.1 Lipid structure	5
4.1.2 Biomembrane structure	7
4.1.2.1 Cell membranes.....	7
4.1.2.2 Stratum corneum.....	8
4.1.3 Drug-membrane interactions	9
4.1.4 Interaction with membrane proteins.....	9
4.2 THEORETICAL STUDIES.....	11
4.2.1 Molecular Dynamics Simulations.....	11
4.2.1.1 Unbiased MD Simulations	12
4.2.1.1 Biased MD Simulations.....	13
4.2.1.1.1 Collective Variables.....	13
4.2.1.1.2 Free energy calculation methods.....	15
Umbrella sampling	15
Z-constraint.....	16
Adaptive biasing force	16
Metadynamics	16
Other approaches.....	17
4.2.2 Semi-continuous approaches	17
4.2.2.1 COSMOmic	17
4.2.3 Applications	18
4.2.3.1 PMF Outcomes	19
4.2.3.2 Partition coefficient	19
4.2.3.3 Permeability.....	21
4.2.3.3.1 Diffusion	22
4.2.3.4 Concentration dependence	23
4.2.3.5 PMF Issues	23
4.2.3.5.1 Methodology Issues	23
4.2.3.5.2 Force fields.....	25
4.2.3.5.3 Other issues	25
4.2.3.6 Role of membrane composition.....	26
4.2.3.6.1 Cholesterol	26
4.2.4 Interaction with membrane proteins.....	27
5. RESULTS	29
5.1 METHODOLOGY	29
5.2 INTERACTIONS WITH FLUID MEMBRANES	30
5.3 INTERACTIONS WITH SKIN-LIKE MEMBRANES	31
5.4 CYTOCHROMES P450	31
6. CONCLUSION	33
7. BIBLIOGRAPHY	34
8. LIST OF PUBLICATIONS	46
9. APPENDICES	47

1. Abstract

The interactions of small molecules with lipid membranes play a major role in drug administration and distribution in human body. Within framework of my Ph.D. thesis I focused on theoretical methods, which can be used for understanding of drug-membrane interactions in terms of distribution of the drugs in the membranes, the thermodynamics and kinetics corresponding to the permeation process. Further, I discuss the impact of drug-membrane interactions with respect to interactions of drugs with membrane-anchored enzymes, involved in drug biotransformation. I provide the basic biological background of membrane and drug-membrane interactions as well as the theoretical background of molecular dynamics (MD) simulations. I describe in details biased methods for drug-membrane interaction studies and the impact and use of potential of mean force (PMF). PMF is the Holy Grail of the estimation of partitioning of drug in the membrane and with diffusion coefficient it provides also the permeability coefficients through the membrane. From MD simulations methodological point of view I showed that drug parameterized with RESP partial charges for GAFF force field and Slipids force field for membrane lipids provide PMFs in a good agreement with experimental data. On the other hand, biased MD simulations are time demanding and for the high throughput PMF screening on fluid membranes I recommend the use of a semi-continuous tool COSMOmic. Its usage is however limited, as it is only designed for fluid membranes and it is unable to describe the gel phase. Further I observed that the amphiphilic drugs tend to accumulate close to the polar head groups region in the fluid membranes, while the lipophilic drugs concentrate in the membrane hydrophobic core. I also observed that the positions of substrates and metabolites of cytochrome P450 (CYP) enzymes in the membrane correspond to the positions of CYP's access and egress channels. And finally I set up the methodology for calculation of PMF of a drug permeating through a highly flexible enzyme channels and used it for identification of a preferred egress channel of CYP3A4 isoform. I believe that the presented thesis covers a wide area of the field of drug-membrane interactions, shows current advances and provides also some useful outlook for further development.

2. Abstrakt

Interakce malých molekul s membránami hrají významnou roli při vstřebávání a distribuci léčiv v našem těle. V předložené práci jsem se soustředila na teoretické metody používané pro pochopení interakcí léčiv s biomembránami z pohledu termodynamiky i kinetiky při permeaci léčiv přes membrány. Dále jsem se věnovala významu chování léčiv v membránách v souvislosti s interakcemi léčiv s biotransformačními enzymy, které jsou kotvené v membránách. V úvodu popisují nezbytné biologické základy týkající se struktury a funkce membrán a jejich interakcí s léčivy, a dále pak teoretické základy molekulově-dynamických (MD) simulací. Detailně popisují pokročilé metody MD, tzv. biased MD methods, poskytující profily volné energie prostupu látek přes membránu. Získaný profil volné energie je základem pro odhad partičního koeficientu léčiva v membráně a společně s difúzním koeficientem i jeho permeability přes membránu. Z pohledu metodologie MD simulací ukazují, že kombinace silového pole Slipids pro membránu a GAFF s parciálními náboji získanými RESP výpočtem pro léčiva poskytují dobré výsledky výpočtu partičního koeficientu v dobré shodě s experimentem. Na druhou stranu, MD simulace jsou časově velmi náročné a pro analýzu velkého množství léčiv doporučuji využít nástroj COSMOmic. Jeho pole působnosti ovšem sahá pouze do oblasti kapalných membrán, jelikož nedokáže dobře popsat gelovou fázi. Amfifilní molekuly se v kapalných membránách vyskytují zejména blízko polárních hlav lipidů, zatímco lipofilní molekuly se nacházejí v hydrofobním jádře membrány. Substráty a metabolity izoformy enzymu cytochromu P450 (CYP) se vyskytují ve stejné hloubce v membráně jako vstupní a výstupní kanály CYP. Nakonec prezentuji pokročilou metodiku pro výpočet profilu volné energie při průchodu léčiva velmi flexibilními a nejasně definovanými tunely enzymů, kterou jsem použila pro identifikaci preferovaného kanálu izoformy CYP3A4. Předložená práce tak pokrývá současný stav poznání v oblasti interakcí léčiv s membránami, ukazuje dosažený pokrok a také nástin budoucího vývoje.

3. Introduction

This thesis summarizes the advances in the field of interactions of small molecules with lipid membranes achieved during my Ph.D. study. The thesis is divided into three major parts; The first part reviews the state of the art of the field of theoretical studies of drug-membrane interactions and their limitations. The second part focuses on the results of my work and in few pages it provides the essence of my fulfilled studies. In my studies I focused on the methodology development and benchmarking and recommended Slipids as a best performing lipid force field for the drug-membrane interaction studies. I also recommended the use of COSMOmic as a fast screening tool well describing the fluid membranes. Further, I analyzed the distribution of drugs in the membranes and showed that the amphiphilic ones were located mostly around the lipid head groups region. I focused also on the skin models and described a high free energy barrier for ceramide membrane permeation. And finally, I focused on membrane-attached cytochromes P450 enzymes, their interactions with the membrane and also with drugs. I developed a methodology for a flexible enzyme channel permeation and successfully used it for estimation of the most preferred channel for 1,3,7-trimethyluric acid in CYP3A4 isoform. In both review and results parts of the thesis I refer to the third part of the thesis, appendices, that presents the copies of all my co-authored publications. I intended to write a clear and understandable description of the topic also for non-experts in the field and I believe that reading this thesis will assist the reader to orient well in the field of theoretical studies of drug-membrane interactions.

4. Review

4.1 Biological background

Understanding of biologically-relevant processes on a molecular level is a field of interest of today's life sciences. Though the largest attention is historically paid to proteins and nucleic acids, the importance and relevance of other biostructures is coming to the light and now we know that for a proper understanding of biological processes we need to pay attention also to other species such as saccharides or lipids. And the focus of this work will be on lipids – their composition and organization in human body, interactions with small molecules and the methods for their studies.

Biomembranes form important separators between various biological environments. In human body we talk mostly about cell membranes or, *e.g.*, skin. The cell membranes are by themselves a very variable group of membranes; consisting from plasma membrane and membranes of variety of organelles. For the detailed molecular biology background we advise to see, *e.g.*, ref.¹. The membranes regulate the flux of substances in and out of the cells or organelles, provide environment for enzyme activity and literally hold the cells or organelles together.¹ Each of the membranes has to some extent different properties, composition or function.² Generally, the cell membranes are composed of lipids and proteins with varying mass ratio (from 1:3 to 3:1 depended on the tissue and organelle).^{1,2} Lipids are arranged into a lipid bilayer and the proteins are either embedded into this bilayer, or they can form pores, or be just covalently or non-covalently attached to the bilayer surface. However, here we focus mostly on the lipid part of the membranes.

4.1.1 Lipid structure

The variability of the molecules in the class of lipids is huge. Overall, lipids are defined as cell molecules, insoluble in water and soluble in organic solvents.¹ They are mostly amphiphilic organic molecules with one or more non-polar tails and a polar head (Figure 1).³ Based on the ratio of the size of their polar head and of the nonpolar tail they form micelles of various shapes.⁴ Based on the shape and function, we can divide lipids in our bodies to storage lipids or membrane lipids.⁵ The storage lipids, mostly triacylglycerols, form lipid droplets and due to their shape they are unable to form bilayers; here we focus on lipids present in the membrane. The membrane lipids can be generally divided, based on their polar heads, to glycerophospholipids, sphingolipids and cholesterol, or some other, less populated species such as carboxylic acids *etc.*

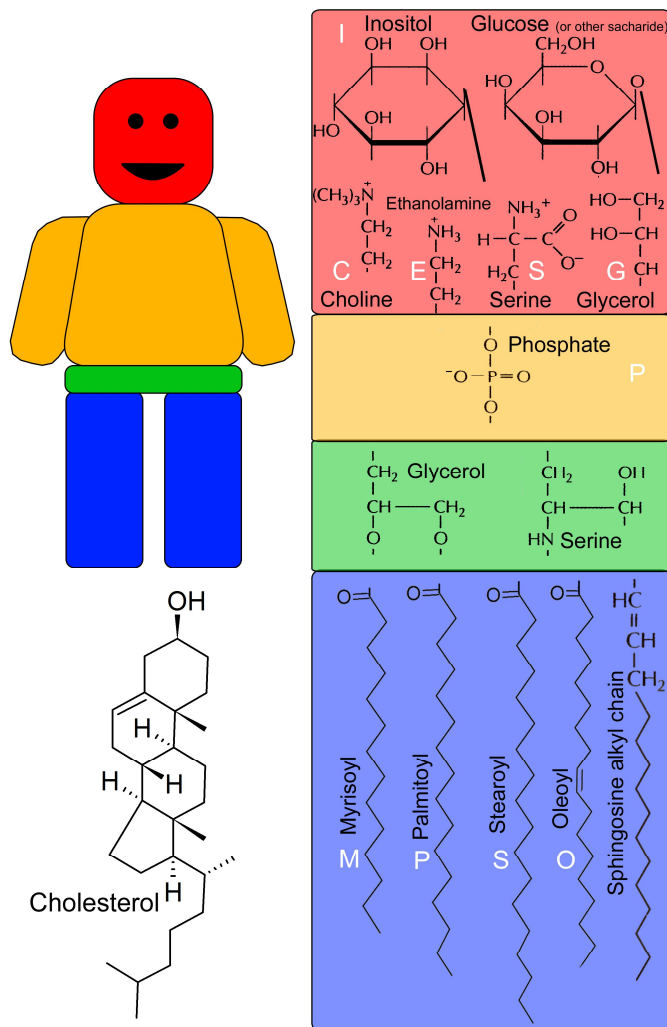


Figure 1: Lipid structure. Majority of membrane lipids can be built almost in a plug-and-play manner, as well as LEGO® doll. Two acyl tails (blue panel) are connected either by serine or glycerol (green panel) that can be also connected to phosphate (orange) and another polar group (red). The abbreviation of the glycerophospholipids is then made of four letters (white) – two for acyl tails, “P” for phosphate and another one for additional polar group. A special case of lipid is cholesterol (down left).

Glycerophospholipids form a major part of cell membrane lipids. They consist of two acyl tails bound to glycerol and subsequently to phosphate group. The phosphate group can bind another polar group of various sizes, from, *e.g.*, small ethanolamine to large inositol (Figure 1).¹ The phosphate group bears a negative charge and the terminal groups present in lipids differ in their charges also. Consequently, glycerophospholipids differ in their charge and therefore in the nature of the interactions with other species. The positive terminal groups (ethanolamine or choline) form, together with negatively charged phosphate, neutrally charged lipids, while the neutrally charged groups (*e.g.*, glycerol or zwitterionic serine) form negatively charged lipids. Naturally, terminal headgroups can differ not only in their charge, but also in their ability of hydrogen bonds formation or other noncovalent interactions.

Sphingolipids consist of sphingosine base connected to an acyl tail and possibly another polar group.⁶ Sphingosine moiety is actually a *trans*-monounsaturated hydrocarbon tail connected to reduced serine. The other acyl tail is connected to serine nitrogen (Figure 1). Both acyl tails are (except for a double bond close to serine) usually saturated and in case of skin the *N*-acylated chain is usually long forming ceramides.⁷ Further, another polar head group can be connected to serine and this can be either phosphocholine forming

sphingomyelin, or a saccharide group in signaling glycolipids.² Overall, sphingolipids are usually more saturated than glycerophospholipids and are often in contact with enzymes in lipid raft⁸ or work as signaling lipids.⁹

Though the role of lipid head group is crucial, the role of the tail is not negligible, especially for the phase behavior. The tail length and saturation affects significantly lipid phase behavior and therefore its properties and function (Figure 2). Lipid phases and the relationship with lipid structures were

nicely reviewed, *e.g.*, in ref. ². Here we just shortly review that the order and consequently the phase of the resulting membrane depends on both the polar head (its size, hydrogen bonding ability, charge, ...) and on the lipid tail (length and saturation, see Figure 2). And the composition of heads and tails is to some extent correlated. The long and saturated tails are very common in sphingolipids⁷ and form very ordered domains and in a pure form they produce gel membranes at a body temperature.¹⁰ (see Appendix A5) The shorter or unsaturated tails form mostly disordered domains. Usually, glycerophospholipids contain one saturated and one unsaturated chain.¹¹ Both ordered and disordered phases are necessary for a proper biological function of the cells and organelles. The cell membranes are mostly disordered, but the enzymes are usually located in ordered domains rich in cholesterol.¹²

Cholesterol is a very specific type of lipid. It consists of tetracyclic sterol ring skeleton with a short iso-octyl hydrocarbon tail with a single hydroxyl group at the other end of the sterol rings than the iso-octyl tail is bound (Figure 1).¹

The cholesterol molecule is planar and two methyl groups at the rings skeleton, hydroxyl group and the hydrocarbon chain are all located at one side of the molecular plane. Cholesterol does not form a bilayer by itself,¹¹ but it plays a crucial role in the structure and function of the biomembranes, as it widely influences the surrounding lipids and makes the lipid phase transition gradual,¹¹ in contrast with the sharp transition in the case of pure lipids. In some cases, cholesterol even inhibits the formation of separated domains of gel and disordered phases in membranes, *e.g.*, when sphingolipids and glycerophospholipids are simultaneously present.¹³ Its polar head consists of a single hydroxyl group that allows a hydrogen bond. But the small size of its head also allows flip-flops between the bilayer leaflets. Cholesterol has a crucial role in between lipids that cannot be compensated by any other lipid.

4.1.2 Biomembrane structure

4.1.2.1 Cell membranes

The lipid membranes were initially described as two-dimensional fluids.¹⁴ This means that the lipids or proteins can move in them in the two dimensions freely, but the third dimension (leaving the membrane or exchange of the membrane leaflet) is constrained (Figure 3). The flip-flop of lipids – meaning the exchange from one leaflet to the other one – is a very rare event and an unsupported flip-flop was described only for cholesterol and not for phospholipids or sphingolipids. The rate of flip-

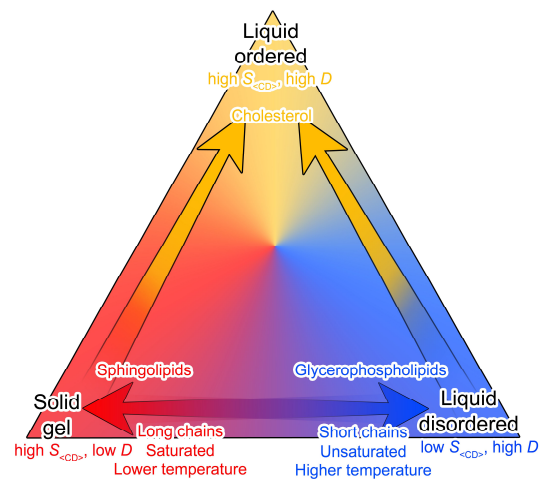


Figure 2: Lipid phases. Liquid disordered (also called fluid of liquid crystalline) phase has low deuterium order parameters $S_{<CD>}$, and high diffusion coefficient D . It consists usually of high fraction of glycerophospholipids with short and unsaturated chains. Solid gel phase consists mostly of sphingolipids with long saturated chains. Both phases transfer to liquid ordered phase by addition of various amount of cholesterol. Naturally, the more disordered phases are present at higher temperature and the lipids form also multiple coexisting phases not specifically displayed here.

flop of cholesterol depends on the saturation of phospholipids in the membrane and is faster in poly-unsaturated membranes.^{15,16} Other lipids need flippase or floppase enzymes to change a leaflet.¹⁷ As a result their movements involve lateral diffusion within the leaflet, rotation in their position or mild floating movements.¹ Naturally, the theory of a two-dimensional fluid is a brute simplification, as now we suggest that the proteins are in so called lipid rafts and therefore cannot diffuse completely freely.¹² Lipid rafts are domains with a higher ordering than the rest of the membrane, they are in a liquid ordered phase, rich in lipids with longer saturated acyl tails, *i.e.*, sphingolipids, and cholesterol.¹⁸ The role of the membrane composition appeared to be crucial and affects its structure and consequently the function of enzymes, interactions with drugs *etc.*

A significant asymmetry was observed in lipids' distribution in plasma membrane leaflets. Cholesterol is equally distributed along the leaflets,¹⁹ whereas the other lipids are predominantly distributed either to the external or cytosolic leaflet. External leaflet contains abundance of phosphatidylcholines (PC) and sphingomyelins (SM) and specifically glycolipids that work here as signaling lipids.¹ On the other hand, phosphatidylserine (PS) and phosphatidylethanolamine (PE) are dominantly localized on the cytosolic leaflet.¹¹ Both PS and PE are aminophospholipids (containing primary amine) with small lipid head group that in a pure form (without other lipids) allows also the formation of inverted hexagonal or other non-lamellar (non-bilayer) phases.¹¹ The cytosolic side of the membranes is negatively charged due to the presence of a fraction of PS and phosphatidylinositol (PI).³ The membrane asymmetry is believed to be important for the membrane and the whole cell biological function.⁴

4.1.2.2 *Stratum corneum*

A very different kind of membrane is on the surface of human body that is protected from the outer environment by skin and especially by its uppermost layer, *stratum corneum*. *Stratum corneum* is 10-15 μm thick layer,²⁰ highly impermeable, protecting the body from water loss and outer pollutants. It is composed of dead cells, corneocytes, embedded in a lipid matrix.²⁰ This layer is regularly renewed, the process of formation of corneocytes takes approximately one month.²¹ While the living cells' membranes are mostly composed of phospholipids, the major lipids in *stratum corneum* are ceramides. The molecular composition of lipid matrix consist of ceramides of various kinds,²² free fatty acids, cholesterol and cholesterol sulphate.²³ Though an incredible effort was focused on resolving of the structure of the lipid matrix (the proposed models are reviewed, *e.g.*, in ²⁴), its structure in the atomistic resolution is still unknown. While cell membranes are organized into bilayers, lipids in *stratum corneum* are in multilayers surrounding the corneocytes as a mortar surrounds bricks.²⁵ It is hypothesized that lipids change their conformations from hairpin that is usual in bilayers to extended form that makes the connection in the multilayers.²⁴ Also a significant contribution of a very long ceramide EOS was observed,²⁶ whose long tail connects two layers and its

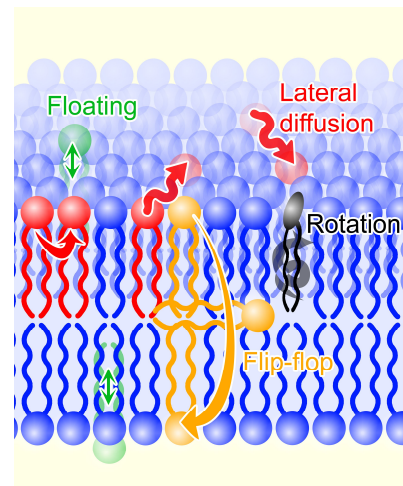


Figure 3: Lipids' moves. Lipids can easily move laterally – diffuse and exchange their positions (red), rotate in their position (black) or mildly float (green). Rare move is flip-flop across the membrane center (orange).

additional polar ester group contributes to another polar head group layer. By X-ray diffraction, two different repeating phases were observed – short periodicity phase (6 nm long) and long periodicity phase (13 nm long).²⁷ But overall, structure of *stratum corneum* is very different from an ordinary bilayer and though several models for its structure were proposed, none of them is definitive and a detailed atomistic understanding here is still a challenge.

4.1.3 Drug-membrane interactions

Understanding of the interactions of drugs with lipid membranes is a fundamental part of the pharmacology understanding of drug metabolic pathways. The small molecules interacting with the membranes can be called by various terms – drugs, solutes, xenobiotics, ligands *etc.* Here, we focus mostly on drugs, but we use here the term ‘drugs’ with the meaning of ‘any solute interacting with the membrane’. Studies of drugs on the membranes are focused mostly on their partitioning^{8,28–80} (see Appendix A1, A3-8) or permeability^{81–104} and consequently on their position in the membrane or diffusion coefficients. Further the function and effect of drugs on the membranes are studied, naturally in the dependence on the membrane composition.^{10,41,54,105} (see Appendix A5, A4) The nature of the drug-membrane interactions is crucial for the drug delivery as it is necessary for the decision between passive transport, passive assisted transport or active transport of drugs, where the drugs interact with membrane enzymes. The passive transport is driven by the concentration gradient with a simple diffusive path.¹ The partitioning into the membrane tells us the amount of drugs dissolved in the membranes, therefore affecting the membrane. Further, the position and lateral diffusion coefficient of the drugs may play a role in the drugs function in the membranes, such as, *e.g.*, antioxidants⁷¹ (see Appendix A8) or anesthetics.^{106,107} The nature of drug-membrane interactions are to some extent general in lipids, but the studies revealed their dependence on the lipid type and overall on their surrounding; and the understanding of the principles is of a high importance to drug development and will be a major topic of this review.

A variety of experimental and theoretical tools have been applied on the membrane studies studying the abovementioned properties. The experimental studies were nicely reviewed elsewhere,¹⁰⁸ it is however worth remembering the neutron diffraction¹⁰⁹ or NMR order parameters measurement for membrane structural parameters,¹¹⁰ PAMPA arrangement for permeability measurement,¹¹¹ solid-phase microextraction for partitioning measurement,¹¹² fluorescence spectroscopy⁴⁰ for positioning or diffusion coefficient calculation *etc.* Naturally, the output gained from experimental studies cannot be always directly compared to the calculated properties, but multiple theoretical approaches were proposed that reproduce well the experimental data.^{66,113,114} (see Appendix A7) With the results corresponding to the experiment, the benchmarking can be performed and the simulations can provide the estimation for experimentally unknown data and offer an atomistic view into the studied phenomena.

4.1.4 Interaction with membrane proteins

The drug path through the membranes does not lead only through lipids, but their transport can be facilitated by proteins. The passive transport of drug is driven by the concentration gradient. The drug transport can also be mediated either by channels or transporters, such as solute carriers (SLC)^{115,116} and this transport is still driven by concentration gradient.¹ Channel proteins simply provide appropriate environment for the drug penetration (*e.g.*, polar environment), while the transporters alternate between two different conformations. Unlike the pathways that do not need energy, active transporters

need additional energy (*e.g.*, from ATP) and can drive either influx or mostly the efflux of drugs, even against the concentration gradient. For instance ATP-binding cassettes (ABC transporters) regularly bind and release ATP for transfer of other drugs.^{117,118} The protein mediated transport allows the membrane permeation also to ions or drugs that would not permeate directly through lipids.

Another possibility of the interactions of drugs with the membrane proteins is the biotransformation of the respective drugs, represented, *e.g.*, by cytochromes P450 (CYPs). Various CYP isoforms are found in majority of living organisms,¹¹⁹ in eukaryotic ones their catalytic domain is attached to the membrane by N-terminal α -helix. They are mostly in endoplasmic reticulum or mitochondria, but in lower amount also in other organelles.¹²⁰ Their deeply buried active site containing heme is connected with the CYP surface by a complex network of channels leading towards the membrane, membrane/water interface or directly to cytosol.¹²¹ The usual result of biotransformation, hydroxylated drugs, are less lipophilic than the original substrates¹²² and by such structural changes CYPs can substantially change the nature of their interactions with membranes, *e.g.*, the affinity or ability to permeate them.

4.2 Theoretical studies

The theoretical studies focused on membranes can be based either on molecular dynamics simulations, semi-continuous approaches or statistical QSPR (quantitative structure-property relationship) methods. Molecular dynamics (MD) simulations describe the development of the behavior of a certain system in time and offer a direct dynamics insight into the studied phenomena. They are however quite costly and therefore a lot of effort have been placed on the increasing of their efficiency. The semi-continuous methods, such as COSMOmic, describe a certain part of the system (usually drug molecule) in an all-atom form, but the membrane is described as a set of continuous layers (though initially represented with atoms). And the QSPR methods are a completely different category based on statistics, as they offer good results for molecules with similar structural features as in the training set, but cannot be used for a completely unknown system. We will discuss their results shortly in the field of permeability, but we will not discuss their principles *etc.* here any more.

In this section, we first discuss the underlying theoretical principles for the drug-membrane interaction studies. We go through the basics of molecular mechanics and molecular dynamics, we will describe the potential of application of biased simulations and the role of the collective variable. Afterwards, we will present major methods for the free energy profiles calculation. We will present then the way, how to obtain the partition or permeability coefficient from the free energy profile. Followingly, we will discuss the issues of the free energy profiles calculation and present our recommendations to obey the common issues. And finally, we will discuss the role of membrane composition, which is very rarely taken into account, though it plays here a crucial role.

4.2.1 Molecular Dynamics Simulations

Molecular dynamics simulations used for membrane studies usually use molecular mechanics principles and calculate the time development of the positions of individual particles in the system. Molecular mechanics (MM) calculates the potential energy of the system as a function of positions of all atoms based on the bond lengths, angles and dihedral angles and the atom distances for calculation of van der Waals and Coulomb interactions (Figure 4). In each calculation step we calculate the potential energy and its gradient on each atom and apply the gradient of the potential energy (*i.e.*, force) on the atoms and followingly the atomic velocity, acceleration and position is calculated (Figure 4). After the movement corresponding to the simulation step, the potential energy coming from molecular mechanics is recalculated, the force is applied again and the velocity and consequently the position are updated. This approach is then called molecular dynamics and is repeated every simulation step. However, MD simulations are heavily dependent on the chosen set of parameters for MM calculations called force field.

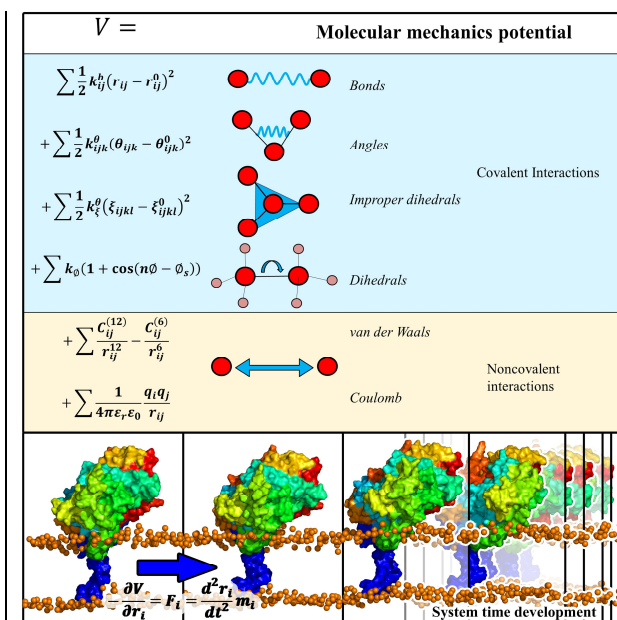


Figure 4: Upper panel: Terms of the molecular mechanics potential (force field).

Lower panel: Molecular dynamic principle. In each step the force applied on the atoms is updated and transferred to the velocity and the system develops.

Several force field families are currently on the market, differing with their fields of focus, way of parameters development or the size of used particles. Currently used force fields for lipids are either all-atomic (CHARMM36,^{123–126} AMBER ff11¹²⁷/ff14¹²⁸, GAFFlipids,¹²⁹ Slipids^{130–132}), united-atoms (Gromos43a1-s3¹³³ or older Berger¹³⁴) or coarse-grained (Martini,¹³⁵ SDK¹³⁶). Generally, force fields are parameterized to reproduce well the experimental properties of lipids, mostly area per lipid (APL), head group – head group distance (D_{HH}), deuterium order parameters ($S_{<CD>}$) or X-ray scattering images.¹¹⁴ A nice review of lipid force field development was published recently¹³⁷ and here we only shortly review the basic principles. The development of the initial set of force field parameters is usually based on quantum-chemical calculations to obtain partial charges and average bonded parameters.¹³⁰ The van der Waal parameters (parameters for Lennard-Jones potentials) of lipid tails can be derived from a simulation of simple alkanes and their physico-chemical properties known from experiment, *e.g.*, density. Finally, the parameters are manually adjusted to reproduce the experimental properties as well as possible. So the force field development is partially a highly precise set of quantum calculations and partially black magic based on the intuition and experience.

The increase of the size of particles representing atoms leads to significant increase in the simulation rate for the cost of a loss of some details. The all-atomic (AA) force fields (FF) represent each atom in the system by one particle. United-atoms (UA) force fields unite the non-polar and non-aromatic hydrogens with the carbon they are attached to and especially in case of lipids this leads to significant increase in the simulation rate,¹³⁴ due to long hydrocarbon chains present in their structure. Both AA and UA force fields use all-atomic representation of water molecules, usually SPC/E^{138,139} or TIPxP (usually TIP3P¹⁴⁰) and as they represent single bonds also with (in case of UA some) hydrogens, the simulation step should correspond to the quickest vibration in the system – usually 1-2 fs. In case of coarse grained (CG) force fields the situation is different. *E.g.*, in Martini, one bead represents about four heavy atoms.¹³⁵ One water bead represents four water molecules. With the absence of hydrogen atoms and overall quick bond vibrations, the integration step of MD simulations can be up to 40 fs and the simulation systems can represent much larger areas due to the limited number of necessary atoms. Though the reduction of the particles brings some limitations to the simulations, *e.g.*, the impossibility of reproducing the single water molecules interactions among the lipid head groups, or some artefacts in diffusion coefficient calculation (as also known in UA FF⁹⁸), the simulation with CG force fields reproduce some experimental parameters surprisingly well.¹⁴¹ The increase in the efficiency of all types of FFs gradually allows studies on biologically interesting space and time scales in an incredible resolution.

4.2.1.1 Unbiased MD Simulations

The unbiased simulations provide a direct view of the studied system behavior, but its sampling is limited to a local free energy minimum. The unbiased simulations in MD mean applying only the potential from MM and the simulation is not biased by any other way than by setting the temperature and pressure. In these simulations we can monitor properties of the systems or their stability (on the used time scales). These simulations are often used, *e.g.*, for comparison or predicting of the experimental properties with the simulations (*e.g.*, force field development¹³⁰) or understanding of experimentally observed differences between very similar systems.¹⁴¹ (see Appendix A10) The unbiased simulation is ideal for monitoring the detailed principles of quick and barrierless phenomena. The observation of some low-barrier processes is possible,³⁸ (see Appendix A1) its probability decreases however exponentially with the height of the energetic barrier.

The distribution of states in unbiased simulation is exponentially dependent on the free energies of these states and this knowledge allows us the estimation of the natural unbiased behavior of the system from the biased simulations and vice versa (Figure 5). Therefore, if we want to estimate the partitioning of a drug into the membrane, we can either run a very long free simulation and analyze directly the drug distribution inside and outside of the membrane, or we can calculate a free energy profile $\Delta G(z)$ along the membrane normal axis and calculate the local (at given z -position) and global partition coefficients $K(z)$, K (Eq. 1):

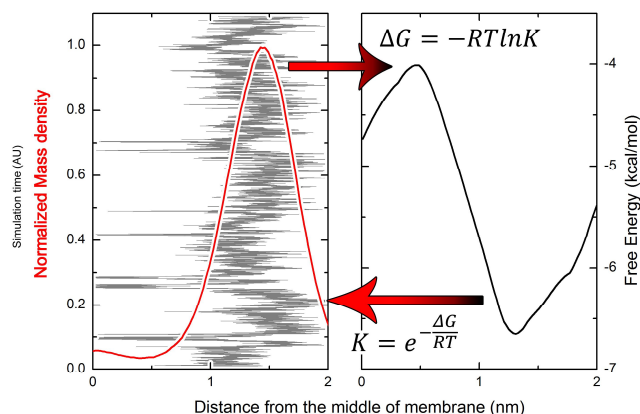


Figure 5: Transfer between a free energy profile (right) and a density profile (left) based on the ratio of density of states K . The free energy profile and the density profile calculated from the unbiased behavior (left background) are equivalent in the resulting information.

$$K = \int_{\text{across membrane}} K(z) dz = \int_{\text{across membrane}} e^{-\frac{\Delta G(z)}{RT}} dz \quad \text{Eq. 1}$$

Similarly, if we are interested in the permeability coefficient, we can monitor the behavior of a studied drug in an unbiased simulation or calculate a free energy profile and local diffusion coefficients from biased ones. For both quantities an extensive discussion is located further in this text. The unbiased simulations allow us to monitor the natural phenomena, including complex formation *etc.* and the biased simulations provide the thermodynamic view into a pre-defined process.

4.2.1.1 Biased MD Simulations

Biased simulations can be used for studies of rare events that could not be monitored by unbiased simulations. In most cases, biased simulations add an external potential to the simulations enhancing sampling in few pre-defined slow motion degrees of freedom denoted as collective variables (CVs), and either directly lead the studied phenomenon in the required way (*e.g.* by pulling a molecule in a specified direction) or monitor the reaction of the system for an external potential. Apart from CV-based methods, one can use also, *e.g.*, replica-exchange based methods, performing exchanges between replicas that can differ, *e.g.*, in temperature (T-REMD)¹⁴² or Hamiltonian (H-REMD);¹⁴³ or use, *e.g.*, accelerated MD (aMD).¹⁴⁴ In membrane simulations, CV-based methods are most commonly used, especially umbrella sampling¹⁴⁵ together with weighted histogram analysis method (WHAM),¹⁴⁶ z -constraint,¹⁴⁷ metadynamics,¹⁴⁸ flooding,¹⁴⁹ adaptive biasing force,¹⁵⁰ *etc.* All of these can calculate a free energy profile along a predefined CV.

4.2.1.1.1 Collective Variables

Definition of a collective variable (CV) fully describing reaction path is a crucial task in preparing and analyzing biased simulation. Multiple studies use different names for the same entity, *e.g.*, order parameters,¹⁵¹ or transition coordinates¹⁵² ..., but here we use the term “collective variable”. In some cases the reaction path can be easily described by a single CV (*e.g.*, distance of two interacting ions in

vacuum), but usually the process is much more complex. Even if the dominant CV is simple (*e.g.*, in drug-membrane interaction studies the CV of the first choice is the distance of drug from the middle of the membrane), the rate limiting steps can be often connected with different variables^{47,90,151} (*e.g.*, the dehydration of the drug in membrane headgroups,³⁸(see Appendix A1) drug conformation,⁴⁷ or, *e.g.*, the drug orientation along the lipid chains). Omitting an important variable leads then to hysteresis in free energy profiles and consequently significantly increases the required simulation time for reaching convergence,¹⁵³ which we will describe later.

For understanding of the underlying principles of calculation of the potential energy in basically all biased simulations, let us consider a single biased CV. The CV for these simulations needs to be defined as a function of atomic coordinates. Let us assume, as an example, a one-dimensional distance d between two molecules. In biased simulations we apply either potential E or a force F_d on the distance d . In case of potential we calculate a partial derivation of the potential by the distance: $(\frac{\partial E}{\partial d})$. This is actually a negative of a force applied on the distance ($-F_d$). This force is however still very abstract, as it is not directly the force applied on the atoms of involved molecules, but it is a negative of a gradient of a free energy profile along the distance and our intent is to calculate the forces F_x applied on atomic coordinates x . But we know the mathematical expression of the distance as a function of positions of the atoms of our molecules. We calculate then the partial derivation of the function defining distance by the atomic coordinates $(\frac{\partial d}{\partial x})$ and here we get the forces F_x applied by the bias on each atom (Eq. 2):

$$F_x = -\frac{\partial E}{\partial d} \frac{\partial d}{\partial x} = F_d \frac{\partial d}{\partial x} \quad \text{Eq. 2}$$

When we exchange in the expression the distance term d by any other CV, the equation is valid in general. From the definition we can see that only the atoms, whose coordinates are involved in our CV are affected by the bias. Naturally, a distance of two groups is a simple example and in reality we use much more complicated CVs, we work in three-dimensional space and we can also bias several CVs and calculate a multi-dimensional free energy landscape. The only limitation is the need of knowledge of a coordinates based function of a desired CV and its derivation. Finally, the force from the bias is added to the force coming from MM potential.

4.2.1.1.2 Free energy calculation methods

Let's revise the free energy calculation methods now. We explain them in simple words and their principles are also depicted in Figure 6. For clarity, a reader can imagine here the distance of a drug from the middle of the membrane as a used CV, but the methods can be used for any other defined CV or CVs.

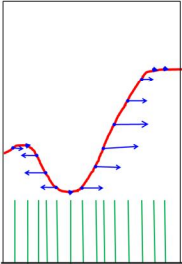
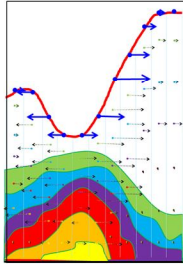
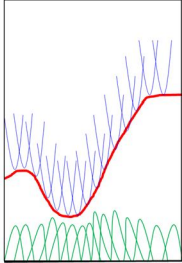
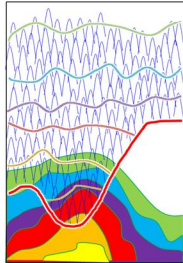
	Static methods Multiple initial conformations	Adaptive methods Single initial conformation
Biasing force methods	<p>Z-constraint</p> $\Delta G(z) = - \int_{outside}^z \langle \vec{F}(z') \rangle_t dz'$ <ul style="list-style-type: none"> • CV is kept constant • Average applied force $\langle F(z) \rangle$ is measured 	<p>Adaptive biasing force</p> $\Delta G(z) = - \int_{outside}^z \langle \vec{F}(z') \rangle_t dz'$ <ul style="list-style-type: none"> • Initially, CV is not biased • After certain visits of bin, force applied by molecular mechanics is calculated • Opposite force $F(z)$ is applied on CV • Force in each bin converges • Finally, CV diffuses along the whole CV space 
Biasing potential methods	<p>Umbrella sampling</p> $\Delta G(z) = -RT \ln P(z) + V(z)$ <ul style="list-style-type: none"> • CV diffuses and feels a biasing potential $V(z)$ • Distribution of CV $P(z)$ with the bias is monitored 	<p>Metadynamics</p> $\Delta \Delta G(z) = - \langle \Delta V(z) \rangle$ <ul style="list-style-type: none"> • Initially, CV is not biased • Once a time a biasing potential is added • The biasing potential is measured and its mean difference represents ΔG • Finally, CV diffuses along the whole CV space 
	Adaptive umbrella sampling Flooding	

Figure 6: Free energy calculation methods. Red – final free energy profile (y-axis). CV position (x-axis). Blue – potentials or forces acting on the CV position (in adaptive biasing force we show its development, in metadynamics the biasing potential is the sum of individual ones). Green – the distribution of sampled states, in adaptive methods displayed for various times.

Umbrella sampling

Up to now, the most used method for obtaining free energy profile is umbrella sampling (US).¹⁴⁵ We use US in a set of various frames along a defined CV and then apply WHAM¹⁴⁶ for the analysis. In US scheme we place a harmonic biasing potential around the initial position in a given CV and monitor the distribution of states with this biasing potential. The free energy profile of the sampled region is based on the assumption that the distribution of states should reflect the 'natural' free energy plus the

biasing potential. In WHAM procedure we perform multiple US simulations. The frames for US simulations are placed along the whole reaction coordinate to gain sufficient sampling in all states. The distribution of states along a defined CV should be steady and the individual distributions overlap. The free energy profile is reconstructed afterwards from the knowledge of biasing potentials and resulting distributions. Though WHAM procedure is actually the proper name of the calculation scheme, in drug-membrane interaction studies this process is called usually simply umbrella sampling and we will stay with this nomenclature.

Z-constraint

The method used for initial theoretical studies of drug-membrane interactions and used up to now is z-constraint¹⁴⁷ (also called average force, blue moon or thermodynamic integration). As well as in US, z-constraint (ZC) uses a set of initial frames along a reaction coordinate. Here we sample only the initial position in a CV space and monitor the average force necessary to keep the system in the desired CV position. The average force shows us the gradient of the free energy in that specific CV position. In ZC we reconstruct the free energy profile as an integral of the force, therefore the free energy profile is often called ‘a potential of mean force’ (PMF).

Both US and ZC require a set of initial frames, either from a previous simulation sampling of the whole reaction coordinate (*e.g.*, pulling a drug through the membrane) or with a direct preparation of the system in a desired position in CV space (*e.g.*, placing a drug in a desired depth). The initial frames generation is a crucial part of the process, as it hugely affects the required time for the convergence of the simulations^{35,38} (Appendix A1, see later) and other methods were developed to obey this issue that require a single initial frame.

Adaptive biasing force

As well as ZC, adaptive biasing force¹⁵⁰ (ABF) uses an average force applied on the system along the predefined CV. This force is however calculated in a different way: The system is let to diffuse freely and its positions in CV space and forces from MM are monitored in specified CV bins (*e.g.*, every 0.1 nm in the distance from the bilayer center for our example CV). After a certain number of visits in a bin a force is applied on the system – the force is opposite to the average force applied from MM. This biasing force widens the sampled CV space, therefore also other bins are visited for the required amount of steps and the biasing force can be applied here. Gradually, after certain number of visits, the biasing force in each of the bins is updated. In the end of the simulation the drug diffuses freely along the CV space.

Metadynamics

A similar, yet different approach is used in metadynamics¹⁴⁸ (META). As well as in ABF, metadynamics does not require generation of initial frames, we just define a CV (or a set of CVs) and from one initial conformation we run the simulation. The principle of metadynamics lies in addition of a biasing potential (in a form of gaussians) to the visited CV position. Addition of a potential drives the system to other regions in the predefined CV space and finally the system diffuses freely along the whole CV space. The free energy is represented by a negative of a mean biasing potential – biasing potential is calculated at different times, fitted to a reference position in a CV space and a statistical block analysis is performed on several profiles.

The differences between metadynamics and adaptive biasing force are not huge and lie in their principles. In ABF we do not set any parameters for the calculation except for the width of the bin. In META we need to set at least width and height of the gaussian, which requires some experience, however this is similar to the width of the bin in ABF. In ABF the resulting average force can be directly integrated to the free energy profile, in META we need a statistical analysis of several free energy profiles as the final biasing potential is not exactly opposite of the free energy profile (otherwise we could use well-tempered META that requires even more knowledge of the system than ordinary META). And finally, the cardinal difference is in the principle of the methods – though the biasing potential is after all transferred to the force applied on the atoms, adding a biasing potential adds the influence of the CV position neighborhood, while ABF is strictly local. Finally, META generates a nonequilibrium sampling, while ABF is generating canonical equilibrium.¹⁵⁴

Other approaches

Naturally, several other approaches can be applied for calculation of free energy profiles. Some of them are based on similar approaches as previous cases, *e.g.*, flooding,¹⁴⁹ some others are completely different. One can mention thermodynamic perturbation methods (sometimes called thermodynamic integration, but this can be misleading as thermodynamic integration is used also for z-constraint), similar Widom particle insertion,¹⁵⁵ oscillating forward-reverse method (OFR)¹⁵⁶ or orthogonal space tempering (OST).¹⁵⁷ These approaches can lead to appropriate results, but in drug-membrane interaction studies are currently used very rarely.

4.2.2 Semi-continuous approaches

A completely different approach than MD simulations in membrane studies can be represented, *e.g.*, by describing the membrane as a set of continuous layers with different dielectric constants.¹⁵⁸ Here the free energy profile of a drug through the membrane can be calculated by the calculation of several solvation free energies into individual layers. Principally a similar approach, but going to much more details, can be represented by COSMOmic.¹⁵⁹

4.2.2.1 COSMOmic

COSMOmic is a semi-continuous tool from a software package COSMOtherm¹⁶⁰ based on a COSMO-RS (Conductor-like Screening Model for Realistic Solvation)¹⁶¹⁻¹⁶³ principle. COSMO-RS implemented in COSMOtherm is based on statistical thermodynamics, where the interactions between solute and fluid or between two fluids are calculated. The calculation requires first a COSMO¹⁶⁴ surface of all molecules in the system of interest, which means the charge induced on a surface of the molecule by a solvent. Further we calculate σ -profiles and σ -potentials. The σ -profile is a histogram of COSMO charges at the molecular surface

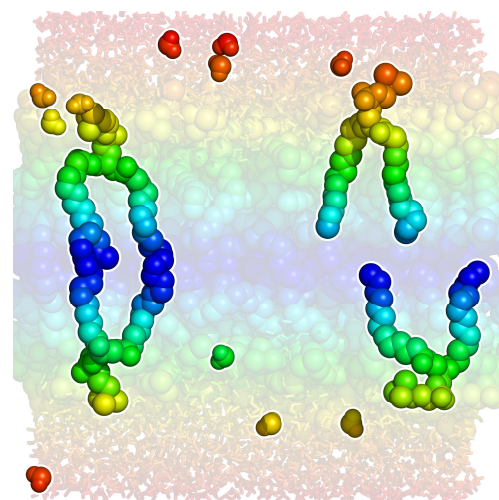


Figure 7: COSMOmic representation of a membrane. Membrane is symmetrically divided into layers depicted here by different colors. Individual atoms are divided according to their positions in the layers (four lipid molecules and water molecules highlighted in the figure). Finally, each membrane layer is treated as an independent fluid.

segments and the σ -potential is the affinity of the molecule to a surface segment of a specific charge (of some other molecule). The interaction energy between two molecules can be then easily calculated. COSMO-RS treats the solvent and solute equally and from the interaction energies it can calculate solubilities, partition coefficient of solute between two phases, phase diagrams *etc.* Further, COSMOtherm is not limited to pure systems, but can calculate σ -profiles and σ -potentials of mixtures composed of unlimited number of species.

COSMOmic uses the idea that the membrane is a two-dimensional fluid. As such, it can be in principle studied by COSMO-RS model designed for fluids. Membrane (or a spherical micelle) is here represented as a set of fluid layers. Therefore, initially we divide the membrane along the membrane normal axis into layers parallel to the membrane plane. (Figure 7) For each layer we calculate the distribution of various atom types. This can be done from a single membrane structure or we can average an MD simulation to include partially the dynamics of the membrane. Simultaneously, we study a lipid molecule (or all lipid types present in the membrane) by DFT methods and calculate its COSMO¹⁶⁴ surface. The distribution of atoms in each membrane layer is then used for construction of a virtual fluid and its σ -profile and σ -potential, representing the properties of the membrane layer. And finally, we can just easily place the drug molecule in a specific layer, rotate it to study its interactions with neighboring layers and study the interaction energy. From the interaction energies in individual layers we can calculate a free energy profile.

4.2.3 Applications

In this section, we will focus directly on already performed PMF studies. First, we will focus on the application of PMF studies in order to calculate partition and permeability coefficients. Then we will shortly review the most common issues stemming from calculation of PMFs. And finally we will discuss the direct output from the studies and the role of both solute and lipid membrane structure and composition.

A majority of drug-membrane interaction studies was focused on calculation of free energy profiles along the membrane normal in order to calculate partition or permeability coefficient. Here we will describe, what can we learn from the free energy profiles and how to obtain the partition and permeability coefficients from PMF studies.

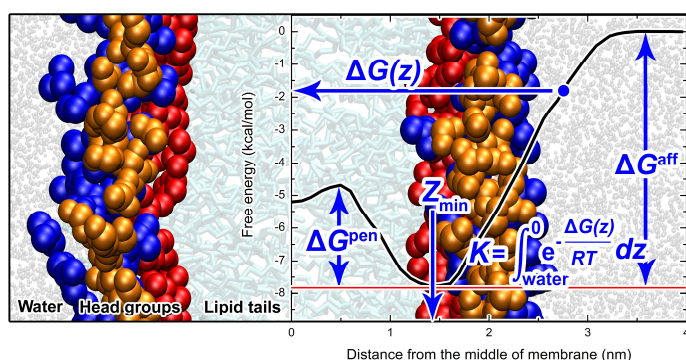


Figure 8: Structure of a lipid membrane (background) and a model free energy profile (right). From the free energy profile $\Delta G(z)$ we can read the position of free energy minimum (Z_{min}), affinity to the membrane ΔG^{aff} , penetration barrier ΔG^{pen} , lipid/water partition coefficient (K) or membrane resistance R (inverse to permeability). We usually calculate the free energy profile only for one half of the bilayer, as it is symmetric.

4.2.3.1 PMF Outcomes

The free energy profile provides numerous data. Apart from partition and permeability coefficient discussed later, we can calculate the affinity to the membrane (ΔG^{aff} in Figure 8) or the penetration barrier ΔG^{pen} . Often used and discussed quantity is the position of the free energy minimum (Z_{min}) that corresponds to the most populated position of the drug in the membrane (see Figure 5). The position of a drug in the membrane plays a role in case of, *e.g.*, antioxidants.^{37,71} (Appendix A8) The position of amphiphilic drugs also corresponds to the position of access channels of cytochromes P450.^{33,165} (Appendix A2) Though these data are important for the understanding of drug-membrane interactions, the most studied and used quantities are partition and permeability coefficients.

4.2.3.2 Partition coefficient

Amphiphilic or lipophilic molecules accumulate in or around the membrane while highly polar molecules prefer the aqueous region.

The partitioning into lipids is depended on the negative of a free energy and can be evaluated as a global or local property. Lipid/water partition coefficient $\log K$ tells us the ratio of concentrations of drug in lipids and in water. The higher $\log K$ is, the more lipophilic the drug is. We can calculate $\log K$ based on the free energy profile of the given molecule (Figures 8 and 10, Eqs. 1 and 3). The calculation of $\log K$ based on Eq. 1 is simple, however depends on setting of a membrane border. Even if the membrane forms a separation between different aqueous environments, the border between lipids and water is not straight, especially in case of fluid membranes. This plays a significant role in case of hydrophilic molecules, where artificial setting of the membrane border for $\log K$ calculation can lead to a significant difference in the result. Therefore, Klamt *et al.*¹⁵⁹ came with another equation (Eq. 3, Figure 10) taking into account the density of water in each membrane region $\rho_{(z)}^{\text{water}}$ in respect to the density of bulk water $\rho_{(n)}^{\text{water}}$ and weighting the free energy based on this amount:

$$K = \int_{\text{water}}^0 \left(e^{-\frac{\Delta G(z)}{RT}} - \frac{\rho_{(z)}^{\text{water}}}{\rho_{(n)}^{\text{water}}} \right) dz \times \frac{APL}{M_{\text{lipids}} m_u} \quad \text{Eq. 3}$$

Here, T is the thermodynamic temperature, R is molar gas constant, APL stands for area per lipid and M_{lipids} is molar mass of lipid molecule, while m_u is the atomic mass constant; we integrate along one membrane leaflet from the bulk water to the middle of the membrane ($z = 0$) along the z axis. In case of lipophilic molecules using Eq. 3 instead of Eq. 1 plays a negligible role, but in case of hydrophilic molecules this improved the results significantly and with current resources available we are able to reproduce experimental $\log K$ s with a high precision.⁶⁶ (Appendix A7)

Recently, Neale *et al.*¹⁵¹ divided the possible results of free energy calculation based on the shape of a free energy profile. The authors studied the free energy profiles of drug-like molecules along the lipid membrane normal axis that were published in last three years. They concluded that most of the studied drugs resulted into profiles that were denoted “3” or “3*” (see figure 9 for the profile shapes) meaning a profile with a free energy minimum around the head groups or below them and with a free energy barrier connected with the membrane center crossing. The star denotes than the situation, where the free energy in the membrane core is higher than the free energy in water. Neale *et al.*¹⁵¹ set also a subclass of profiles denoted “b” that had a small free energy barrier in the head groups region. But we do not take into account this “b” note of the profiles, as the profiles were calculated with

different methodologies and we suppose that the small barrier may be also an artefact of the simulations. Here we generalize the current observations from a slightly different point of view, based on the properties of the drugs, and we attach the findings to the proposed free energy profiles shapes (Figure 9).

Most of the studied molecules from last three years analyzed by Neale *et al.*¹⁵¹ were amphiphilic with octanol/water partition coefficient $\log K_{ow}$ between -1 and 5 (Figure 9). The least lipophilic molecules ($\log K_{ow} < 0$) were mostly included in groups 1 and 3*, meaning higher free energy in the membrane core than in water. Most of the studied molecules in the group 1 were very small (median of molecular weight $M = 37$ g/mol), *e.g.*, water, whose free energy constantly grows with a maximum in the membrane core. In group 3*, there were mostly larger molecules with amphiphilic nature (median of $M = 177$ g/mol). But both groups (1 and 3*) were spread over a larger region of $\log K_{ow}$ s running up to 5. And the other extreme, $\log K_{ow} > 5$ is distributed in groups 2 and 3, meaning a negative free energy in the membrane core. The lipophilic drugs from group 2 (mean $\log K_{ow}$ 3) tend to accumulate in the membrane center and their free energy profile decreases gradually with a free energy minimum in the middle of the membrane. But for amphiphilic drugs with $\log K_{ow} < 5$ we cannot clearly predict the

behavior and some of them were even studied with different results (*e.g.*, caffeine *etc.* in groups 3 and 3*). It was described that amphiphilic drugs, accumulate around the head groups region⁶⁵ and their presence in groups 3 and 3* suggest a barrier for membrane center crossing. But overall we come here to the edge of the predictive potential of $\log K_{ow}$. It was repeatedly reproduced that lipid/membrane partition coefficient $\log K$ correlates significantly with $\log K_{ow}$.⁵ Also, in pharmacology and overall in estimation of lipophilicity an octanol/water partition coefficient is used as a predictive sign of bioavailability. However, the partition coefficient mostly depends on the depth of the free energy well and not on the free energy profile shape. As lipid membrane is a heterogeneous system, unlike octanol/water system with two well defined phases (octanol and water), molecules with similar $\log K_{ow}$ can have very different free energy profile shapes on membranes and vice versa.

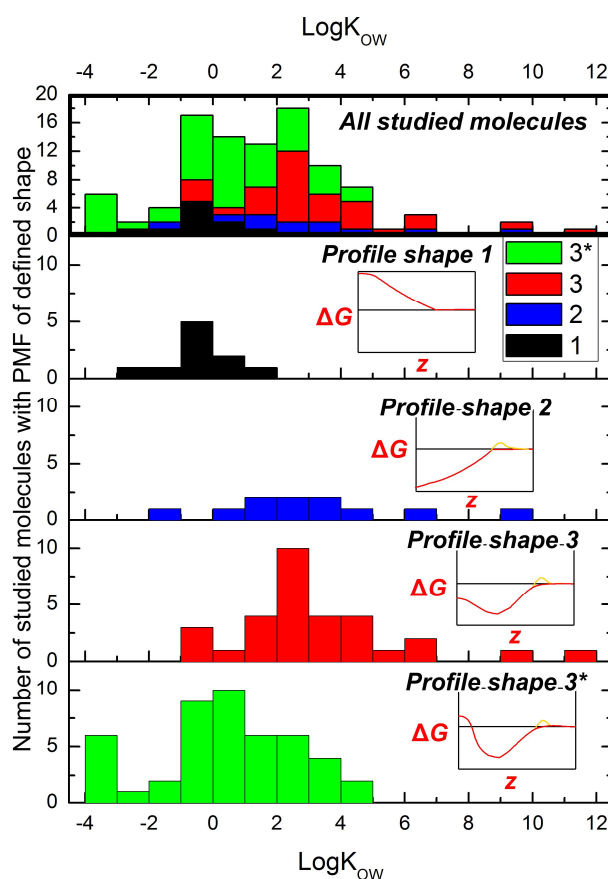


Figure 9: Distribution of studied drugs from ref.¹⁵¹ based on their free energy profile shapes (graph insets – x axis is the distance from the middle of the membrane z , y axis the free energy ΔG , the horizontal black line shows zero ΔG , the orange peaks show a possibility of small barrier at the membrane entrance) and octanol/water partition coefficients. The overall distribution of studied drugs (upper panel) shows the highest distribution of drugs with $\log K_{ow}$ between -1 and 5.

Generally, calculation of $\log K$ can be taken as reliable enough in MD as well as in other methods, such as COSMOmic.⁶⁶ (Appendix A7) Currently, force fields for MM and MD are developed to reproduce the experimental parameters well and this is also reflected in their abilities to reproduce $\log K$ for drug-like molecules.⁶⁶ (Appendix A7) Though not providing the direct atomic insight of the dynamic penetration, studies of $\log K$ in COSMOmic provided us with a high amount of data^{5,166–168} that correlated very well with the experimental results ($r^2 = 0.92$).¹⁶⁸ To summarize, currently we are capable of calculation of $\log K$ with a high precision and without too many issues to overcome.

4.2.3.3 Permeability

Apart from partitioning, other crucial bioproperty is the membrane permeability $\log P$. Permeability P is defined as the steady-state flux of the solute across the bilayer J divided by the concentration difference on both sides of the membrane Δc (Eq. 4).⁹¹

$$P = \frac{J}{\Delta c} \quad \text{Eq. 4}$$

In the theoretical calculations, $\log P$ was initially modeled as a permeation through a homogeneous oil layer with a homogeneous solubility-diffusion model (Eq 5):^{169,170}

$$P = \frac{KD_c}{d_c} \quad \text{Eq. 5}$$

Here K is the partition coefficient of the solute in the oil layer, D_c is the diffusion coefficient and d_c is the thickness of the layer. But with a growing evidence of complexity of membrane structure, a single homogeneous layer was no longer satisfying and an inhomogeneous model was proposed and used.^{104,171} Both models take into account two properties of drug-lipid interaction – partitioning and diffusion, together with the membrane thickness. While the homogeneous model takes a single value for each of these entities, the inhomogeneous model separates the membrane into infinitely thin layers and calculates the permeability gradually (Eq 6, Figure 10).

$$P = \frac{1}{R} = \frac{1}{\int_{\text{water}}^0 R(z) dz} = \frac{1}{\int_{\text{water}}^0 \frac{e^{-\frac{\Delta G(z)}{RT}}}{D(z)} dz} \quad \text{Eq. 6}$$

Where $R(z)$ is a resistance in the depth z and T is the thermodynamic temperature. While the homogenous solubility-diffusion model highlights the partitioning into the membrane layer, the inhomogeneous model almost neglects it and highlights the barrier region, where $\Delta G > 0$ (Figure 10).

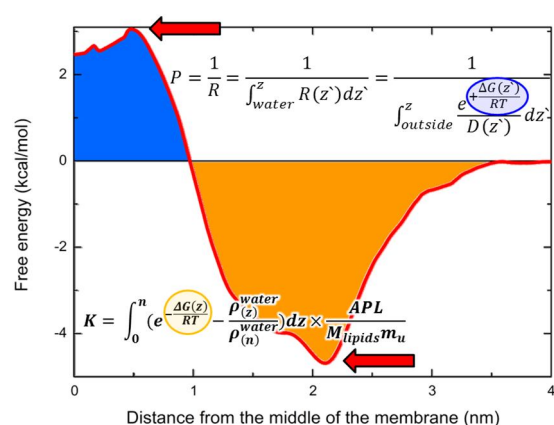


Figure 10: Calculation of partition coefficient K based on Klamt et al. equation depends almost entirely on the negative part of a free energy profile (orange), while the calculation of permeability P depends on the positive part of the free energy profile (blue). $\Delta G(z)$ stands for a free energy in a depth z , $D(z)$ is the diffusion coefficient in depth z , T is the thermodynamic temperature, R is molar gas constant, $\rho^{(water)}(n)$ and $\rho^{(water)}(z)$ is the density of water in furthest n^{th} layer and in the depth z , respectively. APL stands for area per lipid and M_{lipids} is molar mass of lipid molecule, while m_u is the atomic mass constant.

Though a high effort was spent in this field and theoretical estimations are clear, the calculation of $\log P$, and especially its diffusion term, is much less reliable than of previously discussed $\log K$.

4.2.3.3.1 Diffusion

The estimation of a diffusion coefficient of a drug on a non-flat free energy surface is far more complicated than on a flat one. The diffusion coefficient of a drug (or any system on a given CV) on a flat free energy surface can be derived from a mean square displacement of a drug in a long free simulation. The diffusion coefficient calculations require long simulation time depended on a length of the correlation time of the motions. The simulation time can be decreased by the increased number of molecules in the system, *e.g.*, calculations of water diffusion coefficient using a box of water molecules are already in a reasonable agreement with experiment.¹⁷² In drug-membrane studies such calculations can be used either for studying self-diffusion of lipids or for lateral diffusion estimations of drugs.¹⁷³ However, for $\log P$ calculation we need the transversal diffusion that will be calculated differently.

The motion of drug molecules in the membrane is driven by both the free energy gradient and the diffusion itself. For the diffusion coefficient calculation we need to separate these quantities. One of the possible approaches for the diffusion coefficient calculation is based on the fluctuations of a force applied in z-constraint or with the position fluctuations in umbrella sampling. The diffusion coefficient is calculated from the force autocorrelation function $ACF(F(z))$ (Eq. 7):¹⁷⁴

$$D(z) = \frac{(RT)^2}{\int_0^\infty ACF(F(z))dz} \quad \text{Eq. 7}$$

Though such diffusion coefficients are biased by high errors and the convergence time for such calculation is long as well, this is still the most used method for diffusion coefficient calculation.^{81,82,84–86,88,92–99,102,104}

Several other approaches for diffusion coefficient or directly permeability calculations were proposed recently. Ghaemi *et al.*⁹⁰ divided the CV space into several multiple microstates and calculated the free energy difference between them. Naturally, the free energy difference affects the transition rate that can be directly measured either from a single long free simulation of this region (in case of very shallow surfaces) or from multiple short simulations starting from the desired region in CV space. By this approach the transition rates in between microstates were obtained and could be than either used directly for permeability calculation or for local diffusion coefficient calculation. Ghaemi *et al.*⁹⁰ used several CVs, but afterwards Parisio *et al.*⁹¹ using the roto-translational approach adding the orientation of steroids during the permeation concluded that for rigid or small molecules, a single CV in a direction normal to the membrane is sufficient for permeability calculation. But for many molecules the use of other CVs is necessary or at least highly advised, as is discussed later. Further, other approaches were presented, such as oscillating forward-reverse method,^{87,89} generalized langevin method⁹³ or based on a mean first passage time.¹⁰¹ All of these MD approaches intended to reproduce the experimental data, however the precision of the approaches is still below the required level for relevant use.

An absolutely different approach for monitoring the permeation process was applied, *e.g.*, in a coarse-grained study of nanoparticle endocytosis.^{175,176} The permeation of nanoparticles of various shapes

through lipid membrane was monitored and the sampling was enhanced by adjusting the nanoparticle-lipid interactions. The interactions between nanoparticle surface beads and lipid head groups (representing ligand coating) are represented by explicit interaction energy added to the coarse grained force field. Further, the release of the nanoparticle from the lipid coating is driven by switching off this additional interaction energy.¹⁷⁶ These simulations show the abilities of MD to represent many processes on very large space and temporal scale.

Other approaches for estimating log P_s of various molecules are from predictive statistical models. Especially in case of skin permeability, statistical models give a reasonable prediction for a large amount of data available. The earlier models, *e.g.*, Potts&Guy¹⁷⁷ used just the $\log K_{ow}$ as a measure of lipophilicity and molecular weight M_w as a measure of diffusivity. Newer models¹⁷⁸ already take into account the hypothesized pathways of drugs through the skin (and its uppermost layer, *stratum corneum*). We do not provide here the full list of QSPR models here, as it is not the focus of this review. Later in the text we describe the MD works on skin and gel membranes overall.

4.2.3.4 Concentration dependence

All of the abovementioned approaches work in infinite dilution and do not take into account the possibility of drug concentration in the membrane, cluster formation or the membrane disruption. When lipophilic molecules are placed in the membrane neighborhood, they enter the membrane and can change a lateral pressure and consequently affect the function of membrane enzymes, as is hypothesized, *e.g.*, for general anesthetics.¹⁷⁹ Other molecules, mostly surface active one, can work as membrane disruptors, such as DMSO (dimethylsulphoxide), whose presence in the membrane significantly influenced the process of membrane pore formation.¹⁸⁰ The gel bilayer got fluidized by the presence of DMSO and the free energy of pore formation was here much lower. Finally, drugs can form doublets or other clusters and in such a formation they can either permeate through the membrane or perform their metabolic function.⁷¹ (Appendix A8) Overall, the main focus so far was placed on the infinite dilution and the role of a drug concentration in the membrane has not yet been fully described and provides a fascinating field for future studies.

4.2.3.5 PMF Issues

In this section we will discuss the most common issues in the calculation of PMFs that are further used for partitioning or permeability studies. We will discuss the methodology issues concerning the convergence – water defects, number of CVs, initial structures, choice of the method *etc.* and we will provide several recommendations for PMF studies.

4.2.3.5.1 Methodology Issues

One of the most addressed issues of drug-membrane interactions simulations is the convergence of the free energy profile.^{35,38,51} (Appendix A1) The pioneering works in the field of PMF calculations were performed for hundreds of ps per simulation frame¹⁰⁴ and this time was considered enough for convergence. But with the increasing size of studied solutes, it became obvious that this time is highly insufficient. The simulations of amino acids side chains analogues revealed water defects³⁰ in the head group region that can be induced, *e.g.*, by pulling a charged residue into the membrane. Neale *et al.*³⁵ also showed that with using various initial conformations of amino acids side chain analogues (leucine and arginine) one obtains different PMFs that unite at up to 80 ns of umbrella simulation per frame. Paloncýová *et al.*³⁸ (Appendix A1) showed that a careful choice of initial conformations can lead to

significant reduce of necessary simulation time. The water defects, either only in head group region or penetrating deep in the membrane are sources of significant artefacts.

Though the water defect reaching far below the head groups region is an unwanted phenomenon in PMF simulations, formation of a water pore can be a natural transport principle for, *e.g.*, charged molecules. The study of a transfer of arginine analogue through a DOPC lipid membrane revealed that the process was energetically nonadditive.³⁴ This implies that the formation of a pore (no matter how many arginines pass) is thermodynamically more favorable than the presence of arginine analogue in the dry hydrophobic membrane core. And therefore, when the charged arginine is placed in the membrane core, the defect spontaneously forms.³⁰ The formation of a pore in a fluid membrane costs ~ 20 kcal/mol¹⁸¹ and this is also the cost of transfer of charged arginine^{45,102} or a flip-flop of DPPC.¹⁸² From a certain pore size, the energetic cost of the formed pore grows linearly with its radius.¹⁸¹ In case of a gel membrane, the formed pores are not filled with water, but stay hydrophobic (in simulations sometimes with a vacuum inside) for a very high energetic penalty.¹⁸⁰ Though the water penetrating far inside the membrane can be a sign of an artificial structure, in case of fluid membrane and for charged or very hydrophilic species, the pore formation should be considered as a natural scheme for the membrane penetration.

With development of multidimensional methods we started to be able to systematically evaluate the role of other CVs. The first multidimensional free energy profiles were published recently adding an internal torsion angle of ibuprofen to usual CV, distance from the middle of the membrane.⁴⁷ Other possible CV of interest is the tilt angle of the studied solute representing its orientation in the membrane.^{69,74} Another CV that can solve the before-mentioned issue of water defects is the number of contact between a solute and water or lipids. This approach was successfully used by Ghaemi *et al.*⁹⁰ or Galassi *et al.*⁷² using bias-exchange metadynamics. Such an approach (apart from fixing a distal leaflet) can be used also when solving the issue of a system size, where the simple distance of the solute from the membrane cannot describe the membrane undulation.⁴³ Overall, using another CV, that is orthogonal to the obvious distance from the middle of the membrane is highly recommended and can increase the convergence rate significantly.¹⁵¹

Further, the rate of convergence is also affected by simulation method and the choice of other simulation parameters. For simulations with umbrella sampling or z-constraint one should choose a method for initial structure generation to obey the artefacts in head group region, as mentioned above. As many of the initial structures as possible should be chosen by a free simulation,³⁸ (Appendix A1) further method of choice is, *e.g.*, a short metadynamics simulation.¹⁸³ The methods like inflategro should be used with care, as the drug orientation or the adjustment of the membrane to the drug can be very artificial.³⁵ Further, pulling of a drug into the membrane can directly induce artificial water defects that take a long time of biased simulation to vanish.³⁸ (Appendix A1) Overall, spending a time at the initial structure generation is worth it and can reduce significantly the necessary production simulation time.

Another crucial part of the decision is the choice of the PMF calculation method itself. To our best knowledge, no direct comparison of the performance of multiple methods on a same drug-membrane system leading to a clear conclusion was performed. During the time, several general reviews of the PMF methods were published.¹⁸⁴⁻¹⁸⁷ In the case of drug-membrane interactions the most used method was and still is US. This motivated also Palonciová *et al.*³⁸ (Appendix A1) and Jämbeck *et al.*⁴⁷ to

compare US to ZC and META, respectively. US and ZC performed uniquely with undisturbed initial frames, but with a present water defect in membrane head group ZC was able to converge quicker.³⁸ (Appendix A1) META, on the other hand, was able to handle better the flexibility of ibuprofen and its internal torsion angle and it led to a single calculation result adequate to two sets of US. Very recently, Lee *et al.*⁹³ compared US, replica-exchange US, ABF and multiple-walker ABF in their abilities to calculate the PMFs, but did not lead to any definitive answer in the precision or calculation rate of these methods. Naturally, for small, easily permeable molecules one can use a free simulation and wait for the real distribution of the studied solute,⁴⁶ however for larger molecules or overall molecules⁹⁷ with higher energetic barriers to cross in the membrane, one would wait for ages. The choice of the method significantly depends on the desired studied phenomenon, on the habit and knowledge of the methods and the performance of the method in the used MD code.

4.2.3.5.2 Force fields

The use of a best methodology would be useless without a proper performance of a chosen force field. Recently a review was published by Lyubartsev *et al.*¹³⁷ focusing on the principle of various force field development and their performance. Lipid force field development is usually focused on representation of lipid membrane structural parameters, such as area per lipid, membrane thickness, deuterium order parameters *etc.*^{123,127-130} Lipid force fields validation scheme sometimes includes the calculation of free energies of transfers of amino acids analogues into the membrane core¹³⁰ or embedding of a transmembrane helix and comparing its properties with experiment¹³¹ to test the compatibility of a lipid force field with the protein one. Recently, benchmarks of force fields ability to reproduce solutes partition coefficient were published^{66,73} (Appendix A7) and showed a very good compatibility of current force fields with the approaches to parameterize small drug-like molecules. Further, also united atoms and coarse grained force field perform well.^{66,84} (Appendix A7) Current force fields show overall a good compatibility with the rest of the force fields from the appropriate force fields family and with the use of recommended simulation parameters¹¹⁴ they provide very reliable results.

The differences in polarities in water, lipid head groups and lipid tails are huge and lead to development of polarizable force fields.¹⁸⁸⁻¹⁹¹ The nonpolar environment inside the membrane should naturally affect the charge distribution on the solutes penetrating inside the membrane, but this cannot be fully captured by conventional force fields.¹⁸⁸ In a limited way, the atomic polarization of drug molecules was shown by Jämbeck *et al.*⁴⁸ by calculation of two sets of partial charges of drug molecules that were calculated in water and hexane, respectively. Further, polarizable phosphatidylcholine force field was presented by Chowdhary *et al.* and provided a reasonable agreement with experiment for the membrane structural parameters.¹⁹² Though the polarization and depolarization of polar molecules could be of high importance, the use of polarizable force fields in drug-membrane interaction studies is still very rare.

4.2.3.5.3 Other issues

Naturally, other issues may occur in the PMF studies, such as system size or charge of the drug molecule. The larger bilayers can undergo undulations and therefore can lead to systematic errors in the head group region. In large bilayer undulations, the sampling of a same *z* position can be the sampling of drug fully hydrated and also fully embedded in the membrane. The solution for such possibility can be fixing of the distal leaflet.¹⁹³ The charged drugs usually involve large water defects¹⁹⁴ and have a large penetration barrier. The calculation of their free energy profile raises

a question, if they should be treated in their neutral or charged form.³³ The deprotonation is supposed to happen in the head group region,¹⁰ (Appendix A5) but the full agreement of this issue has not yet happened. Both these issues and several others were however nicely reviewed elsewhere.^{151,195}

4.2.3.6 Role of membrane composition

So far we described the drug-membrane interactions from a general point of view, but not we focus on the individual role of lipids, their phases and mixtures which is still quite unknown, but growing field.

The membrane phase significantly affects the permeability of drugs through respective membranes. This field was extensively studied experimentally and revealed a dependence of permeability of acetic acid on deuterium order parameters of lipids (that correspond to area per lipid and consequently the phase).¹⁹⁶ However, only few theoretical studies focused on the role of membrane phase. A PMF study revealed a significantly higher penetration barrier observed for *para*-aminobenzoic acid and its derivatives in gel ceramide membrane in respect to fluid DOPC membrane.¹⁰ (Appendix A5) Further, a higher energetic penalty was paid for a formation of a pore in gel membrane in respect to the fluid one.¹⁸⁰ But most of the studies of membranes in gel state were either focused directly on properties of the membranes¹⁹⁷ or on the role of individual lipids, especially their mixtures.

With the increase in computer power and parameterization of various lipids, an intensive attention became focused on the differences between lipids, *e.g.*, on the role of lipid tail. Though the behavior of multiple species in lipid membranes can be taken generally as ‘lipid behavior’, there are significant exceptions to this presumption. *E.g.*, α -tocopherol was described as oriented with its polar part towards lipid head groups in POPC, in DMPC it was observed as lying in the membrane core, parallel to the membrane plane.¹⁰⁵ Further, in ceramides the length of the lipid tail significantly affects the membrane permeability, as the shorter tails disturb the membrane head group region.^{141,198} (Appendix A10) Both in theoretical and experimental studies, the role of lipid tail plays a role, though it is currently still mostly neglected.

The role of lipid head groups in the PMF studies is even more ignored. Generally, only phosphatidylcholine membranes were used for PMF calculations, with a tiny exception of few studies of phosphatidylglycerol,^{52,199} (Appendix A3) phosphatidylethanolamine⁴¹ and phosphatidylserine.⁵⁵ The head group role in drug-membrane interactions is therefore still not described, but recently, the role of lipid head groups, their charge and ability to form hydrogen bonds was described for membrane enzyme²⁰⁰ (Appendix A13) and we can expect that also in drug membrane interactions the role of lipid head groups will be significant.

4.2.3.6.1 Cholesterol

Apart from ‘ordinary’ lipids a focus is now placed on cholesterol. Cholesterol significantly affects membrane structure and phase. When a cholesterol concentration increases in a fluid membrane, its order parameters increase also, the area per lipid decreases, membrane gets thicker^{31,201} and a phase transition temperature increases. It should be noted that with cholesterol the phase transition is not rapid any more, the transition is more gradual than in case of pure membranes.¹¹ Cholesterol is proposed to be a key component of raft membranes.²⁰² In gel membranes, such as in ceramides, the situation is slightly different. Cholesterol decreases the tilt angle of lipids²⁰³ and decreases the ordering of lipids.¹¹ As well as in fluid membranes, the phase transition temperature becomes less clear and the transition is more gradual. The presence of cholesterol makes the membrane adopting part of the

properties from both liquid-ordered and gel phase and makes so-called liquid ordered phase. Consequently, cholesterol decreases the differences between lipids in the resulting membrane properties.

Naturally, not only other lipids in the membrane are affected by cholesterol, cholesterol is affected by the lipids present in the membrane. Cholesterol was shown to have a different nature of interactions with lipids with various chains. First, Marrink *et al.*²⁰⁴ showed that cholesterol tilt angle increases with the level of lipid unsaturation. Followingly, Kučerka *et al.*²⁰⁵ showed that in polyunsaturated fatty acids cholesterol was oriented in the membrane core, parallel to the membrane plane. The exchange between cholesterol parallel and perpendicular position and the switch to the other leaflet, so called flip-flop, inspired numerous studies. A first two-dimensional free energy surface did not predict a free energy minimum of the parallel cholesterol orientation known from experiment.¹⁵ But further studies identified this minimum⁹¹ and also revealed that a cholesterol flip-flop rate increased dramatically with the level of lipid unsaturation.²⁰⁴

Cholesterol affects also the dynamics of lipids in the membrane. The presence of cholesterol in the membrane decreases the diffusion coefficient of membrane phospholipids in respect to pure phospholipids membranes.²⁰⁶ The PMF calculation of DPPC flip-flop revealed a higher free energy barrier for DPPC flip-flop with the increased concentration of cholesterol in the membrane.³¹ But unlike in pure DPPC bilayer,²⁰⁷ the flip-flop did not go via pore-formation pathway. The affinity of DPPC molecule to the membrane composed of DPPC and cholesterol decreases with increasing cholesterol concentration indicating DPPC preference for cholesterol-free membrane.³¹ Together with the known preference of cholesterol to sphingomyelin,¹¹ cholesterol can be a driving force for the domain formation in membranes.

Naturally, by changing the membrane properties and dynamics, cholesterol affects also the membrane permeability or partitioning. Though experimentally the role of cholesterol on drug-membrane interactions was extensively studied,⁹⁴ theoretically this issue remains almost unsolved. The permeability of hypericin and its derivatives was studied on DPPC lipid bilayer with a various amount of cholesterol and it appeared that hypericin and its derivatives have lower permeability in cholesterol-rich membranes, but the scale of this effect was different for different molecules.⁹⁴ Further, the partitioning of solutes into lipid tails decreases with the addition of cholesterol to the PC and PE membranes and this effect is stronger in saturated lipids.⁴¹ The effect of cholesterol was higher than expected from experiment and therefore we can hypothesize that in real membrane cholesterol is not equally distributed, but form cholesterol-rich and cholesterol-poor regions.⁴¹ Overall, the effect of cholesterol on the drug-membrane interactions has not yet been widely studied and the role of cholesterol or cholesterol packing remains still unresolved.

4.2.4 Interaction with membrane proteins

Embedding a protein into a lipid membrane and its full solvation in atomistic resolution is now possible thanks to the recent development in computer power. Several reviews were recently published about membrane transporters simulations,^{208–211} (Appendix A14) and we do not intend to cover here all performed studies, whose number is steeply growing. The simulation studies are naturally limited, *e.g.*, by the absence of crystal structures of the enzymes, *e.g.*, in case of solute carriers (SLC) transporters and therefore the initial structures for MD simulations need to be prepared, *e.g.*, by the homology modeling.²¹² The studies of SLC transporter revealed that the drug transport is connected

with large conformational changes of transmembrane helices, by a so-called “clamp-and-switch” model of function.²¹³ All the dynamics processes of membrane embedded proteins are naturally rather slow for simple MD simulations and therefore require either a very long simulation or a biased one.

Especially the studies of the mechanism of the transport process used the biased simulations. The mechanism of the pathway of various solutes through SLC transporters was studied by steered and targeted MD.^{214–218} Other possible approach for active transporters, *e.g.*, ABC transporter is to simulate a protein with ATP and after a certain time exchange the ATP by ADP and monitor induced structural changes.^{219,220} Further, in case of pores, the mechanism of transport was studied, *e.g.*, by bias-exchange-metadynamics and metadynamics simulations^{221,222} leading to a free energy profile along the transport pathway. Such simulations are computationally very demanding and currently are on (or perhaps behind) the edge of our abilities.

Other membrane embedded proteins perform the biotransformation of drugs. Here the major focus was on cytochromes P450 (CYPs) with first published models of membrane embedded CYP2C9 that lead to first theoretical atomistic analysis of its membrane position.^{33,223} Further studies of another CYPs^{165,224–228} could use the CYP2C9 structure as an initial model for the depth of the enzyme embedding *etc.*, however the orientation and position of CYP on the membrane differs significantly also in the dependence on lipid composition of the membranes.^{200,229} (Appendix A13, A9) The CYPs` active sites are connected with their surface with a complex network of access and egress channels¹²¹ that open and close during their dynamic motions.^{33,229} (Appendix A9) The channels differ between each other in the drugs` ability to pass through²³⁰ (Appendix A11) and their properties, positions and radii fluctuates and depend on the composition of a membrane they are embedded in.^{200,229} (Appendix A13, A9) The docking into active sites of structures from MD revealed several different structures of the active site whose use in docking lead to good correlation of predicted sites of metabolism of 80 % of studied substrates.²³¹ Though the studies of CYPs revealed a lot of information about their interactions,²³² (Appendix A12) the detailed dynamical view inside the protein and the role of their sequence differences on their activity is still missing.

5. Results

In this section we review shortly our effort in the field of drug-membrane interaction studies. We will focus on the methodology development/benchmarking of calculation free energy profiles and partition coefficients. Afterwards, we will focus on the positions of substrates and metabolites of cytochromes P450 and the role of the membrane composition. Further we will move to skin-like membranes and finally to cytochromes P450 themselves, their orientation and their channels. In the individual cases we review again a small part of the theoretical background mentioned also earlier in the thesis.

5.1 Methodology

Biologically relevant calculation should be based on a functional lipid model, *i.e.*, a set of parameters for MM calculations called force field. Several force field families are currently on the market, differing with their fields of focus, way of parameters development or the size of used particles. Currently used force fields for lipids are either all-atomic (CHARMM36,^{123–126} Amber 11^{127/14}¹²⁸, GAFFlipids,¹²⁹ Slipids^{130–132}), united-atoms (Gromos43a1-s3¹³³ or older Berger lipid force field¹³⁴) or coarse-grained (Martini,¹³⁵ SDK¹³⁶). Generally, force fields are parameterized to reproduce well the experimental properties of lipids, mostly area per lipid, membrane thickness, deuterium order parameters or X-ray scattering images. We benchmarked⁶⁶ (Appendix A7) the force fields available in 2014 with the focus on the structural parameters of the membranes and their ability to reproduce membrane/water partition coefficient of several drugs that were studied also experimentally. We observed that except for the older united-atom Berger lipids force field, all other force fields reproduced the partition coefficient well (Figure 11). The knowledge of a functional model for membrane interactions was crucial for further studies. The ability of the force field to reproduce experimental data is promising for obtaining reliable data in other studies with molecules with experimentally unknown properties or for membrane-protein interactions.

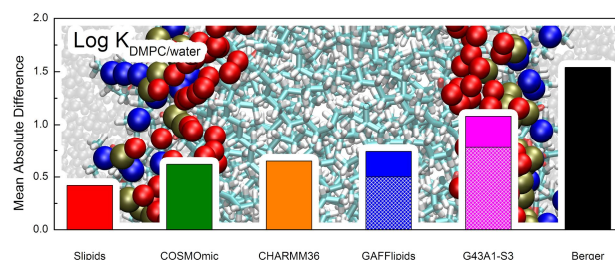


Figure 11: Mean absolute differences of calculated and experimentally measured lipid/water partition coefficients showing a good performance from most of used force fields in MD and COSMOmic.⁶⁶

We focused on the drug-membrane interaction and on the improvement of methods currently used in these studies. We analyzed the convergence rate of calculated free energy profile of a model drug³⁸ (Appendix A1) – coumarin – on a lipid membrane and observed significantly increased rate of convergence when using a z-constraint simulation in comparison with (in that age) commonly used umbrella simulation. While the z-constraint calculates a local gradient of a free energy as a mean force applied on a drug necessary to keep it on place, in umbrella simulation we apply a harmonic potential around an initial position and analyze the distribution of the drug with this external potential. In both cases we needed to perform this calculation for multiple systems with drug in different membrane depths to cover the whole path from water to the middle of the membrane. In both cases we worked with two sets of initial structures, one of them contained an increased hydration in head group region. In z-constraint simulation we observed a quicker relaxation and dehydration of initial structures and use of this method leads to significant increase in the convergence and reduction of a necessary simulation time.

Further increase in the performance of the calculation can come from the COSMOmic calculations.⁶⁵ (Appendix A6) The results from COSMOmic can be gained within the order of minutes, while the MD simulations last days or weeks. In comparison with Berger lipids force field, COSMOmic provided correlated data, however more hydrophobic. But the comparison with experimental data and other newer force fields⁶⁶ (Appendix A7) showed that COSMOmic is a reliable tool and could (and should) be used for fast drug screening projects, though it cannot show the dynamic phenomena as MD.

5.2 Interactions with fluid membranes

With the knowledge of possible methods, we can focus on the drugs' interactions with the membranes and, *e.g.*, monitor their localization and concentration. In case of cytochrome P450 enzymes' substrates and metabolites⁵² (Appendix A3) we observed a deeper immersion of substrates in the membrane and their higher affinity in comparison with the metabolites. We also observed a concentration of all of these amphiphilic molecules around the head group region as well as in case of other amphiphilic molecules.⁶⁵ (Appendix A6) We showed that the concentration of the substrates and metabolites in the membrane corresponds to the positions of access and egress channels of cytochromes P450.¹⁶⁵ (Appendix A2) We also showed that the position of active groups in antioxidants agrees well with the positions of lipid double bonds⁵⁴ (Appendix A4) they are supposed to protect and that they form a sort of a ladder removing the free radicals from the membrane.⁷¹ (Appendix A8)

We analyzed also the role of lipid type in the membrane in the drug-membrane interactions. Comparing two fluid membranes with different charges (Figure 12) showed that the drugs seemed to have a higher affinity to neutral membrane than to a negatively charged membrane.⁵² (Appendix A3)

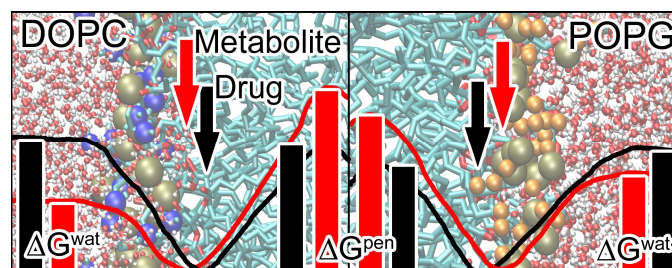


Figure 12: Average position, affinity (ΔG^{wat}) and penetration barrier (ΔG^{pen}) on neutral DOPC (left) and charged POPG (right) membrane

Also, in case of larger molecules, such as argenteane, the thickness of the membrane plays a crucial role and influences significantly the affinity to the membrane.⁵⁴ (Appendix A4) In case of very ordered membranes in a gel phase (such a ceramides in the skin), the affinity to the membrane is similar in comparison with a fluid membrane, but the penetration through such ordered membrane leads across a very high energy barrier.¹⁰ (Appendix A5) Overall, though we can talk about 'lipophilicity' of drug molecules, the type of a lipid influences significantly their interactions with other species.

5.3 Interactions with skin-like membranes

Focusing on the role of lipid type we analyzed the influence of lipid tail length in ceramides membranes on their permeability for drug molecules. These systems were studied experimentally, as the shorter ceramides are present in the skin of atopic eczema patients.²³³ We observed¹⁴¹ (Appendix A10) a behavior well representing experimentally described properties, where the ceramide membrane was highly impermeable, when the tails were long enough. Shortening of lipid chains did not initially lead to the permeability increase, but at a certain tail length (10 carbons) the permeability through these membranes started to grow (Figure 13). The highest permeability was observed for ceramides with 4-6 carbons in their tails and further shortening again reduced the permeability. We created the models of these systems and rationalized this behavior by the head group/lipid tails conformation. In longer ceramides lipids are arranged in a hairpin conformation (both tails go to the same direction). In shorter ceramides the lipids are arranged in L-shape conformation and the shorter tail disrupts the head group region that creates the barrier for the penetration. In the shortest ceramides the lipid tails are too short to disrupt the head group region and therefore the highest permeability is in the middle-long ceramides – short enough to be arranged in L-shape conformation and long enough to disrupt the head groups region.

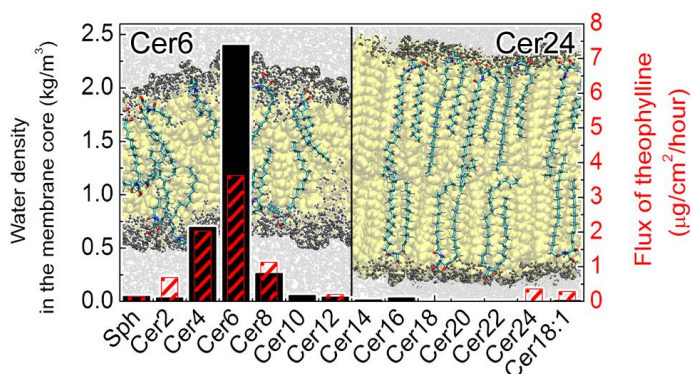


Figure 13:

Background: Structure of a disordered ceramide membrane with a shorter lipid chain (left) and of a gel phase healthy ceramide membrane (right). Lipids in gel phase membrane are ordered in hairpin conformation while the shorter ceramides are in L-shape conformation.

Plot: Experimental (red) and calculated (black) permeability through ceramide membranes.

5.4 Cytochromes P450

Finally, we studied the behavior of drug metabolizing enzymes cytochrome P450 (CYPs)²³² (Appendix A12) on the membranes. We prepared models of CYP 3A4 on a fluid membrane with various concentrations of cholesterol²²⁹ (Appendix A9) and observed changes in CYP 3A4 conformation. In the presence of cholesterol the enzyme was oriented differently and gradually the access and egress channels leading to the membrane closed and other channels leading to water opened. We even identified a channel not observed in any of the crystal structure available. By changes in the channel opening we suggested that the inhibition function of cholesterol experimentally observed²³⁴ can be caused not only by blocking the active site, but also by changes in the enzyme structure caused by the membrane. We also studied the role of lipid head groups of different glycerophospholipids and observed a significant difference in CYP3A4 orientation and embedding depth based on the ability of lipid head groups to form hydrogen bonds and especially on the charge.²⁰⁰ (Appendix A13) In negatively charged membrane CYP3A4 was embedded much deeper and also differently oriented. The negative charge pulled the positively charge CYP3A4 proximal side towards the lipid head groups. Overall, we highlighted here that the membrane, which CYP is attached to, is crucial for analysis of its function.

We introduced also a protocol for permeation studies of drug moving through channel enzymes using a bias-exchange metadynamics (Figure 14).²³⁰ (Appendix A11) We defined a set of variables and for a definition of the position in a flexible channel we defined a new variable metric, DMSDDrug. Metadynamics is based on a regular addition of a biasing potential to a visited place in a defined space that is added to a molecular mechanics potential. Addition of a potential drives the system to other regions in a predefined variable and finally the system diffuses freely along the whole space of a defined variable. The free energy is then calculated as a negative of biasing potential (naturally after a statistical block analysis of several calculated potentials at different times). With a protocol based on a regular exchanges between replicas biased on different variables we identified a favorable egress channel from CYP3A4 for a model drug (1,3,7-trimethyluric acid) and also the energy barrier for the other channels. Our results were in a reasonable agreement with similar experimental data and by this work we introduced a protocol transferable to other enzyme studies that can provide another step in in-silico pharmacology.

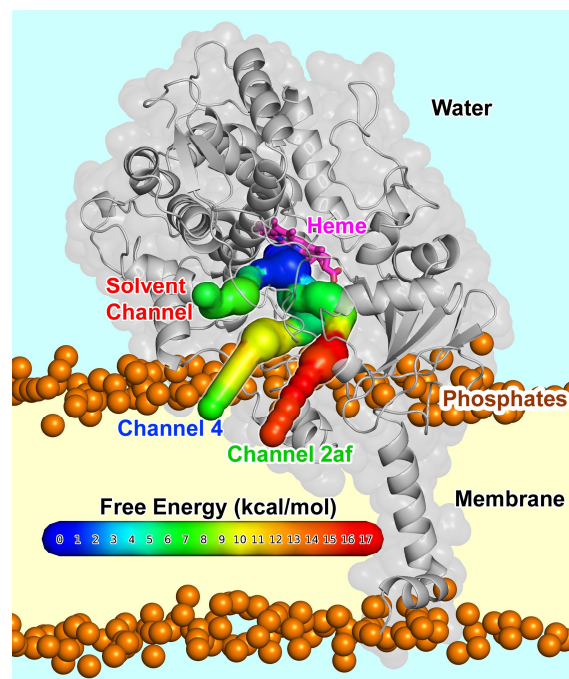


Figure 14: Visualization of free energy of CYP3A4 channels calculated by bias-exchange metadynamics.

6. Conclusion

Here I reviewed the current state of the art of computer-aided studies of drug-membrane interactions and addressed the issues and possible future development. I presented numerous examples that the computer simulations of lipid membranes are advanced enough to provide reliable information on drug-membrane interactions and are in accord with available experimental data. The simulations can be applied in pharmacology for estimation of the drug delivery rates, accessibility of drugs to tissues and organelles and accumulation of drugs in lipids in the body. Further, the understanding of the differences in the interaction with various lipids can provide important information for preferences of drugs to specific membranes present in specific organelles or species and lead to better drug targeting.

The summarized current findings brought a significant increase in the precision and performance of the simulations as well as a deep insight in the drug-membrane interactions. For MD simulations I showed that Slipids force field provided reliable PMF profiles and performed the best from the current available membrane force fields. However, it should be noted that also some other modern force fields (CHARMM36, GAFFlipids, Gromos43a1-s3) provided a good correlation between calculated and experimental partition coefficient in lipid membrane. For the high throughput PMF screening on fluid membranes I recommend to use a semi-continuous tool COSMOmic, however, its usage is limited to fluid membranes only as it cannot describe the differences between fluid and gel phase. I applied these approaches and by MD simulations I monitored the differences between fluid and gel membrane that resisted to the drug permeation much more than the fluid one, however the affinity to both membranes was comparable. Unlike partitioning fully described by PMF, the permeability calculations varied significantly in respect to experiments and the development of the effective methods for its calculation is still in progress. Mostly the diffusion coefficient calculation remains a challenge. I focused further on the drug distribution in the membranes and observed that the amphiphilic drugs tended to accumulate around the head groups region in the fluid membranes, while the lipophilic drugs concentrated in the membrane core. I also compared the positions of substrates and metabolites of CYPs in the membrane to the positions of CYP's access and egress channels and observed a good match supporting the hypothesis of CYPs sucking out the substrates from the membrane. And finally I set up the methodology based on bias-exchange metadynamics for calculation of PMF of a drug permeating through highly flexible enzyme channels and used it for identification of a preferred egress channel of CYP3A4. The solvated complex of enzyme-membrane-drug and their interactions from the thermodynamic point of view lie on a current edge of our abilities in all-atom MD simulations.

The field of computer calculations of drug-membrane interactions is gradually developing and from simple models of lipid bilayers, we move to larger, more complex systems. I envisage that for the next years, plenty of topics can still be addressed. Not only permeability managing, I expect the future focus of drug-membrane interaction community on concentration dependence of permeabilities and also on the role of membrane composition. Step-by-step, we are moving towards modeling structure and properties of the most complex biomembranes, which are present, *e.g.*, in our skin. Modelling of skin membranes may have significant application potential in transdermal drug delivery, cosmetics and risk assessment. Naturally, the drug-membrane-enzyme systems provide an infinite number of questions that need to be addressed. Though the state of the art shows a massive advance during the years, the field of drug-membrane interaction studies provides multiple challenges for next years.

7. Bibliography

- (1) Alberts, B.; Johnson, A.; Lewis, J.; Raff, M.; Roberts, K.; Walter, P. *Molecular Biology of the Cell, 4th Ed.*; Anderson, M.; Granum, S., Eds.; 5th Ed.; New York: Garland Science, 2008.
- (2) van Meer, G.; Voelker, D. R.; Feigenson, G. W. Membrane Lipids : Where They Are and How They Behave. *Nat. Rev. Mol. Cell Biol.* **2008**, *9*, 112–124.
- (3) Cooper, G. M. *The Cell: A Molecular Approach, 2nd Ed.*; 4th ed.; Sinauer Associates, 2000.
- (4) Janmey, P. A.; Kinnunen, P. K. J. Biophysical Properties of Lipids and Dynamic Membranes. *Trends Cell Biol.* **2006**, *16*, 538–546.
- (5) Endo, S.; Escher, B. I.; Goss, K. Capacities of Membrane Lipids to Accumulate Neutral Organic Chemicals. *Environ. Sci. Technol.* **2011**, *45*, 5912–5921.
- (6) Goñi, F. M.; Alonso, A. Biophysics of Sphingolipids I. Membrane Properties of Sphingosine, Ceramides and Other Simple Sphingolipids. *Biochim. Biophys. Acta* **2006**, *1758*, 1902–1921.
- (7) Brown, R. E. Sphingolipid Organization in Biomembranes: What Physical Studies of Model Membranes Reveal. *J. Cell Sci.* **1998**, *111*, 1–9.
- (8) Bennett, W. F. D.; Tieleman, D. P. Molecular Simulation of Rapid Translocation of Cholesterol, Diacylglycerol, and Ceramide in Model Raft and Nonraft Membranes. *J. Lipid Res.* **2012**, *53*, 421–429.
- (9) Escribá, P. V.; Busquets, X.; Inokuchi, J.; Balogh, G.; Török, Z.; Horváth, I.; Harwood, J. L.; Vigh, L. Membrane Lipid Therapy: Modulation of the Cell Membrane Composition and Structure as a Molecular Base for Drug Discovery and New Disease Treatment. *Prog. Lipid Res.* **2015**, *59*, 38–53.
- (10) Paloncýová, M.; DeVane, R. H.; Murch, B. P.; Berka, K.; Otyepka, M. Rationalization of Reduced Penetration of Drugs through Ceramide Gel Phase Membrane. *Langmuir* **2014**, *30*, 13942–13948.
- (11) Ohvo-Rekilä, H.; Ramstedt, B.; Leppimäki, P.; Slotte, J. P. Cholesterol Interactions with Phospholipids in Membranes. *Prog. Lipid Res.* **2002**, *41*, 66–97.
- (12) Pike, L. J. The Challenge of Lipid Rafts. *J. Lipid Res.* **2009**, *50 Suppl*, S323–S328.
- (13) McMullen, T. P. W.; Lewis, R. N. A. H.; McElhaney, R. N. Cholesterol-Phospholipid Interactions, the Liquid-Ordered Phase and Lipid Rafts in Model and Biological Membranes. *Curr. Opin. Colloid Interface Sci.* **2004**, *8*, 459–468.
- (14) Singer, S. J.; Nicolson, G. L. The Fluid Mosaic Model of the Structure of Cell Membrane. *Science (80)*. **1972**, *175*, 720–730.
- (15) Jo, S.; Rui, H.; Lim, J. B.; Klauda, J. B.; Im, W. Cholesterol Flip-Flop: Insights from Free Energy Simulation Studies. *J. Phys. Chem. B* **2010**, *114*, 13342–13348.
- (16) Bennett, W. F. D.; MacCallum, J. L.; Hinner, M. J.; Marrink, S. J.; Tieleman, D. P. Molecular View of Cholesterol Flip-Flop and Chemical Potential in Different Membrane Environments. *J. Am. Chem. Soc.* **2009**, *131*, 12714–12720.
- (17) Seydel, J. K.; Wiese, M. *Drug-Membrane Interactions: Analysis, Drug Distribution, Modeling*; Mannhold, R.; Kubinyi, H.; Folkers, G., Eds.; Wiley-VCH Verlag GmbH: Weinheim, 2002; Vol. 4.
- (18) Brown, D. A.; London, E. Structure and Function of Sphingolipid- and Cholesterol-Rich Membrane Rafts. *J. Biol. Chem.* **2000**, *275*, 17221–17224.
- (19) Eeman, M.; Deleu, M. From Biological Membranes to Biomimetic Model Membranes. *Biotechnol. Agron. Soc. Environ.* **2010**, *14*, 719–736.
- (20) Menon, G. K.; Cleary, G. W.; Lane, M. E. The Structure and Function of the Stratum Corneum. *Int. J. Pharm.* **2012**, *435*, 3–9.
- (21) Houben, E.; De Paepe, K.; Rogiers, V. A Keratinocyte's Course of Life. *Skin Pharmacol. Physiol.* **2007**, *20*, 122–132.
- (22) Masukawa, Y.; Narita, H.; Shimizu, E.; Kondo, N.; Sugai, Y.; Oba, T.; Homma, R.; Ishikawa, J.; Takagi, Y.; Kitahara, T.; *et al.* Characterization of Overall Ceramide Species in Human Stratum Corneum. *J. Lipid Res.* **2008**, *49*, 1466–1476.

- (23) Schurer, N. Y.; Elias, P. M. *The Biochemistry and Function of Stratum Corneum Lipids*; Second Edi.; ACADEMIC PRESS, INC., 1991; Vol. 24.
- (24) Iwai, I.; Han, H.; Hollander, L. Den; Svensson, S.; Ofverstedt, L.-G.; Anwar, J.; Brewer, J.; Bloksgaard, M.; Laloef, A.; Nosek, D.; *et al.* The Human Skin Barrier Is Organized as Stacked Bilayers of Fully Extended Ceramides with Cholesterol Molecules Associated with the Ceramide Sphingoid Moiety. *J. Invest. Dermatol.* **2012**, *132*, 1–11.
- (25) Michaels, A.; Chandrasekaran; Shaw, J. Drug Permeation Through Human Skin: Theory and in Vitro Experimental Measurement. *AIChE J.* **1975**, *21*, 985–996.
- (26) Bouwstra, J. A.; Gooris, G. S.; Dubbelaar, F. E.; Weerheim, A.; Ijzerman, A. P.; Ponc, M. Role of Ceramide 1 in the Molecular Organization of the Stratum Corneum Lipids. *J. Lipid Res.* **1998**, *39*, 186–196.
- (27) Bouwstra, J. A.; Gooris, G. S. The Lipid Organisation in Human Stratum Corneum and Model Systems. *Open Dermatol. J.* **2010**, *4*, 10–13.
- (28) Xiang, T.; Anderson, B. D. A Computer Simulation of Functional Group Contributions to Free Energy in Water and a DPPC Lipid Bilayer. *Biophys. J.* **2002**, *82*, 2052–2066.
- (29) Bemporad, D.; Luttmann, C.; Essex, J. W. Behaviour of Small Solutes and Large Drugs in a Lipid Bilayer from Computer Simulations. *Biochim. Biophys. Acta* **2005**, *1718*, 1–21.
- (30) MacCallum, J. L.; Bennett, W. F. D.; Tieleman, D. P. Distribution of Amino Acids in a Lipid Bilayer from Computer Simulations. *Biophys. J.* **2008**, *94*, 3393–3404.
- (31) Bennett, W. F.; MacCallum, J. L.; Tieleman, D. P. Thermodynamic Analysis of the Effect of Cholesterol on Dipalmitoylphosphatidylcholine Lipid Membranes. *J. Am. Chem. Soc.* **2009**, *131*, 1972–1978.
- (32) Johansson, A. C. V; Lindahl, E. Titratable Amino Acid Solvation in Lipid Membranes as a Function of Protonation State. *J. Phys. Chem. B* **2009**, *113*, 245–253.
- (33) Berka, K.; Hendrychová, T.; Anzenbacher, P.; Otyepka, M. Membrane Position of Ibuprofen Agrees with Suggested Access Path Entrance to Cytochrome P450 2C9 Active Site. *J. Phys. Chem. A* **2011**, *115*, 11248–11255.
- (34) MacCallum, J. L.; Bennett, W. F. D.; Tieleman, D. P. Transfer of Arginine into Lipid Bilayers Is Nonadditive. *Biophys. J.* **2011**, *101*, 110–117.
- (35) Neale, C.; Bennett, W. F. D.; Tieleman, D. P.; Pomès, R. Statistical Convergence of Equilibrium Properties in Simulations of Molecular Solutes Embedded in Lipid Bilayers. *J. Chem. Theory Comput.* **2011**, *7*, 4175–4188.
- (36) Tejwani, R. W.; Davis, M. E.; Anderson, B. D.; Stouch, T. R. Functional Group Dependence of Solute Partitioning to Various Locations within a DOPC Bilayer : A Comparison of Molecular Dynamics Simulations with Experiment. *J. Pharm. Sci.* **2011**, *100*, 2136–2146.
- (37) Košinová, P.; Berka, K.; Wykes, M.; Otyepka, M.; Trouillas, P. Positioning of Antioxidant Quercetin and Its Metabolites in Lipid Bilayer Membranes: Implication for Their Lipid-Peroxidation Inhibition. *J. Phys. Chem. B* **2012**, *116*, 1309–1318.
- (38) Paloncýová, M.; Berka, K.; Otyepka, M. Convergence of Free Energy Profile of Coumarin in Lipid Bilayer. *J. Chem. Theory Comput.* **2012**, *8*, 1200–1211.
- (39) Samanta, S.; Hezaveh, S.; Milano, G.; Roccatano, D. Diffusion of 1,2-Dimethoxyethane and 1,2-Dimethoxypropane through Phosphatidylcholine Bilayers: A Molecular Dynamics Study. *J. Phys. Chem. B* **2012**, *116*, 5141–5151.
- (40) Vazdar, M.; Jurkiewicz, P.; Hof, M.; Jungwirth, P.; Cwiklik, L. Behavior of 4-Hydroxynonenal in Phospholipid Membranes. *J. Phys. Chem. B* **2012**, *116*, 6411–6415.
- (41) Wennberg, C. L.; Van Der Spoel, D.; Hub, J. S.; Spoel, D. Van Der; Hub, J. S. Large Influence of Cholesterol on Solute Partitioning into Lipid Membranes. *J. Am. Chem. Soc.* **2012**, *134*, 5351–5361.
- (42) Yeh, I.; Ripoll, D. R.; Wallqvist, A. Free Energy Difference in Indolicidin Attraction to Eukaryotic and Prokaryotic Model Cell Membranes. *J. Phys. Chem. B* **2012**, *116*, 3387–3396.
- (43) Comer, J.; Schulten, K.; Chipot, C. Calculation of Lipid-Bilayer Permeabilities Using an Average Force. *J. Chem. Theory Comput.* **2014**, *10*, 554–564.

- (44) Hu, Y.; Ou, S.; Patel, S. Free Energetics of Arginine Permeation into Model DMPC Lipid Bilayers: Coupling of Effective Counterion Concentration and Lateral Bilayer Dimensions. *J. Phys. Chem. B* **2013**, *117*, 11641–11653.
- (45) Huang, K.; García, A. E. Free Energy of Translocating an Arginine-Rich Cell-Penetrating Peptide across a Lipid Bilayer Suggests Pore Formation. *Biophys. J.* **2013**, *104*, 412–420.
- (46) Hughes, Z. E.; Malajczuk, C. J.; Mancera, R. L. The Effects of Cryosolvents on DOPC – β - Sitosterol Bilayers Determined from Molecular Dynamics Simulations. *J. Phys. Chem. B* **2013**, *117*, 3362–3375.
- (47) Jämbeck, J. P. M.; Lyubartsev, A. P. Exploring the Free Energy Landscape of Solutes Embedded in Lipid Bilayers. *J. Phys. Chem. Lett.* **2013**, *4*, 1781–1787.
- (48) Jämbeck, J. P. M.; Lyubartsev, A. P. Implicit Inclusion of Atomic Polarization in Modeling of Partitioning Between Water and Lipid Bilayers. *Phys. Chem. Chem. Phys.* **2013**, *15*, 4677–4686.
- (49) Karlsson, B. C. G.; Olsson, G. D.; Friedman, R.; Rosengren, A. M.; Henschel, H.; Nicholls, I. A. How Warfarin's Structural Diversity Influences Its Phospholipid Bilayer Membrane Permeation. *J. Phys. Chem. B* **2013**, *117*, 2384–2395.
- (50) Li, L.; Vorobyov, I.; Allen, T. W. The Different Interactions of Lysine and Arginine Side Chains with Lipid Membranes. *J. Phys. Chem. B* **2013**, *117*, 11906–11920.
- (51) Neale, C.; Madill, C.; Rauscher, S.; Pomés, R. Accelerating Convergence in Molecular Dynamics Simulations of Solutes in Lipid Membranes by Conducting a Random Walk along the Bilayer Normal. *J. Chem. Theory Comput.* **2013**, *9*, 3686–3703.
- (52) Palonciová, M.; Berka, K.; Otyepka, M. Molecular Insight into Affinities of Drugs and Their Metabolites to Lipid Bilayers. *J. Phys. Chem. B* **2013**, *117*, 2403–2410.
- (53) Peters, G. H.; Wang, C.; Cruys-Bagger, N.; Velardez, G. F.; Madsen, J. J.; Westh, P. Binding of Serotonin to Lipid Membranes. *J. Am. Chem. Soc.* **2013**, *135*, 2164–2171.
- (54) Podloucká, P.; Berka, K.; Fabre, G.; Palonciová, M.; Duroux, J.-L. L.; Otyepka, M.; Trouillas, P. Lipid Bilayer Membrane Affinity Rationalizes Inhibition of Lipid Peroxidation by a Natural Lignan Antioxidant. *J. Phys. Chem. B* **2013**, *117*, 5043–5049.
- (55) Qiao, B.; Olvera De La Cruz, M. Driving Force for Water Permeation Across Lipid Membranes. *J. Phys. Chem. Lett.* **2013**, *4*, 3233–3237.
- (56) Tian, J.; Sethi, A.; Swanson, B. I.; Goldstein, B.; Gnanakaran, S. Taste of Sugar at the Membrane: Thermodynamics and Kinetics of the Interaction of a Disaccharide with Lipid Bilayers. *Biophys. J.* **2013**, *104*, 622–632.
- (57) Arcario, M. J.; Mayne, C. G.; Tajkhorshid, E. Atomistic Models of General Anesthetics for Use in in Silico Biological Studies. *J. Phys. Chem. B* **2014**, *118*, 12075–12086.
- (58) Cordeiro, R. M. Reactive Oxygen Species at Phospholipid Bilayers: Distribution, Mobility and Permeation. *Biochim. Biophys. Acta - Biomembr.* **2014**, *1838*, 438–444.
- (59) Filipe, H. A. L.; Joa, M. How To Tackle the Issues in Free Energy Simulations of Long Amphiphiles Interacting with Lipid Membranes: Convergence and Local Membrane Deformations. *J. Phys. Chem. B* **2014**, *118*, 3572–3581.
- (60) Kang, M.; Loverde, S. M. Molecular Simulation of the Concentration-Dependent Interaction of Hydrophobic Drugs with Model Cellular Membranes. *J. Phys. Chem. B* **2014**, 11965–11972.
- (61) Martin, L. J.; Chao, R.; Corry, B. Molecular Dynamics Simulation of the Partitioning of Benzocaine and Phenytoin into a Lipid Bilayer. *Biophys. Chem.* **2014**, *185*, 98–107.
- (62) Nademi, Y.; Amjad Iranagh, S.; Yousefpour, A.; Mousavi, S. Z.; Modarress, H. Molecular Dynamics Simulations and Free Energy Profile of Paracetamol in DPPC and DMPC Lipid Bilayers. *J. Chem. Sci.* **2014**, *126*, 637–647.
- (63) Nategholeslam, M.; Gray, C. G.; Tomberli, B. Implementation of the Forward–Reverse Method for Calculating the Potential of Mean Force Using a Dynamic Restraining Protocol. *J. Phys. Chem. B* **2014**, *118*, 14203–14214.
- (64) Neale, C.; Hsu, J. C. Y.; Yip, C. M.; Pomes, R. Indolicidin Binding Induces Thinning of a Lipid Bilayer. *Biophys. J.* **2014**, *106*, 29–31.

- (65) Paloncýová, M.; Devane, R.; Murch, B.; Berka, K.; Otyepka, M. Amphiphilic Drug-Like Molecules Accumulate in a Membrane below the Head Group Region. *J. Phys. Chem. B* **2014**, *118*, 1030–1039.
- (66) Paloncýová, M.; Fabre, G.; DeVane, R. H.; Trouillas, P.; Berka, K.; Otyepka, M. Benchmarking of Force Fields for Molecule – Membrane Interactions. *J. Chem. Theory Comput.* **2014**, *10*, 4143–4151.
- (67) Riahi, S.; Rowley, C. N. Why Can Hydrogen Sul Fi de Permeate Cell Membranes ? *J. Am. Chem. Soc.* **2014**, *136*, 15111–15113.
- (68) Wang, Y.; Hu, D.; Wei, D. Transmembrane Permeation Mechanism of Charged Methyl Guanidine. *J. Chem. Theory Comput.* **2014**, *10*, 1717–1726.
- (69) Wei, C.; Pohorille, A. Flip-Flop of Oleic Acid in a Phospholipid Membrane: Rate and Mechanism Flip-Flop of Oleic Acid in a Phospholipid Membrane: Rate and Mechanism Department of Pharmaceutical Chemistry , University of California San Francisco. *J. Phys. Chem. B* **2014**, *118*, 12919–12926.
- (70) Bereau, T.; Kremer, K. Automated Parametrization of the Coarse-Grained Martini Force Field for Small Organic Molecules. *J. Chem. Theory Comput.* **2015**, *11*, 2783–2791.
- (71) Fabre, G.; Bayach, I.; Berka, K.; Paloncýová, M.; Starok, M.; Rossi, C.; Duroux, J.-L.; Otyepka, M.; Trouillas, P. Synergism of Antioxidant Action of Vitamins E, C and Quercetin Is Related to Formation of Molecular Associates in Biomembranes. *Chem. Commun.* **2015**, 7713–7716.
- (72) Galassi, V. V.; Arantes, G. M. Partition, Orientation and Mobility of Ubiquinones in a Lipid Bilayer. *Biochim. Biophys. Acta - Bioenerg.* **2015**, *1847*, 1560–1573.
- (73) Genheden, S.; Essex, J. W. A Simple and Transferable All-Atom/Coarse-Grained Hybrid Model to Study Membrane Processes. *J. Chem. Theory Comput.* **2015**, *11*, 4749–4759.
- (74) Lv, C.; Aitchison, E. W.; Wu, D.; Zheng, L.; Cheng, X.; Yang, W. Comparative Exploration of Hydrogen Sulfide and Water Transmembrane Free Energy Surfaces via Orthogonal Space Tempering Free Energy Sampling. *J. Comput. Chem.* **2016**, *37*, 567–574.
- (75) Ma, J.; Domicевичa, L.; Schnell, J. R.; Biggin, P. C. Position and Orientational Preferences of Drug-Like Compounds in Lipid Membranes: A Computational and NMR Approach. *Phys. Chem. Chem. Phys.* **2015**, *17*, 19766–19776.
- (76) Malta De Sá, M.; Sresht, V.; Rangel-Yagui, C. O.; Blankschtein, D. Understanding Miltefosine-Membrane Interactions Using Molecular Dynamics Simulations. *Langmuir* **2015**, *31*, 4503–4512.
- (77) Nierzwicki, L.; Wieczor, M.; Censi, V.; Baginski, M.; Calucci, L.; Samaritani, S.; Czub, J.; Forte, C. Interaction of Cisplatin and Two Potential Antitumoral Platinum(ii) Complexes with a Model Lipid Membrane: A Combined NMR and MD Study. *Phys. Chem. Chem. Phys.* **2015**, *17*, 1458–1468.
- (78) Porasso, R. D.; Ale, N. M.; Ciocco Aloia, F.; Masone, D.; Del Pópolo, M. G.; Ben Altabef, A.; Gomez-Zavaglia, A.; Diaz, S. B.; Vila, J. a. Interaction of Glycine, Lysine, Proline and Histidine with Dipalmitoylphosphatidylcholine Lipid Bilayers: A Theoretical and Experimental Study. *RSC Adv.* **2015**, *5*, 43537–43546.
- (79) Sun, D.; Forsman, J.; Woodward, C. E. Evaluating Force Fields for the Computational Prediction of Ionized Arginine and Lysine Side-Chains Partitioning into Lipid Bilayers and Octanol. *J. Chem. Theory Comput.* **2015**, *11*, 1775–1791.
- (80) Alwarawrah, M.; Hussain, F.; Huang, J. Alteration of Lipid Membrane Structure and Dynamics by Diacylglycerols with Unsaturated Chains. *Biochim. Biophys. Acta - Biomembr.* **2016**, *1858*, 253–263.
- (81) Marrink, S. J.; Berendsen, H. J. C. Permeation Process of Small Molecules across Lipid Membranes Studied by Molecular Dynamics Simulations. *J. Phys. Chem.* **1996**, *100*, 16729–16738.
- (82) Carpenter, T. S.; Kirshner, D. A.; Lau, E. Y.; Wong, S. E.; Nilmeier, J. P.; Lightstone, F. C. A Method to Predict Blood-Brain Barrier Permeability of Drug-Like Compounds Using

- Molecular Dynamics Simulations. *Biophys. J.* **2014**, *107*, 630–641.
- (83) Meng, F.; Xu, W. Drug Permeability Prediction Using PMF Method. *J. Mol. Model.* **2012**, *19*, 991–997.
- (84) Orsi, M.; Sanderson, W. E.; Essex, J. W. Permeability of Small Molecules through a Lipid Bilayer: A Multiscale Simulation Study. *J. Phys. Chem. B* **2009**, *113*, 12019–12029.
- (85) Bemporad, D.; Essex, J. W.; Luttmann, C. Permeation of Small Molecules through a Lipid Bilayer: A Computer Simulation Study. *J. Phys. Chem. B* **2004**, *108*, 4875–4884.
- (86) Zocher, F.; Van Der Spoel, D.; Pohl, P.; Hub, J. S. Local Partition Coefficients Govern Solute Permeability of Cholesterol-Containing Membranes. *Biophys. J.* **2013**, *105*, 2760–2770.
- (87) Holland, B. W.; Gray, C. G.; Tomberli, B. Calculating Diffusion and Permeability Coefficients with the Oscillating Forward-Reverse Method. *Phys. Rev. E - Stat. Nonlinear, Soft Matter Phys.* **2012**, *86*, 036707.
- (88) Fiedler, S. L.; Violi, A. Simulation of Nanoparticle Permeation through a Lipid Membrane. *Biophys. J.* **2010**, *99*, 144–152.
- (89) Holland, B. W.; Berry, M. D.; Gray, C. G.; Tomberli, B. A Permeability Study of O² and the Trace Amine P-Tyramine through Model Phosphatidylcholine Bilayers. *PLoS One* **2015**, *10*, 1–24.
- (90) Ghaemi, Z.; Minozzi, M.; Carloni, P.; Laio, A. A Novel Approach to the Investigation of Passive Molecular Permeation through Lipid Bilayers from Atomistic Simulations. *J. Phys. Chem. B* **2012**, 1–2.
- (91) Parisio, G.; Stocchero, M.; Ferrarini, A. Passive Membrane Permeability: Beyond the Standard Solubility-Diffusion Model. *J. Chem. Theory Comput.* **2013**, *9*, 5236–5246.
- (92) Das, C.; Olmsted, P. P. D.; Noro, M. G. M. Water Permeation through Stratum Corneum Lipid Bilayers from Atomistic Simulations. *Soft Matter* **2009**, *5*, 4549–4556.
- (93) Lee, C. T.; Comer, J.; Herndon, C.; Leung, N.; Pavlova, A.; Swift, R. V.; Tung, C.; Rowley, C.; Amaro, R. E.; Chipot, C.; *et al.* Simulation-Based Approaches for Determining Membrane Permeability of Small Compounds. *J. Chem. Inf. Model.* **2016**, *56*, 721–733.
- (94) Eriksson, E. S. E.; Eriksson, L. A. The Influence of Cholesterol on the Properties and Permeability of Hypericin Derivatives in Lipid Membranes. *J. Chem. Theory Comput.* **2011**, *7*, 560–574.
- (95) Wei, C.; Pohorille, A. Permeation of Membranes by Ribose and Its Diastereomers. *J. Am. Chem. Soc.* **2009**, *131*, 10237–10245.
- (96) Bemporad, D.; Luttmann, C.; Essex, J. W. Computer Simulation of Small Molecule Permeation across a Lipid Bilayer: Dependence on Bilayer Properties and Solute Volume, Size, and Cross-Sectional Area. *Biophys. J.* **2004**, *87*, 1–13.
- (97) Wei, C.; Pohorille, A. Permeation of Nucleosides through Lipid Bilayers. *J. Phys. Chem. B* **2011**, *115*, 3681–3688.
- (98) Shinoda, W.; Mikami, M.; Baba, T.; Hato, M. Molecular Dynamics Study on the Effects of Chain Branching on the Physical Properties of Lipid Bilayers: 2. Permeability. *J. Phys. Chem. B* **2004**, *108*, 9346–9356.
- (99) Orsi, M.; Essex, J. W. Permeability of Drugs and Hormones through a Lipid Bilayer: Insights from Dual-Resolution Molecular Dynamics. *Soft Matter* **2010**, *6*, 3797–3808.
- (100) Notman, R.; den Otter, W. K.; Noro, M. G.; Briels, W. J.; Anwar, J. The Permeability Enhancing Mechanism of DMSO in Ceramide Bilayers Simulated by Molecular Dynamics. *Biophys. J.* **2007**, *93*, 2056–2068.
- (101) Votapka, L. W.; Lee, C. T.; Amaro, R. E. Two Relations to Estimate Membrane Permeability Using Milestoning. *J. Phys. Chem. B* **2016**, Articles ASAP, DOI: 10.1021/acs.jpcc.6b02814.
- (102) Vorobyov, I.; Olson, T. E.; Kim, J. H.; Koeppe, R. E.; Andersen, O. S.; Allen, T. W. Ion-Induced Defect Permeation of Lipid Membranes. *Biophys. J.* **2014**, *106*, 586–597.
- (103) Swift, R. V.; Amaro, R. E. Back to the Future: Can Physical Models of Passive Membrane Permeability Help Reduce Drug Candidate Attrition and Move Us Beyond QSPR? *Chem. Biol. Drug Des.* **2013**, *81*, 61–71.

- (104) Marrink, S.-J.; Berendsen, H. J. C. Simulation of Water Transport through a Lipid Membrane. *J. Phys. Chem.* **1994**, *98*, 4155–4168.
- (105) Marquardt, D.; Williams, J. A.; Kinnun, J. J.; Kuc, N.; Atkinson, J.; Wassall, S. R.; Katsaras, J.; Harroun, T. A. Dimyristoyl Phosphatidylcholine: A Remarkable Exception to α -Tocopherol's Membrane Presence. *J. Am. Chem. Soc.* **2014**, *136*, 203–210.
- (106) Koubi, L.; Saiz, L.; Tarek, M.; Scharf, D.; Klein, M. L. Influence of Anesthetic and Nonimmobilizer Molecules on the Physical Properties of a Polyunsaturated Lipid Bilayer. *J. Phys. Chem. B* **2003**, *107*, 14500–14508.
- (107) Weizenmann, N.; Huster, D.; Scheidt, H. A. Interaction of Local Anesthetics with Lipid Bilayers Investigated by $(1)H$ MAS NMR Spectroscopy. *Biochim. Biophys. Acta* **2012**, *1818*, 3010–3018.
- (108) Deleu, M.; Crowet, J. M.; Nasir, M. N.; Lins, L. Complementary Biophysical Tools to Investigate Lipid Specificity in the Interaction between Bioactive Molecules and the Plasma Membrane: A Review. *Biochim. Biophys. Acta - Biomembr.* **2014**, *1838*, 3171–3190.
- (109) Kucerka, N.; Nagle, J. F.; Sachs, J. N.; Feller, S. E.; Pencer, J.; Jackson, A.; Katsaras, J. Lipid Bilayer Structure Determined by the Simultaneous Analysis of Neutron and X-Ray Scattering Data. *Biophys. J.* **2008**, *95*, 2356–2367.
- (110) Leftin, A.; Brown, M. F. An NMR Database for Simulations of Membrane Dynamics. *Biochim. Biophys. Acta* **2011**, *1808*, 818–839.
- (111) Markovic, B. D.; Vladimirov, S. M.; Cudina, O. A.; Odovic, J. V.; Karljickovic-Rajic, K. D. A PAMPA Assay as Fast Predictive Model of Passive Human Skin Permeability of New Synthesized Corticosteroid C-21 Esters. *Molecules* **2012**, *17*, 480–491.
- (112) Vaes, W. H.; Ramos, E. U.; Hamwijk, C.; van Holsteijn, I.; Blaauboer, B. J.; Seinen, W.; Verhaar, H. J.; Hermens, J. L. Solid Phase Microextraction as a Tool to Determine Membrane/Water Partition Coefficients and Bioavailable Concentrations in in Vitro Systems. *Chem. Res. Toxicol.* **1997**, *10*, 1067–1072.
- (113) Tristram-Nagle, S.; Nagle, J. F. Lipid Bilayers: Thermodynamics, Structure, Fluctuations, and Interactions. *Chem. Phys. Lipids* **2004**, *127*, 3–14.
- (114) Klauda, J. B.; Venable, R. M.; Pastor, R. W. Considerations for Lipid Force Field Development. *Comput. Model. Membr. Bilayers* **2008**, *60*, 1.
- (115) Giacomini, K. M.; Huang, S.-M. Transporters in Drug Development and Clinical Pharmacology. *Clin. Pharmacol. Ther.* **2013**, *94*, 3–9.
- (116) Giacomini, K. M.; Huang, S.-M.; Tweedie, D. J.; Benet, L. Z.; Brouwer, K. L. R.; Chu, X.; Dahlin, A.; Evers, R.; Fischer, V.; Hillgren, K. M.; *et al.* Membrane Transporters in Drug Development. *Nat. Rev. Drug Discov.* **2010**, *9*, 215–236.
- (117) Davidson, A. L.; Maloney, P. C. ABC Transporters: How Small Machines Do a Big Job. *Trends Microbiol.* **2007**, *15*, 448–455.
- (118) Oldham, M. L.; Davidson, A. L.; Chen, J. Structural Insights into ABC Transporter Mechanism. *Curr. Opin. Struct. Biol.* **2008**, *18*, 726–733.
- (119) Anzenbacher, P.; Anzenbacherová, E. Cytochromes P450 and Metabolism of Xenobiotics. *Cell. Mol. Life Sci.* **2001**, *58*, 737–747.
- (120) Seliskar, M.; Rozman, D. Mammalian Cytochromes P450--Importance of Tissue Specificity. *Biochim. Biophys. Acta* **2007**, *1770*, 458–466.
- (121) Cojocaru, V.; Winn, P. J.; Wade, R. C. The Ins and Outs of Cytochrome P450s. *Biochim. Biophys. Acta* **2007**, *1770*, 390–401.
- (122) Kirchmair, J.; Howlett, A.; Peironcely, J. E.; Murrell, D. S.; Williamson, M. J.; Adams, S. E.; Hankemeier, T.; Van Buren, L.; Duchateau, G.; Klaffke, W.; *et al.* How Do Metabolites Differ from Their Parent Molecules and How Are They Excreted? *J. Chem. Inf. Model.* **2013**, *53*, 354–367.
- (123) Klauda, J. B.; Venable, R. M.; Freites, J. A.; O'Connor, J. W.; Tobias, D. J.; Mondragon-Ramirez, C.; Vorobyov, I.; MacKerell, A. D.; Pastor, R. W.; Connor, J. W. O.; *et al.* Update of the CHARMM All-Atom Additive Force Field for Lipids: Validation on Six Lipid Types. *J.*

- Phys. Chem. B* **2010**, *114*, 7830–7843.
- (124) Pastor, R. W.; Mackerell, A. D. Development of the CHARMM Force Field for Lipids. *J. Phys. Chem. Lett.* **2011**, *2*, 1526–1532.
- (125) Lim, J. B.; Rogaski, B.; Klauda, J. B. Update of the Cholesterol Force Field Parameters in CHARMM. *J. Phys. Chem. B* **2012**, *116*, 203–210.
- (126) Venable, R. M.; Sodt, A. J.; Rogaski, B.; Rui, H.; Hatcher, E.; MacKerell, A. D.; Pastor, R. W.; Klauda, J. B. CHARMM All-Atom Additive Force Field for Sphingomyelin: Elucidation of Hydrogen Bonding and of Positive Curvature. *Biophys. J.* **2014**, *107*, 134–145.
- (127) Skjevik, Å. a; Madej, B. D.; Walker, R. C.; Teigen, K. LIPID11: A Modular Framework for Lipid Simulations Using Amber. *J. Phys. Chem. B* **2012**, *116*, 11124–11136.
- (128) Dickson, C. J.; Madej, B. D.; Skjevik, Å. A.; Betz, R. M.; Teigen, K.; Gould, I. R.; Walker, R. C. Lipid14: The Amber Lipid Force Field. *J. Chem. Theory Comput.* **2014**, *10*, 865–879.
- (129) Dickson, C. J.; Rosso, L.; Betz, R. M.; Walker, R. C.; Gould, I. R. GAFFlipid: A General Amber Force Field for the Accurate Molecular Dynamics Simulation of Phospholipid. *Soft Matter* **2012**, *8*, 9617–9627.
- (130) Jämbeck, J. P. M.; Lyubartsev, A. P. Derivation and Systematic Validation of a Refined All-Atom Force Field for Phosphatidylcholine Lipids. *J. Phys. Chem. B* **2012**, *116*, 3164–3179.
- (131) Jämbeck, J. P. M.; Lyubartsev, A. P. An Extension and Further Validation of an All-Atomistic Force Field for Biological Membranes. *J. Chem. Theory Comput.* **2012**, *8*, 2938–2948.
- (132) Jämbeck, J. P. M.; Lyubartsev, A. P. Another Piece of the Membrane Puzzle: Extending Slipids Further. *J. Chem. Theory Comput.* **2012**, *9*, 774–784.
- (133) Chiu, S.-W.; Pandit, S. A.; Scott, H. L.; Jakobsson, E. An Improved United Atom Force Field for Simulation of Mixed Lipid Bilayers. *J. Phys. Chem. B* **2009**, *113*, 2748–2763.
- (134) Berger, O.; Edholm, O.; Jahnig, F. Molecular Dynamics Simulations of a Fluid Bilayer of Dipalmitoylphosphatidylcholine at Full Hydration, Constant Pressure and Constant Temperature. *Biophys. J.* **1997**, *72*, 2002–2013.
- (135) Marrink, S. J.; Risselada, H. J.; Yefimov, S.; Tieleman, D. P.; de Vries, A. H. The MARTINI Force Field: Coarse Grained Model for Biomolecular Simulations. *J. Phys. Chem. B* **2007**, *111*, 7812–7824.
- (136) Shinoda, W.; DeVane, R.; Klein, M. L. Multi-Property Fitting and Parameterization of a Coarse Grained Model for Aqueous Surfactants. *Mol. Simul.* **2007**, *33*, 27–36.
- (137) Lyubartsev, A. P.; Rabinovich, A. L. Force Field Development for Lipid Membrane Simulations. *Biochim. Biophys. Acta - Biomembr.* **2016**.
- (138) Berendsen, H. J. C.; Postma, J. P. M.; Gunsteren, W. F. van; Hermans, J. Interaction Models for Water in Relation to Protein Hydration. In *Intermolecular Forces*; Pullman, B., Ed.; Reidel Publishing Company, 1981; pp. 331–338.
- (139) Berendsen, H. J. C.; Grigera, J. R.; Straatsma, T. P. The Missing Term in Effective Pair Potentials. *J. Phys. Chem.* **1987**, *91*, 6269–6271.
- (140) Jorgensen, W. L.; Chandrasekhar, J.; Madura, J. D.; Impey, R. W.; Klein, M. L. Comparison of Simple Potential Functions for Simulating Liquid Water. *J. Chem. Phys.* **1983**, *79*, 926.
- (141) Palonciová, M.; Vávrová, K.; Sovová, Ž.; DeVane, R. H.; Otyepka, M.; Berka, K. Structural Changes in Ceramide Bilayers Rationalize Increased Permeation through Stratum Corneum Models with Shorter Acyl Tails. *J. Phys. Chem. B* **2015**, *119*, 9811–9819.
- (142) Sugita, Y.; Okamoto, Y. Replica-Exchange Molecular Dynamics Method for Protein Folding Simulation. *Chem. Phys. Lett.* **1999**, *314*, 141–151.
- (143) Meli, M.; Colombo, G. A Hamiltonian Replica Exchange Molecular Dynamics (MD) Method for the Study of Folding, Based on the Analysis of the Stabilization Determinants of Proteins. *Int. J. Mol. Sci.* **2013**, *14*, 12157–12169.
- (144) Hamelberg, D.; Mongan, J.; McCammon, J. A. Accelerated Molecular Dynamics: A Promising and Efficient Simulation Method for Biomolecules. *J. Chem. Phys.* **2004**, *120*, 11919–11929.
- (145) Torrie, G. M.; Calleau, J. P. Nonphysical Sampling Distribution in Monte Carlo Free Energy Estimation: Umbrella Sampling. *J. Comput. Phys.* **1997**, *23*, 187–199.

- (146) Kumar, S.; Rosenberg, J.; Bouzida, D.; Swensen, R. H.; Kollman, P. A. The Weighted Histogram Analysis Method for Free Energy Calculations on Biomolecules. I. The Method. *J. Comput. Chem.* **1992**, *13*, 1011–1021.
- (147) Ciccotti, G.; Kapral, R.; Vanden-Eijnden, E. Blue Moon Sampling, Vectorial Reaction Coordinates, and Unbiased Constrained Dynamics. *ChemPhysChem* **2005**, *6*, 1809–1814.
- (148) Laio, A.; Gervasio, F. L. Metadynamics: A Method to Simulate Rare Events and Reconstruct the Free Energy in Biophysics, Chemistry and Material Science. *Reports Prog. Phys.* **2008**, *71*, 126601.
- (149) Grubmüller, H. Predicting Slow Structural Transitions in Macromolecular Systems: Conformational Flooding. *Phys. Rev. E* **1995**, *52*, 2893–2906.
- (150) Darve, E.; Rodríguez-Gómez, D.; Pohorille, A. Adaptive Biasing Force Method for Scalar and Vector Free Energy Calculations. *J. Chem. Phys.* **2008**, *128*, 1–13.
- (151) Neale, C.; Pomès, R. Sampling Errors in Free Energy Simulations of Small Molecules in Lipid Bilayers. *Biochim. Biophys. Acta - Biomembr.* **2016**, DOI: 10.1016/j.bbamem.2016.03.006.
- (152) Comer, J.; Gumbart, J. C.; Hénin, J.; Lelievre, T.; Pohorille, A.; Chipot, C. The Adaptive Biasing Force Method: Everything You Always Wanted to Know but Were Afraid to Ask. *J. Phys. Chem. B* **2015**, *119*, 1129–1151.
- (153) Piana, S.; Laio, A. A Bias-Exchange Approach to Protein Folding. *J. Phys. Chem. B* **2007**, *111*, 4553–4559.
- (154) Hénin, J.; Fiorin, G.; Chipot, C.; Klein, M. L. Exploring Multidimensional Free Energy Landscapes Using Time-Dependent Biases on Collective Variables. *J. Chem. Theory Comput.* **2010**, *6*, 35–47.
- (155) Widom, B. Some Topics in the Theory of Fluids. *J. Chem. Phys.* **1963**, *39*, 2808.
- (156) Kosztin, I.; Barz, B.; Janosi, L. Calculating Potentials of Mean Force and Diffusion Coefficients from Nonequilibrium Processes without Jarzynski's Equality. *J. Chem. Phys.* **2006**, *124*, 1–12.
- (157) Zheng, L.; Chen, M.; Yang, W. Simultaneous Escaping of Explicit and Hidden Free Energy Barriers: Application of the Orthogonal Space Random Walk Strategy in Generalized Ensemble Based Conformational Sampling. *J. Chem. Phys.* **2009**, *130*, 1–11.
- (158) Sengupta, D.; Smith, J. C.; Ullmann, G. M. Partitioning of Amino-Acid Analogues in a Five-Slab Membrane Model. *Biochim. Biophys. Acta* **2008**, *1778*, 2234–2243.
- (159) Klamt, A.; Huniar, U. COSMOmic: A Mechanistic Approach to the Calculation of Membrane–Water Partition Coefficients and Internal Distributions within Membranes and Micelles. *J. Phys. ...* **2008**, 12148–12157.
- (160) Eckert, F.; Klamt, A. COSMOtherm, 2013.
- (161) Klamt, A. The COSMO and COSMO-RS Solvation Models. *Wiley Interdiscip. Rev. Comput. Mol. Sci.* **2011**, *1*, 699–709.
- (162) Eckert, F.; Klamt, A. Fast Solvent Screening via Quantum Chemistry : COSMO-RS Approach. *AIChE J.* **2002**, *48*, 369–385.
- (163) Klamt, A. *COSMO-RS: From Quantum Chemistry to Fluid Phase Thermodynamics and Drug Design*; Elsevier Science Ltd.: Amsterdam, 2005; Vol. 1.
- (164) Klamt, A.; Schüürmann, G. COSMO - a New Approach To Dielectric Screening in Solvents With Explicit Expressions for the Screening Energy and Its Gradient. *J. Chem. Soc. Perkin Trans.* **1993**, 799–805.
- (165) Berka, K.; Paloncýová, M.; Anzenbacher, P.; Otyepka, M. Behavior of Human Cytochromes P450 on Lipid Membranes. *J. Phys. Chem. B* **2013**, *117*, 11556–11564.
- (166) Ingram, T.; Storm, S.; Kloss, L.; Mehling, T.; Jakobtorweihen, S.; Smirnova, I. V. Prediction of Micelle/ Water and Liposome/ Water Partition Coefficients Based on Molecular Dynamics Simulations, COSMO-RS and COSMOmic. *Langmuir* **2013**, *29*, 3527–3537.
- (167) Jakobtorweihen, S.; Zuniga, A. C.; Ingram, T.; Gerlach, T.; Keil, F. J.; Smirnova, I. Predicting Solute Partitioning in Lipid Bilayers: Free Energies and Partition Coefficients from Molecular Dynamics Simulations and COSMOmic. *J. Chem. Phys.* **2014**, *141*, 045102.

- (168) Jakobtorweihen, S.; Ingram, T.; Smirnova, I. Combination of COSMOmic and Molecular Dynamics Simulations for the Calculation of Membrane-Water Partition Coefficients. *J. Comput. Chem.* **2013**, *34*, 1332–1340.
- (169) Finkelstein, A. Water and Nonelectrolyte Permeability of Lipid Bilayer Membranes. *J. Gen. Physiol.* **1976**, *68*, 127–135.
- (170) Nagle, J. F.; Mathai, J. C.; Zeidel, M. L.; Tristram-Nagle, S. Theory of Passive Permeability through Lipid Bilayers. *J. Gen. Physiol.* **2008**, *131*, 77–85.
- (171) Katz, Y.; Diamond, J. M. Thermodynamic Constants for Nonelectrolyte Partition between Dimyristoyl Lecithin and Water. *J. Membr. Biol.* **1974**, *17*, 101–120.
- (172) Mark, P.; Nilsson, L. Structure and Dynamics of the TIP3P, SPC, and SPC/E Water Models at 298 K. *J. Phys. Chem. A* **2001**, *105*, 9954–9960.
- (173) Hofsäuss, C.; Lindahl, E.; Edholm, O. Molecular Dynamics Simulations of Phospholipid Bilayers with Cholesterol. *Biophys. J.* **2003**, *84*, 2192–2206.
- (174) Roux, B.; Karplus, M. Ion Transport in a Gramicidin-like Channel: Dynamics and Mobility. *J. Phys. Chem.* **1991**, *95*, 4856–4868.
- (175) Vácha, R.; Martinez-Veracoechea, F. J.; Frenkel, D. Receptor-Mediated Endocytosis of Nanoparticles of Various Shapes. *Nano Lett.* **2011**, *11*, 5391–5395.
- (176) Vácha, R.; Martinez-Veracoechea, F. J.; Frenkel, D. Intracellular Release of Endocytosed Nanoparticles upon a Change of Ligand-Receptor Interaction. *ACS Nano* **2012**, *6*, 10598–10605.
- (177) Potts, R. O.; Guy, R. H. Predicting Skin Permeability. *Pharm. Res.* **1992**, *9*, 663–669.
- (178) Mitragotri, S.; Anissimov, Y. G.; Bunge, A. L.; Frisch, H. F.; Guy, R. H.; Hadgraft, J.; Kasting, G. B.; Lane, M. E.; Roberts, M. S. Mathematical Models of Skin Permeability: An Overview. *Int. J. Pharm.* **2011**, *418*, 115–129.
- (179) Kopeć, W.; Telenius, J.; Khandelia, H. Molecular Dynamics Simulations of the Interactions of Medicinal Plant Extracts and Drugs with Lipid Bilayer Membranes. *FEBS J.* **2013**, *280*, 2785–2805.
- (180) Notman, R.; Anwar, J.; Briels, W. J.; Noro, M. G.; den Otter, W. K. Simulations of Skin Barrier Function: Free Energies of Hydrophobic and Hydrophilic Transmembrane Pores in Ceramide Bilayers. *Biophys. J.* **2008**, *95*, 4763–4771.
- (181) Wohler, J.; Den Otter, W. K.; Edholm, O.; Briels, W. J. Free Energy of a Trans-Membrane Pore Calculated from Atomistic Molecular Dynamics Simulations. *J. Chem. Phys.* **2006**, *124*.
- (182) Bennett, W. F. D.; Tieleman, D. P. Water Defect and Pore Formation in Atomistic and Coarse-Grained Lipid Membranes: Pushing the Limits of Coarse Graining. *J. Chem. Theory Comput.* **2011**, *7*, 2981–2988.
- (183) Zhang, Y.; Voth, G. A. Combined Metadynamics and Umbrella Sampling Method for the Calculation of Ion Permeation Free Energy Profiles. *J. Chem. Theory Comput.* **2011**, *7*, 2277–2283.
- (184) Hansen, N.; van Gunsteren, W. F. Practical Aspects of Free-Energy Calculations: A Review. *J. Chem. Theory Comput.* **2014**, *10*, 2632–2647.
- (185) Pohorille, A.; Jarzynski, C.; Chipot, C. Good Practices in Free-Energy Calculations. *J. Phys. Chem. B* **2010**, *114*, 10235–10253.
- (186) Christ, C. D.; Mark, A. E.; Gunsteren, W. F. Van. Basic Ingredients of Free Energy Calculations: A Review. *J. Comput. Chem.* **2009**, *31*, 1569–1582.
- (187) Chipot, C.; Pohorille, A. *Free Energy Calculation*; Springer: Heidelberg, 2007; Vol. 1.
- (188) Bauer, B. A.; Lucas, T. R.; Meninger, D. J.; Patel, S. Water Permeation through DMPC Lipid Bilayers Using Polarizable Charge Equilibration Force Fields. *Chem. Phys. Lett.* **2011**, *508*, 289–294.
- (189) Lucas, T. R.; Bauer, B. A.; Patel, S. Charge Equilibration Force Fields for Molecular Dynamics Simulations of Lipids, Bilayers, and Integral Membrane Protein Systems. *Biochim. Biophys. Acta* **2012**, *1818*, 318–329.
- (190) Davis, J. E.; Rahaman, O.; Patel, S. Molecular Dynamics Simulations of a DMPC Bilayer

- Using Nonadditive Interaction Models. *Biophys. J.* **2009**, *96*, 385–402.
- (191) Davis, J. E.; Patel, S. Revised Charge Equilibration Parameters for More Accurate Hydration Free Energies of Alkanes. *Chem. Phys. Lett.* **2010**, *484*, 173–176.
- (192) Chowdhary, J.; Harder, E.; Lopes, P. E. M.; Huang, L.; MacKerell, A. D.; Roux, B. A Polarizable Force Field of Dipalmitoylphosphatidylcholine Based on the Classical Drude Model for Molecular Dynamics Simulations of Lipids. *J. Phys. Chem. B* **2013**, *117*, 9142–9160.
- (193) Kopelevich, D. I. One-Dimensional Potential of Mean Force Underestimates Activation Barrier for Transport across Flexible Lipid Membranes. *J. Chem. Phys.* **2013**, *139*.
- (194) MacCallum, J. L.; Bennett, W. F. D.; Tieleman, D. P. Partitioning of Amino Acid Side Chains into Lipid Bilayers: Results from Computer Simulations and Comparison to Experiment. *J. Gen. Physiol.* **2007**, *129*, 371–377.
- (195) Tsukanov, A. A.; Psakhie, S. G. A Review of Computer Simulation Studies of Cell Membrane Interaction with Neutral and Charged Nano-Objects. Quasi-Zero-Dimensional Nanoparticles, Drugs and Fullerenes. *Adv. Biomater. Devices Med.* **2015**, *2*, 44–53.
- (196) Xiang, T. X.; Anderson, B. D. Permeability of Acetic Acid across Gel and Liquid-Crystalline Lipid Bilayers Conforms to Free-Surface-Area Theory. *Biophys. J.* **1997**, *72*, 223–237.
- (197) Coppock, P. S.; Kindt, J. T. Atomistic Simulations of Mixed-Lipid Bilayers in Gel and Fluid Phases. *Langmuir* **2009**, *25*, 352–359.
- (198) Janůšová, B.; Zbytovská, J.; Lorenc, P.; Vavryšová, H.; Palát, K.; Hrabálek, A.; Vávrová, K. Effect of Ceramide Acyl Chain Length on Skin Permeability and Thermotropic Phase Behavior of Model Stratum Corneum Lipid Membranes. *Biochim. Biophys. Acta* **2011**, *1811*, 129–137.
- (199) Jalili, S.; Saeedi, M. Study of Curcumin Behavior in Two Different Lipid Bilayer Models of Liposomal Curcumin Using Molecular Dynamics Simulation. *J. Biomol. Struct. Dyn.* **2015**, 1–14.
- (200) Navrátilová, V.; Paloncýová, M.; Berka, K.; Otyepka, M. Effect of Lipid Charge on Membrane Immersion of Cytochrome P450 3A4. *Submitt. to J. Phys. Chem. B*.
- (201) Kucerka, N.; Perlmutter, J. D.; Pan, J.; Tristram-Nagle, S.; Katsaras, J.; Sachs, J. N. The Effect of Cholesterol on Short- and Long-Chain Monounsaturated Lipid Bilayers as Determined by Molecular Dynamics Simulations and X-Ray Scattering. *Biophys. J.* **2008**, *95*, 2792–2805.
- (202) Ollila, S.; Hyvo, M. T.; Karttunen, M.; Vattulainen, I. Assessing the Nature of Lipid Raft Membranes. *PLoS Comput. Biol.* **2007**, *3*.
- (203) Pasenkiewicz-Gierula, M.; Róg, T.; Kitamura, K.; Kusumi, A. Cholesterol Effects on the Phosphatidylcholine Bilayer Polar Region: A Molecular Simulation Study. *Biophys. J.* **2000**, *78*, 1376–1389.
- (204) Marrink, S. J.; de Vries, A. H.; Harroun, T. a; Katsaras, J.; Wassall, S. R. Cholesterol Shows Preference for the Interior of Polyunsaturated Lipid Membranes. *J. Am. Chem. Soc.* **2008**, *130*, 10–11.
- (205) Kucerka, N.; Marquardt, D.; Harroun, T. a; Nieh, M.-P.; Wassall, S. R.; Katsaras, J. The Functional Significance of Lipid Diversity: Orientation of Cholesterol in Bilayers Is Determined by Lipid Species. *J. Am. Chem. Soc.* **2009**, *131*, 16358–16359.
- (206) Falck, E.; Patra, M.; Karttunen, M.; Hyvönen, M. T.; Vattulainen, I. Lessons of Slicing Membranes: Interplay of Packing, Free Area, and Lateral Diffusion in Phospholipid/cholesterol Bilayers. *Biophys. J.* **2004**, *87*, 1076–1091.
- (207) Tieleman, D. P.; Marrink, S.-J. Lipids out of Equilibrium: Energetics of Desorption and Pore Mediated Flip-Flop. *J. Am. Chem. Soc.* **2006**, *128*, 12462–13467.
- (208) Huang, S.-M.; Zhang, L.; Giacomini, K. M. The International Transporter Consortium: A Collaborative Group of Scientists from Academia, Industry, and the FDA. *Clin. Pharmacol. Ther.* **2010**, *87*, 32–36.
- (209) Li, J.; Wen, P. C.; Moradi, M.; Tajkhorshid, E. Computational Characterization of Structural Dynamics Underlying Function in Active Membrane Transporters. *Curr. Opin. Struct. Biol.* **2015**, *31*, 96–105.

- (210) Khalili-Araghi, F.; Gumbart, J.; Wen, P. C.; Sotomayor, M.; Tajkhorshid, E.; Schulten, K. Molecular Dynamics Simulations of Membrane Channels and Transporters. *Curr. Opin. Struct. Biol.* **2009**, *19*, 128–137.
- (211) Ossman, T.; Fabre, G.; Berka, K.; Chantemargue, B.; Paloncýová, M.; Otyepka, M.; Di Meo, F.; Trouillas, P. In Silico Pharmacology: Drug Membrane Partitioning and Crossing. *Pharmacol. Res.* doi:10.1016/j.phrs.2016.06.030
- (212) Dwyer, D. S. Modeling and Molecular Dynamics Simulations of Membrane Transporter Proteins. In *Membrane Transporters*; Yan, Q., Ed.; Humana Press, 2003; Vol. 227, pp. 335–350.
- (213) Quistgaard, E. M.; Löw, C.; Guettou, F.; Nordlund, P. Understanding Transport by the Major Facilitator Superfamily (MFS): Structures Pave the Way. *Nat. Rev. Mol. Cell Biol.* **2016**, *17*, 123–132.
- (214) Wisedchaisri, G.; Park, M.-S.; Iadanza, M. G.; Zheng, H.; Gonen, T. Proton-Coupled Sugar Transport in the Prototypical Major Facilitator Superfamily Protein Xyle. *Nat. Commun.* **2014**, *5*, 4521.
- (215) Park, M.-S. Molecular Dynamics Simulations of the Human Glucose Transporter GLUT1. *PLoS One* **2015**, *10*, e0125361.
- (216) Jensen, M. Ø.; Yin, Y.; Tajkhorshid, E.; Schulten, K. Sugar Transport across Lactose Permease Probed by Steered Molecular Dynamics. *Biophys. J.* **2007**, *93*, 92–102.
- (217) Yin, Y.; Jensen, M. Ø.; Tajkhorshid, E.; Schulten, K. Sugar Binding and Protein Conformational Changes in Lactose Permease. *Biophys. J.* **2006**, *91*, 3972–3985.
- (218) Andersson, M.; Bondar, A.-N.; Freites, J. A.; Tobias, D. J.; Kaback, H. R.; White, S. H. Proton-Coupled Dynamics in Lactose Permease. *Struct. (London, Engl. 1993)* **2012**, *20*, 1893–1904.
- (219) Gyimesi, G.; Ramachandran, S.; Kota, P.; Dokholyan, N. V.; Sarkadi, B.; Hegedűs, T. ATP Hydrolysis at One of the Two Sites in ABC Transporters Initiates Transport Related Conformational Transitions. *Biochim. Biophys. Acta - Biomembr.* **2011**, *1808*, 2954–2964.
- (220) Gyimesi, G.; Ramachandran, S.; Kota, P.; Dokholyan, N. V.; Sarkadi, B.; Hegedűs, T. Corrigendum to “ATP Hydrolysis at One of the Two Sites in ABC Transporters Initiates Transport Related Conformational Transitions” [Biochim. Biophys. Acta 1808 (2011) 2954–2964]. *Biochim. Biophys. Acta - Biomembr.* **2012**, *1818*, 1435.
- (221) Napolitano, L. M. R.; Bisha, I.; De March, M.; Marchesi, A.; Arcangeletti, M.; Demitri, N.; Mazzolini, M.; Rodriguez, A.; Magistrato, A.; Onesti, S.; *et al.* A Structural, Functional, and Computational Analysis Suggests Pore Flexibility as the Base for the Poor Selectivity of CNG Channels. *Proc. Natl. Acad. Sci.* **2015**, 201503334.
- (222) Bisha, I.; Rodriguez, A.; Laio, A.; Magistrato, A. Metadynamics Simulations Reveal a Na⁺ Independent Exiting Path of Galactose for the Inward-Facing Conformation of vSGLT. *PLoS Comput. Biol.* **2014**, *10*, e1004017.
- (223) Cojocaru, V.; Balali-Mood, K.; Sansom, M. S. P.; Wade, R. C. Structure and Dynamics of the Membrane-Bound Cytochrome P450 2C9. *PLoS Comput. Biol.* **2011**, *7*, e1002152.
- (224) Baylon, J. L.; Lenov, I. L.; Sligar, S. G.; Tajkhorshid, E. Characterizing the Membrane-Bound State of Cytochrome P450 3A4: Structure, Depth of Insertion and Orientation. *J. Am. Chem. Soc.* **2013**, *135*, 8542–8551.
- (225) Denisov, I. G.; Shih, A. Y.; Sligar, S. G. Structural Differences between Soluble and Membrane Bound Cytochrome P450s. *J. Inorg. Biochem.* **2012**, *108*, 150–158.
- (226) Cui, Y.-L.; Xue, Q.; Zheng, Q.-C.; Zhang, J.-L.; Kong, C.-P.; Fan, J.-R.; Zhang, H.-X. Structural Features and Dynamic Investigations of the Membrane-Bound Cytochrome P450 17A1. *Biochim. Biophys. Acta - Biomembr.* **2015**, *1848*, 2013–2021.
- (227) Park, J.; Czaplá, L.; Amaro, R. Molecular Simulations of Aromatase Reveal New Insights into the Mechanism of Ligand Binding. *J. Chem. Inf. Model.* **2013**, *53*, 2047–2056.
- (228) Sgrignani, J.; Magistrato, A. Influence of the Membrane Lipophilic Environment on the Structure and on the Substrate Access/Egress Routes of the Human Aromatase Enzyme. A

- Computational Study. *J. Chem. Inf. Model.* **2012**, *52*, 1595–1606.
- (229) Navrátilová, V.; Paloncýová, M.; Kajšová, M.; Berka, K.; Otyepka, M. Effect of Cholesterol on the Structure of Membrane-Attached Cytochrome P450 3A4. *J. Chem. Inf. Model.* **2015**, *55*, 628–635.
- (230) Paloncýová, M.; Navrátilová, V.; Berka, K.; Laio, A.; Otyepka, M. Role of Enzyme Flexibility in Ligand Access and Egress to Active Site: Bias-Exchange Metadynamics Study of 1,3,7-Trimethyluric Acid in Cytochrome P450 3A4. *J. Chem. Theory Comput.* **2016**, *12*, 2101–2109.
- (231) Hritz, J.; De Ruiter, A.; Oostenbrink, C. Impact of Plasticity and Flexibility on Docking Results for Cytochrome P450 2D6: A Combined Approach of Molecular Dynamics and Ligand Docking. *J. Med. Chem.* **2008**, *51*, 7469–7477.
- (232) Scott, E. E.; Wolf, C. R.; Otyepka, M.; Humphreys, S. C.; Reed, J. R.; Henderson, C. J.; McLaughlin, L. A.; Paloncýová, M.; Navrátilová, V.; Berka, K.; *et al.* The Role of Protein-Protein and Protein-Membrane Interactions on P450 Function. *Drug Metab. Dispos.* **2016**, *44*, 576–590.
- (233) Školová, B.; Janušová, B.; Zbytovská, J.; Gooris, G.; Bouwstra, J.; Slepíčka, P.; Berka, P.; Roh, J.; Palát, K.; Hrabálek, A.; *et al.* Ceramides in the Skin Lipid Membranes: Length Matters. *Langmuir* **2013**, *29*, 15624–15633.
- (234) Shinkyo, R.; Guengerich, F. P. Inhibition of Human Cytochrome P450 3A4 by Cholesterol. *J. Biol. Chem.* **2011**, *286*, 18426–18433.

8. List of Publications

- (A1) Paloncýová, M.; Berka, K.; Otyepka, M. Convergence of Free Energy Profile of Coumarin in Lipid Bilayer. *J. Chem. Theory Comput.* **2012**, *8*, 1200–1211. In main text cited as ref³⁸
- (A2) Berka, K.; Paloncýová, M.; Anzenbacher, P.; Otyepka, M. Behavior of Human Cytochromes P450 on Lipid Membranes. *J. Phys. Chem. B* **2013**, *117*, 11556–11564. In main text cited as ref¹⁶⁵
- (A3) Paloncýová, M.; Berka, K.; Otyepka, M. Molecular Insight into Affinities of Drugs and Their Metabolites to Lipid Bilayers. *J. Phys. Chem. B* **2013**, *117*, 2403–2410. In main text cited as ref⁵²
- (A4) Podloucká, P.; Berka, K.; Fabre, G.; Paloncýová, M.; Duroux, J.-L. L.; Otyepka, M.; Trouillas, P. Lipid Bilayer Membrane Affinity Rationalizes Inhibition of Lipid Peroxidation by a Natural Lignan Antioxidant. *J. Phys. Chem. B* **2013**, *117*, 5043–5049. In main text cited as ref³⁴
- (A5) Paloncýová, M.; DeVane, R. H.; Murch, B. P.; Berka, K.; Otyepka, M. Rationalization of Reduced Penetration of Drugs through Ceramide Gel Phase Membrane. *Langmuir* **2014**, *30*, 13942–13948. In main text cited as ref¹⁰
- (A6) Paloncýová, M.; Devane, R.; Murch, B.; Berka, K.; Otyepka, M. Amphiphilic Drug-Like Molecules Accumulate in a Membrane below the Head Group Region. *J. Phys. Chem. B* **2014**, *118*, 1030–1039. In main text cited as ref⁶⁵
- (A7) Paloncýová, M.; Fabre, G.; DeVane, R. H.; Trouillas, P.; Berka, K.; Otyepka, M. Benchmarking of Force Fields for Molecule – Membrane Interactions. *J. Chem. Theory Comput.* **2014**, *10*, 4143–4151. In main text cited as ref⁶⁶
- (A8) Fabre, G.; Bayach, I.; Berka, K.; Paloncýová, M.; Starok, M.; Rossi, C.; Duroux, J.-L.; Otyepka, M.; Trouillas, P. Synergism of Antioxidant Action of Vitamins E, C and Quercetin Is Related to Formation of Molecular Associates in Biomembranes. *Chem. Commun.* **2015**, 7713–7716. In main text cited as ref⁷¹
- (A9) Navrátilová, V.; Paloncýová, M.; Kajšová, M.; Berka, K.; Otyepka, M. Effect of Cholesterol on the Structure of Membrane-Attached Cytochrome P450 3A4. *J. Chem. Inf. Model.* **2015**, *55*, 628–635. In main text cited as ref²²⁹
- (A10) Paloncýová, M.; Vávrová, K.; Sovová, Ž.; DeVane, R. H.; Otyepka, M.; Berka, K. Structural Changes in Ceramide Bilayers Rationalize Increased Permeation through Stratum Corneum Models with Shorter Acyl Tails. *J. Phys. Chem. B* **2015**, *119*, 9811–9819. In main text cited as ref¹⁴¹
- (A11) Paloncýová, M.; Navrátilová, V.; Berka, K.; Laio, A.; Otyepka, M. Role of Enzyme Flexibility in Ligand Access and Egress to Active Site: Bias-Exchange Metadynamics Study of 1,3,7-Trimethyluric Acid in Cytochrome P450 3A4. *J. Chem. Theory Comput.* **2016**, *12*, 2101–2109. In main text cited as ref²³⁰
- (A12) Scott, E. E.; Wolf, C. R.; Otyepka, M.; Humphreys, S. C.; Reed, J. R.; Henderson, C. J.; McLaughlin, L. A.; Paloncýová, M.; Navratilova, V.; Berka, K.; *et al.* The Role of Protein-Protein and Protein-Membrane Interactions on P450 Function. *Drug Metab. Dispos.* **2016**, *44*, 576–590. In main text cited as ref²³²
- (A13) Navrátilová, V.; Paloncýová, M.; Berka, K.; Otyepka, M. Effect of Lipid Charge on Membrane Immersion of Cytochrome P450 3A4. *Submitt. to J. Phys. Chem. B*. Ref²⁰⁰
- (A14) Ossman, T.; Fabre, G.; Berka, K.; Chantemargue, B.; Paloncýová, M.; Otyepka, M.; Di Meo, F.; Trouillas, P. In Silico Pharmacology: Drug Membrane Partitioning and Crossing. *Pharmacol. Res.* doi:10.1016/j.phrs.2016.06.030 In main text cited as ref²¹¹

9. Appendices

Convergence of Free Energy Profile of Coumarin in Lipid Bilayer

Markéta Paloncýová,[†] Karel Berka,^{*,†} and Michal Otyepka^{*,†}[†]Regional Centre of Advanced Technologies and Materials, Department of Physical Chemistry, Faculty of Science, Palacky University, tr. 17 listopadu 12, 771 46, Olomouc, Czech Republic

S Supporting Information

ABSTRACT: Atomistic molecular dynamics (MD) simulations of druglike molecules embedded in lipid bilayers are of considerable interest as models for drug penetration and positioning in biological membranes. Here we analyze partitioning of coumarin in dioleoylphosphatidylcholine (DOPC) bilayer, based on both multiple, unbiased 3 μ s MD simulations (total length) and free energy profiles along the bilayer normal calculated by biased MD simulations ($\sim 7 \mu$ s in total). The convergences in time of free energy profiles calculated by both umbrella sampling and z-constraint techniques are thoroughly analyzed. Two sets of starting structures are also considered, one from unbiased MD simulation and the other from “pulling” coumarin along the bilayer normal. The structures obtained by pulling simulation contain water defects on the lipid bilayer surface, while those acquired from unbiased simulation have no membrane defects. The free energy profiles converge more rapidly when starting frames from unbiased simulations are used. In addition, z-constraint simulation leads to more rapid convergence than umbrella sampling, due to quicker relaxation of membrane defects. Furthermore, we show that the choice of RESP, PRODRG, or Mulliken charges considerably affects the resulting free energy profile of our model drug along the bilayer normal. We recommend using z-constraint biased MD simulations based on starting geometries acquired from unbiased MD simulations for efficient calculation of convergent free energy profiles of druglike molecules along bilayer normals. The calculation of free energy profile should start with an unbiased simulation, though the polar molecules might need a slow pulling afterward. Results obtained with the recommended simulation protocol agree well with available experimental data for two coumarin derivatives.

INTRODUCTION

Passive transport of drugs through membranes is the main process limiting their penetration into cells (in the absence of a specific active transporter) and thus a key step in their administration to the bodies of humans (and animals). Diffusion through membrane and partitioning between water and membrane phases are the key properties for this passive transport affecting kinetics and thermodynamics of permeation process,^{1,2} respectively. Further, the equilibrium position of specific drugs in target membranes also affects their metabolism and transport (both active and passive).^{3–5}

The composition of biological membranes is complex and diverse, varying substantially among the outer and inner leaflets of both organelles and organs.^{6,7} They consist of proteins and lipids, in approximately equal mass proportions.⁸ While proteins are responsible for active transport and signaling, lipids pose the main barrier to passive membrane transport. The most important membrane for drug administration is the plasma membrane, through which drugs must penetrate to reach the internal milieu of target cells. However, mitochondrial and endoplasmic reticulum membranes are also involved in drug metabolism because they accommodate various drug-metabolizing enzymes (e.g., cytochromes P450 and UDP-glucuronosyltransferases).^{5,9,10} The most abundant lipids in mammalian membranes are phosphatidylcholines (PC), although phosphatidylserines, phosphatidylethanolamines, sphingomyelins, and cholesterol are also present,¹¹ thus PC bilayers are commonly used as simple membrane models. However, it must be remembered that in vivo membranes are much more complex, so results obtained using such simple models should be interpreted cautiously.

Several structural frameworks of lipid bilayers have been proposed, including the four-region model of Marrink and Berendsen¹² and others presented by Neale et al.¹³ and Orsi et al.¹⁴ The four-region model, applied in the study presented here, describes the physicochemical properties and densities of lipids in the following four regions along a bilayer's normal axis (Figure 1):

- (i) The *low headgroup density* region (hereafter region 1), a polar zone with similar transport conditions to water, from the point where head groups are first encountered (at minimal density) and ending where the densities of head groups and water are comparable.
- (ii) The highly structured *high headgroup density* region (region 2), from the point where region 1 ends to the point closer to the bilayer center where the density of water decreases to below 1% and bulklike water disappears. Strong Coulombic interactions between polar groups keep polar molecules in the first two regions.¹⁵
- (iii) The *high density of acyl chains* region (region 3) is hydrophobic. Double bonds of unsaturated lipids are typically localized in this region.
- (iv) The fourth, *low density of acyl chains* region (region 4), resides in the middle of the bilayer and terminal methyl groups are primarily located in this region. Here, movement of all molecules is faster due to its low density. The two hydrophobic acyl chain regions are

Received: December 22, 2011

Published: February 24, 2012

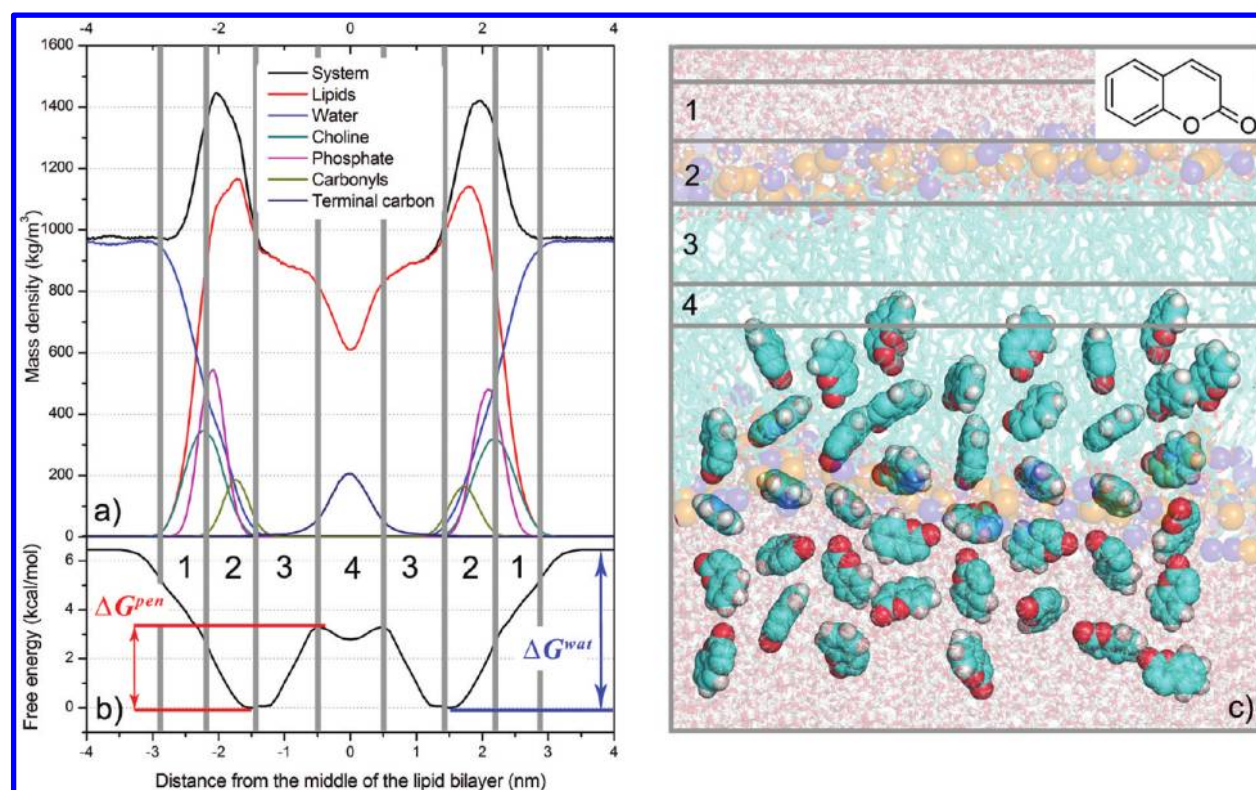


Figure 1. Upper left panel (a): density profile of DOPC bilayer along the normal to the lipid bilayer plane showing densities of the complete system (black), water (blue), DOPC (red), phosphates (magenta), cholines (cyan), carbonyls (green), and terminal carbons (dark blue). Lower left panel (b): free energy profile of coumarin along the DOPC bilayer normal calculated from constraint simulation with initial structures obtained by free simulation (CF). The calculated bilayer center penetration barrier, ΔG^{pen} , and water/lipids barrier, ΔG^{wat} , are labeled. The free energy profile was calculated for one bilayer leaflet and was symmetrized to the other one, the densities of the system were symmetrized along the middle of the bilayer. The vertical bins labeled by numbers denote four bilayer regions: 1 – low density of head groups (2.2–2.9 nm), 2 – high density of head groups (1.45–2.2 nm), 3 – high density of acyl chains (0.5–1.45 nm), and 4 – low density of acyl chains (0–0.5 nm). Right panel (c): structure of DOPC bilayer, together with snapshots of coumarin initial structures. Carbons are colored in cyan, oxygens red, and hydrogens white. The olive and blue balls represent DOPC phosphate and nitrogen atoms.

believed to form the main barrier for most druglike molecules, which are often water-soluble.^{4,16}

Molecular dynamics (MD) simulations can be used to estimate the equilibrium position of a drug in a lipid bilayer, its partition coefficients and diffusion coefficients simultaneously at subpicosecond and atomic resolution.^{4,15,17,18} The partitioning and mean position can be well described by a free energy (ΔG) profile along the normal to the lipid bilayer,^{5,13,18,19} also known as a potential of mean force (PMF). In principle, such free energy profiles can be calculated from partitioning values obtained by long unbiased simulation. However, this approach only provides reliable free energy profiles when all states along the ΔG profile are thoroughly sampled. This is challenging for unbiased MD simulations, because they usually do not sample adequately at the available simulation time scales. The sampling problem is based on the dependence of probability of drug crossing a membrane on the energy barrier for this phenomenon. The probability of membrane crossing decreases exponentially with the energy barrier (Eq. S1 in the Supporting Information). If a barrier for a drug crossing a membrane is higher than ~ 10 kcal/mol, the statistical probability of spontaneous membrane crossing is very low within typical time scales (hundreds of nanoseconds) accessible by unbiased atomistic MD simulations. Therefore during unbiased MD simulations, the polar molecules do not usually enter freely the

deeper parts of bilayer and the nonpolar molecules do not sample enough of the area of bulk water.

Free energy profiles can also be calculated by biased MD simulations. Great advances have been made in this field in recent years, and numerous methods for obtaining free energy profiles have been developed, including umbrella sampling,^{18,19} z-constraint method,^{12,14,15,17,18,22,23} metadynamics,^{24,25} adaptive biasing force,^{26,27} particle insertion,²² and others.^{28,29} However, although these techniques undoubtedly enhance sampling, all of them have drawbacks for estimating free energy profiles along bilayer normals. For example, in an analysis of interactions between charged and neutral forms of ibuprofen and aspirin with a dipalmitoylphosphatidylcholine (DPPC) bilayer, Boggara and Krishnamoorti¹⁸ noted that the drugs (especially charged forms) caused deformations of the lipid bilayer in z-constraint simulations. Similarly, MacCallum et al.³⁰ observed “water defects” at the water–lipid interface in umbrella simulations applied for calculating free energy profiles of amino acids along the normal of a dioleoylphosphatidylcholine (DOPC) bilayer. Such deformation of lipid bilayer in simulations was recently analyzed by Neale et al., who identified it as a systematic sampling error of considerable interest. Neale and co-workers stressed that this systematic sampling error complicated the convergence of free energy profiles of druglike molecules along lipid bilayer normals, especially for charged molecules.

As this systematic error may also originate during the generation of starting structure sets used for biased MD simulations, this issue has been addressed in several previous studies using various strategies. Neale et al.¹³ used an inflatogro procedure,³¹ in which (briefly) a pre-equilibrated bilayer is expanded, a molecule of interest is inserted, and the bilayer is compressed and re-equilibrated. Boggara and Krishnamoorti¹⁸ inserted molecules into a lipid bilayer manually using the VMD visualization program.³² Other approaches for generating starting structures have included growing the molecule inside the bilayer from zero size,¹⁴ pulling simulation,⁵ snapshots from unbiased simulation,³³ and estimation of reaction coordinates using metadynamics.²⁴ However, no methodological analyses of this problem have been previously published.

Here, based on an examination of the embedding of a nonpolar druglike molecule (coumarin; 1,2-benzopyrone) in DOPC bilayer, we show that systematic sampling error is difficult to avoid, but it can be reduced by using appropriate biased simulation and initial structure set generation method. Coumarin naturally occurs in diverse plants, including tonka beans (*Dipteryx odorata*), vanilla grass (*Anthoxanthum odoratum*), sweet woodruff (*Galium odoratum*), sweet clover (*Melilotus* L.), sweet grass (*Hierochloa odorata*), and cassia cinnamon (*Cinnamomum aromaticum*). It is absorbed by humans both orally from food and through the skin from perfumes. Further, it is a valuable test substance because it is a small, planar, rather rigid, nonpolar ($\log P_{\text{oct/wat}} 1.39^{34}$), biologically significant druglike molecule, as its skeleton can be recognized in many drugs (e.g., the anticoagulant warfarin and antispasmodic/insecticide hycromone³⁵) and other biologically active compounds (e.g., scopolin). Therefore, coumarin is an ideal model for assessing the quality of various methods for calculating ΔG profiles of small low-polar druglike molecules along normals of lipid bilayers. DOPC bilayer has been previously used as a model of endoplasmic reticulum membrane, in which coumarin is metabolized by membrane-anchored Cytochrome P450 2A6.^{36,37}

The main aim of the study was to identify the mean position of coumarin in DOPC bilayer from calculations of free energy profiles using different biased MD simulations and different sets of initial structures. We also discuss convergence, advantages and disadvantages of z -constraint, and umbrella sampling methods using starting structures obtained by pulling and unbiased simulations. We focus on the systematic bias caused by choice of the initial structure set and the possibilities of avoiding this bias. The effect of choice of partial charges is also analyzed and results of biased and unbiased MD simulations (3 μs in total) are compared. Finally, a robust simulation protocol for obtaining a convergent free energy profile along a bilayer normal is suggested and tested against available experimental data for two coumarin derivatives embedded in dimyristoylphosphatidylcholine (DMPC) bilayer.

METHODS

The structure and topology of coumarin (1,2-benzopyrone; CAS number 91-64-5) was generated by the PRODRG2 Beta server³⁸ using the GROMOS 53a6 forcefield.³⁹ However, partial charges assigned by PRODRG have been found to lead to unrealistic partitioning between water and cyclohexane phases.⁴⁰ As the partial charges used can introduce another systematic error into free energy calculations, we addressed this problem by also using Mulliken partial charges and restrained fit of electrostatic potential (RESP) partial charges. The RESP

partial charges were successfully adopted by the second generation of AMBER family force fields. The electrostatic potential (ESP) and ESP partial charges were calculated by applying B3LYP/cc-pVDZ method to coumarin geometry optimized at the same level of theory in Gaussian 03.⁴¹ RESP fit⁴² was implemented by Antechamber from the AMBER 11 software package.⁴³ Mulliken partial charges, that were adopted by Berger lipid force field,⁴⁴ were calculated at the HF/6-31G* level in gas phase. Hereafter, all mentioned coumarin charges are RESP charges, except those explicitly named as PRODRG or Mulliken charges.

The lipid bilayer, as prepared and equilibrated by Siu et al.,⁴⁵ contained 128 DOPC molecules, 64 in each leaflet, with a structure generated by the Lipidbook server.⁴⁶ The bilayer was oriented perpendicularly to the z -axis of the simulation box and equilibrated for another 10 ns by a free MD simulation. Water and salt (NaCl) were added to give a physiological concentration, of 0.154 M, of salt in the aqueous phase (excluding the lipid bilayer from the volume calculation). The equilibrated box contained 5,188 molecules of Flexible Simple Point Charge (SPC) water,⁴⁷ 19 Na^+ and 19 Cl^- ions. The equilibrated surface area per lipid was 0.638 nm^2 , and the start of the z -axis was set in the middle of the bilayer.

The GROMACS 4.0.7 package⁴⁸ and united atom Berger lipid force field⁴⁴ were used for MD simulations. The latter reduces the number of atoms in simulations, as it merges nonaromatic and nonpolar hydrogens with their carbons. This simplification likely results in higher diffusion coefficients than those observed in all-atom model simulations.⁴⁹ Berger lipid force field⁴⁴ uses the Mulliken partial charges calculated at the HF/6-31G* level (in gas phase).⁵⁰ Simulations were taken with 2-fs integration time steps under periodic boundary conditions in all directions, with particle-mesh Ewald (PME) electrostatics,⁵¹ a van der Waals cutoff at 1 nm, bond constraints determined by the LINCS algorithm,⁵² V-rescale temperature coupling⁵³ to 310 K, and Berendsen anisotropic pressure coupling⁵⁴ to 1 bar with 10 ps time constant and compressibility of $4.5 \times 10^{-5} \text{ bar}^{-1}$.

A coumarin molecule was placed at the top of the simulation box, a 0.5 ns MD simulation was executed to pre-equilibrate the system, then five independent MD simulations with a total time of 3 μs were generated. From the pre-equilibrated simulation two sets of starting frames for biased MD simulations were generated: one by pulling coumarin to the bilayer center and the other from unbiased MD simulation. The first set of starting frames for biased MD simulations was obtained by pulling the center-of-mass (COM) of coumarin against that of the lipid bilayer (in its center). Coumarin was pulled along the bilayer normal (the z -axis) for 6 ns using a pulling force constant of $10,000 \text{ kJ}\cdot\text{mol}^{-1}\cdot\text{nm}^{-2}$ ($2,390 \text{ kcal}\cdot\text{mol}^{-1}\cdot\text{nm}^{-2}$) and pulling rate of $1 \text{ nm}\cdot\text{ns}^{-1}$. Pulling applies a harmonic potential on molecule and moves the center of this potential with a given pull rate. Starting positions were collected as snapshots from the pulling simulation, spaced $0.1 \pm 0.02 \text{ nm}$ apart along the z -axis from the area of bulk water (4 nm from the bilayer center) to the middle of the bilayer. From the structures at one distance bin, the structure with the lowest potential energy was chosen as the starting frame for biased MD simulations at a given distance from the center of the lipid bilayer. Hereafter, constraint and umbrella simulations with initial structures generated by pulling simulations are referred to as constraint-pulling (CP) and umbrella-pulling (UP), respectively.

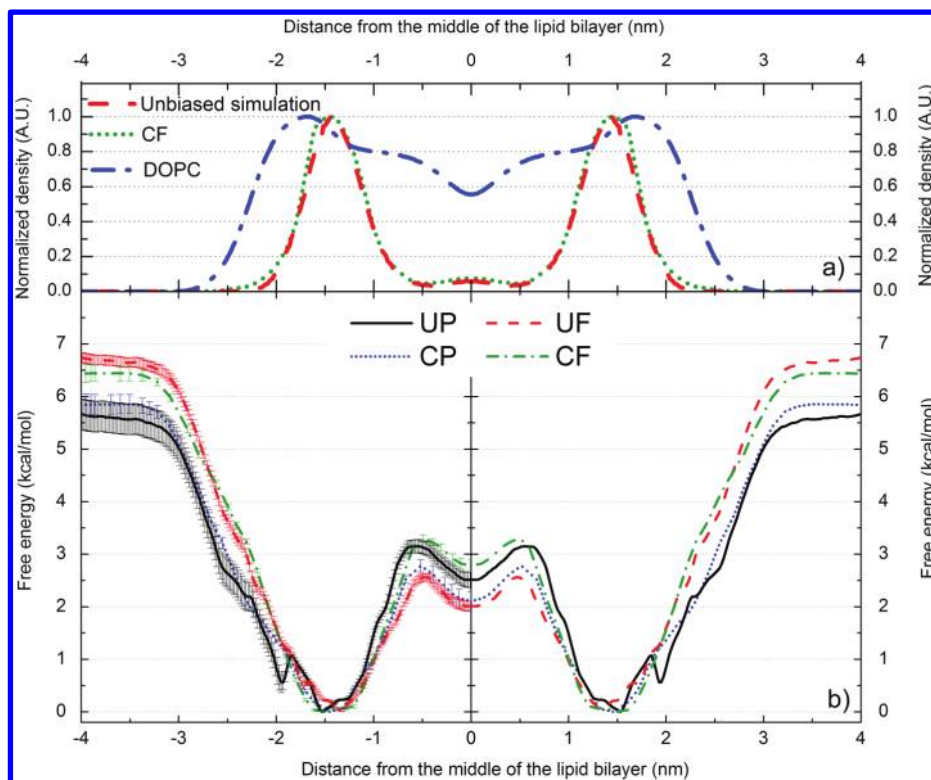


Figure 2. Density profiles of DOPC (blue dash-dotted curves) and coumarin calculated from unbiased MD simulations (3 μ s in total; red dashed curves) and from the free energy profile acquired by the CF method (green dotted curve). The density profiles of coumarin obtained from both methods match each other well (upper panel – a). Free energy profiles obtained from biased simulations (lower panel – b). Both umbrella (UP – black curve and UF – red curve) and constraint (CP – dotted blue curve and CF – dotted green curve) simulations provide free energy minima positions for coumarin that overlap well with the maximum density calculated from the free simulation (cf. upper panel – a). The free energy profiles were calculated for one bilayer leaflet and were symmetrized to the other one; the density was symmetrized along the middle of the bilayer. UP and UF refer to umbrella simulations with initial structures obtained by pulling and free unbiased simulation, respectively; CP and CF refer to constraint simulation with pulling and free initial structures, respectively.

In the other approach for generating starting frames, in which free unbiased simulation (20 ns long) was applied, spontaneous coumarin penetration through the DOPC bilayer was observed. Starting frames (spaced 0.1 ± 0.02 nm apart along the z -axis with the lowest potential energy of the structure at the respective points) for umbrella and constraint simulations were chosen as described above. Simulations with these starting structures are henceforth referred to as umbrella-free (UF) and constraint-free (CF), respectively.

With both sets of starting frames, umbrella sampling and constraint simulations (164 simulation windows in total) were carried out as described below for 30 ns per simulation window, except for simulation bins in the 1.0–2.5 nm z -axis region (for which simulation was prolonged for 50 ns, or up to 100 ns for CP and CF simulations, giving in the latter cases up to 6.9 μ s of biased simulation in total).

In umbrella sampling a harmonic potential is applied between COMs of two groups of molecules, here the drug coumarin and DOPC lipid bilayer. The distance between COMs of coumarin and DOPC was restrained by a harmonic force constant of $2,000 \text{ kJ}\cdot\text{mol}^{-1}\cdot\text{nm}^{-2}$ ($477.9 \text{ kcal}\cdot\text{mol}^{-1}\cdot\text{nm}^{-2}$). The force applied on coumarin was proportional to the square of the displacement from its original position, and a free energy profile was calculated from eq 1^{4,55}

$$\Delta G(z) = -RT \ln P(z) + U(z) \quad (1)$$

where $P(z)$ and $U(z)$ are the coumarin distribution and biasing potential along the bilayer normal, respectively. The force

constant and distance between simulation windows were chosen to achieve equal sampling, as the presence of regions with low sampling density increases the error of umbrella sampling. Forces acting on coumarin were analyzed, and the free energy profile was reconstructed by the weighted histogram analysis method (WHAM)²⁰ using the *g_wham* program.⁵⁶

We also calculated a free energy profile from constraint simulations.^{14,15,18} In this approach, the distance between COMs of the drug and lipid bilayer was constrained, and the constraint force was monitored. Free energy was then calculated from eq 2^{4,16,17,57}

$$\Delta G(z) = - \int_{\text{outside}}^z \langle \vec{F}(z') \rangle_t dz' \quad (2)$$

where the mean force applied on the molecule $\langle \vec{F}(z') \rangle_t$ in certain bilayer depth z' is integrated along the bilayer normal axis beginning in water until the certain bilayer depth z .

Part of the free energy profile was also calculated from the partitioning displayed in an unbiased simulation using eq 3¹⁵

$$\Delta G(z) = -RT \ln K(z) \quad (3)$$

where $K(z)$ is a partition coefficient estimated for a 0.02 nm bin in bilayer depth z , symmetrized for both leaflets. The partition coefficient is calculated from average mass density of coumarin in certain bin and by normalizing this density – the reference state is set to have $K(z) = 1$.

The minimum free energy ($\Delta G = 0$ kcal/mol) of coumarin along the bilayer normal was considered the reference state in all profiles. All free energy profiles were calculated for one lipid leaflet and have been symmetrized for the other one. Error estimates of free energy were calculated as integrated standard deviations of the mean calculated either over the bins of 100 bootstraps generated by Bayesian bootstrap analysis by the *g_wham* program⁵⁶ in umbrella sampling or over the force distribution in 0.1 nm-spaced positions along the *z*-axis in constraint simulations.

For comparison with experimental data (see later) free energy profiles of 7-acetoxy-4-methylcoumarin and 7-acetoxycoumarin along the normal of a DMPC bilayer were calculated (using a DMPC bilayer structure with 128 DMPC molecules and 3,655 water molecules taken from Tieleman's Web site,⁵⁸ after replacing 20 molecules of water by 10 Na⁺ and 10 Cl⁻ ions). The lipid bilayer was equilibrated for 200 ns. 7-Acetoxy-4-methylcoumarin topology was prepared by the simulation protocol described above for coumarin (including the use of RESP partial charges). Initial structure was generated from a 20 ns unbiased free simulation. During this simulation, 7-acetoxy-4-methylcoumarin penetrated to 1.8 nm from the middle of the bilayer and was then pulled into the bilayer for 4 ns with a pulling rate of 1 nm·ns⁻¹ and a pulling force constant of 500 kJ·mol⁻¹·nm⁻² (119.5 kcal·mol⁻¹·nm⁻²). The mild force constant was chosen to avoid water artifacts, as the molecule did not penetrate into region 3 freely during the unbiased simulation and was still in touch with water molecules. A 10 ns constraint simulation was performed with the same simulation protocol as applied in the coumarin CF simulation, but the simulation near the equilibrium position (0.8–1.7 nm) was prolonged to 15 ns per simulation bin.

A free energy profile of 7-acetoxycoumarin was obtained by the same protocol as for 7-acetoxy-4-methylcoumarin, except the free simulation lasted 60 ns and during this time 7-acetoxycoumarin penetrated to 0.5 nm from the center of the lipid bilayer, then the molecule was pulled further into the bilayer for 1 ns with a pulling rate of 1 nm·ns⁻¹ and force constant of 2,000 kJ·mol⁻¹·nm⁻² (477.9 kcal·mol⁻¹·nm⁻²). The molecule freely penetrated close to the bilayer center and thus was pulled with a higher force constant than in the previous case. A free energy profile was obtained by *z*-constraint simulation, which yielded a very large minimum energy zone, with substantial variation in mean forces, so the simulation was prolonged to 15 ns in the interval between 1.0 and 2.0 nm and more frames were added (so the distance between simulation windows was 0.05 nm in the zone between 1.0 and 2.0 nm).

RESULTS

Unbiased MD Simulations. Five independent unbiased simulations starting from coumarin in water, 3 μ s long in total (2 \times 1 μ s, 600 ns, 2 \times 200 ns), showed a tendency for coumarin to stay at the boundary between regions 2 and 3, as coumarin was most frequently located 1.4 \pm 0.1 nm from the bilayer center (see Supporting Information, Figure S1). Once a coumarin molecule entered the bilayer during the first 10 ns of the simulation, it did not leave the lipid bilayer during the rest of simulation (Figure S1). Coumarin occurred in both leaflets because it can transverse the bilayer center spontaneously. Twelve successful (and ten unsuccessful) transitions between leaflets were observed during the 3 μ s of simulations (Figure S1). The transition between both leaflets took place on a 100+ ns time scale, but the transition process itself was rapid

and lasted several nanoseconds. The unbiased simulations also identified a metastable state of coumarin in the bilayer center (Figure 2), where coumarin stayed up to 10 ns. The transition between the bilayer center and one leaflet occurred on time scales of ps up to ns (Figure S1). The bilayer center penetration barrier calculated from the partition coefficient profile (cf. Equation 3) was 2.1 kcal/mol, but the water/lipids barrier could not be calculated, as the distribution of coumarin in water was not properly sampled (Figure S1 and Figure 2).

Biased Simulations. The free energy profiles of coumarin in DOPC lipid bilayer reconstructed from four types of biased (UP, CP, UF, and CF) simulations showed similar trends (Figure 2). Typically, the free energy dropped as coumarin entered region 1 (cf. Figure 1). As it moved deeper into the bilayer, the free energy decreased and the global free energy minimum was reached at the border between regions 2 and 3. When coumarin moved deeper into the bilayer center, the free energy rose. A small local minimum was located in the bilayer center (region 4). So, one global minimum at 1.35–1.53 nm (with a thermally accessible region within 1.05–1.95 nm at 310 K – by thermally accessible region we mean an area with energy barrier of RT (0.616 kcal/mol at 310 K) from the energy minimum) and one local minimum in the middle of the lipid bilayer were common features of all free energy profiles (Figure 2).

The bilayer center penetration barriers (ΔG^{pen}) obtained from the free energy profiles fitted a narrow interval, varying between 2.6–3.3 kcal/mol (Table 1, Figure 2). The water/

Table 1. Properties Extracted from the Free Energy Profiles Calculated by Four Different Simulation Protocols with 50 ns of Biased Simulation Per Window^a

simulation protocol	position of minimum (nm)	area within a reach of a thermal motion at 310 K (nm)		ΔG^{wat} (kcal/mol)	ΔG^{pen} (kcal/mol)
UP	1.53	1.15	1.95	5.7 \pm 0.3	3.2 \pm 0.2
UF	1.35	1.09	1.75	6.7 \pm 0.1	2.6 \pm 0.1
CP	1.47	1.20	1.71	5.9 \pm 0.2	2.8 \pm 0.1
CF	1.49	1.10	1.80	6.4 \pm 0.2	3.3 \pm 0.1

^aUP and UF refer to umbrella simulations with initial structures obtained by pulling and free unbiased simulation, respectively; CP and CF refer to constraint simulation with pulling and free initial structures, respectively. ΔG^{wat} and ΔG^{pen} are water/lipid and bilayer center penetration barriers, respectively. Area within reach of a thermal motion is considered to be the area surrounded by an energy barrier of RT (0.616 kcal/mol, *T* = 310 K).

lipids barrier (ΔG^{wat}) fitted an interval of 5.7–6.7 kcal/mol, and the values calculated with pulling initial structures were lower than those calculated in simulations with initial structures from unbiased simulations (ΔG^{wat} values derived from UP, CP, UF, and CF simulations were 5.7 \pm 0.3, 5.9 \pm 0.2, 6.7 \pm 0.1, and 6.4 \pm 0.2 kcal/mol, respectively; Table 1 and Figure 2). The UP free energy profile also showed a very shallow local minimum at 1.95 nm with an energy barrier of 0.5 kcal/mol (Figure 2). The free energy barrier of this minimum was higher than the free energy error bar estimated by statistical bootstrap analysis (0.1 kcal/mol), but the error seemed to be underestimated. As the depth of the shallow minimum declined with increasing duration of simulation windows (see the following paragraph “Convergence of Biased Simulations”) and no state

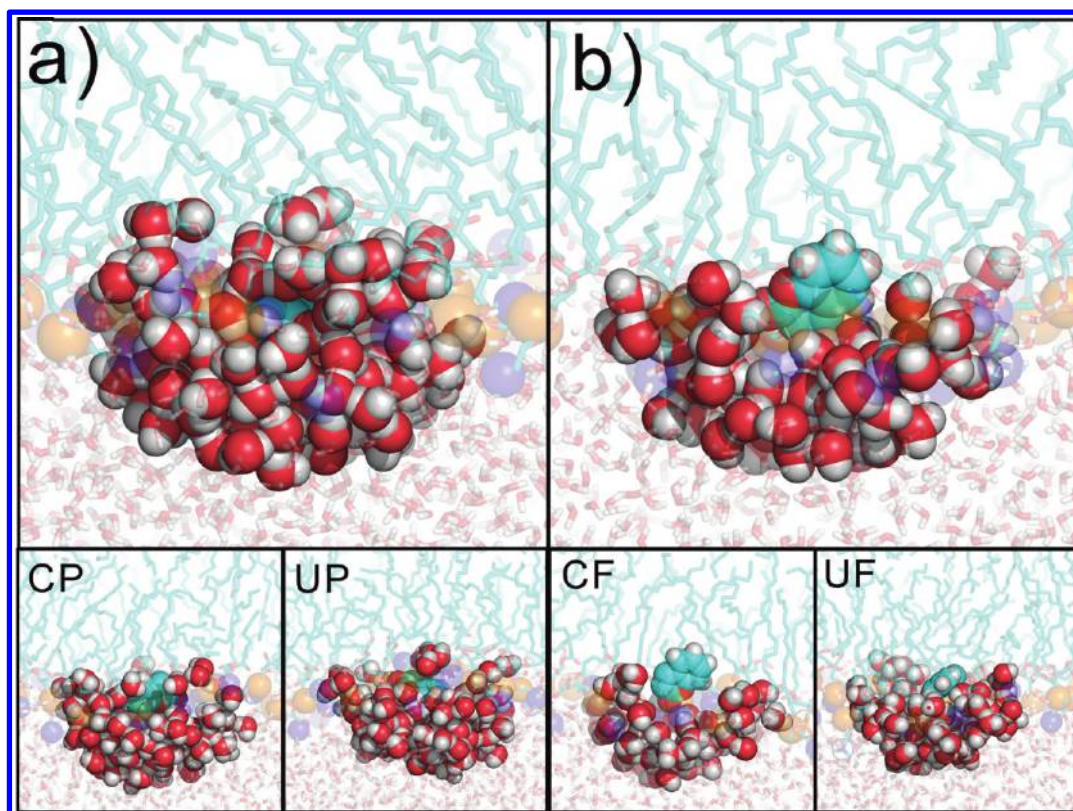


Figure 3. Initial structures (at 1.9 nm from the bilayer center) obtained by pulling (a) and free simulation (b) show a difference in coumarin hydration. The structure generated by pulling simulations indicates that coumarin is pulled to the lipid bilayer with its solvation shell, which causes funnel-like bilayer deformation. Snapshots taken at 10 ns indicate that CP eliminates coumarin hydration more rapidly than UP. Both CF and UF simulations lead to similarly solvated coumarin structures. Carbons are colored in cyan, oxygens red, and hydrogens white. The olive and blue balls represent DOPC phosphate and nitrogen atoms, respectively. Waters surrounding coumarin are colored as red/white balls. UP and UF refer to umbrella simulations with initial structures obtained by pulling and free unbiased simulation, respectively; CP and CF refer to constraint simulation with pulling and free initial structures, respectively.

corresponding to this minimum was observed in the unbiased simulation (Figure S1 in the Supporting Information), we considered this minimum to be an artifact and called it “the artificial minimum”.

As such “artificial minima” may be due to systematic sampling errors, it was of considerable interest to determine the reasons for such behavior. The primary reason lay in the starting structures, which were generated by pulling coumarin along the bilayer normal in the UP and CP simulations. The pulling caused deformation of the lipid bilayer,^{13,18} leading to a funnel-shaped bilayer surface depression (see Supporting Information, Figure S2) induced by solvated coumarin (Figure 3a). In other words, the pulling procedure produced structures in which coumarin embedded in the bilayer was hydrated by a few water molecules. The defects, namely these which were deeper in lipid bilayer, were eliminated during biased MD simulations, as water was expelled from the hydrophobic bilayer interior and bilayer relaxed rapidly on hundreds of picoseconds time scale. The relaxation time grew with increasing distance from the bilayer center. In the area of the artificial minimum ($\sim 1.7\text{--}2.0$ nm), close to the bilayer surface, the water defects were eliminated on a tens of nanoseconds time scale. It is of considerable interest that relaxation occurred significantly more rapidly in the CP than in UP simulations, and thus the membrane deformation was eliminated more rapidly (Figure 3 and Figure 4). The lipid bilayer depression was not observed during a spontaneous embedment of coumarin in the lipid

bilayer in the unbiased simulations, hence the starting structures for biased simulations based on the snapshots from the unbiased simulation were free of this artifact (Figure 3b).

Convergence of Biased Simulations. The position of the global minimum converged more rapidly in biased simulations starting from free (unbiased) simulations (UF and CF) than in simulations starting from pulling (UP and CP) simulations (Figure 4). The free energy profile obtained from UP simulation depended strongly on the length of the simulation windows, and two energetically similar minima in region 2 (one at ~ 1.5 and the other at ~ 2.0 nm) were observed during the beginning of this simulation (Figure 4). After 10 ns the minimum at ~ 1.5 nm became the global minimum and its position converged to 1.53 nm, while the energy barrier of the artificial minimum decreased to 0.5 kcal/mol. During the first 16 ns of UP simulation the area accessible by thermal motion ($\Delta G_{\text{min}} + RT$) gradually widened from 0.90 nm after 5 ns to 1.10 nm, and the region accessible by thermal motion thereafter declined to 0.80 nm. ΔG^{wat} gradually rose throughout the simulation, to a final value (at 50 ns) of 5.7 ± 0.3 kcal/mol, while ΔG^{pen} dropped within the first 16 ns of simulation, slowly rose until 30 ns, and then fluctuated around a final value of 3.2 ± 0.2 kcal/mol (cf. Figure 4).

The free energy profile obtained from CP simulation also displayed two minima initially, while the artificial minimum (at ~ 2.0 nm) quickly vanished, and after ~ 15 ns there was no sign of this minimum. The area within reach of thermal motion

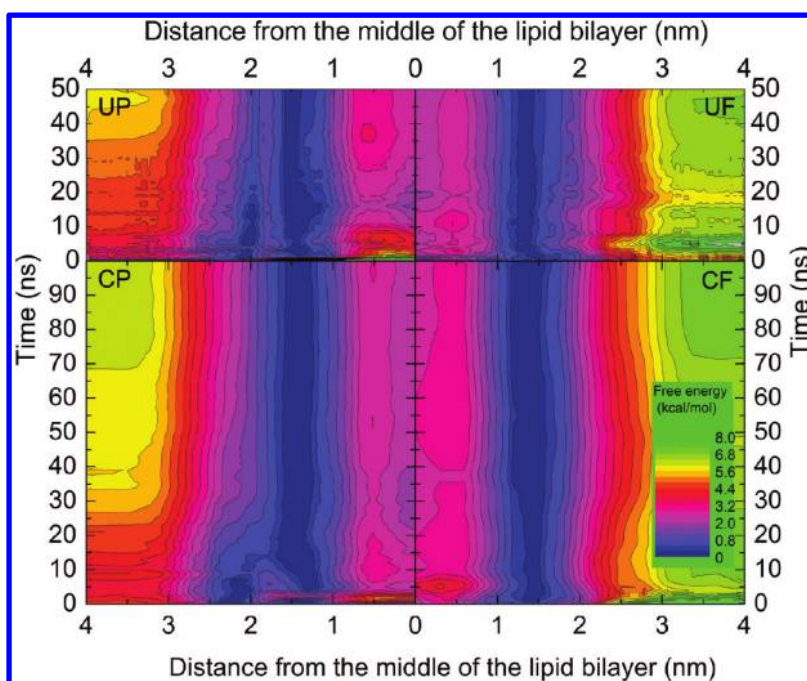


Figure 4. Convergence of free energy profiles, positions of energy minima and energy barriers. The simulation windows within 1.0–2.5 nm have been simulated for 50 and 100 ns in case of UP and UF simulations of CP and CF simulations, respectively; the rest of each profile is calculated from 30 ns of simulation. Free energy profiles calculated from short simulation times (<5 ns) are biased by high error, because of small data set and nonequilibrium starting structures. Free energy profiles obtained by UP and CP simulations (left) show slow elimination of an artificial minimum (~2.0 nm) and deepening of the global minimum (~1.5 nm). Free energy profiles obtained from UF and CF simulation are consistent in coumarin positioning and have deeper energy minima than those obtained from UP and CP simulations. The global minimum energy is considered as reference. UP and UF refer to umbrella simulations with initial structures obtained by pulling and free unbiased simulation, respectively; CP and CF refer to constraint simulation with pulling and free initial structures, respectively.

gradually narrowed from 1.38 nm after 5 ns of simulation to 0.51 nm after 40 ns and thereafter remained constant. ΔG^{wat} gradually rose throughout the simulation, to 5.9 ± 0.2 kcal/mol, while ΔG^{pen} grew during the first 11 ns of simulation, until 20 ns of simulation it gradually declined to 2.8 ± 0.1 kcal/mol and then fluctuated around this value. In the last 50 ns of the simulation prolonged to 100 ns the position of the energy minimum remained constant; ΔG^{pen} fluctuated around 2.8 ± 0.1 kcal/mol and ΔG^{wat} continued to rise, to 6.2 ± 0.2 kcal/mol.

The position of the minimum in the UF free energy profile was almost constant (within 1.29–1.35 nm) during the whole simulation time, with the area accessible by thermal motion slowly widening from 0.44 to 0.66 nm. ΔG^{wat} slowly decreased during the first 19 ns of simulation, then very slowly increased, and after 30 ns ΔG^{wat} converged to 6.7 ± 0.1 kcal/mol, while ΔG^{pen} became convergent after 20 ns, fluctuating within 2.6 ± 0.1 kcal/mol.

The CF free energy profile showed a minimum position within 1.29–1.49 nm, and the area of thermal motion slowly widened from 0.41 to 0.70 nm. ΔG^{wat} fluctuated around 6.4–7.0 kcal/mol during the whole simulation time, while ΔG^{pen} decreased during the first 10 ns of simulation and then fluctuated around 2.9–3.3 kcal/mol. The prolonged simulation to 100 ns showed similar trends – a free energy minimum at 1.29 nm, thermal motion within 0.6 nm, a constant ΔG^{wat} value of 7.0 kcal/mol after 80 ns, and ΔG^{pen} already convergent with a final value of 3.1 ± 0.1 kcal/mol.

Effect of Coumarin Partial Charges. As assignment of partial charges might introduce another systematic sampling error into free energy calculations, we carried out 10 ns long CF

simulations with PRODRG and Mulliken charges (assigned partial charges are listed in Supporting Information Table S1), to assess the extent to which the partial charges affected the free energy profiles. Coumarin with partial charges assigned by PRODRG bore a dipole moment of 9.5 D, assignment of Mulliken partial charges led to 6.0 D, and RESP partial charges resulted in a dipole moment of 4.9 D (Figure 5). The dipole moment based on RESP charges was close to that of coumarin in the gas phase calculated by the hybrid DFT method (B3LYP/cc-pvDZ) of 4.6 D, Mulliken partial charges represent a compromise between the dipole moment in water (represented by continuum dielectrics with $\epsilon_r = 78.39$) and heptane ($\epsilon_r = 1.92$), which we calculated by the CPCM/B3LYP/cc-pVDZ method and that resulted in 6.7 and 5.4 D, respectively. Considering these values, the dipole moment stemming from PRODRG charges seemed to be unreliably overestimated, which could systematically bias free energy profiles based on PRODRG charges. The global minimum of the ΔG profile of coumarin bearing RESP partial charges was located at 1.29 nm (CF with a 10 ns sampling window), energy minimum of coumarin bearing Mulliken partial charges was localized at 1.20 nm, and the minimum for PRODRG-charged coumarin was shifted toward the bilayer/water interface, at 1.62 nm. The global free energy minimum for RESP-charged coumarin was also considerably deeper than for Mulliken-charged or PRODRG-charged coumarin (ΔG^{wat} : 7.5, 5.6, and 3.3 kcal/mol, respectively), and the bilayer center penetration barriers of the systems also differed (ΔG^{pen} : 3.1, 4.6, and 10.1 kcal/mol, respectively) (Figure 5). As expected, the energy cost of bilayer center penetration grows with the increasing

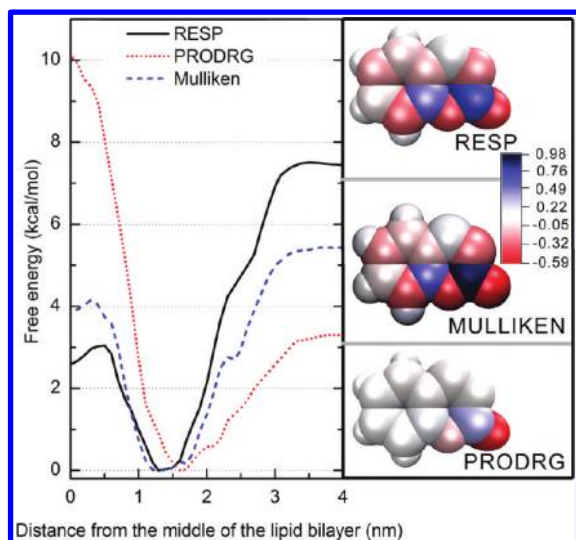


Figure 5. Left panel: free energy profiles calculated for coumarin with PRODRG (red dotted curve), Mulliken (blue dashed curve), and RESP charges (black curve) by constraint simulation (CF) with initial structures obtained by free simulation using 10 ns windows. Coumarin with PRODRG partial charges is shifted to the outer part of the lipid bilayer. The bilayer center penetration barriers grow and the water/lipids barriers decrease with increasing dipole moment. The right panel shows that the partial charges (mapped on the vdW surface) calculated by RESP (upper part) and Mulliken population analysis (middle) are spread along the whole molecule, while partial charges assigned by PRODRG (lower part) are localized close to coumarin oxygens.

dipole moment, and reversely the energy barrier between lipid bilayer and water decreases with the growing dipole moment.

Comparison with Experimental Data. To our knowledge, the precise positioning of bare coumarin in a DOPC bilayer has not yet been studied experimentally; therefore, we compared the results of our theoretical calculations to data obtained in experiments with coumarin derivatives. Depths of several coumarin derivatives in dimyristoylphosphatidylcholine (DMPC) bilayer have been studied in NMR investigations,^{2,46,47} in which chemical shifts of ¹³C-labeled derivatives were used to assess the polarity of the surroundings of ¹³C atoms and hence estimate their depth in the lipid bilayer. Results of the cited experiments indicate that the mean position of 7-acetoxy-4-methylcoumarin is at the border of regions 2 and 3 in DMPC lipid bilayer (0.7 nm from the DMPC choline nitrogens, corresponding to 1.2 nm from the center of the bilayer); ¹³C-labeled carbons of the derivative (C2 and C4, see Figure 6) appeared to be located 0.72 and 0.70 nm from the choline nitrogens, corresponding to 1.18 and 1.20 nm from the bilayer center, respectively. Another coumarin derivative, 7-acetoxycoumarin, was apparently located closer to the bilayer interface in region 2, with its ¹³C-labeled (C2 and C4) carbons 0.44 and 0.59 nm from the choline nitrogen, corresponding to 1.46 and 1.31 nm from the bilayer center, respectively. We recalculated the experimental positions (originally expressed as distances from the bilayer surface) as distances from the bilayer center to facilitate direct comparison with results of this study. In this recalculation, the distance between the DMPC bilayer surface and center was set at 1.9 nm: the mean distance between the bilayer center and maximum density of nitrogens (regarded as the membrane surface in the cited NMR experiments) in corresponding MD simulations.

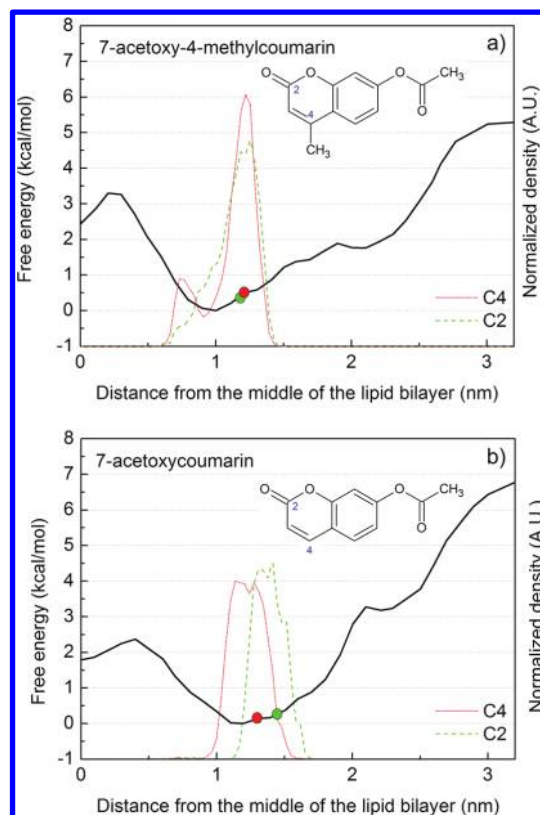


Figure 6. Free energy profiles and structures of coumarin derivatives (7-acetoxy-4-methylcoumarin, upper panel (a), and 7-acetoxycoumarin, lower panel (b)) along a DMPC lipid bilayer normal calculated from constraint simulation with initial structures obtained by free simulation (CF). NMR-observed positions of ¹³C-labeled carbons (C2 and C4) are displayed as red and green circles, respectively, and the positions of C2 and C4 carbons calculated from simulation are depicted as green and red curves, respectively. The positions of marked carbons of both coumarin derivatives are in good agreement with the positions observed by NMR.

For the comparison we employed the most effective simulation protocol of those considered here to calculate the free energy profiles of the coumarin derivatives described above, briefly comprising unbiased simulation followed by constraint simulation with 10 ns simulation bins (see Methods for details). The profile obtained for 7-acetoxy-4-methylcoumarin indicated the free energy minimum position of its COM to be 1.0 nm from the center of the DMPC bilayer (Figure 6), with a thermally accessible region between 0.8 and 1.3 nm. The thermally accessible region estimated from the simulation (0.8–1.3 nm) matched that acquired from NMR experiments, where 7-acetoxy-4-methylcoumarin was located 1.2 ± 0.1 nm from the bilayer center. In addition, the positions of its C2 and C4 carbons calculated from simulations (1.25 and 1.21 nm, respectively) agreed well with those estimated from experiments (1.18 and 1.20 nm, respectively), although the C4 carbon seems to flip-flop between two positions in the bilayer (the other at 0.76 nm, with ca. 14% population, see Figure 6 up).

The free energy minimum position of the COM of 7-acetoxycoumarin in the simulation was located 1.2 nm from the bilayer center, with a thermally accessible region between 0.75 and 1.35 nm. The simulated distances of the C2 and C4 carbons from the bilayer center at this point (1.34 and 1.19 nm, respectively) again matched those obtained from the NMR data

reasonably well (1.46 and 1.31 nm, respectively, see Figure 6 down).

In summary, the MD results for both coumarin derivatives agreed reasonably well with the experimental results, notably 7-acetoxy-4-methylcoumarin was located deeper in the bilayer than 7-acetoxycoumarin, and the carbon atoms' positions calculated from simulations matched those deduced from experiments.

■ DISCUSSION

Coumarin Preferentially Stays in Bilayer Regions 2 and 3 in Unbiased Simulations. During the five independent unbiased simulations (3 μ s long in total) coumarin preferred the lipid bilayer phase rather than the aqueous phase, because it quickly (within <10 ns) entered the lipid bilayer and remained there for the rest of the simulation time (Figure S1 in the Supporting Information). The preferentially occupied position was at 1.4 ± 0.1 nm, at the border of regions 2 and 3, and the molecule was oriented mainly with its oxygens pointing toward the water phase (data not shown). In addition, coumarin penetrated the lipid bilayer spontaneously, i.e., moved from one leaflet to the other, remaining at the preferentially occupied positions in both leaflets for several hundreds of nanoseconds between brief (a few ns) visits to the lipid bilayer center (Figure S1 in the Supporting Information). Similarly, the transition movements were quite rapid, generally occurring within several nanoseconds.

Some key penetration properties were identified from the unbiased simulations, namely positions of local and global free energy minima and qualitative estimates of the height of energy barriers (Figure 2). The water/lipids barrier, ΔG^{wat} , seemed to be higher than the bilayer center penetration barrier, ΔG^{pen} . The number of penetration events allowed us to roughly estimate the absolute value of the bilayer center penetration barrier, at 2.1 kcal/mol (eq 3). However, the estimated ΔG^{pen} value should be interpreted with care, due to the limited sampling as only a small number of transitions between the minima were observed, and ΔG^{wat} could not be calculated as the water phase was not sampled adequately (Figure 2). Nevertheless, the spontaneous embedding of coumarin in DOPC bilayer strongly indicates that this is a barrierless process and that coumarin prefers the bilayer phase, in accordance with expectations based on coumarin's $\log P_{\text{oct/wat}}$ value.

Free Energy Profiles Obtained by Biased and Unbiased Simulation Agree. The final free energy profiles obtained by all simulation protocols (UP, CP, UF, and CF) were in accord (Figure 2), but those obtained from the unbiased simulations provided more accurate information. The global energy minimum was found at 1.44 ± 0.09 nm, while a local energy minimum was localized in the membrane center. The presence of a local energy minimum in the lipid bilayer center agrees with previous findings presented by Bemporad et al.,²³ of such local minima for some other small solutes, e.g. water and acetamide. In our case, the bilayer center penetration barrier (ΔG^{pen}) of coumarin spanned 2.6–3.3 kcal/mol (Table 1, Figure 2), close to the ΔG^{pen} estimated roughly from the unbiased simulation (2.1 kcal/mol). In contrast, the water/lipids barrier (ΔG^{wat}) varied significantly with time and method used (see below). The estimated ΔG^{wat} from CF simulation (which is taken as reference, as constraint biasing eliminates possible artificial errors quicker) was 6.4 ± 0.2 kcal/mol (Figure 2). The free energy profiles therefore confirmed that

coumarin more readily penetrates the bilayer than escapes to the water phase.

Partial Charges – The Force Field Issue. Neither accurate unbiased simulation, nor accurate free energy profile calculation, is possible without a careful choice of force field. The Berger force field (using Mulliken partial charges calculated at HF/6-31G* level (in gas phase)⁵⁰) used for lipids^{39,44} was tested and shown to provide area per lipid and volume per lipid values that correspond well with experimental values.⁴⁴

Further, as coumarin parameters were not available in standard data sets for lipid simulations, they had to be acquired separately. Generally, atom types and corresponding parameters can be adopted for a nonlipid molecule from the standard data sets quite safely, but the set of partial charges had to be carefully considered, as it may introduce a serious systematic sampling error in lipid bilayer-guest molecule simulations. We addressed this issue by using three sets of partial charges (Figure 5, Table S1 in the Supporting Information): one generated by the PRODRG server, one assigned by Mulliken population analysis, and the third generated by applying the RESP procedure in B3LYP/cc-pVDZ calculations of electrostatic potential in gas phase. Generally, increasing the dipole moment of a molecule (by use of PRODRG or Mulliken partial charges) resulted in a lower ΔG^{wat} and higher ΔG^{pen} , in accordance with expectations, given the higher polarity of coumarin bearing PRODRG or Mulliken charges in comparison with RESP partial charges (Figure 5). With only these profiles it would be difficult to decide which partial charges provided more reliable results. However, PRODRG charges led to overestimation of the dipole moment of coumarin and (as mentioned above) partial charges assigned by the PRODRG server lead to unrealistically strong partitioning in water in cyclohexane/water systems as found by Lemkul et al.⁴⁰ The latter finding agrees with the trends observed in our lipid bilayer simulations. In summary, RESP charges seem to provide more accurate models for simulations of lipid bilayer-guest molecule systems than PRODRG charges (although whether the RESP charges should ideally be based on gas phase or solvent-polarized ESP, and if they can be robustly combined with the Berger force field for lipids, remains to be determined).

Convergence of Free Energy Profiles – The Artificial Minimum Issue. We have shown here that the convergence of free energy profiles was significantly influenced by the generation of initial structures when followed by the biasing method. The biased simulations starting from the pulling simulations (UP and CP) suffered from bilayer deformation induced by pulling coumarin from the water phase toward the bilayer center (Figure 3). Similar bilayer deformations have been repeatedly previously observed^{13,18,30} and identified as a systematic sampling artifact in biased lipid bilayer simulations. For example, Neale et al.¹³ observed bilayer deformations when a charged molecule was embedded in the bilayer. We observed a funnel-shape bilayer surface depression (Figure S2 in the Supporting Information), caused by water hydrating the polar parts of coumarin penetrating the lipid bilayer more deeply and thereby exacerbating bilayer deformation during the pulling simulations. The bilayer deformation caused an artificial minimum (~ 2.0 nm) in the free energy profiles in region 2 (Figure 2), whereas in unbiased simulation coumarin never stayed longer in this position, and its behavior showed no sign of reaching a local energy minimum.

This artificial minimum was most profound when short simulation times (<5 ns) for each sampling bin were applied, and it slowly disappeared when the simulation time was prolonged (Figure 4). The main reason for the slow convergence and need for longer simulation times was the slow coumarin water shell elimination in region 2. Furthermore, the presence of the artificial minimum led to underestimation of ΔG^{wat} in simulations using the initial structure set generated by pulling simulation (CP and UP). While ΔG^{wat} values obtained by CF and UF simulations seemed to reach convergence, they did not reach convergence in UP and CP simulations during 50 ns of simulation (or even during 100 ns of CP simulation), although both UP and CP yielded ΔG^{wat} values close to those obtained from CF and UF simulations.

In this respect, constraint biasing was more effective, as the artificial minimum was eliminated within 15 ns per bin (in CP), while there were signs of the artificial minimum in UP simulation even after 50 ns per bin (Figure 4). Even longer times may be needed in simulations of polar or charged residues, as previously shown by MacCallum et al.³⁰ and Neale et al.,¹³ who found that 80 to 205 ns per bin may be required to achieve convergence in umbrella simulations with charged solutes. In contrast, for nonpolar solutes Neale et al. achieved convergence more rapidly (in some cases after 20 ns per bin). These water artifacts seem to be present when nonequilibrated initial structures are used for biased simulation. The higher efficiency of constraint over umbrella biasing is also consistent with the recent observation by Gunsteren et al.,⁶¹ that constraint-biased simulation using force averaging is the most effective method for calculating potential of mean force with respect to a distance from a given reference point.

Convergence of the free energy profiles was clearly achieved more rapidly when using starting structures acquired from unbiased (UF and CF) simulations in comparison with the pulling simulation (UP and CP), since in cases of UF and CF simulation the free energy profiles changed only marginally with increases in the length of the simulation bins (Figure 4). Therefore we recommend starting the calculation of free energy profile with an unbiased simulation for all molecules, in a case of more polar molecules a slow pulling simulation (pulling force constant <500 kJ·mol⁻¹·nm⁻² (119.5 kcal·mol⁻¹·nm⁻²) and a pulling rate <1 nm·ns⁻¹) from the deepest position in the lipid bilayer should follow. Thus, this approach was used for comparing the calculated results with experimental data, and the calculated positions of 7-acetoxy-4-methylcoumarin and 7-acetoxycoumarin in DMPC bilayer agreed well with positions derived from NMR experiments (Figure 6). In summary, whenever possible biased simulations should start from geometries acquired from unbiased MD simulations, and constraint biasing is the recommended and quickly converging method.

CONCLUSION

The convergence in time of free energy profiles of coumarin along a DOPC bilayer normal, calculated by both umbrella sampling and z-constraint techniques, was thoroughly analyzed. Two sets of starting structures were also considered: one based on unbiased MD simulation and the other on “pulling” coumarin along the bilayer normal. Water defects on the lipid bilayer surface were identified in the structures obtained by pulling simulation but not in structures acquired from unbiased simulation. Consequently, the free energy profiles converged more rapidly when starting frames from unbiased simulations

were used. The used methods for free energy profile calculation (umbrella and constraint simulation) are quite equivalent when applied on an error-free set of starting structures. However, if the membrane defects are present, the z-constraint simulation leads to more rapid convergence than umbrella sampling. In summary, for efficient calculation of convergent free energy profiles of druglike molecules along bilayer normals, we recommend using z-constraint biased MD simulations based on as much starting geometries acquired from unbiased MD simulations as possible, otherwise when pulling simulation is employed, the biased simulation might need far longer time to reach convergence.

ASSOCIATED CONTENT

Supporting Information

Details of the recommended simulation protocol, used partial charges, four supplemental figures, and one equation. Table S1: Partial charges on coumarin atoms used in the paper. Figure S1: Position of coumarin in unbiased simulations. Figure S2: Funnel shape water defect caused by pulling coumarin into the membrane. Figure S3: Effect of window spacing in constraint and umbrella simulations. Figure S4: Atom labels as used in Table S1. This material is available free of charge via the Internet at <http://pubs.acs.org>.

AUTHOR INFORMATION

Corresponding Author

*E-mail: karel.berka@upol.cz (K.B.), michal.otyepka@upol.cz (M.O.).

Notes

The authors declare no competing financial interest.

ACKNOWLEDGMENTS

Support through GACR grants 303/09/1001 and P208/12/G016 and Student Project PrF_2011_020 provided by Palacky University is gratefully acknowledged. This work was also supported by the Operational Program Research and Development for Innovations – European Regional Development Fund (CZ.1.05/2.1.00/03.0058) and European Social Fund (CZ.1.07/2.3.00/20.0017).

REFERENCES

- (1) Orsi, M.; Essex, J. W. Passive Permeation Across Lipid Bilayers: a Literature Review. In *Molecular Simulations and Biomembranes*, 1st ed.; Sansom, M. S. P., Biggin, P. C., Eds.; Royal Society of Chemistry: 2010; pp 76–90.
- (2) Balaz, S. Modeling Kinetics of Subcellular Disposition of Chemicals. *Chem. Rev.* **2009**, *109*, 1793–1899.
- (3) Afri, M.; Gottlieb, H. E.; Frimer, A. A. Superoxide Organic Chemistry within the Liposomal Bilayer, part II: a Correlation between Location and Chemistry. *Free Radical Biol. Med.* **2002**, *32*, 605–618.
- (4) Xiang, T.-X.; Anderson, B. D. Liposomal Drug Transport: a Molecular Perspective from Molecular Dynamics Simulations in Lipid Bilayers. *Adv. Drug Delivery Rev.* **2006**, *58*, 1357–1378.
- (5) Berka, K.; Hendrychová, T.; Anzenbacher, P.; Otyepka, M. Membrane Position of Ibuprofen Agrees with Suggested Access Path Entrance to Cytochrome P450 2C9 Active Site. *J. Phys. Chem. A* **2011**, *115*, 11248–11255.
- (6) Alberts, B.; Johnson, A.; Lewis, J.; Raff, M.; Roberts, K.; Walter, P. *Molecular Biology of the Cell*, 4th ed.; Garland Science: New York, 2002.
- (7) Cooper, G. M. *The Cell: A Molecular Approach*, 2nd ed.; Sinauer Associates: Sunderland MA, 2000.

- (8) van Meer, G.; Voelker, D. R.; Feigenson, G. W. Membrane Lipids: Where They Are and How They Behave. *Nat. Rev. Mol. Cell Biol.* **2008**, *9*, 112–124.
- (9) Black, S. D. Membrane Topology of the Mammalian P450 Cytochromes. *FASEB J.* **1992**, *6*, 680–685.
- (10) Ishii, Y.; Takeda, S.; Yamada, H. Modulation of UDP-glucuronosyltransferase Activity by Protein-Protein Association. *Drug Metab. Rev.* **2010**, *42*, 145–158.
- (11) Wu, N. A. N.; Palczewski, K.; Mu, D. J. Vertebrate Membrane Proteins: Structure, Function, and Insights from Biophysical Approaches. *Pharmacol. Rev.* **2008**, *60*, 43–78.
- (12) Marrink, S.-J.; Berendsen, H. J. C. Simulation of Water Transport through a Lipid Membrane. *J. Phys. Chem.* **1994**, *98*, 4155–4168.
- (13) Neale, C.; Bennett, W. F. D.; Tieleman, D. P.; Pomès, R. Statistical Convergence of Equilibrium Properties in Simulations of Molecular Solutes Embedded in Lipid Bilayers. *J. Chem. Theory Comput.* **2011**, *7*, 4175–4188.
- (14) Orsi, M.; Essex, J. W. Permeability of Drugs and Hormones through a Lipid Bilayer: Insights from Dual-Resolution Molecular Dynamics. *Soft Matter* **2010**, *6*, 3797–3808.
- (15) Bemporad, D.; Luttmann, C.; Essex, J. W. Computer Simulation of Small Molecule Permeation across a Lipid Bilayer: Dependence on Bilayer Properties and Solute Volume, Size, and Cross-Sectional Area. *Biophys. J.* **2004**, *87*, 1–13.
- (16) Bemporad, D.; Luttmann, C.; Essex, J. W. Behaviour of Small Solutes and Large Drugs in a Lipid Bilayer from Computer Simulations. *Biochim. Biophys. Acta* **2005**, *1718*, 1–21.
- (17) Orsi, M.; Sanderson, W. E.; Essex, J. W. Permeability of Small Molecules through a Lipid Bilayer: a Multiscale Simulation Study. *J. Phys. Chem. B* **2009**, *113*, 12019–12029.
- (18) Boggara, M. B.; Krishnamoorti, R. Partitioning of Nonsteroidal Antiinflammatory Drugs in Lipid Membranes: a Molecular Dynamics Simulation Study. *Biophys. J.* **2010**, *98*, 586–595.
- (19) MacCallum, J. L.; Tieleman, D. P. Computer Simulation of the Distribution of Hexane in a Lipid Bilayer: Spatially Resolved Free Energy, Entropy, and Enthalpy Profiles. *J. Am. Chem. Soc.* **2006**, *128*, 125–130.
- (20) Kumar, S.; Rosenberg, J.; Bouzida, D.; Swensen, R. H.; Kollman, P. A. The Weighted Histogram Analysis Method for Free Energy Calculations on Biomolecules. I. The Method. *J. Comput. Chem.* **1992**, *13*, 1011–1021.
- (21) Torrie, G. M.; Calleau, J. P. Nonphysical Sampling Distribution in Monte Carlo Free Energy Estimation: Umbrella Sampling. *J. Comput. Phys.* **1997**, *23*, 187–199.
- (22) Marrink, S. J.; Berendsen, H. J. C. Permeation Process of Small Molecules across Lipid Membranes Studied by Molecular Dynamics Simulations. *J. Phys. Chem.* **1996**, *100*, 16729–16738.
- (23) Bemporad, D.; Essex, J. W.; Luttmann, C. Permeation of Small Molecules through a Lipid Bilayer: A Computer Simulation Study. *J. Phys. Chem. B* **2004**, *108*, 4875–4884.
- (24) Zhang, Y.; Voth, G. A. Combined Metadynamics and Umbrella Sampling Method for the Calculation of Ion Permeation Free Energy Profiles. *J. Chem. Theory Comput.* **2011**, *7*, 2277–2283.
- (25) Laio, A.; Parrinello, M. Escaping Free-Energy Minima. *Proc. Natl. Acad. Sci. U. S. A.* **2002**, *99*, 12562–12566.
- (26) Wei, C.; Pohorille, A. Permeation of Membranes by Ribose and Its Diastereomers. *J. Am. Chem. Soc.* **2009**, *131*, 10237–10245.
- (27) Darve, E.; Pohorille, A. Calculating Free Energies Using Average Force. *J. Chem. Phys.* **2001**, *115*, 9169.
- (28) Tai, K. Conformational Sampling for the Impatient. *Biophys. Chem.* **2004**, *107*, 213–220.
- (29) Roux, B. The Calculation of the Potential of Mean Force Using Computer Simulations. *Comput. Phys. Commun.* **1995**, *91*, 275–282.
- (30) MacCallum, J. L.; Bennett, W. F. D.; Tieleman, D. P. Distribution of Amino Acids in a Lipid Bilayer from Computer Simulations. *Biophys. J.* **2008**, *94*, 3393–3404.
- (31) Kandt, C.; Ash, W. L.; Tieleman, D. P. Setting up and Running Molecular Dynamics Simulations of Membrane Proteins. *Methods* **2007**, *41*, 475–488.
- (32) Humphrey, W.; Dalke, A.; Schulten, K. VMD - Visual Molecular Dynamics. *J. Mol. Graphics* **1996**, *14*, 33–38.
- (33) Tejwani, R. W.; Davis, M. E.; Anderson, B. D.; Stouch, T. R. Functional Group Dependence of Solute Partitioning to Various Locations within a DOPC Bilayer: A Comparison of Molecular Dynamics Simulations with Experiment. *J. Pharm. Sci.* **2011**, *100*, 2136–2146.
- (34) Verschuere, K. *Handbook of Environmental Data on Organic Chemicals*, 3rd ed.; Van Nostrand Reinhold: New York, 1996; pp 541–542.
- (35) Gutiérrez-Sánchez, C.; Calvino-Casilda, V.; Pérez-Mayoral, E.; Martín-Aranda, R. M.; López-Peinado, A. J.; Bejblova, M.; Čejka, J. Coumarins Preparation by Pechmann Reaction under Ultrasound Irradiation. Synthesis of Hymecromone as Insecticide Intermediate. *Cat. Lett.* **2008**, *128*, 318–322.
- (36) Anzenbacher, P.; Anzenbacherová, E. Cellular and Molecular Life Sciences Cytochromes P450 and Metabolism of Xenobiotics. *Cell. Mol. Life Sci.* **2001**, *58*, 737–747.
- (37) Pelkonen, O.; Rautio, A.; Raunio, H.; Pasanen, M. CYP2A6: a Human Coumarin 7-hydroxylase. *Toxicology* **2000**, *144*, 139–147.
- (38) Schüttelkopf, A. W.; van Aalten, D. M. F. PRODRG: a Tool for High-Throughput Crystallography of Protein-Ligand Complexes. *Acta Crystallogr., Sect. D: Biol. Crystallogr.* **2004**, *60*, 1355–1363.
- (39) Oostenbrink, C.; Soares, T. A.; van der Vegt, N. F. A.; van Gunsteren, W. F. Validation of the 53A6 GROMOS Force Field. *Eur. Biophys. J.* **2005**, *34*, 273–284.
- (40) Lemkul, J. A.; Allen, W. J.; Bevan, D. R. Practical Considerations for Guiding GROMOS-Compatible Small-Molecule Topologies. *J. Chem. Inf. Model.* **2010**, *50*, 2221–2235.
- (41) Frisch, M. J.; Trucks, G. W.; Schlegel, H. B.; Scuseria, G. E.; Robb, M. A.; Cheeseman, J. R.; Montgomery, Jr., J. A.; Vreven, T.; Kudin, K. N.; Burant, J. C.; Millam, J. M.; Iyengar, S. S.; Tomasi, J.; Barone, V.; Mennucci, B.; Cossi, M.; Scalmani, G.; Rega, N.; Petersson, G. A.; Nakatsuji, H.; Hada, M.; Ehara, M.; Toyota, K.; Fukuda, R.; Hasegawa, J.; Ishida, M.; Nakajima, T.; Honda, Y.; Kitao, O.; Nakai, H.; Klene, M.; Li, X.; Knox, J. E.; Hratchian, H. P.; Cross, J. B.; Bakken, V.; Adamo, C.; Jaramillo, J.; Gomperts, R.; Stratmann, R. E.; Yazyev, O.; Austin, A. J.; Cammi, R.; Pomelli, C.; Ochterski, J. W.; Ayala, P. Y.; Morokuma, K.; Voth, G. A.; Salvador, P.; Dannenberg, J. J.; Zakrzewski, V. G.; Dapprich, S.; Daniels, A. D.; Strain, M. C.; Farkas, O.; Malick, D. K.; Rabuck, A. D.; Raghavachari, K.; Foresman, J. B.; Ortiz, J. V.; Cui, Q.; Baboul, A. G.; Clifford, S.; Cioslowski, J.; Stefanov, B. B.; Liu, G.; Liashenko, A.; Piskorz, P.; Komaromi, I.; Martin, R. L.; Fox, D. J.; Keith, T.; Al-Laham, M. A.; Peng, C. Y.; Nanayakkara, A.; Challacombe, M.; Gill, P. M. W.; Johnson, B.; Chen, W.; Wong, M. W.; Gonzalez, C.; Pople, J. A. Gaussian 03, Revision E.01; Gassuian, Inc.: Wallingford, CT, 2004.
- (42) Cieplak, P.; Caldwell, J.; Kollman, P. Molecular Mechanical Models for Organic and Biological Systems Going Beyond the Atom Centered Two Body Additive Approximation: Aqueous Solution Free Energies of Methanol and N-Methyl Acetamide, Nucleic Acid Base, and Amide Hydrogen Bonding and Chloroform/ Water Partition Coefficients of the Nucleic Acid Bases. *J. Comput. Chem.* **2001**, *22*, 1048–1057.
- (43) Case, D. A.; Darden, T. A.; Cheatham, T. E., III; Simmerling, C. L.; Wang, J.; Duke, R. E.; Luo, R.; Walker, R. C.; Zhang, W.; Merz, K. M.; Roberts, B.; Wang, B.; Hayik, S.; Roitberg, A.; Seabra, G.; Kolossvary, I.; Wong, K. F.; Paesani, F.; Vanicek, J.; Liu, J.; Wu, X.; Brozell, S. R.; Steinbrecher, T.; Gohlke, H.; Cai, Q.; Ye, X.; Hsieh, M.-J.; Cui, G.; Roe, D. R.; Mathews, D. H.; Seetin, M. G.; Sagui, C.; Babin, V.; Luchko, T.; Gusarov, S.; Kovalenko, A.; Kollman, P. A. *AMBER 11*; University of California: San Francisco, 2010.
- (44) Berger, O.; Edholm, O.; Jahnig, F. Molecular Dynamics Simulations of a Fluid Bilayer of Dipalmitoylphosphatidylcholine at Full Hydration, Constant Pressure, and Constant Temperature. *Biophys. J.* **1997**, *72*, 2002–2013.

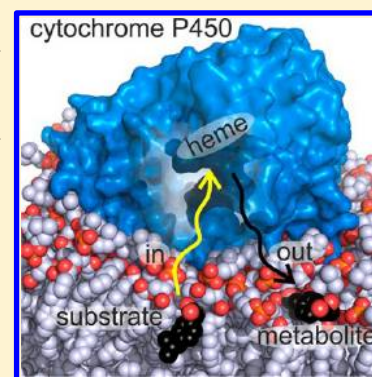
- (45) Siu, S.; Vácha, R.; Jungwirth, P.; Böckmann, R. A. Biomolecular Simulation of Membranes: Physical Properties from Different Force Fields. *J. Chem. Phys.* **2008**, *128*, 125103.
- (46) Domański, J.; Stansfeld, P. J.; Sansom, M. S. P.; Beckstein, O. Lipidbook: a Public Repository for Force-Field Parameters Used in Membrane Simulations. *J. Membr. Biol.* **2010**, *236*, 255–258.
- (47) Berendsen, H. J. C.; Postma, J. P. M.; Gunsteren, W. F. van; Hermans, J. Interaction Models for Water in Relation to Protein Hydration. In *Intermol. Forces*; Pullman, B., Ed.; Reidel Publishing Company: 1981; pp 331–338.
- (48) Hess, B.; Kutzner, C.; van der Spoel, D.; Lindahl, E. GROMACS 4: Algorithms for Highly Efficient, Load-Balanced, and Scalable Molecular Simulation. *J. Chem. Theory Comput.* **2008**, *4*, 435–447.
- (49) Shinoda, W.; Mikami, M.; Baba, T.; Hato, M. Molecular Dynamics Study on the Effects of Chain Branching on the Physical Properties of Lipid Bilayers: 2. Permeability. *J. Phys. Chem. B* **2004**, *108*, 9346–9356.
- (50) Chiu, S. W.; Clark, M.; Balaji, V.; Subramaniam, S.; Scott, H. L.; Jakobsson, E. Incorporation of Surface Tension into Molecular Dynamics Simulation of an Interface: a Fluid Phase Lipid Bilayer Membrane. *Biophys. J.* **1995**, *69*, 1230–1245.
- (51) Darden, T.; York, D.; Pedersen, L. Particle Mesh Ewald: An $N \log(N)$ Method for Ewald Sums in Large Systems. *J. Chem. Phys.* **1993**, *98*, 10089–10092.
- (52) Hess, B.; Bekker, H.; Berendsen, H. J. C.; Fraaije, J. G. E. M. LINCS: A Linear Constraint Solver for Molecular Simulations. *J. Comput. Chem.* **1997**, *18*, 1463–1472.
- (53) Bussi, G.; Donadio, D.; Parrinello, M. Canonical Sampling Through Velocity Rescaling. *J. Chem. Phys.* **2007**, *126*, 014101.
- (54) Berendsen, H.; Postma, J.; Vangunsteren, W.; Dinola, A.; Haak, J. Molecular-Dynamics with Coupling to an External Bath. *J. Chem. Phys.* **1984**, *81*, 3684–3690.
- (55) Van Der Spoel, D.; Lindahl, E.; Hess, B.; Groenhof, G.; Mark, A. E.; Berendsen, H. J. C. GROMACS: Fast, Flexible, and Free. *J. Comput. Chem.* **2005**, *26*, 1701–1718.
- (56) Hub, J. S.; Groot, B. L. D.; Spoel, D. V. D. g_wham-A Free Weighted Histogram Analysis Implementation Including Robust Error and Autocorrelation Estimates. *J. Chem. Theory Comput.* **2010**, *6*, 3713–3720.
- (57) Eriksson, E. S. E.; Eriksson, L. A. The Influence of Cholesterol on the Properties and Permeability of Hypericin Derivatives in Lipid Membranes. *J. Chem. Theory Comput.* **2011**, *7*, 560–574.
- (58) Biocomputing at the University Of Calgary. <http://people.ucalgary.ca/~tieleman/download.html> (accessed Oct. 12, 2011).
- (59) Cohen, Y.; Afri, M.; Frimer, A. A. NMR-Based Molecular Ruler for Determining the Depth of Intercalants within the Lipid Bilayer Part II. The Preparation of a Molecular Ruler. *Chem. Phys. Lipids* **2008**, *155*, 114–119.
- (60) Cohen, Y.; Bodner, E.; Richman, M.; Afri, M.; Frimer, A. A. NMR-Based Molecular Ruler for Determining the Depth of Intercalants within the Lipid Bilayer Part I. Discovering the Guidelines. *Chem. Phys. Lipids* **2008**, *155*, 98–113.
- (61) Trzesniak, D.; Kunz, A.-P. E.; van Gunsteren, W. F. A Comparison of Methods to Compute the Potential of Mean Force. *ChemPhysChem* **2007**, *8*, 162–169.

Behavior of Human Cytochromes P450 on Lipid Membranes

Karel Berka,[†] Markéta Paloncýová,[†] Pavel Anzenbacher,[‡] and Michal Otyepka^{*,†}[†]Department of Physical Chemistry, Regional Centre of Advanced Technologies and Materials, Faculty of Science, Palacký University Olomouc, tř. 17. listopadu 12, 771 46, Olomouc, Czech Republic[‡]Department of Pharmacology, Faculty of Medicine and Dentistry, Palacký University Olomouc, Hněvotínská 3, 775 15 Olomouc, Czech Republic

S Supporting Information

ABSTRACT: Human cytochromes P450 (CYPs) are membrane-anchored enzymes involved in biotransformation of many marketed drugs. We constructed atomic models of six human CYPs (CYP1A2, 2A6, 2C9, 2D6, 2E1, and 3A4) anchored to a lipid bilayer to investigate the positions and orientations of CYPs on a membrane. We equilibrated the models by molecular dynamics simulations on a 100+ ns time scale. Catalytic domains of all studied CYPs were found to be partially immersed in the lipid bilayer, whereas the N-terminal part and F'/G' loop are deeply immersed. The proximal side of the enzyme faces the cytosol, whereas the distal side, where openings of substrate access and product release channels to the active site are primarily located, points toward the lipid bilayer. Access channels with openings in the vicinity of the B/C and F/G loops are typically positioned below the lipid head groups, whereas the solvent channel points toward the membrane–water interface. We found that the access channel opening positions match the preferred substrate positions, whereas the product release channel exit positions correspond closely with the positions of the products. This may indicate that membrane-anchored CYPs have evolutionarily adapted to facilitate uptake of nonpolar substrates from the membrane and uptake/release of polar substrates or products from/to the membrane–water interface.



INTRODUCTION

Mammalian cytochromes P450 (CYPs) are involved in the metabolism of many endogenous compounds as well as xenobiotics. CYPs are attached to the endoplasmic reticulum or inner mitochondrial membranes via their N-terminal anchors.¹ The N-terminal anchor usually adopts an α -helical structure and is connected to the CYP catalytic domain via a loop. The fold of the catalytic domain is known from numerous X-ray experiments,^{2–5} and its shape has been shown to be conserved over the mammalian CYPs.⁶ It is expected that the majority of the catalytic domain is exposed to cytosol. However, the exact immersion (penetration depth) and orientation of CYPs on membranes remains uncertain. The orientations of some CYPs have been deduced from experimental data, e.g., epitope screening,^{1,7,8} tryptophan fluorescence,^{9,10} AFM experiments,^{11,12} protein rotation,¹³ linear dichroism,¹⁴ etc. However, despite providing some basic information about the behavior of CYPs on a membrane, these experiments did not allow construction of an atomic model to predict the CYP orientation on the membrane. Recently, several groups have published atomic models of CYP2C9,^{15,16} CYP3A4,^{14,17} and human aromatase CYP19^{18,19} positioned on a phosphatidylcholine lipid bilayer based on molecular dynamics simulations. All models have indicated that the CYP catalytic domain is partially immersed in the lipid bilayer, but the majority of the catalytic domain remains exposed to the cytosol. In addition, it has been predicted that the N-terminal anchor is immersed in the lipid bilayer and lies almost perpendicular to the bilayer surface, with

the N-terminal apex almost reaching the polar headgroup region of the opposite membrane leaflet (Figure 1).

In our previous work,¹⁵ we showed that the orientation of the CYP2C9 catalytic domain on the dioleoylphosphatidylcholine (DOPC) lipid bilayer was tilted and its proximal side faced the cytosol, whereas the distal side was partially immersed in the membrane. Consequently, the entrances of the active site access channels were located in the vicinity of the F'/G' loop (channels 2a, 2ac, 2f, and 4 according to Wade et al.'s nomenclature²¹) below the polar headgroup region of the lipid bilayer (i.e., below the polar membrane surface). On the other hand, the opening of the solvent channel lies above the membrane surface. The position of the F'/G'-loop channel (2ac, 2f) opening agreed with the preferred (energetically most favorable) position of ibuprofen (typical CYP2C9 substrate) in a DOPC membrane. Similarly, the opening of the solvent channel agreed with the preferred position of 3'-hydroxyibuprofen (product of CYP2C9 oxidation of ibuprofen). These findings may indicate that some channels are involved in the uptake of low polar substrates from the lipid bilayer, whereas others are involved in the release of the respective products to the cytosol.^{15,22}

Recently, we have shown that selected prototypical CYP substrates (caffeine, chlorzoxazone, coumarin, ibuprofen, and

Received: June 17, 2013

Revised: August 29, 2013

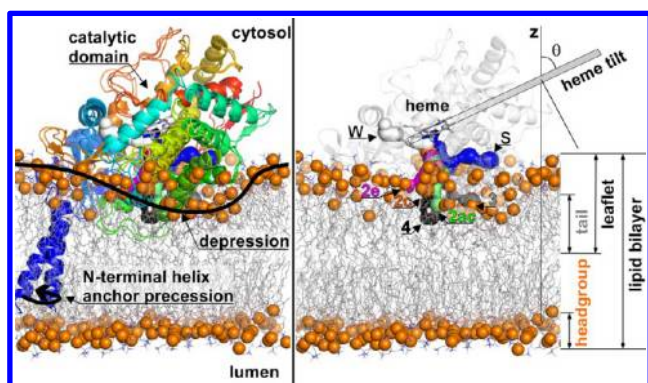


Figure 1. Immersion of CYP2C9 in a dioleoylphosphatidylcholine (DOPC) lipid bilayer. (Left) Overlaid snapshots of CYP2C9 taken at 0.1 and 1 μ s molecular dynamics (MD) simulation, showing that the catalytic domain is immersed in a membrane depression framed by lipid phosphate groups (shown as orange spheres). Water molecules are not shown for clarity. N-terminal helix shows precessional movement about the bilayer normal. Fold of the catalytic domain is conserved and agrees with that observed in X-ray crystallography experiments. (Right) Snapshot taken at 1 μ s of MD simulation showing positions of active site access and egress channels computed from the heme moiety using MOLE 2.0.²⁰ Water channel (white) points toward the cytosolic environment, whereas solvent channel (blue) points above the lipid headgroups. All other channels point inside the bilayer. Channels 2e, 2c, and 3 point into the lipid headgroup region, whereas channels 4 and 2ac point below the lipid headgroups. Heme tilt angle θ (between heme plane and bilayer normal z , i.e., defined according to Baylon et al.¹⁴) is depicted.

debrisoquine) are immersed deeper in DOPC and palmitoyl-oleoylphosphatidylglycerol (POPG) lipid bilayers than their corresponding CYP metabolites.²³ The metabolites also showed lower affinities for the membrane and higher penetration barriers than the substrates. These findings raise an important question as to whether the observed differences in membrane positions of CYP substrates correlate with the enzymes penetration depth, which in turn has implications for the metabolism of drugs.

In the present work, we compared orientations and immersion depths of six CYPs important for drug metabolism (CYP1A2, CYP2A6, CYP2C9, CYP2D6, CYP2E1, and CYP3A4). We constructed atomic models of the CYPs anchored to a DOPC bilayer and relaxed them using molecular dynamics simulations on a 100+ ns time scale. The constructed models agreed well with available experimental data as well as previously published models. We compared the orientations of the catalytic domains and positions of active site access channels of the different CYPs with respect to the lipid bilayer. Despite some differences between the orientation of individual CYPs on the membrane, all studied CYPs showed some common features, i.e., partial immersion of the catalytic domain (N-terminal part and part of F'/G' loop) and a transmembrane N-terminal anchor attached to the catalytic domain via a loop. Entrances of active site access channels belonging to family 2 were generally positioned below the polar headgroup region of the lipid bilayer, whereas exits of the solvent channel were shifted toward the water–membrane interface. Positions of the active site access channels entrances corresponded closely with the lipid positions of substrates, whereas locations of the exits of the solvent channel correlated with the positions of metabolites. We concluded that channels from family 2 may be generally involved in substrate uptake to the CYP active site,

especially of lipophilic substrates, whereas the solvent channel is likely to be involved in product release.

MATERIALS AND METHODS

Model Preparation. Structures of the catalytic domains were taken from the PDB database (Table S1, Supporting Information). Structures for the N-terminal anchor and native-like sequence were obtained by homology modeling using Modeller 9.10.²⁴ Two structural templates were used for each model. The catalytic domain was taken from the respective crystal structure and the missing N-terminal anchor from the atomic model of CYP2C9 equilibrated on a DOPC bilayer.¹⁵

Molecular Dynamics Settings. All models were immersed into dioleoylphosphatidylcholine (DOPC) lipid bilayers using the *g_membed* tool.²⁵ The Berger united atom force field for lipids²⁶ was used together with the G53a6 force field for proteins.²⁷ A physiological concentration of ions (0.1 M NaCl) in SPC/E water was used for solvation of the system. Overall, the simulation system consisted of around 90,000 united atoms in the case of CYP2C9 or around 120,000 united atoms in the case of other CYPs. Simulation of CYP2C9 from ref 15 was extended to 1 μ s.

Gromacs 4.5.4 program package²⁸ was used for all MD simulations, applying a time step of 2 fs, a semi-isotropic Berendsen barostat at 1 bar, and V-rescale thermostat at 310 K. After energy minimization, the simulation was run with position restraints on the protein for 1 ns, followed by 10 consecutive 1 ns long simulations for system equilibration. Final MD simulations were run for 100 ns.

Analysis. The tilt angle between the heme plane, defined by the heme nitrogens, and the lipid bilayer normal, defined as the z axis, was analyzed over the last 50 ns of the production run.

Positions of the access/egress channels were calculated using the command-line version of the MOLE 2.0 software.²⁰ Analysis of the individual structures was also possible using the MOLEonline web server <http://mole.upol.cz>.²⁹ Analysis of the dynamical opening and closing of the channels was based on superimposed 1 ns snapshots from the last 50 ns of the simulations. Two types of simulations were considered: simulations of membrane-embedded CYP structures reported in this paper and CYP simulations in water reported in ref 30. Membrane atoms, as well as ions, waters, and hydrogens, were removed from the structures prior to channel computation. The interior threshold and bottleneck radius, which define the smallest detectable channels, were set to 1 Å. The probe radius and surface cover radius were set to 5 Å in order to sample the rough CYP surface. The starting point was set 4 Å above the heme iron. Snapshot structures were superimposed over the final structure of the catalytic domain. Central points of all channels were transcribed onto a 3D grid with 1 Å spacing in all directions. The maximal value of the radius at each point on the grid was selected. Only points with a radius larger than 1.5 Å (approximate radius of water) were reported. Positions of individual channel openings were defined as a series of channel points located on the surface of the protein.

RESULTS AND DISCUSSION

Model of Membrane-Bound CYP2C9: 1 μ s Molecular Dynamics Simulation. The initial structure of CYP2C9 on the DOPC lipid bilayer was assumed to be the same as the model constructed in our previous study based on available experimental data.¹⁵ A 1 μ s long MD simulation of CYP2C9 on

the membrane was carried out to test the simulation time required to achieve convergence of the orientation of CYP on the lipid bilayer. The catalytic domain fold remained stable, i.e., did not significantly deviate from the crystal structure (the root-mean-square deviation of 490 C α atoms was smaller than 2.5 Å, Table S1, Supporting Information). Typical thermal fluctuations were detected mainly in the loops, similar to the fluctuations observed previously in MD simulations of the catalytic domain in water.³¹

However, the orientation of the catalytic domain with respect to the membrane relaxed during the course of the test simulation. The catalytic domain tilted from its initial orientation and spontaneously embedded deeper to the bilayer within the first 100 ns. Afterward, the orientation and penetration depth remained stable and did not significantly change further over the remainder of the 1 μ s long MD simulation. As mentioned above, the fold of the catalytic domain remained stable and any fluctuations mostly occurred in the loops. The N-terminal helical anchor displayed a small precession movement around the membrane normal inside the lipid bilayer. The above findings suggested that a 100 ns long simulation was sufficient for obtaining a convergent model of CYP immersed in the lipid bilayer (Figure 2).

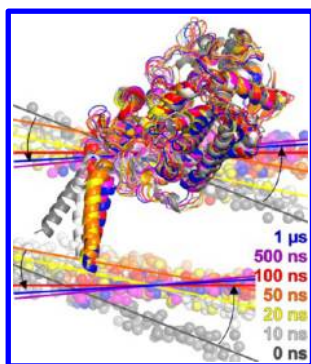


Figure 2. Position of CYP2C9 (represented by a secondary elements model) on a DOPC bilayer (only balls representing lipid phosphates are shown for clarity) showing that it converged on a 100 ns time scale and then remained stable until the end of the 1 μ s long molecular dynamics (MD) simulation. Initial position of CYP2C9 was based on available experimental data and adopted from our previous study.¹⁵ Snapshots extracted at different times (labeled on the right side) during the course of the MD simulation are superimposed over the catalytic domain to highlight the tilting of the initial structure (direction of tilting shown by black arrows).

All other CYP models (CYP1A2, CYP2A6, CYP2D6, CYP2E1, and CYP3A4) were constructed starting from the equilibrated structure of CYP2C9 taken after 100 ns. As expected, the bilayer orientation in these models converged even faster than in the CYP2C9 model, typically within the first 50 ns of the MD simulations (data not shown). During the MD simulations, the folds of all CYP catalytic domains remained stable except for typical thermal fluctuations. However, the depth and orientation in the membrane differed between the individual CYPs, as discussed below.

Immersion of the CYP2C9 catalytic domain in the membrane induced a funnel- or bowl-shaped depression in the lipid bilayer plane at the contact surface between CYP2C9 and bilayer (Figure 1). Due to the depression, the lipid headgroups and even water molecules shifted closer to the bilayer center than in the unperturbed bilayer (Figure S1,

Supporting Information). In principle, four different CYP regions could be distinguished according to their interaction with the lipid bilayer: (i) region inside the lipid bilayer in contact with the nonpolar bilayer interior, (ii) region inside the lipid bilayer in contact with immersed polar headgroups, (iii) region above the lipid bilayer in contact with polar lipid headgroups, and finally (iv) region above the lipid bilayer in contact with the cytosol but not lipids.

Parts of the CYP2C9 catalytic domain that were completely immersed and in contact with the nonpolar lipid bilayer interior included the N-terminal transmembrane helix, tip of the β 1 sheet, A' helix, B' helix in the B/C and F'/G' loops, and N-terminal part of the G helix. However, a significantly larger part of the catalytic domain resided below the lipid bilayer surface plane, in contact with polar headgroups, i.e., large parts of the F and G helices, base of the B/C loop, and tip of the "finger" β 4- β 5 region. The third group consisted of parts lying above the membrane plane but still in contact with polar headgroups, i.e., the Pro-rich region connecting the N-terminal transmembrane helix with the catalytic domain, A helix, ends of the F and G helices, H/I loop, and majority of the "finger" β 4- β 5 region. The last group comprised parts mainly lying on the proximal side of the catalytic domain.

We analyzed the active site access channels using the recently developed MOLE 2.0 software, which has been shown to outperform previous software tools, e.g., CAVER 1.0³² and MOLE 1.4.³³ Channels positioned around or through the F'/G' loop (denoted 2a, 2ac, 2d, 2f, and 4 according to the nomenclature of Wade et al.²¹) and B'/C loop (2b, 2c, or 2e) would open their entrances into the headgroup region of the bilayer, but only channels 2b and 2c were detected open during the simulation. The channel leading between the F and the G helices (channel 3) would also point into the headgroup region. Just above the lipid headgroups, the solvent channel opened its exit and the water channel was found to be open to the proximal side facing the cytosol.

Membrane-Anchored CYPs: Common Features and Variations. Molecular dynamics simulations of CYP models other than CYP2C9 showed quicker convergence of their orientation on the lipid bilayer, most likely because their initial positions were based on the relaxed position of CYP2C9 on the bilayer. All studied CYPs had catalytic domains that were partially immersed in the bilayer, like CYP2C9; however, they displayed slightly different and CYP-specific orientations and immersions (Figures 3 and 4).

The common parts immersed in the nonpolar regions of the membrane were the transmembrane helical anchor, loop of the A' helix, and the F' and G' helices. Parts below the bilayer plane but still in contact with polar headgroups of the lipids were the most variable. They reflected individual and specific CYP orientations on the lipid bilayer (discussed in detail later). The F/G loop displayed contact with the membrane interior, and its tip reached the membrane center. The H/I loop and "finger" β 4-5 region were in contact with the polar headgroups but above the bilayer. The proline-rich region lies above the membrane plane due to the rather high polarity of adjacent amino acids. As a consequence, the arrangement of the membrane-anchoring region was as follows: transmembrane N terminal helix, followed by the rather polar Pro-rich region in contact with the water-membrane interface, followed by the A' helix loop (in cases where it could occur), which was immersed in the membrane. The subsequent A helix was in all cases just above the polar headgroups. Such an arrangement was the

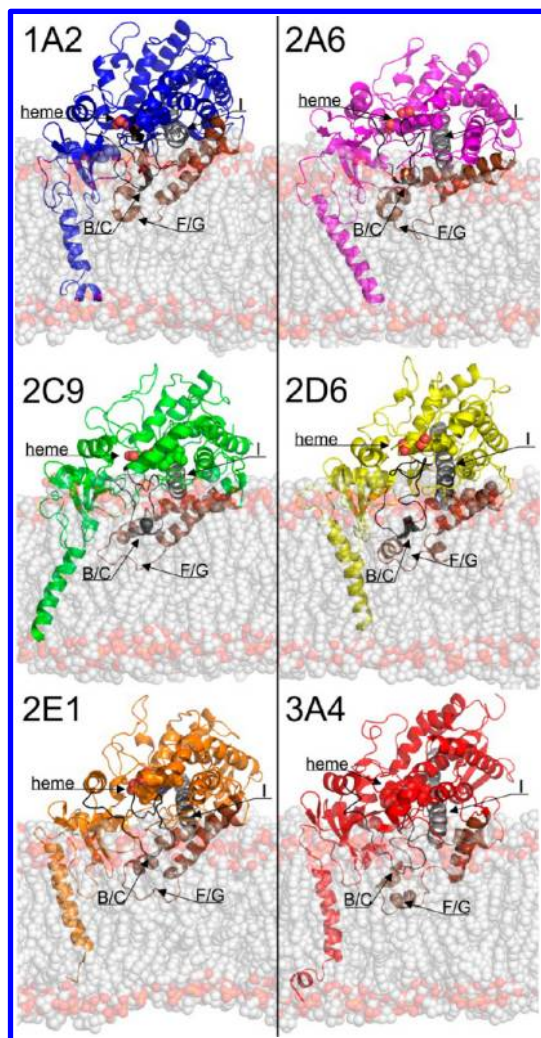


Figure 3. Final snapshots of membrane-anchored CYPs from molecular dynamics simulations showing their orientations on the lipid bilayer. All structures were oriented horizontally with respect to the bilayer plane and perpendicularly with respect to I helix in-plane vector (shown in gray). Different orientations of CYPs can be easily seen from the variation of the tilting angles of I helix with respect to the membrane plane. B/C and F/G loops are shown in black and brown, respectively. As the whole lipid bilayer is shown in a transparent mode, only the frontmost layer of the lipid molecules are visible, and therefore, the membrane depression of the lipids closer to the CYP is partially hidden in this visualization by unperturbed bilayer in front. Water molecules are not shown for clarity.

common membrane anchorage for all studied CYP catalytic domains (Figure 5), but slight differences in immersion and orientation were detected between the individual CYPs.

The individual CYP models on lipid bilayers also displayed some variations in orientation and penetration depth on the lipid bilayer. The orientation of CYP on the membrane can be experimentally characterized by measurement of the tilt angle θ (shown in Figure 1) between the heme plane and the lipid bilayer normal.¹³ A tilt angle θ of $(60 \pm 4)^\circ$ has recently been measured for CYP3A4 in POPC nanodiscs by linear dichroism.¹⁴ The tilt angle calculated from the last 50 ns of our MD simulation was $(56 \pm 5)^\circ$, which agrees with the experimental value within error bars. The MD simulations showed that the tilt angle values varied among the studied CYPs (Table 1), ranging from 56° (CYP3A4) to 72°

(CYP2D6). Tajkhorshid et al.¹⁴ predicted a tilt angle of $(72 \pm 3)^\circ$ for CYP3A4 from MD simulations, but this value differed significantly from the experimental value reported in the same paper. This difference can be attributed to the membrane model (highly mobile membrane model, HMMM) used in the respective article. HMMM consists of two distinctive parts: (i) short lipid tails combined with dichloroethane (to increase the mobility of the membrane interior and thereby convergence of the protein model while retaining the lipid bilayer polarity and density profiles) and (ii) carbonyl groups constrained to their specific positions in the unperturbed membrane to retain the size of the respective membrane. However, the latter constraint does not allow deformation of the CYP/membrane interface (cf. Figure 1) and consequently may prohibit deeper immersion of CYP into the HMMM membrane.

Our simulations showed that the D/E loop of CYP1A2 was more inclined toward the membrane than that of CYP2C9. Consequently, the $\beta 1$ sheet and B/C loop of CYP1A2 were pulled out of the membrane while still retaining some contact with head groups (Figure 3). The F/G loop was immersed below the lipid headgroups, thus allowing channels in its vicinity (2a, 2f, 4) to open into the interior of the lipid bilayer, but these channels were not observed during the simulation. Only channels pointing into the headgroup region were observed between the B/C and the F/G loops (2c) and between the F/G loop and the I helix (S). A channel pointing toward the proximal side (water channel) opened toward the cytosol (Figure 6).

CYP2A6 adopted a similar orientation in the membrane to that of CYP1A2. The only difference was slightly greater immersion of the B' and G helices of CYP2A6 (Figure 3). The positions of the channel openings of CYP2A6 were therefore similar to those discussed in the previous paragraph. The main differences were that channels in the vicinity of the B/C loop were immersed deeper to the bilayer (2c), the channel through the F/G loop (4) pointed toward the lipid bilayer interior, and the remaining channel (2b, S) pointed toward the lipid head groups (Figure 6).

Of all the CYPs studied, CYP2D6 differed in the orientation such that its F and G helices and beta "finger" $\beta 4-5$ loop had the smallest contact with the membrane, which meant that the solvent channel had low contact with the membrane and opened into the cytosol (Figure 3). The D/E loop also had no contact with the membrane; therefore, CYP2D6 had the smallest contact surface with the membrane. On the other hand, the B/C loop had extensive contact with the nonpolar part of the membrane, thus making channels in its vicinity more immersed than in other CYPs and in contact with lipids (2c, 2b, 2e). Also, the tip of the F/G loop pointed toward the nonpolar interior of the bilayer. Therefore, channels in its vicinity (4, 2f) were accessible from the membrane interior (Figure 6).

The orientation of CYP2E1 was similar to CYP2D6, but it was slightly more immersed as it made larger contact with the membrane facilitated by the beta "finger" $\beta 4-5$ region (Figure 3). Only the B' helix of the B/C loop was immersed below the lipid headgroups, and therefore, only a channel through the F/G loop contacted the nonpolar part of the membrane (2f). The rest of the channels around the B/C loop (2c, 2b, 2e) pointed to lipid headgroups, and the solvent channel pointed more to the cytosol (Figure 6).

CYP3A4 exhibited the most similar orientation and immersion to those of CYP2C9. However, CYP3A4 has more polar amino acids in the anchorage region, as shown by its

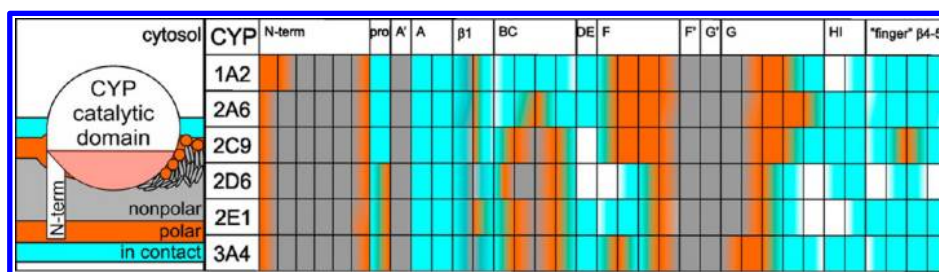


Figure 4. Comparison of immersion and orientation of different regions in equilibrated cytochrome P450 structures. Schematic representation of a CYP on a membrane is shown in the left panel. Lipids on the protein–membrane interface adopt a specific arrangement, as shown in the schematic. Some parts of the CYP are in contact with polar lipid headgroups on the membrane surface (blue). Lipid headgroups in the vicinity of the protein lie below the membrane surface due to interactions with polar residues (orange), and part of the CYP catalytic domain is immersed below the membrane plane (red). In contrast, only a small part of the catalytic domain below the membrane surface interacts with the nonpolar center of the membrane (gray). Right panel displays the positions of important CYP regions in the bilayer (cf. the left panel for color coding).

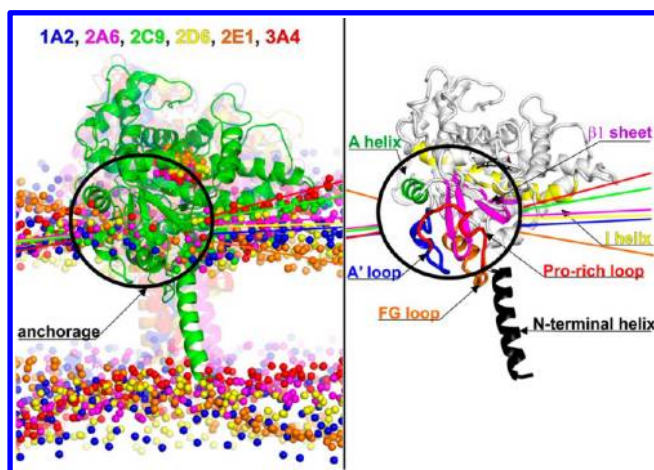


Figure 5. CYP N-terminal anchorage region. Catalytic domains of all final CYP structures on bilayers are shown superimposed. Phosphorus atoms are represented by spheres of different colors for the individual CYPs (CYP1A2, blue; 2A6, magenta; 2C9, green; 2D6, yellow; 2E1, orange; 3A4, red). Pro-rich region followed by a deeply immersed nonpolar loop was found to be the common anchor region in all CYP structures with similar immersion, whereas catalytic domains displayed different degrees of immersion and orientation.

Table 1. Tilt Angle (in degrees) between the Heme Plane and the Lipid Bilayer Normal (cf. Figure 1)

CYP	simulation	experiment	literature ^a
1A2	67 ± 6		
2A6	69 ± 5		
2C9	61 ± 4		55 ± 5, ¹⁵ 50 or 35 ¹⁶
2D6	72 ± 6		
2E1	60 ± 5		
3A4	56 ± 5	60 ± 4 ¹⁴	72 ± 3 ¹⁴

^aValues were recalculated to match the angle between the heme plane and the membrane normal as defined in ref 14.

hydration pattern reported by Hendrychova et al.³⁰ Thus, CYP3A4 makes greater contact with the polar headgroups despite having similar immersion to that of CYP2C9. The parts in contact with the nonpolar part of the bilayer included the A' loop, part of the B/C loop, and the whole F/G loop. The parts in contact with the polar headgroups below the membrane plane were the Pro-rich region, β 1 sheet, B/C loop, and F and G helices. The D/E and H/I loops remained above the plane, retaining contact with the polar headgroups. However, the

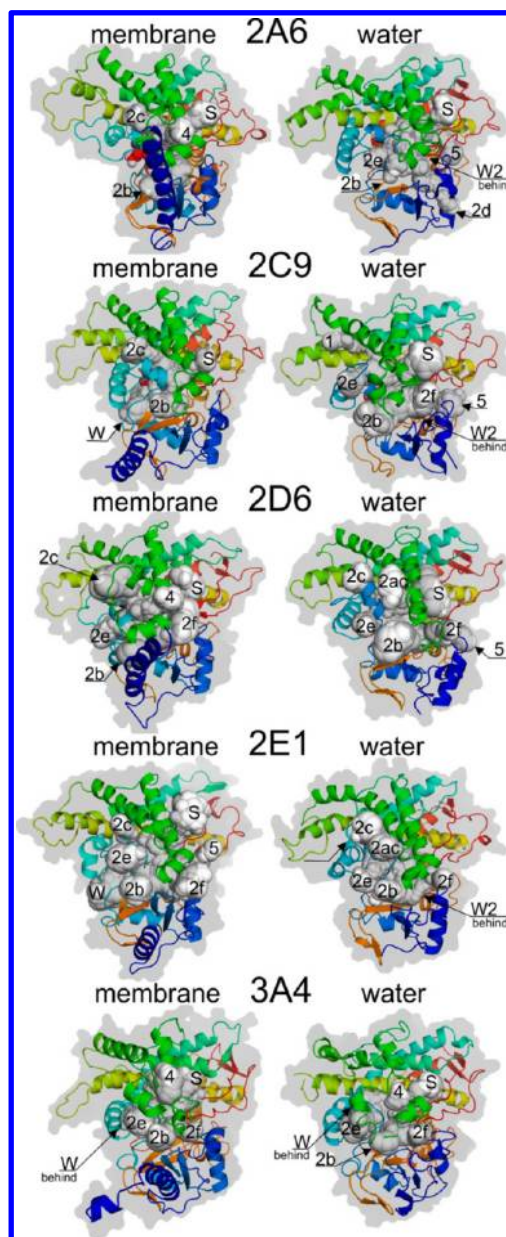


Figure 6. Open channels detected in the CYP membrane (left) and water (right) simulations. Only channels wide enough to enable passage of a probe of radius 1.5 Å are shown.

“finger” $\beta 4$ – $\beta 5$ region was less immersed in the membrane than in the case of CYP2C9 (Figure 3). The channels that opened in contact with the hydrophobic part of the membrane were all located around the F/G loop (2f, 2b, 4). Channel 2e and the solvent channel opened just above the lipid headgroups. Finally, the water channel pointed directly into the cytosol (Figure 6).

Analysis of CYPs’ surface amino acids showed that 12.5% of the surface was in contact with lipid tails, 36.5% faced the lipid headgroups, and 51% of the surface amino acids faced cytosolic water. Aliphatic (V, I, L) and nonpolar phenylalanine (F) and cysteine (C) amino acids occurred preferentially on the contact surface with the lipid tails, whereas all charged (R, K, D, E) and polar amino acids (H, Q) and glycine (G) were underpopulated in this contact region (Tables S2 and S3, Supporting Information). The contact surface with the headgroup region contained a higher amount of tryptophan (W), lysine (K), and glutamine (Q) amino acids, whereas some nonpolar amino acids (I, F, and C) were underpopulated. Charged amino acids (K, R, D) were overpopulated on the cytosolic surface, whereas nonpolar amino acids (V, L, W) were underpopulated in this area. The observed differences in membrane orientations of individual CYPs can be rationalized by different amino acids composition of CYP surfaces. CYPs surface spots rich in nonpolar aliphatic amino acids push these parts toward the membrane interior, while tryptophan to the interface and charged amino acids prefer to be immersed in either the headgroup region or cytosol.

Behavior of Active Site Access/Egress Channel Network in Membrane-Anchored and Solvent-Exposed CYPs. The mechanism of substrate and product channeling to and out of the CYP active site is an important but still not fully answered question of CYP structural biology. Because of a lack of direct experimental data, clues as to the mechanism of substrate/product channeling have relied on analyses of X-ray structures^{21,34} and MD simulations.^{3,34–39} However, recent models of membrane-anchored CYP2C9 have identified significant differences in the behavior of membrane-anchored and fully solvent-exposed enzyme.^{15,16} Phospholipids have been shown to enhance the activity of ethoxyresorufin-*O*-deethylase in recent experiments by Ghosh and Ray.⁴⁰ Thus, to test whether this also applies to CYPs, we compared the behavior of membrane-anchored and fully solvent-exposed CYPs. We focused on the access channels, which were analyzed using a recent version of MOLE 2.0 software. For comparison, CYP MD simulations in water were taken from ref 30 and analyzed using the same protocol.

We found that the channels fluctuated dynamically (opened and closed) during the course of the MD simulations. In contrast, in most of the reported CYP X-ray structures, the channels appear to be closed as they usually have radii below 1.4 Å. If the channels were rigid, passage of CYP substrates to the active site would be hindered because CYP substrates are typically larger than the diameter of the channel bottlenecks. However, if the channels fluctuate (breathe) over time, as the MD simulations imply, molecules may enter and leave the CYP active site. Therefore, the bottleneck can move along the channel line as a “peristaltic wave”, allowing molecules to pass through the active site access/egress channel. The same mechanism has already been reported for passage of water molecules to CYP active sites.³⁰ In addition, adaptive changes in the local channel cross-section may also be induced by the presence of a ligand in the channel. It should be noted that

large conformational changes of the CYP catalytic domain may also occur, e.g., as observed for CYP2B4, leading to wide opening of the CYP2B4 active site.⁴¹ However, these changes are unlikely to be detected in MD simulations due to the still short time scales used (hundreds of nanoseconds).

The membrane-bound CYPs showed fewer open channels than the same CYPs simulated in water (Figure 6 and Table 2).

Table 2. CYP Channels (denoted according to the nomenclature by Wade et al.²¹) Having Radius Above 1.5 Å Calculated from MD Simulations in the Membrane (this work) and Water (taken from ref 1) by MOLE 2.0 Software^a

CYP	membrane	water
1A2	S, 2c, W	N.A.
2A6	S, 2b, 2c, 4	S, 2b, 2d, 2e, 5, W2
2C9	S, 2b, 2c, W	S, 2b, 2e, 2f, 1, 5, W2
2D6	S, 2b, 2c, 2e, 2f, 4	S, 2b, 2c, 2e, 2f, 2ac, 5
2E1	S, 2b, 2c, 2e, 2f, 5, W	2b, 2c, 2e, 2f, 2ac
3A4	S, 2b, 2e, 2f, 4, W	S, 2b, 2e, 2f, 4, W

^aIn **bold** are highlighted channels with radius above 2 Å. MD simulation of CYP1A2 in water was not carried out.

This can be attributed to smaller fluctuations of the membrane-exposed parts of catalytic domains in comparison with solvent-exposed parts of the catalytic domains or when exposed only to a water environment, as movements of protein chains are slower in lipids than in water.^{15,16} The most open CYP structures (having channels with the largest bottleneck radii) were CYP3A4, CYP2D6, and CYP2E1, which also had the most channels opening toward the membrane interior. In contrast, CYP1A2 had the most closed structure. The solvent channel and channel 2b were detected in both the water and the membrane simulations; the former typically had a larger bottleneck radius than the corresponding channel 2b. Open channels 2c and 4 were present more frequently in membrane simulations than in the water simulations, whereas open channels 2e and 2f were preferentially found in the water simulations. It should be noted that open channels 2e and 2f were only identified in the membrane simulation of the most open CYPs (CYP3A4, CYP2D6, and CYP2E1). Channel 5 was closed in all membrane simulations but open in most simulations in water. Channels 1, 2ac, and 2d were open only in the water simulations. On the other hand, the water channel (running from the active site between the I helix and heme and opening on the proximal side) was closed in the water simulations but open in most of the membrane simulations. Thus, the lipid environment resulted in closure of channels 5, 1, and 2d and the water channel. Channels belonging to the 2x family (mostly channels 2b and 2c) were open and had entrances in/below the headgroup region. The solvent channel pointed just above the lipid headgroups, and the water channel opened to the cytosol. Finally, CYPs on the membrane more often had an open channel 4 pointing toward the lipid tails.

In summary, MD simulations showed the dynamic character of the active site access channels, many of which fluctuated (opened and closed) during the course of the simulations. Further, the active site access channel networks differed between the water and the membrane environments, indicating that only data on membrane-anchored CYPs is relevant for determining the substrate/product channeling mechanism in vivo.

Comparison of Positions of Access/Egress Active Site Openings with Penetration Depths of Prototypical CYP Substrates and Metabolites. Simulation results showed that CYPs anchored to a membrane have complex networks of active site access and egress channels, with some opening their entrances inside the membrane while others opening at/above the water–membrane interface. As the orientations of the catalytic domains differ between the individual CYPs, the exact positioning of channel entrances reflects the specific orientation of the individual CYP (Figure 7). Generally, substrates and

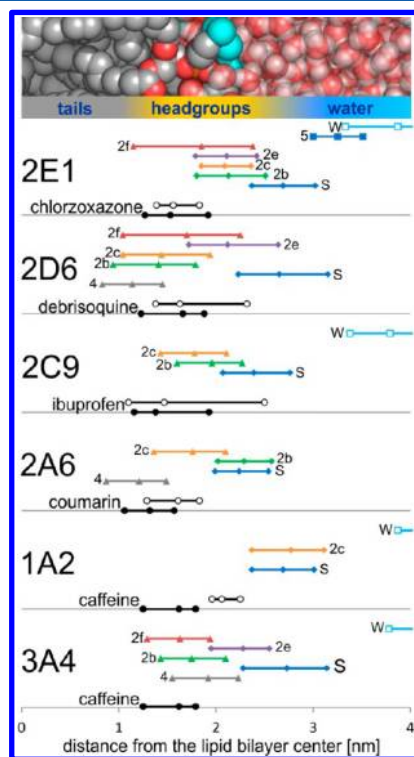


Figure 7. Scheme showing the positions of substrates (filled black circles; central circle represents ligand's center-of-mass membrane position with the lowest free energy, and right and left circles delimit the area accessible at RT, $T = 310$ K) and their respective metabolites (open circles). Average, minimal, and maximal positions of CYP active site access/egress channels openings (denoted according to the nomenclature of Wade et al.²¹) in the membrane were calculated as centers of balls inscribed in the channel's openings. Substrate access channels whose membrane positions overlap with positions of substrates are shown by triangles, while product release channels (i.e., channels whose membrane positions overlap with positions of metabolites) are shown by diamonds. Channels pointing toward the cytosol are shown by squares. (Top) Membrane profile on the same scale for ready comparison.

metabolites localize in the membrane layer, where channel openings are also positioned. Nevertheless, most substrates tend to be closer to the nonpolar phospholipid tail region (deeper in the membrane), whereas most metabolites tend to be closer to the water–membrane interface because metabolites are usually less lipophilic than their respective substrates (cf. Figure S2, Supporting Information).²³ It should be noted that substrates also typically have higher affinities for the membrane than the respective metabolites.²³ The differences in affinities and positioning of substrates and metabolites may generate concentration gradients that are crucial for CYP action, i.e., the high affinity of substrates may enhance the local concentration

of the substrate in the membrane, whereas the low affinity of metabolites may facilitate membrane clearance (release of the respective metabolite to the cytosol for subsequent metabolic steps). In addition, as the membrane positions of the studied substrates correlate with the openings of the active site access channels from the family 2x, we may infer that these channels are involved in substrate trafficking to the CYP active site. On the other hand, as metabolites tend to be positioned near the water–membrane interface where the opening of the solvent channel is located, we may surmise that the solvent channel is involved in product release.

Another important question concerns whether the positions of substrate access channels correlate with substrate preferences of individual CYPs. Some channels retained similar membrane positions in most of the studied CYPs, whereas others varied more significantly. The channels that always pointed toward the lipid interior were channels 2f and 4, which may therefore serve as common access channels for lipophilic substrates. The solvent channel always pointed into the water–membrane interface and therefore may serve as an entrance/release for hydrophilic substrates/products. However, the positions of some channels from the 2x family differed considerably. For instance, channel 2b was inserted deep into the lipid bilayer in CYP3A4, CYP2C9, and CYP2D6, whereas it pointed toward the water–membrane interface in CYP2A6 and CYP2E1. The differences observed in the channel opening positions reflect the variability of the amino acid composition of the region, which is in contact with the membrane.

We also identified variations in amino acid composition in openings of each channel type (Table S4, Supporting Information). The W channel had the least variable channel openings, which were positively charged due to the presence of arginine(s). Solvent channel openings were polar with at least two polar amino acids in all CYPs; however, they contained a variable number of nonpolar amino acids, which was compensated with charged ones. Amino acid composition of other channels was more specific for individual CYPs. Openings of channels 2b and 2c also contained polar or charged amino acids in their openings, but the numbers of nonpolar amino acids present there were larger in channel 2c in CYP1A2 and CYP2C9. Channel 2e openings contained a relatively large amount of charged amino acids. Openings of channels 2f and 4, on the other hand, were rather nonpolar however not in all cases, e.g., CYP2D6 was an exception. Comparing amino acid composition of opening CYP active site access channels we observe the same common features (like the charged W channel and rather polar solvent channel) as well as variations among individual CYPs. This indicates that the composition of channel openings may also contribute to substrate preferences of individual CYPs.

Taking into account the predicted fluctuations of the CYP catalytic domain on the membrane, the thermally accessible space of the substrate in the membrane, and the number (and variability) of CYP substrates, it seems unlikely that there is a straightforward correlation between substrate membrane positions and CYP substrate preferences. However, most membrane-anchored CYPs have probably evolutionarily adapted for flexible uptake of lipophilic substrates from membranes and release of the more hydrophilic metabolites to a membrane–water interface or the cytosol. Nevertheless, we cannot rule out the possibility that some CYP forms (e.g., CYP3A4) may also uptake more hydrophilic substrates directly from the water–membrane interface.

CONCLUSIONS

Human microsomal cytochromes P450 are membrane-anchored enzymes significantly involved in drug metabolism. While a wealth of structural information about water-soluble engineered CYPs has been obtained from X-ray crystallography, information about the membrane orientation and immersion has so far been limited. In this study, we constructed atomic models of several membrane-anchored human CYPs known to be involved in drug metabolism (CYPs 1A2, 2A6, 2C9, 2D6, 2E1, and 3A4). We relaxed the atomic models by MD simulation on a 100+ ns time scale. We showed that the region of the trans-membrane helix attachment to the catalytic site (“anchorage region”) is similarly immersed in the membrane for all CYP models studied, whereas the catalytic domains generally differ in their orientation toward the membrane, as shown by the different heme tilt angles. The heme tilt angle calculated from the MD simulation of membrane-anchored CYP3A4 ($56 \pm 5^\circ$) was in agreement with a recently reported experimental value ($60 \pm 4^\circ$). The lipid bilayer was also influenced by the presence of CYP. In particular, it adopted a funnel- or bowl-like deformation at the enzyme/membrane interface, causing the polar head groups to shift closer to the lipid bilayer center. Comparison of the behavior of fully water-exposed and membrane-anchored CYP showed that the lipid environment also influences the opening of channels. The six forms of membrane-anchored CYP studied here shared several common features, e.g., a catalytic domain partially immersed in the membrane with a solvent-exposed proximal side. However, the orientation of individual CYPs on the membrane displayed some variations. We thoroughly analyzed the network of active site access and egress channels. The opening of channels belonging to the 2x family faced either the membrane interior or the membrane head groups, whereas the solvent channel pointed to the water–membrane interface. We further compared the positions of access and egress channels openings with positions of prototypical CYP substrates and their respective metabolites. The results suggested that the deeply immersed channel openings may facilitate uptake of lipophilic substrates from the membrane to the active site, whereas the solvent channel serves as an entrance or exit for more hydrophilic substrates or products. Our data also indicate that the amino acid composition of access channels openings may contribute to substrate preferences of individual CYPs.

ASSOCIATED CONTENT

Supporting Information

Details about setup and RMSD of catalytic domains, amino acids composition of CYPs surface parts in contact with membrane, headgroup, and cytosol and access channels openings, and supporting figures showing bilayer density profile and prototypical free energy profiles along membrane normal. This material is available free of charge via the Internet at <http://pubs.acs.org>.

AUTHOR INFORMATION

Corresponding Author

*E-mail: michal.otyepka@upol.cz.

Notes

The authors declare no competing financial interest.

ACKNOWLEDGMENTS

This work has been supported by the Operational Program Research and Development for Innovations - European Regional Development Fund (CZ.1.05/2.1.00/03.0058) and Operational Program Education for Competitiveness - European Social Fund (CZ.1.07/2.3.00/20.0017 and /20.0058). M.O. acknowledges support by the Czech Grant Agency through the P208/12/G016 project. K.B. acknowledges support by the Czech Grant Agency through the P303/12/P019 project. M.P. acknowledges support by the student project PrF_2013_028 (Palacký University Olomouc).

REFERENCES

- (1) Black, S. D. Membrane Topology of the Mammalian P450 Cytochromes. *FASEB J.* **1992**, *6*, 680–685.
- (2) Johnson, E. F.; Stout, C. D. Structural Diversity Of Eukaryotic Membrane Cytochromes P450. *J. Biol. Chem.* **2013**, *288*, 17082–17090.
- (3) Otyepka, M.; Berka, K.; Anzenbacher, P. Is There a Relationship Between the Substrate Preferences and Structural Flexibility of Cytochromes P450? *Curr. Drug Metab.* **2012**, *13*, 130–142.
- (4) Domanski, T. L.; Halpert, J. R. Analysis of Mammalian Cytochrome P450 Structure and Function by Site-directed Mutagenesis. *Curr. Drug Metab.* **2001**, *2*, 117–37.
- (5) Poulos, T.; Johnson, E. Structures of cytochrome P450 enzymes. In *Cytochrome P450: Structure, Mechanism, and Biochemistry*; Ortiz de Montellano, P. R., Ed.; Kluwer Academic/Plenum Publishers: New York, 2005; pp 87–114.
- (6) Otyepka, M.; Skopalík, J.; Anzenbacherová, E.; Anzenbacher, P. What Common Structural Features and Variations of Mammalian P450s Are Known to Date? *Biochim. Biophys. Acta, Gen. Subj.* **2007**, *1770*, 376–389.
- (7) Brown, C. A.; Black, S. D. Membrane Topology of Mammalian Cytochromes P-450 from Liver Endoplasmic Reticulum. Determination by Trypsinolysis of Phenobarbital-treated Microsomes. *J. Biol. Chem.* **1989**, *264*, 4442–9.
- (8) von Wachenfeldt, C.; Johnson, E. F. Structures of Eukaryotic Cytochrome P450 Enzymes-Membrane Topology. In *Cytochrome P450: Structure, Mechanism and Biochemistry*; Plenum Press: New York, 1995; pp 183–223.
- (9) Ozalp, C.; Szczesna-Skorupa, E.; Kemper, B. Bimolecular Fluorescence Complementation Analysis of Cytochrome P450 2c2, 2e1, and NADPH-cytochrome P450 Reductase Molecular Interactions in Living. *Drug Metab. Dispos.* **2005**, *33*, 1382–1390.
- (10) Headlam, M. J.; Wilce, M. C. J.; Tuckey, R. C. The F-G Loop Region of Cytochrome P450_{sc} (CYP11A1) Interacts with the Phospholipid Membrane. *Biochim. Biophys. Acta, Biomembr.* **2003**, *1617*, 96–108.
- (11) Kiselyova, O. I.; Yaminsky, I. V.; Ivanov, Y. D.; Kanaeva, I. P.; Kuznetsov, V. Y.; Archakov, A. I. AFM Study of Membrane Proteins, Cytochrome P450 2B4, and NADPH-cytochrome P450 Reductase and Their Complex Formation. *Arch. Biochem. Biophys.* **1999**, *371*, 1–7.
- (12) Nussio, M. R.; Voelcker, N. H.; Miners, J. O.; Lewis, B. C.; Sykes, M. J.; Shapter, J. G. AFM Study of the Interaction of Cytochrome P450 2C9 with Phospholipid Bilayers. *Chem. Phys. Lipids* **2010**, *163*, 182–189.
- (13) Ohta, Y.; Kawato, S.; Tagashira, H.; Takemori, S.; Kominami, S. Dynamic Structures of Adrenocortical Cytochrome P-450 in Proteoliposomes and Microsomes: Protein Rotation Study. *Biochemistry* **1992**, *31*, 12680–12687.
- (14) Baylon, J. L.; Lenov, I. L.; Sligar, S. G.; Tajkhorshid, E. Characterizing the Membrane-Bound State of Cytochrome P450 3A4: Structure, Depth of Insertion and Orientation. *J. Am. Chem. Soc.* **2013**, *135*, 8542–8551.
- (15) Berka, K.; Hendrychová, T.; Anzenbacher, P.; Otyepka, M. Membrane Position of Ibuprofen Agrees with Suggested Access Path

- Entrance to Cytochrome P450 2C9 Active Site. *J. Phys. Chem. A* **2011**, *115*, 11248–11255.
- (16) Cojocaru, V.; Balali-Mood, K.; Sansom, M. S. P.; Wade, R. C. Structure and Dynamics of the Membrane-bound Cytochrome P450 2C9. *PLoS Comput. Biol.* **2011**, *7*, e1002152.
- (17) Denisov, I. G.; Shih, a Y.; Sligar, S. G. Structural Differences Between Soluble and Membrane Bound Cytochrome P450s. *J. Inorg. Biochem.* **2012**, *108*, 150–158.
- (18) Sgrignani, J.; Magistrato, A. Influence of the Membrane Lipophilic Environment on the Structure and on the Substrate Access/egress Routes of the Human Aromatase Enzyme. A Computational Study. *J. Chem. Inf. Model.* **2012**, *52*, 1595–1606.
- (19) Jiang, W.; Ghosh, D. Motion and Flexibility in Human Cytochrome P450 Aromatase. *PLoS ONE* **2012**, *7*, e32565.
- (20) Sehnal, D.; Svobodová Vařeková, R.; Berka, K.; Pravda, L.; Navrátilová, V.; Banáš, P.; Ionescu, C.-M.; Geidl, S.; Otyepka, M.; Koča, J. MOLE 2.0: Advanced Approach for Analysis of Biomacromolecular Channels. *J. Cheminform.* **2013**, *5*, 39.
- (21) Cojocaru, V.; Winn, P. J.; Wade, R. C. The Ins and Outs of Cytochrome P450s. *Biochim. Biophys. Acta* **2007**, *1770*, 390–401.
- (22) Conner, K. P.; Woods, C. M.; Atkins, W. M. Interactions of Cytochrome P450s with Their Ligands. *Arch. Biochem. Biophys.* **2011**, *507*, 56–65.
- (23) Paloncýová, M.; Berka, K.; Otyepka, M. Molecular Insight into Affinities of Drugs and Their Metabolites to Lipid Bilayers. *J. Phys. Chem. B* **2013**, *117*, 2403–2410.
- (24) Sali, A.; Blundell, T. L. Comparative Protein Modelling by Satisfaction of Spatial Restraints. *J. Mol. Biol.* **1993**, *234*, 779–815.
- (25) Wolf, M. G.; Hoefling, M.; Aponte-Santamaría, C.; Grubmüller, H.; Groenhof, G. G_{membed}: Efficient Insertion of a Membrane Protein into an Equilibrated Lipid Bilayer with Minimal Perturbation. *J. Comput. Chem.* **2010**, *31*, 2169–2174.
- (26) Berger, O.; Edholm, O.; Jähnig, F. Molecular Dynamics Simulations of a Fluid Bilayer of Dipalmitoylphosphatidylcholine at Full Hydration, Constant Pressure, and Constant Temperature. *Biophys. J.* **1997**, *72*, 2002–2013.
- (27) Oostenbrink, C.; Villa, A.; Mark, A. E.; Gunsteren, W. F.; Van, A. Biomolecular Force Field Based on the Free Enthalpy of Hydration and Solvation: The GROMOS Force-Field Parameter Sets 53A5 and 53A6. *J. Comput. Chem.* **2004**, *25*, 1656–1676.
- (28) Hess, B.; Kutzner, C.; van der Spoel, D.; Lindahl, E. GROMACS 4: Algorithms for Highly Efficient, Load-Balanced, and Scalable Molecular Simulation. *J. Chem. Theory Comput.* **2008**, *4*, 435–447.
- (29) Berka, K.; Hanák, O.; Sehnal, D.; Banáš, P.; Navrátilová, V.; Jaiswal, D.; Ionescu, C.-M.; Svobodová Vařeková, R.; Koča, J.; Otyepka, M. MOLEonline 2.0: Interactive Web-based Analysis of Biomacromolecular Channels. *Nucleic Acids Res.* **2012**, *40*, W222–W227.
- (30) Hendrychová, T.; Berka, K.; Navrátilová, V.; Anzenbacher, P.; Otyepka, M. Dynamics and Hydration of the Active Sites of Mammalian Cytochromes P450 Probed by Molecular Dynamics Simulations. *Curr. Drug Metab.* **2012**, *13*, 177–189.
- (31) Skopalík, J.; Anzenbacher, P.; Otyepka, M. Flexibility of Human Cytochromes P450: Molecular Dynamics Reveals Differences Between CYPs 3A4, 2C9, and 2A6, Which Correlate with Their Substrate Preferences. *J. Phys. Chem. B* **2008**, *112*, 8165–8173.
- (32) Petřek, M.; Otyepka, M.; Banáš, P.; Košinová, P.; Koča, J.; Damborský, J. CAVER: a New Tool to Explore Routes from Protein Clefts, Pockets and Cavities. *BMC Bioinf.* **2006**, *7*, 316.
- (33) Petřek, M.; Košinová, P.; Koča, J.; Otyepka, M.; Petřek, M.; Kosinová, P.; Koca, J. MOLE: a Voronoi Diagram-based Explorer of Molecular Channels, Pores, and Tunnels. *Structure* **2007**, *15*, 1357–1363.
- (34) Fishelovitch, D.; Shaik, S.; Wolfson, H. J.; Nussinov, R. Theoretical Characterization of Substrate Access/exit Channels in the Human Cytochrome P450 3A4 Enzyme: Involvement of Phenylalanine Residues in the Gating Mechanism. *J. Phys. Chem. B* **2009**, *113*, 13018–13025.
- (35) Wade, R. C.; Winn, P. J.; Schlichting, I.; Sudarko, A. Survey of Active Site Access Channels in Cytochromes P450. *J. Inorg. Biochem.* **2004**, *98*, 1175–1182.
- (36) Schleinkofer, K.; Winn, P. J.; Lüdemann, S. K.; Wade, R. C. Do Mammalian Cytochrome P450s Show Multiple Ligand Access Pathways and Ligand Channelling? *EMBO Rep.* **2005**, *6*, 584–589.
- (37) Li, W.; Liu, H.; Luo, X.; Zhu, W.; Tang, Y.; Halpert, J. R.; Jiang, H. Possible Pathway(s) of Metyrapone Egress from the Active Site of Cytochrome P450 3A4: a Molecular Dynamics Simulation. *Drug Metab. Dispos.* **2007**, *35*, 689–696.
- (38) Li, W.; Shen, J.; Liu, G.; Tang, Y.; Hoshino, T. Exploring Coumarin Egress Channels in Human Cytochrome P450 2A6 by Random Acceleration and Steered Molecular Dynamics Simulations. *Proteins* **2010**, *79*, 271–281.
- (39) Krishnamoorthy, N.; Gajendrarao, P.; Thangapandian, S.; Lee, Y.; Lee, K. W. Probing Possible Egress Channels for Multiple Ligands in Human CYP3A4: a Molecular Modeling Study. *J. Mol. Model.* **2010**, *16*, 607–614.
- (40) Ghosh, M. C.; Ray, A. K. Membrane Phospholipid Augments Cytochrome P4501a Enzymatic Activity by Modulating Structural Conformation During Detoxification of Xenobiotics. *PLoS ONE* **2013**, *8*, e57919.
- (41) Wilderman, P. R.; Halpert, J. R. Plasticity of CYP2B Enzymes: Structural and Solution Biophysical Methods. *Curr. Drug Metab.* **2012**, *13*, 167–176.

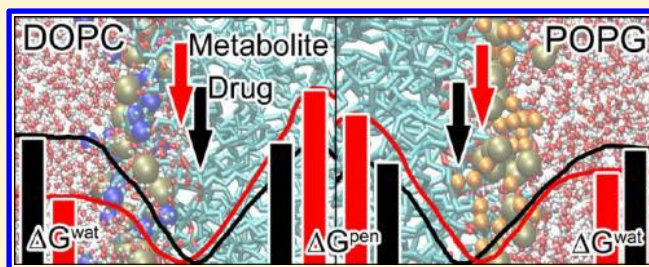
Molecular Insight into Affinities of Drugs and Their Metabolites to Lipid Bilayers

Markéta Paloncýová, Karel Berka,* and Michal Otyepka*

Regional Centre of Advanced Technologies and Materials, Department of Physical Chemistry, Faculty of Science, Palacký University Olomouc, tř. 17. listopadu 12, 771 46, Olomouc, Czech Republic

Supporting Information

ABSTRACT: The penetration properties of drug-like molecules on human cell membranes are crucial for understanding the metabolism of xenobiotics and overall drug distribution in the human body. Here, we analyze partitioning of substrates of cytochrome P450s (caffeine, chlorzoxazone, coumarin, ibuprofen, and debrisoquine) and their metabolites (paraxanthine, 6-hydroxychlorzoxazone, 7-hydroxycoumarin, 3-hydroxyibuprofen, and 4-hydroxydebrisoquine) on two model membranes: dioleoylphosphatidylcholine (DOPC) and palmitoyloleoylphosphatidylglycerol (POPG). We calculated the free energy profiles of these molecules and the distribution coefficients on the model membranes. The drugs were usually located deeper in the membrane than the corresponding metabolites and also had a higher affinity to the membranes. Moreover, the behavior of the molecules on the membranes differed, as they seemed to have a higher affinity to the DOPC membrane than to POPG, implying they have different modes of action in human (mostly PC) and bacterial (mostly PG) cells. As the xenobiotics need to pass through lipid membranes on their way through the body and the effect of some drugs might depend on their accumulation on membranes, we believe that detailed information of penetration phenomenon is important for understanding the overall metabolism of xenobiotics.



INTRODUCTION

The interaction of drugs with cell membranes dictates their pharmacological properties because it affects the drug distribution, transport, accumulation, partitioning, and metabolism.^{1–5} A drug must be passively⁶ or actively^{7–9} transported across the cell membrane before it can reach its target and perform its biological role. Passive transport depends on membrane structure, dynamics,¹⁰ and its permeability for a particular substance.⁶ Recently, we suggested that the positioning of drugs on lipid bilayers might also affect their interaction with drug metabolizing cytochrome P450 (CYP) enzymes,⁴ which are anchored to the membrane of the endoplasmic reticulum,¹¹ and as a consequence affect the metabolism of drugs. In addition, the positioning on and affinity to a membrane may play an important role in other biologically significant processes, such as antioxidant inhibition of lipid peroxidation.¹² The importance of drug–membrane interactions in biology, pharmacology, and medicine has called for extensive research in this field, which is rather challenging due to the complexity of biological membranes. Many experimental and theoretical techniques have been developed to study various aspects of drug membrane interactions.^{1,13–16}

Cell membranes form a protective wall around the cellular interior against an external environment, and separate cytosolic and noncytosolic sides of organelles.^{17,18} The membranes are predominantly composed of lipids, which form a lipid bilayer. Lipid bilayers are widely used as a membrane model in both

experiments and theoretical calculations. The membrane compositions of various cell structures differ, and their properties are mostly determined by their lipid composition,¹⁹ which is highly variable and includes numerous lipid types. However, by careful choice of lipid, a bilayer composed of one lipid type can mimic the key physicochemical features of a particular membrane.¹ In the present work, we chose to use a dioleoylphosphatidylcholine (DOPC) bilayer because phosphatidylcholine makes up about 40% of the human endoplasmic reticulum membrane mass,¹⁹ where the drug metabolizing CYP enzymes are mostly located.²⁰ The other model, a palmitoyloleoylphosphatidylglycerol (POPG) lipid bilayer, was chosen as an example of a negatively charged membrane, which is typically present in bacteria.²¹ Both bilayers differ in headgroup charge, density, thickness, and many other properties (Figure 1). Knowledge of the differences in cell membrane compositions among organelles or various organisms (e.g., between host and pathogen) can be used in rational drug targeting.¹ However, to exploit such information, the nature of drug–membrane interaction needs to be understood in detail.

Molecular dynamics (MD) simulation is a unique technique used in recent years for studying the dynamics of biological systems, simultaneously enabling fine space (atomistic) and

Received: November 30, 2012

Revised: February 6, 2013

Published: February 6, 2013

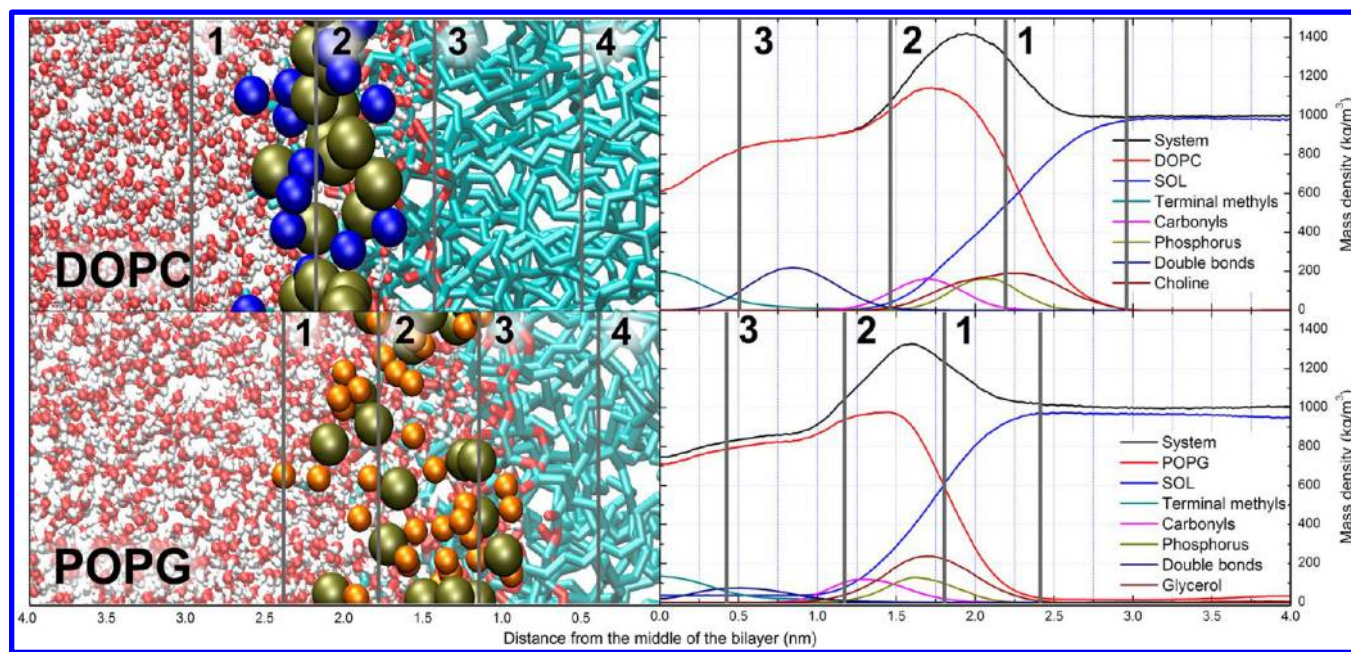


Figure 1. Lipid bilayers of DOPC and POPG analyzed in this study (left) and the density profiles of specified groups (right). The structure of the bilayer is divided into regions according to Marrink's four region model:²² Region 1 – low density of head groups. Polar area, where the conditions are similar to bulk water, ends when the density of water (SOL) and head groups are comparable. Region 2 – high density of head groups. Bulk-like water disappears; this region ends when the density of water is below 1%. Polar molecules are usually located here. Region 3 – high density of acyl tails. Double bonds in unsaturated lipids are located here. Region 4 – low density of acyl tails. The overall density drops and the movement of molecules is usually quicker. Regions 3 and 4 usually form a barrier for polar molecules. Carbon lipid tails are represented by cyan sticks, phosphates are depicted as olive and nitrogens as blue balls, terminal glycerol oxygens in POPG head groups are orange balls, and water molecules are represented by red and white balls.

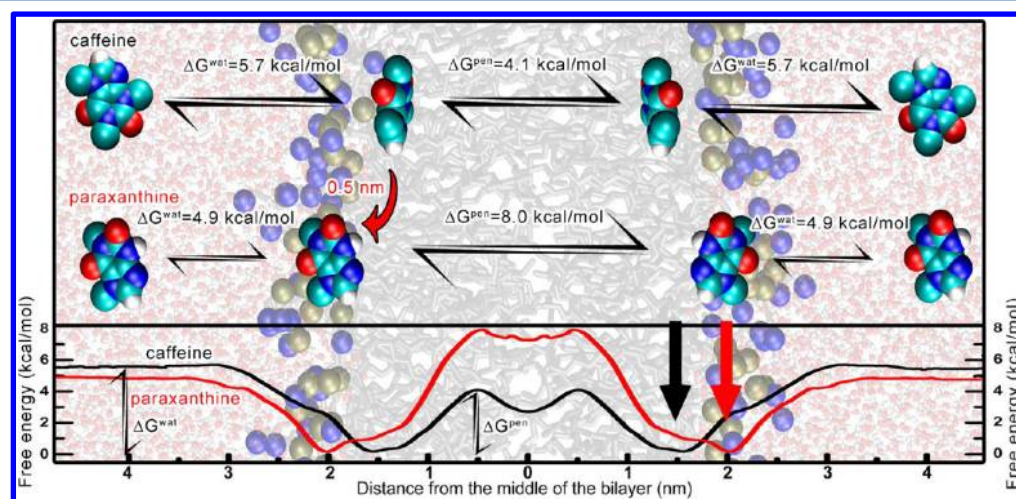


Figure 2. Scheme of caffeine and paraxanthine (caffeine metabolite) molecules moving through the DOPC bilayer (upper panel) highlighting the studied properties. The water/lipid barrier ΔG^{wat} of the drug (here caffeine) is higher than the corresponding value for the metabolite (paraxanthine), whereas the bilayer center penetration barrier ΔG^{pen} is higher for the metabolite. The position of the metabolite is located further from the bilayer center close to the polar headgroup region. The drug enters the membrane spontaneously and concentrates in the region near the entrance of the cytochrome P450 (CYP) active site access tunnel. The drug is metabolized in the active site and leaves CYP, most likely via a channel leading toward the polar headgroup region. The metabolite can escape the membrane more easily than the respective drug. DOPC chains are gray, nitrogens blue balls, phosphates brown, carbons cyan, oxygens red, and hydrogens white. The lower panel shows the free energy profile of caffeine (black) and paraxanthine (red) on a DOPC membrane. The free energy minimum and the heights of the energy barriers (water/lipid barrier ΔG^{wat} and bilayer center penetration barrier ΔG^{pen}) are labeled. The free energy profile is calculated for one leaflet and plotted symmetrically.

time (subpicosecond) resolutions. MD involves integration of simple Newtonian equations and calculates velocities of all atoms in the system from potential energy gradients.²³ The potential energy calculation is based on a simple mechanistic model known as a force field. The force field includes atomic parameters, bonds, angles, dihedrals, and charges in each

molecule. The molecule is then simplified as a system of harmonic oscillators (bonds, angles, and dihedrals), and noncovalent interactions are calculated from electrostatics (applying Coulomb's law to atomic centered partial charges) and using a Lennard-Jones potential (covering dispersion and repulsion).^{21,24} A variety of force fields have been developed,

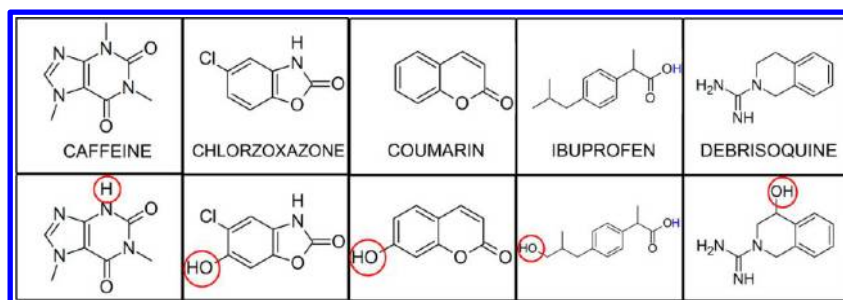


Figure 3. Structures of drugs (upper panel) and their metabolites (lower panel) showing the site of metabolism (red circles). The blue hydrogen in ibuprofen and 3-hydroxyibuprofen shows the location of deprotonation to form a charged molecule.

including all atoms, united atoms, and coarse-grained force fields.²⁵ The all atoms force field explicitly considers all atoms in the system, the united atoms force field (such as Berger lipid force field²⁶) reduces the number of atoms in the system by uniting nonpolar hydrogens with heavy atoms (usually carbons in lipid tails), and the coarse-grained force field uses beads to represent several (usually 4) heavy atoms. The reduction of the number of atoms in the system significantly reduces computational costs, allowing longer time scales to be considered in MD simulations. It should be noted that the quality of MD simulations heavily depends on the chosen force field, and the results of MD simulation should be interpreted with care and, whenever possible, cross-validated with available experimental data.

The penetration properties of small molecules on lipid bilayers can be well described by considering the free energy (ΔG) profile along the bilayer normal, also called the potential of mean force (PMF). The free energy minimum on this profile shows the energetically most favorable position of the molecule on the bilayer. The bilayer center penetration barrier is related to the velocity of transfer of the molecule to the other monolayer (bilayer leaflet), and the water/lipid barrier reflects the affinity to the bilayer in comparison to the water environment (Figure 2). The free energy profile is usually calculated for one leaflet, and the other leaflet is plotted symmetrically. For a polar drug-like molecule, its shape is usually as follows: The free energy of an amphiphilic molecule (used in this study) in a water environment is constant when the molecule is far from the bilayer. As it moves closer to the headgroup regions, the free energy decreases (Figure 2). The polar molecules are most probably located in the water/membrane interface. As the molecule proceeds further into the lipid bilayer, the hydrophobicity of the membrane environment increases and the free energy rises, and thus the molecule must overcome an energy barrier. In the bilayer center, a local energy minimum is usually also observed;²⁷ the mass density of this area is slightly lower than in the outer layers, and the molecules can reside here for some time.²⁸

In the present study, we analyzed the interaction of several model drugs, such as caffeine, chlorzoxazone, coumarin, ibuprofen (both its protonation forms, i.e., charged and uncharged), debrisoquine, and their corresponding major metabolites (Figure 3) with two lipid bilayers consisting of DOPC and POPG in terms of their free energy profiles along the bilayer normal. This enabled us to assess the relative comparison of the affinity of the studied compounds to the respective membranes and estimate their penetration capacities. We observed a higher affinity of drugs to the membrane compared to their CYP metabolites. Drugs and their

corresponding metabolites also differed in their preferred membrane positions; that is, drugs were positioned deeper in the lipid bilayer. This observation suggests that, after the first step of removal, drugs become more hydrophilic and can leave the membrane more easily than their metabolites. We also showed another aspect of drug removal, that is, that cytochrome P450 may clean the membrane of xenobiotics. Further, we observed significant differences in the affinities to DOPC and POPG membranes, which implies that such differences can be exploited in targeting various organisms or cellular compartments.

METHODS

Model lipid bilayers were taken from the Lipidbook server.²⁹ DOPC bilayer was prepared and equilibrated by Siu et al.;³⁰ POPG was prepared by Kukol et al.³¹ Both bilayers consisted of 128 lipid molecules with 64 in each leaflet. Bilayers were oriented perpendicularly to the *z*-axis and re-equilibrated with water and 0.154 M of NaCl. The POPG bilayer had an extra 128 Na⁺ ions to achieve electroneutrality.

Several drugs and their metabolites were chosen as typical substrates for a specific CYP. We studied the stimulating alkaloid caffeine (substrate of CYP1A2), the muscle relaxant chlorzoxazone (CYP2E1), the structure base of some anticoagulants coumarin (CYP2A6), nonsteroidal analgesic and antireumaticum ibuprofen (CYP2C9), antihypertensive debrisoquine (CYP2D6), and their respective major metabolites paraxanthine, 6-hydroxychlorzoxazone, 7-hydroxycoumarin, 3-hydroxyibuprofen, and 4-hydroxydebrisoquine, respectively. As ibuprofen bears a titratable carboxy group, we analyzed both protonation states (protonated $-\text{COOH}$ and unprotonated negatively charged $-\text{COO}^-$) for it and the respective metabolite.

Structures and topologies of drugs and metabolites were built using the PRODRG2Beta³² server. The atom types and bond parameters assigned by PRODRG are compatible with the lipid force field, but the assigned partial charges for hydrophobic groups make these groups too hydrophilic, and therefore these charges are not compatible with GROMOS force fields.³³ The atomic partial charges were derived using the RESP³⁴ (restraint electrostatic potential) procedure from an electrostatic potential calculated on a B3LYP/cc-pVDZ level of theory on structures equilibrated on the same level of theory in Gaussian 03.³⁵ The RESP fit was carried out using Antechamber from the AMBER 11 software package.³⁶ Recently, we have shown that the RESP partial charges provide free energy profiles along bilayer normal, reasonably agreeing with available experimental data.²⁸

Table 1. Free Energy Profiles and Hydration Free Energies (ΔG^{hyd}) of the Studied Molecules^a

	log <i>P</i>	ΔG^{hyd} , kcal/mol	DOPC				POPG					
			<i>P</i> , nm	<i>P</i> _{rel} , %	ΔG^{pen} , kcal/mol	ΔG^{wat} , kcal/mol	<i>P</i> , nm	<i>P</i> _{rel} , %	ΔG^{pen} , kcal/mol	ΔG^{wat} , kcal/mol	<i>pK</i> _m	
caffeine	−0.1 ^b	−8.8	1.6	78	4.1 ± 0.6	5.7 ± 0.1	−2.8	1.6	101	7.6 ± 0.8	6.3 ± 0.1	−3.2
paraxanthine	−0.2 ^b	−11.2	2.1	99	8.0 ± 0.1	4.9 ± 0.1	−2.2	1.5	96	6.9 ± 0.1	5.1 ± 0.3	−2.4
chlorzoxazone	2.2 ^b	−8.4	1.5	72	8.2 ± 1.0	8.9 ± 0.8	−5.2	1.0	66	4.7 ± 0.4	8.1 ± 0.5	−4.2
6-hydroxy- chlorzoxazone	1.7	−11.5	1.6	75	8.3 ± 0.7	8.2 ± 0.4	−4.5	1.7	108	8.9 ± 0.8	7.0 ± 0.8	−3.5
coumarin	1.4 ^b	−6.0	1.3	63	3.0 ± 0.2	6.7 ± 0.2	−3.5	1.4	88	3.6 ± 0.2	5.3 ± 0.1	−2.7
7-hydroxy-coumarin	1.6 ^b	−10.5	1.6	78	4.8 ± 1.0	2.9 ± 1.0	−1.0	1.6	97	4.1 ± 0.6	4.2 ± 0.6	−2.0
ibuprofen	3.7 ^b	−11.3	1.4	65	6.8 ± 1.5	7.7 ± 0.1	−4.4	1.6	100	5.0 ± 0.2	3.1 ± 0.1	−1.2
3-hydroxy-ibuprofen	1.7	−17.5	1.5	70	8.3 ± 0.1	3.0 ± 1.0	−1.3	1.4	86	5.2 ± 0.1	2.2 ± 1.4	−0.5
debrisoquine	0.1 ^b	−18.3	1.7	79	5.6 ± 1.0	4.8 ± 0.7	−2.3	1.4	86	4.6 ± 0.2	2.5 ± 0.5	−0.7
4-hydroxy- debrisoquine	−0.7	−18.3	1.6	77	7.0 ± 0.7	1.8 ± 0.3	−0.2	1.8	113	12.5 ± 2.3	3.5 ± 0.7	−0.9

^aThe positions of the minima (*P*) show the most probable location of the molecule in the membrane. The relative position (*P*_{rel}) shows the ratio of the position of the free energy minimum *P* and the position of phosphates (100% means that the molecule is at the phosphate “plane”; higher and lower numbers indicate positions above and below the phosphates), ΔG^{pen} and ΔG^{wat} are the bilayer center penetration and water/lipid barrier, respectively, while *pK*_m is the negative logarithm of the molar ratio *K*_m of the molecule between the lipid and water phase. ^bExperimental values of octanol/water partition coefficients.

All molecular dynamics (MD) simulations were performed using the GROMACS 4.0.7 software package³⁷ with a Berger lipid force field²⁶ based on the GROMOS 53a6 force field.³⁸ This force field unites nonpolar hydrogens with corresponding carbons and reduces the number of simulated atoms in long hydrocarbon chains present in lipids. However, this simplification is likely to bias the diffusion coefficient calculation and leads to its higher values.³⁹ The simulations were carried out with time steps of 2 fs. The periodic boundary conditions were applied in all directions, electrostatics was solved by the particle-mesh Ewald method,⁴⁰ van der Waals cutoff was set at 1 nm, and bond constraints were determined by LINCS algorithm.⁴¹ We used V-rescale temperature coupling⁴² to 310 K and Berendsen anisotropic pressure coupling⁴³ to 1 bar with a time constant of 10 ps and compressibility of 4.5×10^{-5} bar^{−1}.

The free energy profile can be calculated from biased simulations using various techniques, such as umbrella sampling,^{44,45} *z*-constraint,^{13,27,46–49} metadynamics,^{50,51} and others.⁵² For consistency with our previous study,⁴ we here used the umbrella sampling method. Umbrella sampling applies a harmonic potential around the starting position of a molecule (at a specific depth in a bilayer). The applied force on the molecule is proportional to the square of the displacement from the original distance of the two groups (molecule and lipid bilayer), and the free energy profile can then be calculated from eq 1.^{23,53}

$$\Delta G(z) = -RT \ln P(z) + U(z) \quad (1)$$

Molecules of substrates and metabolites were inserted into the simulation box containing a hydrated lipid bilayer with SPCE water model,⁵⁴ and a short 0.5 ns long simulation was executed to relax water molecules and the simulation box. The initial structures for umbrella simulations were obtained using the following two methods: either the molecule was free to go anywhere by itself (referred to as UF) or the center of mass of the molecule was pulled into the bilayer (UP). Frames separated by 0.1 ± 0.02 nm were chosen from the trajectories, and the frames with the lowest potential energies were selected as initial structures. Usually these two approaches were combined; the free simulation was used to generate as many

starting frames as possible and then followed by a pulling simulation (see Supporting Information Table S1).

The initial structures were subsequently used in the umbrella sampling simulation. The initial distance in the umbrella simulation was restrained by a harmonic force of $2000 \text{ kJ mol}^{-1} \text{ nm}^{-2}$ ($477.9 \text{ kcal mol}^{-1} \text{ nm}^{-2}$). Each window was simulated for 10.25 ns. The first 2250 ps was taken as pre-equilibration of the system. The free energy profiles were analyzed, and the convergence of energy barriers and positions of minima was monitored. The simulations of molecules that did not show stable values of energy barriers' heights and positions of minima were prolonged (see Table S1 and Figures S1 and S2 in the Supporting Information). The free energy profile was calculated by the weighted histogram analysis method⁴⁴ (WHAM) using *g_wham*⁵⁵ from the GROMACS software package. The start of the *z* axis was set to the middle of the membrane.

The free energy profiles of ibuprofen and 3-hydroxyibuprofen were calculated from profiles of their charged and uncharged forms. As the *pK*_A of ibuprofen is 4.44, its free energy in water was shifted by 3.5 kcal/mol (the same value was used as an estimate for 3-hydroxyibuprofen). The lowest energies in the free energy profiles were then used to estimate the preferential form of the molecules in the specified positions.

The hydration free energy ΔG^{hyd} was calculated by the Bennett acceptance ratio (BAR) method⁵⁶ with $\Delta\lambda = 0.05$. A simulation box with an SPCE⁵⁴ water model (~ 500 water molecules) and one molecule of drug/metabolite was prepared and equilibrated. The BAR method calculates the free energy of change when a target molecule “appears” in a solvent. Each (total 21 for each molecule) simulation was executed for 200 ps, with the first 100 ps used for equilibration. The total ΔG^{hyd} was integrated using *g_bar* in the software package GROMACS 4.5.1.

The distribution coefficients of drugs and their metabolites between a membrane and water phase can be calculated from the free energy profile along the membrane normal. Individual distribution coefficients at position *z'* in the membrane, *D*(*z'*), were given by the free energy difference to the reference value of free energy in water, where ΔG was set to 0 kcal/mol. The global distribution coefficient, *D*, for a given molecule was

integrated from the individual $D(z')$ along both membrane leaflets (eq 2):

$$D = \frac{c_{\text{membrane}}}{c_{\text{water}}} = 2 \cdot \int_0^z e^{-\Delta G(z')/RT} dz' \quad (2)$$

where z is one-half of the bilayer thickness (2.5 nm), $\Delta G(z')$ is the free energy of the molecule at depth z' , T is the thermodynamic temperature, and R is the universal gas constant.

To obtain not only the concentration ratio between lipid bilayer and water but also the approximate molar ratio K_m , the volume ratio between water and lipids has to be taken into account. Lipids form about 5% of the mass of human cells, whereas water accounts for as much as 70%;¹⁹ the densities of both phases are approximately the same. The approximate molar ratio K_m of a drug between lipids (n_{membrane}) and water (n_{water}) in the human body can then be estimated from eq 3:

$$K_m = \frac{n_{\text{membrane}}}{n_{\text{water}}} = D \cdot \frac{V_{\text{(membrane)}}}{V_{\text{(water)}}} \quad (3)$$

where $V_{\text{(membrane)}}/V_{\text{(water)}}$ is the volume ratio (5/70). Values are usually reported as pK_m .

Octanol/water partition coefficients ($\log P$) were adopted from experimental values taken from DrugBank⁵⁷ whenever possible, and other values were taken from the ChemSpider⁵⁸ Web site.

The heights of energy barriers were obtained from the free energy profiles along with the positions of the center-of-mass of the molecule in the free energy minima P and the relative position of the energy minimum with respect to the positions of phosphates P_{rel} . The mean values for drugs, metabolites, or all molecules on each bilayer were taken as the median of the obtained values.

RESULTS AND DISCUSSION

Free Energy Profiles Show Typical Behavior of Amphiphilic Drug-like Molecules on Lipid Bilayers. The free energy profiles show the positions of minima, where the molecules are likely to concentrate. The free energy profiles of molecules on a DOPC bilayer (Figure 2 and Table 1) decrease from the water phase to region 2 or 3, where typically one energy minimum is located. One shallow local minimum appears in the middle of the bilayer, where the overall density of the bilayer drops (Figure 1). These profiles indicate that the studied molecules can spontaneously enter the lipid bilayer. The molecules may concentrate in the lipid phase, as is also apparent by the negative pK_m values. The molecules then preferentially stay close to their minima, which are localized in regions 2 and 3. It should be noted that the entrances of active site access channels of CYP enzymes most likely stay in the same regions.^{4,59,60} Here, the drugs can be taken up by CYP to be modified.

The free energy profiles of molecules on a POPG bilayer are similar to those on DOPC bilayers. They display a deep energy minimum in regions 2 or 3. On the other hand, a local energy minimum in the middle of the POPG bilayer is rare. The overall density of the POPG bilayer with respect to DOPC is lower. However, there is only a small decrease in mass density in the POPG bilayer center, and therefore the molecules do not prefer to stay in the bilayer center. Because of the small decrease in mass density, POPG does not have a region near

the bilayer center characterized by rapid lateral diffusion in contrast to DOPC.

Heterogeneity of Membrane Environment Reduces the Correlation of Partitioning in Octanol/Water and Lipids/Water Environments. We have compared the calculated parameters of the free energy profile with the octanol/water partition coefficient ($\log P$), which is widely used to predict a drug bioavailability. We observed a rather poor correlation (correlation coefficient below 0.3, which is not statistically significant at level of significance $\alpha = 0.05$, indeed) for positioning, partitioning, and consequently also ΔG^{wat} on DOPC, and no correlation on POPG bilayer (Figure S3). The low correlation between $\log P$ and ΔG^{wat} values on DOPC can be explained by a more complex structure of the lipid bilayer. The outer parts of the membrane bilayer are more polar than octanol/water surface; therefore, the polar molecules are more concentrated on membranes than they are on octanol/water interface. No correlation of calculated free energy profile properties with $\log P$ was observed on POPG, which might be explained by the fact that the molecules were preferentially located on the bilayer/water interface, where about 20% of mass was formed by water. The octanol/water partition coefficient can therefore reflect partition properties on some membrane types,^{61,62} but cannot be straightforwardly used on all types of membranes and all molecules.

Drugs Have Higher Affinity to the Bilayer than Corresponding Metabolites. The free energy profiles show that the studied drugs have a higher affinity to the lipid bilayer and are located deeper in the bilayers than are the corresponding metabolites. It is supported by the fact that ΔG^{hyd} of the drugs is higher than the corresponding value of the metabolites, and thus the drugs are more hydrophobic than their respective metabolites. The drugs are also on average 0.2 nm deeper in the bilayer than their metabolites (Figures 2 and 4, and Table 1). The bilayer center penetration barrier ΔG^{pen} for drugs is typically lower than that of the metabolites (2.4 kcal/mol on DOPC and 2.2 kcal/mol on POPG). On the other hand, the water/lipid barrier ΔG^{wat} is higher for the drugs than the metabolites (3.7 kcal/mol on DOPC and 1.1 kcal/mol on POPG). The higher membrane affinity of the drugs is clearly visible from the molar ratio pK_m of the molecule in the membrane and water, with the exception of debrisoquine on POPG (Table 1 and Figure 5).

The drugs' metabolites have different charge distributions, and therefore exhibit different orientations on the lipid bilayers. The drugs have polar group(s) located on one side of the molecule (with the exception of caffeine) and are usually oriented with these polar groups pointing toward the polar lipid heads. The metabolites are typically hydroxylated on the other side of the molecule (with the exception of paraxanthine, which is demethylated), and therefore are oriented more parallel to the bilayer.

Implications for Drug Metabolism by Cytochromes P450 (CYP). As mentioned before, the studied drugs concentrate in the lipid bilayer, and their preferred positions correspond with CYP active site access channel influxes (Figure 5). The CYP metabolized drugs are believed to leave the CYPs active sites via egress tunnels that open further from the bilayer center close to the polar headgroup region. It is worth noting that the metabolites can leave the bilayer more easily, as their affinities to the membranes (represented by pK_m and ΔG^{wat}) are lower than the respective affinities of drugs (cf., Figure 5 and Table 1).

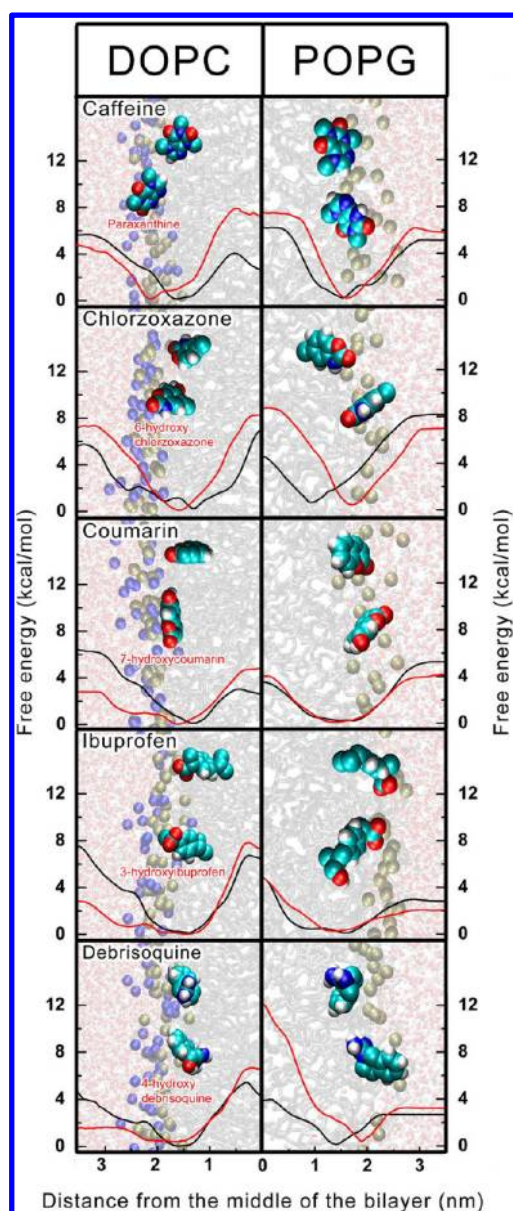


Figure 4. The free energy profiles of the studied molecules in DOPC (left) and POPG (right) bilayers. The free energy profile of the drug (the upper molecule of each box) is plotted in black, whereas the free energy profile of the CYP metabolite (the lower molecule) is in red. The structures of the drugs and their metabolites are shown in their energy minima. The drugs are located deeper in the bilayer than the corresponding metabolites and usually have higher affinities to the lipid bilayer. DOPC and POPG chains are shown in gray, nitrogens are represented as blue balls, phosphates brown, carbons cyan, oxygens red, and hydrogens white.

Molecules Pass through POPG Bilayer More Easily.

The molecules on POPG are usually located closer to the water environment and are bound more weakly than the molecules on DOPC. The POPG bilayer is thinner, but the mean relative position of the molecules on POPG is about 20% closer to the polar headgroup region than on the DOPC bilayer. Molecules on POPG are located in an area where the overall mass is formed by about 20% of water, whereas the mean position of molecules on DOPC is in an area where water comprises only about 2% of the overall mass. This also reduces the water/lipid barrier ΔG^{wat} on POPG as its median is 0.6 kcal/mol lower for

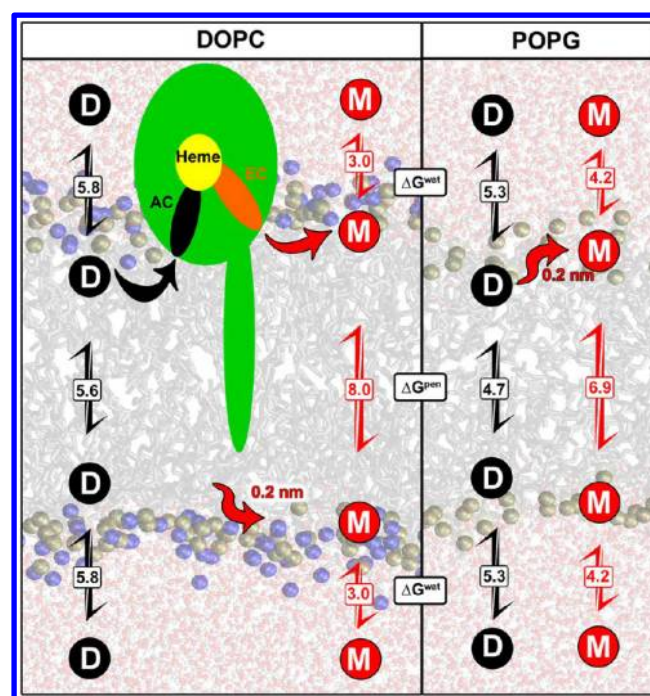


Figure 5. Proposed scheme of drug (D) and metabolite (M) penetration through the DOPC (left panel) and POPG (right panel) bilayers with medians of the obtained energy barriers and proposed scheme of the drug entering and leaving cytochrome P450 (CYP – green object on the left panel), which is anchored to the membrane of endoplasmic reticulum. The water/lipid barrier ΔG^{wat} is higher and the bilayer center penetration barrier ΔG^{pen} is lower for the drugs than for metabolites. The metabolites are located 0.2 nm further from the bilayer center than the drugs in both cases. The overall energy barriers are lower on POPG than on DOPC. The drugs are believed to enter CYP by access channel (AC – in black), it is metabolized in the active site above the heme (in yellow), and leaves CYP via egress channel (EC – orange) as a metabolite. The egress channel opens close to the water region.

molecules on POPG than on DOPC. The bilayer center penetration barrier ΔG^{pen} is also on average 1.8 kcal/mol lower for molecules on POPG. The affinity to the lipid bilayer is higher for molecules on DOPC than on POPG, and therefore the molecules prefer to concentrate in DOPC lipid bilayers. However, small drug-like molecules seem to pass through the POPG bilayer more easily than through DOPC. It should be noted that we used a limited number of molecules in the study and the results gained have to be interpreted with caution as comparison of the data between single pairs of other molecules may lead to different conclusions. However, it is known that membranes of mammals consist mostly of PC, whereas bacterial membranes contain large amounts of negatively charged PG. Thus, the easier penetration and lower concentration of small drugs on POPG membranes could be used in targeted drug delivery.

CONCLUSION

Here, we studied the interaction of five drugs and their respective CYP metabolites with lipid bilayers in terms of their free energy profiles across two prototypical lipid bilayers consisting of DOPC and POPG. We showed that the behavior of the studied drugs and their metabolites on lipid bilayers differed in numerous ways. The drugs (which are more hydrophobic molecules than their respective metabolites)

exhibited higher water/lipid free energy barriers ΔG^{wat} , and therefore a higher affinity to the lipid bilayers than the metabolites. Furthermore, the drugs can penetrate the membrane with lower energy barriers ΔG^{pen} than their respective metabolites. The results imply that the respective metabolites are generally more weakly bound to the membrane and more likely to stay in the cytosol than the drugs. This behavior may have implications for the metabolism of the studied drugs by CYPs. As the drugs prefer to stay in the membrane, they are likely to enter the CYP buried active site via access channels from the membrane. On the other hand, the generally more polar substrates may leave the active site by egress channels pointing toward the membrane surface or cytosol.

Furthermore, the results show that the behavior of drug-like molecules differs on different lipid bilayers. The free energy profiles indicate that the ratio of the number of molecules in the membrane to that in water is slightly higher for DOPC than for POPG. Therefore, the drugs are likely to concentrate more on DOPC bilayers. However, the energy barriers are lower on POPG, and therefore penetration through POPG bilayers seems to be easier. As the penetration through the membrane is crucial for reaching the biological target and also some drug effects are based on the change of bilayer properties as the drugs concentrate in membranes, we believe that such information, along with knowledge of membrane composition, would be useful for drug targeting.

■ ASSOCIATED CONTENT

📄 Supporting Information

Detailed information on simulations. This material is available free of charge via the Internet at <http://pubs.acs.org>.

■ AUTHOR INFORMATION

Corresponding Author

*Phone: +420 585634769 (K.B.); +420 585634756 (M.O.).
Fax: +420 585634761 (M.O.). E-mail: karel.berka@upol.cz (K.B.); michal.otyepka@upol.cz (M.O.).

Notes

The authors declare no competing financial interest.

■ ACKNOWLEDGMENTS

We acknowledge the support by the Operational Program Research and Development for Innovations – European Regional Development Fund (project CZ.1.05/2.1.00/03.0058 of the Ministry of Education, Youth and Sports of the Czech Republic) and the Operational Program Education for Competitiveness – European Social Fund (projects CZ.1.07/2.3.00/20.0017 and CZ.1.07/2.3.00/20.0058). This work was also supported by the Grant Agency of the Czech Republic through the P208/12/G016, 303/09/1001, 203/09/H046, and P303/12/P019 projects and by a student project PrF_2012_028.

■ REFERENCES

- (1) Seydel, J. K.; Wiese, M. In *Drug-Membrane Interactions: Analysis, Drug Distribution, Modeling*; Mannhold, R., Kubinyi, H., Folkers, G., Eds.; Wiley-VCH Verlag GmbH: Weinheim, 2002.
- (2) Peetla, C.; Stine, A.; Labhassetwar, V. *Mol. Pharmaceutics* **2009**, *6*, 1264–1276.
- (3) Lúcio, M.; Lima, J. L. F. C.; Reis, S. *Curr. Med. Chem.* **2010**, *17*, 1795–1809.

- (4) Berka, K.; Hendrychová, T.; Anzenbacher, P.; Otyepka, M. *J. Phys. Chem. A* **2011**, *115*, 11248–11255.
- (5) Nagar, S.; Korzekwa, K. *Drug Metab. Dispos.* **2012**, *40*, 1649–52.
- (6) Orsi, M.; Essex, J. W. In *Molecular Simulations and Biomembranes*; Sansom, M. S. P., Biggin, P. C., Eds.; Royal Society of Chemistry: UK, 2010; pp 76–90.
- (7) Ayrton, A.; Morgan, P. *Xenobiotica* **2001**, *31*, 469–497.
- (8) Shitara, Y.; Horie, T.; Sugiyama, Y. *Eur. J. Pharm. Sci.* **2006**, *27*, 425–446.
- (9) Giacomini, K. M.; Huang, S.-M.; Tweedie, D. J.; Benet, L. Z.; Brouwer, K. L. R.; Chu, X.; Dahlin, A.; Evers, R.; Fischer, V.; Hillgren, K. M.; et al. *Nat. Rev. Drug Discovery* **2010**, *9*, 215–236.
- (10) Mouritsen, O. G.; Jorgensen, K. *Pharm. Res.* **1998**, *15*, 1507–1519.
- (11) Black, S. D. *FASEB J.* **1992**, *6*, 680–685.
- (12) Košinová, P.; Berka, K.; Wykes, M.; Otyepka, M.; Trouillas, P. *J. Phys. Chem. B* **2012**, *116*, 1309–18.
- (13) Orsi, M.; Essex, J. W. *Soft Matter* **2010**, *6*, 3797–3808.
- (14) Kirjavainen, M.; Monkkonen, J.; Saukkosaari, M.; Valjakka-koskela, R.; Kiesvaara, J.; Urtti, A. *J. Controlled Release* **1999**, *58*, 207–214.
- (15) Cohen, Y.; Bodner, E.; Richman, M.; Afri, M.; Frimer, A. A. *Chem. Phys. Lipids* **2008**, *155*, 98–113.
- (16) MacCallum, J. L.; Tieleman, D. P. *J. Am. Chem. Soc.* **2006**, *128*, 125–130.
- (17) Cooper, G. M. *The Cell, A Molecular Approach*; Sinauer Associates: Sunderland, MA, 2000.
- (18) Yeagle, P. L. *Encyclopedia of Life Sciences (ELS)*; Joh Wiley & Sons, Ltd.: Chichester, 2009.
- (19) Alberts, B.; Johnson, A.; Lewis, J.; Raff, M.; Roberts, K.; Walter, P. *Molecular Biology of the Cell*, 4th ed.; Garland Science: New York, 2002.
- (20) Otyepka, M.; Skopalík, J.; Anzenbacherová, E.; Anzenbacher, P. *Biochim. Biophys. Acta* **2007**, *1770*, 376–389.
- (21) Dowhan, W. *Annu. Rev. Biochem.* **1997**, *66*, 199–232.
- (22) Marrink, S.-J.; Berendsen, H. J. C. *J. Phys. Chem.* **1994**, *98*, 4155–4168.
- (23) Van Der Spoel, D.; Lindahl, E.; Hess, B.; Groenhof, G.; Mark, A. E.; Berendsen, H. J. C. *J. Comput. Chem.* **2005**, *26*, 1701–1718.
- (24) Zgarbová, M.; Otyepka, M.; Šponer, J.; Hobza, P.; Jurečka, P. *Phys. Chem. Chem. Phys.* **2010**, *12*, 10476–10493.
- (25) Schlick, T. *Molecular Modeling and Simulation: An Interdisciplinary Guide*, 2nd ed.; Springer: New York, 2010.
- (26) Berger, O.; Edholm, O.; Jahnig, F. *Biophys. J.* **1997**, *72*, 2002–2013.
- (27) Bemporad, D.; Essex, J. W.; Luttmann, C. *J. Phys. Chem. B* **2004**, *108*, 4875–4884.
- (28) Paloncýová, M.; Berka, K.; Otyepka, M. *J. Chem. Theory Comput.* **2012**, *8*, 1200–1211.
- (29) Domański, J.; Stansfeld, P. J.; Sansom, M. S. P.; Beckstein, O. *J. Membr. Biol.* **2010**, *236*, 255–258.
- (30) Siu, S.; Vácha, R.; Jungwirth, P.; Böckmann, R. A. *J. Chem. Phys.* **2008**, *128*, 125103.
- (31) Kukol, A. *J. Chem. Theory Comput.* **2009**, *5*, 615–626.
- (32) Schüttelkopf, A. W.; Van Aalten, D. M. F. *Acta Crystallogr., Sect. D: Biol. Crystallogr.* **2004**, *60*, 1355–1363.
- (33) Lemkul, J. A.; Allen, W. J.; Bevan, D. R. *J. Chem. Inf. Model.* **2010**, *50*, 2221–2235.
- (34) Cieplak, P.; Caldwell, J.; Kollman, P. *J. Comput. Chem.* **2001**, *22*, 1048–1057.
- (35) Frisch, M. J.; Trucks, G. W.; Schlegel, H. B.; Scuseria, G. E.; Robb, M. A.; Cheeseman, J. R.; Montgomery, J. A., Jr.; Vreven, T.; Kudin, K. N.; Burant, J. C.; et al. *Gaussian 03*, revision E.01; Gaussian, Inc.: Wallingford, CT, 2004.
- (36) Case, D. A.; Darden, T. A.; Cheatham, T. E., III; Simmerling, C. L.; Wang, J.; Duke, R. E.; Luo, R.; Walker, R. C.; Zhang, W.; Merz, K. M.; et al. *AMBER 11*; University of California: San Francisco, CA, 2010.

- (37) Hess, B.; Kutzner, C.; Van der Spoel, D.; Lindahl, E. *J. Chem. Theory Comput.* **2008**, *4*, 435–447.
- (38) Oostenbrink, C.; Soares, T. A.; Van der Vegt, N. F. A.; Van Gunsteren, W. F. *Eur. Biophys. J.* **2005**, *34*, 273–284.
- (39) Shinoda, W.; Mikami, M.; Baba, T.; Hato, M. *J. Phys. Chem. B* **2004**, *108*, 9346–9356.
- (40) Darden, T.; York, D.; Pedersen, L. *J. Chem. Phys.* **1993**, *98*, 10089–10092.
- (41) Hess, B.; Bekker, H.; Berendsen, H. J. C.; Fraaije, J. G. E. M. *J. Comput. Chem.* **1997**, *18*, 1463–1472.
- (42) Bussi, G.; Donadio, D.; Parrinello, M. *J. Chem. Phys.* **2007**, *126*, 014101.
- (43) Berendsen, H.; Postma, J.; Vangunsteren, W.; Dinola, A.; Haak, J. *J. Chem. Phys.* **1984**, *81*, 3684–3690.
- (44) Kumar, S.; Rosenberg, J.; Bouzida, D.; Swensen, R. H.; Kollman, P. A. *J. Comput. Chem.* **1992**, *13*, 1011–1021.
- (45) Torrie, G. M.; Calleau, J. P. *J. Comput. Phys.* **1997**, *23*, 187–199.
- (46) Boggara, M. B.; Krishnamoorti, R. *Biophys. J.* **2010**, *98*, 586–595.
- (47) Bemporad, D.; Luttmann, C.; Essex, J. W. *Biophys. J.* **2004**, *87*, 1–13.
- (48) Marrink, S. J.; Berendsen, H. J. C. *J. Phys. Chem.* **1996**, *100*, 16729–16738.
- (49) Orsi, M.; Sanderson, W. E.; Essex, J. W. *J. Phys. Chem. B* **2009**, *113*, 12019–12029.
- (50) Zhang, Y.; Voth, G. A. *J. Chem. Theory Comput.* **2011**, *7*, 2277–2283.
- (51) Laio, A.; Parrinello, M. *Proc. Natl. Acad. Sci. U.S.A.* **2002**, *99*, 12562–12566.
- (52) Roux, B. *Comput. Phys. Commun.* **1995**, *91*, 275–282.
- (53) Xiang, T.-X.; Anderson, B. D. *Adv. Drug Delivery Rev.* **2006**, *58*, 1357–1378.
- (54) Berendsen, H. J. C.; Postma, J. P. M.; Gunsteren, W. F.; van Hermans, J. In *Intermolecular Forces*; Pullman, B., Ed.; Reidel Publishing Co.: Dordrecht, The Netherlands, 1981; pp 331–338.
- (55) Hub, J. S.; Groot, B. L. De; Spoel, D. Van Der *J. Chem. Theory Comput.* **2010**, *6*, 3713–3720.
- (56) Bennett, C. J. *Comput. Phys.* **1976**, *22*, 245–268.
- (57) DrugBank; www.drugbank.ca (accessed Jan 28, 2013).
- (58) ChemSpider – The free chemical database; www.chemspider.com (accessed Jan 25, 2013).
- (59) Cojocar, V.; Balali-Mood, K.; Sansom, M. S. P.; Wade, R. C. *PLoS Comput. Biol.* **2011**, *7*, e1002152.
- (60) Denisov, I. G.; Shih, Y.; Sligar, S. G. *J. Inorg. Biochem.* **2012**, *108*, 150–8.
- (61) Vaes, W. H.; Ramos, E. U.; Hamwijk, C.; Van Holsteijn, I.; Blaauboer, B. J.; Seinen, W.; Verhaar, H. J.; Hermens, J. L. *Chem. Res. Toxicol.* **1997**, *10*, 1067–72.
- (62) Vaes, W. H. J.; Verhaar, H. J. M.; Cramer, C. J.; Hermens, J. L. *M. Chem. Res. Toxicol.* **1998**, *11*, 847–854.

Lipid Bilayer Membrane Affinity Rationalizes Inhibition of Lipid Peroxidation by a Natural Lignan Antioxidant

Pavína Podloucká,[†] Karel Berka,[†] Gabin Fabre,^{†,‡} Markéta Paloncýová,[†] Jean-Luc Duroux,[‡] Michal Otyepka,^{*,†} and Patrick Trouillas^{*,†,‡,§}

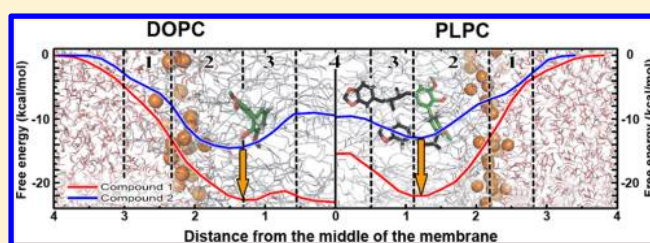
[†]Regional Centre of Advanced Technologies and Materials, Department of Physical Chemistry, Faculty of Science, Palacký University, tř. 17 listopadu 12, 771 46 Olomouc, Czech Republic

[‡]INSERM UMR-S850 / LCSN EA1069, Faculté de Pharmacie, Université de Limoges, 2 rue de Dr. Marcland, 87025 Limoges, France

[§]Service de Chimie des Matériaux Nouveaux, Université de Mons-UMONS, Place du Parc 20, 7000 Mons, Belgium

Supporting Information

ABSTRACT: Lipid peroxidation is a degenerative oxidative process that modifies the structure of membranes, influencing their biological functions. Lignans, natural polyphenolic antioxidants widely distributed in plants, can prevent this membrane damage by free-radical scavenging. Here, we rationalize the difference in lipid peroxidation inhibition activity of argenteane, a natural dilignan isolated from wild nutmeg, and 3,3'-dimethoxy-1,1'-biphenyl-2,2'-diol, which represents the central part of argenteane responsible for its antioxidant activity. Although both compounds have the same capacity to scavenge free radicals, argenteane is a more active inhibitor of lipid peroxidation. We show that both compounds penetrate into DOPC and PLPC lipid bilayers and adopt similar positions and orientations, which therefore does not explain the difference in their lipid peroxidation inhibition activity. However, free energy profiles indicate that argenteane has a significantly higher affinity to the lipid bilayer, and thus a higher effective concentration to scavenge radicals formed during lipid peroxidation. This finding explains the higher activity of argenteane to inhibit lipid peroxidation.



INTRODUCTION

Lipid peroxidation is a three-stage (initiation/propagation/termination) oxidative process occurring in lipid bilayer membranes. It is initiated by reactive species, mainly reactive oxygen species (ROS), induced endogenously by classical biochemical reactions or exogenously by, e.g., pollution or UV light. Lipid peroxidation may strongly modify the lipid bilayer structure, subsequently disrupting various key cell functions associated with membranes. Lipid peroxidation contributes to several pathologies, including neurodegenerative diseases, heart disease, atherosclerosis, liver disease, and aging processes.^{1–6} The oxidative-induced degradation of membranes originates from the formation of aldehydes or lipid peroxides, acyl chain fragments, lipid–lipid cross-linked products, intramolecular cycles, etc.⁷ Lipid bilayers composed of unsaturated fatty acids are more sensitive to such oxidative damage.

Natural antioxidants can prevent membrane damage, mainly by free-radical scavenging at either the initiation or the propagation stages.⁸ Lignans are polyphenols widely distributed in plants. Being present in cereals, fruit, spices, beans, and other vegetables, they are natural components of the human diet.⁹ Their chemical structure is derived from substituted cinnamic alcohols, and they are classified into six subgroups (dibenzylbutanes and skeletons with rings monofuranic lignans, butyrolactones, aryl-naphthalenes, dibenzocyclolactones, furano-

furanic lignans).^{10,11} Lignans exhibit numerous biological activities, including antioxidant, antiproliferative, and protective functions against cardiovascular diseases and other degenerative pathologies associated with oxidative stress.^{9,12–17} As for other polyphenols, their antioxidant activity is attributed to their capacity for H-atom transfer (HAT) from the OH groups to the free radicals.¹⁸

Argenteane (biserythro-5,5'-bis[1-(4-hydroxyl-3-methoxyphenyl)-4-(3,4-methylenedioxyphenyl)-2,3-dimethylbutane]) (1) is a natural dilignan isolated from wild nutmeg (Figure 1A).¹⁹ Its antioxidant activity has been shown in vitro and compared to the activity of 3,3'-dimethoxy-1,1'-biphenyl-2,2'-diol (2), which mimics the central moiety of compound 1 (Figure 1).¹⁸ Both compounds exhibited exactly the same capacity to scavenge DPPH (2,2-diphenyl-1-picrylhydrazyl radical), which was rationalized by quantum calculations showing exactly the same capacity for HAT.²⁰ However, compound 1 was 4 times more active than 2 at lipid peroxidation inhibition as measured on PLPC (1-palmitoyl-2-linoleoyl-*sn*-glycero-3-phosphatidylcholine) vesicles.¹⁸ Moreover, compound 1 has an equivalent activity to vitamin E,

Received: December 27, 2012

Revised: April 4, 2013

Published: April 5, 2013

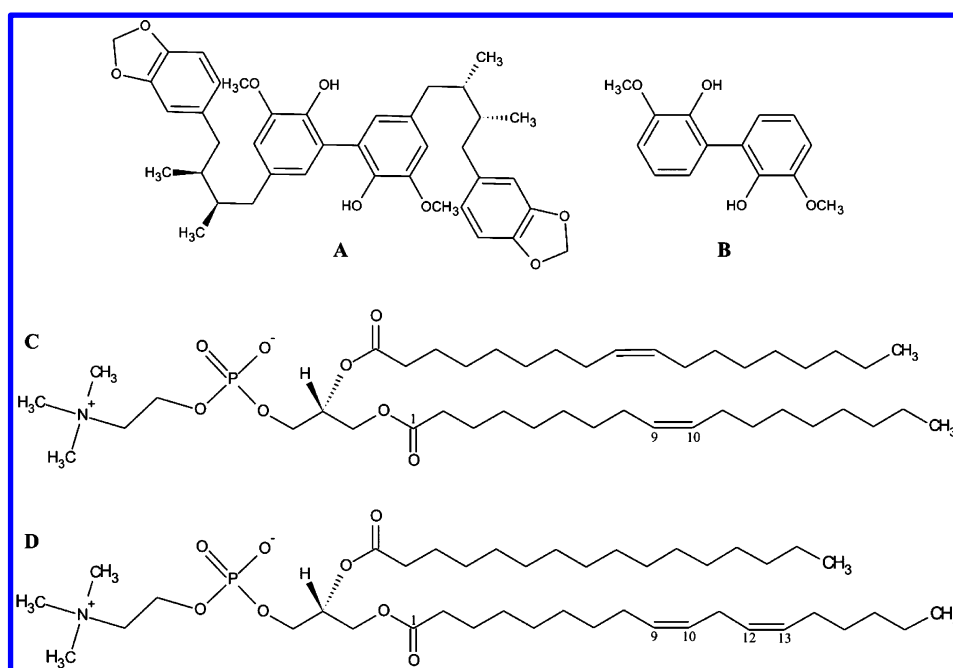


Figure 1. Chemical structures of (A) argenteane (compound 1), (B) 3,3'-dimethoxy-1,1'-biphenyl-2,2'-diol (compound 2), (C) 1,2-dioleoyl-*sn*-glycero-3-phosphatidylcholine (DOPC), and (D) 1-palmitoyl-2-linoleoyl-*sn*-glycero-3-phosphatidylcholine (PLPC).

Table 1. Average Distances (nm) Given with Respect to the Center of the Lipid Bilayers, with the Corresponding Standard Deviations Calculated for the OH Groups in Both the DOPC and PLPC Lipid Bilayers^a

compd	position of COM (nm)		position OH groups (nm)		overlap of OH groups and double bond (%)		$\Delta G(z_{\min})$ (kcal/mol)		IC ₅₀ (μ M)	
	DOPC	PLPC	DOPC	PLPC	DOPC	PLPC	DOPC	PLPC	DPPH scavenging ^b	lipid peroxidation inhibition ^b
1	1.4 ± 0.2	1.2 ± 0.2	1.5 ± 0.2	1.3 ± 0.2	29 ± 15	23 ± 4	-22.7 ± 0.2	-21.9 ± 0.6	70 ± 2	0.68 ± 0.04
2	1.6 ± 0.2	1.3 ± 0.2	1.7 ± 0.2	1.3 ± 0.3	13 ± 6	19 ± 2	-14.5 ± 0.1	-12.8 ± 1.1	70 ± 4	2.70 ± 0.05

^aAll distances were averaged over the last 150 ns of unbiased MD simulations. $\Delta G(z_{\min})$ reflects the affinity of compound to membrane. DPPH scavenging and lipid peroxidation inhibition activities of compounds 1 and 2 were taken from the literature.¹⁸ ^bData from ref 18.

which is well-known as a powerful lipid peroxidation inhibitor (Table 1). Due to the presence of nonpolar side chains in compound 1, the capacity to incorporate into lipid bilayers was proposed to explain such a difference in activity.

In this study, we aimed to rationalize the different capacities of both compounds (1 and 2) to inhibit lipid peroxidation on PLPC membranes.¹⁸ The pair of compounds 1 and 2 provides a useful basis to establish a fine structure activity relationship at the atomic level because both compounds share the same central moiety but differ in the presence/absence of long nonpolar side chains. We calculated the average positions and orientations of both compounds either on the PLPC or DOPC bilayers by molecular dynamics (MD) simulations. MD simulations have been repeatedly shown to provide useful information on the interaction of small molecules with lipid membranes^{21–31} providing a unique view at both an atomic scale and subpicosecond time resolution. The affinity of both compounds to lipid bilayers was investigated in terms of free energy profiles calculated along the bilayer normal. The results showed that both compounds adopt similar positions in the lipid bilayers, but they have significantly different affinities to lipid bilayers as compound 1 exhibited a significantly higher free energy difference between water and lipid phases than compound 2. This finding may explain the higher activity of compound 1 to inhibit lipid peroxidation.

METHODOLOGY

Two types of lipids, namely DOPC (1,2-dioleoyl-*sn*-glycero-3-phosphatidylcholine) as the most abundant lipid in mammal cell membranes³² and PLPC (1-palmitoyl-2-linoleoyl-*sn*-glycero-3-phosphatidylcholine), were used as membrane models to explain experimentally observed differences in the lipid peroxidation activity of compounds 1 and 2.¹⁸ Pure phospholipid bilayers are generally accepted to exhibit many of the important features of real membranes.³³ The former model comprised 128 DOPC molecules, in which the oleoyl chains contain one double bond between carbons C₉ and C₁₀ (Figure 1C). The latter model contained 144 PLPC molecules. For these phospholipids, the palmitic chain is a fully saturated fatty acid, whereas the linoleyl chain contains two double bonds (C₉=C₁₀ and C₁₂=C₁₃, Figure 1D). The presence of the double bonds makes PLPC more sensitive to oxidation. In both lipid bilayer models, both leaflets contain the same number of molecules. The structures of the lipids were taken from the literature^{34,35} and a united-atom Berger's force field was used.³⁶ The bilayers were oriented perpendicularly to the *z*-axis of the box containing the molecular assembly. The bilayers were first equilibrated in the absence of any solute (1 and 2). They were surrounded by an explicit SPC water model³⁷ and the physiological concentration of NaCl (0.15 mol·L⁻¹) in water was used. The MD simulations were carried out using the

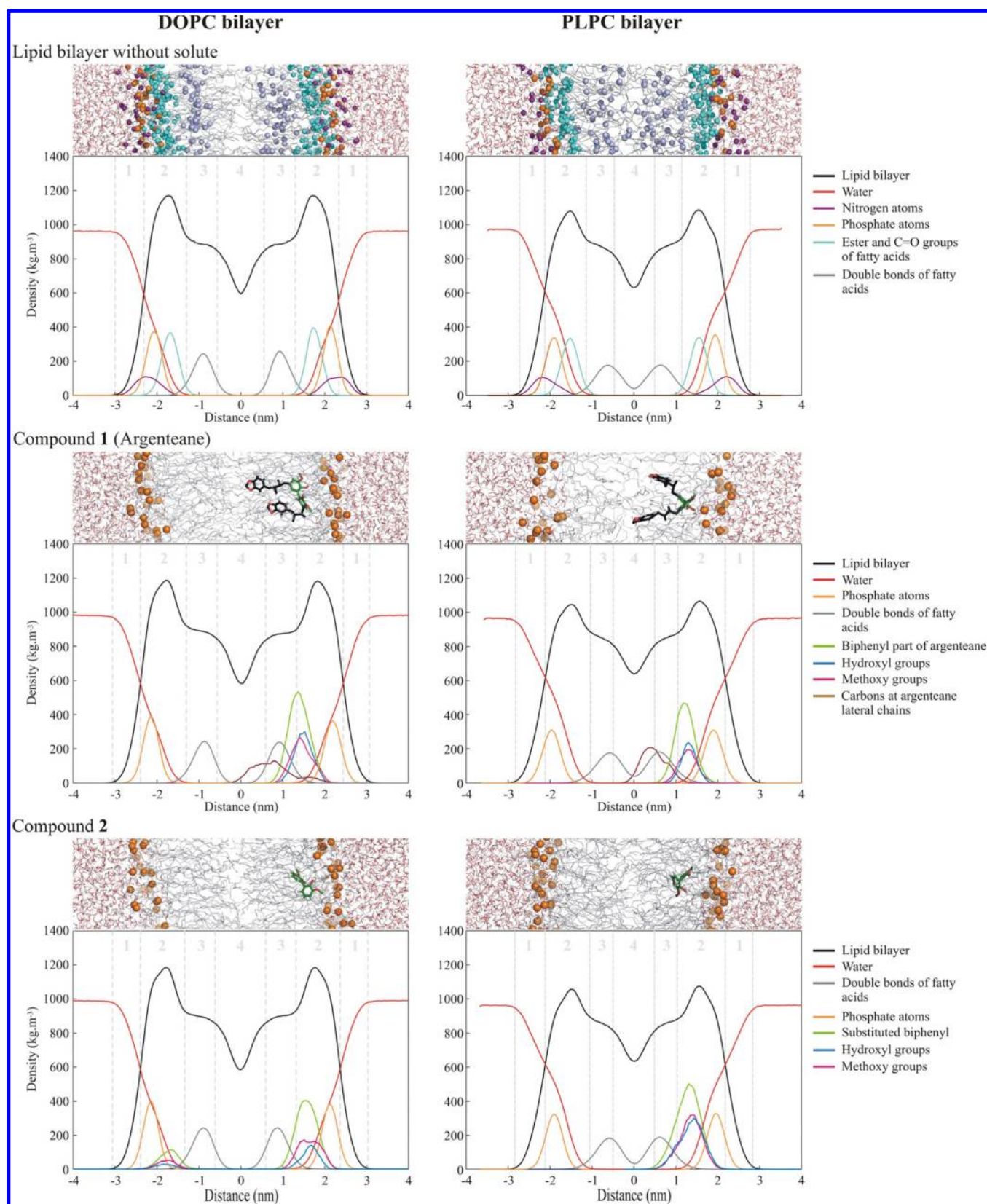


Figure 2. Characteristic snapshots and mass density profiles of DOPC and PLPC bilayers in the absence (upper panel) or presence (middle and lower panel) of **1** and **2**. For clarity, the components (and corresponding densities) are shown in different colors according to the legend and the density profiles of the studied compounds are scaled. The boundaries of regions 1–4 are shown in the upper part of the graphs.

GROMACS 4.0.7 package³⁸ with periodic boundary conditions in all directions.

The conformations of **1** and **2** were optimized using the hybrid DFT functional B3P86 combined with the 6-31+G(d,p)

basis set B3P86/6-31+G(d,p), which has been well adapted for the description of polyphenols.³⁹ The topology was generated from the PRODRG2 Beta server using the Gromos53a6 force field.⁴⁰ The partial atomic charges were assigned using the program Antechamber⁴¹ and RESP method⁴² after single-point calculation at the HF/6-31G* level. Optimization and single-point calculations were carried out in Gaussian03.⁴³

For both lipid bilayers, several MD simulations were carried out from different initial orientations and positions (in the middle of the lipid bilayer or outside the bilayer in the bulk water). To avoid unfavorable atomic contacts, the initial structures were first minimized by the steepest descent method and then equilibrated during a 200 ps simulation. During the equilibration step, the system was heated to 310 K by employing a v-rescale thermostat.⁴⁴ The pressure was kept constant using the anisotropic Berendsen barostat⁴⁵ at 1 bar. All bonds were constrained by the LINCS algorithm.⁴⁶ The electrostatic interactions were evaluated using the smooth particle-mesh Ewald method^{47,48} with a maximum spacing for the FFT grid of 0.12 nm. Both the Coulomb and Lennard-Jones interactions were truncated at 1.4 nm.

The equilibration step was followed by a 300 ns simulation. Thirteen independent unbiased simulations were carried out, differing in starting positions of the compounds. For each simulation the following protocol was used. The temperature was kept constant at 310 K by the v-rescale thermostat⁴⁴ with 0.1 ps coupling. The anisotropic Parrinello–Rahman barostat⁴⁹ was used to keep the pressure at 1 bar with a coupling time constant of 1.0 ps and compressibility of $4.5 \times 10^{-5} \text{ bar}^{-1}$. Integration of Newton's equations was based on the leapfrog algorithm using 2 fs time steps.⁵⁰ The electrostatic interactions were computed by the smooth particle-mesh Ewald method^{47,48} with a space cutoff at 1.4 nm and fast-Fourier grid space of 0.12 nm. The same cutoff was used for short-range interactions. The MD simulations were performed with different random initial velocities sampled according to a Maxwell distribution. All bonds were constrained using the LINCS algorithm.⁴⁶ The trajectories were visualized with VMD.⁵¹

Partitioning into the membrane was computed using the potential of mean force method to obtain free energy profiles.^{23,52–54} A series of initial structures was obtained from unbiased MD simulations to define windows along the bilayer normal (z -axis) separated by $0.10 \pm 0.02 \text{ nm}$. In the case of missing windows, 15 ns pulling simulations were performed. In the latter simulations, the molecule was pulled from the center of the lipid bilayer ($z = 0 \text{ nm}$) to the edge of the box along the z -axis. The rate of change of the reference position was 0.0005 nm/ps . In all windows, the center of mass (COM) of the biphenyl moiety was constrained in that specific depth and the force applied to the molecule was monitored. Neale et al. showed that relatively long simulation times are required for each window to achieve convergence in umbrella simulations with charged solutes,⁵⁵ and Singh and Tieleman⁵⁶ highlighted a necessity of simulation time longer than the slowest relaxation in a system. We recently showed²² that constraint simulations may converge more quickly (the estimated free energies became constant in time) and also that 0.2 nm separation of simulation frames in constraint simulation is sufficient for construction of free energy profiles. In the present work, 50 and 80 ns windows of constraint simulation were used in DOPC and PLPC, respectively. The free energy profiles were reconstructed from the last 30 ns. They were calculated as a

function of the distance of the antioxidant biphenyl moiety from the bilayer center according to the eq 1^{23,29}

$$\Delta G(z) = - \int_{z=-\infty}^z \langle F(z') \rangle_t dz' \quad (1)$$

where $\langle F(z') \rangle_t$ is the average force constraining the biphenyl moiety at a specific position of the simulation. Due to the symmetry of the lipid bilayer, the profile of ΔG was calculated for only half of the box. The error estimates were calculated as a standard deviation of the mean of the constraining force integrated over the z -axis. We assume that error bars may be underestimated.²² For comparison, the free energy profile of compound 2 interacting with PLPC was calculated using 30 ns per simulation window (Figure S4 in the Supporting Information).

The overlap of OH groups of both compounds with lipid double bonds was calculated as an integral over product of normalized densities of both groups along the bilayer normal (Figure S1 and Table S1 in the Supporting Information) according to eq 2

$$S = \int_{-\infty}^{\infty} a(x)b(x) dx \quad (2)$$

where $a(x)$ and $b(x)$ are normalized functions of density profiles of OH groups and double bonds. Last 150 ns of unbiased simulations were used for the calculation.

RESULTS AND DISCUSSION

Comparison of the PLPC and DOPC Lipid Bilayers in the Absence of Solute. Both DOPC and PLPC bilayers exhibited typical features of unsaturated lipid bilayers. Four regions could clearly be distinguished according to the Marrink and Berendsen membrane model,²³ namely the low headgroup density in direct contact with the water phase (region 1), the high headgroup density defining an intermediate region between the water and lipid phases (region 2), the lipid chains (region 3), and the center of the membrane (region 4) with low lipid density (Figure 2). The flexible arrangement of the lipid chains shows that both bilayers were in their liquid phases at 310 K (Figure 2). The area per lipid was 0.59 and 0.63 nm² for the DOPC and PLPC bilayers, respectively, during the simulation. Therefore, in DOPC, the two similar chains containing one double bond allow better lateral packing. In PLPC, the two double bonds in one of the lipid chains produce a kink in the fatty acid chains, disfavoring tight interchain packing (Figure 1), making the bilayer more fluid.³³ However, in the PLPC bilayer, the presence of a shorter saturated chain and the polyunsaturated chain favor better packing along the z -axis and thus a lower thickness, which was by 0.8 nm smaller than that of the DOPC bilayer.

Simple Penetration Process of Compounds 1 and 2. When starting outside of the bilayer, both compounds 1 and 2 intercalated spontaneously between lipid chains (Figure S2 in the Supporting Information), regardless of the type of lipid bilayer used for the unbiased simulations. When starting inside, both compounds stayed in the bilayers. This is attributed to their amphiphatic character. However, a thorough analysis of the unbiased MD simulations showed that the compounds behaved in different ways regarding the penetration process.

When starting out of the bilayer, compound 1 first approached the polar surface, then slowly passed through the polar region, and finally reached its equilibrated position close to the headgroup area of the lipid bilayer (between regions 2

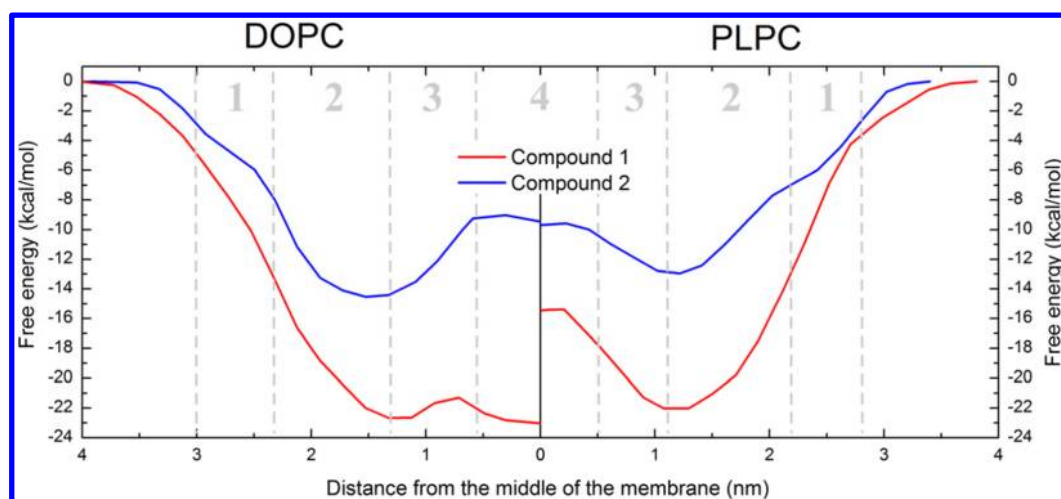


Figure 3. Free energy profiles of compounds 1 and 2 along the z -axis in the DOPC (left) and PLPC (right) lipid bilayers shown for one leaflet.

and 3). The whole process took approximately 200 and 50 ns in the DOPC and PLPC bilayers, respectively. When starting in the center of the bilayer, compound 1 reached its equilibrated position during the first 50 ns in both lipid bilayers. This highlights that the most time-consuming process is transport through regions 1 and 2, in which the water molecules and the polar groups of the membrane create a complex network of hydrogen bonds. Due to its size, the presence of OH groups and two benzodioxole moieties, compound 1 made many intermolecular interactions in these regions, which slowed down the diffusion movement to its equilibrium position. Compound 2 also accumulated inside both bilayers close to the polar groups of the lipids (in region 2). However, due to the absence of the benzodioxole moieties and its smaller size compared to 1, the equilibrated position of 2 was reached within 50 ns regardless of the starting point, i.e., inside or outside the bilayer.

Location and Orientation of Compounds 1 and 2, and Their Antioxidant-Active OH Groups in Lipid Bilayers.

The COM of the central guaiacyl moiety of 1 (responsible for the free radical scavenging capacity of 1)¹⁸ was located at 1.4 ± 0.2 and 1.2 ± 0.2 nm from the center of the DOPC and PLPC bilayers, respectively (Figure 2 and Table 1). This confirms that the molecule was equilibrated in region 2, close to the boundary between regions 2 and 3. The two lateral benzodioxole moieties of 1 were very flexible in all free MD simulations. The mass densities of these lateral moieties were widely distributed from region 2 up to region 4. Having no role in free-radical scavenging, the benzodioxole moieties may participate in the antioxidant action (lipid peroxidation inhibition) from a conformational aspect. The global effect of their presence is a subtle balance between their role as anchor (favoring insertion deep in the membrane) and their steric interaction (disfavoring membrane penetration).

The OH groups of the guaiacyl moiety are the H-atom donors, responsible for the free-radical scavenging activity of 1.¹⁸ They were oriented toward the bilayer surface. Such an orientation was driven by hydrogen-bonding interactions between these groups and both the polar head groups of the bilayer and the water molecules, which penetrated into region 2. It should be noted that the oxygen atoms of the benzodioxole moiety (Figure 1) interacted with neither the polar head groups nor the penetrating water molecules.

In order to establish a correlation between the location of the free-radical-scavenger-active groups and the region in which the propagation stage of lipid peroxidation occurs, an overlapping between both OH groups of the antioxidant and double bonds of unsaturated fatty acids was averaged over the MD simulations (Table S1, Figures S1 and S2 in the Supporting Information). For compound 1, the OH groups are the only free-radical scavengers; thus, the greater the overlap, the more efficient ROO[•] free radical scavenging by the antioxidant. In contrast, it is noteworthy that the lower the overlap, the less efficient its role in the propagation stage, and the more probable its role in the initiation stage (i.e., scavenging of the free radicals penetrating the membrane to oxidize lipids). This overlap was 29 ± 15 and $23 \pm 4\%$ for compound 1 in the DOPC and PLPC lipid bilayer, respectively.

For compound 2, the distance of the COM was 1.6 ± 0.2 and 1.3 ± 0.2 nm from the center of the DOPC and PLPC lipid bilayers, respectively, suggesting it is embedded in region 2 also close to the boundary between regions 2 and 3. In the case of the DOPC bilayer, the density of 2 exhibited two maxima in both leaflets (Figure 2, and Figure S1 in the Supporting Information), indicating that this compound (even during free MD simulations) passed through the lipid bilayer (Figure S2 in the Supporting Information), whereas this behavior was not observed with compound 1, possibly as 1 is larger and therefore its diffusion through the center of bilayer will be slower.

As for compound 1, the OH groups of both guaiacyl moieties of compound 2 were also oriented toward the polar head groups of the bilayers, creating hydrogen bonds with the phosphates and water molecules inserted in region 2. Broad density profiles were obtained (Figure 2), indicating that the molecule fluctuated significantly during the simulations (Figure S2). The overlap of the OH groups of 2 with the double bonds of the unsaturated fatty acids was lower than for 1, mainly in the DOPC membrane ($13 \pm 6\%$ and $19 \pm 2\%$ in the DOPC and PLPC bilayers, respectively). The lower overlap observed in DOPC compared to PLPC originated from the closer location of compound 2 to the center of the PLPC lipid bilayer. In addition, the mobility of 2 was slightly higher in PLPC (see the standard deviation for the OH group in Table 1), probably due to the higher fluidity of this lipid bilayer. However, the lipid peroxidation inhibition activity was measured on PLPC vesicles, whereas only marginal differences were found for the PLPC bilayer, either in overlap of OH groups and lipid double bonds

or in location and orientation. These differences cannot therefore explain the dramatic decrease in lipid peroxidation inhibition from **1** to **2**.

Free Energy Profiles for the Membrane Penetration of **1 and **2**.** The free energy profile of compound **1** exhibited a relatively broad minimum at 1.3 nm for both bilayers. The free energy minimum was located at -22.7 ± 0.2 and -21.9 ± 0.6 kcal/mol with respect to the water phase in the DOPC and PLPC bilayers (Figure 3), respectively. The free energy profile performed in the DOPC bilayer exhibited a second minimum in the middle of the membrane. This position is surprisingly as stable as the former one (Figure 3), which reflects that the DOPC bilayer has an interstitial space in between both leaflets, large enough for compound **1** to adapt and stabilize. Moreover, the energetic barrier for the flip-flop of this compound from one to the other leaflet was low in the DOPC bilayer (1.5 ± 0.1), while it was significantly higher in the PLPC bilayer (6.6 ± 0.4 kcal/mol).

Compound **2** was predicted to have a lower affinity to both membranes than compound **1**. The free energy minima ($\Delta G(z_{\min})$) were at 1.5 and 1.2 nm in the DOPC and PLPC bilayers stabilized by -14.5 ± 0.1 and -12.8 ± 1.1 kcal/mol, respectively (Figure 3). The barrier of passage from one to the other leaflet was 5.5 ± 0.1 and 3.4 ± 0.3 kcal/mol in DOPC and PLPC, respectively.

The free energy profiles indicate that both compounds have significantly different affinities to the lipid bilayers. Compound **1** displays higher affinity to both DOPC and PLPC membranes, which in turn indicates that the effective concentrations of compound **1** in both membranes are higher than concentrations of compound **2**, which is due to the presence of nonpolar side chains of compound **1**. The higher affinity of compound **1** to lipid bilayers can explain higher activity in lipid peroxidation inhibition measured on PLPC vesicles. It may also indicate higher activity on other types of unsaturated lipid bilayer, as is indicated from its affinity to DOPC bilayer (Table 1)

CONCLUDING REMARKS AND CORRELATION TO EXPERIMENTAL DATA

The present theoretical investigation rationalizes the difference in lipid peroxidation inhibition observed between compounds **1** and **2**, despite these two compounds exhibiting the same free-radical scavenging and HAT capacities. Molecular dynamic simulations identified differences in the membrane positions and orientations between the two compounds. However, these differences appeared marginal and not sufficient to rationalize the difference in lipid peroxidation inhibition activities of both compounds. On the other hand, biased MD simulations showed that the compounds significantly differed in their affinities to the lipid bilayers. Compound **1** was stabilized over compound **2** by 8.2 and 9.1 kcal/mol in DOPC and PLPC, respectively. This free energy difference can be associated to the difference in partitioning of both compounds into the lipid bilayer. Therefore, the effective concentration of compound **1** in the studied lipid membranes should be significantly higher than for compound **2**, in agreement with the efficient lipid peroxidation inhibition capacity of compound **1**. This molecular picture for membrane penetration of this compound demonstrates the role of the hydrophobic benzodioxole side moieties, which stabilize the active part of compound **1** between the lipid head groups and unsaturated parts of the lipid chains. Such a position enables inhibition of lipid peroxidation (i) during the

initiation stage (i.e., scavenging of incoming free radicals following their uptake into the membrane) or (ii) during the propagation stage (i.e., propagation of the lipid-based ROO[•] free radicals between lipid chains)

ASSOCIATED CONTENT

Supporting Information

Calculated overlaps of mass densities of OH groups and double bonds during unbiased simulation (Table S1); the density profiles of OH groups of studied compounds during free simulations (Figure S1); the positions of OH groups during unbiased simulations (Figure S2); plot of the free energy profiles vs simulation time (Figure S3); two independent free energy profiles of compound **2** on the PLPC bilayer (Figure S4). This material is available free of charge via the Internet at <http://pubs.acs.org>.

AUTHOR INFORMATION

Corresponding Author

*E-mail: michal.otyepka@upol.cz (M.O.); patrick.trouillas@unilim.fr (P.T.).

Notes

The authors declare no competing financial interest.

ACKNOWLEDGMENTS

The authors gratefully acknowledge support from the Operational Program Research and Development for Innovations—European Regional Development Fund (project CZ.1.05/2.1.00/03.0058 of the Ministry of Education, Youth and Sports of the Czech Republic), the Operational Program Education for Competitiveness—European Social Fund (projects CZ.1.07/2.3.00/20.0017 and CZ.1.07/2.3.00/20.0058 of the Ministry of Education, Youth and Sports of the Czech Republic), and the Grant Agency of the Czech Republic (P208/12/G016). The authors also thank the “Conseil Régional du Limousin” for financial support and CALI (CALcul en LIMousin). The research based in Limoges was also supported by the COST action CM0804 “Chemical Biology with Natural Compounds”.

ABBREVIATIONS

DPPH radical, 2,2-diphenyl-1-picrylhydrazyl radical; DOPC, 1,2-dioleoyl-*sn*-glycero-3-phosphatidylcholine; PLPC, 1-palmitoyl-2-linoleoyl-*sn*-glycero-3-phosphatidylcholine; MD, molecular dynamics; BDE, bond dissociation enthalpy; IC₅₀, half-maximal inhibitory concentration; COM, center of mass

REFERENCES

- (1) Reed, T. T. *Free Radical Biol. Med.* **2011**, *51*, 1302–1319.
- (2) Steinberg, D. *Med. Sci. Symp. Ser.* **1998**, *12*, 141–147.
- (3) Rikans, L. E.; Hornbrook, K. R. *BBA, Mol. Basis Dis.* **1997**, *1362*, 116–127.
- (4) Praticò, D. *Science's SAGE KE* **2002**, *50*, re5.
- (5) Halliwell, B.; Gutteridge, J. M. C. *Free Radicals in Biology and Medicine*, 4th ed.; Oxford University Press: Oxford, UK, 2007.
- (6) Negre-Salvayre, A.; Auge, N.; Ayala, V.; Basaga, H.; Boada, J.; Brenke, R.; Chapple, S.; Cohen, G.; Feher, J.; Grune, T.; et al. *Free Radical Res.* **2010**, *44*, 1125–1171.
- (7) Niki, E. *Free Radical Biol. Med.* **2009**, *47*, 469–484.
- (8) Gutteridge, J. M. C. *Clin. Chem.* **1995**, *41*, 1819–1828.
- (9) Adlercreutz, H. *Crit. Rev. Clin. Lab. Sci.* **2007**, *44*, 483–525.
- (10) Moss, G. P. *Pure Appl. Chem.* **2000**, *72*, 1493–1523.
- (11) Ward, R. S. *Nat. Prod. Rep.* **1999**, *16*, 75–96.
- (12) Filleur, F.; Le Bail, J. C.; Duroux, J. L.; Simon, A.; Chulia, A. J. *Planta Medica* **2001**, *67*, 700–704.

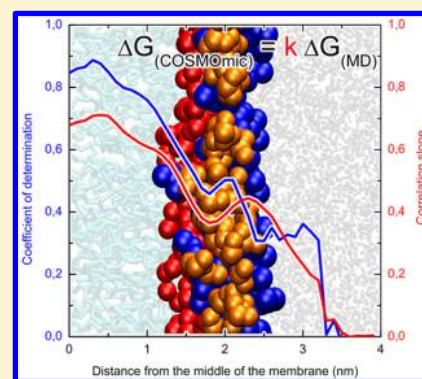
- (13) Adlercreutz, H. *Environ. Health Persp.* **1995**, *103*, 103–112.
- (14) McCann, M. J.; Gill, C. I. R.; McGlynn, H.; Rowland, I. R. *Nutr. Cancer* **2005**, *52*, 1–14.
- (15) Westcott, N. D.; Muir, A. D. *Phytochem. Rev.* **2003**, *2*, 401–417.
- (16) Wang, L. Q. *J. Chromatogr. B* **2002**, *777*, 289–309.
- (17) Ghisalberti, E. L. *Phytomedicine* **1997**, *4*, 151–166.
- (18) Calliste, C. A.; Kozlowski, D.; Duroux, J. L.; Champavier, Y.; Chulia, A. J.; Trouillas, P. *Food Chem.* **2010**, *118*, 489–496.
- (19) Filleur, F.; Pouget, C.; Allais, D. P.; Kaouadji, M.; Chulia, A. J. *Nat. Prod. Lett.* **2002**, *16*, 1–7.
- (20) Anouar, E.; Calliste, C. A.; Košinová, P.; Di Meo, F.; Duroux, J. L.; Champavier, Y.; Marakchi, K.; Trouillas, P. *J. Phys. Chem. A* **2009**, *113*, 13881–13891.
- (21) Košinová, P.; Berka, K.; Wykes, M.; Otyepka, M.; Trouillas, P. *J. Phys. Chem. B* **2012**, *116*, 1309–1318.
- (22) Paloncýová, M.; Berka, K.; Otyepka, M. *J. Chem. Theory Comput.* **2012**, *8*, 1200–1211.
- (23) Marrink, S. J.; Berendsen, H. J. C. *J. Phys. Chem.* **1994**, *98*, 4155–4168.
- (24) Bemporad, D.; Essex, J. W.; Luttmann, C. *J. Phys. Chem. B* **2004**, *108*, 4875–4884.
- (25) dos Santos, D. J. V. A.; Eriksson, L. A. *Biophys. J.* **2006**, *91*, 2464–2474.
- (26) Eriksson, E. S. E.; dos Santos, D. J. V. A.; Guedes, R. C.; Eriksson, L. A. *J. Chem. Theory Comput.* **2009**, *5*, 3139–3149.
- (27) Ulander, J.; Haymet, A. D. *J. Biophys. J.* **2003**, *85*, 3475–3484.
- (28) Qin, S. S.; Yu, Z. W.; Yu, Y. X. *J. Phys. Chem. B* **2009**, *113*, 16537–16546.
- (29) Boggara, M. B.; Krishnamoorti, R. *Biophys. J.* **2010**, *98*, 586–595.
- (30) Vazdar, M.; Jurkiewicz, P.; Hof, M.; Jungwirth, P.; Cwiklik, L. *J. Phys. Chem. B* **2012**, *116*, 6411–6415.
- (31) Paloncýová, M.; Berka, K.; Otyepka, M. *J. Phys. Chem. B* **2013**, *117*, 2403–2410.
- (32) van Meer, G.; Voelker, D. R.; Feigenson, G. W. *Nat. Rev. Mol. Cell Biol.* **2008**, *9*, 112–124.
- (33) Bruce, A.; Alexander, J.; Julian, L.; Martin, R.; Keith, R.; Peter, W. *Molecular Biology of the Cell*, 5th ed.; Garland Science: New York, 2008.
- (34) Siu, S. W. I.; Vácha, R.; Jungwirth, P.; Bockmann, R. A. *J. Chem. Phys.* **2008**, *128*.
- (35) Bachar, M.; Brunelle, P.; Tieleman, D. P.; Rauk, A. *J. Phys. Chem. B* **2004**, *108*, 7170–7179.
- (36) Berger, O.; Edholm, O.; Jahnig, F. *Biophys. J.* **1997**, *72*, 2002–2013.
- (37) Berendsen, H. J. C.; Postma, J. P. M.; van Gunsteren, W. F.; Hermans, J. *Intermolecular Forces*; Reidel Publishing Co.: Dordrecht, The Netherlands, 1981.
- (38) Hess, B.; Kutzner, C.; van der Spoel, D.; Lindahl, E. *J. Chem. Theory Comput.* **2008**, *4*, 435–447.
- (39) Trouillas, P.; Marsal, P.; Siri, D.; Lazzaroni, R.; Duroux, J. L. *Food Chem.* **2006**, *97*, 679–688.
- (40) Schuttelkopf, A. W.; van Aalten, D. M. F. *Acta Crystallogr. D* **2004**, *60*, 1355–1363.
- (41) Case, D. A.; Darden, T. A.; Cheatham, L. T. E.; Simmerling, C. L.; Wang, J.; Duke, R. E.; Luo, R.; Walker, R. C.; Zhang, W.; Merz, K. M.; et al. *AMBER 11*; University of California: San Francisco, 2010.
- (42) Bayly, C. I.; Cieplak, P.; Cornell, W. D.; Kollman, P. A. *J. Phys. Chem.* **1993**, *97*, 10269–10280.
- (43) Frisch, M. J.; Trucks, G. W.; Schlegel, H. B.; Scuseria, G. E.; Robb, M. A.; Cheeseman, J. R.; Montgomery, J. A., Jr.; Vreven, T.; Kudin, K. N.; Burant, J. C.; et al. *Gaussian 03, revision E.01*; Gaussian, Inc.: Wallingford, CT, 2004.
- (44) Bussi, G.; Donadio, D.; Parrinello, M. *J. Chem. Phys.* **2007**, *126*.
- (45) Berendsen, H. J. C.; Postma, J. P. M.; Vangunsteren, W. F.; Dinola, A.; Haak, J. R. *J. Chem. Phys.* **1984**, *81*, 3684–3690.
- (46) Hess, B.; Bekker, H.; Berendsen, H. J. C.; Fraaije, J. G. E. M. *J. Comput. Chem.* **1997**, *18*, 1463–1472.
- (47) Darden, T.; York, D.; Pedersen, L. *J. Chem. Phys.* **1993**, *98*, 10089–10092.
- (48) Essmann, U.; Perera, L.; Berkowitz, M. L.; Darden, T.; Lee, H.; Pedersen, L. G. *J. Chem. Phys.* **1995**, *103*, 8577–8593.
- (49) Parrinello, M.; Rahman, A. *J. Appl. Phys.* **1981**, *52*, 7182–7190.
- (50) Hockney, R. W.; Goel, S. P.; Eastwood, J. W. *J. Comput. Phys.* **1974**, *14*, 148–158.
- (51) Humphrey, W.; Dalke, A.; Schulten, K. *J. Mol. Graph.* **1996**, *14*, 33–38.
- (52) Jämbeck, J. P. M.; Lyubartsev, A. P. *Phys. Chem. Chem. Phys.* **2013**, *15*, 4677–4686.
- (53) Ingram, T.; Storm, S.; Kloss, L.; Mehling, T.; Jakobtorweihen, S.; Smirnova, I. V. *Langmuir* **2013**, *29*, 3527–3537.
- (54) Karlsson, B. C. G.; Olsson, G. D.; Friedman, R.; Rosengren, A. M.; Henschel, H.; Nicholls, I. J. *Phys. Chem. B* **2013**, *117*, 2384–95.
- (55) Neale, C.; Bennett, W. F. D.; Tieleman, D. P.; Pomès, R. *J. Chem. Theory Comput.* **2011**, *7*, 4175–4188.
- (56) Singh, G.; Tieleman, D. P. *J. Chem. Theory Comput.* **2013**, *9*, 1657–1666.

Amphiphilic Drug-Like Molecules Accumulate in a Membrane below the Head Group Region

Markéta Paloncýová,[†] Russell DeVane,[‡] Bruce Murch,[‡] Karel Berka,^{*,†} and Michal Otyepka^{*,†}[†]Department of Physical Chemistry, Faculty of Science, Regional Centre of Advanced Technologies and Materials, Palacký University Olomouc, tř. 17. listopadu 12, 771 46 Olomouc, Czech Republic[‡]Corporate Modeling & Simulation, Procter & Gamble, 8611 Beckett Road, West Chester, Ohio 45069, United States

S Supporting Information

ABSTRACT: The partitioning behavior of drug-like molecules into biomembranes has a crucial impact on the design and efficacy of therapeutic drugs. Thermodynamic properties connected with the interaction of molecules with membranes can be evaluated by calculating free-energy profiles normal to the membrane surface. We calculated the free-energy profiles of 25 drug-like molecules in a 1,2-dioleoyl-*sn*-glycero-3-phosphocholine (DOPC) membrane and free energies of solvation in water and heptane using two methods, molecular dynamics (MD) simulations with the Berger lipid force field and COSMOmic, based on a continuum conductor-like screening model for realistic solvation (COSMO-RS). The biased MD simulations (in total $\sim 22 \mu\text{s}$ long) were relatively computationally expensive, whereas the COSMOmic approach offered a significantly less expensive alternative. Both methods provided similar results and showed that the studied amphiphilic drug-like molecules accumulate in the membrane, with the majority localized below the head group region. The MD simulations were more lipophilic and gave free-energy profiles that were systematically deeper than those calculated by COSMOmic. To investigate the physical nature of the increased lipophilicity, we analyzed a water/heptane system and identified that it is most likely caused by overestimation of the attractive term of the Lennard-Jones potential in lipid tails. We concluded that COSMOmic can be successfully used for high-throughput computations of global thermodynamic properties, for example, partition coefficients and energy barrier heights, in phosphocholine membranes. In contrast, MD is better for investigating local properties like molecular positioning and orientation in the membrane because they more accurately reflect the complex structure of lipid bilayers. MD is also useful for studies of highly complex systems, for example, drug–membrane–protein interactions.



INTRODUCTION

Molecular insight into the interactions of drugs (generally any xenobiotic) with biomembranes broadens our understanding of drug disposition in the human body and, in turn, absorption, distribution, metabolism, and excretion (ADME) processes. Absorption is influenced by the ability of a drug to cross the skin (in the case of a transdermal pathway) or the intestine wall (oral pathway). The distribution depends on the penetration of the drug through cell membranes. Metabolism of the drug is affected by the position and concentration of the drug in the relevant membrane, whereas its excretion depends on the penetration properties of the resulting metabolites and possible accumulation of drugs or metabolites in tissues. As biomembranes form barriers between environments with different properties, the thermodynamic and kinetic properties of drugs interacting with membranes is of particular interest.^{1–8}

Several experimental techniques have been employed for estimating partition and penetration properties of drug-like molecules.^{9–11} Commonly used techniques for partition measurements include, among others, ultracentrifugation, solid phase microextraction, and equilibrium dialysis.¹² Caco2 cells and skin penetration¹³ measurements are commonly used

to estimate penetration rates. These experimental techniques allow estimation of penetration and partitioning properties and their dependence on concentration, temperature, pressure, and so forth. However, they do not provide a detailed molecular-level understanding of drug–membrane interactions.

A considerable effort has been invested in developing *in silico* methods that can assess partitioning and permeation of drugs in membranes.^{5,14–19} The partitioning of a drug in a membrane can be rationalized by a free-energy profile along the lipid bilayer normal. The free-energy profile can be reconstructed from biased molecular dynamics (MD) simulations, typically from constraint simulations, umbrella sampling, metadynamics, or flooding.^{4,20–22} It is worth noting that MD simulations can accurately describe the complex structure of a lipid bilayer,^{23,24} and simultaneously enable fine space (atomic) and time (subpicosecond) resolutions. In addition, MD simulations can be used for dynamical studies of even more complex systems, for example, drug–membrane–protein interactions.²⁵ On the

Received: November 14, 2013

Revised: January 12, 2014

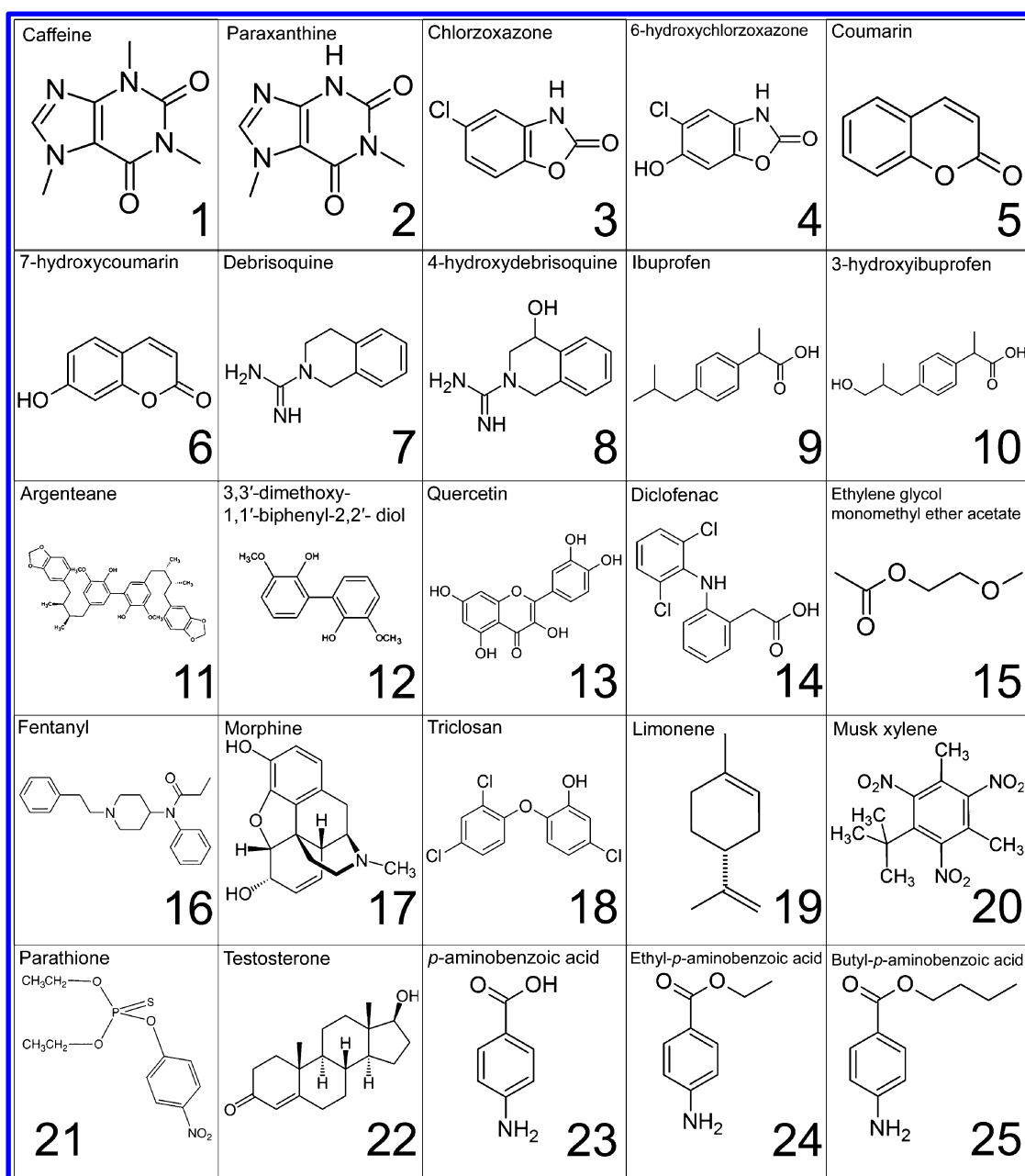


Figure 1. Structures and names of drugs used in this study. The numbers are consistent with the numbering in the rest of the paper.

other hand, the quality of MD simulations is highly dependent on the quality of the force field used (FF; an empirical potential or molecular mechanics potential).^{26–29} Recent studies have shown that the free-energy profiles of drugs on membranes display rather slow convergence,^{18,30} requiring long (typically 100+ ns) and consequently computationally demanding MD simulations. In addition, degrees of freedom other than just the distance from the membrane core need to be taken into account, which makes the calculation even more difficult.³¹ All of the above-mentioned features make MD simulations a powerful but expensive tool in the rationalization of drug partitioning properties.

The enormous computer demands required to obtain free-energy profiles from MD simulations has motivated many researchers to develop less expensive methods. Continuum solvation models based on quantum chemical calculations are a significantly less expensive and reliable alternative to MD

simulations.^{32,33} The COSMOmic approach³⁴ based on the COSMO-RS method³³ allows efficient and accurate prediction of the distribution of molecules in micellar systems and lipid bilayers.^{12,34,35} The COSMO-RS method applies statistical thermodynamics to surface polarization charge densities σ calculated from quantum chemical calculations, typically based on density functional theory (DFT). It has been shown that partition coefficients calculated by COSMOtherm into various homogeneous phases are in a good agreement with experimental data (with the average error of $\log K \approx 10\%$).³⁶ The COSMOmic method further analyzes the structure of a membrane in a solvent environment (water) and estimates the free-energy profile for a given molecule along the membrane normal. First, DFT calculations need to be performed for every molecule type in the system (lipids, water, drug molecules), and σ -profiles (histograms of charge densities σ) are obtained. Simply stated, the more complementary the σ -profiles of two

phases, the more miscible these phases. The following COSMOmic calculation is based only on analysis of geometries, rotation states, and σ -profiles of solute molecules and the membrane. The structure of a membrane is divided into layers, where each layer is considered as a separate fluid with its own σ -profile, which is calculated based on the parts of the molecular surface of each membrane molecular type present in each layer.³⁴ The center of mass of a molecule is placed into each layer, and by rotation of the solute, ~ 162 different directional representations are considered in each layer. For each state, COSMOmic calculates local σ -profiles (considering molecular segments in neighboring layers), which are then used to generate an integral σ -profile. This calculation is again based on the geometrical analysis of molecular orientation and identifies which part of the molecular surface is present in individual membrane layers. From this information, the overall solvation energy of the molecule in each layer is calculated, and the free-energy profile is constructed. The COSMOmic calculation is a relatively quick (it takes just a few minutes on a desktop computer but requires σ -profiles that are calculated within a few hours for considered molecules) and simple method to obtain the free-energy profile of a molecule in a membrane. However, to the best of our knowledge, no comparisons of COSMOmic to other computational approaches have been published.

In this work, we calculated the free-energy profiles of a set of 25 drug-like molecules (Figure 1) in a DOPC membrane and the solvation energies of those molecules in water and heptane. We used both MD simulations with the Berger lipid FF and COSMOmic. Both methods showed that the molecules accumulate in the membrane environment, with the majority lying just below the polar head group region. In the case of DOPC, we observed a significant correlation between the methods with regard to the height of the free-energy barrier between the water and lipid environment. There was also a strong correlation between the partition coefficients and partitioning into the hydrophobic part of the membrane. However, there were large differences in the details around the head group area, mainly in the location of the energy minimum and the energy barrier of crossing the membrane center. Some of these differences were attributed to the higher lipophilicity of the Berger lipid FF stemming from an overestimated Lennard-Jones term.

METHODS

The equilibrated DOPC membrane model²⁷ was downloaded from the Lipidbook web page³⁷ and was equilibrated for 10 ns using classical MD simulation at 310 K. The united-atom Berger lipid FF,³⁸ which simplifies hydrocarbon chains by uniting nonpolar hydrogens with the corresponding carbons, was applied to the lipid bilayer. The drugs were prepared by combining the PRODRG³⁹ tool and RESP^{40–43} calculation (see the Supporting Information). The drug molecules were placed at the top of the simulation box and hydrated with SPC or SPC/E water molecules (see the Supporting Information Table S1). Free-energy profiles, $\Delta G(z)$, were calculated either by umbrella sampling (eq 1), as described in our recent paper,⁴⁴ or by using our proposed simulation protocol³⁰ with z -constraint simulation (eq 2).

$$\Delta G(z) = -RT \ln P(z) + U(z) \quad (1)$$

$$\Delta G(z) = - \int_{\text{outside}}^{z'} \langle \vec{F}(z) \rangle_t dz \quad (2)$$

where $P(z)$ stands for the distribution of the studied molecule in the umbrella sampling simulation window, $U(z)$ stands for the umbrella potential, and $\langle F(z) \rangle_t$ stands for the time-averaged force applied to the molecule during the z -constraint simulation. The start of the z -axis was set to the middle of the membrane, and the reference value ($\Delta G = 0$ kcal/mol) for the free energy was set to that for water. The detailed simulation protocol can be found in the Supporting Information. It is worth noting that the same simulation protocol has been successfully applied to study the penetration properties of various drugs and antioxidants.^{2,5,18,20,30,44,45}

For the COSMOmic calculations, we used a set of 30 structures taken from a 100 ns long MD simulation of a DOPC membrane to increase the precision of the calculations, as recommended in the literature.³⁵ The geometries and σ -profiles of all molecules were calculated by DFT/COSMO calculations at the BP/TZVP level of theory.^{46,47} Free-energy profiles were calculated at 310 K, with the membrane separated into 50 layers and 162 orientations of the solute molecules generated using COSMOmic software³⁴ from the COSMOtherm 13 package.⁴⁸ The free-energy profiles were averaged and compared to those obtained by MD.

The free-energy profiles provided information about (i) the position of the free-energy minimum, (ii) the height of the free-energy barriers (penetration barrier and water/lipids barrier – affinity to membrane), and (iii) the partition coefficient in the water/membrane environment. The overall distribution coefficient D of a molecule between membrane and water phases can be expressed in terms of the free energies in these phases (eq 3) and depends on the partition coefficient into membrane K , membrane surface S_{membrane} and the volume of the water phase V_{water} . As the ratio of the membrane surface and water volume can be considered constant in the human body, we focus here just on the partition coefficient into membrane K that is reconstructed from the free-energy profile along the membrane (L nm thick) using eq 4

$$D = \frac{\iint_{\text{Surface}} dx dy \int_{-L/2}^{L/2} e^{-\Delta G(z)/RT} dz}{\iiint_{\text{Volume}} e^{-\Delta G(\text{water})/RT} dx dy dz} = \frac{S_{\text{membrane}}}{V_{\text{water}}} \cdot K \quad (3)$$

$$K = 2 \int_{L/2}^0 K(z') dz = 2 \int_{L/2}^0 e^{-\Delta G(z')/RT} dz \quad (4)$$

The free-energy profiles obtained by MD and COSMOmic were analyzed, and several parameters were compared (see Figure 2): (i) free-energy values at different membrane depths, $\Delta G(z)$, (ii) positions of the free-energy minima, Z_{min} , (iii) the local partition coefficient as a function of membrane depth, $K(z)$, (iv) the height of penetration barriers, ΔG^{pen} , and (v) the height of water/lipid barriers, ΔG^{wat} (lipophilicity and $\log K$).

Further, we calculated the transfer free energy from water to heptane $\Delta G^{\text{wat/heptane}}$ by COSMOtherm and MD. For the COSMOtherm calculations, we used the same molecular geometries and σ -profiles as described above for COSMOmic and default settings for the free energy of solvation calculation. The MD calculations utilized the thermodynamic integration method with the Bennett acceptance ratio (BAR).⁴⁹ A molecule of heptane was prepared to mimic the properties of a membrane core in the simulations. Therefore, the same charges

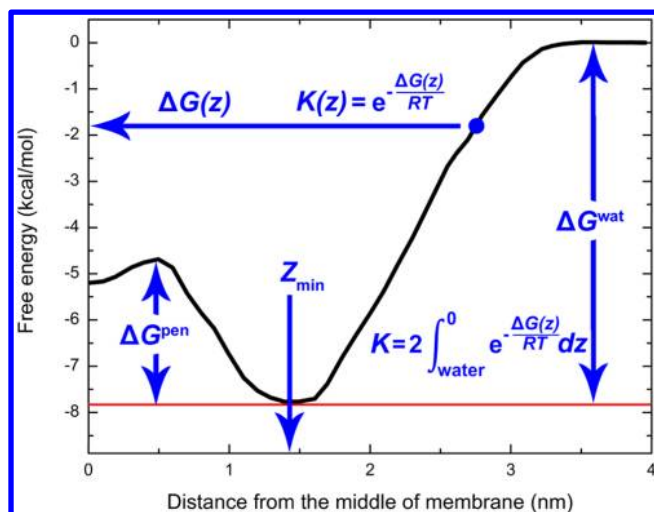


Figure 2. Prototypical free-energy profile of a drug along the bilayer normal showing the free energy $\Delta G(z)$ at different depths (z). $K(z)$ is the local partition coefficient at a distance z from the bilayer center, ΔG^{pen} is the free-energy barrier for penetration across the bilayer core, and Z_{min} is the position of the free-energy minimum. ΔG^{wat} is the water/lipid barrier (affinity to the membrane), which makes the largest contribution to the overall partition coefficient K .

(assigned zero partial charges to all atoms) and atom types were used as those in the lipid tails in the Berger FF. An SPC/E⁵⁰ water model was used to calculate hydration free energies. Each drug molecule was placed in the simulation box and solvated with either water or heptane (~ 1.5 nm distance from drug to box edges). Then, the system was equilibrated for 100 ps. Twenty-one simulation windows ($\Delta\lambda = 0.05$) were run for 200 ps, and the last 100 ps was analyzed using g_{bar} from the GROMACS 4.5.1 software package. We evaluated the correlation of solvation free energies in water ΔG^{hyd} and heptane ΔG^{soliv} by COSMOtherm and MD; we also evaluated $\Delta G^{\text{wat/heptane}}$ between the two methods and, last, compared $\Delta G^{\text{wat/heptane}}$ with the free energies in the middle of the membrane.

We plotted the free-energy profile parameters in DOPC in correlation plots and fitted the data to a straight line of the form $Y_{\text{COSMOmic}} = k(\text{err}) \cdot X_{\text{MD}} + q(\text{err})$, where k is the slope and q the intercept and their errors are in brackets. We evaluated the significance of the intercept parameter at a probability level of 0.975. In the case of a statistically insignificant intercept, we fitted the data to $Y_{\text{COSMOmic}} = k(\text{err}) \cdot X_{\text{MD}}$.

RESULTS AND DISCUSSION

We calculated free-energy profiles for 25 drug-like molecules in a DOPC membrane using biased MD simulations and COSMOmic. A typical free-energy profile of an amphiphilic molecule in a DOPC membrane calculated by MD is shown in Figure 2, and all free-energy profiles calculated in this study are shown in Figure S1 in the Supporting Information. Initially, the free energy decreased as the molecule approached the membrane surface from the water phase. Interestingly, the simulations predicted that some of the molecules have a small barrier to entry (approximately 1 kcal/mol) as they pass through the head group region (2.0–2.5 nm; all depths are reported as the distance from the membrane center). The free-energy minimum was usually located below the head groups (1.1–1.7 nm) and was 2–11 kcal/mol deep for most of the

molecules studied here. The free energy then increased until about 0.5 nm from the membrane center. In the membrane center, there was a shallow local energy minimum. In the case of lipophilic molecules, the free energy decreased to a minimum at the membrane center. The free-energy profiles calculated by COSMOmic displayed similar behavior in the outer parts of the membrane but had a different shape in the membrane interior. The free energies of lipophilic molecules reached an almost constant value at about 1.0 nm from the membrane center, whereas the amphiphilic molecules exhibited an almost constant free energy starting at approximately 0.5 nm from the bilayer center. Neither type of molecule displayed a local free-energy minimum at the membrane center. The free-energy minima calculated by COSMOmic were localized in two regions, at 0.7–1.5 and 2.0–2.6 nm.

Both methods, MD and COSMOmic, ranked the drug's affinity for the membrane in a comparable order, that is, water/lipid barrier ΔG^{wat} (Figure 3 and eq 5)

$$\Delta G_{\text{COSMOmic}}^{\text{wat}} = 0.62(0.08)\Delta G_{\text{MD}}^{\text{wat}} - 0.16(0.74)$$

$$r^2 = 0.73 \quad (5)$$

Linear regression analysis showed that COSMOmic predicted lower free-energy barriers (ΔG^{wat}) by about 40% but did not indicate any statistically significant shift. The coefficient of determination (which is equal to 1 in the case of strict linear dependence) was found to be $r^2 = 0.73$. The penetration barriers ΔG^{pen} predicted by COSMOmic were also about 40% lower than those predicted by MD, but the correlation between the two methods was lower, $r^2 = 0.59$ (eq 6)

$$\Delta G_{\text{COSMOmic}}^{\text{pen}} = 0.63(0.11)\Delta G_{\text{MD}}^{\text{pen}} + 0.13(0.65)$$

$$r^2 = 0.59 \quad (6)$$

The partition coefficients (Figure 3) calculated by both methods showed that all molecules included in this study tended to accumulate in the membrane. However, $\log K$ (eq 4) calculated by COSMOmic was almost 40% smaller than that by MD, but there was a significant linear relationship between the methods (eq 7)

$$\log K_{\text{COSMOmic}} = 0.63(0.07) \log K_{\text{MD}} - 0.01(0.47)$$

$$r^2 = 0.77 \quad (7)$$

These data indicate that drugs described by MD using the Berger lipid FF are more lipophilic than those obtained by COSMOmic. Previous COSMOmic $\log K$ calculations in 1,2-dimyristoyl-*sn*-glycero-3-phosphocholine (DMPC) have shown good correlation with experimentally measured $\log K$ (RMSE of $\log K$ from 0.34 to 0.79),^{12,14,35} with a coefficient of determination of linear fit to experimental data varying from 0.74 to 0.82.³⁴ Therefore, it is likely that COSMOmic would also show good performance for DOPC (DOPC and DMPC possess the same head groups but slightly different alkyl chains). Thus, the results indicate that MD simulations with the Berger lipid FF may systematically overestimate the real partition coefficients, drug affinities for a DOPC bilayer, and heights of penetration barriers (by $\sim 40\%$). Nonetheless, it is able to distinguish between low/high “membranophilic” drugs. This finding is also in agreement with observations by MacCallum et al.,⁵¹ who obtained correct ordering for the binding free energies of amino acids side chains to a POPC membrane.

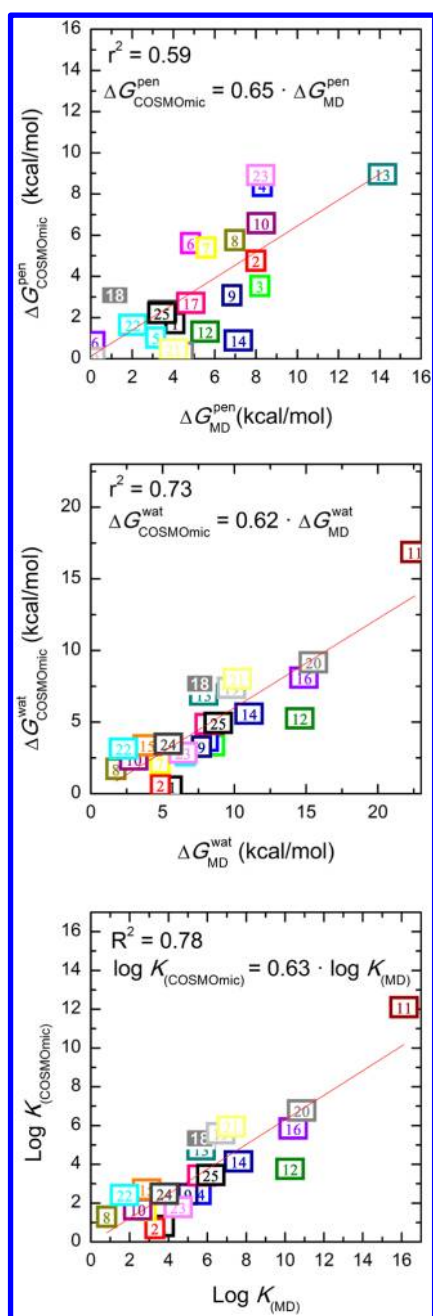


Figure 3. Comparison of the methods used showing the correlation of free-energy profile parameters calculated using COSMOmic (*y*-axis) and MD (*x*-axis). The penetration barrier (upper panel ΔG^{pen}) exhibited a relatively low coefficient of determination, r^2 , between the COSMOmic and MD values, whereas the water/lipid barrier (middle panel ΔG^{wat}) and partition coefficient (lower panel) correlated significantly. The numbers in the charts identify the molecules according to Table S1 (Supporting Information).

The structure of a lipid bilayer is rather complex⁵² (cf. Figure 4), and we anticipate that the local partitioning into different membrane depths by atomistic MD simulations may better reflect the membrane structure compared to the continuous-like model implemented in COSMOmic. The free energy of the drug ($\Delta G(z)$) at a given depth (z) and local partition coefficient ($K(z)$, eq 4) at the same depth calculated from the MD simulations mirrored the structure and density profile of the lipid bilayer. Peaks in the local partition coefficient

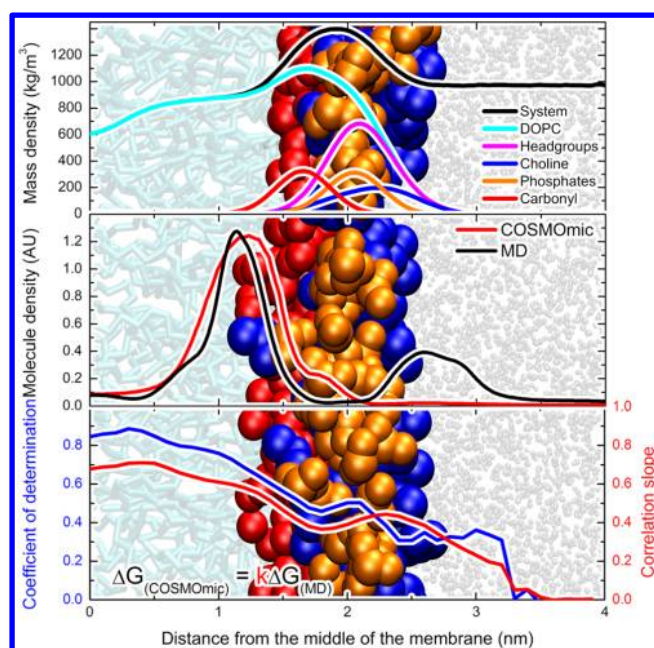


Figure 4. Background image showing the structure of a single leaflet of a hydrated lipid bilayer. Upper panel: mass densities of monitored groups. (Middle panel) Average mass density calculated from the local partition coefficients, $K(z)$, of drug molecules predicted by MD (black) and COSMOmic (red). The partition coefficient profiles were normalized and summed afterward. The MD partitioning favors specific locations in the membrane, whereas COSMOmic places all molecules into one broad region. (Lower panel) Coefficient of determination r^2 (blue) and slope (red) obtained from linear regression analysis of the z -dependent free-energy values between the COSMOmic and MD methods. A correlation slope lower than 1.0 indicates a shallower free-energy profile predicted by COSMOmic.

calculated by MD were found in three regions, (i) just below the head group region, where most of the drug molecules were localized, (ii) outside of the head group region at the interface with water, and (iii) in the middle of the membrane, which has the lowest density of lipids (Figure 4). The local partition coefficients predicted by COSMOmic were mostly localized to one broad area below the head group region. Unlike the MD calculations, COSMOmic showed almost constant partitioning into the region of the lipid tails (cf. Figure S1 (Supporting Information) and Figure 4), indicating that the position in the very middle of the membrane is not favored, as would be expected due to the decreased lipid density in that region. Similarly, MD predicted lower local partition coefficients than COSMOmic in the area of high membrane density (1.7–2.0 nm).

Neither COSMOmic nor MD favored the densest layer of the membrane as a free-energy minimum (Figure 5). However, the positions of the free-energy minima predicted by MD differed substantially from those by COSMOmic; the minima predicted by MD usually lay (i) in the lower parts of the head group region or just below it or (ii) in the middle of the membrane, where the overall density decreases. COSMOmic did not favor the energy minimum in the middle of the membrane and instead placed the molecules in a broad area in the outer parts of head groups (2.0–2.6 nm) or in the lipid tails below the head groups (0.7–1.5 nm). According to the positions of the free-energy minima, the molecules could be separated into three clusters, (i) lipophilic molecules that are localized in the middle of the membrane according to MD and

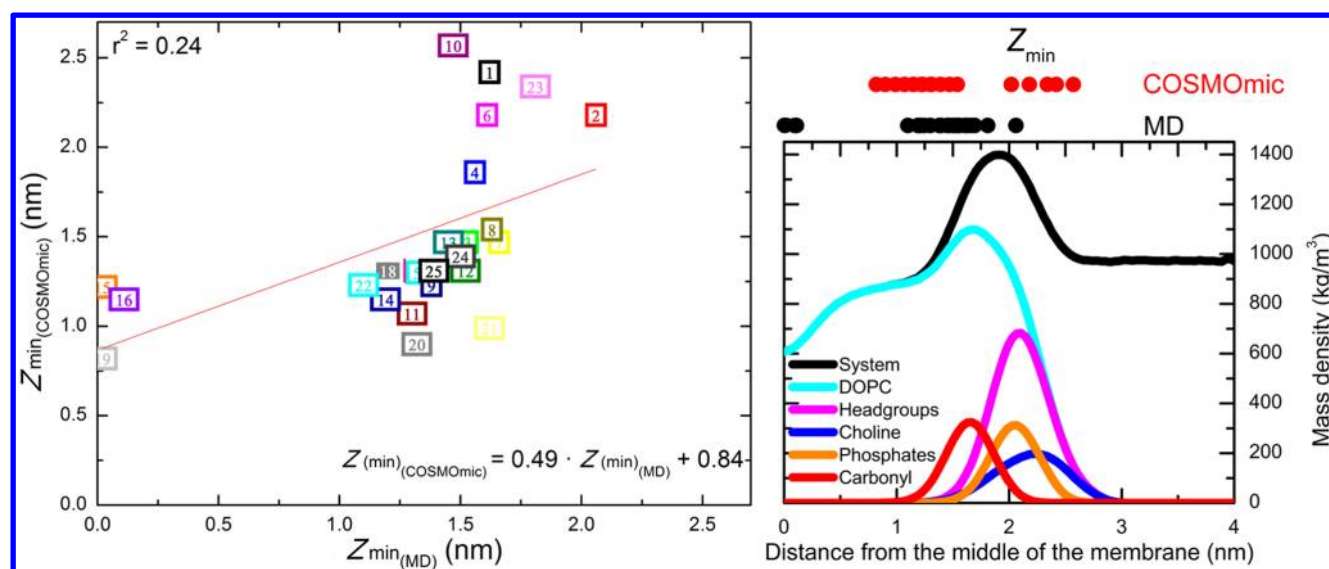


Figure 5. Positions of the free-energy minima Z_{\min} (left panel) proposed by COSMOmic (y-axis) and MD (x-axis) and compared to the system density (right panel). The minima predicted by MD were located in the lower part of the head groups or just below them or in the middle of the membrane (upper right panel, black circles). The minima predicted by COSMOmic were located above the head groups or in the lipid tail region (red circles).

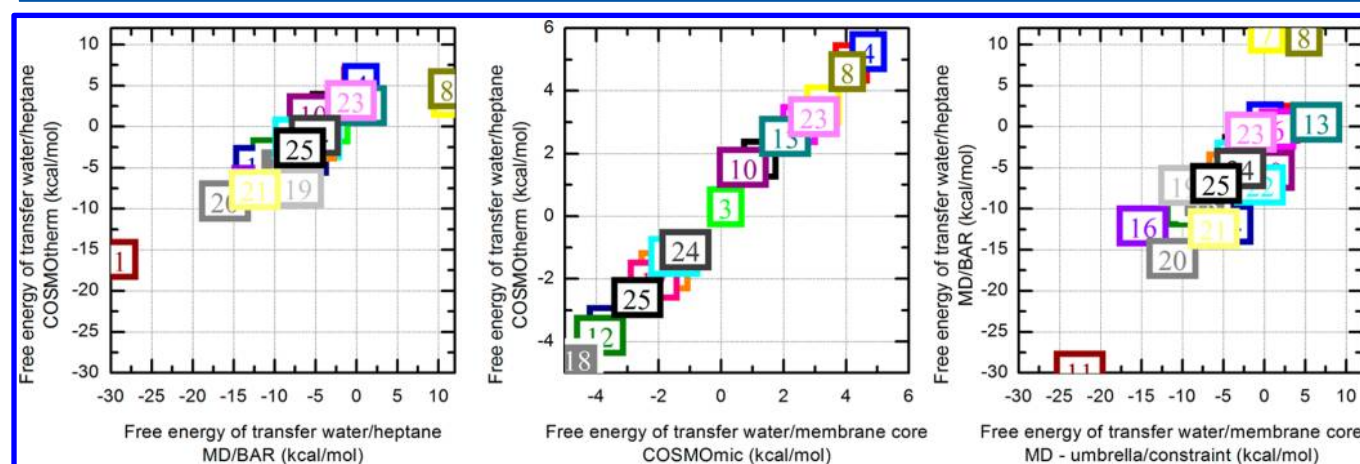


Figure 6. Correlation of the free energies of transfer from water to heptane $\Delta G^{\text{wat/heptane}}$ calculated by COSMOtherm and MD (left). Correlation of the free energies of transfer from water to heptane $\Delta G^{\text{wat/heptane}}$ and to the membrane core $\Delta G^{\text{wat/membrane}}$ for COSMOtherm/COSMOmic (middle) and MD calculated with the Bennett acceptance ratio method (MD-BAR)/MD-umbrella/constraint (right).

around 1.0 nm according to COSMOmic (note again that ΔG^{pen} predicted by COSMOmic was very small), (ii) those localized below the head groups or in lower parts of the head groups according to both methods, and (iii) those localized in the lower parts of the head groups according to MD and at the outer part of head groups according to COSMOmic. It should be noted that the local partition coefficient, $K(z)$, discussed in the previous paragraph reflects both the overall free-energy profile shape (as each $K(z)$ profile was normalized) and also the average of all profiles. Therefore, the local partition coefficient outside of the membrane calculated by COSMOmic was very low even though there were some shallow free-energy minima in this region. The reliability of MD for predicting drug positioning in membranes has been shown in recent studies, where the positions of coumarin derivatives in a DMPC lipid bilayer predicted by MD with the Berger lipid FF³⁰ agreed well with positions determined by NMR.⁵³ The positions of fluorescent probes calculated by MD also agreed well with experimental observations.^{54,55} The molecular positions

suggested by MD seem to more sensitively reflect the local organization and density of the membrane regions than COSMOmic.

We analyzed the free-energy values at different membrane depths and observed an increasing correlation with decreasing distance to the membrane center (Figure 3). The slope, k , of the linear fit, $\Delta G_{\text{COSMOmic}} = k \cdot \Delta G_{\text{MD}}$, reached 0.7 in the membrane core and decreased toward the water phase. On the membrane surface (at 2.8 nm), the slope decreased to $k = 0.3$. The uncertainty (calculated as the percentage of the slope error with respect to the slope value) of the slope rapidly increased from 20% inside of the membrane to 100% in bulk water. The strongest correlation ($r^2 > 0.8$) of the free-energy values was found in the middle of the membrane and decreased toward the outer parts of the membrane. However, it was still statistically significant even at $\alpha = 0.001$. In other words, the free-energy profiles obtained by COSMOmic were shallower than those obtained by MD. However, both profiles could be derived from

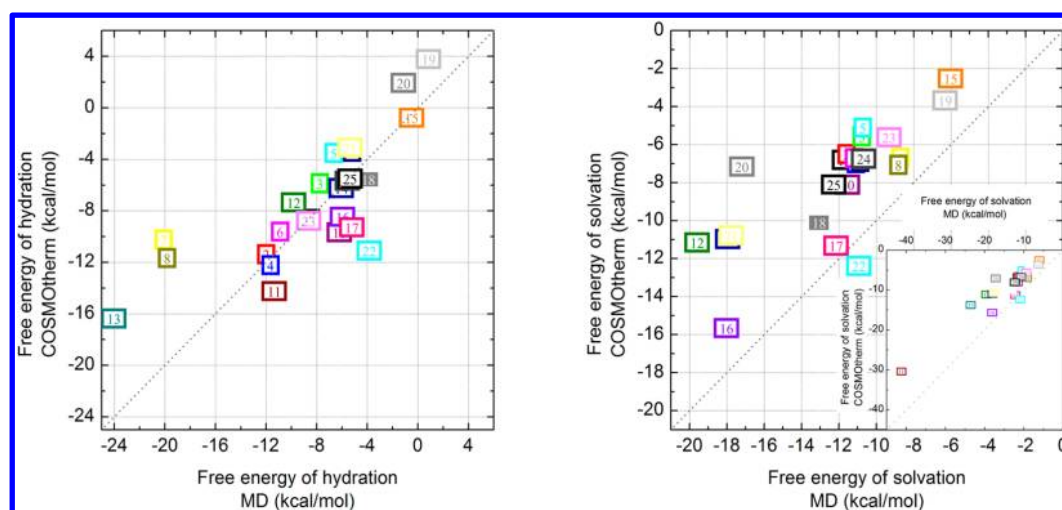


Figure 7. Free energies of solvation in water ΔG^{hyd} (left) and heptane ΔG^{solv} (right) calculated by COSMOtherm and MD. The hydration free energies (left) calculated by COSMOtherm and MD were in closer agreement than the corresponding solvation energies in heptane. The free energies of solvation in heptane were more negative by MD than COSMOtherm in all but one case.

each other with good precision because of the significant linearity.

The heterogeneity of membrane environments complicates direct comparison of free-energy profile properties, especially heights of free-energy barriers, to experimental results. However, such a comparison is straightforward for a binary system where the free energy of transfer between phases can be directly compared to the partition coefficient between the phases, as COSMOtherm has been shown to agree well with experimental partition coefficients.³⁶ The transfer free energies between water and heptane ($\Delta G^{\text{wat/heptane}}$) correlated well between the two methods (eq 8, Figure 6)

$$\Delta G_{\text{COSMOtherm}}^{\text{wat/heptane}} = 0.57(0.06)\Delta G_{\text{MD}}^{\text{wat/heptane}} + 1.42(0.54)$$

$$r^2 = 0.81 \quad (8)$$

These data again show that MD with the Berger lipid FF leads to more lipophilic results, in agreement with the data acquired for MD of a DOPC membrane.

We might expect that the transfer free energies from water to heptane would tightly correlate with the transfer free energies between water and the membrane center.^{51,56} Given this assumption, we compared the transfer free energies from both methods. The fit of COSMOtherm $\Delta G^{\text{wat/heptane}}$ to the COSMOMIC transfer free energies to the membrane core $\Delta G^{\text{wat/membrane}}$ (which literally corresponds to $\Delta G(0)$; see Figure 2) was almost perfect, explaining 99.7% of the data variability (eq 9)

$$\Delta G_{\text{COSMOtherm}}^{\text{wat/heptane}} = 1.04(0.01)\Delta G_{\text{COSMOMIC}}^{\text{wat/membrane}} + 0.34(0.06)$$

$$r^2 = 0.997 \quad (9)$$

$$\Delta G_{\text{MD}}^{\text{wat/heptane}} = 1.12(0.14)\Delta G_{\text{MD}}^{\text{wat/membrane}} - 1.09(1.02)$$

$$r^2 = 0.73 \quad (10)$$

On the other hand, the fit of the MD data explained only 73% of the data variability (eq 10). Possible reasons for this are that the MD data may suffer from insufficient robust sampling and convergence issues^{18,30} or by solute-induced membrane perturbation. Another explanation is that larger molecules may be more affected by the complex membrane structure⁵² because they may reach from the nonpolar membrane core up

to the head groups (or up to the water). As, in principle, this would also affect the comparison of $\Delta G^{\text{wat/heptane(membrane)}}$ calculated by COSMOtherm and COSMOMIC, for which we observed a tight correlation, we may conclude that this effect plays a negligible role.

To obtain a deeper understanding of the physical reasons for the higher lipophilicity of MD simulations, we analyzed the solvation free energies of drugs in water (ΔG^{hyd}) and heptane (ΔG^{solv}) and compared the mean errors in the COSMOtherm and MD values (Table S3 (Supporting Information) and Figure 7). Comparison of the hydration free energies ΔG^{hyd} calculated by COSMOtherm to those calculated by MD revealed a mean difference of -0.86 kcal/mol (mean absolute difference of 2.74 kcal/mol), whereas for ΔG^{solv} , the mean difference was -4.64 kcal/mol (mean absolute difference of 4.76 kcal/mol). These results indicate that ΔG^{hyd} was comparable for the two methods, but ΔG^{solv} was systematically predicted to be 30% lower by MD, that is, more lipophilic, than that by COSMOtherm (Figure 7) as the linear fit to the data (eq 11) was

$$\Delta G_{\text{COSMOtherm}}^{\text{solv}} = 0.71(0.06)\Delta G_{\text{MD}}^{\text{solv}} + 0.66(0.93)$$

$$r^2 = 0.85 \quad (11)$$

where the intercept is statistically insignificant from 0 (at $\alpha = 0.05$).

We modeled partitioning between water and heptane phases to rationalize the differences observed for water–membrane partitioning estimated from MD and COSMOtherm. Such a simplified model enabled comparison of the transfer free energies between water and heptane phases and enumeration of solvation free energies in each phase. This provided a deeper physical–chemical insight into the interaction of solutes with both phases. ΔG^{hyd} calculated by COSMOtherm and MD were biased by lower errors than ΔG^{solv} , which was about 30% more lipophilic according to the MD simulations. In the united atom Berger lipid FF, no charges are present on lipid tails (the same applies for the heptane model used). Therefore, all interactions between the lipid tails or heptane and a drug molecule must originate from the Lennard-Jones term. Taking COSMOtherm data as reference values (as they have been shown to fit the experimental data well³⁶ and partitioning into a homogeneous

phase usually matches experiment), we concluded that combination of the Berger lipid FF with the GROMOS 53a6 FF⁵⁷ (where Lennard-Jones parameters are used to describe interactions of nonlipid atoms of drug-like molecules) leads to overestimation of the attractive term of the Lennard-Jones potential, which in turn overestimates partitioning into lipids. This finding may also help further adjustment of the Berger-like FF.

CONCLUSION

We calculated the free-energy profiles of 25 drug-like amphiphilic molecules in a DOPC lipid bilayer using both MD with the Berger lipid FF and COSMOmic. Solvation free energies of these molecules were also calculated in water and heptane. The calculated free-energy profiles and derived thermodynamic parameters were in good agreement between the two methods. All molecules used in this study were found to accumulate in the membrane, and most localized below the lipid head groups. Detailed analysis of the free-energy profiles in DOPC showed that the MD simulations more sensitively reflected the structural properties of the lipid bilayer. Thus, MD simulations are proposed to be a reliable tool for estimating the membrane localization of drug-like molecules or for analyzing structural features of more complex systems containing, for example, lipids, drugs (antioxidants or other ligands), and proteins. We also showed that the global thermodynamic parameters of drugs on PC membranes (especially ΔG^{wat} and $\log K$) can be calculated by COSMOmic, which offers an inexpensive alternative to computationally demanding MD. By testing a less expensive model of a membrane core (the heptane phase), we identified the origin of the apparent increased lipophilicity of molecules studied by MD with the Berger lipid FF. As the united-atom Berger lipid FF has uncharged lipid tails, the overestimated lipophilicity was attributed to over-attractive Lennard-Jones interactions. Our results show that further studies of lipid FFs and their interactions with other molecules are needed as MD simulations remain the method of choice for dynamic studies of complex systems, such as protein–membrane interactions.

ASSOCIATED CONTENT

Supporting Information

Details of the simulation protocol. Table S1: Simulation protocols for all molecules examined in this study. Table S2: Free-energy profile parameters on DOPC calculated by MD and COSMOmic. Table S3: Free energies of hydration and solvation. Figure S1: Free-energy profiles of all molecules calculated in this study. Figure S2: Correlation plots of free-energy profile values. This material is available free of charge via the Internet at <http://pubs.acs.org>.

AUTHOR INFORMATION

Corresponding Authors

*E-mail: karel.berka@upol.cz. Tel: +420 585 634 756 (K.B.).

*E-mail: michal.otyepka@upol.cz. Tel: +420 585 634 756 (M.O.).

Notes

The authors declare no competing financial interest.

ACKNOWLEDGMENTS

This work was supported by the Operational Program Research and Development for Innovations - European Regional

Development Fund (CZ.1.05/2.1.00/03.0058) and European Social Fund (CZ.1.07/2.3.00/20.0017 and/20.0058). M.O. acknowledges support by the Czech Grant Agency through the P208/12/G016 project. K.B. acknowledges support by the Czech Grant Agency through the P303/12/P019 project. M.P. acknowledges support by the Student Project PrF_2013_028 (Palacký University, Olomouc). This research used resources of the Oak Ridge Leadership Computing Facility at the Oak Ridge National Laboratory, which is supported by the Office of Science of the U.S. Department of Energy under Contract No. DE-AC05-00OR22725. We thank Andreas Klamt for insightful comments concerning COSMOmic methodology.

REFERENCES

- (1) Peters, G. H.; Wang, C.; Cruys-Bagger, N.; Velardez, G. F.; Madsen, J. J.; Westh, P. Binding of Serotonin to Lipid Membranes. *J. Am. Chem. Soc.* **2013**, *135*, 2164–2171.
- (2) Podloucká, P.; Berka, K.; Fabre, G.; Palonciová, M.; Duroux, J.-L.; Otyepka, M.; Trouillas, P. Lipid Bilayer Membrane Affinity Rationalizes Inhibition of Lipid Peroxidation by a Natural Lignan Antioxidant. *J. Phys. Chem. B* **2013**, *117*, 5043–5049.
- (3) Berka, K.; Hendrychová, T.; Anzenbacher, P.; Otyepka, M. Membrane Position of Ibuprofen Agrees with Suggested Access Path Entrance to Cytochrome P450 2C9 Active Site. *J. Phys. Chem. A* **2011**, *115*, 11248–11255.
- (4) Orsi, M.; Essex, J. W. Passive Permeation Across Lipid Bilayers: A Literature Review. In *Molecular Simulations and Biomembranes*; Sansom, M. S. P., Biggin, P. C., Eds.; Royal Society of Chemistry: Cambridge, U.K., 2010; pp 76–90.
- (5) Orsi, M.; Essex, J. W. Permeability of Drugs and Hormones through a Lipid Bilayer: Insights from Dual-Resolution Molecular Dynamics. *Soft Matter* **2010**, *6*, 3797–3808.
- (6) Lúcio, M.; Lima, J. L. F. C.; Reis, S. Drug–Membrane Interactions: Significance for Medicinal Chemistry. *Curr. Med. Chem.* **2010**, *17*, 1795–1809.
- (7) Yamamoto, H.; Liljestrand, H. M. Partitioning of Selected Estrogenic Compounds Between Synthetic Membrane Vesicles and Water: Effects of Lipid Components. *Environ. Sci. Technol.* **2004**, *38*, 1139–1147.
- (8) Seddon, A. M.; Casey, D.; Law, R. V.; Gee, A.; Templer, R. H.; Ces, O. Drug Interactions with Lipid Membranes. *Chem. Soc. Rev.* **2009**, *38*, 2509–2519.
- (9) Seydel, J. K.; Wiese, M. In *Drug–Membrane Interactions: Analysis, Drug Distribution, Modeling*; Mannhold, R., Kubinyi, H., Folkers, G., Eds.; Wiley-VCH Verlag GmbH: Weinheim, Germany, 2002; Vol. 4.
- (10) Grassi, M.; Lapasin, R.; Grassi, G.; Colombo, I. *Understanding Drug Release and Absorption Mechanisms: A Physical and Mathematical Approach*; CRC Press: Boca Raton, FL, 2006.
- (11) Vaes, W. H.; Ramos, E. U.; Hamwijk, C.; Van Holsteijn, I.; Blaauboer, B. J.; Seinen, W.; Verhaar, H. J.; Hermens, J. L. Solid Phase Microextraction as a Tool to Determine Membrane/Water Partition Coefficients and Bioavailable Concentrations in In Vitro Systems. *Chem. Res. Toxicol.* **1997**, *10*, 1067–1072.
- (12) Endo, S.; Escher, B. I.; Goss, K.-U. Capacities of Membrane Lipids to Accumulate Neutral Organic Chemicals. *Environ. Sci. Technol.* **2011**, *45*, 5912–5921.
- (13) Janušová, B.; Skolová, B.; Tüköröová, K.; Wojnarová, L.; Simůnek, T.; Mladěnka, P.; Filipický, T.; Ríha, M.; Roh, J.; Palát, K.; et al. Amino Acid Derivatives as Transdermal Permeation Enhancers. *J. Controlled Release* **2013**, *165*, 91–100.
- (14) Ingram, T.; Storm, S.; Kloss, L.; Mehling, T.; Jakobtorweihen, S.; Smirnova, I. V. Prediction of Micelle/Water and Liposome/Water Partition Coefficients Based on Molecular Dynamics Simulations, COSMO-RS and COSMOmic. *Langmuir* **2013**, *29*, 3527–3537.
- (15) Vácha, R.; Martinez-Veracoechea, F. J.; Frenkel, D. Intracellular Release of Endocytosed Nanoparticles upon a Change of Ligand–Receptor Interaction. *ACS Nano* **2012**, *6*, 10598–10605.

- (16) Bemporad, D.; Luttmann, C.; Essex, J. W. Computer Simulation of Small Molecule Permeation Across a Lipid Bilayer: Dependence on Bilayer Properties and Solute Volume, Size, and Cross-Sectional Area. *Biophys. J.* **2004**, *87*, 1–13.
- (17) Marrink, S. J.; Berendsen, H. J. C. Permeation Process of Small Molecules Across Lipid Membranes Studied by Molecular Dynamics Simulations. *J. Phys. Chem.* **1996**, *100*, 16729–16738.
- (18) Neale, C.; Bennett, W. F. D.; Tieleman, D. P.; Pomès, R. Statistical Convergence of Equilibrium Properties in Simulations of Molecular Solutes Embedded in Lipid Bilayers. *J. Chem. Theory Comput.* **2011**, *7*, 4175–4188.
- (19) Orsi, M.; Sanderson, W. E.; Essex, J. W. Permeability of Small Molecules through a Lipid Bilayer: A Multiscale Simulation Study. *J. Phys. Chem. B* **2009**, *113*, 12019–12029.
- (20) Jämbeck, J. P. M.; Lyubartsev, A. P. Implicit Inclusion of Atomic Polarization in Modeling of Partitioning between Water and Lipid Bilayers. *Phys. Chem. Chem. Phys.* **2013**, *15*, 4677–4686.
- (21) Zhang, Y.; Voth, G. A. Combined Metadynamics and Umbrella Sampling Method for the Calculation of Ion Permeation Free Energy Profiles. *J. Chem. Theory Comput.* **2011**, *7*, 2277–2283.
- (22) Lange, O. F.; Schäfer, L. V.; Grubmüller, H. Flooding in GROMACS: Accelerated Barrier Crossings in Molecular Dynamics. *J. Comput. Chem.* **2006**, *27*, 1693–1702.
- (23) Mouritsen, O. G.; Jorgensen, K. A New Look at Lipid–Membrane Structure in Relation to Drug Research. *Pharm. Res.* **1998**, *15*, 1507–1519.
- (24) Nagle, J. F.; Tristram-Nagle, S. Structure of Lipid Bilayers. *Biochim. Biophys. Acta* **2000**, *1469*, 159–195.
- (25) Berka, K.; Paloncýová, M.; Anzenbacher, P.; Otyepka, M. Behavior of Human Cytochromes P450 on Lipid Membranes. *J. Phys. Chem. B* **2013**, *117*, 11556–11564.
- (26) Taylor, J.; Whiteford, N. E.; Bradley, G.; Watson, G. W. Validation of All-Atom Phosphatidylcholine Lipid Force Fields in the Tensionless NPT Ensemble. *Biochim. Biophys. Acta* **2009**, *1788*, 638–649.
- (27) Siu, S.; Vácha, R.; Jungwirth, P.; Böckmann, R. A. Biomolecular Simulation of Membranes: Physical Properties from Different Force Fields. *J. Chem. Phys.* **2008**, *128*, 125103.
- (28) Prakash, P.; Sankararamkrishnan, R. Force Field Dependence of Phospholipid Headgroup and Acyl Chain Properties: Comparative Molecular Dynamics Simulations of DMPC Bilayers. *J. Comput. Chem.* **2010**, *31*, 266–277.
- (29) Piggot, T. J.; Piñeiro, Á.; Khalid, S. Molecular Dynamics Simulations of Phosphatidylcholine Membranes: A Comparative Force Field Study. *J. Chem. Theory Comput.* **2012**, *8*, 4593–4609.
- (30) Paloncýová, M.; Berka, K.; Otyepka, M. Convergence of Free Energy Profile of Coumarin in Lipid Bilayer. *J. Chem. Theory Comput.* **2012**, *8*, 1200–1211.
- (31) Jämbeck, J. P. M.; Lyubartsev, A. P. Exploring the Free Energy Landscape of Solutes Embedded in Lipid Bilayers. *J. Phys. Chem. Lett.* **2013**, *4*, 1781–1787.
- (32) Tomasi, J.; Mennucci, B.; Cammi, R. Quantum Mechanical Continuum Solvation Models. *Chem. Rev.* **2005**, *105*, 2999–3093.
- (33) Tomasi, J. Selected Features of the Polarizable Continuum Model for the Representation of Solvation. *Wiley Interdiscip. Rev.: Comput. Mol. Sci.* **2011**, *1*, 855–867.
- (34) Klamt, A.; Huniar, U.; Spycher, S.; Keldenich, J. COSMOmic: A Mechanistic Approach to the Calculation of Membrane–Water Partition Coefficients and Internal Distributions within Membranes and Micelles. *J. Phys. Chem. B* **2008**, *112*, 12148–12157.
- (35) Jakobtorweihen, S.; Ingram, T.; Smirnova, I. Combination of COSMOmic and Molecular Dynamics Simulations for the Calculation of Membrane–Water Partition Coefficients. *J. Comput. Chem.* **2013**, *34*, 1332–1340.
- (36) Buggert, M.; Cadena, C.; Mokrushina, L.; Smirnova, I.; Maginn, E. J.; Arlt, W. COSMO-RS Calculations of Partition Coefficients: Different Tools for Conformation Search. *Chem. Eng. Technol.* **2009**, *32*, 977–986.
- (37) Domański, J.; Stansfeld, P. J.; Sansom, M. S. P.; Beckstein, O. Lipidbook: A Public Repository for Force-Field Parameters Used in Membrane Simulations. *J. Membr. Biol.* **2010**, *236*, 255–258.
- (38) Berger, O.; Edholm, O.; Jahnig, F. Molecular Dynamics Simulations of a Fluid Bilayer of Dipalmitoylphosphatidylcholine at Full Hydration, Constant Pressure and Constant Temperature. *Biophys. J.* **1997**, *72*, 2002–2013.
- (39) Schüttelkopf, A. W.; Van Aalten, D. M. F. PRODRG: A Tool for High-Throughput Crystallography of Protein–Ligand Complexes. *Acta Crystallogr., Sect. D* **2004**, *60*, 1355–1363.
- (40) Cieplak, P.; Caldwell, J.; Kollman, P. Molecular Mechanical Models for Organic and Biological Systems Going beyond the Atom Centered Two Body Additive Approximation: Aqueous Solution Free Energies of Methanol and *N*-Methyl Acetamide, Nucleic Acid Base, and Amide Hydrogen Bonding and Chloroform/Water Partition Coefficients of the Nucleic Acid Bases. *J. Comput. Chem.* **2001**, *22*, 1048–1057.
- (41) Lemkul, J. A.; Allen, W. J.; Bevan, D. R. Practical Considerations for Guiding GROMOSCompatible Small-Molecule Topologies. *J. Chem. Inf. Model.* **2010**, *50*, 2221–2235.
- (42) Frisch, M. J.; Trucks, G. W.; Schlegel, H. B.; Scuseria, G. E.; Robb, M. A.; Cheeseman, J. R.; Montgomery, J. A., Jr.; Vreven, T.; Kudin, K. N.; Burant, J. C. et al. *Gaussian 03*, revision E.01; Gaussian, Inc.: Wallingford, CT, 2004.
- (43) Case, D. A.; Darden, T. A.; Cheatham, T. E., III; Simmerling, C. L.; Wang, J.; Duke, R. E.; Luo, R.; Walker, R. C.; Zhang, W.; Merz, K. M.; et al. *AMBER 11*; University of California: San Francisco, CA, 2010.
- (44) Paloncýová, M.; Berka, K.; Otyepka, M. Molecular Insight into Affinities of Drugs and Their Metabolites to Lipid Bilayers. *J. Phys. Chem. B* **2013**, *117*, 2403–2410.
- (45) Košinová, P.; Berka, K.; Wykes, M.; Otyepka, M.; Trouillas, P. Positioning of Antioxidant Quercetin and its Metabolites in Lipid Bilayer Membranes: Implication for Their Lipid- Peroxidation Inhibition. *J. Phys. Chem. B* **2012**, *116*, 1309–1318.
- (46) Becke, A. D. Density-Functional Exchange-Energy Approximation with Correct Asymptotic Behavior. *Phys. Rev. A* **1988**, *38*, 3098–3100.
- (47) Perdew, J. P. Density-Functional Approximation for the Correlation Energy of the Inhomogeneous Electron Gas. *Phys. Rev. B* **1986**, *34*, 7406.
- (48) Klamt, A. *COSMO-RS: From Quantum Chemistry to Fluid Phase Thermodynamics and Drug Design*; Elsevier Science Ltd.: Amsterdam, The Netherlands, 2005.
- (49) Bennett, C. Efficient Estimation of Free Energy Differences from Monte-Carlo Data. *J. Comput. Phys.* **1976**, *22*, 245–268.
- (50) Berendsen, H. J. C.; Grigera, J. R.; Straatsma, T. P. The Missing Term in Effective Pair Potentials. *J. Phys. Chem.* **1987**, *91*, 6269–6271.
- (51) MacCallum, J. L.; Bennett, W. F. D.; Tieleman, D. P. Distribution of Amino Acids in a Lipid Bilayer from Computer Simulations. *Biophys. J.* **2008**, *94*, 3393–3404.
- (52) Tristram-Nagle, S.; Nagle, J. F. Lipid Bilayers: Thermodynamics, Structure, Fluctuations, and Interactions. *Chem. Phys. Lipids* **2004**, *127*, 3–14.
- (53) Afri, M.; Gottlieb, H. E.; Frimer, A. A. Superoxide Organic Chemistry within the Liposomal Bilayer, Part II: A Correlation between Location and Chemistry. *Free Radical Biol. Med.* **2002**, *32*, 605–618.
- (54) Vazdar, M.; Jurkiewicz, P.; Hof, M.; Jungwirth, P.; Cwiklik, L. Behavior of 4-Hydroxynonenal in Phospholipid Membranes. *J. Phys. Chem. B* **2012**, *116*, 6411–6415.
- (55) Nitschke, W. K.; Vequi-Suplicy, C. C.; Coutinho, K.; Stassen, H. Molecular Dynamics Investigations of PRODAN in a DLPC Bilayer. *J. Phys. Chem. B* **2012**, *116*, 2713–2721.
- (56) Marrink, S.-J.; Berendsen, H. J. C. Simulation of Water Transport through a Lipid Membrane. *J. Phys. Chem.* **1994**, *98*, 4155–4168.

(57) Oostenbrink, C.; Soares, T. A.; Van der Vegt, N. F. A.; Van Gunsteren, W. F. Validation of the 53A6 GROMOS Force Field. *Eur. Biophys. J.* **2005**, *34*, 273–284.

Benchmarking of Force Fields for Molecule–Membrane Interactions

Markéta Paloncýová,[†] Gabin Fabre,^{†,‡} Russell H. DeVane,^{||} Patrick Trouillas,^{†,§,⊥} Karel Berka,^{*,†} and Michal Otyepka^{*,†}

[†]Regional Centre of Advanced Technologies and Materials, Department of Physical Chemistry, Faculty of Science, Palacký University Olomouc, tř. 17 Listopadu 12, 771 46 Olomouc, Czech Republic

[‡]LCSN EA1069, Faculté de Pharmacie, Université de Limoges, 2 Rue de Docteur Marcland, 87025 Limoges Cedex, France

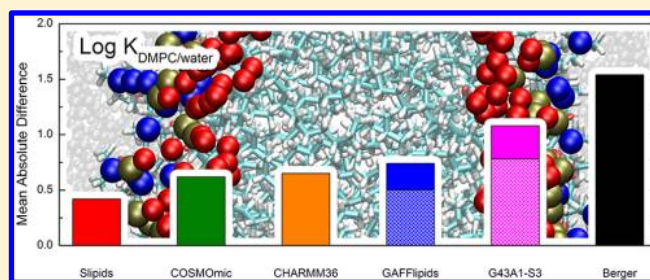
[§]INSERM UMR-S850, Faculté de Pharmacie, Université de Limoges, 2 Rue du Docteur Marcland, 87025 Limoges Cedex, France

^{||}Corporate Modeling and Simulation, Procter and Gamble, 8611 Beckett Road, West Chester, Ohio 45069, United States

[⊥]Laboratoire de Chimie des Matériaux Nouveaux, Université de Mons, Place du Parc 20, B-7000 Mons, Belgium

Supporting Information

ABSTRACT: Studies of drug–membrane interactions witness an ever-growing interest, as penetration, accumulation, and positioning of drugs play a crucial role in drug delivery and metabolism in human body. Molecular dynamics simulations complement nicely experimental measurements and provide us with new insight into drug–membrane interactions; however, the quality of the theoretical data dramatically depends on the quality of the force field used. We calculated the free energy profiles of 11 molecules through a model dimyristoylphosphatidylcholine (DMPC) membrane bilayer using five force fields, namely Berger, Slipids, CHARMM36, GAFFlipids, and GROMOS 43A1-S3. For the sake of comparison, we also employed the semicontinuous tool COSMOmic. High correlation was observed between theoretical and experimental partition coefficients ($\log K$). Partition coefficients calculated by all-atomic force fields (Slipids, CHARMM36, and GAFFlipids) and COSMOmic differed by less than 0.75 \log units from the experiment and Slipids emerged as the best performing force field. This work provides the following recommendations (i) for a global, systematic and high throughput thermodynamic evaluations (e.g., $\log K$) of drugs COSMOmic is a tool of choice due to low computational costs; (ii) for studies of the hydrophilic molecules CHARMM36 should be considered; and (iii) for studies of more complex systems, taking into account all pros and cons, Slipids is the force field of choice.



INTRODUCTION

In nature, biomembranes make selectively permeable walls separating inner and outer cell environments, or inner organelles and cytosol.¹ They play a key role in the control of active transport and passive permeation of endogenous or exogenous compounds.^{2–4} Hence, the molecular interaction of xenobiotics (e.g., drugs and pollutants) with biomembranes is of major importance for understanding their flux through tissue and targeting in the human body.^{5–7} Biomembranes are complex supramolecular systems, which mostly consist of lipids arranged as bilayers. They also contain proteins attached or embedded in the membrane bilayer.⁸ The xenobiotics may interact with all these constituents during their passage through the membrane. Interactions of xenobiotics with the membrane-anchored cytochrome P450 represents a typical example of the complexity of membrane trafficking.^{9–11}

Basic features of the interaction of xenobiotics with biomembranes are known from experimental observations.¹² However, the understanding is fragmented and the molecular picture is often missing. Molecular dynamics (MD) simulations have appeared as an alternative way to gain insight into

structural features¹³ and thermodynamics of interaction of guest molecules with biomembranes.^{14–22} MD follows motions of all atoms of molecular system and generates a wealth of information having extremely fine resolutions both in time (subpicosecond) and space (atomic). This provides MD a major advantage with respect to all other techniques to tackle the interaction of xenobiotics with biomembranes, which nicely complements observations from the experimental techniques. On the other hand, the quality of MD simulations is heavily limited by the underlying empirical potential, also termed force field (FF), and affordable sampling, that is, duration of MD simulation.^{16,23,24} In other words, inaccurate FF parameters may lead to biased structural or thermodynamic membrane parameters, hence, developed FFs are tested to determine the level of agreement with experimental observations.

To date, numerous FFs have been developed for biomembranes, mostly focusing on structural and dynamical features of lipid bilayers. They were based on coarse-grained

Received: May 14, 2014

(e.g., MARTINI,²⁵ SDK²⁶), united-atom (e.g., Berger²⁷ and GROMOS 43A1-S3²⁸), and all-atom models (e.g., Slipids,^{29–31} CHARMM36,^{32,33} GAFFlipids,³⁴ LIPID11,³⁵ LIPID14³⁶). However, the accurate description of not only membrane structural parameters but also molecular interactions between guest molecules and biomembranes requires highly advanced FFs. For even more complicated goals such as membrane protein studies, they should also achieve a properly balanced description of structural and dynamical features of proteins. To this end, advanced FFs compatible with advanced protein FFs would be a promising tool to describe the behavior of guest molecules within realistic complex biomembranes.

To simulate thermodynamics of the interaction between a guest molecule and membrane with MD is computationally demanding as they require robust sampling and in turn accumulation of long simulation times.^{16,20} The huge computer cost of MD simulations has motivated many researchers to develop less expensive approaches to estimate thermodynamic properties of molecule–membrane interaction. An example of such approaches is the COSMOmic³⁷ tool of the COSMO-therm program,³⁸ which is based on the conductor-like screening model for realistic solvation (COSMO-RS) theory.³⁹ It was repeatedly shown that COSMOmic provides thermodynamics of molecule–membrane interactions in good agreement with experimental data.^{40,41} On the other hand, this implicit approach loses the fine time insight into the interaction, which is provided by MD simulations.

This study aims at a critical analysis of molecule–membrane interaction, as evaluated by free energy profiles, which were derived from *z*-constraint MD simulations. In the test set, 11 organic compounds were included, having a broad range of affinities for dimyristoylphosphatidylcholine (DMPC) bilayers and also bearing common organic functional groups. Five advanced FFs dedicated to biomembrane simulations have been evaluated, including Berger, Slipids, CHARMM36, GROMOS 43A1-S3, and GAFFlipids; for the sake of comparison, COSMOmic has been also employed. Based on free energies, the partition coefficients were calculated for each molecule and each FF and were compared to the available experimental data in order to investigate the performance of individual FFs for drug–membrane interactions.

METHODS

Small Molecule Parametrization. A set of 11 molecules was selected for which experimental partition coefficients to DMPC membrane were available (Table 1).⁴⁰ The molecules were chosen to cover a wide range of partition coefficients (from -1.04 to 5.64 measured at temperatures from 20 to 40 °C) and to include common functional groups present in drugs such as hydroxyl, carbonyl, chloro, methyl, nitro, and amino groups on aliphatic chains or aromatic benzene rings. The MD parameters of these molecules were prepared for individual FF, as recommended by their developers. Bonding and van der Waals parameters were taken from (i) GAFF⁴² for Slipids and GAFFlipids, (ii) PRODRG⁴³ for Berger and GROMOS 43A1-S3, and (iii) ParamChem^{44,45} for CHARMM36. For CHARMM36, partial charges were also taken from ParamChem. Special attention was paid to the description of partial charges for Slipids, GAFFlipids, Berger, and GROMOS 43A1-S3 FFs. For these FFs, the partial charges were derived using the restrained fit of electrostatic potential (RESP) procedure and the R.E.D. III software⁴⁶ using multiple conformations and multiple reorientations to ensure reproduc-

Table 1. Molecules Used in This Study^a

no.	compd.	log K_{exp}	method	ref
1	glycerol	-1.04	Ultracentrifugation	52
2	methanol	-0.53	Ultracentrifugation	52
3	acetone	0.06	Ultracentrifugation (0.02 , 0.10)	52
4	1-butanol	0.51	Ultracentrifugation (0.54)	52
			Nondepletion PA-SPME (0.45)	53
5	benzylalcohol	1.14	Ultracentrifugation	52
6	aniline	1.63	Nondepletion PA-SPME	53
7	2-nitrotoluene	2.41	Nondepletion PA-SPME	53
8	<i>p</i> -xylene	2.98	Nondepletion PA-SPME	53
9	4-chloro-3-methylphenol	3.34	Nondepletion PA-SPME	53
10	2,4,5-trichloroaniline	4.16	Nondepletion PA-SPME	53
11	hexachlorobenzene	5.64	<i>n</i> -hexane passive dosing (5.43)	54
			PDMS sheet dosing (5.90)	40
			SPCE-PDMS passive sampling (5.59)	55

^aThe experimental partition coefficients (log K_{exp}) between water and DMPC are given from extensive data set.⁴⁰ They are given as an average of experimental values in case of multiple source of individual partition coefficients (shown in brackets in the Method column).

cibility of charge derivation, as ESP charges are sensitive to orientation.^{46,47} Conformations were generated from 1 ns MD simulation in vacuum followed by clustering using the single linkage method. Only clusters representing more than 10% of the total number of conformations were taken into account. Then, energy minimization and electrostatic potential (ESP) charges were calculated for each conformation with Gaussian09 (rev. A02)⁴⁸ either according to the Duan model⁴⁹ (B3LYP/cc-pVTZ and PCM solvation in diethyl ether) for Slipids, Berger, and GROMOS 43A1-S3 or according to the Cornell model⁵⁰ (HF/6-31G* in vacuum) for GAFFlipids.

MD Simulation Parameters. Fully hydrated membrane patches–bilayers were prepared with 36 DMPC lipids in each monolayer surrounded by 0.15 M NaCl solution to mimic the physiological conditions (Figure 1). The bilayers were then equilibrated and the simulation setup was tested against the experimental structural membrane properties.⁵⁶ The simulation setup was then used for the *z*-constraint simulation (see all specific simulation parameters for all FFs in Table 2). The bilayer normal was oriented parallel to the *z*-axis and the origin of the axis was set in the middle of the bilayer. All MD simulations were performed by the GROMACS 4.5.1 software package with a 2 fs time step and periodic boundary conditions in all directions. Electrostatic interactions were treated by the particle-Mesh Ewald method⁵⁷ and bonds were constrained by the LINCS algorithm.⁵⁸ A Parrinello–Rahman barostat⁵⁹ was used for a semi-isotropic pressure coupling at 1 bar and compressibility of 4.5×10^{-5} bar⁻¹ and Nosé–Hoover thermostat^{60,61} at 310 K.

Z-Constraint Simulation. Two drug molecules were initially placed in the simulation box: one in the middle of the membrane and another on the top of the simulation box, that is, into the water phase. The system was left for 500 ps to equilibrate and then both molecules were pulled in the same direction along the *z*-axis with a pulling rate of 0.05 nm·ns⁻¹ and a harmonic force constant of 500 kJ·mol⁻¹·nm⁻². The initial structures for *z*-constraint simulations were separated from this pulling simulation. In each simulation box two drug

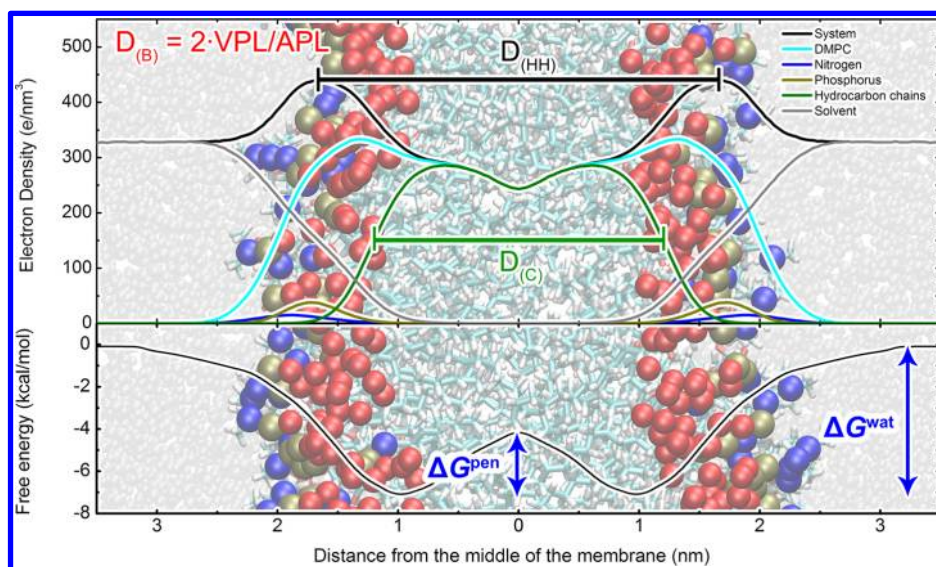


Figure 1. Structure of a dimyristoylphosphatidylcholine (DMPC) bilayer (background) with highlighted glycerol oxygens (red balls), choline nitrogens (blue) and phosphorus (dark yellow). The electron density profile (upper panel) contains labels for membrane thicknesses, that is, headgroup to headgroup distance ($D_{(HH)}$), hydrocarbon core thickness ($D_{(C)}$), and Luzzati thickness ($D_{(B)}$) calculated as a ratio of volume per lipid (VPL) and area per lipid (APL). The free energy profile (lower panel) has highlighted water/lipids barrier ΔG^{wat} , representing the affinity to the membrane, and penetration barrier ΔG^{pen} .

Table 2. Simulation Parameters^a

force field	R_{coulomb} (nm)	R_{vdw} (nm)	$R_{\text{vdw-switch}}$ (nm)	bond constraints	water model	RESP method/basis set	CPUh/project
Berger	1.0	1.0		all-bonds	SPC/E ^{62,63}	B3LYP/cc-pVTZ	21 200
GROMOS 43A1-S3	1.0	1.6		all-bonds	SPC/E ^{62,63}	B3LYP/cc-pVTZ	34 400
CHARMM36	1.4 (1.2)	1.4 (1.2)	0.8	H-bonds	CHARMM TIP3P ⁶⁴		145 200
Slipids	1.0 (1.0)	1.5 (0.9)	1.4 (0.8)	all-bonds	TIP3P ⁶⁵	B3LYP/cc-pVTZ	71 300
GAFFlipids	0.8	0.8		H-bonds	TIP3P ⁶⁵	HF/6-31G*	44 900
COSMOmic							3

^a R_{coulomb} is a short-range electrostatic cut-off, long-range electrostatics are evaluated by PME, R_{vdw} is Lennard-Jones cut-off, in case of switching off the Lennard-Jones interactions, the switching begins at $R_{\text{vdw-switch}}$. In case of CHARMM36 and Slipids, we tested the structural parameters also using different cut-off lengths (in brackets, not affecting the total CPU time in this table). CPUh/project display the total CPU hours for the calculations—for obtaining the topologies and 30 ns z-constraint simulations for MD simulations and for DFT calculations and final free energy profile calculation in case of COSMOmic. The detailed CPU times are in Supporting Information Table S2.

Table 3. Mean Differences (MDi) and Mean Absolute Differences (MAD) of Water/Lipids ΔG^{wat} and Penetration ΔG^{pen} Barriers with Respect to Data Obtained from Slipids FF^a

force field	ΔG^{wat}		ΔG^{pen}	
	MDi (kcal/mol)	MAD (kcal/mol)	MDi (kcal/mol)	MAD (kcal/mol)
Berger	1.94	2.09	0.14	1.06
CHARMM36	-0.27	0.72	-0.15	0.89
GAFFlipids	0.02 (0.14)	0.72 (0.68)	1.04 (0.33)	1.33 (0.65)
GROMOS 43A1-S3	-0.34 (-1.07)	1.65 (1.12)	-0.35 (-0.29)	1.28 (1.31)
COSMOmic	0.12	0.91	-0.73	0.91

^aThe values in brackets show the differences with excluded outlier (2-nitrotoluene in GROMOS 43A1-S3 and acetone in GAFFlipids).

molecules were placed, one in each monolayer. The windows for z-constraint simulations were chosen with separating distance of 0.3 nm, whenever possible.

Z-constraint simulations constrain a distance between different groups and monitors the required force applied on the molecule to keep this distance. The averaged force is then used to calculate the free energy profile also called potential of mean force (eq 1):

$$\Delta G(z) = - \int_{\text{outside}}^{z'} \langle \vec{F}(z) \rangle_t dz \quad (1)$$

where $\langle F(z) \rangle_t$ is the force applied on the molecule in order to keep it at a given depth z . We constrained the two molecules in a box and monitored the applied force separately. Over the last years, we have systematically optimized the simulation protocol for free energy profile calculation in order to minimize the computer time cost.¹⁷ Several authors have identified that the selection of an initial structure can slow the convergence of free energy profiles, especially in area of head groups.^{16,20,66} The z-constraint simulation converges quicker compared to umbrella simulation, even when the initial structure is unequilibrated.¹⁶ As it was also successfully used earlier,⁶⁶ the

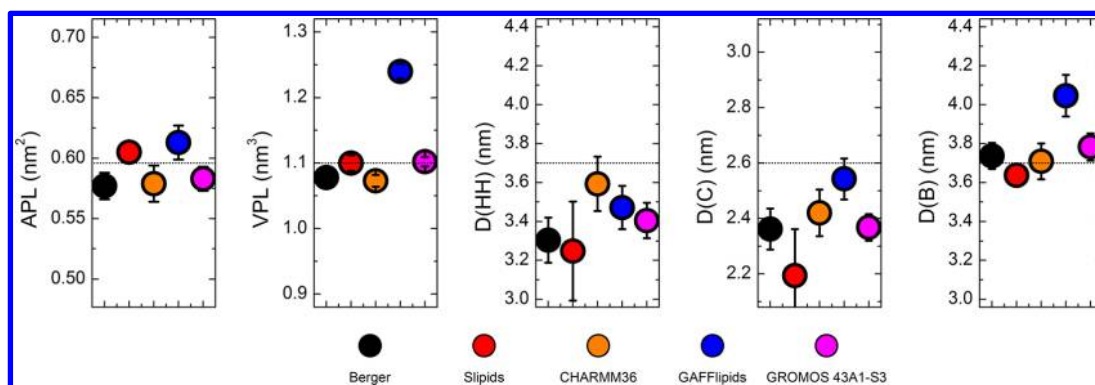


Figure 2. Structural parameters of DMPC bilayer as predicted by MD simulations with various FFs compared to experimental values at 30 °C shown as dotted lines.⁵⁶ APL, area per lipid; VPL, volume per lipid; $D(\text{HH})$, electron–electron density peak distance; $D(\text{C})$, hydrocarbon core thickness; $D(\text{B})$, Luzzati thickness. The error bars show the standard deviation of data obtained from multiple simulations, all the graphs are scaled to show 20% of deviation from experimental values.

amount of simulation windows was halved by adding two solute molecules in one simulation box. Free energy profile by z -constraint simulation allows a window of 0.3 nm. This significantly reduces the computing-time cost. It should be noted that cutoff lengths and water models dramatically influence computational time (Table 3). The z -constraint simulations were run for 30 ns per simulation window and the convergence of free energy profiles was monitored. The initial 15 ns of constraint simulation were left for equilibration and the free energy profiles were calculated from the last 15 ns. In the case of too slow convergence, the window lengths were extended to 50 ns (see the Supporting Information Table S1).

COSMOmic Free Energy Profile Calculation. To increase the precision of COSMOmic calculations, 30 DMPC bilayer structures obtained from Slipids simulation were used; this approach was successfully applied in earlier works.^{17,41} The geometries and σ -profiles of DMPC, water, and guest molecules were obtained by DFT/COSMO calculations at the BP/TZVP level of theory.^{67,68} A single conformation as a result of geometry optimization was used. Free energy profiles were calculated at 310 K. Using the COSMOmic software³⁷ from the COSMOtherm 13 package, the bilayers were separated into 50 layers.⁶⁹ A total of 162 orientations of the solute molecules were used for each membrane to produce individual free energy profiles. The final free energy profile was averaged over the individual free energy profiles of all the DMPC bilayer structures.

Log K Calculation. The free energy profiles obtained with MD (all FFs) and COSMOmic were analyzed and the partition coefficients were calculated according to an implemented method of COSMOmic^{37,41} that removes the need for setting a membrane border and which is independent of the system size (eq 2):

$$K = \int_0^n \left(e^{-\Delta G(z)/RT} - \frac{\rho_{(z)}^{\text{water}}}{\rho_{(n)}^{\text{water}}} \right) dz \frac{\text{APL}}{M_{\text{lipids}} m_u} \quad (2)$$

where $\Delta G(z)$ stands for a free energy at depth z , $\rho_{(z)}^{\text{water}}$ stands for water density at depth z , and $\rho_{(n)}^{\text{water}}$ stands for density of bulk water. The multiplying factor converts the partition coefficient into units used in experimental works $\text{kg}_{(\text{lipid})}/\text{L}_{(\text{water})}$. APL is the area per lipid, M_{lipids} is the molecular weight of lipids and m_u is the atomic mass constant.

Statistical Evaluation. Predicted $\log K_{\text{calc}}$ were compared to the $\log K_{\text{exp}}$ experimental values in terms of mean difference

(MDi) $(1/N \sum_i^N (\log K_{\text{calc},i} - \log K_{\text{exp},i}))$ and mean absolute difference (MAD) $(1/N \sum_i^N |\log K_{\text{calc},i} - \log K_{\text{exp},i}|)$, and in terms of the parameters of the linear $\log K_{\text{exp}}$ vs $\log K_{\text{calc}}$ fit (eq 3):

$$\log K_{\text{exp}} = a \cdot \log K_{\text{calc}} + b \quad (3)$$

which was constructed by the least-squares method. The significance of the slope differing from 1 and intercept differing from 0 were evaluated at the probability level of 0.975. We analyzed the outliers of $\log K$ predictions based on a Williams plot⁷⁰ and identified acetone in GAFFlipids, 2-nitrotoluene in GROMOS 43A1-S3, and 2-nitrotoluene and hexachlorobenzene in Berger. Due to the limited number of molecules investigated, we included the outliers in our analysis. However, for analysis in a given FF, the outliers were excluded. We also analyzed the predictability of proper ordering of molecules according to their lipophilicity based on Spearman's rank correlation coefficient. Further we analyzed the heights of free energy barriers—the water/lipids barrier ΔG^{wat} , the membrane center penetration barrier ΔG^{pen} and the free energy at various membrane depths—and compared them to the values from Slipids that provided $\log K_{\text{calc}}$ in the best agreement with experimental data.

RESULTS AND DISCUSSION

Structure of DMPC Bilayer Is Well Represented by All

FFs. During both unbiased and z -constraint simulations, most of the membrane structural parameters stayed reasonably close to experimental values,⁵⁶ though most of the FFs produced a bilayer with thickness lower than that measured experimentally (Figure 2). The values of area per lipid (APL) were reproduced reasonably well by all FFs considered here. The volume per lipid (VPL) predicted by GAFFlipids significantly differed from the other FFs. On the other hand, GAFFlipids showed headgroup distance ($D(\text{HH})$) and hydrocarbon thickness ($D(\text{C})$) in agreement with the experimental data. The Luzzati thickness ($D(\text{B})$), which depends on a ratio of VPL and APL (see Figure 1 for thickness explanation),⁵⁶ was again well reproduced by all other FFs but GAFFlipids (Figure 2). In summary, all FFs tested in this study accurately reproduce the structural features of the DMPC bilayer reasonably well.

Additional relevant structural characteristics of fluid membranes are the order parameters of lipid tails.⁷¹ The average order parameters were monitored (i.e., both sn1 and sn2 chains

were averaged, Figure 3) during both unbiased and z-constraint simulations. Slipids, Berger, and GROMOS 43A1-S3 FFs

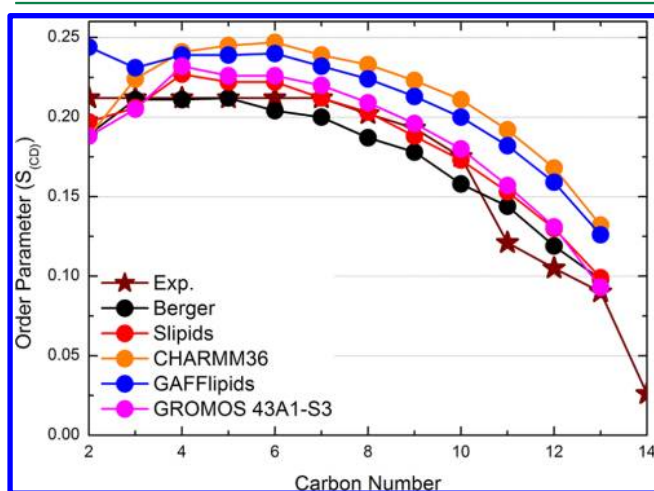


Figure 3. Order parameters experimentally measured (stars) and calculated by MD simulations with five FFs.

reproduced the order parameters as best (MAD equal to 0.012, 0.013, and 0.015, respectively). On the other hand, the order parameters calculated by GAFFlipids and CHARMM36 were slightly overestimated (MAD 0.031 and 0.035). These findings agree with a recent work by Piggot et al.,¹³ comparing structural parameters of DPPC and POPC; the calculated order parameters of lipid tails in the plateau region below the head groups were the lowest with Berger, followed by GROMOS 43A1-S3 and CHARMM36. It should be noted that in the original publication of GAFFlipids³⁴ the order parameters were also slightly overestimated. However, DMPC membranes were in fluid phase with all FFs, for the full simulation time.

The structural features of the DMPC membrane are sensitive to the simulation setup, especially cut-offs and water models. So, we used the setup suggested by the developers of each FF and when necessary we optimized the setup to acquire structural parameters best agreeing with the experimental data (see Table 2). As expected, from the point of view of computational time, the united atom FFs (i.e., Berger and GROMOS 43A1-S3) were the most efficient (Table 1 and Supporting Information Table S2). There were also differences among the all-atom FFs, the most effective being GAFFlipids due to a very short cutoff (0.8 nm). Slipids take advantage of uncharged carbons and hydrogens in the middle of aliphatic tails, while CHARMM36 was the slowest among all tested FFs, because of the long cutoff used, and the CHARMM modified TIP3P water model. In order to use parameters compatible with AMBER ff99SB FF for proteins, we also carried out Slipids simulations with 1.0 nm cutoff and tested CHARMM36 simulations with a 1.2 nm cutoff. In this case, the DMPC bilayer structural parameters stayed reasonably close to the experimental values (data not shown). Decreasing the cutoff is an attractive way to increase performance for future simulations on larger membrane systems.

Calculated Partition Coefficients Agreed with the Experimental Values. Membrane/water partition coefficients were calculated by eq 2 and compared with the experimental values (Table 1 and Supporting Information Table S2). The relative ranking of the molecules according to their partition coefficients, which was evaluated by the Spearman's rank order correlation coefficient, was reproduced best by Slipids and CHARMM36 (Supporting Information Table S2). The differences in ranking appeared for the medium lipophilic molecules for both CHARMM36 and Slipids, while both FFs ranked all lipophilic molecules properly. CHARMM36 ranked adequately even the most hydrophilic molecules ($\log K < 0.5$) while Slipids ranked well all molecules with $\log K$ higher than 1.7. The COSMOmic approach also ranked properly the lipophilic

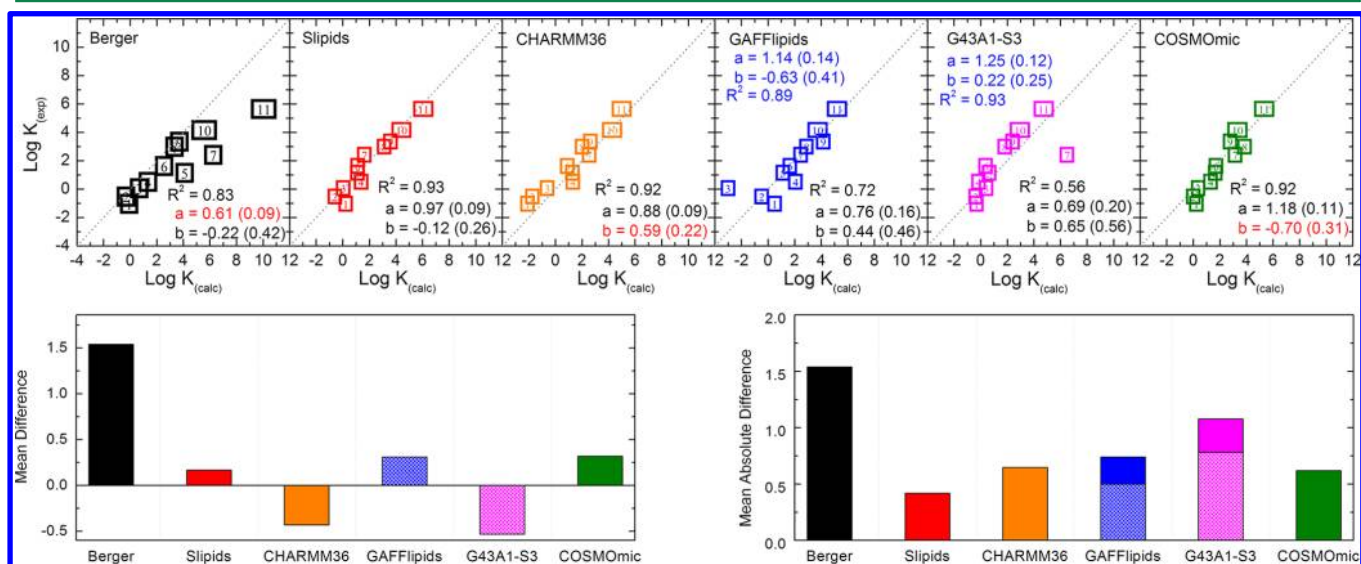


Figure 4. Experimental partition coefficients plotted against the respective calculated values (upper panel) with parameters of the linear fit, that is, coefficient of determination, R^2 , slope (a) (standard deviation in bracket) and intercept (b). Slopes significantly differing from 1.0 and intercepts from 0.0 significantly on the probability level of 0.975 are highlighted in red. Each data point is labeled by a number, which corresponds to the number of the molecule in Table 1. The fitting parameters for GROMOS 43A1-S3 (G43A1-S3) and GAFFlipids recalculated by omitting outliers (acetone and 2-nitrotoluene, in GAFFlipids and GROMOS 43A1-S3, respectively) are shown in blue. The bar charts (lower panel) depict the mean differences and the mean absolute differences (MAD). The patterned bars show values when excluding outliers.

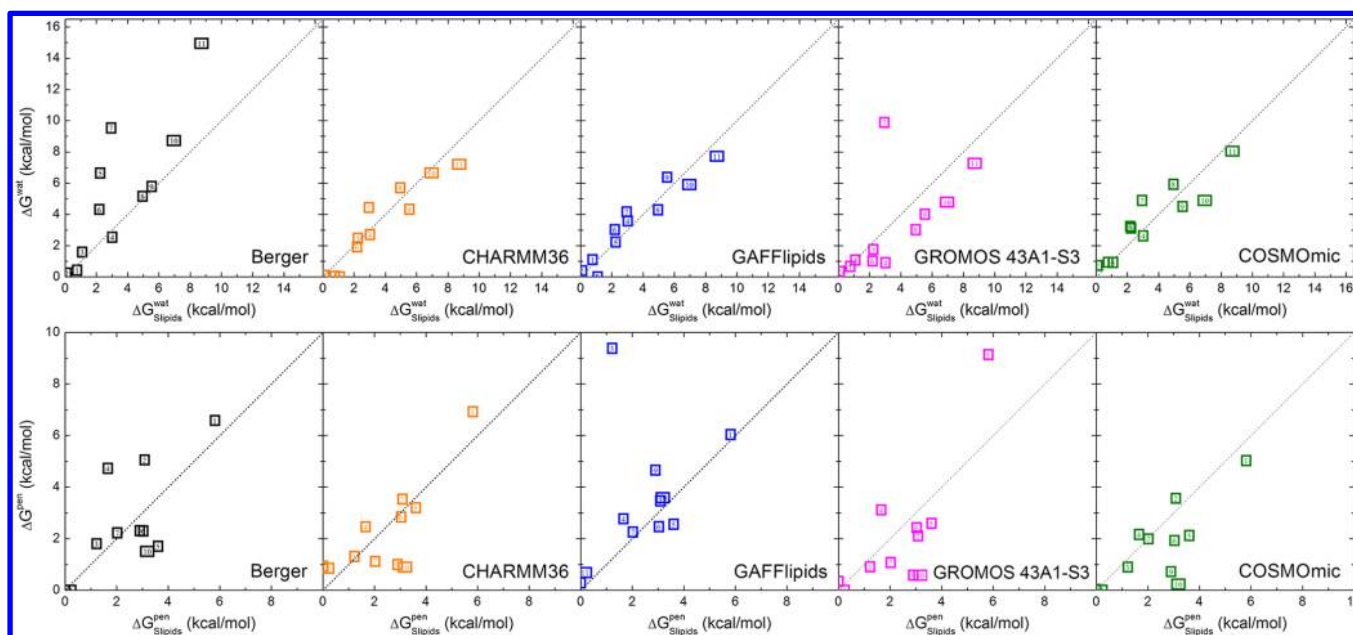


Figure 5. Water/lipid barriers ΔG^{wat} and penetration barriers ΔG^{pen} calculated by all FFs and COSMOmic vs the values obtained with Slipids.

molecules and performed just a little worse than Slipids and CHARMM36. GAFFlipids, Berger, and GROMOS 43A1-S3 showed worse ranking performance over the whole lipophilicity scale (Supporting Information Table S2). It should be stressed that all FFs and COSMOmic reproduce the right ranking of affinities to DMPC membrane, with $\alpha = 0.05$ statistical significance.

The absolute predicted values of the partition coefficients $\log K_{\text{calc}}$ also agreed with the corresponding experimental values $\log K_{\text{exp}}$ (Figure 4, Supporting Information Table S3). The mean absolute difference with respect to $\log K_{\text{exp}}$ of $\log K_{\text{calc}}$ obtained with Slipids was 0.42 log unit, which is comparable with the experimental uncertainty for determination of $\log K_{\text{exp}}$. With this FF, the linear fit between calculated and experimental partition coefficients (cf. eq 3) led to a slope of effectively 1 and a y -intercept of effectively 0 (0.97(0.09) and $-0.12(0.26)$, respectively, see Figure 4). CHARMM36 and COSMOmic exhibited similar performance (MAD 0.65 and 0.62, respectively), but CHARMM36 showed systematic shifts toward hydrophilic results ($b = 0.59(0.22)$), whereas COSMOmic toward hydrophobic results ($b = -0.70(0.31)$). GAFFlipids (MAD 0.74) gave one outlier (acetone), and GROMOS 43A1-S3 (MAD 1.08) gave 2-nitrotoluene as outlier. When omitting the outliers the mean absolute differences dropped to more reasonable values, namely 0.50 and 0.78 for GAFFlipids and GROMOS 43A1-S3 FFs, respectively. The reason for the existence of these respective outliers has not been rationalized. Berger FF is known to overestimate lipophilicity of guest molecules and showed the largest deviation from experimental values.¹⁷ In summary, taking the mean absolute differences and the linear fit of $\log K$ into consideration, the best performing FF among those tested here appears to be Slipids. However, the other FFs appear predictive enough, with the significant exception of Berger FF. Taking the predictive power (see also ref 17) into consideration and regarding low computer cost, COSMOmic can be recommended for high throughput screening of interaction of small molecules, for example, drugs, cosmetics, antioxidants, pollutants, pesticides, and warfare agents with lipid bilayers.

Properties of the Free Energy Profiles. From the previous section, Slipids was taken as a reference, and the performance of the other FFs was tested in terms of water/lipids barrier ΔG^{wat} and penetration barrier ΔG^{pen} with respect to the corresponding values obtained with Slipids. The water/lipid barriers ΔG^{wat} (that strongly correlates with $\log K_{\text{calc}}$, $r^2 = 0.96$) predicted by CHARMM36, GAFFlipids, and COSMOmic were similar to those obtained with Slipids (Table 3, Supporting Information Tables S4, S5, and Figure 5). GAFFlipids exhibited the lowest mean difference (MDI 0.02 kcal/mol) and both GAFFlipids and CHARMM36 yielded the best mean absolute difference (MAD 0.72 kcal/mol, or even better—0.68 kcal/mol—when excluding the acetone outlier from GAFFlipids data set). ΔG^{wat} values calculated by GROMOS 43A1-S3 exhibited a MAD 1.65 kcal/mol; when removing the 2-nitrotoluene outlier from the data set, the MAD dropped to 1.12 kcal/mol. Berger as expected predicted higher values of ΔG^{wat} with a MAD of 2.09 kcal/mol due to its over attractive Lennard-Jones interactions as we suggested earlier.¹⁷

Concerning the mean difference of the penetration barrier ΔG^{pen} , the best agreement with Slipids was achieved with CHARMM36 having a MDI -0.15 kcal/mol and a MAD 0.89 kcal/mol. COSMOmic predicted ΔG^{pen} values lower than Slipids with a MDI -0.73 kcal/mol and a MAD 0.91 kcal/mol. The mean absolute difference calculated from GAFFlipids data was 1.33 kcal/mol (and 0.65 if acetone was excluded). The mean absolute differences calculated from GROMOS 43A1-S3 and Berger data were 1.28 and 1.06 kcal/mol, respectively. Though ΔG^{pen} range is lower the range of ΔG^{wat} with Slipids (5.8 and 8.7 kcal/mol, respectively), the relative mean absolute difference (with respect to Slipids) of ΔG^{wat} of CHARMM36, COSMOmic, and GAFFlipids is less than or equal to the mean absolute difference of ΔG^{pen} . Therefore, CHARMM36, COSMOmic, and GAFFlipids agreed with Slipids better for ΔG^{wat} than ΔG^{pen} . However, it must be stressed that in the case of GAFFlipids, the ΔG^{pen} description was affected by the presence of one outlier (Figure 5). On the other hand, the mean absolute difference of both free energy barriers of CHARMM36 and COSMOmic compared to Slipids was lower

than 1.0 kcal/mol. This confirms the ability of Slipids, CHARMM36, and COSMOmic to provide comparable and rather accurate predictions of the free energy barriers.

The free energy profiles were also compared at different membrane depths calculated by all methods vs the free energy profile from Slipids (Figure 6). The reference free energy value

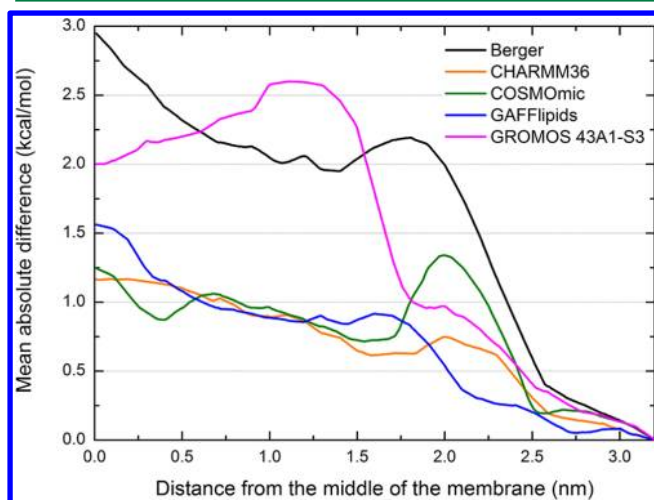


Figure 6. Mean absolute difference of free energy profile values with respect to Slipids as a function of distance from the middle of the membrane.

($\Delta G = 0$ kcal/mol) was set to water and the largest increase in the differences occurred at the water/membrane interface (2.5–1.5 nm from the membrane center). For COSMOmic, the maximum mean absolute difference (MAD 1.3 kcal/mol) was reached at 2.0 nm, dropped back to 0.7 kcal/mol at 1.75 nm, and slowly increased again to 1.2 kcal/mol in the middle of the membrane. With CHARMM36, it increased gradually up to 1.2 kcal/mol at the membrane center and the bump at the interface is less pronounced. GAFFlipids exhibited a slightly similar behavior with a mean absolute difference below 1.0 kcal/mol except at the center of the membrane. Berger and GROMOS 43A1-S3 failed in the description of the free energy profiles with respect to Slipids. Berger produced an excessively lipophilic description (i.e., too deep, Supporting Information Figure S1) with a mean absolute difference reaching 2.9 kcal/mol in the center of the membrane. Concerning the united atom FFs, GROMOS 43A1-S3 is a better choice than Berger and all-atomic FFs and COSMOmic performed better than any of the united atoms FFs.

CONCLUSION

This work compared the performance of five (two united atom and three all atom) FFs and the implicit COSMOmic method to reproduce the experimentally observed partition coefficients of 11 molecules into the DMPC membrane. Slipids appeared to be the most precise method, followed by COSMOmic, CHARMM36, GAFFlipids, GROMOS 43A1-S3, and Berger. COSMOmic and the all-atomic FFs performed well and reproduced the $\log K$ with a mean absolute difference lower than 0.8 log units. Perhaps a more relevant result is that Slipids, CHARMM36, and COSMOmic performed well in the prediction of free energy barriers; GAFFlipids predicted ΔG^{wat} very well. In terms of computational time, COSMOmic is by far the best choice at predicting $\log K$ for fluid membranes. To study hydrophilic molecules, CHARMM36 is the only FF

able to predict a correct ranking of lipophilicity. However, in the GROMACS software due the specific TIP3P water model required, CHARMM36 is the slowest, which might be limiting for larger systems, such as proteins and lipids. Taking all pros and contras into account, we recommend Slipids as the versatile FF for simulations of complex molecular systems containing lipid bilayers. It should be noted that an inclusion of polarization effects might be successful strategy how to improve predictions of partition coefficients from MD simulations.⁵¹

ASSOCIATED CONTENT

Supporting Information

Table S1: Duration of z-constraint simulations. Table S2: CPU times. Table S3: Calculated and experimental partition coefficients. Table S4: Calculated penetration barriers. Table S5: Calculated water/lipids barriers. Table S6: Calculated positions of free energy minima. Figure S1: Mean difference of free energy profiles with respect to Slipids. This material is available free of charge via the Internet at <http://pubs.acs.org>.

AUTHOR INFORMATION

Corresponding Authors

*Tel: +420 585 634 756. Email: karel.berka@upol.cz.

*Tel: +420 585 634 756. Email: michal.otyepka@upol.cz.

Notes

The authors declare no competing financial interest.

ACKNOWLEDGMENTS

This work was supported by the Grant Agency of the Czech Republic (P208/12/G016), the Operational Program Research and Development for Innovations—European Regional Development Fund (CZ.1.05/2.1.00/03.0058), the Operational Program Education for Competitiveness—European Social Fund (CZ.1.07/2.3.00/20.0058), and a student project of Palacký University (IGA_PrF_2014023). P.T. and G.F. thank the “Conseil Régional du Limousin” for financial support and CALI (CALcul en LIMousin).

REFERENCES

- Alberts, B.; Johnson, A.; Lewis, J.; Raff, M.; Roberts, K.; Walter, P. *Molecular Biology of the Cell*, 4th ed.; Garland Science: New York, 2002.
- Nagle, J. F.; Mathai, J. C.; Zeidel, M. L.; Tristram-Nagle, S. Theory of Passive Permeability through Lipid Bilayers. *J. Gen. Physiol.* **2008**, *131*, 77–85.
- Orsi, M.; Essex, J. W. Passive Permeation Across Lipid Bilayers: A Literature Review. In *Molecular Simulations and Biomembranes*; Sansom, M. S. P., Biggin, P. C., Eds.; Royal Society of Chemistry: Cambridge, U.K., 2010; pp 76–90.
- Ayrton, A.; Morgan, P. Role of Transport Proteins in Drug Absorption, Distribution, and Excretion. *Xenobiotica* **2001**, *31*, 469–497.
- Seddon, A. M.; Casey, D.; Law, R. V.; Gee, A.; Templer, R. H.; Ces, O. Drug Interactions with Lipid Membranes. *Chem. Soc. Rev.* **2009**, *38*, 2509–2519.
- Lúcio, M.; Lima, J. L. F. C.; Reis, S. Drug–Membrane Interactions: Significance for Medicinal Chemistry. *Curr. Med. Chem.* **2010**, *17*, 1795–1809.
- Balaz, S. Modeling Kinetics of Subcellular Disposition of Chemicals. *Chem. Rev.* **2009**, *109*, 1793–1899.
- Cooper, G. M. *The Cell, A Molecular Approach*; Sinauer Associates: Sunderland, MA, 2000.
- Berka, K.; Hendrychová, T.; Anzenbacher, P.; Otyepka, M. Membrane Position of Ibuprofen Agrees with Suggested Access Path

- Entrance to Cytochrome P450 2C9 Active Site. *J. Phys. Chem. A* **2011**, *115*, 11248–11255.
- (10) Palonc'ová, M.; Berka, K.; Otyepka, M. Molecular Insight into Affinities of Drugs and Their Metabolites to Lipid Bilayers. *J. Phys. Chem. B* **2013**, *117*, 2403–2410.
- (11) Berka, K.; Palonc'ová, M.; Anzenbacher, P.; Otyepka, M. Behavior of Human Cytochromes P450 on Lipid Membranes. *J. Phys. Chem. B* **2013**, *117*, 11556–11564.
- (12) Seydel, J. K.; Wiese, M. *Drug-Membrane Interactions: Analysis, Drug Distribution, Modeling*; Mannhold, R., Kubinyi, H., Folkers, G., Eds.; Wiley-VCH Verlag GmbH: Weinheim, 2002; Vol. 4.
- (13) Piggot, T. J.; Piñeiro, Á.; Khalid, S. Molecular Dynamics Simulations of Phosphatidylcholine Membranes: A Comparative Force Field Study. *J. Chem. Theory Comput.* **2012**, *8*, 4593–4609.
- (14) Košinová, P.; Berka, K.; Wykes, M.; Otyepka, M.; Trouillas, P. Positioning of Antioxidant Quercetin and Its Metabolites in Lipid Bilayer Membranes: Implication for Their Lipid-Peroxidation Inhibition. *J. Phys. Chem. B* **2012**, *116*, 1309–1318.
- (15) Podloucká, P.; Berka, K.; Fabre, G.; Palonc'ová, M.; Duroux, J.-L.; Otyepka, M.; Trouillas, P. Lipid Bilayer Membrane Affinity Rationalizes Inhibition of Lipid Peroxidation by a Natural Lignan Antioxidant. *J. Phys. Chem. B* **2013**, *117*, 5043–5049.
- (16) Palonc'ová, M.; Berka, K.; Otyepka, M. Convergence of Free Energy Profile of Coumarin in Lipid Bilayer. *J. Chem. Theory Comput.* **2012**, *8*, 1200–1211.
- (17) Palonc'ová, M.; Devane, R.; Murch, B.; Berka, K.; Otyepka, M. Amphiphilic Drug-Like Molecules Accumulate in a Membrane below the Head Group Region. *J. Phys. Chem. B* **2014**, *118*, 1030–1039.
- (18) Orsi, M.; Essex, J. W. Permeability of Drugs and Hormones through a Lipid Bilayer: Insights from Dual-Resolution Molecular Dynamics. *Soft Matter* **2010**, *6*, 3797–3808.
- (19) Bemporad, D.; Essex, J. W.; Luttmann, C. Permeation of Small Molecules through a Lipid Bilayer: A Computer Simulation Study. *J. Phys. Chem. B* **2004**, *108*, 4875–4884.
- (20) Neale, C.; Bennett, W. F. D.; Tieleman, D. P.; Pomès, R. Statistical Convergence of Equilibrium Properties in Simulations of Molecular Solutes Embedded in Lipid Bilayers. *J. Chem. Theory Comput.* **2011**, *7*, 4175–4188.
- (21) Jämbeck, J. P. M.; Lyubartsev, A. P. Exploring the Free Energy Landscape of Solutes Embedded in Lipid Bilayers. *J. Phys. Chem. Lett.* **2013**, *4*, 1781–1787.
- (22) Marrink, S. J.; Berendsen, H. J. C. Permeation Process of Small Molecules across Lipid Membranes Studied by Molecular Dynamics Simulations. *J. Phys. Chem.* **1996**, *100*, 16729–16738.
- (23) Mackerell, A. D. Empirical Force Fields for Biological Macromolecules: Overview and Issues. *J. Comput. Chem.* **2004**, *25*, 1584–1604.
- (24) Schlick, T.; Neidle, S.; Scheraga, H. A.; MacKerell, A. D. J. *Innovations in Biomolecular Modeling and Simulations*; Schlick, T., Ed.; RSC Biomolecular Sciences; Royal Society of Chemistry: Cambridge, U.K., 2012; Vol. 1.
- (25) Marrink, S. J.; Risselada, H. J.; Yefimov, S.; Tieleman, D. P.; de Vries, A. H. The MARTINI Force Field: Coarse Grained Model for Biomolecular Simulations. *J. Phys. Chem. B* **2007**, *111*, 7812–7824.
- (26) Shinoda, W.; DeVane, R.; Klein, M. L. Multi-Property Fitting and Parameterization of a Coarse Grained Model for Aqueous Surfactants. *Mol. Simul.* **2007**, *33*, 27–36.
- (27) Berger, O.; Edholm, O.; Jahnig, F. Molecular Dynamics Simulations of a Fluid Bilayer of Dipalmitoylphosphatidylcholine at Full Hydration, Constant Pressure, and Constant Temperature. *Biophys. J.* **1997**, *72*, 2002–2013.
- (28) Chiu, S.-W.; Pandit, S. A.; Scott, H. L.; Jakobsson, E. An Improved United Atom Force Field for Simulation of Mixed Lipid Bilayers. *J. Phys. Chem. B* **2009**, *113*, 2748–2763.
- (29) Jämbeck, J. P. M.; Lyubartsev, A. P. Derivation and Systematic Validation of a Refined All-Atom Force Field for Phosphatidylcholine Lipids. *J. Phys. Chem. B* **2012**, *116*, 3164–3179.
- (30) Jämbeck, J. P. M.; Lyubartsev, A. P. An Extension and Further Validation of an All-Atomistic Force Field for Biological Membranes. *J. Chem. Theory Comput.* **2012**, *8*, 2938–2948.
- (31) Jämbeck, J. P. M.; Lyubartsev, A. P. Another Piece of the Membrane Puzzle: Extending Slipids Further. *J. Chem. Theory Comput.* **2012**, *9*, 774–784.
- (32) Klauda, J. B.; Venable, R. M.; Freites, J. A.; Connor, J. W. O.; Tobias, D. J.; Mondragon-Ramirez, C.; Vorobyov, I.; Mackerell, A. D.; Pastor, R. W. Update of the CHARMM All-Atom Additive Force Field for Lipids: Validation on Six Lipid Types. *J. Phys. Chem. B* **2010**, *114*, 7830–7843.
- (33) Pastor, R. W.; Mackerell, A. D. Development of the CHARMM Force Field for Lipids. *J. Phys. Chem. Lett.* **2011**, *2*, 1526–1532.
- (34) Dickson, C. J.; Rosso, L.; Betz, R. M.; Walker, R. C.; Gould, I. R. GAFFlipid: A General Amber Force Field for the Accurate Molecular Dynamics Simulation of Phospholipid. *Soft Matter* **2012**, *8*, 9617–9627.
- (35) Skjevik, Å. a.; Madej, B. D.; Walker, R. C.; Teigen, K. LIPID11: A Modular Framework for Lipid Simulations Using Amber. *J. Phys. Chem. B* **2012**, *116*, 11124–11136.
- (36) Dickson, C. J.; Madej, B. D.; Skjevik, Å. A.; Betz, R. M.; Teigen, K.; Gould, I. R.; Walker, R. C. Lipid14: The Amber Lipid Force Field. *J. Chem. Theory Comput.* **2014**, *10*, 865–879.
- (37) Klamt, A.; Huniar, U.; Spycher, S.; Keldenich, J. COSMOmic: A Mechanistic Approach to the Calculation of Membrane–Water Partition Coefficients and Internal Distributions within Membranes and Micelles. *J. Phys. Chem. B* **2008**, *112*, 12148–12157.
- (38) Eckert, F.; Klamt, A. *COSMOtherm*; COSMOlogic GmbH & Co. KG: Leverkusen, Germany, 2013.
- (39) Klamt, A. The COSMO and COSMO-RS Solvation Models. *Wiley Interdiscip. Rev. Comput. Mol. Sci.* **2011**, *1*, 699–709.
- (40) Endo, S.; Escher, B. I.; Goss, K.-U. Capacities of Membrane Lipids to Accumulate Neutral Organic Chemicals. *Environ. Sci. Technol.* **2011**, *45*, 5912–5921.
- (41) Jakobtorweihen, S.; Ingram, T.; Smirnova, I. Combination of COSMOmic and Molecular Dynamics Simulations for the Calculation of Membrane–Water Partition Coefficients. *J. Comput. Chem.* **2013**, *34*, 1332–1340.
- (42) Wang, J.; Wolf, R. M.; Caldwell, J. W.; Kollman, P. a.; Case, D. a. Development and Testing of a General Amber Force Field. *J. Comput. Chem.* **2004**, *25*, 1157–1174.
- (43) Schüttelkopf, A. W.; van Aalten, D. M. F. PRODRG: A Tool for High-Throughput Crystallography of Protein-Ligand Complexes. *Acta Crystallogr. Sect. D Biol. Crystallogr.* **2004**, *60*, 1355–1363.
- (44) Vanommeslaeghe, K.; Mackerell, A. D. Automation of the CHARMM General Force Field (CGenFF) I: Bond Perception and Atom Typing. *J. Chem. Inf. Model.* **2012**, *52*, 3144–3154.
- (45) Vanommeslaeghe, K.; Raman, E. P.; Mackerell, A. D. Automation of the CHARMM General Force Field (CGenFF) II: Assignment of Bonded Parameters and Partial Atomic Charges. *J. Chem. Inf. Model.* **2012**, *52*, 3155–3168.
- (46) Dupradeau, F.-Y.; Pigache, A.; Zaffran, T.; Savineau, C.; Lelong, R.; Grivel, N.; Lelong, D.; Rosanski, W.; Cieplak, P. The R.E.D. Tools: Advances in RESP and ESP Charge Derivation and Force Field Library Building. *Phys. Chem. Chem. Phys.* **2010**, *12*, 7821–7839.
- (47) Woods, R. J.; Khalil, M.; Pell, W.; Moffat, S. H.; Smith, V. H. Net Atomic Charges from Molecular Electrostatic Potentials. *J. Comput. Chem.* **1990**, *11*, 297–310.
- (48) Frisch, M. J.; Trucks, G. W.; Schlegel, H. B.; Scuseria, G. E.; Robb, M. A.; Cheeseman, J. R.; Scalmani, G.; Barone, V.; Mennucci, B.; Petersson, G. A.; et al. *Gaussian 09*, Revision A.02, Gaussian, Inc.: Wallingford, CT, 2009.
- (49) Cieplak, P.; Caldwell, J.; Kollman, P. Molecular Mechanical Models for Organic and Biological Systems Going Beyond the Atom Centered Two Body Additive Approximation: Aqueous Solution Free Energies of Methanol and N-Methyl Acetamide, Nucleic Acid Base, and Amide Hydrogen Bonding and Chloroform/Water Partition Coefficients of the Nucleic Acid Bases. *J. Comput. Chem.* **2001**, *22*, 1048–1057.

- (50) Cornell, W. D. A Second Generation Force Field for the Simulation of Proteins, Nucleic Acids, and Organic Molecules. *J. Am. Chem. Soc.* **1995**, *117*, 5179–5197.
- (51) Jämbeck, J. P. M.; Lyubartsev, A. P. Implicit Inclusion of Atomic Polarization in Modeling of Partitioning Between Water and Lipid Bilayers. *Phys. Chem. Chem. Phys.* **2013**, *15*, 4677–4686.
- (52) Katz, Y.; Diamond, J. M. Thermodynamic Constants for Nonelectrolyte Partition between Dimyristoyl Lecithin and Water. *J. Membr. Biol.* **1974**, *17*, 101–120.
- (53) Vaes, W. H.; Ramos, E. U.; Hamwijk, C.; van Holsteijn, I.; Blaauboer, B. J.; Seinen, W.; Verhaar, H. J.; Hermens, J. L. Solid Phase Microextraction as a Tool to Determine Membrane/Water Partition Coefficients and Bioavailable Concentrations in In Vitro Systems. *Chem. Res. Toxicol.* **1997**, *10*, 1067–1072.
- (54) Gobas, F. A. P. C.; Lahittete, J. M.; Garofalo, G.; Shiu, W. Y.; Mackay, D. A Novel Method for Measuring Membrane–Water Partition Coefficients of Hydrophobic Organic Chemicals: Comparison with 1-Octanol–Water Partitioning. *J. Pharm. Sci.* **1988**, *77*, 265–272.
- (55) Van der Heijden, S. A.; Jonker, M. T. O. Evaluation of Liposome–Water Partitioning for Predicting Bioaccumulation Potential of Hydrophobic Organic Chemicals. *Environ. Sci. Technol.* **2009**, *43*, 8854–8859.
- (56) Nagle, J. F.; Tristram-Nagle, S. Structure of Lipid Bilayers. *Biochim. Biophys. Acta* **2000**, *1469*, 159–195.
- (57) Darden, T.; York, D.; Pedersen, L. Particle Mesh Ewald: An N.log(N) Method for Ewald Sums in Large Systems. *J. Chem. Phys.* **1993**, *98*, 10089–10092.
- (58) Hess, B.; Bekker, H.; Berendsen, H. J. C.; Fraaije, J. G. E. M. LINCS: A Linear Constraint Solver for Molecular Simulations. *J. Comput. Chem.* **1997**, *18*, 1463–1472.
- (59) Parrinello, M.; Rahman, A. Polymorphic Transitions in Single Crystals: A New Molecular Dynamics Method. *J. Appl. Phys.* **1981**, *52*, 7182–7190.
- (60) Nosé, S. A Unified Formulation of the Constant Temperature Molecular Dynamics Methods. *J. Chem. Phys.* **1984**, *81*, 511.
- (61) Hoover, W. G. Canonical Dynamics: Equilibrium Phase-Space Distributions. *Phys. Rev. A* **1985**, *31*, 1695–1697.
- (62) Berendsen, H. J. C.; Postma, J. P. M.; Gunsteren, W. F. van; Hermans, J. Interaction Models for Water in Relation to Protein Hydration. In *Intermolecular Forces*; Pullman, B., Ed.; Reidel Publishing Company, 1981; pp 331–338.
- (63) Berendsen, H. J. C.; Grigera, J. R.; Straatsma, T. P. The Missing Term in Effective Pair Potentials. *J. Phys. Chem.* **1987**, *91*, 6269–6271.
- (64) Durell, S. R.; Brooks, B. R.; Ben-Naim, A. Solvent-Induced Forces between Two Hydrophilic Groups. *J. Phys. Chem.* **1994**, *98*, 2198–2202.
- (65) Jorgensen, W. L.; Chandrasekhar, J.; Madura, J. D.; Impey, R. W.; Klein, M. L. Comparison of Simple Potential Functions for Simulating Liquid Water. *J. Chem. Phys.* **1983**, *79*, 926.
- (66) MacCallum, J. L.; Bennett, W. F. D.; Tieleman, D. P. Distribution of Amino Acids in a Lipid Bilayer from Computer Simulations. *Biophys. J.* **2008**, *94*, 3393–3404.
- (67) Becke, A. D. Density-Functional Exchange-Energy Approximation with Correct Asymptotic Behavior. *Phys. Rev. A* **1988**, *38*, 3098–3100.
- (68) Perdew, J. P. Density-Functional Approximation for the Correlation Energy of the Inhomogeneous Electron Gas. *Phys. Rev. B* **1986**, *34*, 7406.
- (69) Klamt, A. *COSMO-RS: From Quantum Chemistry to Fluid Phase Thermodynamics and Drug Design*; Elsevier Science Ltd.: Amsterdam, 2005.
- (70) Meloun, M.; Bordovská, S.; Kupka, K. Outliers Detection in the Statistical Accuracy Test of a pK_a Prediction. *J. Math. Chem.* **2010**, *47*, 891–909.
- (71) Leftin, A.; Brown, M. F. An NMR Database for Simulations of Membrane Dynamics. *Biochim. Biophys. Acta* **2011**, *1808*, 818–839.

Rationalization of Reduced Penetration of Drugs through Ceramide Gel Phase Membrane

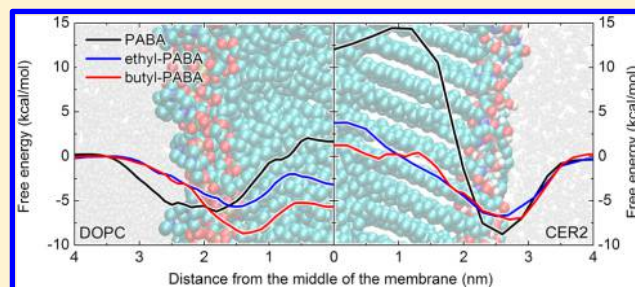
Markéta Paloncýová,[†] Russell H. DeVane,[‡] Bruce P. Murch,[‡] Karel Berka,^{*,†} and Michal Otyepka^{*,†}

[†]Regional Centre of Advanced Technologies and Materials, Department of Physical Chemistry, Faculty of Science, Palacký University Olomouc, tř. 17. listopadu 12, 771 46, Olomouc, Czech Republic

[‡]Corporate Modeling & Simulation, Procter & Gamble, 8611 Beckett Road, West Chester, Ohio 45069, United States

S Supporting Information

ABSTRACT: Since computing resources have advanced enough to allow routine molecular simulation studies of drug molecules interacting with biologically relevant membranes, a considerable amount of work has been carried out with fluid phospholipid systems. However, there is very little work in the literature on drug interactions with gel phase lipids. This poses a significant limitation for understanding permeation through the stratum corneum where the primary pathway is expected to be through a highly ordered lipid matrix. To address this point, we analyzed the interactions of *p*-aminobenzoic acid (PABA) and its ethyl (benzocaine) and butyl (butamben) esters with two membrane bilayers, which differ in their fluidity at ambient conditions. We considered a dioleoylphosphatidylcholine (DOPC) bilayer in a fluid state and a ceramide 2 (CER2, ceramide NS) bilayer in a gel phase. We carried out unbiased (100 ns long) and biased *z*-constraint molecular dynamics simulations and calculated the free energy profiles of all molecules along the bilayer normal. The free energy profiles converged significantly slower for the gel phase. While the compounds have comparable affinities for both membranes, they exhibit penetration barriers almost 3 times higher in the gel phase CER2 bilayer. This elevated barrier and slower diffusion in the CER2 bilayer, which are caused by the high ordering of CER2 lipid chains, explain the low permeability of the gel phase membranes. We also compared the free energy profiles from MD simulations with those obtained from COSMOmic. This method provided the same trends in behavior for the guest molecules in both bilayers; however, the penetration barriers calculated by COSMOmic did not differ between membranes. In conclusion, we show how membrane fluid properties affect the interaction of drug-like molecules with membranes.



■ INTRODUCTION

The penetration of small xenobiotic molecules such as drugs or pollutants through various biomembranes plays a crucial role in disposition among biological environments and organisms. Phosphatidylcholine (PC) represents the most abundant lipid type in human cell membranes,^{1,2} and consequently PC bilayers are used as prototypical membrane models. PC membranes are usually present in their fluid phases under physiological conditions because their gel-to-fluid phase transition temperatures vary approximately from 200 to 360 K.³ The interactions of xenobiotics with fluid PC membranes have been widely studied both experimentally and theoretically.^{4–7} These studies provide detailed atomistic insight into the interaction of molecules with membranes, e.g., into partitioning,^{8–11} location, and permeation^{6,12,13} of guest molecules through the membranes. On the contrary, little attention has been paid to the gel membrane phases,^{14–17} which are also biologically important and occur for instance in the outermost layer of skin termed the *stratum corneum* (SC).

Several pathways have been proposed for permeation through the skin, whereas the key rate-limiting step for the majority of the molecules is the penetration through SC membranes.¹⁸ SC superstructure can be described with a brick

and mortar model, where (im)permeable bricks represent corneocytes (dead cells), surrounded by a mortar which represents a lipid matrix made of ceramides, fatty acids, and cholesterol.¹⁹ Most compounds have been shown to penetrate by the intercellular pathway, i.e., through the lipid matrix.²⁰ The presence of ceramides and fatty acids with long saturated chains and cholesterol predispose the SC lipids to occur in the gel phase under physiological conditions. While experimental studies of the permeability of SC have been largely based on isolated SC,^{21–25} some groups have developed artificial models of the SC membrane.

Recently, a synthetic experimental model for SC permeability studies was introduced by Bouwstra et al.²⁶ Unlike other studies on SC extracted directly from the skin, a stratum corneum substitute (SCS) membrane enables an adaptive composition that can be modified to model both healthy and diseased skin. The authors studied the permeation of *p*-aminobenzoic acid (PABA, Figure 1) and two of its anesthetically active esters: ethyl ester (ethyl-PABA; benzocaine, Figure 1) and butyl ester

Received: August 17, 2014

Revised: October 24, 2014

Published: October 29, 2014

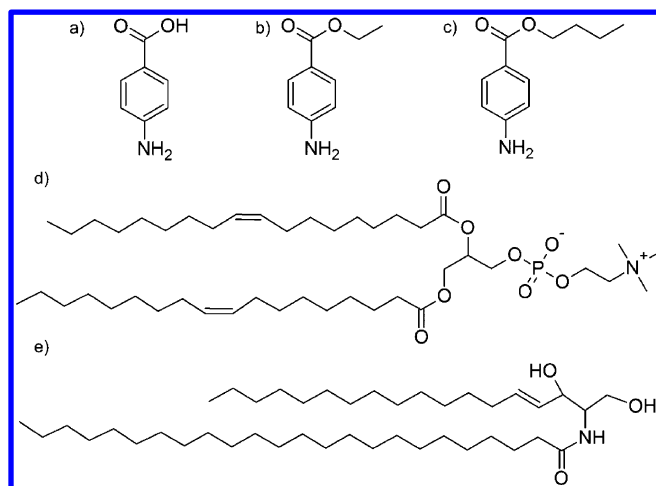


Figure 1. Structures of (a) *p*-aminobenzoic acid (PABA, blue hydrogen shows the place of deprotonation), (b) ethyl-PABA, (c) butyl-PABA, (d) DOPC (1,2-dioleoyl-*sn*-glycero-3-phosphatidylcholine), and (e) ceramide 2 (CER2, *N*-(tetracosanoyl)sphingosine), also termed ceramide NS.

(butyl-PABA; butamben, Figure 1) through the SCS membrane and concluded that the permeability was ordered based on lipophilicities of these molecules. The most lipophilic butyl-PABA being the best penetrant was closely followed by ethyl-PABA, whereas PABA was shown as the worst penetrant. However, PABA permeability was lower by an order of magnitude, even though the differences in $\log P_{\text{oct/wat}}$ were relatively uniform (XLogP3: PABA: 0.8, ethyl-PABA: 1.9, butyl-PABA: 2.9). Generally, the permeability of SC is low in comparison with the fluid membranes, and it was hypothesized that this difference is caused by the gel phase of SC lipids.^{23,27,28}

The behavior, e.g., structure and fluidity, of lipids in various phases is significantly different, and we may also expect that the interaction of guest molecules with membranes would reflect their phase state, which depends on both the temperature and composition of the membrane.¹ Lipid phase behavior can be taken as characteristic of the lipid type at a specific temperature and evaluated based on two properties: chain order parameters (S_{CD}) and lateral diffusion coefficients of lipids (D_{lat}). The liquid crystalline phase (L_d or L_{or} also called liquid disordered or fluid), often observed for unsaturated phosphatidylcholine membranes, has a low S_{CD} and high D_{lat} . The liquid ordered phase (L_o) is often formed by lipid mixtures with cholesterol and has a high S_{CD} and high D_{lat} . The gel phase (L_β or solid-ordered s_o) is usually formed by lipids with long saturated tails and has high S_{CD} and low D_{lat} .¹ There are numerous studies on fluid phase membranes mimicking the plasma membrane;^{6,8–12} however, surprisingly only a few theoretical studies have used a gel phase membrane to model the lipid component of the SC.^{14,16,29} This lack of work in the literature is partly due to the rather complex and yet totally unresolved structure of SC lipid matrix³⁰ as well as high computational costs required for study of dynamical behavior of the gel phase membranes.

Theoretical studies of the interaction of guest molecules with biomembranes provide useful physical-chemical insights with very fine spatial and temporal resolutions and can nicely paint the picture drawn from experiments. Namely molecular dynamics (MD) simulations and COSMOmic have been

repeatedly shown to widen our understanding in this field.^{8,31–33} Both methods can decipher the thermodynamic nature of the interactions, while MD has an advantage of being able to also tackle the dynamic and transport phenomena. MD simulations evolve the trajectory of atoms by integrating Newton equations based on an empirical potential called a force field. MD naturally has femtosecond and atomic resolutions simultaneously. COSMOmic, on the other hand, works with the idea of a membrane as a set of fluid layers of different composition and properties and calculates the partitioning into these layers. We recently showed that the results from COSMOmic and MD are qualitatively comparable,⁸ although MD is heavily dependent on the chosen force field.³⁴

Here, we studied the interactions of PABA and its two anesthetically active esters ethyl-PABA and butyl-PABA with fluid phase dioleoylphosphatidylcholine (DOPC, Figure 1) and gel phase ceramide 2 (CER2, Figure 1) bilayers. Using molecular dynamics, we describe the different behavior of both model membranes and also the different nature of the thermodynamic interactions of drugs with fluid and gel phases. Finally, we studied both systems in COSMOmic and describe here the benefits and the limitations of this approach.

METHODS

A DOPC bilayer (1,2-dioleoyl-*sn*-glycero-3-phosphatidylcholine, CAS number 56648-95-4, Figure 1) was used to model a fluid phase. DOPC is a double unsaturated lipid from the most common fluid lipid type (PC) in the cell membrane. Its phase transition occurs at 255 K,³ and it is therefore present in the fluid phase at physiological conditions. The bilayer was downloaded from the Lipidbook server³⁵ and was prepared and equilibrated by Siu et al.³⁶ with the Berger lipid force field.³⁷ It contained 128 molecules of DOPC, 64 in each leaflet. To reach the physiological concentration 0.154 M of salt, 13 Na⁺ and 13 Cl⁻ ions were added. The fully hydrated box contained 4731 molecules of SPC/E water.^{38,39}

The gel phase was modeled by using a CER2 bilayer (*N*-(tetracosanoyl)sphingosine, CAS number 102917-80-6, also called ceramide NS). CER2 is the most common ceramide in the SC lipid matrix¹⁶ with a phase transition temperature of ~340–360 K (depending on the hydration state).⁴⁰ The Berger force field parameters for the CER2 bilayer were taken from the literature.⁴¹ The bilayer consisted of 128 molecules of CER2 (64 in each layer) and 4085 molecules of SPC/E water. Both bilayers were then left to equilibrate and were oriented perpendicular to the *z*-axis of the simulation box and the *z*-axis start (*z* = 0 nm) was set to the middle of the membrane.

The topologies of PABA (Figure 1) in both protonation states and its two (ethyl and butyl) esters were generated by PRODRG2Beta server,⁴² but the partial charges were set up as follows: the Gaussian 03 program⁴³ with B3LYP/cc-pVDZ method was used to optimize the structures and to calculate their electrostatic potentials. The partial charges were then calculated using the restrained electrostatic potential method (RESP)^{44,45} in Antechamber from the AMBER 11 software package.⁴⁶ The geometry parameters were generated by tleap from the same software package. The derived parameters were then transferred to the format compliant with the GROMACS 4.0.7 simulation package using amb2gmx.pl program.

MD simulations were carried out in the GROMACS 4.0.7 software package⁴⁷ using a 2 fs integration time step under periodic boundary conditions in all directions. Particle-mesh Ewald (PME) was applied to the long-range electrostatic interactions, and the van der Waals interactions were cut off at 1 nm. Covalent bonds including hydrogen atoms were constrained by the LINCS algorithm.⁴⁸ Temperature was controlled using V-rescale temperature coupling to 310 K,⁴⁹ and pressure was controlled using a Berendsen anisotropic barostat at 1 bar with 10 ps time constant and a compressibility of $4.5 \times 10^{-5} \text{ bar}^{-1}$. For

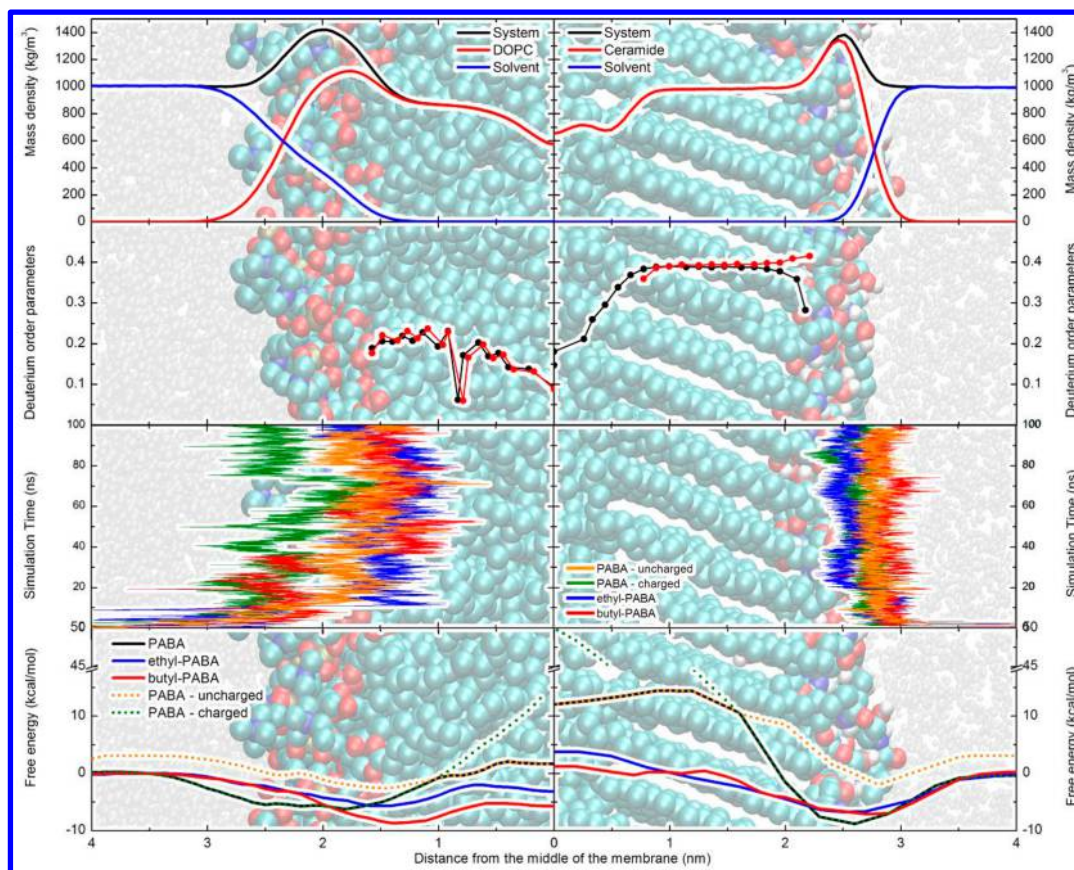


Figure 2. Structural parameters of fluid DOPC and gel CER2 bilayers and behavior of PABA molecules. Upper two panels: density profile (upper panel) and deuterium order parameters (second panel) of DOPC (left panel) and ceramide (right panel) bilayers during free simulations of a pure bilayer. While properties of the DOPC bilayer change gradually, the changes in CER2 bilayer are very sharp. The drop of the density and order parameters in the middle of the membrane is connected with termination of sphingosine lipid chains. The water molecules are shown as gray balls, united carbons cyan, oxygens red, phosphates olive, and nitrogens blue. Lower two panels: evolution of the drug distance from the bilayer center during the unbiased simulations (third panel). The molecules penetrated into the DOPC membrane; however, they stayed outside of the CER2 bilayer. Free energy profiles of PABA, ethyl-PABA, and butyl-PABA with separated free energy profiles for the charged and uncharged form of PABA (lower panel). The penetration barrier from MD in the gel phase CER2 bilayer is far higher than in the fluid DOPC.

analysis of the membrane structure, we used additional GROMACS tools such as `g_msd` to calculate diffusion coefficients and `g_order` to calculate order parameters. All structural parameters of the membranes were calculated as averages on the trajectories of equilibrated membranes.

Initial structures for the biased simulations of DOPC and CER2 were obtained as follows: we placed each studied molecule at the top of the membrane simulation box (in the water phase) and then executed a 100 ns long free simulation. Structures from this unbiased simulation approach should lead to a more quickly converging free energy profile.⁹ From the deepest position in the membrane (or near the membrane) that the drug reached during the free simulation, the drug was pulled inside the membrane with a pull rate of 0.1 nm ns^{-1} and a pulling force constant of $500 \text{ kJ mol}^{-1} \text{ nm}^{-2}$. Pulling applies a harmonic potential to the molecule and moves the center of this potential with a given pull rate. The starting structures for further z -constraint simulations were the structures with the lowest potential energy from an ensemble of structures in the specific depth separated by $0.1 \pm 0.02 \text{ nm}$.

The z -constraint simulation was executed for 11–100 ns per simulation window for the DOPC bilayer systems. The simulation windows in the water area had the shortest simulation times (11 ns), with the typical length of simulation in the membrane at 30 ns. At the location of the free energy minimum the simulations were prolonged to 100 ns; as needed, in specific windows (separated by 0.5 nm) the simulation times were also prolonged to 100 ns.

The simulations of the CER2 bilayer based systems needed a longer time to equilibrate and were simulated for 100–150 ns per simulation window. Because of the high computational costs, a longer distance between simulation windows was chosen (up to 0.4 nm). It should be noted that this is a safe way to reduce computational costs without significant effect on the final free energy profile.⁹ The free energy profiles were calculated from the last 50 ns of each simulation window. The influence of the presence of PABA and its esters on the global properties of the simulation system (e.g., global average order parameter change, number of hydrogen bonds, etc.) was calculated for each window from the z -constraint simulations.

The free energy profile was constructed by integrating the mean force applied on the molecule $\langle F(z') \rangle$ along the membrane normal z (eq 1).

$$\Delta G(z) = - \int_{\text{outside}}^z \langle F(z') \rangle_t dz' \quad (1)$$

The free energy profile of PABA was calculated as a combination of the charged and uncharged form of PABA. The protonated PABA free energy profile was shifted by 3.1 kcal/mol in water, reflecting the pK_a of 4.85 for PABA at a pH of 7. The convergence of free energy profiles was evaluated on the basis of differences of neighboring time frames.

For COSMOmic calculations, we took 30 structures of DOPC and CER2 bilayers from a free simulation. We calculated geometries and σ -profiles of PABA and its esters and the lipid molecules by DFT/COSMO calculations at the BP/TZVP level of theory in Turbomole 6.3. The free energy profiles were calculated with membranes

separated into 50 layers and with 162 solute orientations at 310 K by COSMOmic from COSMOtherm X13 package (COSMOlogic GmbH, Leverkusen, Germany).⁵⁰ Finally, we averaged the calculated free energy profiles to a final profile as recommended in the literature.⁵³

RESULTS AND DISCUSSION

Pure Membrane Simulation. The density profile and structure of a DOPC bilayer display typical regions which can be distinguished in fluid membranes.⁵¹ The densest region occurs around the head groups at roughly 2 nm from the bilayer core. The head groups are solvated with water, reaching as deep as 1.5 nm from the bilayer core. The lipid tails show a slight plateau in density near the middle of the membrane with a sharp drop in overall density near the bilayer core (Figure 2). The deuterium order parameters of individual tail atoms are around 0.2, which are the typical values for fluid bilayers.^{52–54} The deuterium order parameters slowly decrease toward the middle of the membrane with a steep drop at the double bond positions. This is consistent with their inherent tendency of unsaturated bonds to disorder lipid chains. On the other hand, the CER2 bilayer density profile and structure show much sharper boundaries between the regions. The highest density for the system occurs at roughly 2.5 nm. Water does not permeate inside the membrane to the same extent as in DOPC and instead stays just at the outer edges of the head groups. The lipid tails display a distinct “plateau” corresponding to a region that is highly ordered and tilted. This is consistent with deuterium order parameters of around 0.4. The density in this region is higher than the respective density of the DOPC bilayer. This plateau extends until ~ 0.8 nm from the middle of the membrane with tilted lipid tails in both leaflets. Then a sharp decrease of the density follows due to the asymmetry in the lipid chains. This area at the core of the CER2 bilayer is fluid. The lipid diffusion coefficients differ significantly in the two bilayers, with DOPC ($(17.9 \pm 2.1) \times 10^{-8}$ cm²/s) showing a much higher value than CER2 ($(4.4 \pm 1.6) \times 10^{-8}$ cm²/s).

Behavior of PABA Derivatives on Bilayers in Free Simulations. During the free simulations, the molecules penetrated into the DOPC bilayer; however, this was not observed for the CER2 bilayer (Figure 2). For the DOPC bilayer, the uncharged molecules penetrated deep into the hydrophobic tails and most often stayed below the head groups. The charged form of PABA stayed in the polar head groups region. For the CER2 bilayer simulations, all molecules remained outside of the bilayer interacting only with its surface. These simulations indicate that the molecules studied here are localized below the polar headgroup region of DOPC, which is consistent with other drug molecules.^{8,10} On the other hand, the free simulation results might suggest that the free energy minima are outside of the CER2 head groups (on the CER2 bilayer surface) or are deeper in the bilayer but with kinetically unreachable minima on simulation time scales, i.e., separated by a significant energy barrier. This ambiguity demonstrates the need for free energy profile calculations to quantify the different behavior of drugs in DOPC and CER2 bilayers.

Convergence of Free Energy Profiles from MD. For DOPC, the rate-limiting step affecting the convergence of the biased *z*-constraint simulations usually lies in the estimation of the free energy barrier from the bulk water phase to the minimum free energy position in the lipids, ΔG^{wat} .^{9,55} This is mostly because of introduction of perturbed bilayer structures

(e.g., funnel-like surface protrusions^{55,56}), which require several tens or hundreds of nanoseconds to achieve full relaxation.^{9,55} Using the protocol optimized for free energy estimations,⁹ the profiles reached convergent values (stable ΔG values in simulation time) after ~ 15 ns. On the other hand, the free energy penetration barrier ΔG^{pen} , defined as the barrier of passing from the free energy minimum in the lipid bilayer through the bilayer core, was the slowest converging barrier in the biased simulations for the CER2 bilayer systems (Figure 3)

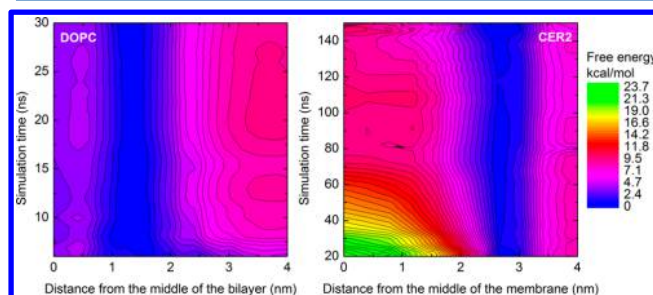


Figure 3. Convergence of free energy profiles of butyl-PABA in DOPC (left) and CER2 (right) in simulation time. In each plot, zero free energy was set to the free energy minimum in order to highlight the convergence of free energy barriers. The convergence in the fluid DOPC membrane is much quicker than the convergence in gel CER2 bilayer. The water/lipids barrier is the slowest converging barrier in the fluid phase, while in the gel phase the slowest converging barrier is the penetration barrier.

with convergence achieved after ~ 100 ns. It is of note that the ΔG^{pen} values play an important role in evaluation of the permeability coefficients because either the most positive free energy value (in the case of exponential permeability calculation)¹² or the highest energy barrier (see the Supporting Information) contribute significantly to the permeability coefficients.⁵⁷

Free Energy Profiles of PABA Derivatives on Both Bilayers from MD. Drug partitioning into lipid bilayers is a rather complex process, and its thermodynamics includes the major contribution from hydrophobic interactions, which are accompanied by contributions stemming from changes in the structure of the lipid bilayer.⁵⁸ The free energy profiles show water/lipids free energy differences ΔG^{wat} , reflecting the drug's affinities to the membrane, 6.1, 5.6, and 8.6 kcal/mol in DOPC bilayer and 8.6, 6.7, and 7.0 kcal/mol in CER2 bilayer for PABA, ethyl-PABA, and butyl-PABA, respectively (Figure 2 and Table 1). Both ethyl-PABA and butyl-PABA esters were positioned deeper in the DOPC bilayer (~ 0.3 and ~ 0.4 nm deeper, respectively) compared to PABA, while all three molecules shared the same position close to the CER2/water interface. In both membranes, butyl-PABA had higher affinity for the membrane than ethyl-PABA with its shorter aliphatic chain. As nonpolar molecules, PABA esters gain more from their dehydration,⁸ and the hydrophobic effect drives them deeper into the DOPC lipid bilayer to the position where amphiphilic drugs accumulate in PC bilayers.⁸ Butyl-PABA has a higher affinity to DOPC than ethyl-PABA by 3 kcal/mol, which agrees with observations that molecules having longer aliphatic chains have higher membrane affinities and that the affinity increases by ~ 1 kcal/mol per carbon atom.⁵⁸ The charged PABA moiety showed the strongest interactions with the polar head groups of both bilayers, and thus it had a higher affinity in this region. However, the overall affinity for the

Table 1. Penetration Barrier, ΔG^{pen} (kcal/mol), and Water/Lipids Barrier, ΔG^{wat} (kcal/mol), Calculated by Molecular Dynamics (MD) and COSMOmic for PABA and Its Esters in DOPC and CER2 Bilayers

molecule	MD				COSMOmic			
	DOPC		CER2		DOPC		CER2	
	ΔG^{pen}	ΔG^{wat}	ΔG^{pen}	ΔG^{wat}	ΔG^{pen}	ΔG^{wat}	ΔG^{pen}	ΔG^{wat}
PABA	8.1	6.1	22.5	8.6	9.4	3.0	6.5	0.0
ethyl-PABA	3.6	5.6	10.4	6.7	2.5	3.4	2.3	3.2
butyl-PABA	3.4	8.6	8.3	7.0	2.5	4.9	2.2	4.6

DOPC bilayer was lower compared to CER2. The higher affinity of PABA to CER2 may stem from the situation in which the hydrophobic part of PABA gains from its dehydration and the carboxylate group stays in contact with the polar headgroup region, making hydrogen bonds with CER2 heads and water molecules. It should be noted that the DOPC headgroup lacks a proton donor, which can make favorable hydrogen bonds to the carboxylate moiety of PABA (Figures S1 and S2). In turn, the positioning and affinity of PABA to DOPC are determined by a counterbalance between favorable dehydration of the hydrophobic moiety and favorable hydration of the carboxylate group.

The penetration barriers in a CER2 bilayer are much higher than in a DOPC bilayer. Obviously, the increased lipophilicity of the molecules lowered ΔG^{pen} in both bilayers. The penetration barriers ΔG^{pen} were 8.1, 3.6, and 3.4 kcal/mol in the DOPC bilayer and 22.5, 10.4, and 8.3 kcal/mol in CER2 bilayer for PABA, ethyl-PABA, and butyl-PABA, respectively. The relative ordering of ΔG^{pen} in CER2 was also in qualitative agreement with the experimentally measured permeabilities, which indicated butyl-PABA as the best penetrator with ethyl-PABA closely following and PABA as the worst penetrator.²⁶ It should be noted that PABA penetrated through both membranes in its protonated neutral form. The protonation of PABA carboxylate group occurred inside the membrane (Figure 2) and was connected with a dehydration of carboxylate group.

As the gain from the drug dehydration is the same in DOPC and CER2 membranes, the observed variations in free energies inside both bilayers must stem from different drug–lipid interactions and different changes in the structure of both bilayers. A comparison of free energies of ethyl- and butyl-PABA inside both bilayers may indicate that a penalty for disruption of the membrane structure is by ~ 7 kcal/mol higher in CER2 than in DOPC bilayer, assuming that the drug–lipid interactions in the membrane center are comparable in DOPC and CER2. The higher energetic penalty connected with the penetration through the CER2 bilayer is caused by the high chain ordering of the CER2 bilayer (Figure 2), which is not significantly perturbed during the drug passage (Figure S3). It is of note that the free energy profiles derived from simulations on artificially fluid CER2 membrane (see Supporting Information for details) were closer to profiles on DOPC membrane than those on the gel CER2 membrane (Figures S4 and S5). The significant role of chain ordering in partitioning and transport was also observed experimentally on mixed DMPC:cholesterol bilayers in the L_0 phase.⁵⁹

The kinetics of the penetration depends on the height of the energy barrier and on the diffusion across the lipid bilayer. The penetration through the CER2 bilayer is slowed down by two factors: the higher ΔG^{pen} barriers and lower diffusion coefficients in CER2 bilayer than in DOPC bilayer (Figure S6). As the affinities for both membranes are comparable, the

high ordering of CER2 bilayer influences more significantly the permeation across the membrane than the partitioning into, at least for amphiphilic molecules.

Free Energy Profiles of PABA Derivatives on Both Bilayers from COSMOmic. For comparison, we also calculated the free energy profiles of PABA and its esters in both bilayers using COSMOmic (Figure 4 and Table 1), which

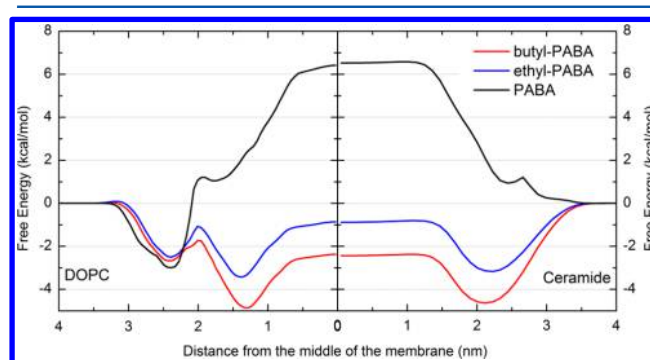


Figure 4. Free energy profiles of PABA and its esters in DOPC (left) and CER2 (right) bilayers calculated by COSMOmic shows differences in the headgroup area; however, COSMOmic does not differentiate the membranes free energies in the core.

is a computationally less expensive alternative to MD. The affinities for the DOPC membrane predicted by COSMOmic ($\Delta G^{\text{wat}} = 3.0, 3.4,$ and 4.9 kcal/mol for PABA, ethyl-PABA, and butyl-PABA in DOPC) are about 40% lower than the values predicted by MD with the Berger force field (Table 1), which agrees with our recent findings.⁸ For CER2, PABA did not preferentially interact with the membrane, but the ΔG^{wat} values for ethyl-PABA and butyl-PABA were comparable to DOPC (COSMOmic $\Delta G^{\text{wat}} = 0.0, 3.2,$ and 4.6 kcal/mol for PABA, ethyl-PABA and butyl-PABA in CER2). The penetration barrier, ΔG^{pen} in DOPC predicted by COSMOmic should be about 35% lower than MD predictions with Berger force field,⁸ which applies for the PABA esters but not for PABA (COSMOmic $\Delta G^{\text{pen}} = 9.4, 2.5,$ and 2.5 kcal/mol for PABA, ethyl-PABA, and butyl-PABA in DOPC). COSMOmic predictions of ΔG^{pen} in CER2 were 6.5, 2.3, and 2.2 kcal/mol for PABA, ethyl-PABA, and butyl-PABA. The COSMOmic free energy profiles for DOPC and CER2 differ in the headgroup region, where it shows two minima in DOPC and only one in CER2. The position of the major minima agrees for DOPC bilayer in both computational methods. However, COSMOmic predicts that the minima in CER2 are located at deeper z -positions in the bilayer compared to the MD results. Also, in contrast to the MD results, the COSMOmic profiles for DOPC and CER2 have almost the same free energy values in the middle of the membrane. This can be rationalized by considering that although the area per headgroup differs between DOPC and CER2 membranes, the membrane cores

have similar densities (cf. Figure 2) and the same atom types. Therefore, COSMOmic estimates similar partitioning into this region despite the differences in ordering. It should be noted that MD simulations reflect the difference in the free energy profiles between both lipid phases.

CONCLUSION

We studied the interactions of *p*-aminobenzoic acid and its two anesthetically active esters in DOPC and CER2 bilayers in order to gain a better understanding of the interactions of drugs with fluid and gel phase membranes. The relevance for probing such systems is to highlight the different environments that drugs encounter via traditional cellular uptake versus skin absorption. The studied molecules penetrated into the DOPC bilayers during MD simulation; however, they did not enter the CER2 bilayers within the simulation times and stayed at the outer side of head groups. Despite this observation, free energy simulations indicated comparable affinities for both membranes. On the other hand, the penetration barriers were significantly higher in the ceramide membrane, and their absolute ranking agreed with the experimentally observed permeability values. Further, we explained that the different behavior on both membranes is dominantly caused by the high ordering of lipid chains in the CER2 bilayer. The non-MD tool, COSMOmic, provided the same relative orders of permeants, however, it was not able to differentiate between penetration in liquid and gel phase membranes. It should be noted that COSMOmic was used outside of its recommended range of applicability. In conclusion, we show how the membrane fluid properties affect the interaction of drug-like molecules with membranes and may help in understanding of slower penetration of drugs through SC layer of skin in comparison with plasma membrane.

ASSOCIATED CONTENT

Supporting Information

Permeability calculation based on Marrink et al.⁶⁰ and Orsi et al.⁵⁷ equations; Figure S1: number of hydrogen bonds between various groups in the dependence on position of solute molecules; Figure S2: number of hydrogen bonds between drug and rest of the system; Figure S3: influence of presence of the solute on the order parameters of lipid chains; Figure S4: free energy profiles on artificially fluid CER2 bilayer compared to free energy profiles on gel phase CER2 bilayer and fluid DOPC bilayer; Figure S5: density profile and order parameters of artificially fluid CER2 bilayer; Figure S6: lateral and transversal diffusion coefficients; derived force field parameters for drug molecules. This material is available free of charge via the Internet at <http://pubs.acs.org>.

AUTHOR INFORMATION

Corresponding Authors

*E-mail karel.berka@upol.cz, Tel +420 585 634 756 (K.B.).

*E-mail michal.otyepka@upol.cz, Tel +420 585 634 756 (M.O.).

Notes

The authors declare no competing financial interest.

ACKNOWLEDGMENTS

This work was supported by the Operational Program Research and Development for Innovations—European Regional Development Fund (CZ.1.05/2.1.00/03.0058) and European Social

Fund (CZ.1.07/2.3.00/20.0058). M.O. acknowledges support by the Czech Grant Agency through the P208/12/G016 project. M.P. acknowledges support by the Student Project IGA_PrF_2014023 (Palacký University, Olomouc). This research used resources of the Oak Ridge Leadership Computing Facility at the Oak Ridge National Laboratory, which is supported by the Office of Science of the U.S. Department of Energy under Contract DE-AC05-00OR22725.

REFERENCES

- (1) Van Meer, G.; Voelker, D. R.; Feigenson, G. W. Membrane Lipids: Where They Are and How They Behave. *Nat. Rev. Mol. Cell Biol.* **2008**, *9*, 112–124.
- (2) Alberts, B.; Johnson, A.; Lewis, J.; Raff, M.; Roberts, K.; Walter, P. *Molecular Biology of the Cell*, 4th ed.; Garland Science: New York, 2002.
- (3) Koynova, R.; Caffrey, M. Phases and Phase Transitions of the Phosphatidylcholines. *Biochim. Biophys. Acta* **1998**, *1376*, 91–145.
- (4) Cohen, Y.; Afri, M.; Frimer, A. A. NMR-Based Molecular Ruler for Determining the Depth of Intercalants within the Lipid Bilayer. Part II. The Preparation of a Molecular Ruler. *Chem. Phys. Lipids* **2008**, *155*, 114–119.
- (5) Vazdar, M.; Jurkiewicz, P.; Hof, M.; Jungwirth, P.; Cwiklik, L. Behavior of 4-Hydroxynonenal in Phospholipid Membranes. *J. Phys. Chem. B* **2012**, *116*, 6411–6415.
- (6) Orsi, M.; Essex, J. W. Passive Permeation Across Lipid Bilayers: A Literature Review. In *Molecular Simulations and Biomembranes*; Sansom, M. S. P., Biggin, P. C., Eds.; Royal Society of Chemistry: Cambridge, 2010; pp 76–90.
- (7) Seydel, J. K.; Wiese, M. *Drug-Membrane Interactions: Analysis, Drug Distribution, Modeling*; Mannhold, R., Kubinyi, H., Folkers, G., Eds.; Wiley-VCH Verlag GmbH: Weinheim, 2002; Vol. 4.
- (8) Palončyová, M.; Devane, R.; Murch, B.; Berka, K.; Otyepka, M. Amphiphilic Drug-Like Molecules Accumulate in a Membrane below the Head Group Region. *J. Phys. Chem. B* **2014**, *118*, 1030–1039.
- (9) Palončyová, M.; Berka, K.; Otyepka, M. Convergence of Free Energy Profile of Coumarin in Lipid Bilayer. *J. Chem. Theory Comput.* **2012**, *8*, 1200–1211.
- (10) Palončyová, M.; Berka, K.; Otyepka, M. Molecular Insight into Affinities of Drugs and Their Metabolites to Lipid Bilayers. *J. Phys. Chem. B* **2013**, *117*, 2403–2410.
- (11) Bemporad, D.; Luttmann, C.; Essex, J. W. Behaviour of Small Solutes and Large Drugs in a Lipid Bilayer from Computer Simulations. *Biochim. Biophys. Acta* **2005**, *1718*, 1–21.
- (12) Marrink, S. J.; Berendsen, H. J. C. Permeation Process of Small Molecules across Lipid Membranes Accumulate by Molecular Dynamics Simulations. *J. Phys. Chem.* **1996**, *100*, 16729–16738.
- (13) Orsi, M.; Sanderson, W. E.; Essex, J. W. Permeability of Small Molecules through a Lipid Bilayer: A Multiscale Simulation Study. *J. Phys. Chem. B* **2009**, *113*, 12019–12029.
- (14) Notman, R.; den Otter, W. K.; Noro, M. G.; Briels, W. J.; Anwar, J. The Permeability Enhancing Mechanism of DMSO in Ceramide Bilayers Simulated by Molecular Dynamics. *Biophys. J.* **2007**, *93*, 2056–2068.
- (15) Notman, R.; Anwar, J. Breaching the Skin Barrier - Insights from Molecular Simulation of Model Membranes. *Adv. Drug Delivery Rev.* **2012**, *65*, 237–250.
- (16) Das, C.; Noro, M. G.; Olmsted, P. D. Simulation Studies of Stratum Corneum Lipid Mixtures. *Biophys. J.* **2009**, *97*, 1941–1951.
- (17) Redmill, P. S.; McCabe, C. Molecular Dynamics Study of the Behavior of Selected Nanoscale Building Blocks in a Gel-Phase Lipid Bilayer. *J. Phys. Chem. B* **2010**, *114*, 9165–9172.
- (18) Naegel, A.; Heisig, M.; Wittum, G. Detailed Modeling of Skin Penetration—an Overview. *Adv. Drug Delivery Rev.* **2013**, *65*, 191–207.
- (19) Menon, G. K.; Cleary, G. W.; Lane, M. E. The Structure and Function of the Stratum Corneum. *Int. J. Pharm.* **2012**, *435*, 3–9.
- (20) Guy, R. H. Skin—“That Unfakeable Young Surface”. *Skin Pharmacol. Physiol.* **2013**, *26*, 181–189.

- (21) Janušová, B.; Skolová, B.; Tükörová, K.; Wojnarová, L.; Simůnek, T.; Mladěnka, P.; Filipický, T.; Říha, M.; Roh, J.; Palát, K.; et al. Amino Acid Derivatives as Transdermal Permeation Enhancers. *J. Controlled Release* **2013**, *165*, 91–100.
- (22) Vávrová, K.; Hrabálek, A.; Doležal, P.; Šámalová, L.; Palát, K.; Zbytovská, J.; Holas, T.; Klimentová, J. Synthetic Ceramide Analogues as Skin Permeation Enhancers: Structure–Activity Relationships. *Bioorg. Med. Chem.* **2003**, *11*, 5381–5390.
- (23) Xiang, T. X.; Anderson, B. D. Permeability of Acetic Acid across Gel and Liquid-Crystalline Lipid Bilayers Conforms to Free-Surface-Area Theory. *Biophys. J.* **1997**, *72*, 223–237.
- (24) Bolzinger, M.-A.; Briçon, S.; Pelletier, J.; Chevalier, Y. Penetration of Drugs through Skin, a Complex Rate-Controlling Membrane. *Curr. Opin. Colloid Interface Sci.* **2012**, *17*, 156–165.
- (25) Hadgraft, J.; Lane, M. E. Skin: The Ultimate Interface. *Phys. Chem. Chem. Phys.* **2011**, *13*, 5215–5222.
- (26) De Jager, M.; Groenink, W.; Bielsa i Guivernau, R.; Andersson, E.; Angelova, N.; Ponec, M.; Bouwstra, J. A Novel in Vitro Percutaneous Penetration Model: Evaluation of Barrier Properties with p-Aminobenzoic Acid and Two of Its Derivatives. *Pharm. Res.* **2006**, *23*, 951–960.
- (27) Forslind, B. A Domain Mosaic Model of the Skin Barrier. *Acta Derm. Venerol.* **1994**, *74*, 1–6.
- (28) Norlén, L. Current Understanding of Skin Barrier Morphology. *Skin Pharmacol. Physiol.* **2013**, *26*, 213–216.
- (29) Rim, J. E.; Pinsky, P. M.; van Osdol, W. W. Multiscale Modeling Framework of Transdermal Drug Delivery. *Ann. Biomed. Eng.* **2009**, *37*, 1217–1229.
- (30) Iwai, I.; Han, H.; Hollander, L. Den; Svensson, S.; Ofverstedt, L.-G.; Anwar, J.; Brewer, J.; Bloksgaard, M.; Laloëuf, A.; Nosek, D.; et al. The Human Skin Barrier Is Organized as Stacked Bilayers of Fully Extended Ceramides with Cholesterol Molecules Associated with the Ceramide Sphingoid Moiety. *J. Invest. Dermatol.* **2012**, *132*, 1–11.
- (31) Klamt, A.; Huniar, U.; Spycher, S.; Keldenich, J. COSMOmic: A Mechanistic Approach to the Calculation of Membrane–Water Partition Coefficients and Internal Distributions within Membranes and Micelles. *J. Phys. Chem. B* **2008**, *112*, 12148–12157.
- (32) Ingram, T.; Storm, S.; Kloss, L.; Mehling, T.; Jakobtorweihen, S.; Smirnova, I. Prediction of Micelle/Water and Liposome/Water Partition Coefficients Based on Molecular Dynamics Simulations, COSMO-RS, and COSMOmic. *Langmuir* **2013**, *29*, 3527–3537.
- (33) Jakobtorweihen, S.; Ingram, T.; Smirnova, I. Combination of COSMOmic and Molecular Dynamics Simulations for the Calculation of Membrane–Water Partition Coefficients. *J. Comput. Chem.* **2013**, *34*, 1332–1340.
- (34) Palončyová, M.; Fabre, G.; Devane, R. H.; Trouillas, P.; Berka, K.; Otyepka, M. Benchmarking of Force Fields for Molecule – Membrane Interactions. *J. Chem. Theory Comput.* **2014**, *10*, 4143–4151.
- (35) Domański, J.; Stansfeld, P. J.; Sansom, M. S. P.; Beckstein, O. Lipidbook: A Public Repository for Force-Field Parameters Used in Membrane Simulations. *J. Membr. Biol.* **2010**, *236*, 255–258.
- (36) Siu, S. W. I.; Vácha, R.; Jungwirth, P.; Böckmann, R. a. Biomolecular Simulations of Membranes: Physical Properties from Different Force Fields. *J. Chem. Phys.* **2008**, *128*, 125103.
- (37) Berger, O.; Edholm, O.; Jahnig, F. Molecular Dynamics Simulations of a Fluid Bilayer of Dipalmitoylphosphatidylcholine at Full Hydration, Constant Pressure and Constant Temperature. *Biophys. J.* **1997**, *72*, 2002–2013.
- (38) Berendsen, H. J. C.; Postma, J. P. M.; van Gunsteren, W. F.; Hermans, J. Interaction Models for Water in Relation to Protein Hydration. In *Intermolecular Forces*; Pullman, B., Ed.; Reidel Publishing Company: Dordrecht, 1981; pp 331–338.
- (39) Berendsen, H. J. C.; Grigera, J. R.; Straatsma, T. P. The Missing Term in Effective Pair Potentials. *J. Phys. Chem.* **1987**, *91*, 6269–6271.
- (40) Shah, J.; Atienza, J. M.; Rawlings, A. V.; Shipley, G. G. Physical Properties of Ceramides: Effect of Fatty Acid Hydroxylation. *J. Lipid Res.* **1995**, *36*, 1945–1955.
- (41) Hoopes, M. I.; Noro, M. G.; Longo, M. L.; Faller, R. Bilayer Structure and Lipid Dynamics in a Model Stratum Corneum with Oleic Acid. *J. Phys. Chem. B* **2011**, *115*, 3164–3171.
- (42) Schüttelkopf, A. W.; van Aalten, D. M. F. PRODRG: A Tool for High-Throughput Crystallography of Protein-Ligand Complexes. *Acta Crystallogr., Sect. D: Biol. Crystallogr.* **2004**, *60*, 1355–1363.
- (43) Frisch, M. J.; Trucks, G. W.; Schlegel, H. B.; Scuseria, G. E.; Robb, M. A.; Cheeseman, J. R.; Montgomery, Jr., J. A.; Vreven, T.; Kudin, K. N.; Burant, J. C.; et al. *Gaussian 03, Revision E.01*; Gaussian, Inc.: Wallingford, CT, 2004.
- (44) Lemkul, J. A.; Allen, W. J.; Bevan, D. R. Practical Considerations for Guiding GROMOS-Compatible Small-Molecule Topologies. *J. Chem. Inf. Model.* **2010**, *50*, 2221–2235.
- (45) Cieplak, P.; Caldwell, J.; Kollman, P. Molecular Mechanical Models for Organic and Biological Systems Going Beyond the Atom Centered Two Body Additive Approximation: Aqueous Solution Free Energies of Methanol and N-Methyl Acetamide, Nucleic Acid Base, and Amide Hydrogen Bonding and Chloroform/. *J. Comput. Chem.* **2001**, *22*, 1048–1057.
- (46) Case, D. A.; Darden, T. A.; Cheatham, T. E., III; Simmerling, C. L.; Wang, J.; Duke, R. E.; Luo, R.; Walker, R. C.; Zhang, W.; Merz, K. M.; et al. *AMBER 11*; University of California: San Francisco, 2010.
- (47) Hess, B.; Kutzner, C.; van der Spoel, D.; Lindahl, E. GROMACS 4: Algorithms for Highly Efficient, Load-Balanced, and Scalable Molecular Simulation. *J. Chem. Theory Comput.* **2008**, *4*, 435–447.
- (48) Hess, B.; Bekker, H.; Berendsen, H. J. C.; Fraaije, J. G. E. M. LINC: A Linear Constraint Solver for Molecular Simulations. *J. Comput. Chem.* **1997**, *18*, 1463–1472.
- (49) Bussi, G.; Donadio, D.; Parrinello, M. Canonical Sampling Through Velocity Rescaling. *J. Chem. Phys.* **2007**, *126*, 014101.
- (50) Eckert, F.; Klamt, A.; Gmbh, C.; kg, C.; Leverkusen, D. Fast Solvent Screening via Quantum Chemistry. *COSMO-RS Approach.* **2002**, 369–385.
- (51) Tieleman, D. P.; Marrink, S. J.; Berendsen, H. J. C. A Computer Perspective of Membranes: Molecular Dynamics Studies of Lipid Bilayer Systems. *Biochim. Biophys. Acta* **1997**, *1331*, 235–270.
- (52) Taylor, J.; Whiteford, N. E.; Bradley, G.; Watson, G. W. Validation of All-Atom Phosphatidylcholine Lipid Force Fields in the Tensionless NPT Ensemble. *Biochim. Biophys. Acta* **2009**, *1788*, 638–649.
- (53) Leftin, A.; Brown, M. F. An NMR Database for Simulations of Membrane Dynamics. *Biochim. Biophys. Acta* **2011**, *1808*, 818–839.
- (54) Leekumjorn, S.; Sum, A. K. Molecular Studies of the Gel to Liquid-Crystalline Phase Transition for Fully Hydrated DPPC and DPPE Bilayers. *Biochim. Biophys. Acta* **2007**, *1768*, 354–365.
- (55) Neale, C.; Bennett, W. F. D.; Tieleman, D. P.; Pomès, R. Statistical Convergence of Equilibrium Properties in Simulations of Molecular Solutes Embedded in Lipid Bilayers. *J. Chem. Theory Comput.* **2011**, *7*, 4175–4188.
- (56) Boggara, M. B.; Krishnamoorti, R. Partitioning of Nonsteroidal Antiinflammatory Drugs in Lipid Membranes: A Molecular Dynamics Simulation Study. *Biophys. J.* **2010**, *98*, 586–595.
- (57) Orsi, M.; Essex, J. W. Permeability of Drugs and Hormones through a Lipid Bilayer: Insights from Dual-Resolution Molecular Dynamics. *Soft Matter* **2010**, *6*, 3797–3808.
- (58) Rowe, E. S.; Zhang, F.; Leung, T. W.; Parr, J. S.; Guy, P. T. Thermodynamics of Membrane Partitioning for a Series of N-Alcohols Determined by Titration Calorimetry: Role of Hydrophobic Effects. *Biochemistry* **1998**, *37*, 2430–2440.
- (59) Xiang, T.; Anderson, B. D. Phospholipid Surface Density Determines the Partitioning and Permeability of Acetic Acid in DMPC:Cholesterol Bilayers. *J. Membr. Biol.* **1995**, *167*, 157–167.
- (60) Marrink, S.-J.; Berendsen, H. J. C. Simulation of Water Transport through a Lipid Membrane. *J. Phys. Chem.* **1994**, *98*, 4155–4168.



Cite this: *Chem. Commun.*, 2015, 51, 7713

Received 22nd January 2015,
Accepted 30th March 2015

DOI: 10.1039/c5cc00636h

www.rsc.org/chemcomm

Synergism of antioxidant action of vitamins E, C and quercetin is related to formation of molecular associations in biomembranes†

Gabin Fabre,^{ab} Imene Bayach,^a Karel Berka,^b Markéta Paloncýová,^b Marcelina Starok,^c Claire Rossi,^c Jean-Luc Duroux,^a Michal Otyepka^{*b} and Patrick Trouillas^{*bd}

Vitamins E, C and polyphenols (flavonoids and non-flavonoids) are major natural antioxidants capable of preventing damage generated by oxidative stress. Here we show the capacity of these antioxidants to form non-covalent association within lipid bilayers close to the membrane/cytosol interface. Antioxidant regeneration is significantly enhanced in these complexes.

Over the last decades, natural antioxidants have attracted increasing interest, largely because they have been shown to exhibit preventive effects against various disorders caused by oxidative stress, including cardiovascular and neurodegenerative diseases, ageing and also certain cancers.¹ Despite recent progress in the field, there are still many open and fundamental questions concerning antioxidant mechanisms and biological targets, and the exact role in various pathologies is still under scrutiny.² A deep understanding of antioxidant action is mandatory for a safe and efficient usage in nutrition, health prevention, cosmetics and food preservation. Most of the known antioxidants are efficient scavengers of reactive oxygen species (ROS), which are over-produced during oxidative stress. Oxidation of lipids (namely lipid peroxidation, LPO) is a major process in oxidative stress, which is initiated by various endogenous (*e.g.*, inflammation, enzymatic processes) or exogenous (*e.g.*, radiation, smoking, pollution) effects. The propagation stage of LPO³ can be inhibited by lipophilic or amphiphilic antioxidants sufficiently incorporated in lipid bilayers.⁴ In addition, hydrophilic and polar antioxidants are able to scavenge ROS that diffuse toward membranes, thus inhibiting the initiation stage of LPO. Vitamin E (α -tocopherol,

henceforth referred to as vitE),⁵ vitamin C (ascorbic acid, vitC) and natural polyphenols are major antioxidants found in food. Depending on their bioavailability,^{2,6} these antioxidants are known to be highly efficient ROS scavengers in different phases, namely vitE in membranes,^{7,8} vitC in plasma or cytosol⁹ and flavonoids at the membrane/water interface.^{4,10} When acting simultaneously, their overall antioxidant activity is synergistically enhanced.^{3,11,12} Free radical scavenging by vitE yields the corresponding α -tocopheroxyl radical by hydrogen atom transfer (HAT), which in turn can be regenerated back to vitE by vitC.^{3,11,12} This synergistic effect has been shown enhanced by flavonoids,^{11–13} which are efficient hydrogen atom donor antioxidants.^{14,15}

Here, we present a molecular description of the interaction between vitE, vitC and a representative flavonoid antioxidant, namely quercetin¹⁶ (Fig. 1), in lipid bilayer membranes. Using both *in vitro* and *in silico* models, the formation of mutual associations at the membrane/water interface is described for the first time. This description enables better rationalization of vitE regeneration by vitC, which is often enhanced in the presence of flavonoids.

The penetration and positioning of vitC, vitE and quercetin in membrane was evaluated using a lipid bilayer model comprising DOPC molecules, as phosphatidylcholines are major components of biological membranes in plant and animal cells.¹⁷ Molecular dynamic (MD) simulations were used, which have been repeatedly shown to predict the positioning of small molecules in lipid bilayers in agreement with experimental data.^{4,18–20} The behavior of those three (non-interacting) antioxidants was evaluated by

^a LCSN EA1069, Univ. Limoges, Faculté de Pharmacie, 2 rue du Docteur Marcland, 87025 Limoges Cedex, France

^b Regional Centre of Advanced Technologies and Materials, Department of Physical Chemistry, Faculty of Science, Palacký University, tř. 17 listopadu 12, 771 46 Olomouc, Czech Republic. E-mail: michal.otyepka@upol.cz

^c FRE CNRS 3580, Génie Enzymatique et Cellulaire, Université de Technologie de Compiègne, CS 60319, 60203 Compiègne, France

^d UMR 850 INSERM, Univ. Limoges, Faculté de Pharmacie, 2 rue du Docteur Marcland, 87025 Limoges Cedex, France. E-mail: patrick.trouillas@unilim.fr

† Electronic supplementary information (ESI) available. See DOI: 10.1039/c5cc00636h

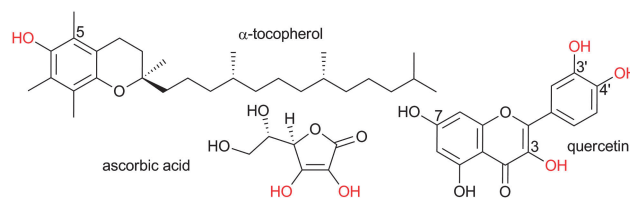


Fig. 1 Antioxidant compounds evaluated in this study. The active antioxidant OH groups (prone to HAT) are shown in red.

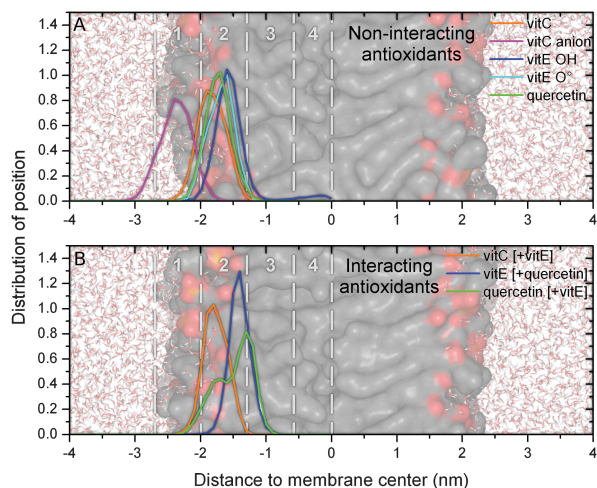


Fig. 2 Position of center of mass of vitC and quercetin, and the antioxidant OH group of vitE in DOPC. (A) Individual molecules, (B) close contact pairs.

placing a single molecule in the lipid bilayer model during the MD simulations.

The simulations showed that vitE localizes below the membrane/water interface and can penetrate through the membrane center. The peak position of the C5-methyl group of vitE was found to be 1.5 ± 0.3 nm from the bilayer center (Fig. 2A), which agrees with recent experimental data in DOPC bilayers (1.7 ± 0.4 nm).⁸ The OH group of vitE, which is responsible for free radical scavenging by HAT,²¹ was mainly located close to the lipid polar head groups, *i.e.*, at the lipid/water interface suggesting inhibition of both the LPO-initiation (directly) and LPO-propagation (if the lipid chains adopt a transient snorkel-like shape^{8,22}). Moreover, flip-flops may occur with an energetic barrier of 0.65 kcal mol⁻¹ as obtained by COSMOmic (Fig. S1, ESI[†]). This roughly corresponds to an occurrence of 1 flip-flop event every 1 μ s at a 10^{-6} μ M concentration, in agreement with observations from our MD simulations. The flip-flop process is accompanied by the transient presence of the active OH group inside the bilayer (Fig. 2A) hence scavenging the deeply buried peroxy radicals and playing a direct role in inhibition of LPO-propagation.

VitC is less buried in the lipid bilayer than vitE and resides in the outer layer close to the water phase (1.9 ± 0.3 nm) because of the lower lipophilicity of vitC with respect to vitE. Interestingly, the average location of quercetin and its aryloxy radical formed under oxidative stress (1.7 ± 0.3 nm) was found to lie between that of vitC and vitE (Fig. 2A). The flip-flop of quercetin is much less efficient than that of vitE, due to higher energetic barrier of 10.2 kcal mol⁻¹ (Fig. S1, ESI[†]), corresponding to a 1 s time-scale occurrence at 10^{-6} μ M.

Under physiological conditions (pH 7.4) and in an aqueous environment, vitC and quercetin are deprotonated (first pK_a equal 4.2 and 5.7 in water for vitC and quercetin, respectively). As expected²³ the corresponding anions lie outside the membrane (Fig. 2A) *i.e.* 2.5 ± 0.3 nm and 2.4 ± 0.2 nm for ascorbate and the phenolate form of quercetin (deprotonated at C-7), respectively. Acid-base equilibrium is likely to occur in the overlapping regions with the protonated forms (Fig. 2A).

The lateral (x,y -plane) diffusion coefficients of vitC, quercetin and vitE were 17 ± 2 , 17 ± 2 and $22 \pm 5 \times 10^{-8}$ cm² s⁻¹, respectively, as obtained from averaging MD trajectories (Table S1, ESI[†]). These values are in agreement with the experimental self-diffusion coefficients of DOPC at 313 K (14×10^{-8} cm² s⁻¹),²⁴ confirming that the MD simulation time was sufficient to allow correct sampling of all intermolecular motions. The diffusion coefficients along the z -axis were lower by one order-of-magnitude for the three antioxidants (Table S1, ESI[†]), confirming rather extended residence time in the equilibrium locations.

According to the respective locations of the three studied antioxidants, quercetin may act (i) by scavenging free radicals diffusing into the membrane like vitE, both quercetin and vitE being regenerated by vitC; and/or (ii) as vitE regenerator, thus enhancing the regeneration by acting in synergy alongside vitC. The active OH group of vitE overlapped that of the center of mass of vitC and quercetin in the head group region (Fig. 2A) highlighting the proximity of the three antioxidants, so that the formation of mutual complexes seems likely, in the membrane layer close to the surface.

To confirm that such intermolecular complexes can be formed in the membrane, a series of 300 ns free MD simulations of the lipid bilayer containing several vitC, vitE and quercetin molecules was performed. This procedure allowed sufficient sampling of all possible non-covalent rearrangements and interactions (see Methodology, ESI[†]). During the MD simulations, long-lasting (>90% of the time) and close-contact pairs were observed, namely hetero-association complexes quercetin:vitE, quercetin:vitC and vitC:vitE, and self-association complexes quercetin:quercetin and vitE:vitE (Fig. S2, Table S2, ESI[†]). An extensive set of one hundred of 100 ns-long MD simulations quantified formation of self- and hetero-association, amounting to 27:45:28% for quercetin:quercetin, quercetin:vitE and vitE:vitE, respectively (Table S3, ESI[†]). This does not significantly differ from a random distribution (25:50:25%); however, this should be interpreted with care, as the sampling is still quite limited despite all the effort.

The driving force of such non-covalent association was thoroughly analyzed with quantum chemical calculations. Quercetin:quercetin, quercetin:vitE and vitE:vitE pairs were mainly held together by π -stacking interactions, whereas pairs involving vitC were stabilized only by intermolecular H-bonding. The stability of these non-covalent interactions was confirmed with density functional theory (DFT) augmented by an empirical dispersion term, namely B3P86-D2 recently re-parameterized to accurately evaluate stabilities of polyphenol non-covalent complexes.²⁵ Different intermolecular arrangements were predicted, namely head-to-head and head-to-tail, in which the importance of π -stacking (ring-to-ring distance of around 3.6 Å, as typical for π -stacking of aromatic rings²⁶) and H-bonding was confirmed (see Fig. 3 for the most stable geometries and Dataset S1 for all xyz geometries).

The *in vacuo* enthalpies of association ranged from -24.4 to -10.8 kcal mol⁻¹ (Table 1). The presence of aqueous environment lowered the absolute values of these association enthalpies by 10.0, 5.8, 8.0 and 14.2 kcal mol⁻¹ for quercetin:vitE, quercetin:vitC,

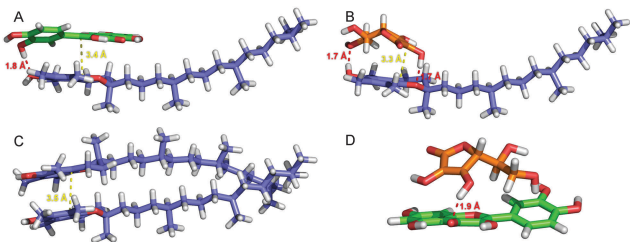


Fig. 3 Most stable associations as obtained from DFT-D. (A) Quercetin: vitE, (B) vitC: vitE, (C) vitE: vitE, and (D) quercetin: vitC.

Table 1 Association energies and enthalpies (kcal mol^{-1}) calculated as the difference in energy (enthalpy) between the most stable complex and the isolated fragments, in the gas phase and in PCM-type benzene and water solvents. Negative values indicate that the association is thermodynamically favored compared to the pair of isolated fragments quercetin and vitE

System	ΔE_{gas}	ΔH_{gas}	$\Delta H_{\text{C}_6\text{H}_6}$	$\Delta H_{\text{H}_2\text{O}}$
Quercetin: vitE	-15.8	-15.1	-9.0	-5.1
Quercetin: vitC	-11.1	-10.8	-9.3	-5.0
VitC: vitE	-15.4	-15.3	-9.0	-7.2
VitE: vitE	-28.0	-24.4	-13.6	-10.2
Quercetin: quercetin	-13.7 ^a	—	—	—

^a From ref. 25 with B3P86-D2/cc-pVDZ (BSSE corrected).

vitC: vitE and vitE: vitE, respectively (Table 1). An entropy loss is expected accompanying formation of the non-covalent complexes, probably counterbalancing the strongly negative enthalpies of association. However, this entropy loss is most probably lower in the organized membrane phase with respect to vacuum²⁷ (see Methodology section, ESI[†]).

In any event, the quantum calculations confirmed that the associations are stabilized by a combination of intermolecular hydrogen bonding and π -stacking. According to this quantum evaluation, attractive forces definitely exist between the three antioxidants, favoring the formation of non-covalent (self- and hetero-) associations of antioxidants.

An experimental confirmation was obtained from the fluorescence quenching of vitE embedded in DOPC liposomes in the presence of quercetin, added at increasing concentrations. VitE-containing liposomes were formed by addition of vitE to DOPC prior to liposome formation. These liposomes were then pelleted and re-suspended in buffer by a double ultra-centrifugation/re-suspension procedure so that non-inserted vitE molecules were discarded (see Materials and methods for details, ESI[†]). Following this procedure, the measured vitE fluorescence (Fig. 4A, condition: 0 μM of quercetin) was unambiguously assigned to vitE molecules embedded in the bilayer and not lying on the liposome surface.

With increasing quercetin concentration to the vitE-containing liposomes, a significant decrease in vitE fluorescence intensity was observed (Fig. 4A). Quercetin did not exhibit any fluorescence when excited at 291 nm (excitation wavelength of vitE, Fig. S3A, ESI[†]) in both aqueous solutions and liposomes (Fig. S3, ESI[†]), therefore ruling out interference. The quercetin concentration-dependent fluorescence quenching thus suggests that (i) quercetin molecules have the capacity to insert into the DOPC bilayer, and (ii) quercetin: vitE complexes are formed.

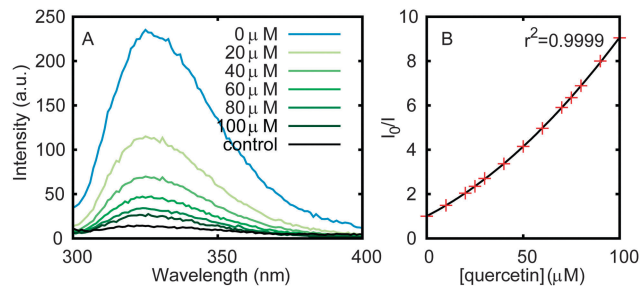


Fig. 4 Fluorescence emission of vitE in liposomes with increasing concentrations of quercetin (0 to 100 μM). (A) Fluorescence spectra, (B) Stern–Volmer plot. VitE was excited at $\lambda_{\text{exc}} = 291 \text{ nm}$ after incorporation into liposomes. The control condition was performed by incubation of vitE (50 μM) with vitE-free DOPC liposomes. Prior to quercetin addition, the non inserted vitE molecules were eliminated from the liposome suspension by double centrifugation and resuspension.

The $I_0/I = f([\text{quercetin}])$ Stern–Volmer plot is clearly non-linear and follows a quadratic function (Fig. 4B), which is unambiguously attributed to the presence of both static and dynamic quenching.²⁸ The linearity of $[I_0/I - 1]/[\text{quercetin}] = f([\text{quercetin}])$ also confirms this concomitant quenching (Fig. S4, ESI[†]). The confirmed occurrence of static quenching supports the results of MD simulations, indicating that quercetin penetrates the membrane and forms non-covalent complexes with vitE.

Our findings help to rationalize the results of previous experimental studies showing that addition of flavonoids synergistically increases the antioxidant activity of a vitE and vitC mixture in membranes.¹¹ The existence of non-covalent complexes between these antioxidants explains how pairs can dramatically improve LPO inhibition by increasing intermolecular contacts between antioxidants, enhancing recycling and subsequent synergic effects.

Indeed, from a thermodynamic point of view, the capacity of regeneration is confirmed by comparing the bond dissociation enthalpies (BDEs) of the most labile hydroxyl group of each antioxidant (Fig. 1). The BDEs were calculated as 75.5, 78.7, and 78.7 kcal mol^{-1} for vitE, quercetin (4'-OH group) and vitC, respectively. These low values agree with previous experimental data that have been strongly supported theoretically,^{15,29} showing that these three compounds have a strong capacity to scavenge free radicals by HAT. The BDE values were similar for all three compounds, which indicates that HAT between the different antioxidants (native or oxidized) is thermodynamically allowable *i.e.*, enabling the regeneration process. The only limitation to this process is the capacity of two antioxidants to come into contact. Here, we have shown that non-covalent interactions (mainly π -stacking and hydrogen bonding) drive this association process and put in close contact the active OH groups (Fig. 3 and Fig. S2, ESI[†]). This geometrically and statistically enables quercetin undergo HAT towards vitE to regenerate it. Because the BDEs of both compounds are rather close in energy, the reverse process (regeneration of quercetin by vitE) is likely as well, despite being less preferred. Due to π -stacking interactions between aromatic rings in a given complex, electron transfer between the two π -conjugated antioxidant partners is also likely to occur.

These effects would be even more enhanced in larger aggregates, e.g. in nanodomains (lipid rafts). VitE has already been experimentally shown to preferentially localize in lipid rafts.³⁰ Aggregation and formation of domains have also been evidenced at the membrane surface for catechin derivatives,³¹ but also inside the bilayer for quercetin²³ and curcumin.¹⁹

The average position of the non-covalent associations in the membrane was also evaluated. No significant location difference was detected between the antioxidants in the complexes and their respective individual partners, except for quercetin: vitE. Indeed, in these pairs, quercetin exhibited a probability density with two peaks (Fig. 2B). Although 50% of the quercetin molecules remained at a similar location to the individual molecules (1.7 ± 0.2 nm), 50% were pulled deeper into the membrane (1.3 ± 0.1 nm). This latter location allows the quercetin: vitE pair to span a larger part of membrane with respect to the non-interacting quercetin. This shift towards the center of the membrane may increase the capacity of quercetin to directly inhibit the propagation stage of LPO by scavenging lipid peroxy free radicals, which may also contribute to the synergetic effects.

We have presented a molecular insight into the synergism of vitE, vitC and polyphenols. Our results showed that vitE can reach vitC in the polar head group region of the membrane and form associations that favor its recycling. Quercetin can readily form non-covalent associations with vitE and vitC in membranes, therefore enabling regeneration of vitE and mediating vitE regeneration by vitC. The occurrence of such associations should be systematically considered to support the research in new cocktails of collaborative antioxidants.

CALI, Czech Science Foundation (P208/12/G016), Ministry of Education, Youth and Sports of Czech Rep. (LO1305), ECOP-ESF (CZ.1.07/2.3.00/20.0058), Marie Curie RTN CHEBANA, FP7 ITN 2010-264772, and ADF are gratefully acknowledged.

Notes and references

- M. Valko, D. Leibfritz, J. Moncol, M. T. D. Cronin, M. Mazur and J. Telsler, *Int. J. Biochem. Cell Biol.*, 2007, **39**, 44–84.
- O. Dangles, *Curr. Org. Chem.*, 2012, **16**, 692–714.
- E. Niki, Y. Yoshida, Y. Saito and N. Noguchi, *Biochem. Biophys. Res. Commun.*, 2005, **338**, 668–676.
- P. Košinová, K. Berka, M. Wykes, M. Otyepka and P. Trouillas, *J. Phys. Chem. B*, 2011, **116**, 1309–1318; P. Podloucká, K. Berka, G. Fabre, M. Palonciová, J.-L. Duroux, M. Otyepka and P. Trouillas, *J. Phys. Chem. B*, 2013, **117**, 5043–5049.
- M. G. Traber and J. Atkinson, *Free Radical Biol. Med.*, 2007, **43**, 4–15.
- C. Manach, G. Williamson, C. Morand, A. Scalbert and C. Rémésy, *Am. J. Clin. Nutr.*, 2005, **81**, 230S–242S; J. M. Landete, *Crit. Rev. Food Sci. Nutr.*, 2012, **52**, 936–948.
- J. Atkinson, T. Harroun, S. R. Wassall, W. Stillwell and J. Katsaras, *Mol. Nutr. Food Res.*, 2010, **54**, 641–651.
- D. Marquardt, J. A. Williams, N. Kučerka, J. Atkinson, S. R. Wassall, J. Katsaras and T. A. Harroun, *J. Am. Chem. Soc.*, 2013, **135**, 7523–7533.
- J. M. May, *FASEB J.*, 1999, **13**, 995–1006.
- B. Pawlikowska-Pawłęga, W. Ignacy Gruszecki, L. Misiak, R. Paduch, T. Piersiak, B. Zarzyka, J. Pawelec and A. Gawron, *Biochim. Biophys. Acta, Biomembr.*, 2007, **1768**, 2195–2204.
- A. Nègre-Salvayre, A. Affany, C. Hariton and R. Salvayre, *Pharmacology*, 1991, **42**, 262–272; C.-Y. Che, P. E. Milbury, K. Lapsley and J. B. Blumberg, *J. Nutr.*, 2005, **135**, 1366–1373; S. Fujisawa, M. Ishihara, T. Atsumi and Y. Kadoma, *In Vivo*, 2006, **20**, 445–452.
- P. Lambelet, F. Saucy and J. Lölliger, *Experientia*, 1985, **41**, 1384–1388; L. Hon-Wing, M. J. Vang and R. D. Mavis, *Biochim. Biophys. Acta, Lipids Lipid Metab.*, 1981, **664**, 266–272; M. Scarpa, A. Rigo, M. Maiorino, F. Ursini and C. Gregolin, *Biochim. Biophys. Acta*, 1984, **801**, 215–219; D. C. Liebler, D. S. Kling and D. J. Reed, *J. Biol. Chem.*, 1986, **261**, 12114–12119; K. Fukuzawa, *J. Nutr. Sci. Vitaminol.*, 2008, **54**, 273–285.
- K. Mukai, S. Itoh and H. Morimoto, *J. Biol. Chem.*, 1992, **267**, 22277–22281; Q. Y. Zhu, Y. Huang, D. Tsang and Z.-Y. Chen, *J. Agric. Food Chem.*, 1999, **47**, 2020–2025; K. Mukai, S. Mitani, K. Ohara and S.-I. Nagaoka, *Free Radical Biol. Med.*, 2005, **38**, 1243–1256.
- K. Mukai, S. Nagai and K. Ohara, *Free Radical Biol. Med.*, 2005, **39**, 752–761.
- F. Di Meo, V. Lemaury, J. Cornil, R. Lazzaroni, J.-L. Duroux, Y. Olivier and P. Trouillas, *J. Phys. Chem. A*, 2013, **117**, 2082–2092; M. Leopoldini, N. Russo and M. Toscano, *Food Chem.*, 2011, **125**, 288–306.
- A. W. Boots, G. R. M. M. Haenen and A. Bast, *Eur. J. Pharmacol.*, 2008, **585**, 325–337.
- G. van Meer, D. R. Voelker and G. W. Feigenson, *Nat. Rev. Mol. Cell Biol.*, 2008, **9**, 112–124.
- W. Kopeček, J. Telenius and H. Khandelia, *FEBS J.*, 2013, **280**, 2785–2805.
- S. M. Loverde, *J. Phys. Chem. Lett.*, 2014, **5**, 1659–1665.
- M. Palonciová, K. Berka and M. Otyepka, *J. Chem. Theory Comput.*, 2012, **8**, 1200–1211; M. Palonciová, G. Fabre, R. H. DeVane, P. Trouillas, K. Berka and M. Otyepka, *J. Chem. Theory Comput.*, 2014, **10**, 4143–4151.
- C. Schneider, *Mol. Nutr. Food Res.*, 2005, **49**, 7–30.
- J. Garrec, A. Monari, X. Assfeld, L. M. Mir and M. Tarek, *J. Phys. Chem. Lett.*, 2014, **5**, 1653–1658.
- L. Movileanu, I. Neagoe and M. L. Flonta, *Int. J. Pharm.*, 2000, **205**, 135–146.
- A. Filippov, G. Oradd and G. Lindblom, *Biophys. J.*, 2003, **84**, 3079–3086.
- F. Di Meo, J. C. Sancho Garcia, O. Dangles and P. Trouillas, *J. Chem. Theory and Comput.*, 2012, **8**, 2034–2043.
- K. E. Riley and P. Hobza, *Wiley Interdiscip. Rev.: Comput. Mol. Sci.*, 2011, **1**, 3–17.
- X. Siebert and L. M. Amzel, *Proteins: Struct., Funct., Bioinf.*, 2004, **54**, 104–115.
- M. Hof, R. Hutterer and V. Fidler, *Fluorescence Spectroscopy in Biology: Advanced Methods and their Applications to Membranes, Proteins, DNA, and Cells*, Springer Science & Business Media, 2006; L. K. Fraiji, D. M. Hayes and T. C. Werner, *J. Chem. Educ.*, 1992, **69**, 424.
- P. Trouillas, P. Marsal, D. Siri, R. Lazzaroni and J.-L. Duroux, *Food Chem.*, 2006, **97**, 679–688.
- S. Lemaire-Ewing, C. Desrumaux, D. Néel and L. Lagrost, *Mol. Nutr. Food Res.*, 2010, **54**, 631–640.
- T. W. Sirk, E. F. Brown, M. Friedman and A. K. Sum, *J. Agric. Food Chem.*, 2009, **57**, 6720–6728.

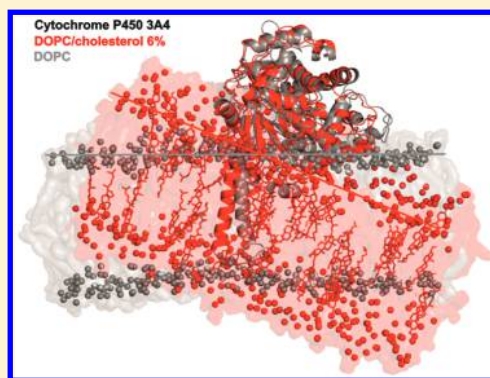
Effect of Cholesterol on the Structure of Membrane-Attached Cytochrome P450 3A4

Veronika Navrátilová, Markéta Paloncýová, Michaela Kajšová, Karel Berka,* and Michal Otyepka*

Regional Centre of Advanced Technologies and Materials, Department of Physical Chemistry, Faculty of Science, Palacký University Olomouc, tř. 17. listopadu 12, 771 46, Olomouc, Czech Republic

Supporting Information

ABSTRACT: Cholesterol is a widely researched component of biological membranes that significantly influences membrane properties. Human cytochrome P450 3A4 (CYP3A4) is an important drug-metabolizing enzyme, wherein the catalytic domain is attached to a membrane by an N-terminal α -helical transmembrane anchor. We analyzed the behavior of CYP3A4 immersed in a 1,2-dioleoyl-*sn*-glycero-3-phosphocholine (DOPC) membrane with various amounts of cholesterol. The presence of cholesterol caused ordering and thickening of the membrane and led to greater immersion and inclination of CYP3A4 toward the membrane. Cholesterol also lowered the flexibility of and tended to concentrate around membrane-immersed parts of CYP3A4. Further, the pattern of the CYP3A4 active-site access channels was altered in the presence of cholesterol. In summary, cholesterol in the membrane affected the positioning and structural features of CYP3A4, which in turn may have implications for the activity of this enzyme in various membranes and membrane parts with different cholesterol content.



INTRODUCTION

Human cytochrome P450 (CYP) enzymes are involved in biotransformation processes of endogenous compounds and xenobiotics. Although they typically catalyze monooxygenation reactions, their catalytic potential is more diverse.^{1,2} CYPs attach to membranes of the endoplasmic reticulum (ER) and mitochondria³ by an N-terminal anchor, and their catalytic domains are partially immersed in the membrane.^{4–6} It has been suggested that the membrane is not merely a passive medium but may actively contribute to the biotransformation processes by accumulation of nonpolar compounds.^{7–9} Such compounds may also enter the CYP active site from the membrane via the active-site access channels.^{5,6,9,10} The behavior of CYP on a membrane may be affected by the membrane composition and in turn the breathing (dynamical opening/closing) of access channels.^{6,11} Moreover, CYP activity is dependent on the presence of certain redox partners, which attach to the membrane via transmembrane helices.^{12,13} Thus, it is important to gain a deeper understanding of the role of membranes in the above-mentioned processes.

Direct structural insight into the behavior of membrane-anchored enzymes is still very challenging for experimental techniques. Until now, only NMR^{14,15} and linear dichroism¹⁶ measurements have been able to provide direct information on the membrane attachment of CYPs. It took more than 10 years after publication of the first X-ray structure of mammalian CYP¹⁷ for the first crystal structure of CYP to be reported, which showed a resolved N-terminal anchor but only applied to outside the membrane environment.¹⁸ However, it has been

shown that missing information on the structural behavior of CYP on membrane can be gleaned by molecular dynamics (MD) simulations.^{6,11} As the membranes of mitochondria and the ER are mainly composed of phosphatidylcholines, MD studies have so far largely focused on lipid bilayers consisting of unsaturated phospholipids, such as 1,2-dioleoyl-*sn*-glycero-3-phosphocholine (DOPC)^{5,6} and 1-palmitoyl-2-oleoyl-*sn*-glycero-3-phosphocholine (POPC),^{9,11,19,20} and membrane-mimicking models.¹⁶ A recent study on membrane anchored aromatase considered the more complex composition of the ER membrane.²¹ However, to date, no systematic study into the effect of membrane composition on the positioning of CYP has been published.

The ER membrane comprises glycerolipids, such as phosphatidylcholine (PC), phosphatidylethanolamine (PE), phosphatidylinositol (PI), and phosphatidylserine (PS), as well as cholesterol, cardiolipin, and sphingomyelin.²² Among these lipids, cholesterol is known to significantly alter membrane properties by (i) enhancing the stiffness,²³ (ii) decreasing lateral diffusion,^{24,25} (iii) causing “thickening” of the membrane with increasing cholesterol content,^{26,27} and (iv) increasing membrane ordering.²⁸ The presence of cholesterol in the membrane also affects solute partitioning between the membrane and water^{29,30} and interactions with proteins.³¹ In eukaryotes, the membrane content of cholesterol varies depending on location: the smallest amount is present in the

Received: October 27, 2014

mitochondrial membrane (3 wt%, 6 mol%), followed by the ER (6 wt%), whereas the largest amount occurs in the plasma membrane (20 wt%).³² There is also some evidence that the concentration of cholesterol is not homogeneous in membranes and can be locally higher, i.e., in structures called lipid rafts, where cholesterol may also interact with proteins.^{31,33,34} The cholesterol gradient from the ER to the cell surface can also regulate sorting of membrane proteins to their correct membrane site.³⁵ As cholesterol significantly influences membrane properties, it is plausible that it may also affect the structure, orientation, and dynamics of CYP on membranes and in turn the interaction of CYP with its substrates. Recently, Park and co-workers³⁶ showed that individual CYPs differed in localization in ordered and disordered membrane domains, which had various cholesterol concentrations.

We conducted MD simulations to analyze the structure of CYP3A4 attached to DOPC bilayers with various concentrations of cholesterol (0, 3, 6, 20, and 50 wt%). We chose CYP3A4, as it plays a prominent role in the metabolism of the more than 50% of marketed drugs and is the most abundant CYP in human hepatocytes.³⁷ CYP3A4 has a deeply buried, large, and malleable active site,^{38–40} which can be occupied by more than one ligand.^{41–43} It should be noted that cholesterol acts as a CYP3A4 substrate, undergoing 4 β -hydroxylation.⁴⁴ On the other hand, cholesterol also inhibits several CYP3A4 reactions in a noncompetitive manner.⁴⁵ Our MD simulations showed that the presence of cholesterol changes the orientation and rigidifies the membrane-immersed parts of CYP3A4, which could inhibit entry of lipophilic substrates directly from the membrane.

METHODS

Structures. The structure of the catalytic domain of CYP3A4³⁸ was taken from the Protein Data Bank (PDB ID 1TQN), and the N-terminal anchor, which was missing in the X-ray structure, was added to the structure as an α -helix using methodology described in detail elsewhere.⁶ We prepared five lipid bilayers: one consisting of pure DOPC and four composed of DOPC and various (3, 6, 20, and 50 wt%) concentrations of cholesterol. CYP3A4 was inserted into the equilibrated bilayers using the GROMACS tool `g_membed`.⁴⁶ CYP3A4 anchored to the bilayer was then immersed into a rectangular periodic box and solvated by SPC/E⁴⁷ explicit water molecules (~30 000). Counter ions were added to maintain a physiological concentration of 0.1 mol/L in the water phase.

MD Procedure. All simulations were carried out with using the Gromacs 4.5.4 program package.⁴⁸ We used the Berger lipid force field⁴⁹ for the membrane, which was compatible with the GROMOS 53a6⁵⁰ force field used for CYP3A4. The lipid bilayer was initially simulated without protein for 200 ns. After the protein was embedded in the membrane, all systems were minimized with the steepest descent method, followed by a short (10 ns long) MD simulation with positional restraints applied on $C\alpha$ atoms. Afterward, a 200 ns long MD simulation of each system was carried out. Parameters of the MD simulations were set as follows: integration time step, 2 fs with the LINCS algorithm; Berendsen pressure coupling, semi-isotropic Berendsen barostat with pressure 1 bar; isothermal compressibility, 4.5×10^{-5} bar⁻¹; and for temperature coupling, V-rescale thermostat at 310 K with 0.1 ps time constant. The long-range electrostatics was treated with the particle mesh Ewald method, and a pair-list was generated with the group cut-off scheme.

Analysis. As equilibration of systems with CYPs requires at least 50 ns,⁶ the first 100 ns of the simulation was set aside for equilibration of CYP3A4, and only data for the last 100 ns were analyzed. For analysis of the membrane properties, we used Gromacs tools.⁴⁸ The heme tilt angle was defined as the angle between the heme plane (defined by the heme nitrogens) and the lipid bilayer normal, set as the z axis.⁶ Access and egress channels⁵¹ were identified using the MOLE 2.0 tool⁵² with the following setup: interior threshold and bottleneck radius, 1.0; probe radius, 8.0; surface cover radius, 3.0; origin radius, 3.0; and starting point located ~3 Å above the heme iron atom (distal side). Water molecules, hydrogens, ions, and membrane atoms were not considered in this analysis. In total, 201 structural snapshots taken every 500 ps (of the last 100 ns) were analyzed. Identified channels were sorted according to the nomenclature introduced by Wade and co-workers,⁵³ with the exception of channels 2a and 2f, which were united into one channel (henceforth called 2af) because of their high structural similarity.

RESULTS AND DISCUSSION

Addition of Cholesterol Changes the Basic Structural Characteristics of a DOPC Membrane. The presence of cholesterol altered the structure of the DOPC bilayer. DOPC lipid bilayers were generally thicker in the presence of cholesterol, with the headgroup–headgroup distance (D_{HH}) changing from 4.2 nm in the case of a pure DOPC membrane to 4.6 nm for a membrane containing 20 wt% cholesterol (Table 1). The area per lipid (APL) decreased from 0.59 to 0.42 nm². Density profiles also showed that the presence of cholesterol increased the density of the lipid plateau region in terms of the maximal density in the membrane headgroups but did not alter the density in the middle of the membrane

Table 1. Mean Distances of Phosphate (d_p), Cholesterol OH Group (d_{OH}), and Heme Cofactor (d_{heme}) from the Bilayer Center, Area Per Lipid (APL), Average Order Parameters of Lipid Tails (S_{CD}), Average Fraction of Gauche Bonds (f_g), Heme and Transmembrane (TM) Helix Tilt Angles, and Number of Amino Acid Residues (N) Buried in the Hydrophobic Membrane Interior (below DOPC Carbonyls)

	cholesterol content (wt%)				
	0%	3%	6%	20%	50%
	Membranes without CYP				
d_p (nm)	2.1	2.1	2.1	2.3	2.2
d_{OH} (nm)	–	1.6	1.6	1.8	1.9
APL (nm ²)	0.59	0.58	0.54	0.48	0.42
S_{CD}	0.182	0.190	0.219	0.259	0.294
f_g	0.157	0.156	0.154	0.150	0.147
	Membranes with CYP				
d_p (nm)	2.0	2.1	2.2	2.3	2.1
d_{OH} (nm)	–	1.5	1.5	1.8	1.8
S_{CD}	0.172	0.188	0.201	0.246	0.270
f_g	0.156	0.154	0.152	0.148	0.144
d_{heme} (nm)	3.8 ± 0.1	3.7 ± 0.1	3.5 ± 0.1	3.7 ± 0.1	3.5 ± 0.1
heme tilt angle (deg)	52 ± 8	59 ± 3	60 ± 4	69 ± 5	68 ± 4
TM helix tilt angle (deg)	8 ± 4	10 ± 4	11 ± 4	12 ± 5	9 ± 4
N	54	60	82	79	73

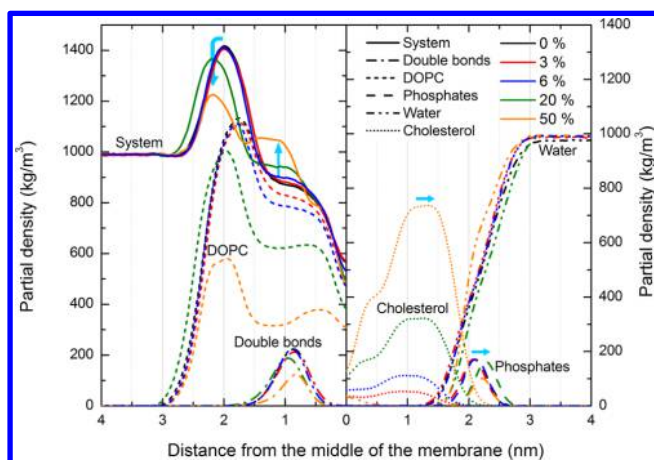


Figure 1. Density profiles of the studied membrane system (without CYP). The membrane was averaged and considered to be symmetric. However, for clarity, the partial densities of groups are shown for just one leaflet.

(Figure 1). As the concentration of cholesterol was increased, the cholesterol OH group shifted further from the membrane center. All these findings are in agreement with previous simulations^{25,54,55} and experimental data⁵⁵ and confirm that the force field used adequately represented the structural properties of these mixed membranes. Thus, the membrane model was considered valid and used to study the effect of cholesterol content on CYP3A4 anchoring.

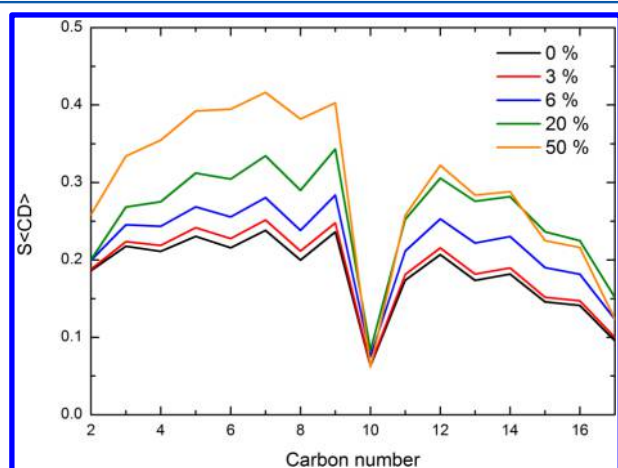


Figure 2. Average order parameter $S_{<CD>}$ for the carbon atoms of DOPC lipid tails calculated from MD simulations with varying cholesterol concentrations.

The presence of cholesterol also induced higher ordering of the DOPC lipid tails (Figure 2). A pure DOPC membrane comprises a diunsaturated lipid with a phase transition temperature of ~ 255 K⁵⁶ and is therefore fluid at ambient temperatures, as documented by the rather low mean order parameter $S_{<CD>}$ of 0.182. Ordering of the lipid membrane was found to increase with increasing cholesterol content, together with a decrease in the fraction of gauche torsion angles of the DOPC lipid chains (Table 1). Higher ordering (above ~ 0.25) can occur in a liquid-ordered lipid phase, which is generally a cholesterol-rich domain.^{25,30,55,57}

Cholesterol Interacts with the N-Terminal Anchor and F/G-Loop of CYP3A4. The simulations showed that CYP3A4

was attached to the membrane by the N-terminal anchor helix, which intersected the membrane, and its catalytic domain was partially immersed in the membrane. The DOPC head groups are pushed aside and DOPC molecules form a funnel-like shape in the membrane occupied by the protein. The N-terminal helix tilt angle, i.e., angle between the helix axis and bilayer normal, was $\sim 10^\circ$ and was rather insensitive to the cholesterol content (Table 1). This angle is smaller than the transmembrane anchor tilt angle of 17° recently measured by NMR on CYP2B4 anchored to DMPC/DHPC bicelles,¹⁵ which makes sense as the latter lipids have shorter tails and head-to-head distance than DOPC.

The radial distribution function (RDF) of the anchor and cholesterol centers of mass (COMs) showed that cholesterol had some tendency to accumulate in the vicinity of the anchor (Figure 3). Cholesterol also accumulated close to the immersed F/G loop (Figure 4). The number of hydrogen bonds between lipids and CYP3A4 rose with cholesterol content (Table S1) and cholesterol had higher capacity to make hydrogen bonds to membrane buried amino acids. Neither cholesterol nor DOPC molecules penetrated into the protein and stayed in the membrane. Fluctuations of the lipids around CYP were massively reduced (Figure S2 in Supporting Information).

Orientation and Immersion Depth of CYP3A4 on DOPC Membrane Is Affected by the Presence of Cholesterol. The presence of cholesterol in the membrane changed the penetration depth of CYP3A4 in the membrane. Besides the mentioned N-terminal anchor, the F/G loop (bearing F' and G' helices) was buried in the lipophilic membrane interior of the pure DOPC membrane (Figure 5). The $\beta 1$ and $\beta 2$ -sheets, B/C loop, F and G helices, and tip of the I helix interacted with the lipid head groups in same positions as reported earlier.⁶ It is worth noting that despite some differences in membrane immersion depths and orientations of individual CYPs, all recent studies have consistently reported insertion of the N-terminal, F', and G' helices into the membrane interior,^{9,11,16,21} while the B/C loop and F and G helices in CYP3A4¹¹ have been reported to interact with the membrane. Figure 5 shows that with increasing content of cholesterol, the F and G helices and B/C loop become systematically sunk deeper into the membrane interior. The number of amino acids in contact with the membrane (Tables 1 and S2 in Supporting Information) was the lowest in the pure DOPC membrane and reached a maximum at 6 wt% cholesterol content.

The orientation of the CYP3A4 catalytic domain with respect to the membrane changed with the increasing content of cholesterol in the DOPC membrane (Figure 6), as evaluated from the heme tilt angle (see Methods for definition). The tilt angle systematically increased from 52° in the pure DOPC membrane to 68° in membranes containing 50 wt% cholesterol (Table 1). It should be noted that the experimentally measured tilt angle of CYP3A4 on POPC nanodiscs is $(60 \pm 4)^\circ$.¹⁶ A higher cholesterol content in the DOPC membrane led to increased contact of the CYP3A4 catalytic domain with the membrane, mostly in the vicinity of the F and G helices and β -finger (containing $\beta 4$ and $\beta 5$ sheets, and $\beta 4/\beta 5$ loop). However, the secondary structural elements of the CYP3A4 catalytic domain did not significantly change with increasing cholesterol content (Figures S1 and S3 in Supporting Information).

Cholesterol Presence in the Membrane Alters Active-Site Access Channels Openings. CYP3A4 active-site access

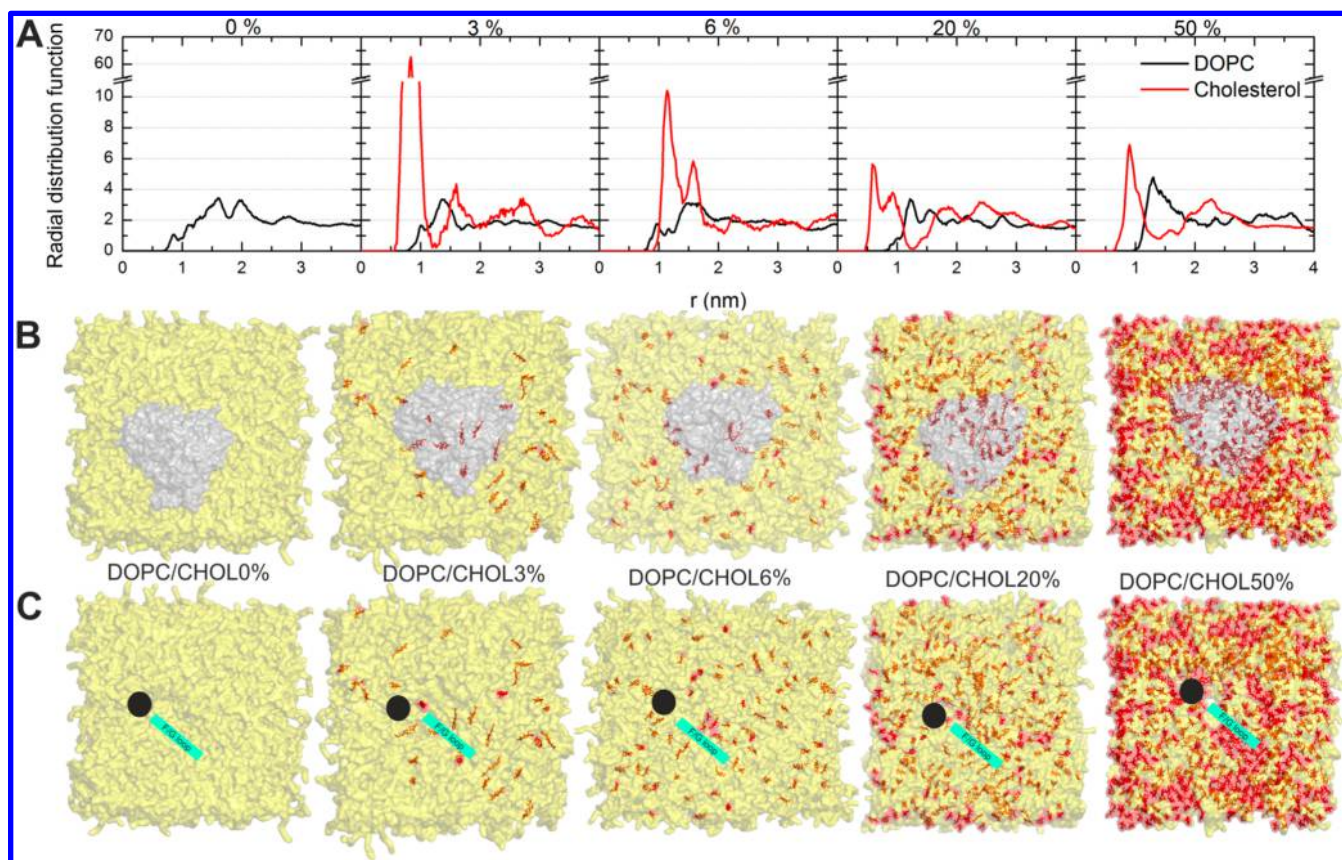


Figure 3. Distribution of cholesterol in membranes. (A) Radial distribution functions of the COMs of DOPC and cholesterol with respect to the transmembrane anchor. (B) Positions of cholesterol molecules (red) in membranes (yellow) with immersed CYP3A4 (gray); frames were taken from 200 ns snapshots. (C) The same view but with CYP3A4 deleted for clarity; positions of the CYP3A4 anchor (black circle) and F/G-loop (green) are shown. Cholesterol showed some tendency to concentrate close to the transmembrane anchor and F/G-loop.

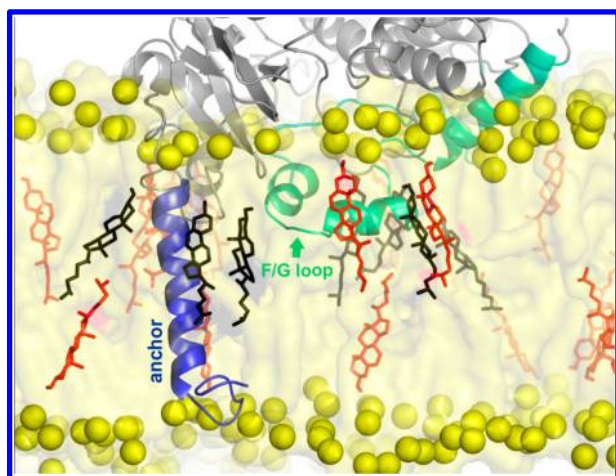


Figure 4. Snapshot taken from MD simulation of CYP3A4 embedded in 6 wt% cholesterol in DOPC membrane showing a typical view of cholesterol molecules interacting with the N-terminal anchor (blue) and F/G loop (green). Membrane phosphates are represented by yellow spheres, cholesterol molecules within 5 Å of CYP3A4 by black sticks and more distal cholesterol molecules by red sticks.

channels connected the active site to both membrane and water phases because their openings were localized inside, on and outside the membrane (Figure 7). The channels 2af, 2b, 2c (around F/G loop), and 4 (through F/G loop) pointed toward the hydrophobic membrane interior. The solvent channel (S; between F, I helices and β -finger) and channels 2e (running

through B/C loop) and 3 (between F and G helices) were open to the membrane/water interface. The water channel (W; leading to the proximal side around B, C helices or B/C loop) and channels 1 (among C, H, and L helices) and 5 (between K and K' helices) opened into the water phase. The positions of these channels are in good agreement with previously published data.^{5,6,9} The channels were hydrated and enabled traffic of water molecules in/out CYP3A4 active site (Table S4).

The addition of cholesterol to the DOPC membrane changed the pattern of channel openings. At low cholesterol content (3 and 6 wt%), the water channel was closed and the solvent channel open, but there were no significant changes in the channels pointing to the membrane interior. Channels leading deepest into the membrane, i.e., channels 2af and 2b, closed when CYP was embedded into the cholesterol-rich membrane (with 20 and 50 wt% cholesterol content). The bottlenecks of membrane-exposed channels were narrower in cholesterol rich membranes (Table 2). As well as closure of the channels leading to the membrane, channels leading to the membrane/water interface, such as channels 2e or the solvent channel, opened. Channels leading toward the water phase were highly hydrated (Table S4) and enabled traffic of water molecules out/in CYP3A4 active site. A new channel, labeled 7, whose opening pointed toward the water phase, was identified. Channel 7 passed near the K helix and K/L loop to the proximal side of CYP 3A4 (Figure S2 in Supporting Information). The opening of this channel was caused by subtle movement of the F/G loop and K and L helices.

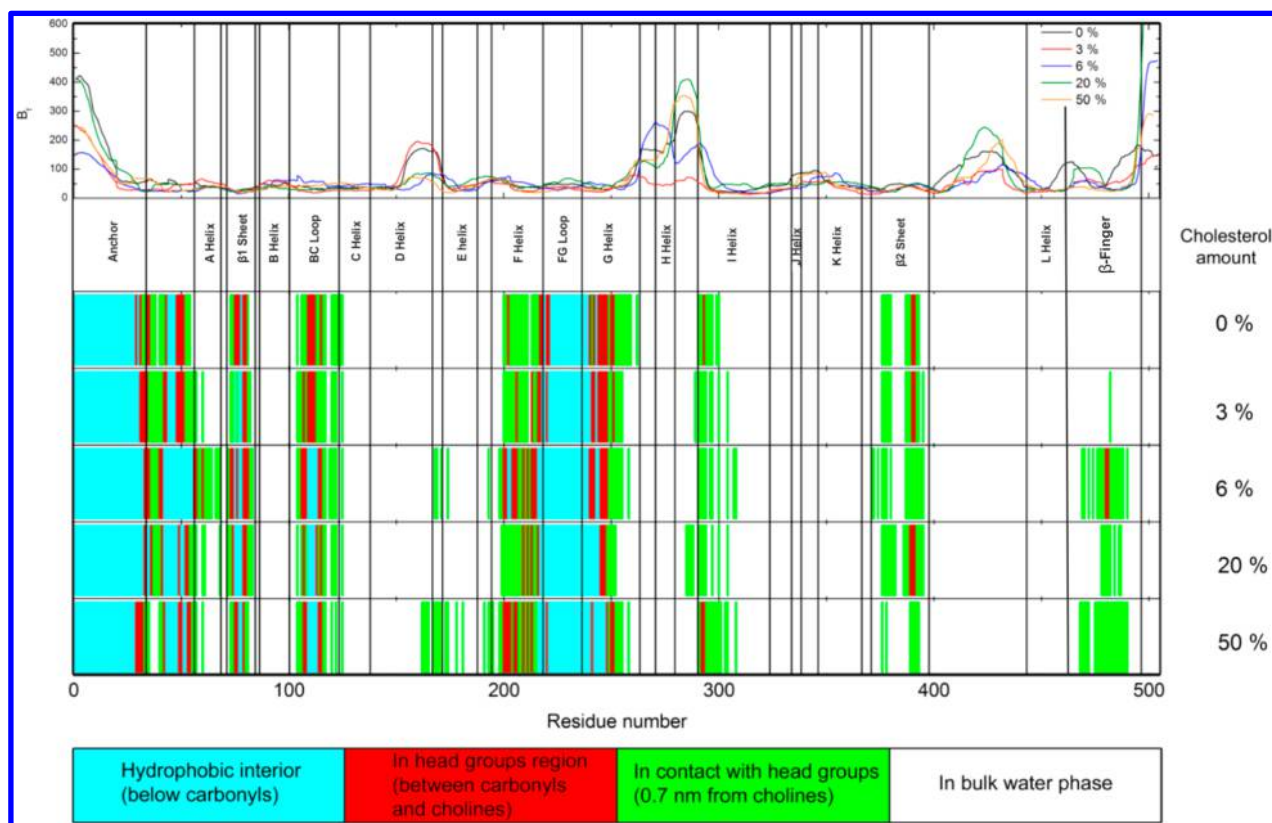


Figure 5. Structural features of CYP3A4 in different membranes. The average B-factors (upper panel) along the protein chain show that the regions in contact with water are the most flexible. The locations of residues differ with respect to the membrane composition (bottom): higher cholesterol leads to more immersed CYP structures, especially in the B/C and F/G loop regions. The colors indicate CYP3A4 parts that are in direct contact with the hydrophobic membrane interior (blue), interact with membrane head groups, i.e., between carbonyl groups and cholines (red), and contact the membrane upper layer (green). The white regions indicate parts in contact with bulk water (cytosol).

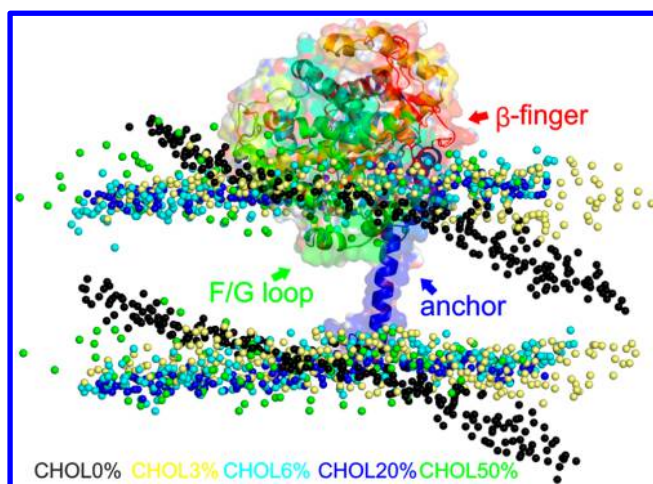


Figure 6. Effect of cholesterol on the orientation of CYP3A4 in the membrane. Structures of CYP3A4 catalytic domain have been superimposed to highlight changes in the CYP3A4 orientation with respect to the DOPC membrane. The membrane is represented by spheres of phosphorus atoms (for clarity) and colored according to the cholesterol content: 0 wt%, black; 3 wt%, yellow; 6 wt%, cyan; 20 wt%, blue; and 50 wt%, green. CYP3A4 is shown as a cartoon with transparent surfaces.

Generally, conformational changes of channel lining amino acid residues and small variations in arrangement of secondary structural elements, which bear the channel lining amino acids can cause channel opening/closing. The subtle movement of

the F/G loop toward the membrane and concurrent opening of the K and L helix region in the CYP structures immersed in membranes containing cholesterol lead to opening of the channel 7. Solvent channel opening and closing was mostly connected with the orientation of R212, which closed solvent channel of CYP3A4 immersed to membranes with 0% and 3% of cholesterol, whereas the channel was open in the membrane containing 20% cholesterol.

CONCLUSION

We studied the effect of increasing the cholesterol content in a DOPC membrane on the behavior of membrane-anchored cytochrome P450 3A4 (CYP3A4). The presence of cholesterol in the lipid membrane significantly changed the membrane thickness, ordering, and diffusion. The position and orientation of CYP3A4 on the membrane were also affected by the cholesterol content. With increasing cholesterol concentration, CYP3A4 was immersed about 0.4 nm deeper into the membrane and was more inclined toward the membrane. In addition, the contact area between the catalytic domain and membrane increased. As a result, about 34% more CYP3A4 amino acids were in contact with the membrane. The presence of cholesterol in the membrane also affected opening of the active-site access channels, but the most pronounced changes occurred for high (20 and 50 wt%) cholesterol concentrations. One can hypothesize that the above-discussed changes might also contribute to the noncompetitive inhibition of CYP3A4 by cholesterol observed by Shinkyo and Guengerich.⁴⁵ Our results show that cholesterol content significantly influences the

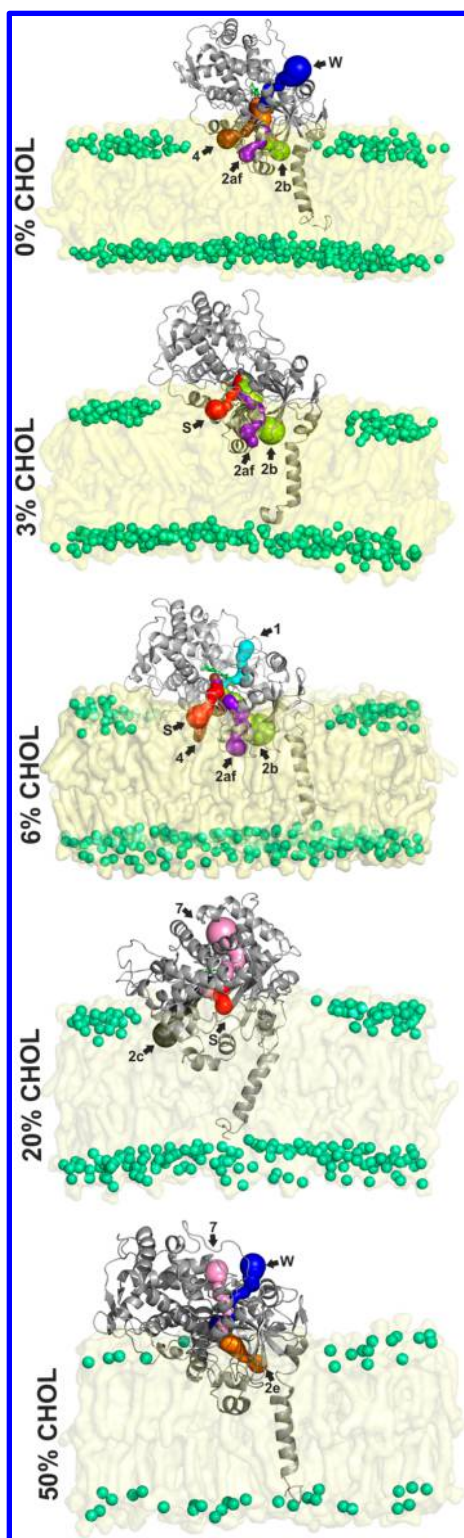


Figure 7. Channel openings (highlighted by arrows) of CYP3A4 active-site access channels (open with bottleneck radius of 1 Å and higher in 15% of frames) are shown in DOPC membranes with increasing cholesterol content. Access channels are labeled according to the nomenclature introduced by Wade and co-workers,⁵³ and colored as follows: 1, cyan; 4, brown; 7, pink; W, blue; S, red; 2af, magenta; 2b, bright green; 2c, gray; 2e, orange. Membrane lipids are represented as transparent surfaces and phosphates in green spheres; CYP3A4 is shown as a cartoon.

Table 2. Normalized Frequency of CYP Channel Opening (nfreq) and Average Radius (Rmax) of Bottlenecks^a

	chol 0%		chol 3%		chol 6%		chol 20%		chol 50%	
#	nfreq	Rmax	nfreq	Rmax	nfreq	Rmax	nfreq	Rmax	nfreq	Rmax
membrane										
2af	47	1.46	30	1.45	29	1.39	2	1.19	4	1.24
2b	76	1.73	95	1.64	88	1.53	1	1.09	10	1.41
4	18	1.29	8	1.26	17	1.31	1	1.16	11	1.31
2c	5	1.42	1	1.13			21	1.43	4	1.26
2e	33	1.61	1	1.01	2	1.13	78	1.77	62	1.59
S			27	1.28	45	1.47	75	1.89	5	1.17
3	5	1.22			2	1.01	2	1.05	1	1.2
5							9	1.39	5	1.23
1	10	1.25	2	1.17	20	1.36	10	1.47	10	1.24
W	56	1.38	5	1.27	3	1.07	1	1.01	21	1.36
7					11	1.62	34	1.57	78	1.55
r		0.74		0.89		0.62		0.92		0.90

^aRmax values are colored according to their bottleneck radius, from dark green for the most open to red for the most closed channels. According to the Rmax and nfreq values, the most frequently occurring channels were also the most open, whereas rarely observed channels tended to have rather narrow bottlenecks. The last line shows the correlation coefficients between nfreq and Rmax.

structural features of a membrane-anchored enzyme, which in turn may affect the substrate preferences and catalytic efficiency of the respective membranes or membrane domains. The described changes may influence biotransformation processes in different membrane parts and various cellular compartments, which differ in membrane composition and cholesterol content.

■ ASSOCIATED CONTENT

📄 Supporting Information

Root-mean-square fluctuations of the systems with different cholesterol content (Figure S1); detailed view of newly observed channel 7 (Figure S2); number of hydrogen bonds between lipids, protein, and water (Table S1); numbers of protein residues located in various parts of the membrane and potentially interacting with the membrane (Table S2); numbers of solvent and ions in the simulated system (Table S3); number of water molecules in various channels (Table S4); evolution of secondary structure elements (Figure S3); overview of all channels found in the CYPs in membranes with different cholesterol content (Figure S4). This material is available free of charge via the Internet at <http://pubs.acs.org>.

■ AUTHOR INFORMATION

Corresponding Authors

*K.B.: phone +420 585634769, fax +420 585634761, E-mail karel.berka@upol.cz.

*M.O.: phone +420 585634756, fax +420 585634761, E-mail michal.otyepka@upol.cz.

Notes

The authors declare no competing financial interest.

■ ACKNOWLEDGMENTS

This research was supported by the Operational Program Research and Development for Innovations—European Social Fund (CZ.1.07/2.4.00/31.0130 ChemPharmNet) from the Ministry of Education Youth and Sports, Czech Republic. We acknowledge support from the Czech Grant Agency through the projects P303/12/P019 to K.B. and P208/12/G016 to M.O. We also acknowledge support from a student project of Palacký University Olomouc (IGA_PrF_2014023) to M.P. and V.N. The authors gratefully acknowledge support through the

project LO1305 of the Ministry of Education, Youth and Sports of the Czech Republic.

ABBREVIATIONS

CYP, cytochrome P450; ER, endoplasmic reticulum; DOPC, 1,2-dioleoyl-*sn*-glycero-3-phosphocholine; POPC, 1-palmitoyl-2-oleoyl-*sn*-glycero-3-phosphocholine; MD, molecular dynamics; PC, phosphatidylcholine; PE, phosphatidylethanolamine; PI, phosphatidylinositol; PS, phosphatidylserine; APL, area per lipid; TM, transmembrane; DMPC, 1,2-dimyristoyl-*sn*-glycero-3-phosphocholine; DHCP, 1,2-diheptanoyl-*sn*-glycero-3-phosphocholine; CHOL, cholesterol; RDF, radial distribution function; COM, center of mass

REFERENCES

- (1) Guengerich, F. P. Common and Uncommon Cytochrome P450 Reactions Related to Metabolism and Chemical Toxicity. *Chem. Res. Toxicol.* **2001**, *14*, 611–650.
- (2) Ortiz de Montellano, P. R., Ed. *Cytochrome P450: Structure, Mechanism, and Biochemistry*, 3rd ed.; Kluwer Academic/Plenum Publishers: New York, 2005; Vol. 21, p 690.
- (3) Black, S. D. Membrane Topology of the Mammalian P450 Cytochromes. *FASEB J.* **1992**, *6*, 680–685.
- (4) Williams, P. A.; Cosme, J.; Sridhar, V.; Johnson, E. F.; McRee, D. E. Microsomal Cytochrome P450 2C5: Comparison to Microbial P450s and Unique Features. *J. Inorg. Biochem.* **2000**, *81*, 183–190.
- (5) Berka, K.; Hendrychová, T.; Anzenbacher, P.; Otyepka, M. Membrane Position of Ibuprofen Agrees with Suggested Access Path Entrance to Cytochrome P450 2C9 Active Site. *J. Phys. Chem. A* **2011**, *115*, 11248–11255.
- (6) Berka, K.; Palončyová, M.; Anzenbacher, P.; Otyepka, M. Behavior of Human Cytochromes P450 on Lipid Membranes. *J. Phys. Chem. B* **2013**, *117*, 11556–11564.
- (7) Endo, S.; Escher, B. I.; Goss, K.-U. Capacities of Membrane Lipids to Accumulate Neutral Organic Chemicals. *Environ. Sci. Technol.* **2011**, *45*, 5912–5921.
- (8) Palončyová, M.; Devane, R.; Murch, B.; Berka, K.; Otyepka, M. Amphiphilic Drug-Like Molecules Accumulate in a Membrane below the Head Group Region. *J. Phys. Chem. B* **2014**, *118*, 1030–1039.
- (9) Cojocar, V.; Balali-Mood, K.; Sansom, M. S. P.; Wade, R. C. Structure and Dynamics of the Membrane-Bound Cytochrome P450 2C9. *PLoS Comput. Biol.* **2011**, *7*, No. e1002152.
- (10) Kingsley, L. J.; Lill, M. An Ensemble Generation and the Influence of Protein Flexibility on Geometric Tunnel Prediction in Cytochrome P450 Enzymes. *PLoS One* **2014**, *9*, No. e99408.
- (11) Denisov, I. G.; Shih, A. Y.; Sligar, S. G. Structural Differences between Soluble and Membrane Bound Cytochrome P450s. *J. Inorg. Biochem.* **2012**, *108*, 150–158.
- (12) Sündermann, A.; Oostenbrink, C. Molecular Dynamics Simulations Give Insight into the Conformational Change, Complex Formation, and Electron Transfer Pathway for Cytochrome P450 Reductase. *Protein Sci.* **2013**, *22*, 1183–1195.
- (13) Yamamoto, K.; Dürr, U. H. N.; Xu, J.; Im, S.-C.; Waskell, L.; Ramamoorthy, A. Dynamic Interaction between Membrane-Bound Full-Length Cytochrome P450 and Cytochrome b5 Observed by Solid-State NMR Spectroscopy. *Sci. Rep.* **2013**, *3*, No. 2538.
- (14) Dürr, U. H. N.; Waskell, L.; Ramamoorthy, A. The Cytochromes P450 and b5 and their Reductases—Promising Targets for Structural Studies by Advanced Solid-State NMR Spectroscopy. *Biochim. Biophys. Acta* **2007**, *1768*, 3235–3259.
- (15) Yamamoto, K.; Gildenberg, M.; Ahuja, S.; Im, S.-C.; Pearcy, P.; Waskell, L.; Ramamoorthy, A. Probing the Transmembrane Structure and Topology of Microsomal Cytochrome-P450 by Solid-State NMR on Temperature-Resistant Bicelles. *Sci. Rep.* **2013**, *3*, No. 2556.
- (16) Baylon, J. L.; Lenov, I. L.; Sligar, S. G.; Tajkhorshid, E. Characterizing the Membrane-Bound State of Cytochrome P450 3A4: Structure, Depth of Insertion and Orientation. *J. Am. Chem. Soc.* **2013**, *135*, 8542–8551.
- (17) Williams, P. A.; Cosme, J.; Sridhar, V.; Johnson, E. F.; McRee, D. E. Mammalian Microsomal Cytochrome P450 Monooxygenase: Structural Adaptations for Membrane Binding and Functional Diversity. *Mol. Cell* **2000**, *5*, 121–131.
- (18) Monk, B. C.; Tomasiak, T. M.; Keniya, M. V.; Huschmann, F. U.; Tyndall, J. D. A. Architecture of a Single Membrane Spanning Cytochrome P450 Suggests Constraints that Orient the Catalytic Domain Relative to a Bilayer. *Proc. Natl. Acad. Sci. U.S.A.* **2014**, *111*, 3865–3870.
- (19) Jiang, W.; Ghosh, D. Motion and Flexibility in Human Cytochrome P450 Aromatase. *PLoS One* **2012**, *7*, No. e32565.
- (20) Sgrignani, J.; Magistrato, A. Influence of the Membrane Lipophilic Environment on the Structure and on the Substrate Access/Egress Routes of the Human Aromatase Enzyme. A Computational Study. *J. Chem. Inf. Model.* **2012**, *52*, 1595–1606.
- (21) Park, J.; Czaplá, L.; Amaro, R. Molecular Simulations of Aromatase Reveal New Insights into the Mechanism of Ligand Binding. *J. Chem. Inf. Model.* **2013**, *53*, 2047–2056.
- (22) Van Meer, G.; de Kroon, A. I. P. M. Lipid Map of the Mammalian Cell. *J. Cell Sci.* **2011**, *124*, 5–8.
- (23) Needham, D.; McIntosh, T.; Evans, E. Thermomechanical and Transition Properties of Dimyristoylphosphatidylcholine/Cholesterol Bilayers. *Biochemistry* **1988**, *27*, 4668–4673.
- (24) Evans, E.; Needham, D. Physical Properties of Surfactant Bilayer Membranes: Thermal Transitions, Elasticity, Rigidity, Cohesion and Colloidal Interactions. *J. Phys. Chem.* **1987**, *2*, 4219–4228.
- (25) Ohvo-Rekilä, H.; Ramstedt, B.; Leppimäki, P.; Slotte, J. P. Cholesterol Interactions with Phospholipids in Membranes. *Prog. Lipid Res.* **2002**, *41*, 66–97.
- (26) Raffy, S.; Teissié, J. Control of Lipid Membrane Stability by Cholesterol Content. *Biophys. J.* **1999**, *76*, 2072–2080.
- (27) Drolle, E.; Kučerka, N.; Hoopes, M. I.; Choi, Y.; Katsaras, J.; Karttunen, M.; Leonenko, Z. Effect of Melatonin and Cholesterol on the Structure of DOPC and DPPC Membranes. *Biochim. Biophys. Acta* **2013**, *1828*, 2247–2254.
- (28) Hung, W.-C.; Lee, M.-T.; Chen, F.-Y.; Huang, H. W. The Condensing Effect of Cholesterol in Lipid Bilayers. *Biophys. J.* **2007**, *92*, 3960–3967.
- (29) Trandum, C.; Westh, P.; Jorgensen, K.; Mouritsen, O. G. A Thermodynamic Study of the Effects of Cholesterol on the Interaction Between Liposomes and Ethanol. *Biophys. J.* **2000**, *78*, 2486–2492.
- (30) Wennberg, C. L.; Spoel, D. Van Der; Hub, J. S. Large Influence of Cholesterol on Solute Partitioning into Lipid Membranes. *J. Am. Chem. Soc.* **2012**, *134*, 5351–5361.
- (31) Pike, L. J. The Challenge of Lipid Rafts. *J. Lipid Res.* **2009**, *50* (Suppl), S323–328.
- (32) Sackman, E. Biological Membranes Architecture and Function. In *Structure and Dynamics of Membranes From Cells to Vesicles*; Lipowsky, R., Sackmann, E., Eds.; Elsevier: Amsterdam, 1995; pp 1–63.
- (33) Epanand, R. M. Cholesterol and the Interaction of Proteins with Membrane Domains. *Prog. Lipid Res.* **2006**, *45*, 279–294.
- (34) Fantini, J. Interaction of Proteins with Lipid Rafts through Glycolipid-Binding Domains: Biochemical Background and Potential Therapeutic Applications. *Curr. Med. Chem.* **2007**, *14*, 2911–2917.
- (35) Coskun, Ü.; Simons, K. Cell Membranes: the Lipid Perspective. *Structure* **2011**, *19*, 1543–1548.
- (36) Park, J. W.; Reed, J. R.; Brignac-Huber, L. M.; Backes, W. L. Cytochrome P450 System Proteins Reside in Different Regions of the Endoplasmic Reticulum. *Biochem. J.* **2014**, *464*, 241–249.
- (37) Anzenbacher, P.; Anzenbacherová, E. Cytochromes P450 and Metabolism of Xenobiotics. *Cell. Mol. Life Sci.* **2001**, *58*, 737–747.
- (38) Yano, J. K.; Wester, M. R.; Schoch, G. A.; Griffin, K. J.; Stout, C. D.; Johnson, E. F. The Structure of Human Microsomal Cytochrome P450 3A4 Determined by X-ray Crystallography to 2.05-Å Resolution. *J. Biol. Chem.* **2004**, *279*, 38091–38094.

(39) Otyepka, M.; Skopalík, J.; Anzenbacherová, E.; Anzenbacher, P. What Common Structural Features and Variations of Mammalian P450s Are Known to Date? *Biochim. Biophys. Acta* **2007**, *1770*, 376–389.

(40) Hendrychová, T.; Anzenbacherová, E.; Hudeček, J.; Skopalík, J.; Lange, R.; Hildebrandt, P.; Otyepka, M.; Anzenbacher, P. Flexibility of Human Cytochrome P450 Enzymes: Molecular Dynamics and Spectroscopy Reveal Important Function-Related Variations. *Biochim. Biophys. Acta* **2011**, *1814*, 58–68.

(41) Bren, U.; Oostenbrink, C. Cytochrome P450 3A4 Inhibition by Ketoconazole: Tackling the Problem of Ligand Cooperativity Using Molecular Dynamics Simulations and Free-Energy Calculations. *J. Chem. Inf. Model.* **2012**, *52*, 1573–1582.

(42) Bren, U.; Fuchs, J. E.; Oostenbrink, C. Cooperative Binding of Aflatoxin B 1 by Cytochrome P450 3A4: A Computational Study. *Chem. Res. Toxicol.* **2014**, *27*, 2136–2147.

(43) Davydov, D. R.; Halpert, J. R. Allosteric P450 Mechanisms: Multiple Binding Sites, Multiple Conformers, or Both? *Exp. Opin. Drug Metab. Toxicol.* **2008**, *4*, 1523–1535.

(44) Bodin, K.; Bretillon, L.; Aden, Y.; Bertilsson, L.; Broomé, U.; Einarsson, C.; Diczfalussy, U. Antiepileptic Drugs Increase Plasma Levels of 4beta-Hydroxycholesterol in Humans: Evidence for Involvement of Cytochrome P450 3A4. *J. Biol. Chem.* **2001**, *276*, 38685–38689.

(45) Shinkyo, R.; Guengerich, F. P. Inhibition of Human Cytochrome P450 3A4 by Cholesterol. *J. Biol. Chem.* **2011**, *286*, 18426–18433.

(46) Wolf, M. G.; Hoefling, M.; Aponte-Santamaría, C.; Grubmüller, H.; Groenhof, G. g _ mbed: Efficient Insertion of a Membrane Protein into an Equilibrated Lipid Bilayer with Minimal Perturbation. *J. Comput. Chem.* **2010**, *31*, 2160–2174.

(47) Berendsen, H. The Missing Term in Effective Pair Potentials. *J. Phys. Chem.* **1987**, *91*, 6269–6271.

(48) Hess, B.; Kutzner, C.; van der Spoel, D.; Lindahl, E. GROMACS 4: Algorithms for Highly Efficient, Load-Balanced, and Scalable Molecular Simulation. *J. Chem. Theory Comput.* **2008**, *4*, 435–447.

(49) Berger, O.; Edholm, O.; Jahnig, F. Molecular Dynamics Simulations of a Fluid Bilayer of Dipalmitoylphosphatidylcholine at Full Hydration, Constant Pressure and Constant Temperature. *Biophys. J.* **1997**, *72*, 2002–2013.

(50) Oostenbrink, C.; Villa, A.; Mark, A. E.; van Gunsteren, W. F. A Biomolecular Force Field Based on the Free Enthalpy of Hydration and Solvation: the GROMOS Force-Field Parameter Sets 53A5 and 53A6. *J. Comput. Chem.* **2004**, *25*, 1656–1676.

(51) Pravda, L.; Berka, K.; Svobodová Vařeková, R.; Sehnal, D.; Banáš, P.; Laskowski, R. A.; Koča, J.; Otyepka, M. Anatomy of enzyme channels. *BMC Bioinformatics* **2014**, *15*, 379.

(52) Sehnal, D.; Svobodová Vařeková, R.; Berka, K.; Pravda, L.; Navrátilová, V.; Banáš, P.; Ionescu, C.-M.; Otyepka, M.; Koča, J. MOLE 2.0: Advanced Approach for Analysis of Biomacromolecular Channels. *J. Cheminform.* **2013**, *5*, 39.

(53) Cojocaru, V.; Winn, P. J.; Wade, R. C. The Ins and Outs of Cytochrome P450s. *Biochim. Biophys. Acta* **2007**, *1770*, 390–401.

(54) Hofsäss, C.; Lindahl, E.; Edholm, O. Molecular Dynamics Simulations of Phospholipid Bilayers with Cholesterol. *Biophys. J.* **2003**, *84*, 2192–2206.

(55) Róg, T.; Pasenkiewicz-Gierula, M.; Vattulainen, I.; Karttunen, M. Ordering Effects of Cholesterol and its Analogues. *Biochim. Biophys. Acta* **2009**, *1788*, 97–121.

(56) Koynova, R.; Caffrey, M. Phases and Phase Transitions of the Phosphatidylcholines. *Biochim. Biophys. Acta* **1998**, *1376*, 91–145.

(57) Rawicz, W.; Smith, B. A.; McIntosh, T. J.; Simon, S. A.; Evans, E. Elasticity, Strength, and Water Permeability of Bilayers that Contain Raft Microdomain-Forming Lipids. *Biophys. J.* **2008**, *94*, 4725–4736.

Structural Changes in Ceramide Bilayers Rationalize Increased Permeation through Stratum Corneum Models with Shorter Acyl Tails

Markéta Paloncýová,[†] Kateřina Vávrová,[‡] Žofie Sovová,[†] Russell DeVane,[§] Michal Otyepka,[†] and Karel Berka^{*,†}

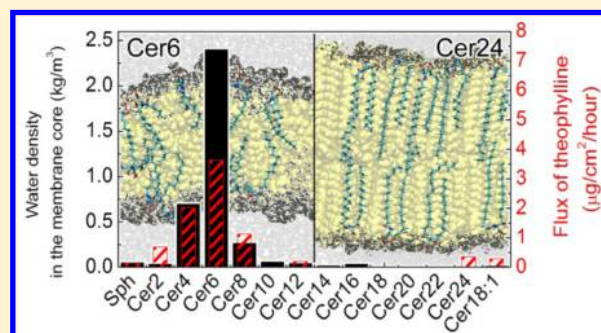
[†]Regional Centre of Advanced Technologies and Materials, Department of Physical Chemistry, Faculty of Science, Palacký University Olomouc, tř. 17. listopadu 12, 771 46 Olomouc, Czech Republic

[‡]Skin Barrier Research Group, Faculty of Pharmacy in Hradec Králové, Charles University in Prague, Heyrovského 1203, 500 05 Hradec Králové, Czech Republic

[§]Corporate Modeling & Simulation, Procter & Gamble, 8611 Beckett Road, West Chester, Ohio 45069, United States

Supporting Information

ABSTRACT: Ceramides are indispensable constituents of the stratum corneum (SC), the uppermost impermeable layer of human skin. Ceramides with shorter (four- to eight-carbon acyl chains) fatty acid chains increase skin and model membrane permeability, while further shortening of the chain leads to increased resistance to penetration almost as good as that of ceramides from healthy skin (24 carbons long on average). Here we address the extent to which the atomistic CHARMM36 and coarse-grain MARTINI molecular dynamics (MD) simulations reflect the skin permeability data. As a result, we observed the same bell-shaped permeability trend for water that was observed in the skin and multilayer membrane experiments for model compounds. We showed that the enhanced permeability of the short ceramides is mainly caused by the disturbance of their headgroup conformation because of their inability to accommodate the shorter lipid acyl chain into a typical hairpin conformation, which further led to their destabilization and phase separation. As MD simulations described well delicate structural features of SC membranes, they seem to be suitable for further studies of the SC superstructure, including the development of skin penetration enhancers for transdermal drug delivery and skin toxicity risk assessment studies.



INTRODUCTION

Ceramides (Cer) are key constituents of the skin barrier protecting our bodies against water loss and the entrance of undesirable chemicals from our environment.¹ As such, skin and especially its uppermost layer, stratum corneum (SC), are vital for maintaining stable conditions in the human body. Cer are sphingolipids, which in skin usually contain long saturated tails. Unlike phosphatidylglycerols, typical for cell membranes,² the Cer headgroup is rather small and serine-based, forming a network of hydrogen bonds.^{3,4} Also, pure Cer in aqueous solution does not form fluid bilayers but rather V-shaped gel phase lipid membranes of Cer or even lipid crystals,^{5,6} or spongelike structures that are dependent on the level of hydration and temperature.⁷ SC lipid mixtures also contain almost equimolar amounts of free fatty acid (FFA) and cholesterol (Chol) and other minor constituents.³ These lipids form highly ordered and weakly permeable membranes.⁸ This unusual membrane composition with a high Cer content is essential for maintaining the skin barrier function.⁹

The permeability of SC lipid membranes depends strongly on the Cer composition of these membranes.¹⁰ An increased

fraction of Cer with shorter fatty acid chains [with approximately 16 carbons (16C)] and a decreased amount of Cer with a typical fatty acid chain of around 24C (long Cer) is one of the signs of several skin diseases [apart from variations in Cer subclasses (for a review, see ref 11)], such as atopic dermatitis, psoriasis, or ichthyoses,^{12–16} and leads to an increased water loss and a reduced level of protection from allergens, pollution, and other xenobiotics. The permeability properties of the skin can be mimicked by model lipid membranes.¹⁷ In a recent study that aimed to elucidate the role of Cer chain length, it was shown that short Cer (4–8C) alone significantly increases skin permeability with maxima at 4–6C acyl.¹⁸ Such substantial changes in Cer acyl chain length are not encountered in diseased skin; however, understanding the chain length-dependent permeability would be interesting, in particular because Cer with 6C acyl are frequently used as easier-to-handle Cer mimics. However, both theoretical and

Received: June 9, 2015

Revised: July 7, 2015

Published: July 7, 2015

experimental studies of the mechanism of such increased skin permeability seem to be complicated by the complexity of the skin composition and structure.

To reveal the effect of Cer acyl chain length on the SC lipid barrier, Školová et al.¹⁹ prepared model membranes consisting of equimolar mixtures of CerNS (*N*-lignoceroylsphingosine) or its shorter analogue, lignoceric acid (most abundant FFA in SC), and Chol with addition of a small amount of cholesterol sulfate. The lipid mixtures arranged themselves into multilayer membranes with a nontrivial bell-shaped permeability trend with the highest values for short Cer containing fatty acid chains with around 4–8C that was similar to the trend found in SC.¹⁸ Because the trend was reproduced well in the SC model multilayer membranes experimentally,¹⁹ it would be valuable to gain insight into this phenomenon by modern molecular dynamics (MD) simulations on a simple bilayer model.

MD simulations allow studies of complex systems simultaneously at atomistic and subpicosecond resolution, which is not possible using any of the experimental techniques. Most of the initial MD studies^{20,21} on lipid membranes were performed on fluid phosphatidylcholine bilayers, representing cell membranes, but until now, only a limited number of studies have focused on peculiarities of the simulations of gel phase membranes similar to the SC membrane.^{8,22} As the structure of the SC membrane is still not entirely known, most recent simulation studies focused on the structural properties of bilayers containing one or more SC components, e.g., Cer,^{5,23–26} while only recently were the first attempts to analyze SC multilayer superstructure performed.^{27,28} One of the main struggles in gel phase membranes is its rigidity, which increases the computational costs of such simulations. As the analysis of the penetration through the membrane requires even greater computational resources,^{29,30} it is not surprising that there are just a handful of MD simulations trying to analyze the penetration through the Cer-containing gel phase membrane.^{8,31–33} Although the representation of the SC multilayer membrane by a Cer SC-like bilayer is a crude simplification, the penetration through the artificially built gel phase bilayer alone was shown to impose a barrier for penetration much higher than that of a fluidic cell-like membrane.⁸ The major questions here are whether MD simulation would be capable of capturing the permeability trend and if a bilayer is a sufficient model for analyzing skin permeabilities of more complex lipid multilayers such as skin.

In this paper, we rationalized the bell-shaped relationship between Cer acyl chain length and the permeability of the SC lipid membranes at the atomistic and coarse-grain (CG) level using MD simulations. MD results depend heavily on a chosen force field (FF). The atomistic CHARMM36 FF for phosphatidylglycerols³⁴ was shown to reproduce well the available experimental properties.³⁵ However, this study is one of the first tests of the newly developed CHARMM36 FF for sphingolipids and Cer in particular.³⁶ Membranes are also being more frequently studied using a coarse-grain force field, such as MARTINI,³⁷ where typically a foursome of heavy atoms is replaced by so-called beads. This reduction of particles leads to a large acceleration of the simulations. As new MARTINI-compatible force field parameters for Cer were developed recently,⁷ we also decided to compare their ability to describe physicochemical properties of Cer bilayers with the results of atomistic simulations. Because experimental investigation of Cer mixtures showed phase separation to Cer-rich, FFA-rich, and Chol domains, we modeled not only the mixture

of the major components but also pure FFA and pure Cer bilayers. Finally, we monitored the structural parameters of the bilayers as well as the conformations of Cer that play a crucial role in the resulting permeability.

METHODS

We prepared bilayers of equimolar mixtures of ceramide NS [with appropriate chain lengths from the shortest Sph and Cer2 through short Cer with C4–C10 until long Cer with C12–C24 (see Figure 1)], lignoceric acid [free fatty acid (FFA)], and

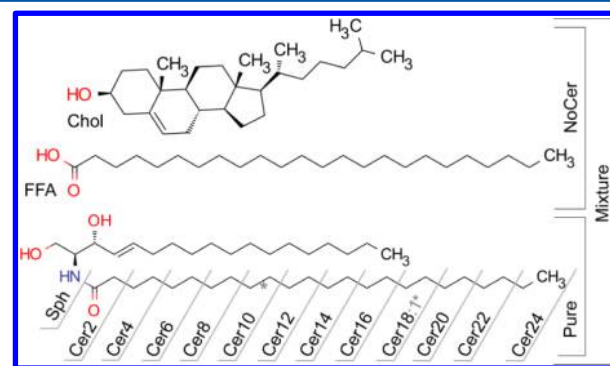


Figure 1. Molecular components of the lipid bilayers used in this study with abbreviations of the ceramide (Cer) analogues and free sphingosine (Sph). An asterisk denotes the position of the cis double bond in the Cer18:1 fatty acid tail.

cholesterol (Chol) and bilayers composed of a mixture of Chol and FFA (NoCer), which correspond to the experimental compositions of Školová et al.¹⁹ Though the experimental measurements were performed on either multilayers or monolayers of lipids, we studied their properties by lipid bilayer models. Also, a CG simulation suggested the formation of a spongelike phase⁷ instead of bilayers separated by water layers. However, this phenomenon cannot be seen in a small simulation box with a single bilayer hydrated with a thick layer of water. To better mimic experimentally observed conditions, as a phase separation of Cer-rich regions has been experimentally proposed,¹⁹ we prepared pure bilayers composed of only Cer and a bilayer composed of only FFA (FFA) to mimic Cer-rich and FFA-rich phases. In addition to focusing on the Cer studied experimentally,¹⁹ we also conducted simulations using other chain lengths in the series.

Topologies for ceramide NS (Cer) and Chol were derived from sphingomyelin parameters in the CHARMM36^{34,36,38} format and are presented in the [Supporting Information](#). Topologies for Cer with shorter lipid chains were adjusted by removing the aliphatic middle atoms of the 24:0 chain. The topology of uncharged FFA was prepared by combining the acyl chain parameters from Cer and the acetic acid headgroup of the CHARMM General Force Field (cgenff).³⁹ All parameters were then transferred into GROMACS format and are presented in the [Supporting Information](#).

Both mixed and pure bilayer structures were obtained using an in-house membrane builder. The pure bilayers contained 128 lipids arranged in a fully hydrated lipid bilayer with TIPS3P water. The mixed membranes contained an equimolar mixture of 108 total lipid molecules equally distributed into a fully hydrated bilayer with at least 20 waters per lipid. The hydrated membranes were then equilibrated, and the remaining water was removed from the membrane core.

All atomistic MD simulations were performed using the GROMACS 5.0 simulation package.^{40,41} The simulations were performed under periodic boundary conditions in all directions with a 2 fs time step, using the Nosé–Hoover thermostat method^{42,43} and semi-isotropic pressure (1 bar) coupling using the Parrinello–Rahman barostat method.⁴⁴ As used also previously³⁵ for the CHARMM36 force field, van der Waals interactions were switched off to zero between 0.8 and 1.2 nm distances of interacting atoms and electrostatic interactions were treated by particle mesh Ewald from 1.2 nm.

For isothermal simulations, we performed 500 ns simulations at 310 K for both mixed and pure bilayers. After initial equilibration (50 ns), the systems reached stable properties, and we analyzed the macroscopic structural properties of the bilayers, such as area per lipid and membrane thickness (defined as the distance between the highest density of nitrogen atoms); we also monitored deuterium order parameters of acyl tails (S_{CD}), by standard GROMACS tool `g_order`). Further, we evaluated the water content in the middle of the pure Cer membranes and Cer headgroup organization.

As the lipid phase is directly related to the area per lipid (APL),⁴⁵ we evaluated the stability and phase transitions of the membranes based on the variation in area per lipid during heating. We let the bilayers equilibrate for 20 ns at 300 K and then heated them gradually to 400 K over the next 180 ns. We are aware of the high rate of heating (0.56 K/ns); therefore, we took into account only large and irreversible changes in the area per lipid versus temperature slope.

For coarse-grain (CG) simulations using the MARTINI-compatible force field,³⁷ we also prepared fully hydrated (at least 28 water beads per lipid; each water bead represents four water molecules) bilayers consisting of 512 Cer. These bilayers were constructed using the `insane.py` script (freely available at <http://md.chem.rug.nl/cgmartini>). For full length Cer, we used our recently introduced CG parameters,⁷ while for the short Cer, topologies were derived by shortening the C24 acyl tail. The acyl tail of oleoyl-Cer was mapped in the same manner as the sn-2 tail of POPC.³⁷ CG systems were denoted with the same system as in all atom simulation, CerNCG, where *N* stands for the number carbon atoms that would correspond to the number of carbons in an all atom representation. Thus, Cer4CG corresponds to (atomistic) Cer4 and has one CG bead, Cer24CG corresponds to Cer24 and has six CG beads, etc. All CG simulations were performed using the GROMACS 4.0.7 simulation package.⁴⁰ Systems were relaxed by 1000 steps using steepest descent geometry optimization followed by a series of short *NVT* and *NPT* MD simulations (1000 steps each) with increasing time steps of 1, 2, 5, and 10 fs. Finally, a 30 fs time step was used for production simulations (6 μ s for each system) at 310 K with separate velocity-rescaling thermostats⁴⁶ for Cer and water and Berendsen pressure coupling⁴⁷ (10^5 Pa) with the compressibility set to 4.6×10^{-10} Pa⁻¹. van der Waals interactions were shifted to zero between 0.9 and 1.2 nm, and Coulombic interactions were not considered. Pair lists were updated every 10 steps. Analyses of the last 5 μ s of simulations were performed using standard GROMACS tools. APL and membrane thickness were computed as described previously.⁴⁸ The order parameter S_{CC} was computed using the `do-order.py` script (freely available at <http://md.chem.rug.nl/cgmartini>). The conformations of Cer were determined on the basis of the angle between the terminal tail beads and the H1 headgroup bead (containing a nitrogen atom).

RESULTS

The Area per Lipid and Membrane Thickness Depend on Ceramide Chain Length. We analyzed the macroscopic structural parameters of Cer bilayers and observed an increase in the bilayer volume with an increasing Cer chain length (Figure 2). The chain length and area per lipid (APL) are

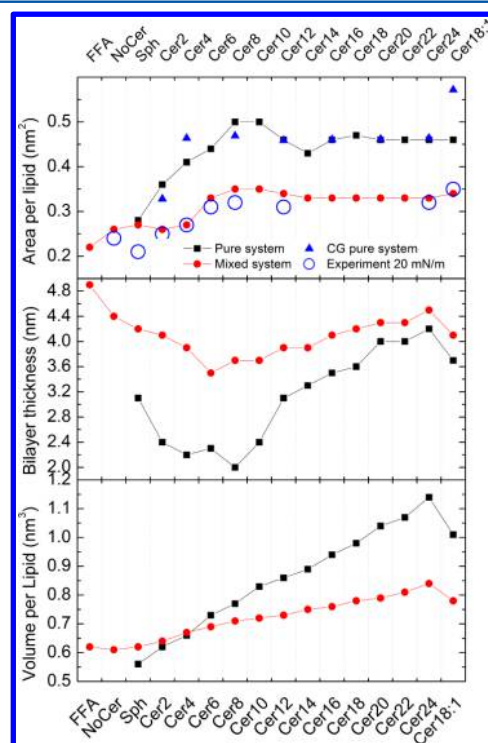


Figure 2. Area per lipid (top), bilayer thickness (middle), and volume per lipid (bottom) of pure (black line with squares) and mixed (red line with dots) Cer bilayers. The area per lipid is compared to the experimental area per lipid of the monolayer mixture at 20 mN/m from ref 19 (top, blue circles) and to CG pure systems (blue triangles). NoCer stands for a membrane composed of only FFA and Chol; FFA is composed of only FFA.

initially linearly correlated in pure bilayers; APL grows from Sph (0.28 nm^2) to Cer8 (0.50 nm^2 for both Cer8 and Cer10). However, further elongation does not lead to an additional APL increase (Cer12 and longer Cer all have similar APLs of $\sim 0.46 \text{ nm}^2$), but rather to an increase in membrane thickness for a pure bilayer (Figure 2). Pure bilayers have the smallest bilayer thickness at Cer8 (2.0 nm), whereas shortening or lengthening the chain leads to an increase in bilayer thickness. The APL from CG simulations nicely fits the atomistic simulation for pure bilayers with the exception of Cer18:1 (Figure S8 of the Supporting Information). In mixed bilayers, the thickness decreases from FFA (4.9 nm of the bilayer) to Cer6 (3.5 nm). From Cer6, the bilayer thickness grows with lipid chain length to Cer24 (4.5 nm). A double bond in Cer18:1 increases APL and decreases D_{HH} . APL values of Cer4–Cer8 show larger fluctuations (Figure S1 of the Supporting Information). In mixed bilayers, both APL and bilayer thickness are less dependent on the chain length than in the case of pure bilayers. Further, in mixed systems, the APL is almost constant above Cer6 ($\sim 0.33 \text{ nm}^2$).

The Lowest Level of Ordering Was Observed in Cer6 and Cer8 Membranes. We also analyzed average deuterium

order parameters [$S_{(\text{CD})}$ (see the Supporting Information for the proper definition)] of the lipid tails and observed lower $S_{(\text{CD})}$ in bilayers with short Cer (Figure 3). Overall, the $S_{(\text{CD})}$

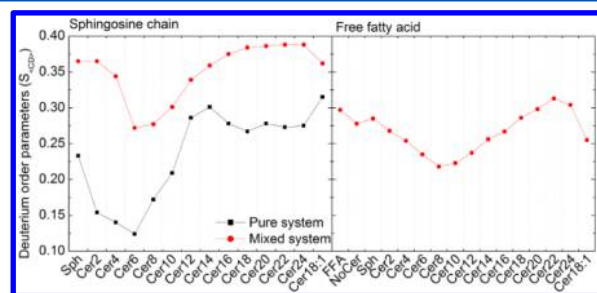


Figure 3. Average deuterium order parameters calculated for sphingosine chains of Cer (left) and FFA in the mixtures (right).

values of sphingosine chains were lower in pure bilayers than in the mixed bilayers, which was also affected by a smaller tilt angle in mixed bilayers (Figure S2 of the Supporting Information). In the case of pure lipid bilayers, we observed the lowest $S_{(\text{CD})}$ for Cer2–Cer6 (~ 0.14) and in mixed bilayers for Cer6 and Cer8 (0.27). We analyzed the $S_{(\text{CD})}$ for FFA in the mixed system, and here we observed the lowest $S_{(\text{CD})}$ for Cer8 and Cer10 membranes [0.22 (Figure 3 and Figure S3 of the Supporting Information)]. The order parameters of the plateau region of FFA in the Cer24 mixture go to ~ 0.4 , which agrees with experimental findings for stearic acid in a Cer mixture (~ 0.4).⁴⁹ The pure FFA bilayer was also significantly ordered, with ordering and tilt angles similar to those of the pure Cer24 bilayer (tilt angles of $\sim 27^\circ$ and $\sim 24^\circ$ for FFA and Cer24 bilayers, respectively). Increasing or decreasing the chain length below six or above eight carbons leads to an increase in the order parameters for both FFA and Cer24.

Ceramides Undergo a Phase Transition toward a Nonlamellar or Liquid-Disordered Phase. We monitored the temperature dependence of APL and evaluated the phase behavior based on the changes in APL while heating the simulation system. Experimentally, Cer24 exhibits two phase transitions, from an orthorhombic gel to a hexagonal gel phase at ~ 333 K and from a hexagonal gel phase to a disordered phase (liquid crystalline, LQ) at ~ 371 K.¹⁸ However, while the transition between the orthorhombic and hexagonal phases is visible in FTIR spectra as a disappearance of the splitting of

methylene scissoring or rocking band, the experimental APL measurement for that phase transition is almost unchanged,⁵⁰ and therefore, we focused on large changes in APL trends showing more visible transitions. The phase transition temperature between the gel and LQ can be visible during the evolution of APL during heating scans of simulated lipid bilayers, while it is impossible to read it from cooling scans of the same samples.⁵¹ In our simulations in pure Cer bilayers, long Cer [Cer24, Cer18:1, and Cer12 (Figure 4)] show a steep enlargement of APL, indicating gel \rightarrow LQ phase transitions. As the Cer tails become shorter, transition temperatures become lower, as well. Note also that in our case the system is heated throughout the simulation quite quickly (0.56 K/ns), resulting in a nonequilibrium simulation, unlike in the case of isothermal simulations. This leads to large APL fluctuations, and therefore, we can evaluate only permanent and sharp changes in the APL versus temperature scans and use them for approximate predictions of the phase transition temperature; however, we are unable to describe all possible transitions, e.g., orthorhombic \rightarrow hexagonal gel phase transitions. Sph and short Cer [Cer6 and Cer8 (Figure 4)] show rather complex behavior; the APL of rather disordered bilayer even at low temperatures is gradually growing with increased temperature with several steps and drops that cannot be significantly evaluated because of the nonequilibrium conditions. Above ~ 380 – 390 K, the bilayers lose their lamellar structure. This is, however, not the case for Cer2 and Cer4, which seem to be more stable than Cer6 and Cer8 (though Cer4 seems to be less stable than Cer2). In a manner consistent with the known ability of cholesterol to broaden the phase transition,⁵² we observed continuous growth of the APL with temperature for Cer mixtures with no irreversible transitions as observed for pure Cer (Figure S4 of the Supporting Information). In all, the most unstable systems were formed with pure Cer4, Cer6, Cer8, and Sph.

Water Penetrates inside Pure Ceramide Membranes.

During the free simulations, a significant amount of water molecules spontaneously penetrated into the pure short Cer bilayers but not in the mixed membranes. The water content of pure Cer bilayers increased with chain length from Sph to Cer6 and dropped again for Cer8 (Figure 5). Water molecules penetrated as funnel-like strings forming a semipore reaching the middle of the bilayer (Figures 6 and 7). Very few water molecules penetrated into long Cer bilayers. However, in the case of a water drop artificially formed in the middle of the membrane during the equilibration step, this drop stayed

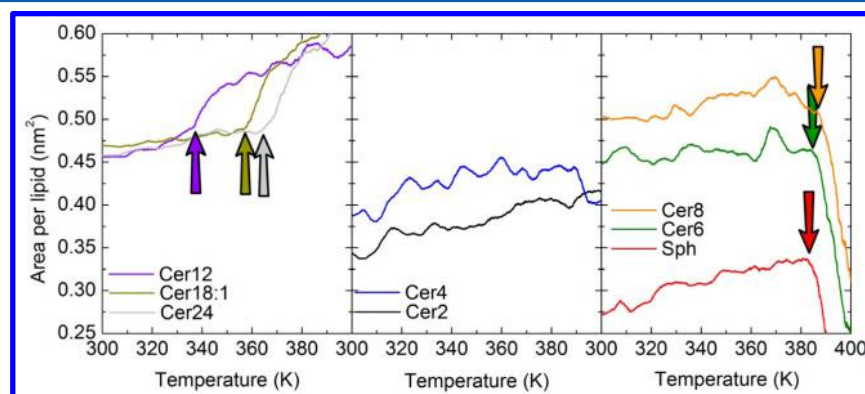


Figure 4. Dependence of area per lipid on temperature in pure Cer membranes (only experimentally studied lipids are shown for the sake of clarity). The steep increase in area per lipid in the left panel shows a gel–liquid crystalline transition. The strong decrease in the right panel in Sph, Cer6, and Cer8 shows a transition toward a nonlamellar phase.

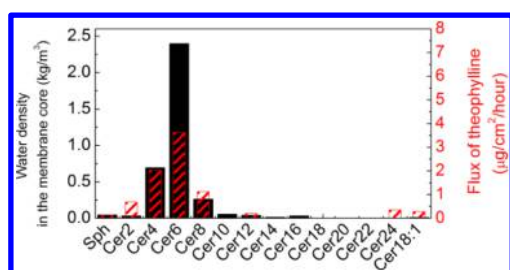


Figure 5. Water content in the middle of the membrane (black bars) compared to experimentally measured flux of theophylline (red bars) from ref 19.

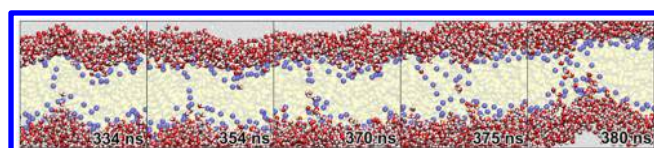


Figure 6. Snapshots of water penetrating into the membrane in a pure Cer6 bilayer. Cer6 is colored yellow. Nitrogens are colored blue. Bulk water is shown as gray dots. Water molecules in contact with Cer are shown as white and red spheres.

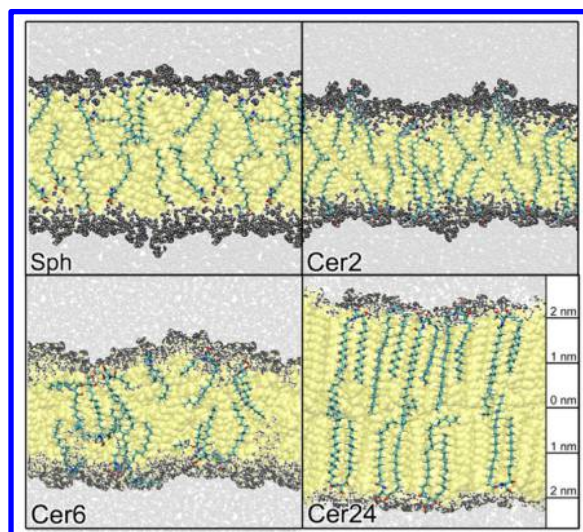


Figure 7. Snapshots of Sph, Cer2, Cer6, and Cer24 membranes. In Cer6, the water penetrating into the middle of the membrane is visible, while the Cer24 bilayer “stayed dry”. The Cer6 membrane has significant undulation, while Sph and Cer2 are flatter. The gray dots represent water molecules; the yellow background displays the membrane, and some (not all) Cer molecules are shown as sticks.

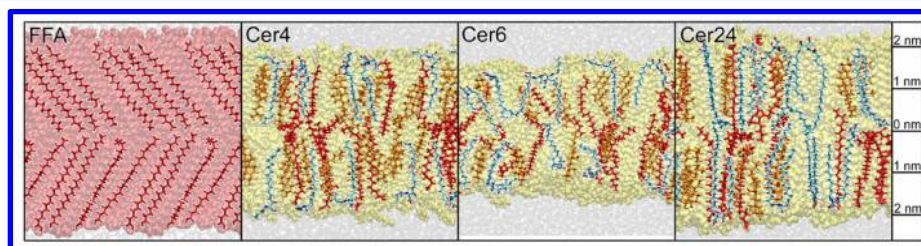


Figure 8. Membrane composed of pure FFA (left) and mixed membranes composed of Cer4, Cer6, and Cer24 (blue) with Chol (orange) and FFA (red). In Cer4, the middle of the membrane is formed almost entirely with FFA, and Cer chain elongation leads to an increasing level of interdigitation of Cer tails.

trapped in the membrane of long Cer but was repelled when the membrane formed in short Cer (these data were not included in water content analysis). The density of water in the middle of pure Cer membranes corresponds closely to the permeability of these membranes to small hydrophilic molecules.

Longer Aliphatic Chains Interdigitate in the Membrane Core. At the atomistic level, we observed interdigitation of FFA or long Cer chains in the bilayer core (Figures 7 and 8). Pure Cer with shorter chains (from Sph until Cer10) formed disordered layers. The long lipids (from Cer12 up) formed highly ordered gel bilayers with significant chain interdigitation, resulting in a flexible disordered region in the bilayer center. The significant exception to the trends here is the FFA system; FFA molecules are not interdigitated and are highly ordered across the whole membrane region (Figure 8 and Figure S5 of the Supporting Information). In mixed bilayers, short Cer formed two ordered layers separated by a disordered region composed mostly of FFA tails in the membrane center. Cer chains are localized either in headgroups [shorter chain (see the next paragraph)] or in ordered layers (longer chains, sphingosine chain). Cholesterol is also located mostly in the ordered layers. The NoCer system is arranged in a similar way; both bilayer leaflets are organized and composed of FFA and Chol and are separated by a disordered region composed of interdigitated FFA chains. Elongation of Cer leads to incorporation of Cer chains into the middle FFA tail rich disordered layer, thus ordering it.

Shorter Ceramide Tails Are Oriented into the Headgroup Region. A detailed analysis of the angles between terminal methyl carbons and nitrogen in headgroups showed significant conformational changes depending on the chain length. In well-ordered long Cer bilayers, the angle between the tail carbons is $\sim 17^\circ$ (Figures 8 and 9 and Table S1 of the Supporting Information). Decreasing the acyl chain length below 10 carbons leads to a significant increase in this angle, and the shorter acyl chains are then oriented into the headgroup area instead of being incorporated into the lamellar lipid structure. This is consistent in both pure and mixed Cer bilayers.

DISCUSSION

Pure Ceramide Bilayers Are More Sensitive to Acyl Chain Length Than Mixed Systems. In our model simulations of pure bilayer systems, long Cer are highly ordered while short Cer adopt a more disordered phase. When initially arranged into the bilayer, the most abundant Cer in the human SC (Cer24) forms an ordered bilayer with a dry interior, tilted lipid chains, and a sharp boundary between Cer

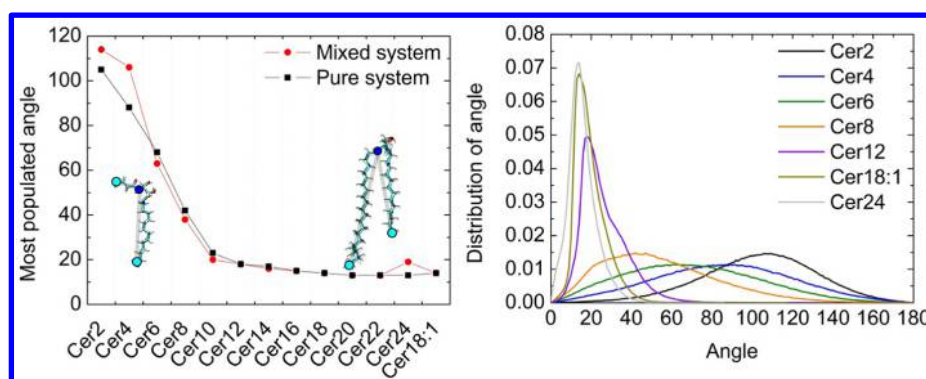


Figure 9. Most populated angles between terminal methyls of Cer chains and nitrogen (left) and angle distribution plots (right; only some of the Cer are shown) are very similar for both pure (displayed) and mixed membranes.

and water (Figure 7). In agreement with previous studies, the part of the bilayer occupied by both lipid tails is highly ordered,^{8,24} while the middle layer formed by interdigitated Cer acyl chains is disordered. Shortening of Cer acyl chain leads to more disordered membranes with significant undulation at 310 K and lower order parameters (Figure 3), affected by a significant tilt angle (Figure S2 of the Supporting Information). The decreased ordering was also experimentally observed on Cer6, Cer8, and Cer12 using FTIR spectra of pure Cer; the typical orthorhombic packing was not observed in those experiments.¹⁸ The disordered regions were also reported experimentally in Cer/FFA/Chol/CholS mixtures, where short Cer showed larger portions of disordered phase content probably located in phase-separated Cer-rich domains.¹⁹ Though the preference of short Cer for the disordered phase has been repeatedly reported,^{19,53} the phase transition temperature (T_m) experimentally measured for short Cer is interpreted as the gel \rightarrow liquid crystalline phase transition. We suggest here the reconsideration of this interpretation, as the short Cer may be as well in the disordered or partially disordered phase at body temperature.

The adoption of the disordered phase is mainly caused by arrangement of a shorter lipid chain. When inspected in simulations, short Cer are not present in a hairpin orientation, but they are more likely arranged in an L shape or even an extended-like conformation (Figure 9 and Table S1 of the Supporting Information). The elongation of the acyl chain arranged in an L shape leads to an increase in the APL, while the hairpin-oriented Cer all possess similar APL values (Figure 2 and Figure S8 of the Supporting Information for the CG model). Though we did not observe long Cer arranged in an extended conformation, they might be arranged in this way in multilayers or crystals with slightly different structural properties, such as the lamellar repeat distance. When heated, long Cer go through a phase transition from the gel phase to the liquid crystalline phase, while the shorter ones collapse into a nonlamellar phase (Figure 4). Overall, pure Cer membranes are very sensitive to Cer chain length.

The addition of Chol and FFA stabilizes Cer bilayers and makes them less sensitive to the length of the Cer chain. The APL of mixed bilayers is lower than those of pure bilayers (Figure 2), with the only exception being Sph bilayers that possess the same APL as the NoCer mixture (FFA and Chol). On the other hand, bilayer thickness is larger in mixed bilayers than in pure ones. The development of APL during heating is more complex in mixed bilayers (Figure S4 of the Supporting Information); however, no nonlamellar transition was observed

for any of the systems. The behavior of Cer mixtures is in agreement with former studies of cholesterol and phosphatidylcholines, where increases in order parameters and broadening of the phase transition were also observed.⁵⁴ However, increasing the S_{CD} and bilayer thickness is here mostly caused by a reduction in the tilt angle of Cer in mixed system (Figure S2 of the Supporting Information) and not by ordering of the bilayer, though visually, the pure bilayers are more ordered (Figures 7 and 8). The NoCer system also formed an ordered bilayer (Figure 3), but in the simulations of mixtures, FFA arranged into ordered leaflets and their tails formed a disordered mobile region in the bilayer core. This is in contrast with FTIR spectra that show a high degree of order for FFA even in the most permeable membranes¹⁹ and supports the experimental observation of phase separation. The FTIR spectra are in agreement with the FFA bilayer that formed a highly ordered, tilted layer (Figure 8 and Figure S5 of the Supporting Information). Because of time and size limitations, mixture simulations did not reproduce the phase separation experimentally expected. Consequently, from the atomistic simulation point of view, a mixed bilayer is not the best model for experimental Cer/FFA/Chol/CholS mixtures. Two independent models, including (1) impermeable FFA or NoCer bilayers and (2) a permeable pure Cer bilayer, better capture the experimental behavior.

The Incorporation of the Shorter Acyl Chain into the Headgroups Destabilizes Short Cer Bilayers. We observed that the permeability of small hydrophilic molecules through multilayers of Cer mixtures could be successfully modeled by a pure Cer bilayer. One would expect that the mixed lipid bilayer should reproduce theophylline/water penetration in mixed experimental systems, but no water penetrating into those bilayer models was observed. The phase separation, as was discussed in the previous section, suggests different interactions of molecules with various membrane phases. We monitored water molecules spontaneously penetrating into pure Cer bilayers and observed good correlation with the experimental flux of the small hydrophilic molecule theophylline (Figure 5). Small hydrophilic molecules permeate via free volume diffusion,⁵⁵ and we suggest that theophylline uses a mechanism similar to that of water; also, a mild correlation of the permeation of theophylline and TEWL was observed previously.⁵⁶ Moreover, theophylline permeation might be directly influenced by the presence of water in the membrane. The different permeability and quantity of water inside short Cer (Cer4–Cer6) membranes stem from a different structural organization.

The major contribution for the permeability of the membrane for hydrophilic molecules seems to be the conformation of lipids in the headgroup area driven by the length of the acyl tail. The significant conformational changes that we observed in this region result in a lower phase stability (Figure 4) and a higher permeability for water (Figure 5). While all long chain Cer molecules are in the hairpin conformation with a narrow peak in the terminal carbon angle distribution (Figure 9 and Table S1 of the Supporting Information), a decrease in the acyl chain length leads to broadening of the angle distribution and the acyl chain is oriented in the headgroup region (Figures 7–9). Similar behavior was previously observed in oxidized PC membranes, where it was linked with increased water permeability as well as enhancement of formation of water defects and pores.⁵⁷ Naturally, such a disturbance also influences the stability of the bilayer (Figure 4). We observed a nonlamellar transition for Sph, Cer6, and Cer8 and a drop in the APL in Cer4. The lower stability of these membranes also results in a lower energy barrier for their disturbance by a permeating substrate, which can be hypothesized as a local membrane phase transition event.

The permeability of lipophilic molecules is proposed to follow lateral diffusion in the membranes^{55,58} and is also affected by the mobility or ordering of membrane lipids. A correlation between the order parameters of lipid chains and permeability was found for phosphatidylcholine mixtures with cholesterol,⁴⁵ and we can assume a similar relationship in Cer: the higher the order parameters, the lower the permeability. The lowest order parameters were found for Cer6 and Cer8 in mixed systems and also for Cer6 in the pure system (Figure 3) and reflect well the most permeating systems.

MD Simulations with Used Force Field Parameters Reproduce Well Experimental Properties of Cer. We focused here on the ability of MD simulations to capture the trend of different permeabilities of Cer with varying tail lengths. The APL, trends in $S_{\langle CD \rangle}$, or spontaneous water permeability reproduces well the experimentally observed properties (for more discussion of FF issues, see the Supporting Information). Though the only difference between the systems is the length of one acyl chain, the crucial differences appeared to be localized mainly in the headgroup conformation. The input parameters (FFs) of the headgroups were identical in all simulations in the respective force fields and appeared to be capable of modeling hairpin, L shape, and extended Cer conformations. As multiple experimentally derived SC models have been published and all of them have been based on a multilayer structure, this can be crucial for such modeling. For example, the Norlén⁵⁹ and Kiselev⁶⁰ models consider the extended conformation of Cer as a crucial connection between the SC layers. Moreover, the water spontaneously penetrating into pure Cer reflects very precisely the experimentally observed permeabilities of theophylline. From knowledge gained by comparison of experimentally observed permeabilities and simulated properties, we can assume that Cer10 (not studied by experiment) will still belong to more permeable Cer, while all other long Cer possess strong barrier properties. Together, MD simulations with MARTINI and CHARMM36 FF appeared to be very effective for SC superstructure and CHARMM36 FF also for the permeability studies.

CONCLUSION

In this paper, we rationalized in the atomistic resolution the increased permeability of model skin lipid membranes composed of short Cer. Though the experimental observations are performed on model mixture multilayers, we focused on the ability of the MD simulation to model their properties by simple bilayers. In our simulation models composed of either lipid mixtures or pure Cer arranged into bilayers, we observed that the shorter Cer chains do not incorporate into the lipid chain matrix of the bilayer but instead reside in the membrane headgroup region. Their shorter chains disrupt the close packing that is typical for the skin lipids. Consequently, they influence the area per lipid, lipid ordering, mobility of lipid atoms, phase stability of the bilayer, and bilayer permeability. The experimental evidence of the preference of shorter chain Cer for the disordered phase has been also observed,^{19,53} and here we present a similar theoretical proposal. Therefore, we suggest a reconsideration of this experimental interpretation as the shorter chain Cer (Sph-Cer10) may be present in a phase more disordered than previously thought as they have a weaker preference for hairpin conformation typical for Cer bilayers mimicking gel phase membranes. The crucial property of the disturbing chain appeared to be its length. Although the shortest Cer (Cer2) chains reside more in the headgroup region, they are not long enough to sufficiently disturb the membrane structure to allow increased permeability. With increasing lipid chain length, this disturbance grows until the hairpin conformation prevails. The short Cer (Cer4, Cer6, and Cer8) are then shown to be the most permeable in agreement with the experiment with addition of Cer10, which was not studied by experiment, while this effect was more pronounced in pure Cer membranes effectively modeling the effects of experimentally observed phase separation. We believe that knowledge of the relationship between lipid composition and arrangement and, consequently, the permeability of the skin lipid barrier will bring another perspective to our understanding of skin diseases such as atopic dermatitis, psoriasis, or ichthyoses. This knowledge should also extend to toxicological risk assessment and more rational development of barrier repair strategies. Finally, more mechanistic knowledge of permeation through the stratum corneum lipids would be beneficial in the field of transdermal/topical drug delivery, including permeation enhancing strategies.

ASSOCIATED CONTENT

Supporting Information

Area per lipid fluctuation during isothermal evolution (Figure S1), average tilt angles of sphingosine chains (Figure S2), individual deuterium order parameters and definition of order parameters (Figure S3), dependence of area per lipid on temperature in mixed Cer membranes (Figure S4), structure of the FFA and NoCer system (Figure S5), Cer headgroup organization (Table S1), a discussion concerning force field performance, structures of CG simulation systems (Figure S6), $S_{\langle CC \rangle}$ order parameters in the CG simulation (Figure S7), structural parameters stemming from CG simulations (Figure S8), average B factors for the most fluctuating carbons and corresponding results (Figure S9), and topologies for Cer, FFA, and Chol in Gromacs format. The Supporting Information is available free of charge on the ACS Publications website at DOI: 10.1021/acs.jpccb.5b05522.

AUTHOR INFORMATION

Corresponding Author

*E-mail karel.berka@upol.cz. Phone: +420-58 563 4769.

Notes

The authors declare no competing financial interest.

ACKNOWLEDGMENTS

Thanks to Jeff Klauđa for sharing CHARMM36 parameters of Cer ahead of publication. We gratefully acknowledge support through Project LO1305 of the Ministry of Education, Youth and Sports of the Czech Republic. M.O. acknowledges support from the Czech Grant Agency through Project P208/12/G016. M.P. acknowledges support from a student project of Palacký University Olomouc (IGA_PrF_2015_027). Ž.S. was supported by the Operational Program Education for Competitiveness European Social Fund (Projects CZ.1.07/2.3.00/30.0041). The access of Ž.S. to computing and storage facilities owned by parties and projects contributing to the National Grid Infrastructure MetaCentrum and IT4Innovations (LM2010005 and LM2011033) is greatly appreciated.

REFERENCES

- (1) Menon, G. K.; Cleary, G. W.; Lane, M. E. The Structure and Function of the Stratum Corneum. *Int. J. Pharm.* **2012**, *435*, 3–9.
- (2) Van Meer, G.; Voelker, D. R.; Feigenson, G. W. Membrane Lipids: Where They Are and How They Behave. *Nat. Rev. Mol. Cell Biol.* **2008**, *9*, 112–124.
- (3) Wertz, P. W. Lipids and Barrier Function of the Skin. *Acta Dermato-Venereologica, Suppl.* **2000**, *80*, 7–11.
- (4) Pascher, I. Molecular Arrangements in Sphingolipids. Conformation and Hydrogen Bonding of Ceramide and Their Implication on Membrane Stability and Permeability. *Biochim. Biophys. Acta, Biomembr.* **1976**, *455*, 433–451.
- (5) Guo, S.; Moore, T. C.; Iacovella, C. R.; Strickland, L. A.; McCabe, C. Simulation Study of the Structure and Phase Behavior of Ceramide Bilayers and the Role of Lipid Head Group Chemistry. *J. Chem. Theory Comput.* **2013**, *9*, 5116–5126.
- (6) Pascher, I.; Sundell, S. Molecular Arrangements in Sphingolipids: Crystal Structure of the Ceramide. *Chem. Phys. Lipids* **1992**, *62*, 79–86.
- (7) Sovová, Ž.; Berka, K.; Otyepka, M.; Jurečka, P. Coarse-Grain Simulations of Skin Ceramide NS with Newly Derived Parameters Clarify Structure of Melted Phase. *J. Phys. Chem. B* **2015**, *119*, 3988–3998.
- (8) Paloncýová, M.; DeVane, R. H.; Murch, B. P.; Berka, K.; Otyepka, M. Rationalization of Reduced Penetration of Drugs through Ceramide Gel Phase Membrane. *Langmuir* **2014**, *30*, 13942–13948.
- (9) Wertz, P. W. Current Understanding of Skin Biology Pertinent to Skin Penetration: Skin Biochemistry. *Skin Pharmacol. Physiol.* **2013**, *26*, 217–226.
- (10) Elias, P. M.; Friend, D. S. The Permeability Barrier in Mammalian Epidermis. *J. Cell Biol.* **1975**, *65*, 180–191.
- (11) Bouwstra, J. A.; Ponc, M. The Skin Barrier in Healthy and Diseased State. *Biochim. Biophys. Acta, Biomembr.* **2006**, *1758*, 2080–2095.
- (12) Holleran, W. M.; Takagi, Y.; Uchida, Y. Epidermal Sphingolipids: Metabolism, Function, and Roles in Skin Disorders. *FEBS Lett.* **2006**, *580*, 5456–5466.
- (13) Janssens, M.; van Smeden, J.; Gooris, G. S.; Bras, W.; Portale, G.; Caspers, P. J.; Vreeken, R. J.; Hankemeier, T.; Kezic, S.; Wolterbeek, R.; et al. Increase in Short-Chain Ceramides Correlates with an Altered Lipid Organization and Decreased Barrier Function in Atopic Eczema Patients. *J. Lipid Res.* **2012**, *53*, 2755–2766.
- (14) Janssens, M.; van Smeden, J.; Gooris, G. S.; Bras, W.; Portale, G.; Caspers, P. J.; Vreeken, R. J.; Kezic, S.; Lavrijsen, A. P. M.; Bouwstra, J. A. Lamellar Lipid Organization and Ceramide Composition in the Stratum Corneum of Patients with Atopic Eczema. *J. Invest. Dermatol.* **2011**, *131*, 2136–2138.
- (15) Tawada, C.; Kanoh, H.; Nakamura, M.; Mizutani, Y.; Fujisawa, T.; Banno, Y.; Seishima, M. Interferon- γ Decreases Ceramides with Long-chain Fatty Acids: Possible Involvement in Atopic Dermatitis and Psoriasis. *J. Invest. Dermatol.* **2014**, *134*, 712–718.
- (16) Eckl, K.-M.; Tidhar, R.; Thiele, H.; Oji, V.; Hausser, I.; Brodessa, S.; Preil, M.-L.; Onal-Akan, A.; Stock, F.; Müller, D.; et al. Impaired Epidermal Ceramide Synthesis Causes Autosomal Recessive Congenital Ichthyosis and Reveals the Importance of Ceramide Acyl Chain Length. *J. Invest. Dermatol.* **2013**, *133*, 2202–2211.
- (17) Abraham, W.; Downing, D. T. Preparation of Model Membranes for Skin Permeability Studies Using Stratum Corneum Lipids. *J. Invest. Dermatol.* **1989**, *93*, 809–813.
- (18) Janušová, B.; Zbytovská, J.; Lorenc, P.; Vavryšová, H.; Palát, K.; Hrabálek, A.; Vávrová, K. Effect of Ceramide Acyl Chain Length on Skin Permeability and Thermotropic Phase Behavior of Model Stratum Corneum Lipid Membranes. *Biochim. Biophys. Acta, Mol. Cell Biol. Lipids* **2011**, *1811*, 129–137.
- (19) Školová, B.; Janušová, B.; Zbytovská, J.; Gooris, G.; Bouwstra, J.; Slepíčka, P.; Berka, P.; Roh, J.; Palát, K.; Hrabálek, A.; et al. Ceramides in the Skin Lipid Membranes: Length Matters. *Langmuir* **2013**, *29*, 15624–15633.
- (20) Marrink, S.-J.; Berendsen, H. J. C. Simulation of Water Transport through a Lipid Membrane. *J. Phys. Chem.* **1994**, *98*, 4155–4168.
- (21) Orsi, M.; Essex, J. W. Permeability of Drugs and Hormones through a Lipid Bilayer: Insights from Dual-Resolution Molecular Dynamics. *Soft Matter* **2010**, *6*, 3797–3808.
- (22) Notman, R.; Anwar, J. Breaching the Skin Barrier - Insights from Molecular Simulation of Model Membranes. *Adv. Drug Delivery Rev.* **2013**, *65*, 237–250.
- (23) Höltje, M.; Förster, T.; Brandt, B.; Engels, T.; von Rybinski, W.; Höltje, H. D. Molecular Dynamics Simulations of Stratum Corneum Lipid Models: Fatty Acids and Cholesterol. *Biochim. Biophys. Acta, Biomembr.* **2001**, *1511*, 156–167.
- (24) Das, C.; Noro, M. G.; Olmsted, P. D. Simulation Studies of Stratum Corneum Lipid Mixtures. *Biophys. J.* **2009**, *97*, 1941–1951.
- (25) Torin Huzil, J.; Sivaloganathan, S.; Kohandel, M.; Foldvari, M. Drug Delivery through the Skin: Molecular Simulations of Barrier Lipids to Design More Effective Noninvasive Dermal and Transdermal Delivery Systems for Small Molecules, Biologics, and Cosmetics. *Wiley Interdiscip. Rev. Nanomed. Nanobiotechnol.* **2011**, *3*, 449–462.
- (26) Pandit, S. A.; Scott, H. L. Molecular-Dynamics Simulation of a Ceramide Bilayer. *J. Chem. Phys.* **2006**, *124*, 014708.
- (27) Hadley, K. R.; McCabe, C. A Simulation Study of the Self-Assembly of Coarse-Grained Skin Lipids. *Soft Matter* **2012**, *8*, 4802–4814.
- (28) MacDermaid, C. M.; DeVane, R. H.; Klein, M. L.; Fiorin, G. Dehydration of Multilamellar Fatty Acid Membranes: Towards a Computational Model of the Stratum Corneum. *J. Chem. Phys.* **2014**, *141*, 22D526.
- (29) Neale, C.; Bennett, W. F. D.; Tieleman, D. P.; Pomès, R. Statistical Convergence of Equilibrium Properties in Simulations of Molecular Solutes Embedded in Lipid Bilayers. *J. Chem. Theory Comput.* **2011**, *7*, 4175–4188.
- (30) Paloncýová, M.; Berka, K.; Otyepka, M. Convergence of Free Energy Profile of Coumarin in Lipid Bilayer. *J. Chem. Theory Comput.* **2012**, *8*, 1200–1211.
- (31) Notman, R.; den Otter, W. K.; Noro, M. G.; Briels, W. J.; Anwar, J. The Permeability Enhancing Mechanism of DMSO in Ceramide Bilayers Simulated by Molecular Dynamics. *Biophys. J.* **2007**, *93*, 2056–2068.
- (32) Das, C.; Olmsted, P.; Noro, M. Water Permeation through Stratum Corneum Lipid Bilayers from Atomistic Simulations. *Soft Matter* **2009**, *5*, 4549–4556.
- (33) Notman, R.; Anwar, J.; Briels, W. J.; Noro, M. G.; den Otter, W. K. Simulations of Skin Barrier Function: Free Energies of Hydro-

phobic and Hydrophilic Transmembrane Pores in Ceramide Bilayers. *Biophys. J.* **2008**, *95*, 4763–4771.

(34) Klauda, J. B.; Venable, R. M.; Freites, J. A.; O'Connor, J. W.; Tobias, D. J.; Mondragon-Ramirez, C.; Vorobyov, I.; MacKerell, A. D.; Pastor, R. W.; Connor, J. W. O.; et al. Update of the CHARMM All-Atom Additive Force Field for Lipids: Validation on Six Lipid Types. *J. Phys. Chem. B* **2010**, *114*, 7830–7843.

(35) Palonciová, M.; Fabre, G.; Devane, R. H.; Trouillas, P.; Berka, K.; Otyepka, M. Benchmarking of Force Fields for Molecule – Membrane Interactions. *J. Chem. Theory Comput.* **2014**, *10*, 4143–4151.

(36) Venable, R. M.; Sodt, A. J.; Rogaski, B.; Rui, H.; Hatcher, E.; MacKerell, A. D.; Pastor, R. W.; Klauda, J. B. CHARMM All-Atom Additive Force Field for Sphingomyelin: Elucidation of Hydrogen Bonding and of Positive Curvature. *Biophys. J.* **2014**, *107*, 134–145.

(37) Marrink, S. J.; Risselada, H. J.; Yefimov, S.; Tieleman, D. P.; de Vries, A. H. The MARTINI Force Field: Coarse Grained Model for Biomolecular Simulations. *J. Phys. Chem. B* **2007**, *111*, 7812–7824.

(38) Pastor, R. W.; Mackerell, A. D. Development of the CHARMM Force Field for Lipids. *J. Phys. Chem. Lett.* **2011**, *2*, 1526–1532.

(39) Vanommeslaeghe, K.; Hatcher, E.; Acharya, C.; Kundu, S.; Zhong, S.; Shim, J.; Darian, E. CHARMM General Force Field: A Force Field for Drug-Like Molecules Compatible with the CHARMM All-Atom Additive Biological Force Fields. *J. Comput. Chem.* **2009**, *31*, 671–690.

(40) Van Der Spoel, D.; Lindahl, E.; Hess, B.; Groenhof, G.; Mark, A. E.; Berendsen, H. J. C. GROMACS: Fast, Flexible, and Free. *J. Comput. Chem.* **2005**, *26*, 1701–1718.

(41) Hess, B.; Kutzner, C.; van der Spoel, D.; Lindahl, E. GROMACS 4: Algorithms for highly efficient, load-balanced, and scalable molecular simulation. *J. Chem. Theory Comput.* **2008**, *4*, 435–447.

(42) Nosé, S. A Unified Formulation of the Constant Temperature Molecular Dynamics Methods. *J. Chem. Phys.* **1984**, *81*, 511–519.

(43) Hoover, W. G. Canonical Dynamics: Equilibrium Phase-Space Distributions. *Phys. Rev. A: At., Mol., Opt. Phys.* **1985**, *31*, 1695–1697.

(44) Parrinello, M.; Rahman, A. Polymorphic Transitions in Single Crystals: A New Molecular Dynamics Method. *J. Appl. Phys.* **1981**, *52*, 7182–7190.

(45) Xiang, T. X.; Anderson, B. D. Permeability of Acetic Acid across Gel and Liquid-crystalline Lipid Bilayers Conforms to Free-Surface-Area Theory. *Biophys. J.* **1997**, *72*, 223–237.

(46) Bussi, G.; Donadio, D.; Parrinello, M. Canonical Sampling Through Velocity Rescaling. *J. Chem. Phys.* **2007**, *126*, 014101.

(47) Berendsen, H.; Postma, J.; Vangunsteren, W.; Dinola, A.; Haak, J. Molecular-Dynamics with Coupling to an External Bath. *J. Chem. Phys.* **1984**, *81*, 3684–3690.

(48) Poger, D.; van Gunsteren, W. F.; Mark, A. E. A New Force Field for Simulating Phosphatidylcholine Bilayers. *J. Comput. Chem.* **2010**, *31*, 1117–1125.

(49) Engelbrecht, T. N.; Schroeter, A.; Hauß, T.; Demé, B.; Scheidt, H. a.; Huster, D.; Neubert, R. H. H. The Impact of Ceramides NP and AP on the Nanostructure of Stratum Corneum Lipid Bilayer. Part I: Neutron Diffraction and ²H NMR Studies on Multilamellar Models Based on Ceramides with Symmetric Alkyl Chain Length Distribution. *Soft Matter* **2012**, *8*, 2599–2607.

(50) Vaknin, D.; Kelley, M. S. The Structure of D-Erythro-C18 Ceramide at the Air-Water Interface. *Biophys. J.* **2000**, *79*, 2616–2623.

(51) Leekumjorn, S.; Sum, A. K. Molecular Studies of the Gel to Liquid-Crystalline Phase Transition for Fully Hydrated DPPC and DPPE Bilayers. *Biochim. Biophys. Acta, Biomembr.* **2007**, *1768*, 354–365.

(52) Krause, M. R.; Regen, S. L. The Structural Role of Cholesterol in Cell Membranes: From Condensed Bilayers to Lipid Rafts. *Acc. Chem. Res.* **2014**, *47*, 3512–3521.

(53) Westerlund, B.; Grandell, P. M.; Isaksson, Y. J. E.; Slotte, J. P. Ceramide Acyl Chain Length Markedly Influences Miscibility with Palmitoyl Sphingomyelin in Bilayer Membranes. *Eur. Biophys. J.* **2010**, *39*, 1117–1128.

(54) Ohvo-Rekilä, H.; Ramstedt, B.; Leppimäki, P.; Slotte, J. P. Cholesterol Interactions with Phospholipids in Membranes. *Prog. Lipid Res.* **2002**, *41*, 66–97.

(55) Mitragotri, S. Modeling Skin Permeability to Hydrophilic and Hydrophobic Solutes Based on Four Permeation Pathways. *J. Controlled Release* **2003**, *86*, 69–92.

(56) Vávrová, K.; Hrabálek, A.; Mac-Mary, S.; Humbert, P.; Muret, P. Ceramide Analogue 14S24 Selectively Recovers Perturbed Human Skin Barrier. *Br. J. Dermatol.* **2007**, *157*, 704–712.

(57) Jurkiewicz, P.; Olżyńska, A.; Cwiklik, L.; Conte, E.; Jungwirth, P.; Megli, F. M.; Hof, M. Biophysics of Lipid Bilayers Containing Oxidatively Modified Phospholipids: Insights from Fluorescence and EPR Experiments and from MD Simulations. *Biochim. Biophys. Acta, Biomembr.* **2012**, *1818*, 2388–2402.

(58) Johnson, M. E.; Blankschtein, D.; Langer, R. Evaluation of Solute Permeation through the Stratum Corneum: Lateral Bilayer Diffusion as the Primary Transport Mechanism. *J. Pharm. Sci.* **1997**, *86*, 1162–1172.

(59) Norlén, L.; Gil, I. P.; Simonsen, A.; Descouts, P. Human Stratum Corneum Lipid Organization as Observed by Atomic Force Microscopy on Langmuir-Blodgett Films. *J. Struct. Biol.* **2007**, *158*, 386–400.

(60) Kiselev, M. A.; Ryabova, N. Y.; Balagurov, A. M.; Dante, S.; Hauss, T.; Zbytovska, J.; Wartewig, S.; Neubert, R. H. H. New Insights into the Structure and Hydration of a Stratum Corneum Lipid Model Membrane by Neutron Diffraction. *Eur. Biophys. J.* **2005**, *34*, 1030–1040.

Role of Enzyme Flexibility in Ligand Access and Egress to Active Site: Bias-Exchange Metadynamics Study of 1,3,7-Trimethyluric Acid in Cytochrome P450 3A4

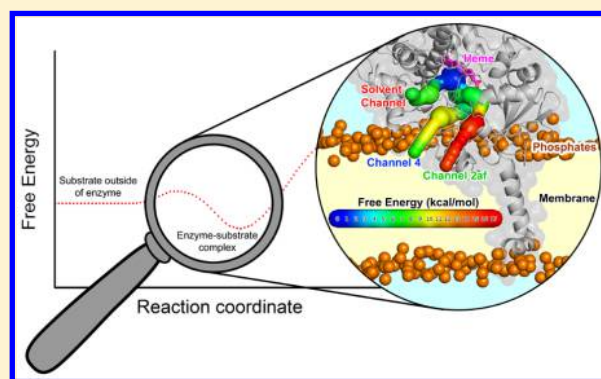
Markéta Paloncýová,^{†,#} Veronika Navrátilová,^{†,#} Karel Berka,[#] Alessandro Laio,^{*,||} and Michal Otyepka^{*,#}

[#]Regional Centre of Advanced Technologies and Materials, Department of Physical Chemistry, Faculty of Science, Palacký University Olomouc, tř. 17 Listopadu 12, 771 46 Olomouc, Czech Republic

^{||}SISSA - Scuola Internazionale Superiore di Studi Avanzati, via Bonomea 265, 34136 Trieste, Italy

S Supporting Information

ABSTRACT: Although the majority of enzymes have buried active sites, very little is known about the energetics and mechanisms associated with substrate and product channeling in and out. Gaining direct information about these processes is a challenging task both for experimental and theoretical techniques. Here, we present a methodology that enables following of a ligand during its passage to the active site of cytochrome P450 (CYP) 3A4 and mapping of the free energy associated with this process. The technique is based on a combination of a bioinformatics tool for identifying access channels and bias-exchange metadynamics and provides converged free energies in good agreement with experimental data. In addition, it identifies the energetically preferred escape routes, limiting steps, and amino acids residues lining the channel. The approach was applied to mapping of a complex channel network in a complex environment, i.e., CYP3A4 attached to a lipid bilayer mimicking an endoplasmic reticulum membrane. The results provided direct information about the energetics and conformational changes associated with the ligand channeling. The methodology can easily be adapted to study channeling through other flexible biomacromolecular channels.



INTRODUCTION

Enzyme catalyzed biotransformation processes take place in active sites,^{1–3} which are usually either localized in surface pockets or buried within the protein, as shown for more than 60% of annotated enzymes.⁴ Hence, substrates and products (henceforth referred to as ligands) must typically access the enzyme's active site through access channels (ACs),⁵ which connect the site with the surrounding environment.⁶ The amino acids lining such channels contribute to the substrate specificity and enzyme efficiency^{7–9} because they determine the channel geometry, physical-chemical properties, and flexibility. Thus, identification of ACs and AC lining amino acids is important for understanding the enzyme substrate specificity, which in turn can be used for the rational design of biocatalysts in biotechnology and sensing applications.^{9,10} In addition ACs may behave as uniform pathways which connect the buried active site with the protein surface or form a complex channel network where the channels may either merge into the others or branch.¹¹ This can hinder the ACs description. Nonetheless, the identification of ACs and AC lining amino acids and evaluation of their behavior and role in ligand permeation are challenging tasks for both experimental techniques and theoretical tools.

Unfortunately, traditional structural methods, i.e., single crystal X-ray diffraction and NMR spectrometry, do not provide a sufficient picture of the ligand passage. X-ray diffraction provides mostly a static view of the enzyme and its ACs from either analysis of enzyme structures by dedicated software tools (e.g., MOLE 2.0,¹² CAVER 3.0,¹³ and MolAxis,¹⁴ to name a few) or comparison of enzyme structures with and without bound ligands.^{15,16} However, NMR techniques can reveal information on multiple time-scales about the conformational enzyme dynamics,¹⁷ e.g., product release during an isomerization reaction.¹⁸ Yet another view is provided by single molecule fluorescence spectroscopy, which can be used to describe the structural dynamics and fluctuations of enzymes at molecular resolution.^{19,20} Fluorescence spectroscopy has also successfully been applied in studies of catalytic properties of enzymes with buried active sites.^{21,22} Apart from spectroscopy methods, the role of specific amino acids in the ACs or active site on the activity of enzymes can be evaluated by mutational studies.^{23–27} However, such experimental techniques have so far provided only limited details of the mechanism of ligand

Received: January 21, 2016

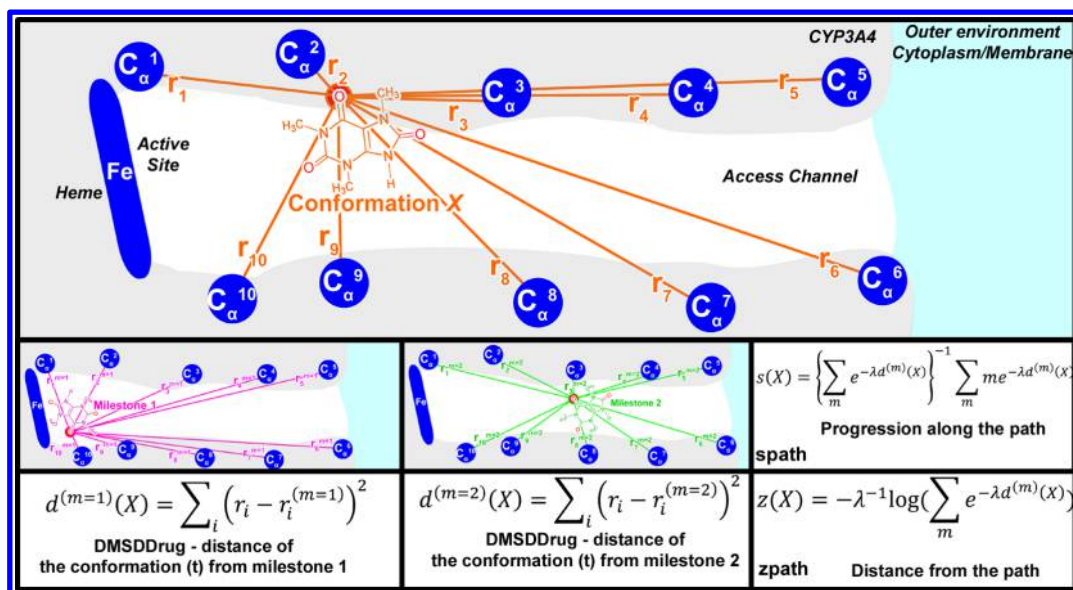


Figure 1. Schematic representation of 1,3,7-trimethyluric acid (TMU) passage through one of the CYP3A4 enzyme channels. The path through the channel (spath) was defined by several milestones—reference structures equally distributed in the chosen space. The metric defining the milestones was the drug distance mean square deviation (DMSDDrug) (one of the pair of atoms used for DMSDDrug enumeration was a TMU heavy atom (red), the other was the C_α atom of the channel lining residues or heme atoms (blue), for clarity we only show contacts to one oxygen atom of the ligand). The value of spath determines the position along the path (for conformation in time t (orange) in the figure spath ~1.5—between milestones 1 and 2). The value of zpath determines the distance from the path.

passage through ACs and degree of adaptive conformation changes of ACs associated with ligand passage.

The identification and characterization of ACs and lining amino acids by theoretical methods are also a nontrivial task as channels may dynamically open/close in response to water or ligand passage and enzyme breathing motions.^{28–30} Random acceleration (originally termed expulsion) molecular dynamics (RAMD)³¹ and steered molecular dynamics (SMD)^{11,32,33} are two techniques developed to identify potential ACs.^{34,35} These techniques are derived from classical molecular dynamics (MD) and use an additional force to pull the ligand molecule through the channel. They can suggest the mechanism of ligand passage and assess free energies of ligand binding ΔG^{bind} and the transition state ΔG^{\ddagger} , which are related to the experimentally observed Michaelis constant and rate constant of ligand binding and unbinding, respectively. However, it should be noted, that the latter methods tend to overestimate the free energies associated with ligand passage^{33,36–38} as they do not sample the configurational space effectively. A recently published approach, based on Hamiltonian replica exchange molecular dynamics (HREMD), allows studying the process of pulling the ligand from the active site or binding the ligand to the protein cavity obtaining results in the good agreement with experiments.^{39,40} Its use with a newly defined variable—distance field distance—allowed studying binding of aspirin to a shallow active pocket in PLA₂ enzyme without the exact prior definition of the path.⁴¹ Nevertheless, to our best knowledge, these methods were never applied to systems with a complex network of malleable ACs, such as those identified in cytochrome P450 (CYP) enzymes: the passage from one state to another in such complicated systems can depend on several collective variables and sampling of such a multidimensional space is not possible by simply pulling the ligand out of the active site. In recent years, metadynamics with a well chosen set of collective variables has been shown to allow sampling the configurational space of complex systems and provide converged free energies.^{47,48} This

approach was introduced in 2002, building on ideas from other free energy methods, such as the Wang–Landau algorithm⁴² and adaptive force bias,⁴³ and conformational search methods such as Tabu search,⁴⁶ conformational flooding,⁴⁵ and local elevation.⁴⁴ However, metadynamics has not yet been applied to such highly flexible systems as CYPs. Overall, an efficient and robust method capable of providing information about the passage of ligands through multiple flexible channels has not been described yet.

Human cytochrome P450 (CYP) enzymes are membrane anchored proteins that catalyze biotransformation processes of many endogenous and exogenous compounds.⁴⁹ They are important targets of pharmacological studies, being responsible for transformations of more than 60% of marketed drugs^{50,51} and many drug–drug interactions.⁵² CYP active sites are deeply buried in compact catalytic domains^{53–55} and are connected to the outside via a complex network of flexible ACs.^{34,56} The CYP3A4 isoform is a prominent member of the CYP family¹⁵ owing to its promiscuity and relevance in drug metabolism.^{50,57} Despite its importance, CYP3A4 represents a challenge for molecular dynamics simulations (MD): the catalytic cycle involving the heme cofactor is complex⁵⁸ and the enzyme is flexible and most frequently anchored to an endoplasmic reticulum membrane. MD simulations of membrane attached CYP3A4 have been published very recently^{59,60} mostly thanks to advances in force field development and membrane simulations. The above-mentioned features make CYP3A4 a highly challenging but ideal touchstone of theoretical methods for the identification of ACs, their lining amino acids and free energy changes accompanying ligand passage through flexible ACs.

Here, we present a synergy of the standard structure-based approach for identifying ACs (MOLE) and bias-exchange metadynamics (BE-META) to study the mechanism of ligand passage through the malleable ACs of CYP3A4. As the ligand we used one of the CYP3A4 caffeine metabolites,

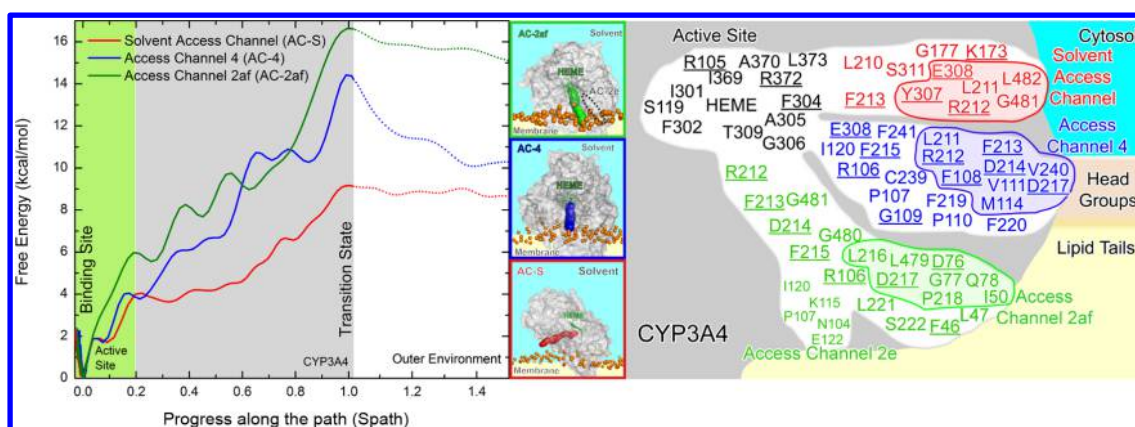


Figure 2. Free energy profiles (left panel) of TMU passage via three ACs of CYP3A4 embedded in a DOPC lipid bilayer (middle panel). CYP3A4 is shown as a gray surface, heme as green sticks, and DOPC phosphates as orange balls. Initially identified AC-2e is shown in black dots. The schematic in the right panel shows the depth of the channel entrances in the membrane and the channel lining amino acids residues. Bulky channel lining residues are underlined, whereas transition state residues within 4 Å of TMU are depicted in the bordered regions.

1,3,7-trimethyluric acid (TMU). For this purpose, we developed a new metric describing the movement of a ligand along a highly flexible AC, named *DMSDDrug* (Figure 1). Using *DMSDDrug* together with a set of other collective variables (CVs), we obtained converged free energy profiles along three independent ACs valid for both access and egress of a ligand. Using these profiles, we identified the preferred AC, transition states for all three ACs and lining and gate-keeping amino acids, whose mutations may alter enzyme function. We observed adaptive conformational changes of CYP3A4 during ligand passage and demonstrated that the flexibility and adaptability of ACs are crucial for ligand passage. The knowledge gained into the ligand passage mechanism represents a key step forward for rational enzyme design, and the presented technique could be easily adapted to analyze other enzymes.

METHODS

We prepared the model of CYP3A4 using the X-ray structure 1TQN according to the procedure described elsewhere⁶⁰ (see also the [Supporting Information](#)). We then inserted CYP3A4 into a pre-equilibrated 1,2-dioleoyl-*sn*-glycero-3-phosphocholine (DOPC) bilayer and performed 100 ns of unbiased MD simulation with GROMACS 4.5.5.⁶¹ Using the MD trajectory, we identified potential access channels by MOLE 2.0.¹² Among the 7 channels found by this algorithm (see [Table S1](#)), we selected three channels that were open (bottleneck radius larger than 1 Å) in total for more than 1 ns during the whole MD run. The channels satisfying this criterion are depicted in [Figure 2](#): the channel depicted in black (AC-2e) joins the enzymatic cavity with the hydrophobic core of the membrane; the one depicted in blue (AC-4) ends in the headgroup region of the phospholipids; and finally, the one depicted in red ends in the cytoplasm.

We then performed MD simulations for a total of approximately 6 μs and computed the free energy associated with the passage of 1,3,7-trimethyluric acid (TMU, [Figure S1](#)) through the three channels using bias-exchange metadynamics (BE-META).⁶² This technique is based on running in parallel a large number of metadynamics,⁴⁸ each biasing a different collective variable (CV). Exchanges between the replicas are attempted at regular time intervals according to a replica-exchange scheme. As a consequence of the exchanges, this

procedure enhances the convergence of the free energy estimates on each replica and allows multidimensional free energy landscapes associated with complex biochemical processes to be computed, e.g., protein folding.⁶³

In BE-META simulations, choosing the correct CVs is crucial for reaching convergence. BE-META has already been applied for studying the translocation of a ligand through a channel.⁶⁴ Building on this work, we introduced a metric (named *DMSDDrug*) specifically tailored for studying the translocation of ligands through very flexible and faintly defined channels. The metric was used for enumeration of the path collective variable introduced in ref 65. In ref 64 it was shown that in some cases the distance CV does not allow reaching convergence, and only by using a suitably defined spath variable it is possible to reconstruct a meaningful free energy landscape.⁶⁴ Progression along the channel was defined by 5–10 milestones, in which the ligand was placed in a regularly spaced sequence of configurations between the enzymatic cavity and mouth of the channel. These milestones were generated by docking the ligand in the channel identified by MOLE 2.0¹² by AutoDock Vina⁶⁶ (see the [Supporting Information](#)). To estimate the value of *DMSDDrug* on configuration *X*, the distance between *X* and milestone *m* was computed as follows

$$d^{(m)}(X) = \frac{1}{N_{\text{ligand}}N_{\text{channel}}} \sum_{i=1}^{N_{\text{ligand}}} \sum_{j=1}^{N_{\text{channel}}} (r_{ij} - r_{ij}^{(m)})^2$$

where r_{ij} and $r_{ij}^{(m)}$ are the distance between atom *i* and *j* in configuration *X* and the configuration of milestone *m*, respectively. The sums on *i* and *j* run from 1 to N_{ligand} atoms belonging to the ligand and N_{channel} atoms belonging to the channel wall, respectively (see [Figure 1](#)). This is the main difference to the *DMSD* metric detailed in ref 65, for which both sums run over the same set of atoms. This modification was crucial for using a *spath* variable for the process studied in this work because in the original formulation, the value of $d^{(m)}$ was dominated by fluctuations in the distance between the atoms of the channel wall, making its value a noisy measure of the position of the ligand. Following ref 65, we then defined the channel *spath* collective variable as follows

$$s(X) = \frac{\sum_m m e^{-\lambda d^{(m)}(X)}}{\sum_m e^{-\lambda d^{(m)}(X)}}$$

The set of CVs used for the three BE-META simulations of the three channels included the *spath* variable defined above (CV1) and seven other variables aimed at describing the orientation of the ligand, the size of the channel and chemical nature of the interaction of the ligand with the channel walls: CV2 and CV3 covered the number of hydrophobic and hydrophilic contacts between the ligand and channel, CV4 and CV5 described the orientation of the ligand with respect to the channel axis, CV6 was the radius of gyration (R_g) of the channel mouth/s, CV7 was the distance from the heme, and CV8 was the *zpath* variable defined according to ref 65 (see the Supporting Information and Table S2 for exact definition and Figure S2). For increasing the sampling in channel AC-2af and its R_g (see later) we performed another 130 ns BE-META simulation with 5 replicas – AC-2e *spath* and *zpath*, distance from the heme, R_g of AC-2af, and contacts with AC-2e. The sampling and convergence is discussed in the Supporting Information (see Figures S10–S15).

RESULTS AND DISCUSSION

We studied the thermodynamics of TMU permeation through membrane-attached CYP3A4 via its access channels. Based on MOLE 2.0 analysis of an unbiased simulation (Table S1), we chose channels AC-S, AC-2e, and AC-4 for further study. We then defined a set of eight collective variables (CV1–CV8) for BE-META calculations as using multiple CVs in BE-META simulations was shown to increase the convergence rate.⁶² Since we aimed at monitoring the translocation of TMU through different channels, the simple distance from the heme was insufficient for this purpose. Therefore, and owing to the flexibility of the channels, we employed the new *DMSDDrug* metric for *spath* CV, which allowed distinguishing the motion of a ligand and motion of the channel (see Methods). For each channel, we performed $\sim 2 \mu\text{s}$ of BE-META simulations. By a detailed analysis of the trajectories of the individual replicas we observed that for some of them (especially those biased on the orientation of TMU with respect to the channel direction) the sampling was produced almost entirely with the TMU in the active site and therefore we discarded these replicas from further analysis (Figures S12–14). In other words, these CVs (two orientation CV replicas, hydrophobic contacts replica and hydrophilic contacts replica in AC-2af) contribute to the final free energy results only by enhancing the convergence of the other replicas (for example by generating configurations with the TMU in different orientations). The *zpath* CV was introduced in order to control the distance from the predefined path. In the case of AC-S, a soft potential wall on this variable was introduced in order to keep a drug within the channel for an initial part of the simulation; however, finally this appeared to be useful only in the case of very disfavored channels. In principle, we would recommend keeping as many CV replicas as possible, because it leads to convergent BE-META simulations of a rather complex system and enabled enough flexibility for similar simulations; however, in the case of need the discarded replicas could be under consideration and the CVs can be mapped afterward. During the analysis, we noticed that in the simulation of TMU transport through AC-2e, the ligand preferred to permeate through the nearby channel

AC-2af. Therefore, we interpreted the results of this simulation as for AC-2af.

In Figure 2, free energy profiles are plotted as a function of the *spath* variable, which describes the progress of TMU along the channels. All the free energy profiles showed a minimum in the active site. For all three cases after this minimum, we observed a low barrier of 4–6 kcal/mol related to the unbinding of TMU from the active site. After this barrier, the free energy progressively increased up to the transition state, which was localized just below the CYP3A4 surface in all three cases, with barriers of 10.2 ± 0.6 kcal/mol for AC-S, 14.5 ± 0.9 for AC-4, and 16.5 ± 0.9 for AC-2af. This shows that TMU is released preferentially through the AC-S channel. The computational setup did not allow computing the binding free energy ΔG^{bind} . Indeed, the milestones used in *spath* only properly describe the translocation through the channels, though some milestones were located also outside of the channels (dotted line in Figure 2). However, by using the milestones we cannot take into account the entropy gain deriving from releasing the confinement effect of the channel. Thus, to compute ΔG^{bind} , one should perform another free energy calculation with different collective variables aimed at describing the detachment of the ligand from the transition state at the channel mouth, add a correction to the entropic gain (e.g., using the method described in ref 67), or perform alchemical free energy calculation. For amphiphilic molecules, the free energy of the transition state of AC-S provides an upper bound for ΔG^{bind} . The ΔG^{bind} calculated by the alchemical simulation (see the Supporting Information) was -10.4 ± 2.5 kcal/mol, which is in good agreement with ΔG of the transition state.

Apart from BE-META, we also computed the free energy profile associated with the translocation of TMU through a DOPC membrane by COSMOmic⁶⁸ (see Figure S3). The state in which TMU was solvated in water was favored by ~ 6 kcal/mol with respect to the membrane core, consistent with the difference between the free energy barriers for the AC-S and the AC-2af channels connecting the active site with the cytoplasm and membrane interior. This indicates that the pathway toward the hydrophobic tail region is strongly disfavored for this ligand. Interestingly, COSMOmic also predicted that TMU can localize close to the headgroup region (notice the minimum at $z = 1.5$ nm in Figure S3). Remarkably, the barrier for channel AC-4 directing TMU to the region below the head groups was significantly higher than for the channel leading to the solvent; however, the free energy profiles after the transition states (outside of protein) suggest a small free energy decrease as TMU samples both solvent and headgroup region. Our calculations also unambiguously demonstrate that two of the channels (AC-S and AC-2af) of CYP3A4 are remarkably flexible and change their conformations in response to the passage of TMU.

In Figure 3, we plot the free energy for each channel as a function of the mouth opening (henceforth mouth) radius R_m and the *spath* variable. R_m represents the maximal radius of a sphere docked to the mouth opening at the end point of the channel starting from the active site and leading to the respective mouth as calculated by MOLE 2.5¹² software with a probe radius 5.0 Å. End points of channels were defined by the same amino acids as those used for the definition of R_g (Figure 3, Figure S6). We observed small changes in R_m during TMU permeation through AC-4, indicating that this specific channel is rather rigid, at least in the mouth region. The mouth of the

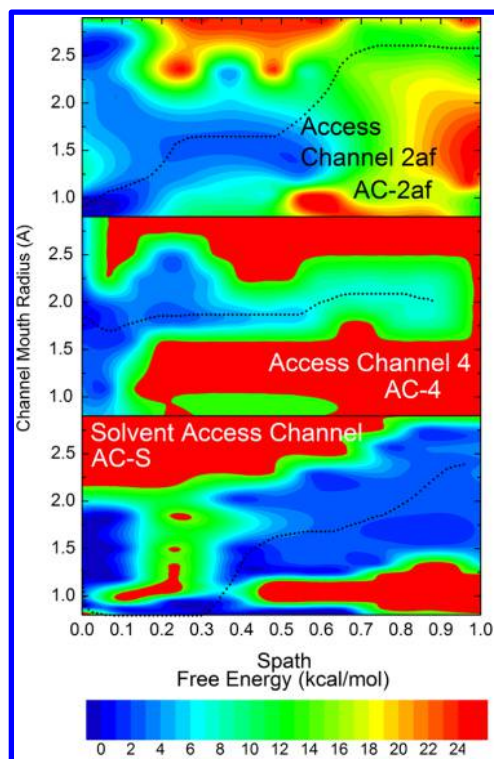


Figure 3. Free energy as a function of the mouth radius and spath variable. Red regions did not have sufficient sampling for reliable calculation of the free energy. The dashed line represents the approximate path followed by the ligand.

AC-2af was rather in a closed state when TMU was in the active site with $R_m \sim 0.9 \text{ \AA}$, but TMU permeation opened the channel mouth to $R_m \sim 2.5 \text{ \AA}$. It should be remarked that the initially studied channel AC-2e did not open sufficiently for TMU permeation. Indeed, the one-dimensional free energy profile of R_g of channel AC-2e showed a high free energy barrier for its opening (see Figure S4). Interestingly, both AC-4 and AC-2e lead through CYP3A4 F/G or B/C loops with defined backbone lengths, and the adjustment of these loops to the presence of ligand is rather limited. The AC-S channel was very flexible and gradually adjusted its geometry in response to the ligand passage. When TMU was in the active site, the channel was either closed ($R_m \sim 0.9 \text{ \AA}$) or moderately open ($R_m \sim 1.7 \text{ \AA}$), as indicated also by the one-dimensional free energy profile (see Figures S4, S5, and Figure 3). As soon as the ligand left the active site, the channel stayed closed ($R_m \sim 0.9 \text{ \AA}$). Finally, at the transition state, the channel opened completely, and R_m reached 2.5 \AA . In a free unbiased simulation with TMU in the active site, the channel remained closed ($R_m \sim 0.85 \text{ \AA}$) for the whole simulation (500 ns, Figure S7), indicating that the open state is separated from the closed state by a significant free energy barrier associated with a variable not directly related to R_g and therefore not visible in the free energy projections of Figures 3 and S4. The results clearly indicate that biased MD simulations directly addressing passage of a ligand may identify different preferred access channels than analyses based on classical MD simulations or X-ray structures. This is demonstrated by the fact that in the free simulations, channel AC-S appeared to open very rarely, whereas with BE-META, it was the most favorable channel. In other words, the enzyme access channels are malleable,^{55,69–72} reflecting ligand passage, and such adaptive conformation changes of access channels

may not necessarily be reflected in structures taken from X-ray analysis and classical MD simulations.

The multidimensional free energy profiles obtained from the BE-META simulations allowed identification of the transition states for the release of TMU via the three channels (Figure 4). In all three cases, the transition states corresponded to configurations where TMU was at least partially in contact with the surrounding environment, i.e., either water or lipids. The nature of the environment outside the individual ACs differed significantly, especially in terms of hydration level: TMU in the transition state of AC-S was partially hydrated, in AC-4, the hydration was localized on a small part of TMU, and in AC-2af, TMU was not in contact with bulk water but in contact with lipids (Figure 4). The amino acid residues of the local environment also reflected the nature of the transition states also reflected the nature of the local environment: in AC-S, TMU made polar contacts with E308, Y307, and the backbone of L211; in AC-4, a hydrogen bond was formed between TMU and the backbone of F108; and in AC-2af, the only polar contact was with the backbone of D76 and otherwise TMU was surrounded by nonpolar residues. A common residue of transition states for two of the three channels (AC-S and AC-4) was R212. This residue was also present close to the transition state of AC-2af, and therefore it seems to play an important role in channel opening. The mentioned residues and also other residues important to the transition states are depicted in Figure 4. Mutations of these amino acid residues may alter access channel properties and, in turn, enzyme substrate preferences, as shown also for other enzymes.

Large amino acids lining the channels, such as R106, E308, F213, D214, and D217, are also perspective candidates for mutation (Figures 2, S8, and S9), as their size and ability for forming hydrogen bonds can significantly affect the malleability of ACs. The importance of some of these residues has been confirmed experimentally (Appendix #1, Supporting Information).^{23–26,74,75} We identified that the enzyme flexibility is a crucial property for ligand permeation, and therefore reducing the flexibility (especially in AC-S) may reduce the AC permeability. Hence, mutation of residues on loops forming the mouth of AC-S (glycines 480–481 or leucines 210–211) to other residues (especially forming a hydrogen bond with the I-helix or larger amino acids blocking AC entrance) may restrict the opening of AC-S. Indeed, mutation of L211 to tyrosine has been shown to decrease the affinity toward several xenobiotics.⁷⁶

These results show that the presented method is not only capable of predicting the free energy of release of a ligand from the binding site but also of finding new access channels not detectable by the analysis of the enzyme structure, which usually focuses on lining amino acids or on the AC diameter.^{38,56,77,78} In our approach the identification and characterization of the ACs is based on a synergy between the structural bioinformatics tool, MOLE 2.0, and BE-META simulation. Here, it was possible to achieve a satisfactory statistical accuracy only by using a newly employed metric used in the *spath* variable. Unlike other in silico techniques for free energy calculations of ligand passage through enzyme ACs^{31,79,80} that drive the ligand from the active site and usually overestimate the free energy barrier, the proposed BE-META approach allowed several permeations of TMU to be observed through ACs and provided converged free energy profiles valid both for access and egress. Previous studies employing the BE-META method to analyze ligand passage have only focused on

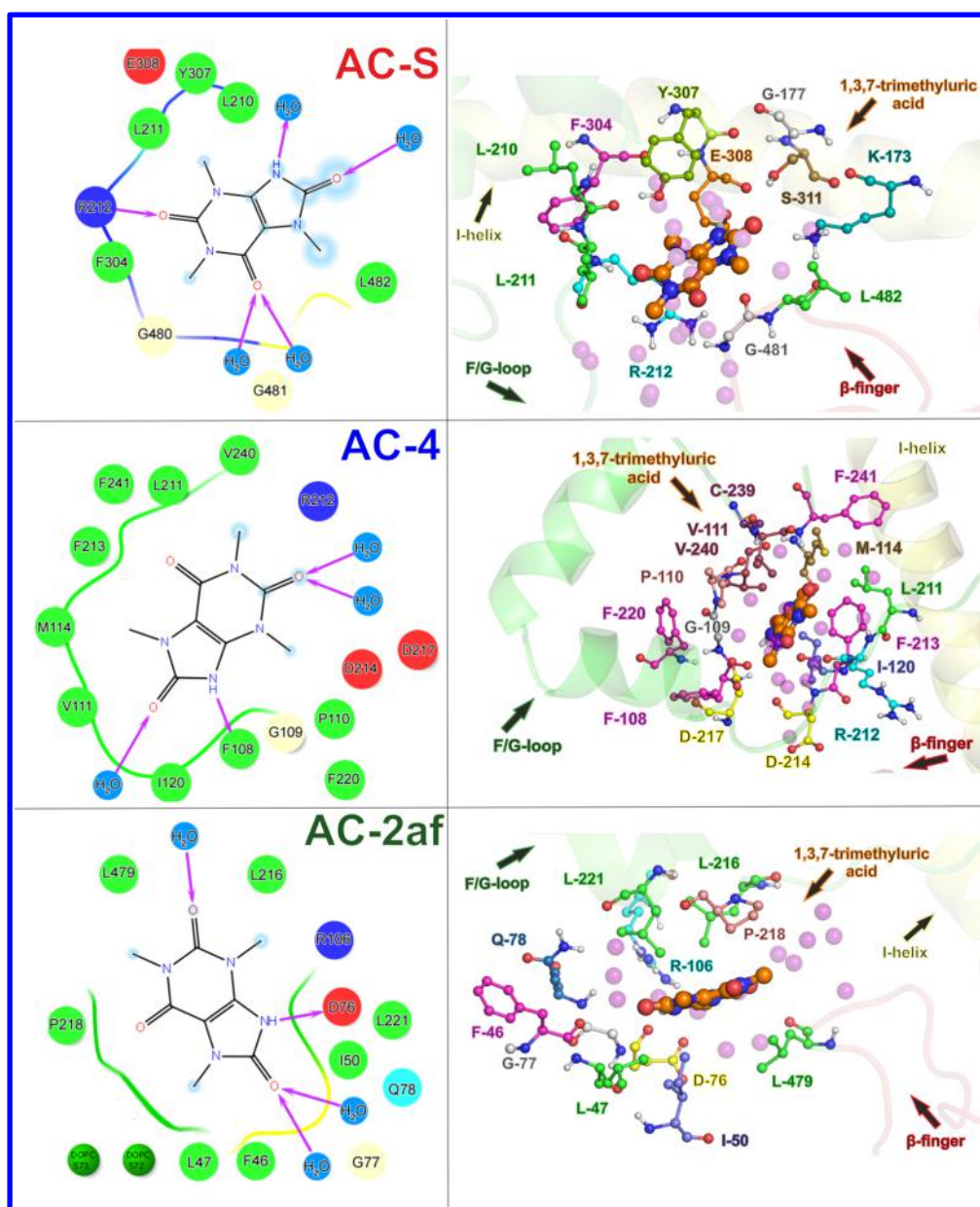


Figure 4. Amino acid residues near TMU in the transition states of studied ACs in schematic representation (left) and atomic representation (right). **Left:** Blue shadow represents hydration level of TMU atoms, green curves represent nonpolar contacts, yellow and blue curves show polar contacts, and magenta arrows correspond to hydrogen bonds.⁷³ **Right:** Residues are shown as balls-and-sticks representations, nonpolar hydrogens are not shown for clarity, secondary structural elements are represented as transparent cartoons and colored according to their position in the sequence: β -5-region (labeled as β -finger) – red, F/G loop–green, I-helix–yellow. TMU is shown as orange/blue/red balls and sticks, and water molecules are shown as purple transparent spheres.

rigid and clearly defined pathways through enzymes.^{64,81} However, we have shown that the approach presented here also allows identification of mutable AC-lining residues and analysis of their function in malleable enzyme ACs.

CONCLUSION

We have presented a method for studying ligand passage through malleable enzyme ACs and applied it to the passage of 1,3,7-trimethyluric acid (TMU) through membrane attached CYP3A4 ACs. We used a synergy of the MOLE 2.0 bioinformatics tool for identifying access channels and bias-exchange metadynamics (BE-META). This combination of methods allowed differentiating well between multiple ACs and allowed performing a detailed thermodynamic and structural

analysis without the restriction to previously identified channels. To achieve convergence, it was necessary to introduce a new metric for *spath* enumeration (*DMSDDrug*), which was shown to closely describe the position of TMU in the ACs.

Our results suggested that CYP3A4 flexibility has a significant influence on the permeation ability of TMU. Whereas MOLE 2.0 analysis of a classical MD simulation identified AC-2e and AC-4 as the mostly opened channels, the BE-META simulation suggested that TMU does not pass through AC-2e, mostly due to the rigidity and insufficient size of its mouth. Further, we analyzed a channel (AC-S) that opened very rarely during the classical MD simulation. BE-META indicated that AC-S was the most favorable channel for TMU release, followed by AC-4 and AC-2af. From analysis of

transition states located on the CYP3A4 surface and the channel lining residues, we identified several amino acids (R212, E308, F304, S119 and F108, F213, D214, D217) whose mutations may significantly affect CYP3A4 activity. Some of these residues have already been identified experimentally as amino acids altering CYP3A4 function.^{23–26,74,75} These results provide new insights into the mechanism of ligand release from CYP3A4. Overall, the approach presented here appears to be robust, transferable, and capable of distinguishing between multiple pathways. We anticipate it will be a valuable tool for enzymatic studies and rational enzyme design.

■ ASSOCIATED CONTENT

● Supporting Information

The Supporting Information is available free of charge on the ACS Publications website at DOI: 10.1021/acs.jctc.6b00075.

Detailed description of simulation protocol. Figure S1: C8 hydroxylation/oxylation of caffeine in CYP3A4. Figure S2: Scheme showing used collective variables. Figure S3: Free energy profile of caffeine and TMU on a DOPC membrane calculated by COSMOmic. Figure S4: One dimensional free energy profiles for radius of gyration of channel mouths. Figure S5: 3D chart of free energy above all monitored radii of gyration and S-path variable. Figure S6: Recalculation of radius of gyration mouth radius R_g into physical mouth radius R_m (radius of maximally inscribed ball calculated by MOLE 2.0). Figure S7: Development of radii of gyration of monitored mouths during an unbiased simulation. Figure S8: Channel lining residues of the respective channels. Figure S9: Binding state in atomic and schematic representation. Figure S10. Free energy profiles along the spath with estimated errors. Figure S11. Monitoring spath variable during the BE-META simulation in spath replica. Figures S12–14: Monitoring of other CVs in all replicas. Figure S15: The history dependent potential along the time extracted from BE-META simulations. Figure S16: Multiple free simulations starting from various positions in channel AC-S. Table S1: Frequency of channel opening during free simulation analyzed by MOLE 2.0. Table S2: Amino acid residues defining the milestones, contacts, and mouths. Appendix #1: Mutation studies. Appendix #2: Input files for Plumed calculation (PDF)

Modified source codes of Plumed 2.1 (ZIP)

■ AUTHOR INFORMATION

Corresponding Authors

*E-mail: michal.otyepka@upol.cz.

*E-mail: laio@sissa.it.

Author Contributions

†Both authors contributed equally to this paper.

Notes

The authors declare no competing financial interest.

■ ACKNOWLEDGMENTS

We gratefully acknowledge support through Project LO1305 of the Ministry of Education, Youth and Sports of the Czech Republic. M.O. acknowledges support from the Czech Grant Agency through Project P208/12/G016. V.N. and M.P. acknowledge support from a student project of Palacký University Olomouc (IGA_PrF_2016_028).

■ REFERENCES

- (1) Garcia-Viloca, M.; Gao, J.; Karplus, M.; Truhlar, D. G. How Enzymes Work: Analysis by Modern Rate Theory and Computer Simulations. *Science* **2004**, *303*, 186–195.
- (2) Benkovic, S. J.; Hammes-Schiffer, S. A Perspective on Enzyme Catalysis. *Science* **2003**, *301*, 1196–1202.
- (3) Koeller, K. M.; Wong, C. H. Enzymes for Chemical Synthesis. *Nature* **2001**, *409*, 232–240.
- (4) Pravda, L.; Berka, K.; Svobodová Vařeková, R.; Sehnal, D.; Banáš, P.; Laskowski, R. A.; Koča, J.; Otyepka, M. Anatomy of Enzyme Channels. *BMC Bioinf.* **2014**, *15*, 379.
- (5) Bui, J. M.; Tai, K.; McCammon, J. A. Acetylcholinesterase: Enhanced Fluctuations and Alternative Routes to the Active Site in the Complex with Fasciculin-2. *J. Am. Chem. Soc.* **2004**, *126*, 7198–7205.
- (6) Bailey, L. J.; McCoy, J. G.; Phillips, G. N.; Fox, B. G. Structural Consequences of Effector Protein Complex Formation in a Diiron Hydroxylase. *Proc. Natl. Acad. Sci. U. S. A.* **2008**, *105*, 19194–19198.
- (7) Lindberg, R. L.; Negishi, M. Alteration of Mouse Cytochrome P450coH Substrate Specificity by Mutation of a Single Amino-Acid Residue. *Nature* **1989**, *339*, 632–634.
- (8) Scrutton, N. S.; Berry, A.; Perham, R. N. Redesign of the Coenzyme Specificity of a Dehydrogenase by Protein Engineering. *Nature* **1990**, *343*, 38–43.
- (9) Pavlova, M.; Klvana, M.; Prokop, Z.; Chaloupkova, R.; Banas, P.; Otyepka, M.; Wade, R. C.; Tsuda, M.; Nagata, Y.; Damborsky, J. Redesigning Dehalogenase Access Tunnels as a Strategy for Degrading an Anthropogenic Substrate. *Nat. Chem. Biol.* **2009**, *5*, 727–733.
- (10) Bernhardt, R.; Urlacher, V. B. Cytochromes P450 as Promising Catalysts for Biotechnological Application: Chances and Limitations. *Appl. Microbiol. Biotechnol.* **2014**, *98*, 6185–6203.
- (11) Kingsley, L. J.; Lill, M. a Including Ligand-Induced Protein Flexibility into Protein Tunnel Prediction. *J. Comput. Chem.* **2014**, *35*, 1748–1756.
- (12) Sehnal, D.; Svobodová Vařeková, R.; Berka, K.; Pravda, L.; Navrátilová, V.; Banáš, P.; Ionescu, C.-M.; Otyepka, M.; Koča, J. MOLE 2.0: Advanced Approach for Analysis of Biomacromolecular Channels. *J. Cheminf.* **2013**, *5*, 39.
- (13) Chovancova, E.; Pavelka, A.; Benes, P.; Strnad, O.; Brezovsky, J.; Kozlikova, B.; Gora, A.; Sustr, V.; Klvana, M.; Medek, P.; et al. CAVER 3.0: a Tool for the Analysis of Transport Pathways in Dynamic Protein Structures. *PLoS Comput. Biol.* **2012**, *8*, e1002708.
- (14) Yaffe, E.; Fishelovitch, D.; Wolfson, H. J.; Halperin, D.; Nussinov, R. MolAxis: Efficient and Accurate Identification of Channels in Macromolecules. *Proteins: Struct., Funct., Genet.* **2008**, *73*, 72–86.
- (15) Ekroos, M.; Sjögren, T. Structural Basis for Ligand Promiscuity in Cytochrome P450 3A4. *Proc. Natl. Acad. Sci. U. S. A.* **2006**, *103*, 13682–13687.
- (16) Zhao, Y.; White, M. A.; Muralidhara, B. K.; Sun, L.; Halpert, J. R.; Stout, C. D. Structure of Microsomal Cytochrome P450 2B4 Complexed with the Antifungal Drug Bifonazole: Insight into P450 Conformational Plasticity and Membrane Interaction. *J. Biol. Chem.* **2006**, *281*, 5973–5981.
- (17) Henzler-Wildman, K. A.; Lei, M.; Thai, V.; Kerns, S. J.; Karplus, M.; Kern, D. A Hierarchy of Timescales in Protein Dynamics is Linked to Enzyme Catalysis. *Nature* **2007**, *450*, 913–916.
- (18) Rozovsky, S.; Jogl, G.; Tong, L.; McDermott, A. E. Solution-state NMR Investigations of Triosephosphate Isomerase Active Site Loop Motion: Ligand Release in Relation to Active Site Loop Dynamics. *J. Mol. Biol.* **2001**, *310*, 271–280.
- (19) Ha, T.; Ting, A. Y.; Liang, J.; Caldwell, W. B.; Deniz, A. A.; Chemla, D. S.; Schultz, P. G.; Weiss, S. Single-Molecule Fluorescence Spectroscopy of Enzyme Conformational Dynamics and Cleavage Mechanism. *Proc. Natl. Acad. Sci. U. S. A.* **1999**, *96*, 893–898.
- (20) Weiss, S. Measuring Conformational Dynamics of Biomolecules by Single Molecule Fluorescence Spectroscopy. *Nat. Struct. Biol.* **2000**, *7*, 724–729.
- (21) Yang, H. Protein Conformational Dynamics Probed by Single-Molecule Electron Transfer. *Science* **2003**, *302*, 262–266.

- (22) Sykora, J.; Brezovsky, J.; Koudelakova, T.; Lahoda, M.; Fortova, A.; Chernovets, T.; Chaloupkova, R.; Stepankova, V.; Prokop, Z.; Smatanova, I. K.; et al. Dynamics and Hydration Explain Failed Functional Transformation in Dehalogenase Design. *Nat. Chem. Biol.* **2014**, *10*, 428–430.
- (23) Davydov, D. R.; Rumfeldt, J. a O.; Sineva, E. V.; Fernando, H.; Davydova, N. Y.; Halpert, J. R. Peripheral Ligand-binding Site in Cytochrome P450 3A4 Located with Fluorescence Resonance Energy Transfer (FRET). *J. Biol. Chem.* **2012**, *287*, 6797–6809.
- (24) Domanski, T. L.; He, Y. a.; Khan, K. K.; Roussel, F.; Wang, Q.; Halpert, J. R. Phenylalanine and Tryptophan Scanning Mutagenesis of CYP3A4 Substrate Recognition Site Residues and Effect on Substrate Oxidation and Cooperativity. *Biochemistry* **2001**, *40*, 10150–10160.
- (25) Sevrioukova, I. F.; Poulos, T. L. Structural and Mechanistic Insights into the Interaction of Cytochrome P4503A4 with Bromocryptine, a Type I Ligand. *J. Biol. Chem.* **2012**, *287*, 3510–3517.
- (26) Yamaguchi, Y.; Khan, K. K.; He, Y. A.; He, Y. Q.; Halpert, J. R. Topological Changes in the CYP3A4 Active Site Probed with Phenyl diazene: Effect of Interaction with NADPH-Cytochrome P450 Reductase and Cytochrome b 5 and of Site-Directed Mutagenesis. *Drug Metab. Dispos.* **2004**, *32*, 155–161.
- (27) Urban, P.; Truan, G.; Pompon, D. Access Channels to the Buried Active Site Control Substrate Specificity in CYP1A P450 Enzymes. *Biochim. Biophys. Acta, Gen. Subj.* **2015**, *1850*, 696–707.
- (28) Hendrychová, T.; Berka, K.; Navrátilová, V.; Anzenbacher, P.; Otyepka, M. Dynamics and Hydration of the Active Sites of Mammalian Cytochromes P450 Probed by Molecular Dynamics Simulations. *Curr. Drug Metab.* **2012**, *13*, 177–189.
- (29) Scoriapino, M. A.; Robertazzi, A.; Casu, M.; Ruggerone, P.; Ceccarelli, M. Breathing Motions of a Respiratory Protein Revealed by Molecular Dynamics Simulations. *J. Am. Chem. Soc.* **2009**, *131*, 11825–11832.
- (30) Shen, T.; Tai, K.; Mccammon, J. A. Molecular Dynamics Simulations of Acetylcholinesterase. *Acc. Chem. Res.* **2002**, *35*, 332–340.
- (31) Lüdemann, S. K.; Lounnas, V.; Wade, R. C. How Do Substrates Enter and Products Exit the Buried Active Site of Cytochrome P450cam? 1. Random Expulsion Molecular Dynamics Investigation of Ligand Access Channels and Mechanisms. *J. Mol. Biol.* **2000**, *303*, 797–811.
- (32) Isralewitz, B.; Gao, M.; Schulten, K. Steered Molecular Dynamics and Mechanical Functions of Proteins. *Curr. Opin. Struct. Biol.* **2001**, *11*, 224–230.
- (33) Fishelovitch, D.; Shaik, S.; Wolfson, H. J.; Nussinov, R. Theoretical Characterization of Substrate Access/Exit Channels in the Human Cytochrome P450 3A4 Enzyme: Involvement of Phenylalanine Residues in the Gating Mechanism. *J. Phys. Chem. B* **2009**, *113*, 13018–13025.
- (34) Wade, R. C.; Winn, P. J.; Schlichting, I.; Sudarko. A Survey of Active Site Access Channels in Cytochromes P450. *J. Inorg. Biochem.* **2004**, *98*, 1175–1182.
- (35) Kalyanamoorthy, S.; Chen, Y. P. P. Exploring Inhibitor Release Pathways in Histone Deacetylases Using Random Acceleration Molecular Dynamics Simulations. *J. Chem. Inf. Model.* **2012**, *52*, 589–603.
- (36) Li, W.; Liu, H.; Luo, X.; Zhu, W.; Tang, Y. Possible Pathway (s) of Metyrapone Egress from the Active Site of Cytochrome P450 3A4: a Molecular Dynamics Simulation. *Drug Metab. Dispos.* **2007**, *35*, 689–696.
- (37) Li, W.; Liu, H.; Scott, E. E.; Gräter, F.; Halpert, J. R.; Luo, X.; Shen, J.; Jiang, H. Possible Pathway(s) of Testosterone Egress from the Active Site of Cytochrome P450 2B1: A Steered Molecular Dynamics Simulation. *Drug Metab. Dispos.* **2005**, *33*, 910–919.
- (38) Shen, Z.; Cheng, F.; Xu, Y.; Fu, J.; Xiao, W.; Shen, J.; Liu, G.; Li, W.; Tang, Y. Investigation of Indazole Unbinding Pathways in CYP2E1 by Molecular Dynamics Simulations. *PLoS One* **2012**, *7*, e33500.
- (39) Oostenbrink, C.; de Ruiter, A.; Hritz, J.; Vermeulen, N. Malleability and Versatility of Cytochrome P450 Active Sites Studied by Molecular Simulations. *Curr. Drug Metab.* **2012**, *13*, 190–6.
- (40) Venhorst, J.; Onderwater, R. C.; Meerman, J. H. N.; Commandeur, J. N. M.; Vermeulen, N. P. E. Influence of N-Substitution of 7-Methoxy-4- (Aminomethyl) -Coumarin on Cytochrome P450 Metabolism and Selectivity. *Drug Metab. Dispos.* **2000**, *28*, 1524–1532.
- (41) de Ruiter, A.; Oostenbrink, C. Protein – Ligand Binding from Distancefield Distances and Hamiltonian Replica Exchange Simulations. *J. Chem. Theory Comput.* **2013**, *9*, 883–892.
- (42) Wang, F.; Landau, D. P. Efficient, Multiple-Range Random Walk Algorithm to Calculate the Density of States. *Phys. Rev. Lett.* **2001**, *86*, 2050–2053.
- (43) Darve, E.; Pohorille, A. Calculating Free Energies Using Average Force. *J. Chem. Phys.* **2001**, *115*, 9169.
- (44) Huber, T.; Torda, A. E.; van Gunsteren, W. F. Local Elevation: A Method for Improving the Searching Properties of Molecular Dynamics Simulation. *J. Comput.-Aided Mol. Des.* **1994**, *8*, 695–708.
- (45) Grubmüller, H. Predicting Slow Structural Transitions in Macromolecular Systems: Conformational Flooding. *Phys. Rev. E: Stat. Phys., Plasmas, Fluids, Relat. Interdiscip. Top.* **1995**, *52*, 2893–2906.
- (46) Glover, F. Tabu Search - Part I. *ORSA J. Comput.* **1989**, *1*, 190–206.
- (47) Laio, A.; Parrinello, M. Escaping Free-Energy Minima. *Proc. Natl. Acad. Sci. U. S. A.* **2002**, *99*, 12562–12566.
- (48) Laio, A.; Gervasio, F. L. Metadynamics: a Method to Simulate Rare Events and Reconstruct the Free Energy in Biophysics, Chemistry and Material Science. *Rep. Prog. Phys.* **2008**, *71*, 126601.
- (49) Guengerich, F. P. Common and Uncommon Cytochrome P450 Reactions Related to Metabolism and Chemical Toxicity. *Chem. Res. Toxicol.* **2001**, *14*, 611–650.
- (50) Anzenbacher, P.; Anzenbacherová, E. Cytochromes P450 and Metabolism of Xenobiotics. *Cell. Mol. Life Sci.* **2001**, *58*, 737–747.
- (51) Evans, W. E.; Relling, M. V. Pharmacogenomics: Translating Functional Genomics into Rational Therapeutics. *Science* **1999**, *286*, 487–491.
- (52) Guengerich, F. P. Role of Cytochrome P450 Enzymes in Drug-Drug Interactions. *Adv. Pharmacol.* **1997**, *43*, 7–35.
- (53) Otyepka, M.; Skopalík, J.; Anzenbacherová, E.; Anzenbacher, P. What Common Structural Features and Variations of Mammalian P450s Are Known to Date? *Biochim. Biophys. Acta, Gen. Subj.* **2007**, *1770*, 376–389.
- (54) Johnson, E. F.; Stout, C. D. Structural Diversity of Human Xenobiotic-Metabolizing Cytochrome P450 Monooxygenases. *Biochem. Biophys. Res. Commun.* **2005**, *338*, 331–6.
- (55) Otyepka, M.; Berka, K.; Anzenbacher, P. Is There a Relationship Between the Substrate Preferences and Structural Flexibility of Cytochromes P450? *Curr. Drug Metab.* **2012**, *13*, 130–142.
- (56) Cojocar, V.; Winn, P. J.; Wade, R. C. The Ins and Outs of Cytochrome P450s. *Biochim. Biophys. Acta, Gen. Subj.* **2007**, *1770*, 390–401.
- (57) Rendic, S. Summary of Information on Human CYP Enzymes: Human P450 Metabolism Data. *Drug Metab. Rev.* **2002**, *34*, 83–448.
- (58) Denisov, I. G.; Makris, T. M.; Sligar, S. G.; Schlichting, I. Structure and Chemistry of Cytochrome P450. *Chem. Rev.* **2005**, *105*, 2253–77.
- (59) Baylon, J. L.; Lenov, I. L.; Sligar, S. G.; Tajkhorshid, E. Characterizing the Membrane-Bound State of Cytochrome P450 3A4: Structure, Depth of Insertion and Orientation. *J. Am. Chem. Soc.* **2013**, *135*, 8542–8551.
- (60) Berka, K.; Palonciová, M.; Anzenbacher, P.; Otyepka, M. Behavior of Human Cytochromes P450 on Lipid Membranes. *J. Phys. Chem. B* **2013**, *117*, 11556–11564.
- (61) Pronk, S.; Páll, S.; Schulz, R.; Larsson, P.; Bjelkmar, P.; Apostolov, R.; Shirts, M. R.; Smith, J. C.; Kasson, P. M.; van der Spoel, D.; et al. GROMACS 4.5: A High-Throughput and Highly Parallel Open Source Molecular Simulation Toolkit. *Bioinformatics* **2013**, *29*, 845–854.

(62) Piana, S.; Laio, A. A Bias-Exchange Approach to Protein Folding. *J. Phys. Chem. B* **2007**, *111*, 4553–4559.

(63) Granata, D.; Camilloni, C.; Vendruscolo, M.; Laio, A. Characterization of the Free-Energy Landscapes of Proteins by NMR-Guided Metadynamics. *Proc. Natl. Acad. Sci. U. S. A.* **2013**, *110*, 6817–6822.

(64) Bisha, I.; Rodriguez, A.; Laio, A.; Magistrato, A. Metadynamics Simulations Reveal a Na⁺ Independent Exiting Path of Galactose for the Inward-Facing Conformation of vSGLT. *PLoS Comput. Biol.* **2014**, *10*, e1004017.

(65) Branduardi, D.; Gervasio, F. L.; Parrinello, M. From A to B in Free Energy Space. *J. Chem. Phys.* **2007**, *126*, 054103.

(66) Trott, O.; Olson, A. J. AutoDock Vina: Improving the Speed and Accuracy of Docking with a New Scoring Function, Efficient Optimization, and Multithreading. *J. Comput. Chem.* **2010**, *31*, 455–461.

(67) Doudou, S.; Burton, N. A.; Henchman, R. H. Standard Free Energy of Binding from a One-Dimensional Potential of Mean Force. *J. Chem. Theory Comput.* **2009**, *5*, 909–918.

(68) Klamt, A.; Huniar, U.; Spycher, S.; Keldenich, J. COSMOmic: A Mechanistic Approach to the Calculation of Membrane–Water Partition Coefficients and Internal Distributions within Membranes and Micelles. *J. Phys. Chem. B* **2008**, *112*, 12148–12157.

(69) Skopalík, J.; Anzenbacher, P.; Otyepka, M. Flexibility of Human Cytochromes P450: Molecular Dynamics Reveals Differences between CYPs 3A4, 2C9, and 2A6, which Correlate with Their Substrate Preferences. *J. Phys. Chem. B* **2008**, *112*, 8165–8173.

(70) Poulos, T. L. Cytochrome P450 Flexibility. *Proc. Natl. Acad. Sci. U. S. A.* **2003**, *100*, 13121–13122.

(71) Hammes-Schiffer, S.; Benkovic, S. J. Relating Protein Motion to Catalysis. *Annu. Rev. Biochem.* **2006**, *75*, 519–541.

(72) Hendrychová, T.; Anzenbacherová, E.; Hudeček, J.; Skopalík, J.; Lange, R.; Hildebrandt, P.; Otyepka, M.; Anzenbacher, P. Flexibility of Human Cytochrome P450 Enzymes: Molecular Dynamics and Spectroscopy Reveal Important Function-Related Variations. *Biochim. Biophys. Acta, Proteins Proteomics* **2011**, *1814*, 58–68.

(73) Schrödinger Release 2015-1: Maestro Schrödinger Release 2015-1: Maestro 2015.

(74) Moore, C. D.; Shahrokh, K.; Sontum, S. F.; Cheatham, T. E.; Yost, G. S. Improved Cytochrome P450 3A4 Molecular Models Accurately Predict the Phe215 Requirement for Raloxifene Dehydrogenation Selectivity. *Biochemistry* **2010**, *49*, 9011–9019.

(75) Domanski, T. L.; He, Y. A.; Harlow, G. R.; Halpert, J. R. Dual Role of Human Cytochrome P450 3A4 Residue Phe-304 in Substrate Specificity and Cooperativity. *J. Pharmacol. Exp. Ther.* **2000**, *293*, 585–591.

(76) Fowler, S. M.; Taylor, J. M.; Friedberg, T.; Roland Wolf, C.; Riley, R. J. CYP3A4 Active Site Volume Modification by Mutagenesis of Leucine 211. *Drug Metab. Dispos.* **2002**, *30*, 452–456.

(77) Hayashi, T.; Harada, K.; Sakurai, K.; Shimada, H.; Hirota, S. A Role of the Heme-7-Propionate Side Chain in Cytochrome P450cam as a Gate for Regulating the Access of Water Molecules to the Substrate-Binding Site. *J. Am. Chem. Soc.* **2009**, *131*, 1398–1400.

(78) Krishnamoorthy, N.; Gajendrarao, P.; Thangapandian, S.; Lee, Y.; Lee, K. W. Probing Possible Egress Channels for Multiple Ligands in Human CYP3A4: A Molecular Modeling Study. *J. Mol. Model.* **2010**, *16*, 607–614.

(79) Jarzynski, C. A Nonequilibrium Equality for Free Energy Differences **1996**, *11* arXiv:cond-mat/9610209.

(80) Lüdemann, S. K.; Lounnas, V.; Wade, R. C. How Do Substrates Enter and Products Exit the Buried Active Site of Cytochrome P450cam? 2. Steered Molecular Dynamics and Adiabatic Mapping of Substrate Pathways. *J. Mol. Biol.* **2000**, *303*, 813–830.

(81) Napolitano, L. M. R.; Bisha, I.; De March, M.; Marchesi, A.; Arcangeletti, M.; Demitri, N.; Mazzolini, M.; Rodriguez, A.; Magistrato, A.; Onesti, S.; et al. A Structural, Functional, and Computational Analysis Suggests Pore Flexibility as the Base for the Poor Selectivity of CNG Channels. *Proc. Natl. Acad. Sci. U. S. A.* **2015**, *112*, E3619–E3628.

Symposium Report

The Role of Protein-Protein and Protein-Membrane Interactions on P450 Function[□]

Emily E. Scott, C. Roland Wolf, Michal Otyepka, Sara C. Humphreys, James R. Reed, Colin J. Henderson, Lesley A. McLaughlin, Markéta Paloncýová, Veronika Navrátilová, Karel Berka, Pavel Anzenbacher, Upendra P. Dahal, Carlo Barnaba, James A. Brozik, Jeffrey P. Jones, D. Fernando Estrada, Jennifer S. Laurence, Ji Won Park, and Wayne L. Backes

Departments of Medicinal Chemistry and Pharmaceutical Chemistry, The University of Kansas, Lawrence, Kansas (D.F.E., J.S.L., E.E.S.); Division of Cancer Research, School of Medicine, University of Dundee, Ninewells Hospital, Dundee, United Kingdom (C.R.W., C.J.H., L.A.M.); Regional Center of Advanced Technologies and Materials, Department of Physical Chemistry, Faculty of Science (M.O., M.P., V.N., K.B.) and Department of Pharmacology, Faculty of Medicine and Dentistry (P.A.), Palacký University, Olomouc, Czech Republic; Department of Chemistry, Washington State University, Pullman, Washington (S.C.H., U.P.D., C.B., J.A.B., J.P.J.); and Department of Pharmacology and Experimental Therapeutics, and the Stanley S. Scott Cancer Center, Louisiana State University Health Sciences Center, New Orleans, Louisiana (J.R.R., J.W.P., W.L.B.)

Received December 29, 2015; accepted February 3, 2016

ABSTRACT

This symposium summary, sponsored by the ASPET, was held at Experimental Biology 2015 on March 29, 2015, in Boston, Massachusetts. The symposium focused on: 1) the interactions of cytochrome P450s (P450s) with their redox partners; and 2) the role of the lipid membrane in their orientation and stabilization. Two presentations discussed the interactions of P450s with NADPH-P450 reductase (CPR) and cytochrome *b*₅. First, solution nuclear magnetic resonance was used to compare the protein interactions that facilitated either the hydroxylase or lyase activities of CYP17A1. The lyase interaction was stimulated by the presence of *b*₅ and 17 α -hydroxypregnenolone, whereas the hydroxylase reaction was predominant in the absence of *b*₅. The role of *b*₅ was also shown in vivo by selective hepatic knockout of *b*₅ from mice expressing CYP3A4 and CYP2D6; the lack of *b*₅ caused a

decrease in the clearance of several substrates. The role of the membrane on P450 orientation was examined using computational methods, showing that the proximal region of the P450 molecule faced the aqueous phase. The distal region, containing the substrate-access channel, was associated with the membrane. The interaction of NADPH-P450 reductase (CPR) with the membrane was also described, showing the ability of CPR to “helicopter” above the membrane. Finally, the endoplasmic reticulum (ER) was shown to be heterogeneous, having ordered membrane regions containing cholesterol and more disordered regions. Interestingly, two closely related P450s, CYP1A1 and CYP1A2, resided in different regions of the ER. The structural characteristics of their localization were examined. These studies emphasize the importance of P450 protein organization to their function.

Introduction

The cytochrome P450 (P450) system in eukaryotic organisms comprises numerous proteins that interact within the confines of a

This work was supported in part by National Institutes of Health [R01 GM076343, GM102505] to E.E.S.; [F32 GM103069] to D.F.E.; [GM110790] to J.P.J.; and [R01 ES004344] and [P42 ES013648] to W.L.B.; the Ministry of Education, Youth and Sports of the Czech Republic, project LO1305 to M.O. and the Grant Agency of the Czech Republic, [P303/12/G163] to P.A.; and Cancer Research UK Programme Grant [C4639/A10822] to C.R.W.

This report is a summary of a session at Experimental Biology 2015 sponsored by the Drug Metabolism Division of ASPET.

Emily E. Scott, C. Roland Wolf, Michal Otyepka, Sara C. Humphreys, and James R. Reed were speakers at the symposium and are considered co-first authors.

dx.doi.org/10.1124/dmd.115.068569.

[□]This article has supplemental material available at dmd.aspetjournals.org.

membrane environment. The microsomal P450s reside in the endoplasmic reticulum (ER) and catalyze numerous oxidative reactions of both exogenous and endogenous substrates (Omura and Sato, 1962; Omura et al., 1965; Rendic and Guengerich, 2015). Because the proteins are crowded in the ER, there are numerous “opportunities” for protein-protein interactions, leading to questions regarding how the P450 system proteins are organized in the membrane. The requirement for P450 enzymes to interact with their redox partners, NADPH-cytochrome P450 reductase and cytochrome *b*₅ (*b*₅), is well known (Hildebrandt and Estabrook, 1971); however, the mechanism that governs formation of these complexes remains unclear. Additionally, recent studies have shown that some P450 enzymes are capable of forming both homomeric and heteromeric P450•P450 complexes that affect monooxygenase function (Davydov, 2011; Reed and Backes, 2012). Consequently, P450 activities can be modulated by

ABBREVIATIONS: *b*₅, cytochrome *b*₅; CHAPS, (3-[3-cholamidopropyl]dimethylammonia]-1-propanesulfonate); CPR, NADPH-cytochrome; DRM, detergent-resistant membrane; ER, endoplasmic reticulum; GFP, green fluorescent protein; HBN, hepatic *b*₅ null; NMR, nuclear magnetic resonance; P450, cytochrome P450; SM-TIRF, single-molecule total internal reflectance microscopy; SPLIM, super-resolution protein-lipid interaction map; 2D, two-dimensional.

the specific substrates present, the relative amount of the catalytically pertinent P450 present, the relative amounts of the electron donors CPR and b_5 , whether the specific reaction is stimulated by the presence of b_5 , and whether a second P450 is present that can interact with the P450 responsible for substrate hydroxylation (Jansson and Schenkman, 1987; Im and Waskell, 2011).

The multiple interactions among P450 system proteins occur within a heterogeneous lipid environment of the ER membrane (Brignac-Huber et al., 2011). At one level, insertion of these proteins within the membrane restricts their ability to interact to two dimensions; however, owing to the flexibility of the proteins within the membrane, their movement around their membrane-binding segments results in a greater range of motion and increases their ability to form complexes (Baylon et al., 2013). The heterogeneity of the membrane can also affect P450 function by either concentrating or segregating proteins within membrane regions.

The goal of this symposium was to address issues related to how proteins of the P450 system are organized and how these proteins interact with the membrane. Dr. Emily Scott examined the interactions among CPR, b_5 , and CYP17A1 using solution NMR. Dr. Scott identified residues involved in the interaction of both CPR and b_5 with CYP17A1, and showed that the b_5 •CYP17A1 complex was enhanced by the presence of 17α -hydroxypregnenolone, the substrate for the CYP17A1-mediated lyase reaction.

Dr. Roland Wolf examined the interactions of P450s with their redox partners *in vivo* by generating a series of mice having the murine P450 gene clusters deleted and then engineered to express the corresponding human P450 enzymes. These investigators then selectively knocked out hepatic b_5 and showed the effect on the *in vivo* metabolism of CYP3A4- and CYP2D6-selective substrates. In these experiments, both CYP3A4 and CYP2D6 substrates that were known to require b_5 were cleared from the hepatic b_5 knockout mice.

Because the interactions among these proteins occur in a membrane environment, the role of the lipid membrane also serves as an integral component affecting P450 system function. Dr. Michal Otyepka used a computational approach to better understand the relationship among substrate, P450, and the membrane. He showed that the proximal side of the P450 molecule faced the aqueous environment, whereas the distal side was associated with the membrane-water interface. Substrate was modeled to approach the active site from the membrane through channels.

Using single-molecule total internal reflectance microscopy, Sara Humphreys reported on the interaction between CPR and the lipid bilayer and showed that this interaction was affected by the presence of detergent. In these studies, CPR was shown to move in and out of the membrane, a response exacerbated by the presence of detergent. Interestingly, this effect, referred to as *helicoptering*, is diminished by the presence of P450 proteins in the membrane.

The heterogeneity of the lipid components of the ER membrane were considered in the report by Dr. James (Rob) Reed, who showed that two closely related P450s, CYP1A1 and CYP1A2, reside in different regions of the ER. Whereas CYP1A2 exists in regions where the lipids are more ordered, CYP1A1 exists in the disordered regions. The investigators identified sequence motifs that governed their localization into the different membrane regions by generation of CYP1A1-CYP1A2 chimeric proteins.

Taken together, these studies show the interplay not only among of the protein components of the P450 system but also the role of the membrane on their organization. These protein-protein and protein-lipid interactions have a profound effect on the function of the P450 system.

Steroidogenic Cytochrome P450 17A1 Interactions with Catalytic Partners (D.F.E., J.S.L., and E.E.S.)

During the course of mono-oxygenation reactions, human P450 enzyme interaction with CPR is required to sequentially deliver the two electrons required for P450 catalysis, whereas interaction with b_5 is not usually required but is variously reported to accelerate, inhibit, or have no effect on P450 catalysis, depending on the P450 and substrate (Akhtar et al., 2005; Zhang et al., 2008; Ortiz de Montellano, 2015). A biophysical and biochemical understanding of these critical protein-protein interactions has been limited by the absence of crystallographic structures for human P450 proteins interacting with these protein partners, although mutagenesis, crosslinking, *in silico* docking, and other techniques have provided substantial information (Bridges et al., 1998; Naffin-Olivos and Auchus, 2006; Im and Waskell, 2011; Zhao et al., 2012). The generation of X-ray structures of such P450-protein complexes is likely hindered by the transient nature of these P450-protein interactions and the fact that they are largely thought to be mediated by electrostatic interactions; however, defining and characterizing such P450-protein interactions at high-resolution are possible using solution NMR, which generates information on protein dynamics and conformations but is amenable to the lower affinities of P450-protein interactions. The generation of isotopically labeled, catalytically active, truncated forms of the human steroidogenic CYP17A1, CPR, and b_5 proteins has permitted tracking the isotopically labeled resonances for individual amino acid residues as they broaden and/or shift upon experiencing changes in environment. In the set of experiments described herein, one of the three proteins is ^{15}N -labeled and titrated with one or more of the other proteins that compose the P450 catalytic system. The human steroidogenic P450 used, CYP17A1, is saturated with pregnenolone, its substrate for an initial hydroxylase reaction; 17α -hydroxypregnenolone, the product of this hydroxylation reaction and substrate for a subsequent lyase reaction generating androgens; or the type II steroidal inhibitor abiraterone. CYP17A1 is

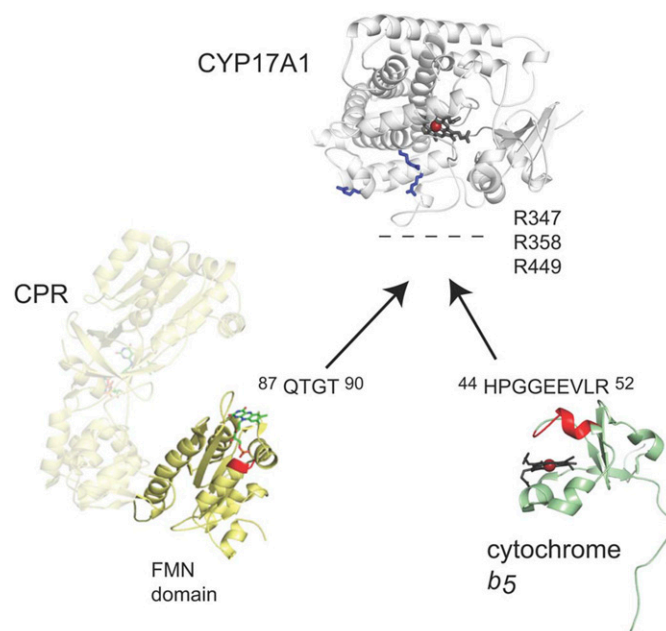


Fig. 1. Surfaces of CYP17A1, cytochrome b_5 , and CPR involved in protein-protein interactions. The respective binding surfaces are shown as blue sticks for positively charged residues of CYP17A1, red for the negatively charged $\alpha 2$ helix of b_5 , and red for the positively charged loop 1 of the CPR FMN domain. Aggregated from data from Estrada et al., 2013, 2014, and 2015.

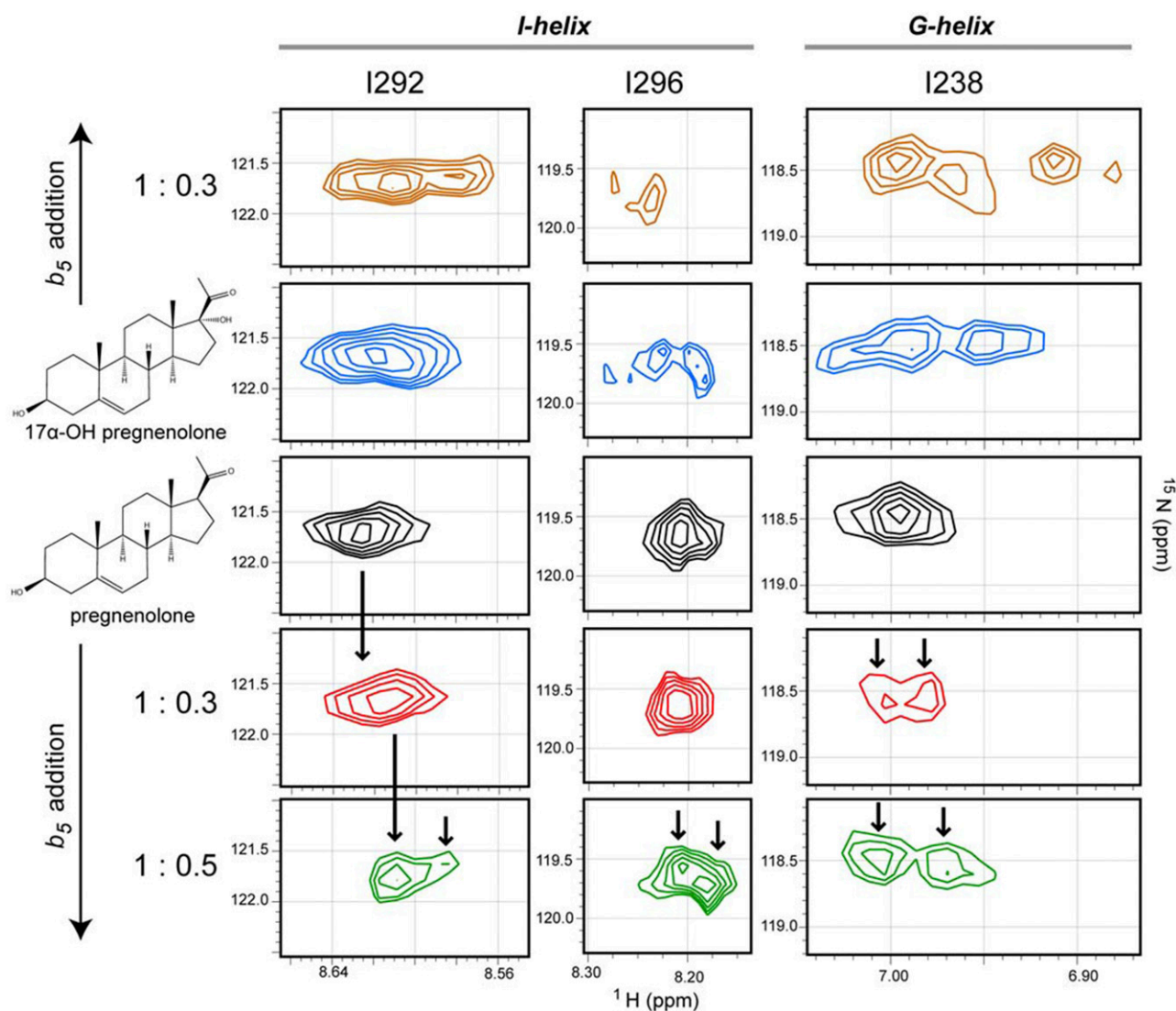


Fig. 2. Effect of substrate and b_5 on the conformational dynamics of CYP17A1. Distinct conformations are observed in the I-helix and G-helix residues of ^{15}N -labeled CYP17A1 when pregnenolone (black) versus 17α -hydroxypregnenolone (blue) is present in the active site. The addition of b_5 to either substrate-bound sample further perturbs the conformations for these residues (top and bottom panels). When saturated with the hydroxylase substrate pregnenolone, serial titration of CYP17A1 with b_5 [1:0.3 (red) and 1:0.5 (green)] induced a shift toward conformations more closely resembling those observed for CYP17A1 saturated with the lyase substrate 17α -hydroxypregnenolone in the absence of b_5 . Vertical arrows emphasize differences between spectra. This research was originally published in Estrada et al. 2014.

an important system for evaluating P450-protein interactions because although CPR is required for both hydroxylase and lyase reactions, b_5 results in a 10-fold increase in the lyase reaction without directly transferring electrons or substantially affecting the hydroxylation reaction (Auchus, et al., 1998). This selective b_5 facilitation of the lyase reaction is physiologically important as adrenal increases in b_5 levels drive androgen sex steroid production immediately before puberty in human development (Nakamura et al., 2009).

Previously published NMR studies (Estrada et al., 2013) have used ^{15}N - b_5 titrated with CYP17A1 to identify residues on b_5 that are differentially line broadened (G47, E48, E49, V50, and surrounding residues) and compose the anionic b_5 surface of the b_5 -CYP17A1 interface. Repeating such titration experiments with the R347H, R358Q, and R449L mutants of CYP17A1 reported to selectively depress the lyase activity (Geller et al., 1999) similarly prevented NMR changes indicative of b_5 -CYP17A1 physical complex formation. Thus, key residues of the CYP17A1- b_5 interface were identified on the proximal surface of CYP17A1 and the $\alpha 2$ helix of b_5 (Fig. 1). These

interacting surfaces were the same regardless of the CYP17A1 ligand, but the strength of the b_5 -CYP17A1 interaction was modulated by the identity of the CYP17A1 substrate, suggesting communication between the b_5 binding site on the proximal surface of CYP17A1 and the buried active site.

The reverse experiments titrating ^{15}N -CYP17A1 with unlabeled b_5 (Estrada et al., 2014) are much more complex owing to the number of resonances in CYP17A1 (494 amino acids) compared with b_5 (114 amino acids) and, at present, can be only partially interpreted because of the availability of only partial resonance assignments; however b_5 binding on the proximal surface of CYP17A1 clearly results in resonance splitting indicative of new backbone conformations for residues in the N terminus of the I helix (e.g., Fig. 2, I292 and I296) and the F and G helices (e.g., Fig. 2, I238) on the opposite, distal side of the protein from the b_5 binding site—and does so in a substrate-dependent manner. Bending and straightening of the I helix and repositioning of the F and G secondary structure elements are often associated with ligand entry and exit, consistent with the idea that when the initial

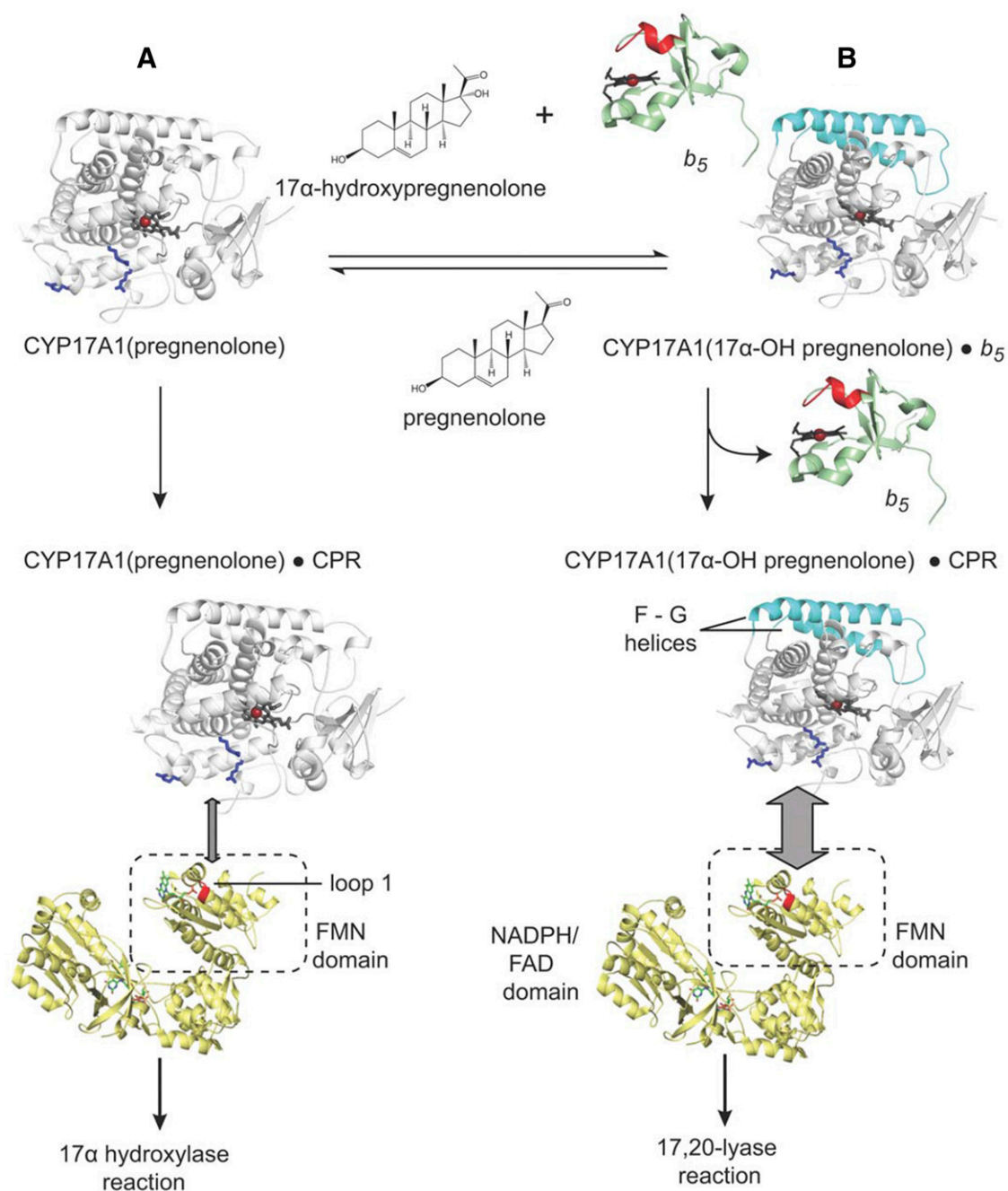


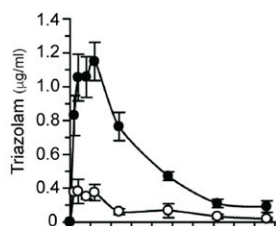
Fig. 3. Model of CYP17A1 interaction with substrates, NADPH-cytochrome P450 reductase, and cytochrome b_5 to perform either the 17α -hydroxylation (state A) or 17,20-lyase (state B) reaction consistent with current knowledge of the system. Interacting residues are shown as in Fig. 1. The CYP17A1 F-G helices that are altered by b_5 binding are shown in cyan. Adapted from research originally published in Estrada et al. (2015).

hydroxylase product 17α -hydroxypregnenolone occupies the CYP17A1 active site that b_5 binding could promote a conformation that decreases ligand release, thereby promoting the second, lyase reaction to yield the androgen product. Differences in processivity have previously been observed for the two CYP17 enzymes in zebrafish, although in that case, processivity was not modulated by b_5 (Pallan et al., 2015).

The CPR interactions with CYP17A1 have been probed using solution NMR in a similar manner; however, instead of using the multidomain CPR protein in which the CPR FAD domain primarily interacts with its FMN domain and is only transiently available for interaction with CYP17A1, the isolated ^{15}N -FMN domain of CPR was

used. Titration of the CPR ^{15}N -FMN domain with unlabeled CYP17A1 revealed that residues in a loop near the flavin (Q87-T90, Fig. 1) experienced the most significant line broadening, suggesting that this region is involved in the interaction between the FMN domain and CYP17A1; however, line broadening was much more broadly distributed and more severe for ^{15}N -FMN domain binding to CYP17A1 than for ^{15}N - b_5 binding to CYP17A1, consistent with a higher-affinity interaction in the former case. Like the b_5 -CYP17A1 interactions, the affinity for the CYP17A1-FMN domain interaction was modulated by the identity of the CYP17A1 substrate.

When the experiment was inverted and ^{15}N -CYP17A1 was titrated with the FMN domain of CPR, select residues in the B' helix, the F and



Drug	PK Parameter	CYP3A4	CYP3A4-HBN
TRIAZOLAM	C_{max} ($\mu\text{g/ml}$)	0.26 \pm 0.11	1.03 \pm 0.2 ***
	Half-life (min)	112.9 \pm 54.6	98.9 \pm 34.6
	AUC_{0-8h} ($\text{min} \cdot \mu\text{g/ml}$)	29.4 \pm 10.5	167.5 \pm 29.1 **
	$AUC_{0-\infty}$ ($\text{min} \cdot \mu\text{g/ml}$)	32.3 \pm 14	181.8 \pm 24.3 ***
	Cl (ml/min/kg)	104.6 \pm 36.5	18.5 \pm 2.2 **

Fig. 4. In vivo pharmacokinetic profiles of triazolam in CYP3A4 and CYP3A4-HBN mice. CYP3A4 (open circle) and CYP3A4-HBN (black circle) mice (female, $n = 4$) were treated with pregnenolone-16 α -carbonitrile (PCN) at a dose of 10 mg/kg daily i.p. for 3 days. On day 4, mice were dosed p.o. with triazolam at 3 mg/kg body weight, and a pharmacokinetic study was carried out over 8 hours with blood sampling via the tail vein at the time points shown. Samples were analyzed for triazolam content by LC-MS/MS, and table shows pharmacokinetic parameters (mean \pm S.E.M.). This figure was reproduced from Henderson et al. (2015).

G helices, and the N terminus of the I helix were line-broadened more than the average CYP17A1 residue. These resonances did not demonstrate peak splitting indicative of new backbone conformations, however, as they had upon addition of b_5 (not shown). This suggests that the binding of the FMN domain alters the dynamics of CYP17A1, with specific effects on certain structural elements but does not alter the CYP17A1 conformation like b_5 does. In other words, b_5 has been shown to allosterically modulate CYP17A1 conformation, as suggested previously (Auchus et al., 1998).

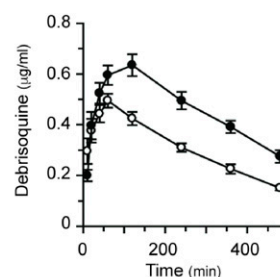
Interactions between CYP17A1 and its catalytic partners can be further compared using solution NMR by evaluating the three proteins together. Experiments with ^{15}N - b_5 added to CYP17A1 demonstrate formation of the CYP17A1- b_5 complex, which is then disrupted when full-length CPR (or the CPR FMN domain) is added, consistent with mutually exclusive binding and the partially overlapping binding sites for CPR and b_5 on the proximal face of P450 enzymes as previously proposed (Zhang et al., 2007; Im and Waskell, 2011). Although single point mutations of R347H or R449L on the proximal surface of CYP17A1 were sufficient to prevent binding of b_5 , neither the R449L nor the R358Q mutation is individually sufficient to disrupt binding of the FMN domain of CPR. This result may indicate that these CYP17A1 residues are not involved in binding of the FMN domain or that the interaction with the CPR FMN domain is not easily disrupted by single point mutations, either of which is consistent with the functional observations (Geller et al., 1999).

In aggregate, solution NMR studies, functional data, and structural data suggest a relatively simple comprehensive model for the observed CYP17A1 biochemistry, including selective facilitation of the lyase reaction by b_5 (Fig. 3). NMR studies clearly demonstrate that in solution CYP17A1 exists in different conformational states with the hydroxylase substrate pregnenolone, the lyase substrate 17 α -hydroxypregnenolone, and in the presence of b_5 . Binding of the hydroxylase substrate pregnenolone is likely to promote a conformational state that interacts with CPR and facilitates formation of the typical Fe(IV) oxo catalytic intermediate for the hydroxylation reaction. CYP17A1 can release the 17 α -hydroxypregnenolone product or bind it de novo; however, it is likely that the 17 α -hydroxy intermediate can also remain in the active site

to undergo the second sequential reaction. Regardless, the presence of the lyase substrate in the CYP17A1 active site and b_5 binding generate a distinct conformational state, which is likely to ultimately facilitate the subsequent lyase reaction. Because the presence of b_5 facilitates the lyase reaction and because binding of b_5 alters the backbone of elements implicated in substrate entry and exit, it is tempting to suggest that the binding of b_5 to the CYP17A1/17 α -hydroxypregnenolone complex promotes the processivity of the enzyme by promoting a closed conformational state. Regardless of how b_5 does so, b_5 and CPR binding are mutually exclusive, requiring b_5 to dissociate for CPR to bind and deliver the two electrons necessary for catalysis. This is consistent with the NMR studies herein, which suggest that either CPR or the CPR FMN domain can outcompete b_5 . This model is internally consistent with the present state of knowledge regarding the interactions of CYP17A1, CPR, and b_5 and significantly expands our knowledge of P450 dynamics and protein interactions beyond that previously understood for the human steroidogenic CYP17A1, with implications for other human P450 enzymes.

Role of NADPH-Cytochrome P450 Reductase and Cytochrome b_5 as Electron Donors to P450 (C.J.H., L.A.M., and C.R.W.)

Although the role of CPR in P450 function has been extensively studied and relatively well defined, that of b_5 is less well understood, and, until recently, information on b_5 had been essentially generated exclusively from in vitro experiments, yielding data that were not only difficult to interpret but often contradictory and not easily extrapolated to the in vivo situation. Within the last few years, however, we have generated mouse models with either a conditional (liver) or global deletion of b_5 and used these, in conjunction with our previously described model of hepatic CPR deletion (hepatic reductase null mice) to investigate the role of both CPR and b_5 in P450-mediated drug metabolism, disposition, and toxicity. Whereas CPR deletion was found, as expected, to have a significant effect on P450 activity both in vitro and in vivo, we also demonstrated, for the first time in vivo, that b_5 deletion had a profound effect on P450 drug metabolism in a tissue- and



Drug	PK Parameter	CYP2D6	CYP2D6-HBN
DEBRISOQUINE	C_{max} ($\mu\text{g/ml}$)	0.53 \pm 0.06	0.67 \pm 0.1 **
	Half-life (min)	265 \pm 43.9	325.4 \pm 59.2*
	AUC_{0-8h} ($\text{min} \cdot \mu\text{g/ml}$)	149.7 \pm 17.3	223.8 \pm 35.9 ***
	$AUC_{0-\infty}$ ($\text{min} \cdot \mu\text{g/ml}$)	207.8 \pm 27.5	357.3 \pm 89.7 ***
	Cl (ml/min/kg)	48.8 \pm 6	29.5 \pm 7.4 ***

Fig. 5. In vivo pharmacokinetic profiles of debrisoquine in CYP2D6 and CYP2D6-HBN mice. CYP2D6 (open circle) and CYP2D6-HBN (black circle) mice (female, $n = 4$) were dosed p.o. with debrisoquine at 10 mg/kg of body weight, and a pharmacokinetic study was carried out over 8 hours with blood sampling via the tail vein at the time points shown. Samples were analyzed for debrisoquine content by LC-MS/MS, and table shows pharmacokinetic parameters (mean \pm S.E.M.). This figure was reproduced from Henderson et al. (2015).

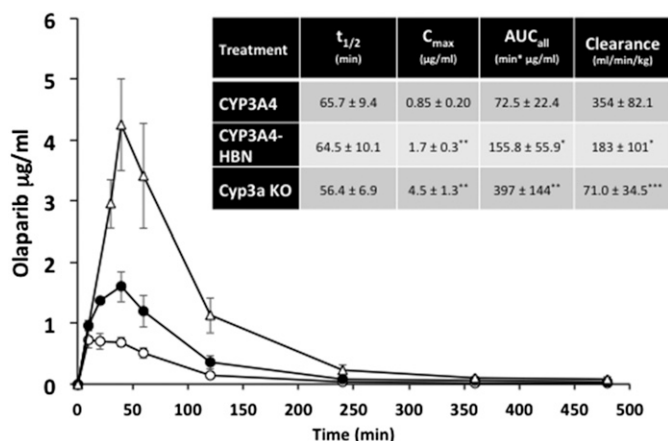


Fig. 6. In vivo pharmacokinetic profiles of olaparib in CYP3A4, CYP3A4-HBN, and Cyp3a null mice. CYP3A4 (open circle), CYP3A4-HBN (black circle), and Cyp3a null (open triangle) mice (female; $n = 4$) were fed on a powdered diet (RM1) containing 250 mg/kg pregnenolone-16 α -carbonitrile (PCN) for 3 days (equivalent to 50 mg/kg daily). On day 4, mice were dosed p.o. with olaparib at a final concentration of 25 mg/kg body weight, and a pharmacokinetic study carried out over 8 hours with blood sampling via the tail vein at the time points shown. Samples were analyzed for olaparib content by LC-MS/MS. Inset table shows pharmacokinetic parameters (mean \pm S.D.). * $P < 0.05$, ** $P < 0.01$ *** $P < 0.001$; CYP3A4-HBN or Cyp3a KO versus CYP3A4, t test.

substrate-dependent manner (Finn et al., 2008, 2011; McLaughlin et al., 2010). Furthermore, investigation of a residual P450 activity (~10%) in vitro in HRN samples through the generation of a mouse line in which both CPR and b_5 were deleted in the liver (hepatic b_5 reductase null) led us to demonstrate that b_5 -Cyb5R can act as sole electron donors to the P450 system both in vitro and in vivo (Henderson et al., 2013).

The importance of b_5 in drug metabolism is underlined by the finding that expression of the enzyme varies significantly—by at least 5-fold—across the human population (Kurian et al., 2007; Henderson and Wolf, unpublished). Coupled with a recently discovered genetic variant in b_5 (McKenna et al., 2014), there is clearly a need to better understand the role of b_5 in relation to human P450 activity and to establish—in vivo—the extent to which human P450s exhibit a b_5 dependency. To this end, we crossed the hepatic b_5 null (HBN) (Finn et al., 2008) mouse with two mouse lines in which key human P450s—CYP2D6 or CYP3A4—are expressed on a Cyp2d or Cyp3a gene cluster null background (Hasegawa et al., 2011; Scheer et al., 2012). CYP2D6-HBN and CYP3A4-HBN mice (Henderson et al., 2015) were fertile and phenotypically normal and had only minor changes in hepatic lipids, perhaps surprising given the known involvement of b_5 in lipid desaturation (Jeffcoat et al., 1977; Finn et al., 2011). Using substrates for human CYP3A4 (triazolam) and CYP2D6 (debrisoquine), it was shown in vitro in hepatic microsomes that the metabolism of these drugs was significantly reduced in the absence of b_5 . Moreover, in both cases, addition of exogenous b_5 to reaction mixtures restored activity in a dose-dependent manner (Henderson et al., 2015). When triazolam (Fig. 4) and debrisoquine (Fig. 5) pharmacokinetics were determined in vivo in CYP3A4-HBN and CYP2D6-HBN mice, respectively, metabolism was again shown to be profoundly reduced in mice lacking hepatic b_5 , with significant increases in C_{max} and AUC and decreased clearance relative to control animals. The minor perturbations in hepatic lipids reported in the CYP3A4-HBN and CYP2D6-HBN mice (Henderson et al., 2015) strongly support the view that the effects observed on drug disposition in vivo are not a result of changes to the lipid composition of the ER but rather reflect the consequences of a lack of b_5 . It is thus possible that the expression of b_5 , and its functionality, may make a significant contribution to the observed heterogeneity in plasma levels

of many commonly prescribed drugs. To further illustrate this, the pharmacokinetics of the anticancer drugs and poly ADP ribose polymerase inhibitors olaparib (primarily metabolized by CYP3A4) and veliparib (primarily metabolized by CYP2D6) were determined in CYP3A4 and CYP2D6 mice, in the presence or absence of hepatic b_5 . For olaparib (Fig. 6), b_5 significantly affected metabolism of this drug, with C_{max} and area under the curve being increased and clearance decreased, in mice lacking b_5 relative to CYP3A4 mice, whereas for veliparib (Fig. 7), b_5 made no difference to metabolism. These data emphasize the importance of taking b_5 expression into account for in vitro-in vivo extrapolation.

Positioning of Microsomal P450s and Drugs in Lipid Bilayers (M.O., M.P., V.N., K.B., P.A.)

Drugs enter cells via active and passive transport processes through lipid membranes and inside cells; both transport modes significantly contribute to the final drug disposition (Smith et al., 2014). Besides the mentioned processes, membrane partitioning, nonspecific protein binding, and biotransformation dominantly contribute to drug disposition in a cell (Anzenbacher and Anzenbacherova, 2001; Guengerich, 2006; Balaz, 2009; Seddon et al., 2009; Lucio et al., 2010; Endo et al., 2011; Nagar and Korzekwa, 2012). In humans, most marketed drugs undergo biotransformation processes catalyzed by P450 enzymes (Evans and Relling, 1999; Anzenbacher and Anzenbacherova, 2001; Zanger and Schwab, 2013), which are attached to membranes of the ER and mitochondria (Black, 1992). Experimental measurements suggested that P450 catalytic domains flow on the membrane surface being anchored to the lipid bilayer by an N-terminal α -helix; however the exact positioning of P450 in the membrane has not been yet determined by a direct experiment. This ignited an interest in modeling of P450s on the lipid bilayer. The early empirical models, which appeared soon after release of the crystal structures of mammalian P450s, were, however, not conclusive as they suggested very different membrane orientations of P450s (cf. Fig. 5 in Berka et al., 2011). Two independent models of membrane anchored CYP2C9 based on molecular dynamics simulations (Berka et al., 2011; Cojocaru et al., 2011) published in 2011 shared many similarities indicating that molecular dynamics might provide convergent and reliable membrane

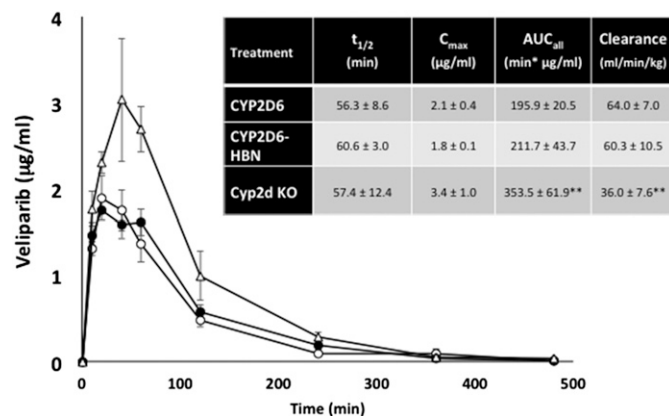


Fig. 7. In vivo pharmacokinetic profiles of veliparib in CYP2D6, CYP2D6-HBN, and Cyp2d KO mice. CYP2D6 (open circle), CYP2D6-HBN (black circle), and Cyp2d null (open triangle) mice (female; $n = 4$) were dosed p.o. with veliparib at a final concentration of 12.5 mg/kg body weight, and a pharmacokinetic study was carried out over 8 hours with blood sampling via the tail vein at the time points shown. Samples were analyzed for olaparib content by LC-MS/MS. Inset table shows pharmacokinetic parameters (mean \pm S.D.). ** $P < 0.01$; Cyp2d KO versus CYP2D6-HBN or CYP2D6, t test.

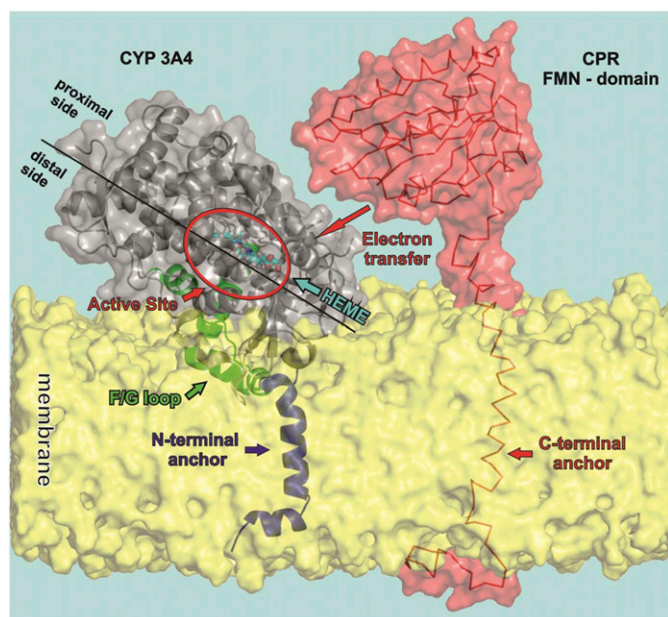


Fig. 8. Model of the orientation of CYP3A4 and CPR with respect to the membrane. The figure shows a model of CYP3A4, taken from molecular dynamics simulations, floating on the membrane having a partially immersed catalytic domain and being anchored by one N-terminal α -helix crossing the membrane. The distal side faces to the membrane while the proximal side is oriented toward the cytosol and available for interaction with redox partners (here the FMN domain of CPR is shown).

models of P450s. Since then, many independent models of membrane anchored P450s have been published, so we can discuss common features and differences among individual P450 forms (Denisov et al., 2012; Sgrignani and Magistrato, 2012; Baylon et al., 2013; Berka et al., 2013; Ghosh and Ray, 2013; Yu et al., 2015).

Common features of P450 membrane anchoring include the catalytic domain, which resides on the lipid bilayer being partially immersed to the membrane interior. The N-terminal part and F/G loop on the distal side of P450s are typically immersed to the nonpolar membrane interior (Fig. 8). The proximal side of P450 is exposed to the aqueous environment being available for interactions with redox partners. The active site, which is deeply buried in P450 structures (Otyepka et al., 2007; Johnson and Stout, 2013), is above the membrane surface and is accessible through a network of access channels (Cojocaru et al., 2007). Analysis of access channels by software tools CAVER (Petrek et al., 2006) and MOLE (Petrek et al., 2007) showed that openings of active-site access channels are positioned inside the membrane and the solvent channel exit (passing between F and I helices) faces the water/membrane interface (Fig. 9). The individual P450 forms (CYPIA2, 2A6, 2C9, 2D6, 2E1, and 3A4) show rather small variations in their membrane orientations, which affect positions of the channel openings with respect to the membrane (Berka et al., 2013).

Most of the marketed drugs are amphiphilic compounds, and they have a large potential to accumulate in lipid bilayers (Seddon et al., 2009; Endo et al., 2011; Nagar and Korzekwa, 2012). It should be noted that the drug-metabolizing P450s catalyze the monooxygenase reaction as the most typical reaction. Formally, an oxygen atom is inserted onto a substrate molecule in the reaction, and one may expect that the amphiphilic substrate becomes more hydrophilic after the oxidation reaction. Comparison of affinities of drugs and their respective P450 metabolites to membranes shows that substrates have higher affinities for the membranes and are positioned deeper in the membrane structure than their respective metabolites (Paloncýová et al., 2013; Paloncýová

et al., 2014). The drugs are typically localized inside the lipid bilayers just below the polar head group region, and the positions of P450 access active site channels openings are in the same membrane layer. Membrane positions of metabolites correspond to the solvent channel exit, which point toward the water-membrane interface (Fig. 10). Based on these findings, one may hypothesize that the drugs penetrate from the membrane to the P450 active sites. They are oxidized and released to the cytosol via the solvent channel.

Super-resolution Protein-Lipid Interaction Mapping of P450 Reductase and Cytochrome P450 2C9 Interacting with Ternary Planar Lipid Bilayers (S.C.H., U.P.D., C.B., J.A.B., and J.P.J.)

Single-molecule techniques provide insight into protein-protein and protein-lipid interactions at a molecular level that is unresolvable by ensemble methods. Here, we investigated interactions between CPR, CYP2C9, and planar supported lipid bilayers using single molecule total internal reflectance microscopy (SM-TIRF) to generate super resolution protein-lipid interaction maps (SPLIMs). Specifically, we looked at how detergent concentration and time can affect protein-lipid interactions between CPR and planar lipid bilayers. We also examined how CYP2C9 perturbs this system.

Both CPR and CYP2C9 are localized to the cytoplasmic face of the hepatic ER in vivo via N-terminal α -helices (Williams and Kamin, 1962; Black, 1992). There is mounting evidence to suggest that under certain experimental conditions, CPR and P450s form higher-order complexes (Reed et al., 2010; Davydov, 2011; Davydov et al., 2015); however, the stoichiometry of these complexes and the dynamics governing their association and disassociation are not well understood. To understand how such complexes are formed, it is first important to investigate the simpler protein-lipid and protein-protein interactions essential to the system.

Detection and measurement of single ER proteins or protein complexes and their membrane counterparts are difficult in live cells owing to the complexity of the system and labeling shortcomings. Consequently, over decades, researchers have developed a range of cell membrane mimics to satisfy the finicky energetic requirements of membrane proteins for biphasic amphiphilic environments while removing much of the complexity of biologic membranes. Examples of P450 reconstituted systems include planar lipid bilayers, liposomes, and nanodiscs (Denisov and Sligar, 2011).

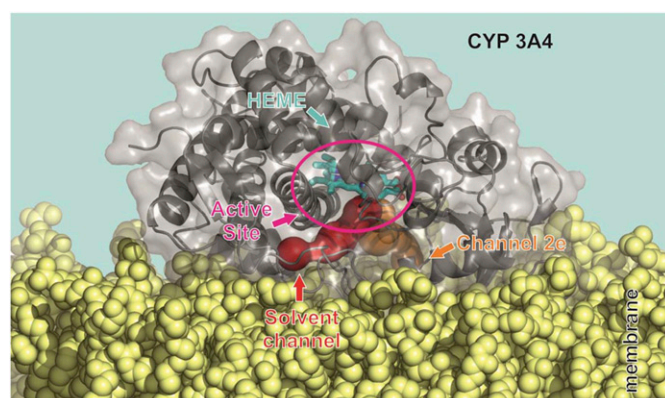


Fig. 9. Orientation of the CYP3A4 solvent channel and active site with respect to the membrane. The P450 catalytic domain (i.e., here CYP3A4 taken from molecular dynamics simulation) floats on the membrane and the access and exit channels (calculated by MOLE 2.0 software) to the deeply buried active site point toward the membrane opening above (for the solvent channel) and below (for channel no. 2e) the membrane surface.

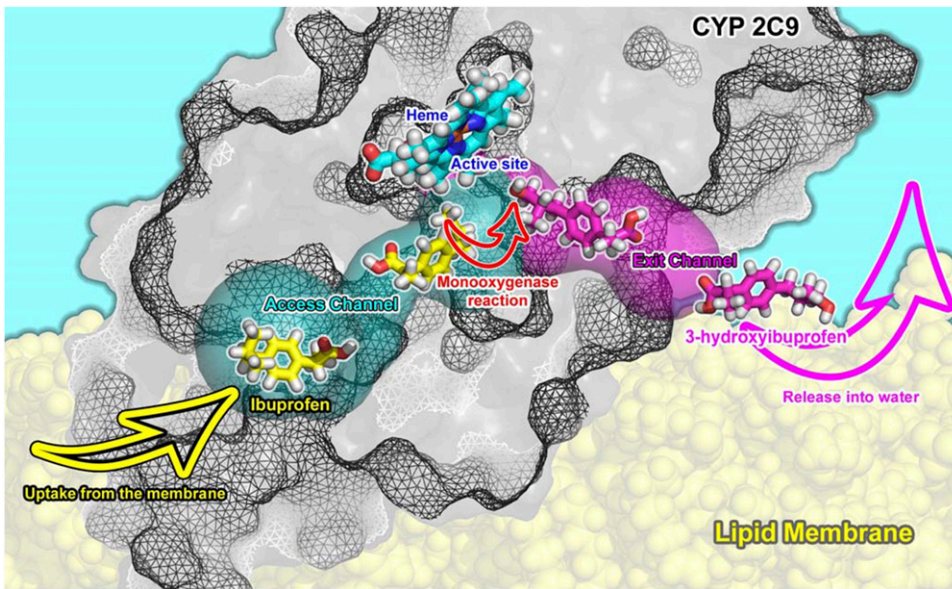


Fig. 10. Model of the substrate access channel of CYP2C9. Lipophilic and amphiphilic drugs can bind to CYP2C9 (taken from molecular dynamics simulation) active site from membrane, where they may accumulate. They pass via an access channel (calculated by MOLE 2.0) to the active site and there are transformed typically by a monooxygenase reaction and released via an exit channel to the water-membrane interface.

Although there are many advantages in using this type of reductionist approach, one distinct disadvantage is that reconstituted systems are prepared using detergents. Detergents are required to solubilize membrane proteins, maintain their stability, and facilitate their incorporation into the phospholipid bilayer (Helenius and Simons, 1975); however, detergents interfere with native protein-lipid and protein-protein interactions, and it is difficult to remove them from the system completely when they are no longer needed. The paradoxical beneficial and adverse roles of detergents in reconstituted systems can be explained by their chemical and thermodynamic properties. Commonly

used detergents, such as (3-[3-cholamidopropyl]dimethylammonia]-1-propanesulfonate (CHAPS), structurally resemble cell membrane-associated compounds, including sterols and bile acids. In addition, akin to phospholipids, under certain conditions, detergents undergo organizational transformations to form lamellar micelles and bicelles.

Although attempts are often made to remove detergents using dialysis, hydrophobic adsorption, and gel filtration chromatography, based on our observations, we hypothesize that some unknown amount always remains. This could explain why incorporation of CPR and P450 into reconstituted systems is never complete (Reed et al., 2006). In

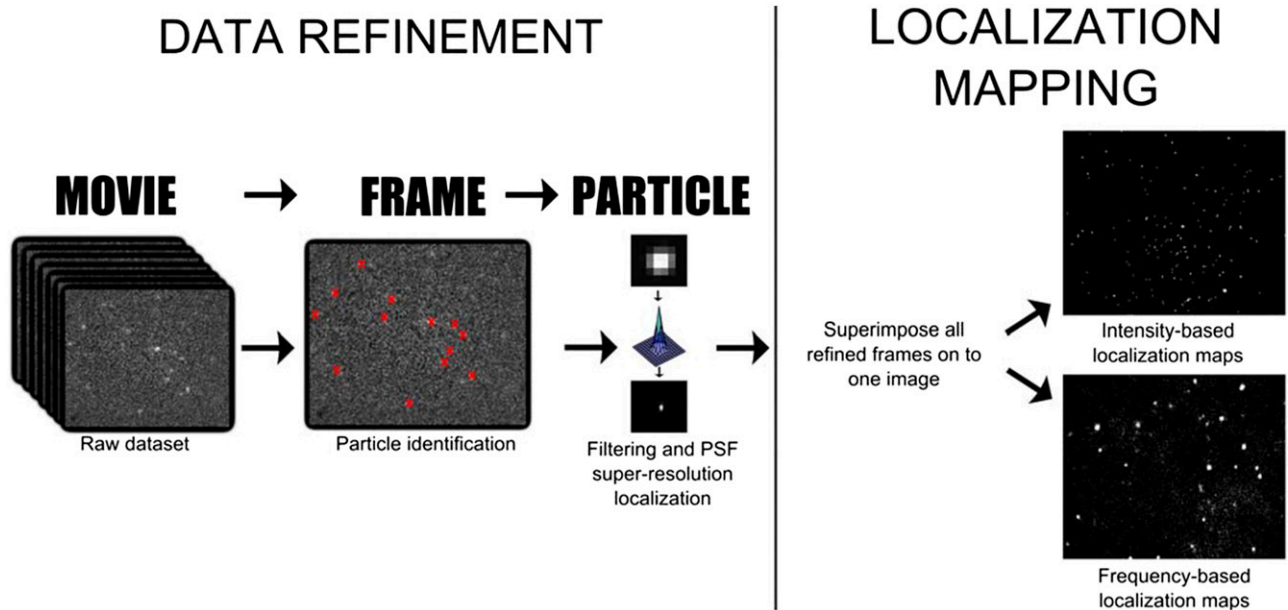


Fig. 11. Super-resolution protein-lipid interaction mapping (SPLIM) workflow. Single-molecule data collected by exciting individual Alexa-555-CPR proteins at the lipid bilayer in a TIRF evanescent field using a 532-nm laser. Emitted light was detected on an EM-CCD camera. Tens to hundreds of thousands of continuous 10-millisecond frames were collected from a single sample at a specific bilayer location. The ThunderSTORM plugin for ImageJ identifies individual proteins frame-by-frame. The super-resolution location of each protein was found by approximating the point spread function with a 2D Gaussian and finding the center. CPR-lipid interactions were 'mapped' by superimposing all super-resolution refined frames. Two different types of 2D grayscale maps can be generated: intensity-based maps (top left) and frequency-based maps (bottom left). Whereas cumulative molecular brightness (intensity) may be of interest in some applications, for example, in fixed cells, for SPLIM, we postulate that frequency-based localization better represents transient protein-lipid interactions, where 'whiter' regions are locations in the heterogeneous bilayer where the incidence of interaction is higher.

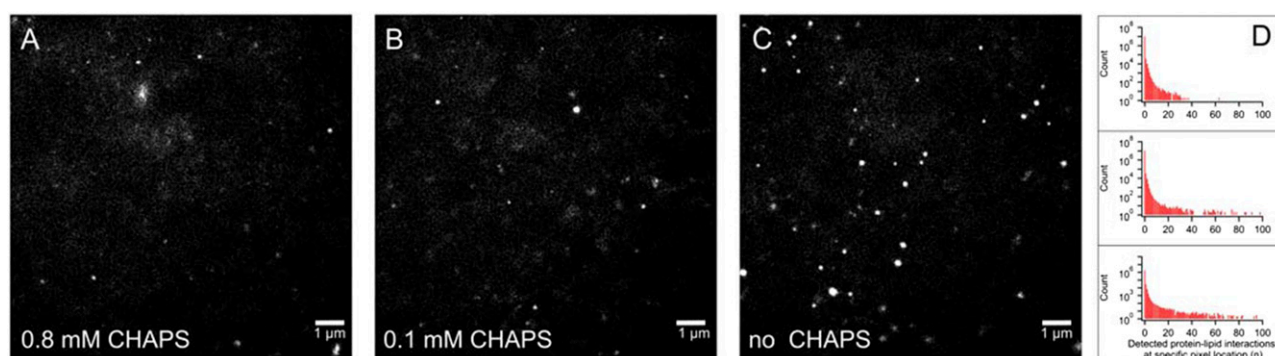


Fig. 12. SPLIM indicates diminishing detergent leads to changes in the frequency and distribution of protein-lipid interactions. Alexa 555-CPR (CPR purified according to Rock et al., (2001) and conjugated to Alexa 555 C2 maleimide according to the manufacturer (ThermoFisher)) was added to a final concentration of 3.5 nM to ternary lipid bilayers (prepared in 200 mM K-HEPES (pH 7.4), 15 mM MgCl₂, and 0.8 mM CHAPS). The degree of labeling of the final Alexa 555-CPR was 80%. After 30 minutes incubation at 37°C, the bilayer was rinsed in buffer containing 200 mM K-HEPES (pH 7.4), 15 mM MgCl₂, and either 0.8 mM CHAPS (A), 0.1 mM CHAPS (B) or no CHAPS (C). These SPLIM images have been normalized for the number of particles instances (84,000 ± 600). A *particle instance* is defined as one spatially resolved CPR-lipid interaction in one 10-millisecond frame using ThunderSTORM. (A, B) were each generated by superimposing 20,000 frames, whereas (C) was generated from 12,200 frames. Changes in the spatial frequency distribution demonstrated in these SPLIM images are further shown by one-dimensional histograms (D) where (A), (B), and (C) are the top, middle, and bottom, respectively. All SPLIM experiments were carried out at 37°C. Because SPLIM images are essentially 2D histograms that follow poissonian distributions, to enhance contrast, grayscale levels were adjusted. The same adjustments were applied to each SPLIM image. Thus, all pixels in all SPLIM images were treated identically.

support of this hypothesis, using SM-TIRF, we directly observed fluorescently labeled proteins transiently interacting with lipid bilayers. This apparent dynamic binding and debinding phenomenon—helicoptering—was first described by (Ingelman-Sundberg and Glaumann, 1980) and is demonstrated in the (Supplemental Video S1). Furthermore, we examined how helicoptering is dependent on detergent concentration and time, as well on the strength of the protein-lipid interaction or protein complex-lipid interaction.

It is first important to provide a brief background on our CPR-CYP2C9 planar lipid bilayer system, SM-TIRF, and a data visualization technique we are calling super-resolution protein-lipid interaction mapping (SPLIM). We produce our reconstituted systems by laying down planar lipid bilayers on glass coverslips and allowing fluorescently labeled protein (Alexa 555 CPR and/or CYP2C9) to self-incorporate from above by incubation at 37°C. We prepare liposomes based on a method described by Guengerich and colleagues (Ingelman-Sundberg et al., 1996). From the liposomes, we prepare planar supported lipid bilayers using a method described by our group (Pouidel et al., 2013).

SM-TIRF involves focusing a laser beam through a high numerical aperture lens in such a way that it creates an evanescent field. This restricts the excitation of fluorophores to within ~100 nm of the coverslip. Consequently, only fluorescently labeled proteins that are in or very close to the 5-nm-thick lipid bilayer on the surface of the coverslip are monitored. The light emitted from the excited fluorophores in a specific 2D region of the bilayer is captured by an electron multiplying charge coupled device camera in sequential 10-ms exposure frames (seen in S1). We use the ThunderSTORM plugin for ImageJ to process this movie data to achieve super-resolution localization of CPR interacting with the lipid bilayer (Fig. 11) (Ovesny et al., 2014). Briefly, each movie frame is filtered to improve the signal-to-noise ratio, and then fluorophores within each frame are identified according to a set of parameters (intensity, ellipticity, diameter, etc.). The center of each fluorophore's point spread function is approximated to one pixel by fitting it with a two-dimensional (2D) Gaussian. Finally, the superlocalized positions of all fluorophores from all frames of the movie are superimposed to generate a 2D grayscale histogram that represents the spatial frequency distribution of all protein-lipid

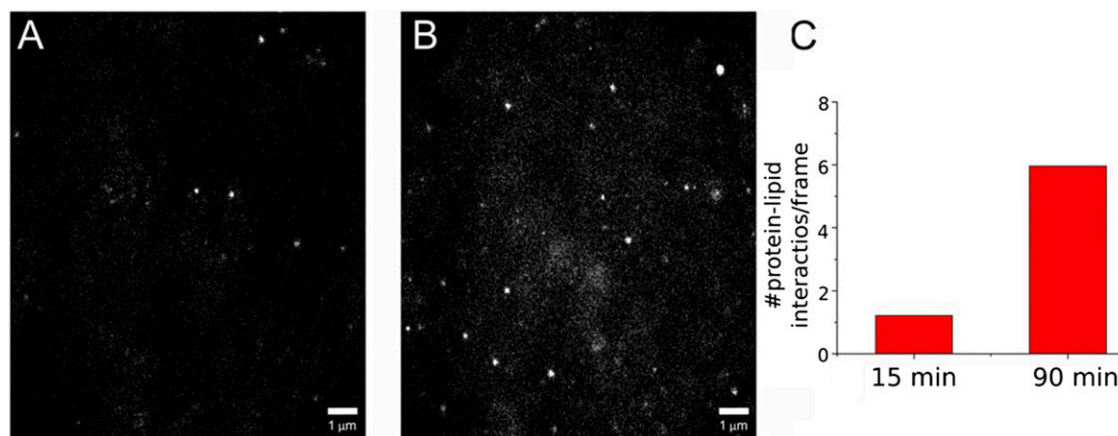


Fig. 13. Time-dependent CPR-lipid interactions using SPLIM. (A, B) are SPLIM images generated from 15,000 frames each (a total of 150 seconds). (A) Data were collected 15 minutes after CPR addition. (B) Data were collected 90 minutes after CPR addition. (C) Average number of particle instances detected per frame. Samples were prepared as in Fig. 12, using the 0.8 mM CHAPS-containing buffer. Contrast adjustments were performed as in Fig. 12.

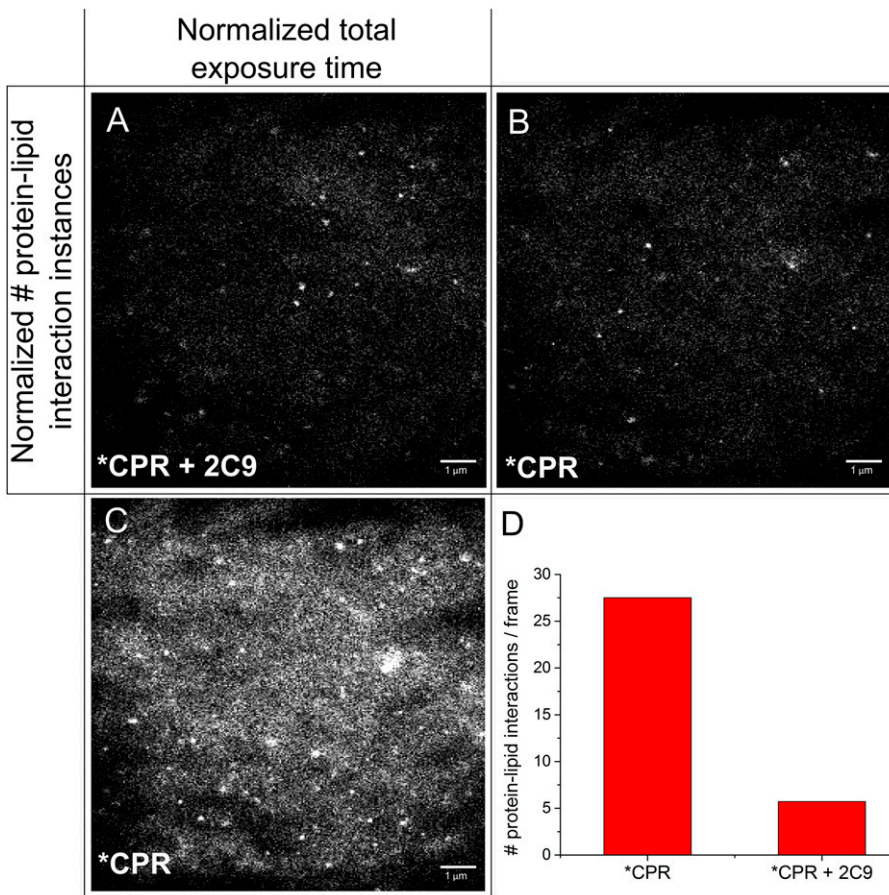


Fig. 14. Using SPLIM to visually demonstrate perturbation of CPR-lipid interactions by CYP2C9. (A) A SPLIM image of a bilayer that has been incubated with Alexa 555-CPR and unlabeled CYP2C9 [3.5 nM each; CYP2C9 prepared according to Shimoji et al., (1998)]. It contains data from 19,801 frames and has 57,218 particle instances. (B, C) SPLIM images of the same Alexa-555 CPR sample (no CYP2C9), normalized according to (B) particle instances or (C) number of frames. (B) Generated from 4,508 frames. (C) Had 275,123 particle instances. (D) Bar graph showing the average number of particle instances per frame for each sample. Samples were prepared, and contrast adjustments were made as in Fig. 12.

interactions within a precise region of the bilayer over a given period of time—hence, SPLIM.

SPLIM differs from more conventional super-resolution image-reconstruction techniques because we plot frequency per pixel rather than cumulative intensity per pixel (Fig. 11, right). To explain, we use a grayscale 2D matrix to represent the region of the bilayer we collect data from; in the matrix, each element represents one pixel, and the pixel dimensions define the ultimate resolution of the image. Black is represented by zero, so before data collection begins, the matrix is populated with zeros. Shades of gray through to white are represented by integers greater than zero. Each time a protein “visits” a particular location on the bilayer, the value for that pixel in the matrix increases by one. The pixel that is “visited” the greatest number of times during data collection will be white and will have the highest corresponding integer value in the matrix. All other shades of gray will fall somewhere in between.

In conventional super-resolution imaging and reconstruction, the aim is to “map” fluorophore locations under the assumption that they are fixed. The blinking properties of fluorophores are exploited to attain sparsely populated images that are then superimposed to “fill in the gaps.” The cumulative intensity at each pixel location is used to populate the grayscale matrix. Cumulative intensity represents the total number of photons generated at a given pixel location rather than the number of times a protein is located there. A cumulative intensity image can differ significantly from a frequency plot because of dynamic changes in fluorophore quantum efficiencies with respect to their photophysical processes and local environment (i.e., in solution versus in the bilayer). We believe our SPLIM treatment better addresses the dynamic nature of our system, as we are most interested in the number of times a particle “visits” a certain location on the bilayer.

Using SM-TIRF and SPLIM, we investigated the role of detergent in CPR-bilayer interactions (Fig. 12). At high concentrations of detergent (CHAPS) (Fig. 12, A and B), CPR-bilayer interactions appear more spatially random, occupying more of the pixels in the field of view. In contrast, we observed that as the CHAPS concentration decreases, CPR appears to become less laterally mobile and is seen in the same pixel location more frequently (Fig. 12, C and D). It is important to note that based on these observations alone, we cannot distinguish between one particle that visits a particular region on the bilayer and is detected over many frames versus many particles visiting the same region.

One explanation for these observations is that CPR partitioning between the bilayer and solution is detergent-dependent. As detergent is removed, there are fewer solution-based amphiphilic molecules to interact with and stabilize CPRs’ hydrophobic N-terminal helix. This results in greater partitioning of CPR into the membrane, and the on/off rates of CPR-lipid helicoptering adjust accordingly. With less detergent, CPR is “on” the bilayer longer or permanently. This could account for the increased frequency of protein-lipid interactions at specific bilayer locations (i.e., we are detecting the same protein multiple times over multiple frames).

An alternative explanation is that at low detergent concentrations, helicoptering CPR could have higher affinity for specific regions within the heterogeneous bilayer [here, we used a ternary mix of DLPC, DOPC, DLPS (1:1:1 (w/w/w)), and what we are observing is it “visiting” these regions more often. It has been shown that CPR harbors a specific affinity for anionic phospholipids such as phosphatidylserine (Balvers et al., 1993). To investigate this question further, we looked at annexin V, a self-inserting transmembrane protein, interacting with bilayers under the high detergent conditions (0.8 mM CHAPS). Annexin V is

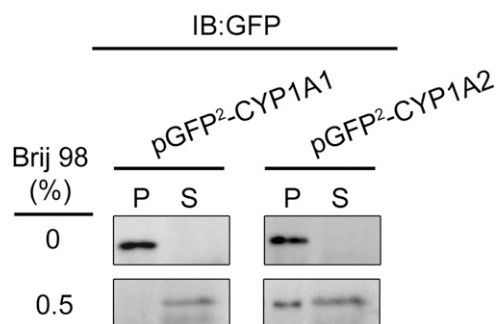


Fig. 15. Localization of CYP1A2-GFP and CYP2B4-GFP fusion proteins in different lipid microdomains. The ordered and disordered lipid domains from HEK293T cells expressing either GFP-CYP1A1 or GFP-CYP1A2 were treated with 0.5% Brij 98 followed by high-speed centrifugation at 100,000g for 1 hour in a buffer containing 50 mM HEPES (pH 7.25), 150 mM NaCl, and 5 mM EDTA. S and P represent the supernatant (disordered) and P (ordered) fractions of the modified CYP1A proteins, showing that the fusion proteins reside in different membrane regions. (This research was originally reported in Park et al., unpublished.)

known to interact specifically with phosphatidylserine (Tait and Gibson, 1992). We found that annexin V was localized to spatially distinct regions in a pattern similar to that seen in the “no CHAPS” sample, indicating that CPR does in fact localize to PS-rich domains (data not shown).

To ascertain whether CPR-lipid interactions displayed time-dependent variability, we collected SM-TIRF data from the same sample at two different time points after addition of CPR to the bilayer. From the SPLIM profiles (Fig. 13, A and B), we observed a change in the spatial distribution of protein-lipid interactions over time that was similar to what was seen with detergent removal. After a longer incubation, CPR appeared to frequent specific regions of the bilayer more often. In addition, the number of detected CPR-lipid interactions increased from 1.22 per frame to 5.97 per frame (Fig. 13C), confirming that we are observing a dynamic process that has not yet reached equilibrium. This finding corroborates the work of many groups who have described long protein-lipid incubation periods (hours to days) to achieve higher levels of protein incorporation into their reconstituted systems (Causey et al., 1990; Reed et al., 2006; Davydov et al., 2010). It is important to note, however, that we have been unable to find experimental evidence to suggest that protein incorporation is complete and irreversible, even after the removal of detergent.

To investigate how CYP2C9 affects CPR-lipid interactions, we compared the SPLIM profiles of our CPR-lipid samples before and after the addition of CYP2C9 (Fig. 14). Once again, there were differences in the spatial distribution patterns (Fig. 14, A and B), as well as changes in the number of protein-lipid interaction instances over time (Fig. 14, A, C, and D). Most interestingly, there appeared to be a significant reduction (80%) in the number of recorded protein-lipid interaction instances when CYP2C9 was present. We believe this could be due to Förster resonance energy transfer quenching of Alexa 555-CPR fluorescence by the P450 heme, a phenomenon that has been previously described in the literature (Isin and Guengerich, 2008). This would indicate that under these conditions, approximately 80% of all CPR molecules are within the Förster radius of a CYP2C9 molecule, signifying that CPR and CYP2C9 are forming heterodimers or oligomers. An alternative explanation could be that in the presence of CYP2C9, CPR “visits” the bilayer less frequently, although this is unlikely given that other groups have described the opposite to be true (Reed et al. 2006).

In conclusion, we directly observed that CPR-lipid interactions are dependent on detergent concentration and time and that in the presence of CYP2C9, the CPR fluorophore is likely quenched via Förster

resonance energy transfer to the P450 heme. Together, these findings highlight the unique information that can be extracted from reconstituted systems using SM-TIRF. In addition, we introduced SPLIM as a method to display protein-lipid interactions by localization frequency and spatial distribution. We postulate that by visualizing the data in this way, we can unveil information about the underlying structure of the lipid bilayer. In the future, SPLIM could be used to dynamically “map” lipid rafts and phase domains within membranes on cell or organelle surfaces. Cluster analysis such as the work described by Owen et al. (2010) may help to quantify SPLIM interactions further.

Elucidating the Macromolecular Determinants of Lipid Domain Localization for CYP1A1 and CYP1A2 in the ER (J.w.P., J.R.R., and W.L.B.)

Biologic membranes are heterogeneous with respect to both the composition and the ordering of the constituent lipids. These lipid bilayers are comprised primarily of a variety of phospholipids with varying lengths of fatty acyl chain moieties. Cholesterol is another component of biologic membranes that modulates the ordering of certain types of phospholipids in its proximity (Berkowitz, 2009). As a result, clusters of cholesterol and phospholipids containing a high proportion of saturated, straight-chained fatty acyl groups coalesce in the membranes as discrete zones that have been termed “lipid rafts” or “lipid microdomains” (Pike, 2009). The lipids in the microdomains are tightly packed which results in their lateral motion being highly restricted. These regions are described as being in the “liquid-ordered” state (Brown and London, 2000). The lipid microdomains are present in

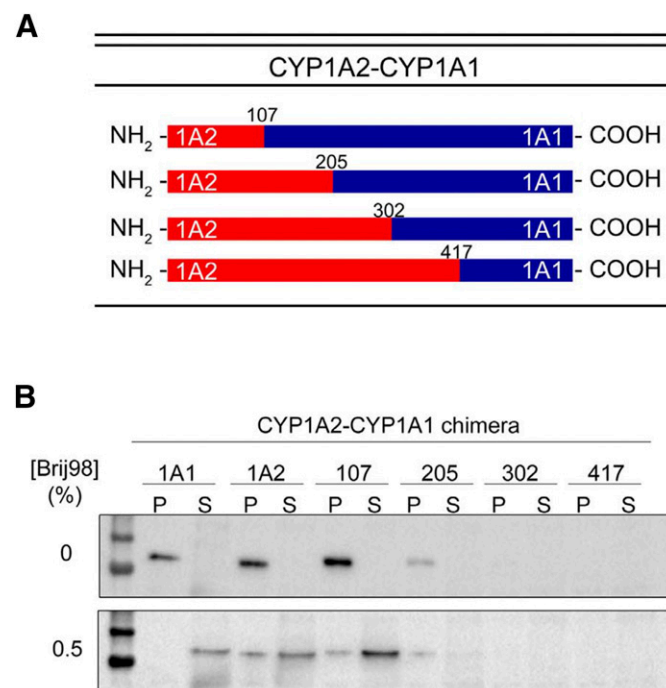


Fig. 16. Membrane localization of CYP1A2-CYP1A1 chimeric proteins in HEK293T cells. Chimeric proteins were constructed that contained the N-terminal region of CYP1A2 fused to the C-terminal region of CYP1A1. (A) A diagram of the cut sites representing the junction of cDNAs for the chimeras. (B) The relative distribution of the expressed chimeras into ordered (P) and disordered (S) regions after cell lysis, isolation of the postnuclear supernatant, and high-speed centrifugation (100,000g for 1 hour). The 0% panel shows the immune blots resulting from no detergent treatment and the 0.5% panel shows the distribution after solubilization in 0.5% Brij 98. (This research was originally reported by Park et al., unpublished.)

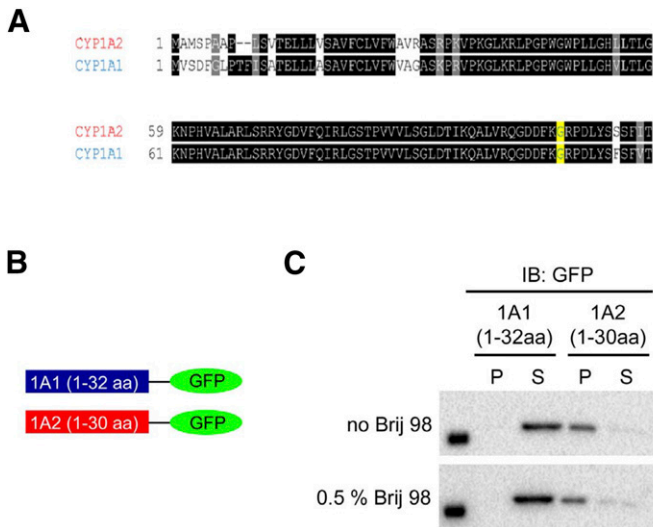


Fig. 17. Membrane localization of CYP1A1-GFP and CYP1A2-GFP fusion proteins containing only their N-terminal regions. Construction of CYP1A-GFP chimeras derived by attaching the N-terminal regions of CYP1A1 (aa 1–32) and CYP1A2 (aa 1–30), respectively to the cDNA for GFP and their relative distribution into ordered and disordered lipid domains. (A) Comparison of the N-terminal regions of rabbit CYP1A1 and CYP1A2. (B) Illustration of the constructed fusion proteins. (C) Localization of the proteins before and after Brij 98 solubilization. CYP1A2 resides in the pellet before Brij 98 treatment and remains in the membrane after partial membrane solubilization. In contrast, the expressed fusion protein containing the CYP1A1 N-terminus does not reside in the membrane, even before to Brij 98. (This research was originally reported by Park et al., unpublished.)

a surrounding medium containing phospholipids with a high degree of unsaturation in the fatty-acyl chains. This aspect of the lipids surrounding the microdomains prevents them from being tightly packed and results in the constituent lipids displaying an extreme state of random motion. As a result, this milieu has been referred to as being in the liquid-disordered phase (Brown and London, 2000).

One physical characteristic of the ordered domains that has allowed for their study is the fact that they are resistant to being solubilized by detergent treatment of the membrane (Ahmed et al., 1997; London and Brown, 2000). Thus, lipid microdomains have also been referred to as *detergent-resistant membranes* (DRMs). In studies with lipid microdomains, researchers have used detergent solubilization to identify the proteins in the membrane that predominantly localize to DRMs. In addition, researchers have commonly used a compound that tightly binds to cholesterol, methyl- β -cyclodextrin, to deplete cellular membranes of cholesterol. In addition to showing the dependence of lipid microdomains on the presence of cholesterol (Brignac-Huber et al., 2011), these studies have also elucidated some of the cellular functions of the microdomains. In the plasma membrane, DRMs have been shown to regulate diverse cellular processes, including signal transduction, endocytosis, cellular trafficking, and cytoskeletal tethering (reviewed in Head et al., 2014).

Lipid microdomains have recently been demonstrated to also exist in the ER (Browman et al., 2006), although their functions have not been well established. Our laboratory examined whether lipid microdomains influenced the distribution and activities of P450 in the ER membrane. Our initial studies determined that CYP1A2 predominantly resided in ordered membranes (Brignac-Huber et al., 2011). Furthermore, its localization in the membrane and its catalytic activity were greatly affected by cholesterol depletion. We subsequently used fluorescent lipid probes to demonstrate that ordered lipid domains were present in purified CYP1A2-reconstituted systems, with the lipid composition of total ER and that CYP1A2 resided in ordered domains as indicated by

its resistance to detergent solubilization (Brignac-Huber et al., 2013). When comparing a homogeneous membrane reconstituted system prepared from bovine liver phosphatidylcholine and one prepared from a mixture of lipids that would favor the generation of ordered lipid microdomains, the presence of ordered domains was associated with a much higher apparent binding affinity between CYP1A2 and CPR (Brignac-Huber et al., 2011). Interestingly, the localization of CYP2B4 and CYP2E1 in the ER was distinct from that of CYP1A2 as the former distributed equally between ordered and disordered regions, whereas CYP2E1 was almost entirely within disordered regions (Park et al., 2014).

In the course of investigating the membrane distribution of CYP1A2, we noticed an intriguing distinction in the localization of CYP1A2 and CYP1A1 (Fig. 15). After the DRMs were isolated by high-speed centrifugation after treatment with 1% Brij 98, immune blotting was performed to monitor the P450 distribution by using a primary antibody reactive with both forms of CYP1A enzymes. As reported previously, CYP1A2 localized predominantly in ordered domains; however, CYP1A1 was found to reside almost entirely in disordered regions of the ER.

Because CYP1A1 and CYP1A2 share about 80% sequence identity, the protein regions responsible for the varying localization of the two P450s could be clearly determined by the generation of CYP1A1-CYP1A2 chimeras. Initially, it was important to ensure that we could accurately monitor the expression and localization of the two P450s in HEK293T cells. To easily monitor transient expression in the cells, we linked the cDNA of green fluorescent protein (GFP) to the C-terminal end of the CYP1A cDNAs and cloned into the pGFP²-N2 expression vector. After expression in the human embryonic kidney cell line HEK-293T cells, it was determined that the modified CYP1A proteins were expressed in the ER of the cells; after detergent solubilization with 0.5% Brij 98 of the postnuclear supernatant of the cells and high-speed centrifugation (100,000g for 1 hour), it was found that CYP1A1 and CYP1A2 were localized to disordered and ordered domains, respectively (data not shown). Thus, the cell system could be used with mutagenesis of the CYP1A sequences to determine the regions responsible for domain localization.

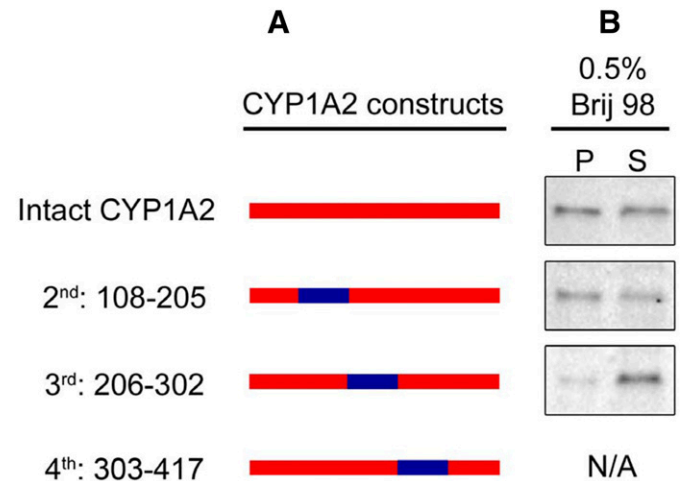


Fig. 18. Role of the internal regions of CYP1A on membrane localization. Chimeric proteins where internal regions of CYP1A1 were inserted into the CYP1A2 sequence were generated. The constructs were then transfected into HEK293T cells and their localization determined. (A) Illustration of the chimeric constructs. (B) Localization of the chimeras after Brij 98 treatment of the membranes. This research was originally reported published by Park et al., unpublished.

Chimeras were generated by overlap extension PCR (Ho et al., 1989). Four cut sites in the cDNA sequences of the P450s were selected based on their location in meander regions of the crystal structures (Sansen et al., 2007) and thus were not expected to interrupt key regions of secondary structure that were important for function. The cut sites were used to generate a combination of chimeras (shown in Fig. 16A). A complementary set of chimeras were also generated using the same cut sites by adding different lengths of the CYP1A1 N terminus to the C-terminal end of CYP1A2 (not shown). Substitution of the shortest N-terminal sequence in both chimera systems was sufficient to reverse the domain localization of the wild-type enzymes. More specifically, when the first 100 amino acids of CYP1A2 were combined with the C-terminal end of CYP1A1, the enzyme partially localized to the ordered domain (Fig. 16B), and with the opposite substitution, the chimera was found to reside entirely in the disordered region (not shown).

All the mammalian P450s involved in drug metabolism have an N-terminal sequence of approximately 30 amino acids in length that is hydrophobic and anchors the proteins to the membrane (Black and Coon, 1982). It is known that this segment functions to target the enzymes to the ER. Given the effect of substituting the N terminal ≈ 100 amino acids of CYP1A2 and CYP1A1 on domain localization, however, we suspected that the N-terminal hydrophobic tail of the P450 may also have a role in the lipid domain selectivity of the enzyme. Therefore, we generated expression plasmids with the N-terminal tails of CYP1A1 and CYP1A2 linked to the cDNA for GFP (Fig. 17B). These modified GFP proteins were then expressed in HEK 293T cells, and their membrane localization was determined by cell lysis and detergent solubilization of the postnuclear supernatant. After detergent treatment and high-speed centrifugation, it was found that the GFP with N-terminal CYP1A1 did not express in the membrane; however, the GFP with N-terminal CYP1A2 did express in the membrane and was predominantly localized in the ordered microdomains (Fig. 17C). Thus, the hydrophobic, N-terminal sequence (≈ 30 amino acids) of CYP1A2 appears to play a key role in targeting this enzyme to the ordered domains.

Examination of Fig. 16 shows that the N-terminal ≈ 100 amino acids of CYP1A2 resulted in only partial relocation of the CYP1A2-CYP1A1 chimera to ordered domains. As a result, we suspected that there might be an internal amino acid sequence of the P450s that also contributes to domain localization. To test this possibility, the same cleavage sites in the amino acid sequences of CYP1A1 and CYP1A2 were used to generate cDNAs for three chimeras in which one of the CYP1A1 internal sequences was substituted for that of CYP1A2 (Fig. 18). The chimera containing the CYP1A1 sequence from amino acid 303–417 did not express in the cells. The CYP1A1 substitution at amino acids 108 to 205 did not seem to alter the relative distribution into ordered and disordered domains; however, when amino acids 206–302 of CYP1A1 were substituted, a higher proportion of the P450 localized to disordered domains, suggesting this region also contributes to the domain selectivity of these enzymes. This region of the protein contains the F and G helices and F-G loop, which interact with the membrane, are involved in substrate binding from the membrane and constitute part of the ceiling of the P450 active site above the heme group (Williams et al., 2003; Yano et al., 2004; Pochapsky et al., 2010; Johnson et al., 2014). Our data show that both the hydrophobic N-terminal sequence and the F-G helices region confer the ordered microdomain selectivity of CYP1A enzymes. Because there is considerable sequence homology for CYP1A1 and CYP1A2 in these regions, future studies will focus on identifying the specific amino acids in these two sequences that are responsible for targeting the enzymes to disordered and ordered regions in the ER.

P450s have been shown to associate with one another in lipid membranes. Both homomeric and heteromeric complexes of P450 have been demonstrated using a variety of techniques (reviewed in Davydov, 2011; Reed and Backes, 2012). Almost 40 years ago (Peterson et al., 1976), it was proposed and has been subsequently shown that the aggregation of P450s would allow for more efficient electron transfer by the CPR as electrons could be rapidly transferred to the aggregating P450s in a single interaction with the complex. The P450-P450 associations also directly influence the function of these enzymes because form-specific interactions have been shown to result in activation and/or inhibition of P450 catalytic activities (Hazai and Kupfer, 2005; Kelley et al., 2006; Subramanian et al., 2009, 2010; Reed et al., 2010). Thus, factors that influence the protein-protein associations of P450s in the ER can have important effects on P450 function. We are currently examining the effect of microdomain localization of different P450 enzymes on their ability to form P450-P450 complexes.

Summary

Although much is known about the factors controlling the expression and catalytic function of P450 system proteins, numerous questions remain regarding how these proteins are organized in the ER and how they interact with their protein partners and even with the membrane itself. These reports show that the interactions among these proteins are complex, and we must consider the specific proteins that are present as well as the membrane environment in which they reside.

Authorship Contributions

Participated in research design: Park, Reed, Backes, Otyepka, Humphreys, Barnaba, Dahal, Brozik, Jones, Estrada, Laurence, Scott, Wolf, Henderson.

Conducted experiments: Park, Reed, Palončyová, Navrátilová, Berka, Humphreys, Dahal, Estrada, McLaughlin.

Performed data analysis: Otyepka, Berka, Anzenbacher, Park, Reed, Backes, Humphreys, Estrada, Laurence, Scott, McLaughlin.

Wrote or contributed to the writing of the manuscript: Otyepka, Park, Reed, Backes, Humphreys, Brozik, Jones, Estrada, Laurence, Scott, Henderson.

References

- Ahmed SN, Brown DA, and London E (1997) On the origin of sphingolipid/cholesterol-rich detergent-insoluble cell membranes: physiological concentrations of cholesterol and sphingolipid induce formation of a detergent-insoluble, liquid-ordered lipid phase in model membranes. *Biochemistry* **36**:10944–10953.
- Akhtar MK, Kelly SL, and Kaderbhai MA (2005) Cytochrome b(5) modulation of 17 α hydroxylase and 17-20 lyase (CYP17) activities in steroidogenesis. *J Endocrinol* **187**:267–274.
- Anzenbacher P and Anzenbacherová E (2001) Cytochromes P450 and metabolism of xenobiotics. *Cell Mol Life Sci* **58**:737–747.
- Auchus RJ, Lee TC, and Miller WL (1998) Cytochrome b5 augments the 17,20-lyase activity of human P450c17 without direct electron transfer. *J Biol Chem* **273**:3158–3165.
- Balaz S (2009) Modeling kinetics of subcellular disposition of chemicals. *Chem Rev* **109**:1793–1899.
- Balvers WG, Boersma MG, Vervoort J, Ouweland A, and Rietjens IM (1993) A specific interaction between NADPH-cytochrome reductase and phosphatidylserine and phosphatidylinositol. *Eur J Biochem* **218**:1021–1029.
- Baylon JL, Lenov IL, Sliagar SG, and Tajkhorshid E (2013) Characterizing the membrane-bound state of cytochrome P450 3A4: structure, depth of insertion, and orientation. *J Am Chem Soc* **135**:8542–8551.
- Berka K, Hendrychová T, Anzenbacher P, and Otyepka M (2011) Membrane position of ibuprofen agrees with suggested access path entrance to cytochrome P450 2C9 active site. *J Phys Chem A* **115**:11248–11255.
- Berka K, Palončyová M, Anzenbacher P, and Otyepka M (2013) Behavior of human cytochromes P450 on lipid membranes. *J Phys Chem B* **117**:11556–11564.
- Berkowitz ML (2009) Detailed molecular dynamics simulations of model biological membranes containing cholesterol. *Biochim Biophys Acta* **1788**:86–96.
- Black SD (1992) Membrane topology of the mammalian P450 cytochromes. *FASEB J* **6**:680–685.
- Black SD and Coon MJ (1982) Structural features of liver microsomal NADPH-cytochrome P-450 reductase: hydrophobic domain, hydrophilic domain, and connecting region. *J Biol Chem* **257**:5929–5938.
- Bridges A, Gruenke L, Chang YT, Vakser IA, Loew G, and Waskell L (1998) Identification of the binding site on cytochrome P450 2B4 for cytochrome b5 and cytochrome P450 reductase. *J Biol Chem* **273**:17036–17049.
- Brignac-Huber L, Reed JR, and Backes WL (2011) Organization of NADPH-cytochrome P450 reductase and CYP1A2 in the endoplasmic reticulum—microdomain localization affects monooxygenase function. *Mol Pharmacol* **79**:549–557.

- Brignac-Huber LM, Reed JR, Eyer MK, and Backes WL (2013) Relationship between CYP1A2 localization and lipid microdomain formation as a function of lipid composition. *Drug Metab Dispos* **41**:1896–1905.
- Browman DT, Resek ME, Zajchowski LD, and Robbins SM (2006) Erlin-1 and erlin-2 are novel members of the prohibitin family of proteins that define lipid-raft-like domains of the ER. *J Cell Sci* **119**:3149–3160.
- Brown DA and London E (2000) Structure and function of sphingolipid- and cholesterol-rich membrane rafts. *J Biol Chem* **275**:17221–17224.
- Causey KM, Eyer CS, and Backes WL (1990) Dual role of phospholipid in the reconstitution of cytochrome P-450 LM2-dependent activities. *Mol Pharmacol* **38**:134–142.
- Cojocar V, Balali-Mood K, Sansom MSP, and Wade RC (2011) Structure and dynamics of the membrane-bound cytochrome P450 2C9. *PLoS Comput Biol* **7**:e1002152.
- Cojocar V, Winn PJ, and Wade RC (2007) The ins and outs of cytochrome P450s. *Biochim Biophys Acta* **1770**:390–401.
- Davydov DR (2011) Microsomal monooxygenase as a multienzyme system: the role of P450-P450 interactions. *Expert Opin Drug Metab Toxicol* **7**:543–558.
- Davydov DR, Davydova NY, Sineva EV, Halpert JR, and Halpert JR (2015) Interactions among cytochromes P450 in microsomal membranes: oligomerization of cytochromes P450 3A4, 3A5, and 2E1 and its functional consequences. *J Biol Chem* **290**:3850–3864.
- Davydov DR, Sineva EV, Sistla S, Davydova NY, Frank DJ, Sligar SG, and Halpert JR (2010) Electron transfer in the complex of membrane-bound human cytochrome P450 3A4 with the flavin domain of P450BM-3: the effect of oligomerization of the heme protein and intermittent modulation of the spin equilibrium. *Biochim Biophys Acta* **1797**:378–390.
- Denisov IG, Shih AY, and Sligar SG (2012) Structural differences between soluble and membrane bound cytochrome P450s. *J Inorg Biochem* **108**:150–158.
- Denisov IG and Sligar SG (2011) Cytochromes P450 in nanodiscs. *Biochim Biophys Acta* **1814**:223–229.
- Endo S, Escher BI, and Goss KU (2011) Capacities of membrane lipids to accumulate neutral organic chemicals. *Environ Sci Technol* **45**:5912–5921.
- Estrada DF, Laurence JS, and Scott EE (2013) Substrate-modulated cytochrome P450 17A1 and cytochrome b5 interactions revealed by NMR. *J Biol Chem* **288**:17008–17018.
- Estrada DF, Laurence JS, and Scott EE (2016) Cytochrome P450 17A1 interactions with the FMN domain of its reductase as characterized by NMR. *J Biol Chem* **291**:3990–4003.
- Estrada DF, Skinner AL, Laurence JS, and Scott EE (2014) Human cytochrome P450 17A1 conformational selection: modulation by ligand and cytochrome b5. *J Biol Chem* **289**:14310–14320.
- Evans WE and Relling MV (1999) Pharmacogenomics: translating functional genomics into rational therapeutics. *Science* **286**:487–491.
- Finn RD, McLaughlin LA, Hughes C, Song C, Henderson CJ, and Roland Wolf C (2011) Cytochrome b5 null mouse: a new model for studying inherited skin disorders and the role of unsaturated fatty acids in normal homeostasis. *Transgenic Res* **20**:491–502.
- Finn RD, McLaughlin LA, Ronseaux S, Rosewell I, Houston JB, Henderson CJ, and Wolf CR (2008) Defining the in Vivo Role for cytochrome b5 in cytochrome P450 function through the conditional hepatic deletion of microsomal cytochrome b5. *J Biol Chem* **283**:31385–31393.
- Geller DH, Auchus RJ, and Miller WL (1999) P450c17 mutations R347H and R358Q selectively disrupt 17,20-lyase activity by disrupting interactions with P450 oxidoreductase and cytochrome b5. *Mol Endocrinol* **13**:167–175.
- Ghosh MC and Ray AK (2013) Membrane phospholipid augments cytochrome P4501a enzymatic activity by modulating structural conformation during detoxification of xenobiotics. *PLoS One* **8**:e57919.
- Guengerich FP (2006) Cytochrome P450s and other enzymes in drug metabolism and toxicity. *AAPS J* **8**:E101–E111.
- Hasegawa M, Kapelyukh Y, Tahara H, Seibler J, Rode A, Krueger S, Lee DN, Wolf CR, and Scheer N (2011) Quantitative prediction of human pregnane X receptor and cytochrome P450 3A4 mediated drug-drug interaction in a novel multiple humanized mouse line. *Mol Pharmacol* **80**:518–528.
- Hazai E and Kupfer D (2005) Interactions between CYP2C9 and CYP2C19 in reconstituted binary systems influence their catalytic activity: possible rationale for the inability of CYP2C19 to catalyze methoxychlor demethylation in human liver microsomes. *Drug Metab Dispos* **33**:157–164.
- Head BP, Patel HH, and Insel PA (2014) Interaction of membrane/lipid rafts with the cytoskeleton: impact on signaling and function: membrane/lipid rafts, mediators of cytoskeletal arrangement and cell signaling. *Biochim Biophys Acta* **1838**:532–545.
- Helenius A and Simons K (1975) Solubilization of membranes by detergents. *Biochim Biophys Acta* **415**:29–79.
- Henderson CJ, McLaughlin LA, Scheer N, Stanley LA, and Wolf CR (2015) Cytochrome b5 is a major determinant of human cytochrome P450 CYP2D6 and CYP3A4 activity in vivo. *Mol Pharmacol* **87**:733–739.
- Henderson CJ, McLaughlin LA, and Wolf CR (2013) Evidence that cytochrome b5 and cytochrome b5 reductase can act as sole electron donors to the hepatic cytochrome P450 system. *Mol Pharmacol* **83**:1209–1217.
- Hildebrandt A and Estabrook RW (1971) Evidence for the participation of cytochrome b5 in hepatic microsomal mixed-function oxidation reactions. *Arch Biochem Biophys* **143**:66–79.
- Ho SN, Hunt HD, Horton RM, Pullen JK, and Pease LR (1989) Site-directed mutagenesis by overlap extension using the polymerase chain reaction. *Gene* **77**:51–59.
- Im SC and Waskell L (2011) The interaction of microsomal cytochrome P450 2B4 with its redox partners, cytochrome P450 reductase and cytochrome b5. *Arch Biochem Biophys* **507**:144–153.
- Ingelman-Sundberg M and Glaumann H (1980) Incorporation of purified components of the rabbit liver microsomal hydroxylase system into phospholipid vesicles. *Biochim Biophys Acta* **599**:417–435.
- Ingelman-Sundberg M, Hagbjörk AL, Ueng YF, Yamazaki H, and Guengerich FP (1996) High rates of substrate hydroxylation by human cytochrome P450 3A4 in reconstituted membranous vesicles: influence of membrane charge. *Biochem Biophys Res Commun* **221**:318–322.
- Isin EM and Guengerich FP (2008) Substrate binding to cytochromes P450. *Anal Bioanal Chem* **392**:1019–1030.
- Jansson I and Schenkman JB (1987) Influence of cytochrome b5 on the stoichiometry of the different oxidative reactions catalyzed by liver microsomal cytochrome P-450. *Drug Metab Dispos* **15**:344–348.
- Jeffcoat R, Brawn PR, Safford R, and James AT (1977) Properties of rat liver microsomal stearyl-coenzyme A desaturase. *Biochem J* **161**:431–437.
- Johnson EF, Connick JP, Reed JR, Backes WL, Desai MC, Xu L, Estrada DF, Laurence JS, and Scott EE (2014) Correlating structure and function of drug-metabolizing enzymes: progress and ongoing challenges. *Drug Metab Dispos* **42**:9–22.
- Johnson EF and Stout CD (2013) Structural diversity of eukaryotic membrane cytochrome p450s. *J Biol Chem* **288**:17082–17090.
- Kelley RW, Cheng D, and Backes WL (2006) Heteromeric complex formation between CYP2E1 and CYP1A2: evidence for the involvement of electrostatic interactions. *Biochemistry* **45**:15807–15816.
- Kurian JR, Longlais BJ, and Trepanier LA (2007) Discovery and characterization of a cytochrome b5 variant in humans with impaired hydroxylamine reduction capacity. *Pharmacogenet Genomics* **17**:597–603.
- London E and Brown DA (2000) Insolubility of lipids in triton X-100: physical origin and relationship to sphingolipid/cholesterol membrane domains (rafts). *Biochim Biophys Acta* **1508**:182–195.
- Lúcio M, Lima JLFC, and Reis S (2010) Drug-membrane interactions: significance for medicinal chemistry. *Curr Med Chem* **17**:1795–1809.
- McKenna JA, Sacco J, Son TT, Trepanier LA, Callan MB, Harvey JW, and Arndt JW (2014) Congenital methemoglobinemia in a dog with a promoter deletion and a nonsynonymous coding variant in the gene encoding cytochrome bs. *J Vet Intern Med* **28**:1626–1631.
- McLaughlin LA, Ronseaux S, Finn RD, Henderson CJ, and Roland Wolf C (2010) Deletion of microsomal cytochrome b5 profoundly affects hepatic and extrahepatic drug metabolism. *Mol Pharmacol* **78**:269–278.
- Naffin-Olivos JL and Auchus RJ (2006) Human cytochrome b5 requires residues E48 and E49 to stimulate the 17,20-lyase activity of cytochrome P450c17. *Biochemistry* **45**:755–762.
- Nagar S and Korzekwa K (2012) Commentary: nonspecific protein binding versus membrane partitioning: it is not just semantics. *Drug Metab Dispos* **40**:1649–1652.
- Nakamura Y, Gang HX, Suzuki T, Sasano H, and Rainey WE (2009) Adrenal changes associated with adrenarache. *Rev Endocr Metab Disord* **10**:19–26.
- Omura T and Sato R (1962) A new cytochrome in liver microsomes. *J Biol Chem* **237**:1375–1376.
- Omura T, Sato R, Cooper DY, Rosenthal O, and Estabrook RW (1965) Function of cytochrome P-450 of microsomes. *Fed Proc* **24**:1181–1189.
- Ortiz de Montellano PR (2015) *Cytochrome P450: Structure, Mechanism, and Biochemistry*. Springer International Publishing, Switzerland.
- Otyepka M, Skopalík J, Anzenbacherová E, and Anzenbacher P (2007) What common structural features and variations of mammalian P450s are known to date? *Biochim Biophys Acta* **1770**:376–389.
- Ovesný M, Krížek P, Borkovec J, Svindrych Z, and Hagen GM (2014) ThunderSTORM: a comprehensive ImageJ plug-in for PALM and STORM data analysis and super-resolution imaging. *Bioinformatics* **30**:2389–2390.
- Owen DM, Rentero C, Rossy J, Magenau A, Williamson D, Rodriguez M, and Gaus K (2010) PALM imaging and cluster analysis of protein heterogeneity at the cell surface. *J Biophotonics* **3**:446–454.
- Pallan PS, Nagy LD, Lei L, Gonzalez E, Kramlinger VM, Azumaya CM, Wawrzak Z, Waterman MR, Guengerich FP, and Egli M (2015) Structural and kinetic basis of steroid 17 α ,20-lyase activity in teleost fish cytochrome P450 17A1 and its absence in cytochrome P450 17A2. *J Biol Chem* **290**:3248–3268.
- Palonciová M, Berka K, and Otyepka M (2013) Molecular insight into affinities of drugs and their metabolites to lipid bilayers. *J Phys Chem B* **117**:2403–2410.
- Palonciová M, DeVane R, Murch B, Berka K, and Otyepka M (2014) Amphiphilic drug-like molecules accumulate in a membrane below the head group region. *J Phys Chem B* **118**:1030–1039.
- Park JW, Reed JR, Brignac-Huber LM, and Backes WL (2014) Cytochrome P450 system proteins reside in different regions of the endoplasmic reticulum. *Biochem J* **464**:241–249.
- Park JW, Reed JR, and Backes WL (2015) The Localization of Cytochrome P450s CYP1A1 and CYP1A2 into Different Lipid Microdomains is Governed by their NH2-terminal and Internal Protein Regions. *J Biol Chem* **290**:29449–29460.
- Peterson JA, Ebel RE, O'Keefe DH, Matsubara T, and Estabrook RW (1976) Temperature dependence of cytochrome P-450 reduction. A model for NADPH-cytochrome P-450 reductase:cytochrome P-450 interaction. *J Biol Chem* **251**:4010–4016.
- Petek M, Kosinová P, Koca J, and Otyepka M (2007) MOLE: a Voronoi diagram-based explorer of molecular channels, pores, and tunnels. *Structure* **15**:1357–1363.
- Petek M, Otyepka M, Banás P, Kosinová P, Koca J, and Damborský J (2006) CAVER: a new tool to explore routes from protein clefts, pockets and cavities. *BMC Bioinformatics* **7**:316–324.
- Pike LJ (2009) The challenge of lipid rafts. *J Lipid Res* **50** (Suppl):S323–S328.
- Pochapsky TC, Kazanis S, and Dang M (2010) Conformational plasticity and structure/function relationships in cytochromes P450. *Antioxid Redox Signal* **13**:1273–1296.
- Pouidel KR, Jones JP, and Brozik JA (2013) A guide to tracking single transmembrane proteins in supported lipid bilayers. *Methods Mol Biol* **974**:233–252.
- Reed JR and Backes WL (2012) Formation of P450 · P450 complexes and their effect on P450 function. *Pharmacol Ther* **133**:299–310.
- Reed JR, Eyer M, and Backes WL (2010) Functional interactions between cytochromes P450 1A2 and 2B4 require both enzymes to reside in the same phospholipid vesicle: evidence for physical complex formation. *J Biol Chem* **285**:8942–8952.
- Reed JR, Kelley RW, and Backes WL (2006) An evaluation of methods for the reconstitution of cytochromes P450 and NADPH P450 reductase into lipid vesicles. *Drug Metab Dispos* **34**:660–666.
- Rendic SP and Guengerich FP (2015) Survey of Human Oxidoreductases and Cytochrome P450 Enzymes Involved in the Metabolism of Chemicals. *Chem Res Toxicol* **28**:38–42.
- Rock D, Rock D, and Jones JP (2001) Inexpensive purification of P450 reductase and other proteins using 2',5'-adenosine diphosphate agarose affinity columns. *Protein Expr Purif* **22**:82–83.
- Sansen S, Yano JK, Reynald RL, Schoch GA, Griffin KJ, Stout CD, and Johnson EF (2007) Adaptations for the oxidation of polycyclic aromatic hydrocarbons exhibited by the structure of human P450 1A2. *J Biol Chem* **282**:14348–14355.
- Scheer N, Kapelyukh Y, McEwan J, Beuger V, Stanley LA, Rode A, and Wolf CR (2012) Modeling human cytochrome P450 2D6 metabolism and drug-drug interaction by a novel panel of knockout and humanized mouse lines. *Mol Pharmacol* **81**:63–72.
- Seddon AM, Casey D, Law RV, Gee A, Templar RH, and Ces O (2009) Drug interactions with lipid membranes. *Chem Soc Rev* **38**:2509–2519.

- Sgrignani J and Magistrato A (2012) Influence of the membrane lipophilic environment on the structure and on the substrate access/egress routes of the human aromatase enzyme: a computational study. *J Chem Inf Model* **52**:1595–1606.
- Shimoji M, Yin H, Higgins L, and Jones JP (1998) Design of a novel P450: a functional bacterial-human cytochrome P450 chimera. *Biochemistry* **37**:8848–8852.
- Smith D, Artursson P, Avdeef A, Di L, Ecker GF, Faller B, Houston JB, Kansy M, Kerns EH, and Krämer SD, et al. (2014) Passive lipoidal diffusion and carrier-mediated cell uptake are both important mechanisms of membrane permeation in drug disposition. *Mol Pharm* **11**:1727–1738.
- Subramanian M, Low M, Locusion CW, and Tracy TS (2009) CYP2D6-CYP2C9 protein-protein interactions and isoform-selective effects on substrate binding and catalysis. *Drug Metab Dispos* **37**:1682–1689.
- Subramanian M, Tam HZhang H and Tracy TS (2010) CYP2C9-CYP3A4 protein-protein interactions: role of the hydrophobic N terminus. *Drug Metab Dispos* **38**:1003–1009.
- Tait JF and Gibson D (1992) Phospholipid binding of annexin V: effects of calcium and membrane phosphatidylserine content. *Arch Biochem Biophys* **298**:187–191.
- Williams CH, Jr and Kamin H (1962) Microsomal triphosphopyridine nucleotide-cytochrome c reductase of liver. *J Biol Chem* **237**:587–595.
- Williams PA, Cosme J, Ward A, Angove HC, Matak Vinković D, and Jhoti H (2003) Crystal structure of human cytochrome P450 2C9 with bound warfarin. *Nature* **424**:464–468.
- Yano JK, Wester MR, Schoch GA, Griffin KJ, Stout CD, and Johnson EF (2004) The structure of human microsomal cytochrome P450 3A4 determined by X-ray crystallography to 2.05-Å resolution. *J Biol Chem* **279**:38091–38094.
- Yu X, Cojocaru V, Mustafa G, Salo-Ahen OMH, Lepesheva GI, and Wade RC (2015) Dynamics of CYP51: implications for function and inhibitor design. *J Mol Recognit* **28**:59–73.
- Zanger UM and Schwab M (2013) Cytochrome P450 enzymes in drug metabolism: regulation of gene expression, enzyme activities, and impact of genetic variation. *Pharmacol Ther* **138**:103–141.
- Zhang H, Hamdane D, Im SC, and Waskell L (2008) Cytochrome *b5* inhibits electron transfer from NADPH-cytochrome P450 reductase to ferric cytochrome P450 2B4. *J Biol Chem* **283**:5217–5225.
- Zhang H, Im SC, and Waskell L (2007) Cytochrome *b5* increases the rate of product formation by cytochrome P450 2B4 and competes with cytochrome P450 reductase for a binding site on cytochrome P450 2B4. *J Biol Chem* **282**:29766–29776.
- Zhao C, Gao Q, Roberts AG, Shaffer SA, Doneanu CE, Xue S, Goodlett DR, Nelson SD, and Atkins WM (2012) Cross-linking mass spectrometry and mutagenesis confirm the functional importance of surface interactions between CYP3A4 and holo/apo cytochrome b(5). *Biochemistry* **51**:9488–9500.

Address correspondence to: Wayne L. Backes, PhD Department of Pharmacology and Experimental Therapeutics, Louisiana State University Health Sciences Center, 1901 Perdido Street, New Orleans, LA 70112. E-mail: wbacke@lsuhsc.edu

Behavior of Cytochrome P450 3A4 on Membranes with Different Lipid Composition

Effect of Lipid Composition and Charge on Cytochrome P450 3A4

*Veronika Navrátilová, Markéta Paloncýová, Karel Berka, Michal Otyepka**

Regional Centre of Advanced Technologies and Materials, Department of Physical Chemistry,
Faculty of Science, Palacký University Olomouc, tř. 17. listopadu 12, 771 46, Olomouc, Czech
Republic

*Corresponding author

KEYWORDS: cytochrome P450; heme tilt angle; membrane lipid; DOPC; DOPE; DOPG;
DOPS; charge; membrane lipid; drug metabolism

ABSTRACT

Microsomal cytochrome P450 enzymes are membrane attached enzymes playing indispensable roles in biotransformation of numerous endo and exogenous compounds. Due to recent progress in experiments and simulations, many important features of CYP-membrane interactions were described, however, many other aspects are underexplored. Using microsecond-long molecular dynamics simulations, we analyzed interaction of CYP3A4 to bilayers composed of lipids differing in their polar head groups – phosphatidylcholine, phosphatidylethanolamine, phosphatidylserine, and phosphatidylglycerol. In the negatively charged lipids, CYP3A4 was immersed deeper and more oriented toward the membrane, because of the favorable electrostatic interactions between CYP catalytic domain and the lipid polar head groups. The significant role of electrostatic interaction in CYP-membrane interactions helped us to explain experimentally observed preferences of individual CYP isoform to distribute to (dis)ordered membrane microdomains.

Introduction

The microsomal cytochrome P450 (CYP) enzymes are membrane-anchored proteins involved in many biotransformation processes of drugs and other endo and exogenous compounds^{1,2}. They are known to metabolize more than 50 % of marketed drugs² and are responsible for some adverse effects of drugs, e.g., drug-drug interactions. It is not surprising that CYPs are in a focus of pharmacology and drug development. Catalytic domain of CYPs contain deeply buried active site housing a heme cofactor³ connected with environment by a complex network of channels.⁴ The CYP catalytic domain sits on the cytoplasmic side of endoplasmic reticulum (ER) membrane being anchored by an N-terminal transmembrane α -helical anchor to the membrane.⁵⁻⁹

Membrane orientations of CYPs were studied by various methods. Molecular dynamics simulations⁵⁻⁹ identified common hydrophobic regions of CYP interacting with the membrane (N-terminal, A', F', and G' helices), and only small variations among individual CYP isoforms.¹⁰ The orientation agreed with the experimental evidences from atomic force microscopy^{11,12} and tryptophan fluorescence scanning,¹³ epitope labeling^{14,15} and NMR experiments.¹⁶ These findings about CYP membrane orientation were recently corroborated by the first X-ray structures of CYP with resolved transmembrane N-terminal anchor from *Saccharomyces cerevisiae*.^{17,18} In addition, there is ever growing evidence that the membrane is not just a passive environment but affects CYP orientation, localization, ligand binding and catalytic activity.

Individual CYP isoforms differ in localization in the ordered and disordered microdomains of ER membrane.¹⁹⁻²¹ While CYP1A1 and CYP2E1 preferred the disordered domains, CYP1A2 and CYP reductase (CPR) preferred the ordered domains and CYP2B4 was equally distributed in both domains.¹⁹⁻²⁵ The difference in localization could affect catalytic efficiency of individual

CYPs as the excessive addition of the order-inducing cholesterol lipid significantly suppressed the activity of CYP3A4.^{26,27}

Activity of CYP also depends on membrane lipid composition. The addition of phosphatidylethanolamine (PE) to phosphatidylcholine (PC) was shown to increase the catalytic activity of CYP2B4,²⁸ while it had stabilization effect on CYP1A2.²⁹ The catalytic activity of CYP1A2 was increased by the presence of anionic lipids 2-3 folds at 50 % addition of phosphatidyl acid (PA) or phosphatidylserin (PS).³⁰ When CYP3A4 was attached to mixed phosphatidylcholine/phosphatidylserine membrane, an increase in maximal velocity V_{\max} for nifedipine oxidation occurred but Michaelis constant K_m did not change.³¹ The enzymatic activity of CYP3A4 in the presence of anionic lipids increased ~6-fold at 50 mol % of PS in comparison with pure phosphatidylcholine (PC) membrane. Further increase in the PS concentration (above 60 %) lead to a concomitant rapid decrease of the enzyme activity.³² As the rate of NADPH oxidation was unaffected by the presence of anionic lipids, it was suggested that the negative charge of the membrane lipid might affect electron flow between CYP and redox partners.³¹⁻³⁴ However, the mechanism how lipids mediate the electron transfer still remains unclear.³⁵ Despite the importance of membrane in the catalytic function of CYP, there is still a lack of information about structural details of interaction of CYPs with various membranes and how changes in membrane composition is pronounced in CYP biophysics.

In this work, we describe the interactions between CYP3A4 and various membrane lipids differing in a head group region. We have chosen dioleoyl phospholipids and monitored the influence of the differently charged head groups on CYP3A4 interaction with the membrane (Figure 1). We observed significant differences in the structure, position and orientation of CYP3A4 in the membrane composed of lipids with variously charged lipids. We discussed the

observations in the context of activity of CYPs and in context of the CYP charges. We have hypothesized that the charge of CYP may induce electrostatic interactions between CYP and (negatively charged) membranes and may lead not only to the changes in catalytic efficiency and access or egress of the substrate/metabolite, but also to the CYP localization.

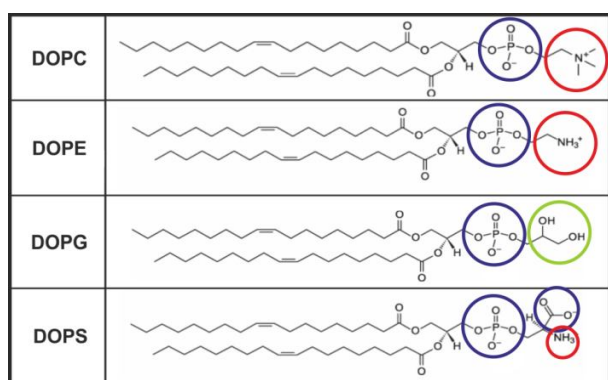


Figure 1: Lipids of biological membranes addressed in this study, i.e., dioleylphosphatidylcholine (DOPC), dioleylphosphatidyl-ethanolamine (DOPE), 1,2-dioleoyl-*sn*-glycero-3-[phospho-*rac*-(3-lysyl(1-glycerol))] (DOPG), and 1,2-dioleoyl-*sn*-glycero-3-phosphoserine (DOPS). The charges are highlighted in circles in following colors: blue – negative, red – positive, green – neutral polar.

Methods

We prepared membrane models using four different lipid bilayers, each composed of pure dioleoylphosphoglycerolipid (DOPx) containing 121 molecules per leaflet. We used 1,2-dioleoyl-*sn*-glycero-3-phosphocholine (DOPC), 1,2-dioleoyl-*sn*-glycero-3-phosphoethanolamine (DOPE), dioleylphosphatidyl-glycerol (DOPG), and dioleylphosphatidyl-serine (DOPS). The lipids differed only in the head groups (Figure 1) in order to separate the role of the head groups

from the effect of lipid tails. We used Slipids³⁶ force field for the lipids. We hydrated the bilayer with TIP3P water model.³⁷ As prepared bilayer models were equilibrated for 200 ns.

We used all-atom structure of CYP3A4 pre-equilibrated on the DOPC membrane from our previous study.³⁸ In the next step, we attached CYP3A4 into each of four different equilibrated bilayers using Gromacs tool `g_membed`.³⁹ CYP3A4 attached to the membrane was inserted into a rectangular box and solvated with TIP3P water model.³⁷ After solvation we added Na⁺ and Cl⁻ ions to neutralize the system and to obtain physiological concentration 0.1 mol/L (see Table S1 in Supporting information).

All simulations were performed using Gromacs package 5.0.⁴⁰ We used AMBER ff99SB⁴¹ for CYP3A4, which is compatible with Slipids force field.³⁶ We used parameters developed by Cheatham et al⁴² for the heme cofactor. For ions was used parameters developed by Aqvist and Applequist et al.^{43,44} Each system was energy minimized using steepest descent method. After the initial minimization, a short 10-ns-long MD simulation with positional restraints applied for C α atoms was executed. The next step was 200-ns-long equilibration MD simulation of all membranes with CYP3A4 with following parameters; 2-fs-long time step (LINCS algorithm⁴⁵); semiisotropic Berendsen barostat⁴⁶ with pressure 1 bar, V-rescale thermostat at 310 K. The trajectories were collected from the 1,000+ ns long production run. We used following parameters of $[N, p, T]$ MD simulations: 2-fs-long time step, Nosé-Hoover thermostat^{47,48} set to 310 K and Parrinello-Rahman barostat⁴⁹ set to 1.013 bar with semi-isotropic conditions; isothermal compressibility $4.5 \times 10^{-5} \text{ bar}^{-1}$ and pair-list was generated with the group cut-off scheme. The particle Mesh Ewald method⁵⁰ was used for treatment of the electrostatics interactions from 1 nm and van der Waals interactions were switched from 0.8 to 1.0 nm.

Constraints were applied on all bonds with hydrogens. In all directions we applied periodic boundary conditions.

All analyses were performed over the last 500 ns of MD simulation. For analysis of CYP3A4 and membrane properties the Gromacs tools were used.⁴⁰ For measure of distances between CYP, parts of CYP and membrane, `g_dist` tool was used for centers of masses of individual moieties. The `g_sgangle` was used for the computation of heme tilt angle which was characterized as the angle between heme plane and membrane normal (z axis).¹⁰ The heme plane was represented by set of three nitrogen atoms of the heme porphyrin. The area per lipid (APL) was calculated from size of the plane and number of lipids. Monolayer thickness ($D_{HH}/2$) was calculated from the z-distance between maximum densities of phosphate group in both leaflets obtained by `g_density` tool. Deuterium order parameters were measured with using `g_order` tool and the radial distribution function of terminal nitrogens (in case of DOPG a terminal oxygen), phosphorus atoms, ions and water around a surface of CYP3A4, was calculated by `g_rdf` tool. RMSD was calculated using `g_rms` tool. Figures were provided using PyMOL 1.8 (The PyMOL Molecular Graphics System, Version 1.8 Schrödinger, LLC).

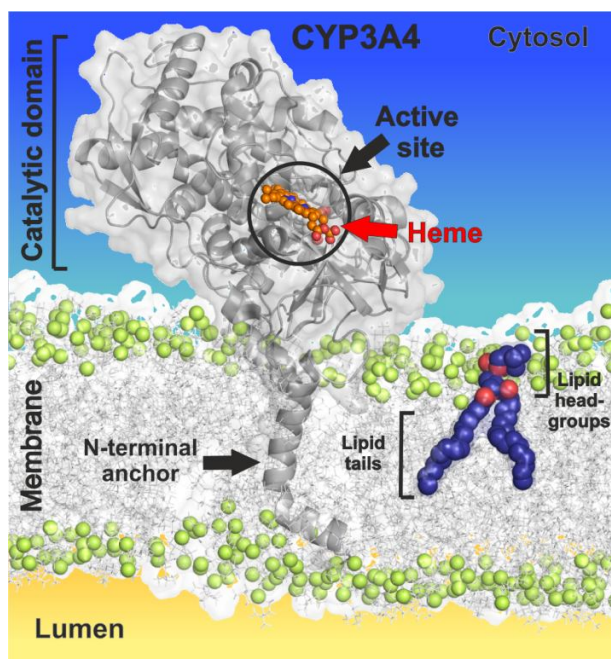


Figure 2: Structural view of CYP3A4 attached to DOPC membrane CYP3A4 is represented as grey cartoon and transparent surface, the active site is shown in black circle and the heme cofactor as orange (carbons) and red spheres (oxygens), detail of one DOPC lipid (blue spheres) shows position of lipid head group and tails in the bilayer; the oxygens are represented as red spheres and phosphate atoms as pale green spheres.

Results

We embedded CYP3A4 into four different DOPx bilayers (Figure 2, 3) and carried out 1- μ s-long MD simulations in order to decipher the role of lipid head groups on the interaction of CYP3A4 with the membrane. The structural details of pure membranes (without CYP3A4) are listed in Table 1 and they show that the area per lipid (APL) of pure membranes varied between 0.59 nm² (DOPE) to 0.70 nm² (DOPG) and was negatively linearly correlated ($r^2 = 0.96$) with the membrane thickness varying from 4.2 nm (DOPE) to 3.6 nm (DOPG). The DOPE membrane

was significantly more ordered (average deuterium order parameters $S_{\langle CD \rangle}$ of 0.16) than other lipids with a significant increase of $S_{\langle CD \rangle}$ on its sn-2 chain (Figure S1 in Supporting Information). The differences in chain ordering between sn-1 and sn-2 chains were observed near head groups, but apart from DOPE, $S_{\langle CD \rangle}$ in lipids chains in membrane core were equivalent. These observations agree with literature^{51–53} and document that the used parameters and protocols provide relevant data ready for further interpretation.

Table 1: Measured properties from lipid membrane simulations.

Lipid type	Pure Membrane		Membrane with CYP3A4					
	APL	$D_{HH}/2$	$S_{\langle CD \rangle}$	CYP-DOPx distance	Interacting AA residues with membrane		Average # hydrogen bonds of CYP3A4 to lipids	Heme tilt angle
	[nm ²]	[nm]		[nm]	Inside	Above*		[Deg.]
DOPC	0.69	1.89	0.11	3.77 ± 0.14	47	38	12.7	63.6 ± 6.1
DOPE	0.59	2.12	0.16	3.83 ± 0.14	52	34	25.3	73.2 ± 5.6
DOPG	0.70	1.80	0.10	3.10 ± 0.11	112	98	40.3	77.3 ± 5.0
DOPS	0.65	1.97	0.13	3.58 ± 0.15	68	46	32.1	68.6 ± 5.2

Area per lipid (APL) and monolayer thickness ($D_{HH}/2$) calculated as half of the head group – head group distance of lipid bilayers in pure bilayer simulations; the distance between center of masses of CYP3A4 and lipid membrane, the number of CYP3A4 AA residues located inside the membrane or within 7 Å from polar head groups, average number of hydrogen bonds between CYP3A4 and lipids and the heme tilt angle.

*within 7 Å from the membrane

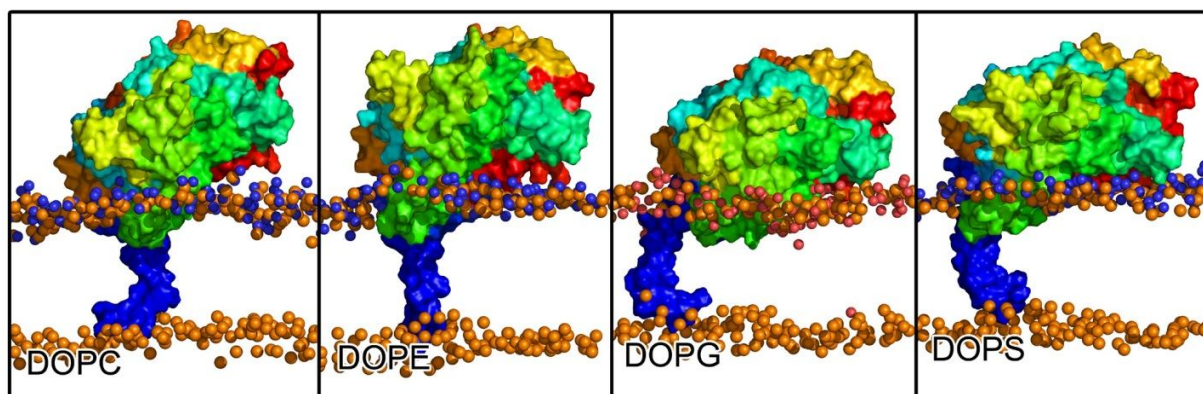


Figure 3: CYP3A4 on different membranes adopt a different orientation and depth of the embedding. In lipid only phosphates are shown as orange balls and in upper layer of the membrane the nitrogens or glycerol oxygens (in DOPG) are shown as blue and pink balls, respectively.

The embedded CYP3A4 catalytic domain kept its native fold as RMSD of $C\alpha$ atoms from the last frame to the X-ray structure were below 0.4 nm with notable exception of CYP3A4 on DOPS membrane (Figures S2 and S3 in Supporting Information) and the systems achieved convergence after 500 ns of production simulation. The difference of RMSD value in the case of CYP3A4 on DOPS membrane is caused by the partial deformation and loss of CYP3A4 secondary structure of membrane-attached parts – C, F, G, H helices, as a result former C and H helices sunk towards the membrane and drag the I-helix causing the distortions in the middle part of I-helix. During 1 μ s of unbiased simulations the CYP3A4 structures reached a stable distance to the centre of the membrane with fluctuations in range of 0.15 nm (Table S2 in Supporting Information). CYP3A4 was anchored to the membrane by its N-terminal transmembrane helix, but also by the tip of F/G loop, A, F and G helices and partially B/C loop (Figure 4) in a good consensus with known observations.^{5–10} In case of DOPS membrane, additional contacts of K-helix with the membrane head groups were found and in case of DOPG β 3- β 5 sheets were in

contact to the membrane. These additional contacts indicated deeper immersion of CYP3A4 into the respective membranes. Subsequently, the mouth openings of active site access channels were located deeper in the negatively charged membranes (Figure 4).

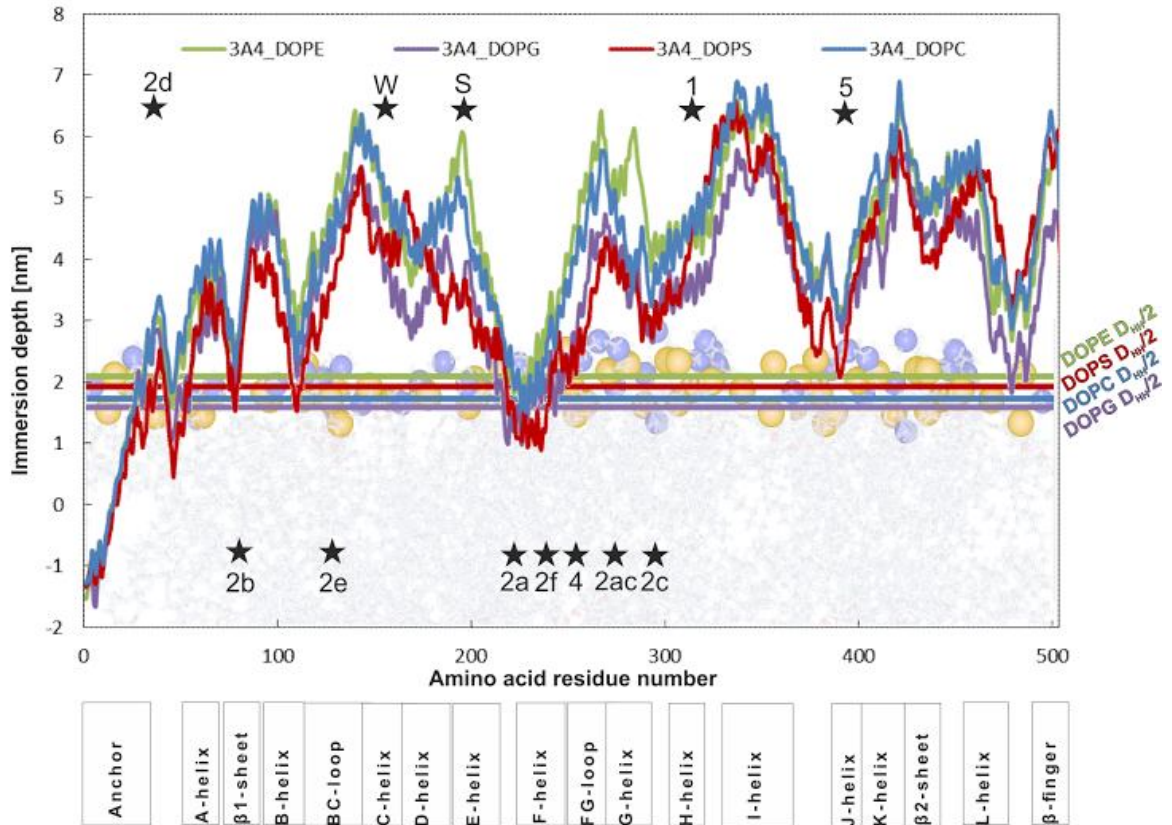


Figure 4: Distribution of amino acids in the contact with membrane. The respective system is represented in following color: 3A4-DOPC – blue, 3A4-DOPE - green, 3A4-DOPG – purple, 3A4-DOPS – red. Boxes below the graph represent the position of respective secondary structural feature of the CYP3A4. The color lines depict monolayer thickness according to $D_{HH}/2$ values (from Table 1). Black stars depict the positions of mouth openings of active site access channels: 2a, 2ac, 2b, 2c, 2d, 2e, 2f, 1, 4, 5, water (W) and solvent (S) channels (labeled by Wade et al. nomenclature⁴).

The immersion depths of CYP3A4 in the DOPx membranes correlated with the number of CYP3A4 amino acid (AA) residues embedded in the membrane and their contacts with the membrane ($r^2 = 0.98$; Table 1). The deepest immersion of CYP3A4 was observed in DOPG membrane (distance of CYP centre of mass to membrane centre 3.1 ± 0.1 nm) followed by DOPS (and 3.6 ± 0.1 nm; Table 1, Table S2 and Figure S4 in Supporting Information). In neutral DOPC and DOPE membranes, CYP3A4 was located significantly further from the membrane center ($\sim 3.8 \pm 0.1$ nm in both cases). We also monitored distance of CPR binding AA residues (N441-R446) to the membrane center, and identified similar trends as described for the distance of the catalytic domain from the membrane center (Figure S5 in Supporting Information). The number of hydrogen bonds between CYP3A4 and membrane head groups increased with the shorter distance of CYP3A4 from the membrane center ($r^2 = 0.67$; Table 1).

The lipid type of the membrane influenced, besides the immersion depth, the orientation of CYP3A4 on the membrane (Figure 3). The different orientation of the catalytic domain can be analyzed in terms of heme tilt angle (Figure 5), which defined the orientation of the heme cofactor plane with respect to the membrane plane and which is experimentally accessible from linear dichroism measurements.⁵⁴ The highest heme tilt angle of CYP3A4 was observed in DOPG membrane (77 ± 5) reflecting largest inclination towards this membrane. Heme tilt angle decreased gradually afterwards from DOPE, DOPS towards smallest angle for DOPC ($64 \pm 6^\circ$, Table 1), which agreed (within the error bars) with the experimentally obtained value $60 \pm 4^\circ$ measured for CYP3A4 on 1-palmitoyl-2-oleyl-sn-glycero-3-phosphocholine (POPC) nanodisc.⁵⁴ In all cases heme tilt angle displayed large fluctuation on ~ 100 ps and ~ 100 ns time scales during the MD simulation (Figure 5).

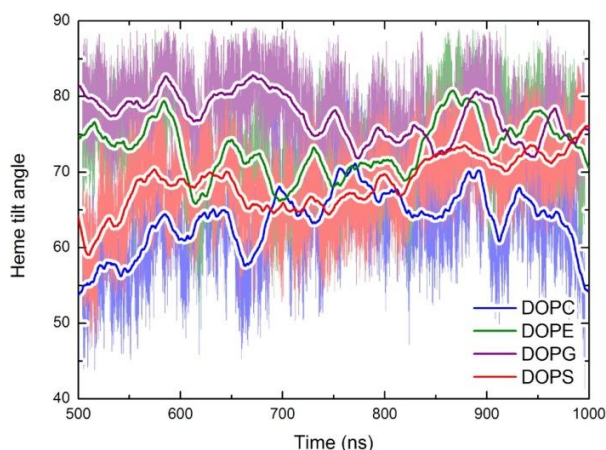


Figure 5: Heme tilt angle of CYP3A4 on different membranes (DOPC – blue, DOPE - green, DOPG – purple, DOPS – red, the thick lines represent a smooth development of heme tilt angle and the background shows the detailed trajectory analysis), from the last 500 ns of MD simulation.

Discussion

In this study, we were focused on description how CYP3A4 interacts with the membrane and also the effect of different head groups of membrane lipids on CYP3A4 behavior. We found that our results are in agreement with known data. Most of in silico CYP studies so far were performed on phosphatidylcholine (PC) membranes and the position and orientation of CYP3A4 on DOPC membrane observed here agree well with the known structures and experiments.^{17,54,55} In our model, CYP3A4 was embedded into the PC membrane in common pattern by N-terminal α -helix, tips of F/G loop and B/C loop and parts of F and G loops (Figures 2 and 4).⁵⁶

The orientation of CYP3A4 on DOPC, evaluated from heme tilt angle, corresponded with the experimental value determined by linear dichroism measurement for CYP3A4 on POPC nanodiscs,⁵⁴ which supports validity of our model. Higher heme tilt angle is connected with lower number of hydrogen bonds between CYP3A4 and the membrane and the number of

hydrogen bonds is also connected with the depth of immersion of the CYP3A4 into the membrane (Figure S6). However, we have observed large fluctuations with slow frequency in the characteristics of depth and orientation of CYP3A4 on all membranes. Though the systems were left to relax for 200 ns, which used to be considered as a long enough time for the equilibration,⁵⁷ the analysis of the first 500 ns of our production simulation (so in fact after 700 ns of MD simulation since start) revealed a time evolution of distribution of heme tilt angle e.g. for the relaxation of DOPE system (Figure S7 in Supporting information). As we defined heme tilt angle by a small region, tiny fluctuations or reversible deformations of heme are reflected by fluctuation in ps time scale without a significant influence on the whole CYP3A4 structure. The long term fluctuations, on the other hand, on 100 ns+ time scale are already significant and reflect the enzyme orientation changes on the membrane. These observations showed that the membrane-attached proteins such as CYP3A4 underwent slow floating motions, which could be observed on 100+ ns time scales. Hence, we recommend executing MD simulations of membrane-attached proteins on at least 500 ns time scale in order to observe such motions. On the other hand, we could not rule out that some relevant motions were not detected due to still short time scale with respect to real biophysical and biochemical experiments.

In our simulations we observed changes in CYP3A4 depth and orientation on membranes that might affect activity of CYP3A4 in various membranes depending on chemical properties of lipid head groups. In neutral lipids, DOPE had a small head group (ethanolamine) terminated by a charged ammonium group, which served as the hydrogen bonds proton donor, in contrast DOPC with the charged choline group was unable to form hydrogen bonds. Thanks to the capacity to make hydrogen bonds, DOPE bilayer was more ordered than DOPC and could create more hydrogen bonds with CYP3A4 (Table 1). The negatively charged DOPG and DOPS may

serve as both proton donors and acceptors for hydrogen bonds. DOPG possessed a single negative charge on phosphoryl group terminated by neutral glycerol moiety. DOPS beard zwitterion serine moiety attached to the phosphoryl group, and had therefore three charged groups interacting more strongly via electrostatic interactions. The different binding properties of lipid head groups were reflected in the total amount of hydrogen bonds to CYP3A4 that was the highest for DOPG followed by DOPS and DOPE, and the lowest for DOPC (Table 1). Naturally, the ability of DOPG to form extensive network of hydrogen bonds drove CYP3A4 to bend towards the membrane (Figure 3).

Contacts between CYP3A4 and lipids hence differed for individual membranes as could be seen from their radial distribution functions (RDF, Figure S8 in Supporting information). In all four cases, a clear peak in the RDF between CYP3A4 surface and phosphorus atoms could be seen at approximately the same position (~ 0.30 nm). In DOPS, lipids head groups are more organized due to stronger interactions and a second head group layer could be observed at ~ 0.45 nm. The positions of terminal nitrogens (in case of DOPG the terminal oxygen) were the same (~ 0.27 nm) except for DOPC, which cannot form hydrogen bonds as its nitrogen is shielded by methyl groups and it is located at ~ 0.38 nm. In DOPG we observed an additional shoulder in RDF function closer to CYP3A4 surface (~ 0.20 nm) reflecting close hydrogen bonding interactions between uncharged terminal hydroxyl group of DOPG glycerol with CYP3A4. In DOPG and DOPS we also observed a high concentration of Na^+ cations interacting with negatively charged head groups, whereas water pattern is similar in all cases. Here a different orientation and depth of CYP3A4 creates a unique environment in the contact region, rich in hydrogen bonds, ions and charged head groups (Figure S9 in Supporting information).

CYP3A4 was immersed more deeply into the negatively charged membranes (DOPG and DOPS) than into neutral ones (DOPC and DOPE). This is consistent with the fact that the distal side of the CYP3A4, which is in direct contact with the membrane (see Figure 6), is positively charged and therefore attracted more to the negatively charged lipids. DOPG showed the deepest immersion of CYP3A4 into the membrane as its negatively charged group was deeper than in serine carboxylic acid on DOPS. On the other hand, the surplus of negatively charged lipids in DOPS also caused distortions of the CYP3A4 structure (as seen on RMSD in Figure S3 in Supporting information), which can explain a rapid decrease of the enzyme activity with large concentration of PS (>60%) in the membrane.³² Electrostatic interactions between CYP and the membrane can therefore have an impact on also on catalytic activity of the enzyme.

Overall, differences in the interactions of CYPs with the membrane can be based on their respective charges. Lipid membranes present in, e.g., human body can vary from neutral lipids (PC, PE) to negatively charged lipids (e.g., PS or PG). They vary also in their ordering, ability to form hydrogen bonds etc. Individual CYP isoforms vary in charge from negatively charged CYP2D6 to highly positively charged CYP1A2 (Table 2). The charge is unevenly distributed between distal and proximal sides of the catalytic domain. The proximal side is usually negatively charged, which is consistent with the structures of its redox partners interacting in this area.^{56,58,59} The distal side, which makes majority of CYP3A4-membrane interface, is usually positively charged. A different preference for the ordered and disordered membrane domains was observed also for very homologous CYPs 1A1 and 1A2.^{20,21} As these two CYP isoforms significantly differ in their charge, we may hypothesize that the different membrane localization is controlled by the charge and charge distribution over the CYP catalytic domain. Table 2 indicates that CYPs with positive total charge prefer ordered membrane domains as these can

contain anionic lipids.⁶⁰ In these new findings of the interactions of CYPs with differently charged membranes, the effect of the membranes to the enzyme immersion level, orientation, interaction with its redox partners and membrane domain localization and overall function is crucial and should be taken into account in all further studies (Figure 6).

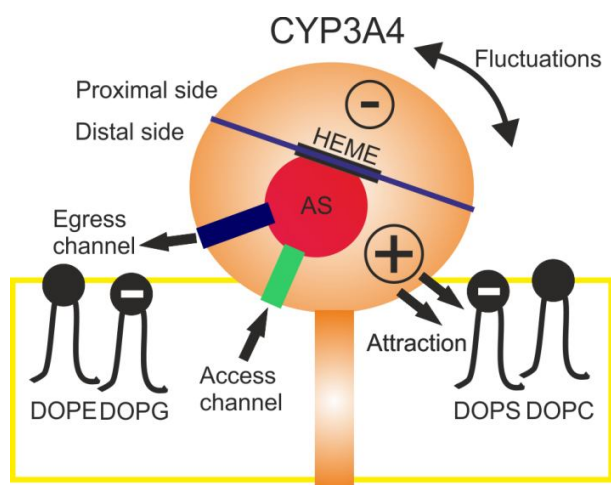


Figure 6: Schematic view of CYP3A4 - membrane lipid interactions and the effect on the CYP function. CYP3A4 is represented as orange circle and N-terminal transmembrane anchor as orange rectangle. The CYP active site (AS) is showed as red circle and blue and green rectangles symbolize egress and access channels respectively. The membrane is depicted as yellow box and membrane lipids in black; the distal side of the CYP3A4 is positively charged which leads to the attraction between catalytic domain and the negatively charged membrane lipids (in this case DOPS, DOPG) and may influence also substrate access or product release. In addition the interactions of the membrane lipids with the CYP catalytic domain cause fluctuations of the CYP on the membrane surface.

Table 2. Preference for CYP membrane domains based on charges of important mammalian CYPs.

CYP	total	distal	prox.	PDBID	Domain
rabbit 1A2	12	N/A	N/A	N/A	ordered ^{21,22,24,25} , anionic-rich ⁶¹
human 1A2	10	2	7	2hi4	
human 2C8	9	11	-5	2mj	
rabbit 2B4	6	7	-2	1po5	disordered+ordered ²⁰
human 1A1	5	4	-1	4i8v	
rabbit 1A1	3	N/A	N/A	N/A	disordered ^{20,21,25}
rabbit 2E1	3	N/A	N/A	N/A	disordered ²⁰
human 2C9	3	7	-4	1r9o	
human 2B6	3	6	-3	3ua5	
human 2E1	3	6	-3	3koh	
human 3A4	3	5	1	1tqn	
human 2C19	0	0	-1	4gqs	
human 2D6	-2	-1	-3	3qm4	

Total charge was taken from UNIPROT canonical sequence. Distribution of the charge between the distal or proximal (prox) side was calculated on crystal structure resembling the most native form. Charges are estimated by the presence of Arg, Lys, Asp and Glu amino acids.

Conclusion

Here we studied the influence of lipid membrane composition on the behavior of cytochrome P450 3A4. Overall, CYP3A4 is embedded in the membrane with in N-terminal α -helix, F/G loop and neighboring hydrophobic regions, however significant differences in embedding depth and orientation were observed in the dependence on the membrane charge. As CYP3A4 is positively charged, it is attracted to the negatively charged membrane lipids. We propose that the charge of the enzyme and of the membrane plays a significant role in the enzyme orientation and embedding depth and therefore it may affect CYP function or domain localization. As CYP3A4 is involved in a variety of drug metabolism, we believe that this knowledge is of a high interest of pharmacologists and molecular biologists.

Supporting Information

Number of ions and water molecules in simulations of CYP3A4 of various lipid bilayers (Table S1); Average deuterium order parameters (Figure S1); Comparison of crystal structure of CYP3A4 with 1000 ns DOPC, DOPE, DOPG and DOPS membranes after 1000 ns of MD simulation (Figure S2); RMSD evolution of CYP3A4 on individual membranes (Figure S3); Average values and standard deviations of measured characteristics from whole 1000 ns, from last 200 and last 500 ns of MD simulation (Table S2); Distance of CYP3A4 and respective DOPx membrane of 1000 ns long MD simulation (Figure S4); Distance between CPR contact amino acids (441, 442, 445 and 446) and center of mass of the membrane during 1000 ns long MD simulation (Figure S5); Correlation of some of the monitored properties during the simulation (Figure S6); Heme tilt angle of CYP3A4 on different membranes (Figure S7); Radial distribution functions of terminal nitrogens (Figure S8); Side view and bottom view at CYP3A4 with displayed ions (Figure S9). This material is available free of charge via the Internet at <http://pubs.acs.org>.

Corresponding Authors

*MO, Phone: +420 585634756, fax: +420 585634761, e-mail: michal.otyepka@upol.cz

Notes

The authors declare no competing financial interest.

ACKNOWLEDGMENT

This research was supported by the Czech Grant Agency through the project P208/12/G016. M.P. and V.N. acknowledge support from a student project of Palacký University Olomouc (IGA_PrF_2016_028). The authors gratefully acknowledge support through the project LO1305 of the Ministry of Education, Youth and Sports of the Czech Republic.

ABBREVIATIONS

CYP – cytochrome P450

DOPC - 1,2-dioleoyl-sn-glycero-3-phosphocholine

DOPE - 1,2-dioleoyl-sn-glycero-3-phosphoethanolamine

DOPG - 1,2-dioleoyl-sn-glycero-3-[phospho-rac-(3-lysyl(1-glycerol))]

DOPS - 1,2-dioleoyl-sn-glycero-3-phosphoserine

POPC – 1-palmitoyl-2-oleyl-sn-glycero-3-phosphocholine

MD – molecular dynamics

CPR – cytochrome P450 reductase

AA – amino acid

REFERENCES

- (1) Ortiz de Montellano, P. R. *Cytochrome P450: Structure, mechanism, and biochemistry*; P.R. Ortiz de Montellano, Ed.; 3ed ed.; Kluwer Academic/Plenum Publishers: New York, 2005; Vol. 21.
- (2) Anzenbacher, P.; Anzenbacherová, E. *Cell. Mol. Life Sci.* **2001**, *58*, 737–747.
- (3) Shaik, S.; Kumar, D.; de Visser, S. P.; Altun, A.; Thiel, W. *Chem. Rev.* **2005**, *105*, 2279–

2328.

- (4) Cojocaru, V.; Winn, P. J.; Wade, R. C. *Biochim. Biophys. Acta* **2007**, *1770*, 390–401.
- (5) Sgrignani, J.; Magistrato, A. *J. Chem. Inf. Model.* **2012**, *52*, 1595–1606.
- (6) Cojocaru, V.; Balali-Mood, K.; Sansom, M. S. P.; Wade, R. C. *PLoS Comput. Biol.* **2011**, *7*, e1002152.
- (7) Berka, K.; Hendrychová, T.; Anzenbacher, P.; Otyepka, M. *J. Phys. Chem. A* **2011**, *115*, 11248–11255.
- (8) Denisov, I. G.; Shih, A. Y.; Sligar, S. G. *J. Inorg. Biochem.* **2012**, *108*, 150–158.
- (9) Johnson, E. F.; Stout, C. D. *J. Biol. Chem.* **2013**, *288*, 17082–17092.
- (10) Berka, K.; Paloncýová, M.; Anzenbacher, P.; Otyepka, M. *J. Phys. Chem. B* **2013**, *117*, 11556–11564.
- (11) Bayburt, T. H.; Sligar, S. G. *Proc. Natl. Acad. Sci. U. S. A.* **2002**, *99*, 6725–6730.
- (12) Nussio, M. R.; Voelcker, N. H.; Miners, J. O.; Lewis, B. C.; Sykes, M. J.; Shapter, J. G. *Chem. Phys. Lipids* **2010**, *163*, 182–189.
- (13) Ozalp, C.; Szczesna-Skorupa, E.; Kemper, B. *Biochemistry* **2006**, *45*, 4629–4637.
- (14) Black, S. D. *FASEB J.* **1992**, *6*, 680–685.
- (15) Von Wachenfeldt, C.; Johnson, E. F. In *Cytochrome P450*; Springer US: Boston, MA, 1995; pp. 183–223.
- (16) Yamamoto, K.; Dürr, U. H. N.; Xu, J.; Im, S.-C.; Waskell, L.; Ramamoorthy, A. *Sci. Rep.*

2013, 3, 2538.

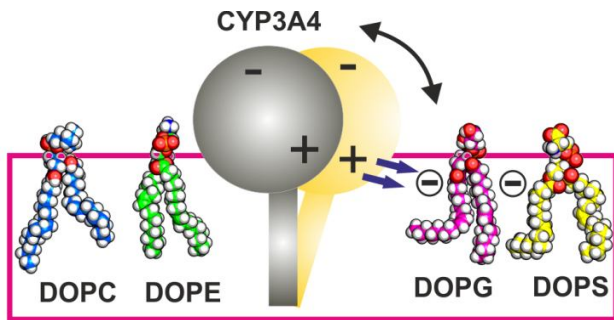
- (17) Monk, B. C.; Tomasiak, T. M.; Keniya, M. V.; Huschmann, F. U.; Tyndall, J. D. a.; O'Connell, J. D.; Cannon, R. D.; McDonald, J. G.; Rodriguez, A.; Finer-Moore, J. S.; Stroud, R. M. *Proc. Natl. Acad. Sci.* **2014**, *111*, 3865–3870.
- (18) Sagatova, A. A.; Keniya, M. V.; Wilson, R. K.; Monk, B. C.; Tyndall, J. D. A. *Antimicrob. Agents Chemother.* **2015**, *59*, 4982–4989.
- (19) Reed, J. R.; Backes, W. L. *Pharmacol. Ther.* **2012**, *133*, 299–310.
- (20) Park, J. W.; Reed, J. R.; Brignac-Huber, L. M.; Backes, W. L. *Biochem. J.* **2014**, *464*, 241–249.
- (21) Park, J. W.; Reed, J. R.; Backes, W. L. *J. Biol. Chem.* **2015**, *290*, 29449–29460.
- (22) Brignac-Huber, L. M.; Reed, J. R.; Eyer, M. K.; Backes, W. L. *Drug Metab. Dispos.* **2013**, *41*, 1896–1905.
- (23) Berman, H.; Henrick, K.; Nakamura, H.; Markley, J. L. *Nucleic Acids Res.* **2007**, *35*, D301–D303.
- (24) Brignac-Huber, L. M.; Reed, J. R.; Backes, W. L. *Mol. Pharmacol.* **2011**, *79*, 549–557.
- (25) Scott, E. E.; Wolf, C. R.; Otyepka, M.; Humphreys, S. C.; Reed, J. R.; Henderson, C. J.; McLaughlin, L. A.; Paloncýová, M.; Navratilova, V.; Berka, K.; Anzenbacher, P.; Dahal, U. P.; Barnaba, C.; Brozik, J. A.; Jones, J. P.; Estrada, F.; Laurence, J. S.; Park, J. W.; Backes, W. L. *Drug Metab. Dispos.* **2016**.
- (26) Navrátilová, V.; Paloncýová, M.; Kajšová, M.; Berka, K.; Otyepka, M. *J. Chem. Inf.*

- Model.* **2015**, *55*, 628–635.
- (27) Shinkyō, R.; Guengerich, F. P. *J. Biol. Chem.* **2011**, *286*, 18426–18433.
- (28) Ingelman-Sundberg, M.; Haaparanta, T.; Rydström, J. *Biochemistry* **1981**, *20*, 4100–4106.
- (29) Ahn, T.; Yun, C. H.; Oh, D. B. *Biochemistry* **2005**, *44*, 9188–9196.
- (30) Ahn, T.; Guengerich, F. P.; Yun, C. H. *Biochemistry* **1998**, *37*, 12860–12866.
- (31) Ingelman-Sundberg, M.; Hagbjork, A. L.; Ueng, Y. F.; Yamazaki, H.; Guengerich, F. P. *Biochem Biophys Res Commun* **1996**, *221*, 318–322.
- (32) Kim, K. H.; Ahn, T.; Yun, C. H. *Biochemistry* **2003**, *42*, 15377–15387.
- (33) Macdonald, P. M.; Seelig, J. *Biochemistry* **1988**, *27*, 6769–6775.
- (34) Laursen, T.; Jensen, K.; Møller, B. L. *Biochim. Biophys. Acta - Proteins Proteomics* **2011**, *1814*, 132–138.
- (35) Bayburt, T. H.; Sligar, S. G. *Proc Natl Acad Sci U S A* **2002**, *99*, 6725–6730.
- (36) Jämbeck, J. P. M.; Lyubartsev, A. P. *J. Chem. Theory Comput.* **2013**, *9*, 774–784.
- (37) Mahoney, M. W.; Jorgensen, W. L. *J. Chem. Phys.* **2000**, *112*, 8910.
- (38) Paloncýová, M.; Navrátilová, V.; Berka, K.; Laio, A.; Otyepka, M. *J. Chem. Theory Comput.* **2016**, *12*, 2101–2109.
- (39) Wolf, M. G.; Hoefling, M.; Aponte-santamaría, C.; Grubmüller, H.; Groenhof, G. *J. Comput. Chem.* **2010**, *31*, 2169–2174.

- (40) Van Der Spoel, D.; Lindahl, E.; Hess, B.; Groenhof, G.; Mark, A. E.; Berendsen, H. J. C. *J. Comput. Chem.* **2005**, *26*, 1701–1718.
- (41) Hornak, V.; Abel, R.; Okur, A.; Strockbine, B.; Roitberg, A.; Simmerling, C. *Proteins Struct. Funct. Bioinforma.* **2006**, *65*, 712–725.
- (42) Shahrokh, K.; Orendt, A.; Yost, G. S.; Cheatham, T. E. *J. Comput. Chem.* **2011**, *0742249*, 1–15.
- (43) Åqvist, J. *J. Phys. Chem.* **1990**, *94*, 8021–8024.
- (44) Applequist, J.; Carl, J. R.; Fung, K. *J. Am. Chem. Soc.* **1972**, *261*, 2952–2960.
- (45) Hess, B.; Bekker, H.; Berendsen, H. J. C.; Fraaije, J. G. E. M. *J. Comput. Chem.* **1997**, *18*, 1463–1472.
- (46) Berendsen, H. J. C.; Postma, J. P. M.; van Gunsteren, W. F.; DiNola, a; Haak, J. R. *J. Chem. Phys.* **1984**, *81*, 3684–3690.
- (47) Nosé, S. *J. Chem. Phys.* **1984**, *81*, 511.
- (48) Hoover, W. G. *Phys. Rev. A* **1985**, *31*, 1695–1697.
- (49) Parrinello, M.; Rahman, A. *J. Appl. Phys.* **1981**, *52*, 7182–7190.
- (50) Darden, T.; York, D.; Pedersen, L. *J. Chem. Phys.* **1993**, *98*, 10089–10092.
- (51) Kucerka, N.; Nagle, J. F.; Sachs, J. N.; Feller, S. E.; Pencser, J.; Jackson, A.; Katsaras, J. *Biophys. J.* **2008**, *95*, 2356–2367.
- (52) Tristram-Nagle, S.; Nagle, J. F. *Chem. Phys. Lipids* **2004**, *127*, 3–14.

- (53) Petrache, H. I.; Tristram-Nagle, S.; Gawrisch, K.; Harries, D.; Parsegian, V. A.; Nagle, J. F. *Biophys. J.* **2004**, *86*, 1574–1586.
- (54) Baylon, J. L.; Lenov, I. L.; Sligar, S. G.; Tajkhorshid, E. *J. Am. Chem. Soc.* **2013**, *135*, 8542–8551.
- (55) Strandberg, E.; Tiltak, D.; Ehni, S.; Wadhvani, P.; Ulrich, A. S. *Biochim. Biophys. Acta* **2012**, *1818*, 1764–1776.
- (56) Otyepka, M.; Skopalík, J.; Anzenbacherová, E.; Anzenbacher, P. *BBA-Gen. Subj.* **2007**, *1770*, 376–389.
- (57) Freddolino, P. L.; Liu, F.; Gruebele, M.; Schulten, K. *Biophys. J.* **2008**, *94*, L75–L77.
- (58) Clarke, T. A.; Im, S. C.; Bidwai, A.; Waskell, L. *J. Biol. Chem.* **2004**, *279*, 36809–36818.
- (59) Bridges, A.; Gruenke, L.; Chang, Y. T.; Vakser, I. A.; Loew, G.; Waskell, L.; Eng, L. P. *J. Biol. Chem.* **1998**, *273*, 17036–17049.
- (60) Himeno, H.; Shimokawa, N.; Komura, S.; Andelman, D.; Hamada, T.; Takagi, M. *Soft Matter* **2014**, *10*, 7959–7967.
- (61) Ahn, T.; Kim, M.; Yun, C.; Chae, H. *Curr. Protein Pept. Sci.* **2007**, *8*, 496–505.

Table of Contents Graphic



***In Silico* Pharmacology: Drug Membrane Partitioning and Crossing**

Florent Di Meo,^a Gabin Fabre,^b Karel Berka,^c Tahani Ossman,^a Benjamin Chantemargue,^{a,c} Markéta Paloncýová,^c Pierre Marquet,^a Michal Otyepka^c and Patrick Trouillas^{a,c,*}

^a *INSERM UMR 850, Univ. Limoges, Faculty of Pharmacy, 2 rue du Dr Marcland, F-87025, Limoges, France*

^b *LCSN, Univ. Limoges, Faculty of Pharmacy, 2 rue du Dr Marcland, F-87025, Limoges, France*

^c *Regional Centre for Advanced Technologies and Materials, Department of Physical Chemistry, Faculty of Science, Palacký University, Olomouc, Czech Republic*

* *Corresponding author: patrick.trouillas@unilim.fr*

¹ Acronyms

1

ABC, ATP-binding cassette; **ADME**, Absorption, Distribution, Metabolism and Excretion; **AMP**, Antimicrobial peptide; **CG**, Coarse-grained; **COX**, Cyclooxygenase; **CYP**, Cytochrome P450; **DLiPC**, Dilinoeyl-phosphatidylcholine; **DOPC**, 1,2-dioleoyl-sn-glycero-3-phosphocholine; **GA**, General anesthetic; **GlpT**, Glycerol-3-phosphate:phosphate transporter; **GLUT1**, Glucose transporter; **GST**, Glutathione S-transferase; **IF**, Inward facing; **LA**, Local anesthetic; **LacY**, Lactose permease; **MATE**, Multi-antimicrobial extrusion protein; **MD**, Molecular dynamics; **MFS**, Major facilitator superfamily; **MM/PBSA**, **Molecular Mechanics / Poisson-Boltzmann Surface Area**; **MM/GBSA**, **Molecular Mechanics / Generalized Born Surface Area**; **Msba**, Bacterial ABC lipid flippase; **NAT**, N-acetyltransferases; **NBD**, Nucleotide-binding domains; **NSAID**, Non-steroidal anti-inflammatory drug; **NSS**, Neurotransmitter:sodium symporter; **OAT**, Organic anion transporter; **OF**, Outward facing; **PEPT**, Peptide transporter; **PIP2**, Phosphatidylinositol 4,5-bisphosphate; **PMF**, potential of mean force; **POPC**, 1-Palmitoyl,2-oleoyl-sn-glycero-3-phosphocholine; **POPG**, 1-Palmitoyl-2-oleoyl-sn-glycero-3-phosphoglycerol; **QM/MM**, Quantum mechanics/Molecular mechanics; **SLC**, Solute carrier; **SULT**, Sulfotransferase; **TM**, Transmembrane helice; **TMD**, Transmembrane domain; **UGT**, Uridine 5'-diphospho-glucuronosyltransferase; **Xyle**, Xylose:H⁺ symporter.

Abstract

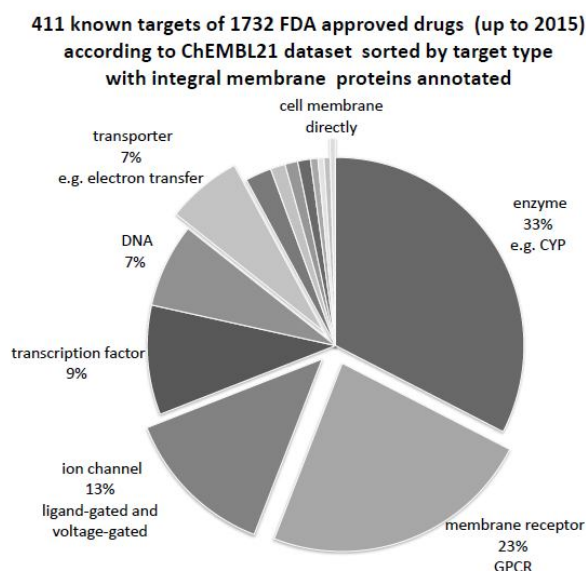
Over the past decade, molecular dynamics (MD) simulations have become particularly powerful to rationalize drug insertion and partitioning in lipid bilayers. MD simulations efficiently support experimental evidences, with a comprehensive understanding of molecular interactions driving insertion and crossing. Prediction of drug partitioning is discussed with respect to drug families (anesthetics; β -blockers; non-steroidal anti-inflammatory drugs; antioxidants; antiviral drugs; antimicrobial peptides). To accurately evaluate passive permeation coefficients turned out to be a complex theoretical challenge; however the recent methodological developments based on biased MD simulations are particularly promising. Particular attention is paid to membrane composition (*e.g.*, presence of cholesterol), which influences drug partitioning and permeation. Recent studies concerning *in silico* models of membrane proteins involved in drug transport (influx and efflux) are also reported here. These studies have allowed gaining insight in drug efflux by, *e.g.*, ABC transporters at an atomic resolution, explicitly accounting for the mandatory forces induced by the surrounded lipid bilayer. Large-scale conformational changes were thoroughly analyzed.

1. Introduction

Drug-membrane interaction is a crucial pharmacological step that directly affects ADME (absorption, distribution, metabolism and excretion) of drugs, and subsequently drug action or toxicity [1,2]. Biological membranes are complex dynamical systems composed of a huge number of different lipids and proteins, with mass ratio ranging from 1:3 to 3:1 [3]. According to the fluid mosaic model proposed by Singer and Nicholson in 1972, the plasma membrane forms "islands" of proteins immersed in the "two-dimensional sea" of lipids [4]. This model is still a valid description of most biological membranes with some significant exceptions, *e.g.*, skin membrane [5].

In this review, we will mainly focus on drug interactions with the lipid bilayer and with membrane proteins. Although only about 30 % of human genes encode for

membrane proteins [6], more than 60 % of molecular targets of commonly used drugs are membrane proteins (Scheme 1) [7]. Drug-protein interactions, related mechanism of a drug action, have been under close consideration [8], which is often better documented than drug-lipid interactions and membrane crossing. Drug-lipid interactions are pharmacologically significant as i) drug partitioning to membranes is more common than nonspecific protein binding [9]; ii) nonpolar xenobiotics can accumulate in lipid bilayers [10]; and passive transport contributes to drug disposition [11].



Scheme 1: 411 known targets of 1732 FDA approved drugs (up to 2015) according to ChEMBL21 dataset sorted by target type. Membrane bound targets consist about 62.4 % are annotated by expansion of triangle.

The biophysical techniques used to investigate drug-membrane interactions provide meaningful but fragmented information on: drug insertion; average location in the inner or outer parts of lipid bilayers; conformational and orientational behaviors; diffusion coefficients; partition coefficients; and membrane (passive) permeation. The mentioned biophysical methods are rather expensive, time consuming and cannot be employed easily in high-throughput screening.

Alternatively, *in silico* molecular modeling has gained substantial attention and maturity over the past decade. Since their conceptualization [12–14], the *in silico* membrane models have witnessed an extensive development [15–17]. The exponential growth of computing resources also drives the development in accuracy at reasonable time. Molecular dynamics (MD) simulations of lipid bilayer membranes evaluate drug-membrane interaction at both atomic and femtosecond resolutions, which is hardly reached simultaneously by experimental methods. This review will show how theoretical methods can now be considered as a new pharmacological tool, supporting or predicting experimental evidence, explicitly addressing: i) lipid bilayer insertion (Section 3); ii) passive membrane permeation (Section 4.1); iii) facilitated transport by membrane proteins (Section 4.2); iv) biotransformation by membrane proteins (Section 5); and v) efflux by active membrane transporters (Section 6)². Concerning the last three points, a particular attention will be paid to the role of lipid bilayers. The strengths of different *in silico* methodologies will be discussed, emphasizing on the importance of lipid bilayer composition (Section 7).

2. Glossary of *in silico* terms

The aim of this section is only to guide non-experts in the specialized vocabulary, so as to facilitate and focus on understanding of the physical-chemical picture of drug-membrane crossing.

Molecular Mechanics: Methods to calculate the potential energy of a given molecular system as a function of position of the atoms in the system. The calculation

2

Active transport proteins require ATP-hydrolysis to function contrary to the facilitated transport, in which transporters use electrochemical gradient arising from the co-transport of smaller substrates (e.g., H⁺, Na⁺).

is based on the classical (Newtonian) mechanics and empirical non-covalent terms as described by a force field.

Force field: Empirical formula of the potential energy together with tabulated empirical atomic parameters. Formula usually includes the bond deformation energy, the angle deformation energy, the energy associated with changes in dihedrals, the energy due to electrostatic (Coulomb) interactions, and the energy associated with van der Waals interactions. Some force fields also include specific terms such as H-bonding, or an energetic term describing polarization effects.

All atom force field: All atoms are explicitly treated as partially charged van der Waals balls on springs. Van der Waals interactions between distant atoms (*e.g.*, above 1 nm) are usually neglected, so to reduce the computational costs.

United atom force field: All atoms are treated as in all atom force fields, except nonpolar hydrogens that are united with the carbon they are attached to. United atom force fields are known to overestimate diffusion coefficients due to smaller friction.

Coarse-grained (CG) force field: The number of degrees of freedom (*e.g.*, atoms) is decreased (with respect to all atom force field description) by associating some atoms into atomic (super)-groups, called beads. These beads are treated as interacting polar, non-polar, apolar, or charged moieties.

Classical, free or unbiased MD simulations: The evolution (trajectory) of a molecular system in time by integration of Newtonian equations of motion at given conditions (*e.g.*, pressure, temperature, ionic strength, etc.). Currently, we achieve timescales from hundreds of nanoseconds to a few microseconds depending on system size and available computational power.

Biased MD simulations: Dedicated MD algorithms designed to speed up the exploration of potential energy either by constraining or focusing on geometrical

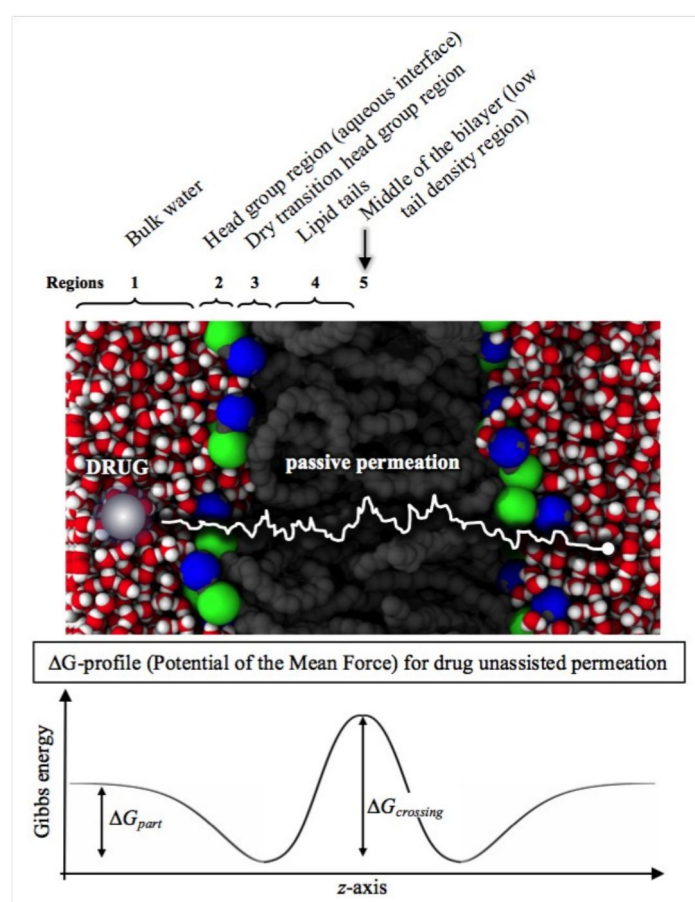
variables of interest, *e.g.*, steered MD; constrained MD; targeted MD, metadynamics, replica exchange MD.

Homology modeling: A theoretical approach, which provides structural models of proteins based on sequence homology (similarity). Assuming that two similar protein sequences should adopt remarkably close 3D structures, an unknown structure can be built by aligning its amino acid sequence onto a known structure of a reference (homologue) protein.

3. Drug insertion and partitioning into lipid bilayers

One of the main advantages of MD simulations is the ability to describe the preferred location and orientation of drugs in membranes at atomic resolution. Locations and orientations have been successfully predicted for a wide variety of drugs, in agreement with experimental data obtained on biomimetic membrane models [18]. In addition to providing locations and orientations, biased MD simulations enable evaluation of Gibbs energy (ΔG)-profiles along a chosen direction, *e.g.*, the membrane normal (z -axis) to picture membrane crossing and estimate membrane partitioning (Scheme 2). This energetic profile reflects the selective drug affinity to the different membrane regions. Along the z -axis, a bilayer can conceptually be divided into five regions: region 1) bulk water ($z > \sim 2.5$ nm); region 2) the aqueous interface between water and phosphate groups ($\sim 2.0 < z < \sim 2.5$ nm); region 3) the dry transition region between phosphate groups and acyl chains ($\sim 1.5 < z < \sim 2.0$ nm); region 4) the hydrophobic region of the bilayer ($\sim 0.5 < z < \sim 1.5$ nm); and region 5) the middle of the bilayer with low tail density ($z < \sim 0.5$ nm).³ The difference in Gibbs energies between the bulk water and the potential well

in the membrane (ΔG_{part} , see Scheme 2) provides a much more complex view on drug-membrane partitioning than the commonly used 1-octanol/water partition coefficients $\log P$ [19,20], which cannot catch complexity of membrane bilayer structure [21]. Here a non-exhaustive list is given, in which we exemplify the success of MD studies at predicting or confirming membrane insertion of a number of drugs, sorted by therapeutic classes.



Scheme 2: Pictorial description of unassisted (passive) permeation and energetic profile for drug crossing. ΔG_{part} is related to drug partitioning, whereas $\Delta G_{crossing}$ is the highest energetic barrier met by drugs through the bilayer (*i.e.*, limiting step of crossing event). The potential well and the $\Delta G_{crossing}$ may be localized in different regions; this very scheme reflects the behavior of a polar or an amphiphilic compound (high barrier in the lipid tail region).

Although the boundaries, given in bracket for a neat 1,2-dioleoyl-sn-glycero-3-phosphocholine (DOPC) bilayer, may differ with membrane composition, they are pertinent to the present analysis.

3.1 Anesthetics

Local anesthetics (LAs), including articaine, lidocaine, prilocaine, tetracaine and phenytoin bear titratable amino groups and may exist in both charged and uncharged states at physiological pH. MD simulations predict that all charged forms partition in the polar head group region in contact with water molecules (region 2), whereas uncharged forms insert deeper into the bilayers (regions 3-5) and cross membrane by passive permeation [22–32]. MD simulations help to decide whether LAs directly inhibit voltage-sensitive sodium and potassium channels [33–35], or as suggested by their location in membranes, increase lipid bilayer fluidity hence decreasing lipid order [22,27,29,31,32]. Membrane modifications associated with LA insertion in lipid bilayer most likely occur in the surrounding of ion channels, thus affecting ion exchanges.

The general anesthetics' (GAs) family includes: small gases such as neon and NO; fluorinated molecules (*e.g.*, halothane, desflurane); amphiphilic compounds (*e.g.*, benzodiazepines, propofol, ketamine); and 1-alkanols. Two main mechanisms of action have been considered, namely via receptors [36] or via membrane disruption. MD simulations confirmed X-ray diffraction studies showing that, at therapeutic concentration, ketamine inserts in membranes at the lipid/water interface affecting neither membrane thickness nor area per lipid, however inducing significant changes in lateral pressure profile that could affect ion channels [37]. Additionally, several MD studies addressed the relationship between lateral pressure and pressure reversal (cessation of anesthesia by hyperbaric pressure) [38]. Molecular descriptors rationalizing pressure reversal were identified, *e.g.*, location of some GAs' moieties; orientation of lipid head groups or tails [39]; and intra-membrane GA aggregation [40,41].

3.2 β -blockers

Beside their β -adrenergic blocking activities, β -blockers can also affect lipid bilayer properties, especially the non-selective β -blockers such as alprenolol, oxprenolol and propranolol. This mechanism of action is known as the non-specific membrane effect; it results in anesthetic [42] and cardioprotective effects [43]. Non-selective β -blockers were reported to fluidize 1,2-dipalmitoylphosphatidylcholine (DPPC) lipid bilayer membranes [44], whereas they significantly rigidified liposomes made of 1-palmitoyl,2-oleoyl-sn-glycero-3-phosphocholine (POPC) [45]. MD simulations were recently carried out to describe the interactions between propranolol and POPC bilayer. Propranolol was shown to specifically bind the carbonyl and phosphate groups, resulting in an increase and decrease of packing in the polar head group and the lipid tail regions, respectively [45]. This result agrees with the modification of lateral pressure observed for LAs, and may explain the anesthetic effects of β -blockers. However, to confirm this mechanism a particular attention has to be paid to specificity of β -blockers and membrane composition.

3.3 Non-steroidal anti-inflammatory drugs

Non-steroidal anti-inflammatory drugs (NSAIDs) are widely used as inhibitors of cyclooxygenases (COX). The most common drugs in this family are ibuprofen, aspirin and naproxen. Several studies highlighted that the related gastro-intestinal toxicity could result from intercalation of NSAIDs in-between phospholipids and subsequent perturbations of the bilayer structure [46], including membrane thinning and fluidizing effects [47–49]. Interaction between NSAIDs and lipid bilayers is mainly driven by the fact that they all bear a carboxylic acid moiety that can be

deprotonated at relatively low pH values (*e.g.*, pK_a values of ibuprofen, aspirin and naproxen are 4.5-5.2, 3.5 and 4.2, respectively). It means that at physiological pH, the negatively charged forms predominate and can locate just below the polar head groups of lipid bilayers (regions 2 to 3), as seen theoretically and experimentally [48,50]. When MD simulations are carried out on the neutral form, NSAIDs are predicted to be much deeper in bilayers, lying between lipid chains close to the middle of membrane (regions 4-5) [48,49,51,52]. Membrane alteration may increase membrane permeability to H⁺, which may participate in rationalizing gastro-intestinal toxicity [47].

3.4 Antioxidants

Antioxidants have been extensively studied for their beneficial effects on human health, despite the fact that from a medical viewpoint, only a few applications exist, *e.g.*, usage in organ conservation [53,54]. Among other processes, antioxidants are capable of inhibiting lipid peroxidation, which requires location sufficiently deep inside lipid bilayer membranes, where oxidation occurs (propagation and termination stages). Several MD-based studies have rationalized the insertion of polyphenol antioxidants in lipid bilayers, with a preferred location in contact with the polar head group region (region 3), in agreement with experimental studies [55–58]. Structure-property relationships were thoroughly established, showing, *e.g.*, the role of OH groups at orienting the molecules towards membrane surface [59–62]. Methylation or hydrophobic moieties drive antioxidants deeper in membranes, increasing lipid peroxidation inhibition, as clearly confirmed theoretically for α -tocopherol (having one phenolic OH group, adjacent methyl groups and a long lipid tail) that penetrates deeper into lipid bilayers (regions 3-5) than most of polyphenols [63]. Additionally, it

is capable of 'flip-flop' from one to the other leaflet, increasing contact with lipid chains [63]. Ascorbic acid (or vitamin C) is also a very common antioxidant that partitions outside lipid bilayer, in contact with the water phase (region 2) [63]. Membrane complexity can also be taken into consideration, *e.g.*, the depth of penetration for α -tocopherol in bilayer strongly depends on lipid composition [64–66]. Also synergy effects between antioxidants were shown, by MD simulations [63], to occur inside lipid bilayer due to the formation of noncovalent complexes (Fig. 1), which may increase their total antioxidant activity [67,68].

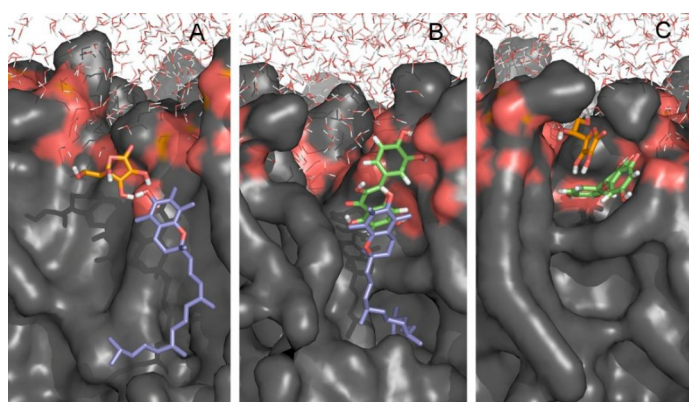


Fig. 1. Location of α -tocopherol, ascorbic acid and a prototypical polyphenol (quercetin) in a DOPC lipid bilayer.

3.5 Antiviral drugs

Adamantane derivatives such as amantadine, rimantadine and memantine are antiviral drugs widely used against influenza A. They are suggested to block the so-called M2 ion channel [69]. This process is partially attributed to the interactions of these drugs with the lipid bilayer surrounding the channel. MD simulations showed that both the protonated and deprotonated forms of adamantane derivatives preferentially locate in lipid bilayers, in contact with the polar head groups (region 3) [70,71]. MD simulations showed that at such a location, these antiviral compounds

disrupt the intramolecular interactions between choline and carbonyl groups in lipids, subsequently distorting significantly their conformations.

The photoactivated antiviral activities of hypericin and its brominated derivatives were shown to dramatically affect membrane cell by causing lipid peroxidation [72,73]. MD simulations were carried out for hypericin, mono- and tetra-brominated hypericin, showing a preferred location close to the polar head group region at the lipid/water interface (region 2) in a pure DPPC bilayer [73]. Such location was favored by the existence of several hydrogen bonds between the drugs and water molecules. The depth of penetration increased with the level of bromination of hypericin. Higher concentration of cholesterol also drove the drugs slightly deeper in the bilayer, suggesting a better capacity to cross membranes [72]. At high concentrations, hypericin molecules could also self-assemble to form strong noncovalent aggregates in both the water phase and the bilayer [72].

MD simulations showed that the oleuropein aglycone antiviral agent (from virgin olive oil) preferentially locates in the hydrophobic core of different lipid bilayers, *i.e.*, POPC / cholesterol and POPC / POPG (1-palmitoyl-2-oleoyl-sn-glycero-3-phosphoglycerol) / cholesterol [74]. This compound located deeper in the latter model due to stronger effects of the negatively charged lipids on the order parameters compared to zwitterionic ones. This antiviral agent affected the thickness of the bilayers as well as locations of phosphate atoms in the membrane, mainly for POPG-containing membranes.

3.6 Antimicrobial peptides

Due to their structural properties (amino acid composition, amphiphilic properties, cationic charges and small size) antimicrobial peptides (AMPs) are ideal candidates to

penetrate or cross cell membranes of microbes, either to affect them or to reach intracellular targets, respectively [75]. There are several mechanisms for AMPs to kill cells and four of which involve membrane interactions: i) disruption of the bacterial membrane structure; ii) pore formation; iii) membrane thinning; iv) translocation of the peptide across membrane; v) receptor inhibition; and vi) inhibition of nucleic acid synthesis [75–78]. MD simulations showed a high ability to picture what can be considered here as the first step of the mechanism for AMP antimicrobial action, namely the binding mode with membrane. Various AMPs (CM15, cyclo(RRWRF), piscidins, β -hairpin tachyplesins, bacteriocins such as plantaricin EF) were indeed theoretically confirmed to efficiently insert in lipid bilayers [78–83]. The role of hydrophobic effects, H-bonding and electrostatic interactions rationalize the peptide positioning. Due to the molecular weight of these peptide drugs, the physical chemical properties of membranes are much influenced, including fluidity, order parameter and Gibbs energy barrier of water penetration. Atomistic models revealed conformational flexibility of AMPs in lipid bilayers [79] but also the formation of aggregates that may influence lateral diffusion and membrane integrity [78,80,83].

4. Drug entrance into cytoplasmic media

4.1. Drug passive diffusion and permeation

Even though pores, vesicle formation or protein transporters may control influx, in particular for charge species or essential elements such as sugars and amino acids, unassisted (spontaneous) passive permeation through the lipid bilayers is the major drug influx process. Permeation could in principle be observed with fully sampled free MD simulations. As far as sufficient sampling is reached, free (unbiased) MD simulations allow prediction of permeability in terms of simple models, according to

number of crossing events. Crossing events and permeability through both pores and lipid bilayers were thereby predicted [84]. To improve statistics, these authors have counted the semipermeation events (crossing over one membrane leaflet). However, most of drugs passively permeate within at least several milliseconds [85], while the time scale that is accessible by unbiased MD simulation with nowadays-regular computational power is somewhat not more than several microseconds. It means that, for most of drugs, permeation is a rare event within the microsecond-time-scale, as reached by MD simulations. CG calculations allow accessing longer simulation time scale, as well as biased MD simulations (*e.g.*, *z*-constrained, Umbrella-sampling or metadynamics) that somehow "force" membrane-crossing events. The accurate computation of all aspects of passive permeation turned out to be a theoretical challenge [86], in which all-dynamical aspects of local solute-environment interactions have to be thoroughly described.

The "homogeneous solubility-diffusion" model can partially depict permeation. Here the process is decomposed into three stages, namely dissolution into the lipid bilayer, diffusion through membrane interior, and dissolution back to the surrounding environment (water) [87]. To make the description more realistic, the "inhomogeneous solubility-diffusion" model account for inhomogeneity (defects) in the membrane interior. Ideally any defect (even rare) should be taken into consideration, *e.g.*, transient pores favoring drug permeation. These formalisms are likely to provide a picture of the dominant mechanism for passive permeation through biological membranes. An elegant alternative approach, borrowed from polymer science, is to consider hopping transport via free volumes. This approach highlights the importance of evaluating all free volumes in membranes, a task for which MD is

ideally suited. This is particularly relevant to rationalize permeation of small molecules.

The evaluation of permeability coefficients should consider the Gibbs energy barriers required to cross the different sections of the lipid bilayer $\Delta G(z)$ profile along the z -axis (perpendicular to membrane surface), as well as the local diffusion coefficients $D(z)$. The global permeation then combines both $\Delta G(z)$ and $D(z)$ expressions within a single expression of the local resistance to membrane crossing:

$$R = \int_{z_1}^{z_2} R(z) dz = \int_{z_1}^{z_2} \frac{\exp[\Delta G(z)/kT]}{D(z)} dz = \frac{1}{P} = \frac{\Delta c}{J} \quad (1)$$

where P is the predicted membrane permeability coefficient; Δc is the concentration difference between z_1 and z_2 ; and J is the flux of solute from z_1 to z_2 , *i.e.*, through membrane.

The Gibbs energy profile provides the $\Delta G(z)$ values (Scheme 2). Although it is inaccessible to the experimental techniques in an atomistic detail, several theoretical methods are available. Gibbs energy profile is alternatively called potential of mean force (PMF), as the main objective is to calculate the energetic cost required by the drug to follow its way through the membrane. Some methods indeed evaluate the average force exerted on a drug to be constrained at a given depth, specifically z -constraint method.

Concerning the diffusion coefficients $D(z)$, it is highly dependent on drug location and it strongly changes through membrane crossing. Again, if correctly employed, (biased or unbiased) MD simulations are the way, how to depict the local effects driving $D(z)$. During the z -constraint simulations, the forces applied to drug are monitored. The force autocorrelation function then allows calculation of the friction coefficient $\xi(z, t)$, obtained from the difference $\Delta F(z, t)$ between the instantaneous force and the averaged force acting on the drug:

$$\xi(z, t) = \frac{\langle \Delta F(z, t) \cdot \Delta F(z, t=0) \rangle}{kT} \quad (2)$$

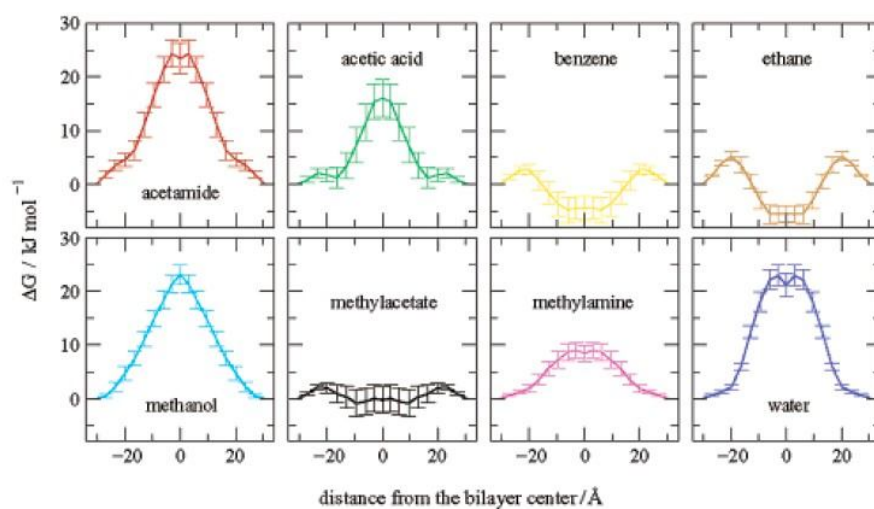
The local diffusion coefficient is then given by:

$$D(z) = \frac{kT}{\xi} = \frac{(kT)^2}{\int \langle \Delta F(z, t) \cdot \Delta F(z, t=0) \rangle dt} \quad (3)$$

The atomic-level simulations intrinsically account for all intermolecular interactions, as far as sufficient sampling is reached.

The permeation of eight small organic compounds with various polarities (acetamide, acetic acid, benzene, ethane, methanol, methyl acetate, methylamine, and water) was evaluated using the Eqn. 1-3 and MD simulations [87,88]. The Gibbs energy profiles confirmed high-energy barriers in the middle of the membrane for polar (hydrophilic) compounds, whereas more apolar (hydrophobic) compounds showed barrier only in the polar head group region (Fig. 2A). The same trend was confirmed for resistance to permeation. The diffusion coefficient was shown to be sensitive to membrane crossing, namely: i) decreasing in the polar head group region; ii) being uniform in between lipid chains; and iii) increasing when reaching the middle of the membrane as a result of the presence of free space (Fig. 2B). Interestingly, diffusion coefficients turned out to be somewhat isotropic, as seen when comparing the predicted lateral and normal (z-axis) diffusion coefficients of water molecules in a DPPC bilayer [87]; this isotropy should however be considered with care for larger molecular-weight systems. Although the general trend for the predicted permeabilities was correct, their predicted values were roughly higher by 1 order of magnitude with respect to experimental values [87,88].

(A)



(B)

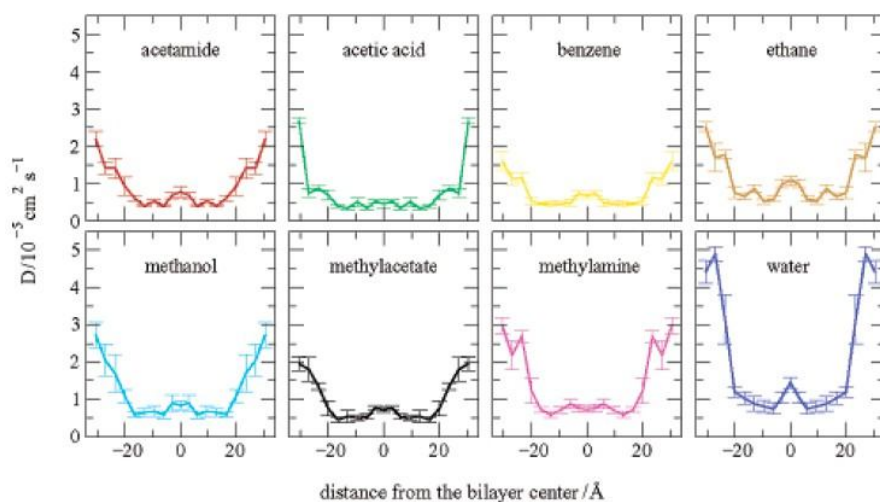


Fig. 2. Predicted (A) Gibbs energy profiles and (B) diffusion coefficients of eight derivatives. Adapted from Ref. [88].

Biased MD simulations were also used to predict passive permeability of various drugs [89], *e.g.*, a nifedipine analogue (an early attempt performed by a 4-ns MD simulation in DMPC bilayer) [90]; valproic acid [91]; β -blockers [92]; psoralen derivatives [93]; hypericin [94]. It must be stressed that to reach similar estimations from both theoretical simulations and experimental measurements is still a delicate issue, even more complex because different systems and different conditions are often

used. However, relative permeability seems to be fairly predicted, which is particularly useful when dealing with families of drugs obtained from a lead compound [89,95].

More recently, a multiscale approach was proposed, in which compatible (mainly in terms of electrostatics) CG and atomic-level force fields were used on a 1,2-dimyristoyl-sn-glycero-3-phosphocholine (DMPC) lipid bilayer model [96]. Here the same list of eight organic solutes as used in Ref. [97] was considered. Within an inhomogeneous solubility-diffusion formalism, the permeability values were within two orders of magnitude from the experimental values. However, this approach has appeared particularly promising as it allows working on larger membranes (thus minimizing artifacts induced by the boundary conditions), while at the same time ensuring better sampling. With this approach, the diffusion coefficients in the middle of the bilayer were higher than in the water phase, contrary to what was obtained with the standard atomic-level MD simulations [97]. However this can be an inherent artifact of CG simulations, as in this case a CG bead is represented by four water molecules. The transmembrane permeations of two steroid hormones (progesterone and testosterone) were evaluated using the same methodology [98]. The proposed limiting step for membrane crossing was that related to the highest Gibbs energy barrier required to cross the membrane, the transversal diffusion coefficient being roughly constant along the bilayer. The estimated lateral coefficients were lower than those along the normal z-axis. This study also highlighted the contribution of other membrane perturbation occurring during drug crossing, in particular intrusion of water molecules rather deep in the bilayer, in interaction with the drug. Regarding the size of the two steroid hormones, a particular attention was also paid to orientational effects.

Along this line, a recent work evaluated permeability coefficients using bias-exchange metadynamics [99]. To ensure better sampling of the whole hypersurface (including conformational and orientational variability of the drug), four collective variables were considered to benchmark the permeation of ethanol through a POPC bilayer. Among these variables was the position of the center of mass of ethanol along the *z*-axis, but also distances between specific moieties of both molecules. A permeability coefficient of 6×10^{-2} cm/s was obtained in a reasonable concord with performed unbiased MD simulations using 60 ethanol molecules in a POPC bilayer made of 128 lipids, corresponding to 8 permeation events, *i.e.*, a mean permeation time estimation of 2.3 ± 1.1 μ s [99].

4.2. Facilitated diffusion mediated by membrane transport protein

An alternative way for drugs to influx is by facilitated diffusion, which is mediated by a superfamily of membrane transport proteins named solute carrier (SLC) [100,101]. This influx is a secondary active transport, which means that it only uses the energy stored in electrochemical gradients. More than 380 different SLC proteins, divided into 52 families, have been annotated in the human genome [102–107]. Most of the SLC transporters can be grouped into two large structural folds in membrane transporters, namely major facilitator superfamily (MFS) and neurotransmitter:sodium symporter (NSS) or LeuT-like fold [105]. Here a particular attention is paid to the MFS superfamily since only those influx transporters are described as being of "emerging clinical importance" in drug discovery [101] by the International Transporter Consortium [108].

In silico studies on human MFS transporters are rather limited, mainly due to the absence of X-ray crystallographic structures. However, homologous models (mostly bacterial) have provided substantial insights in SLC transporter functions [106,109–

111]. It is important to note that the surrounding membrane is not necessarily involved directly in the large-scale events; however, it naturally restrains protein movements to some extents. The use of protein models embedded in lipid bilayers is thus mandatory to simulate the transport cycle. In this section, we will only focus on *in silico* studies in which the membrane is explicitly included.

MFS transporters all adopt similar secondary structure consisting of twelve transmembrane helices (TM) organized into two N-terminal (TM1-TM6) and C-terminal domain (TM7-TM12) substructures (Fig. 3A). The X-ray crystallographic structures supported by computational studies described two main conformations, namely inward- or outward-facing (IF and OF, respectively, see Fig. 3B). The drug/substrate transport across the membrane is thus driven by large-scale conformation changes from one to the other state, following a "clamp-and-switch" model of function [112]. This suggests the existence of intermediate occluded conformations in IF- and/or OF-states, later confirmed by the X-ray structure of the Xylose:H⁺ symporter (Xyle) [113,114]. Such mechanical pathway was also suggested by means of steered and targeted (biased)-MD simulations in several transporters (namely, xylose Xyle [115], glucose⁴ GLUT1 [117] and lactose LacY [118–120] transporters). It is worth noting that the "clamp-and-switch" model is actually a recent enhancement of the "rocker-switch" model [112]. Particular attention should be paid to a recent computational study on the glycerol-3-phosphate:phosphate transporter (GlpT) [121]. Although this transporter drives efflux, this study provides useful insights in the deep understanding of influx since all MFS transporters are very

4

It must be stressed that this model was built by homology modeling using Xyle as reference [115]. The theoretical results agreed with the recently crystallized human GLUT1 in the IF-state [116].

likely to share the "clamp-and-switch" mechanical pathway. The complete potential energy surface of the transport process was elucidated using a MD iterative protocol including biased-MD simulations and string method with swarm of trajectories.

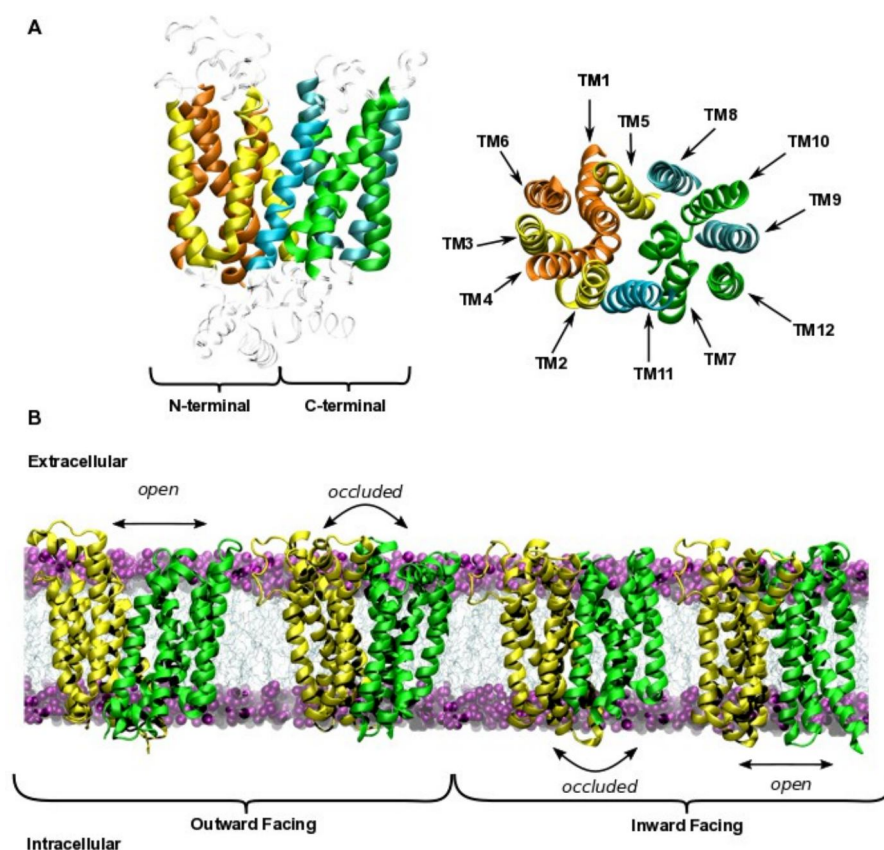


Fig. 3. (A) X-ray structure of Glucose transporter type 3 (PDB-ID: 4ZW9 - GLUT3 [122], a detailed structural description is also available in Ref. [112]). (B) Examples of the several conformations detailed in the “clamp-and-switch” model from X-ray structures. Occluded-OF and occluded/open-IF structures were taken from X-ray structures of Xyle transporters (PDB-ID: 4GBY [114], 4JA3 [113] and 4JA4 [113], respectively); open-OF structure was taken from the GLUT3 transporter. N- and C-terminal domains are depicted in yellow and green, respectively.

The complete Gibbs energy landscape of transport cycle was then calculated with and without substrate underlining the "catalytic" role of the substrate. The existence of occluded-IF and -OF states was also confirmed to be thermodynamically stable states if and only if the substrate is bound to the transporter. This should explain why

occluded states are so challenging to observe experimentally, since the substrate is not always present in crystal structures. Furthermore, details about the role of specific TMs along the transport cycle were investigated to correlate local and global conformational changes. The role of TM1 and TM7 to the periplasmic gating process was stressed as observed in GLUT1 influx transporter [117], whereas TM4, TM5, TM10 and TM11 were shown to be involved in the cytoplasmic gating. Such observations have strengthened the hypothesis of the asymmetrical global conformational changes along the transport cycle of MFS.

Joint experimental and computational studies are likely to elucidate more local events. For example in H⁺-cotransporters (*e.g.*, LacY and XyleE), the H⁺-conduction (electrochemical gradient) from the periplasmic to cytoplasmic side is shown to provide the energy required to the transport cycle. Such conduction along amino acid side chains (mainly Glu, Asp and His) proceeds by proton transfer reactions that locally change charge states of protonatable residues, leading to salt-bridge breaking/formation that trigger the IF-to-OF transition [115,119,120,123,124].

Although MFS transport cycles have been extensively investigated theoretically, only a few studies have tackled the direct influence of the surrounding membrane. Yet, studying lipid-protein supramolecular assemblies [120,125] as well as considering membrane composition [120] have repeatedly been suggested to be of crucial importance. Another currently missing aspect is the direct study of human transporters of clinical interest. Only three human MFS transporter structures have been elucidated so far [116,126]. To the best of our knowledge, either homolog (*e.g.*, with PEPT-1/2, see [127]) or homology-modeling-made (*e.g.*, with PEPT-1 and OAT1, see Refs. [128,129]) transporters were used so far. Interestingly, the dynamic of the overall mechanism of PEPT-1 was found to be very close to that of LacY

although they belong to two different distant SLC families. This supports the hypothesis that MFS transporters exhibit large-scale conformational transitions during transport cycle regardless substrates. MFS transporters mainly differ in local binding events that govern their substrate selectivity [127].

5. Membrane proteins for biotransformations

Drug-membrane interactions can be altered via biotransformation processes. Usually we distinguish two phases (I and II) of biotransformation of drugs [130]. In both phases, membrane-bound proteins are involved, *e.g.*, cytochrome P450 (CYP) in phase I, uridine 5'-diphospho-glucuronosyltransferase (UGT) in phase II, or multidrug-resistance proteins later in excretion.

Phase I biotransformation of majority of drugs, is executed by CYP enzymes [131]. CYP enzymes are found in a majority of living organisms [132], but while bacterial CYPs are soluble enzymes, eukaryotic ones are attached to the membrane of either endoplasmic reticulum or mitochondria, and to the a much lower extent in the Golgi apparatus, peroxisomes or plasma membranes [133]. The sequence length of mammalian CYPs is around 500 amino acids including a ~20-25 amino acid long N-terminal transmembrane helix attached to a catalytic domain encompassing heme prosthetic group.

The important role of membrane topology in action of mammalian CYP was shown first by molecular simulations connecting together fragmental pieces of experimental evidences. The first atomistic membrane models of human CYP2C9 anchored to phosphatidylcholine bilayers [52,134] were constructed using homology modeling of the human CYP2C9 sequence over available crystal structures of catalytic domain [135,136] with added N-terminal helix. Those preliminary models

were then positioned in different orientations into a lipid bilayer model; the whole molecular assembly was further equilibrated with 100 ns+ long MD simulations. Equilibrated consensus orientation showed that not only transmembrane N-terminal helix but also F/G loop of the catalytic domain was immersed into the membrane as it was confirmed by experimental evidence from epitope labeling, tryptophan fluorescence scanning and others [137–139]. CYP membrane orientation was later supported by additional MD simulations of other CYP family members [140–145], and recent experiments [146–148], including whole *Saccharomyces cerevisiae* CYP51 structures [147]. Importantly, CYP positioning and orientation allow drugs to pass from the membrane into the active site of CYP via a membrane-facing active site access channel, whereas more polar drugs and metabolites can access to, or egress, the active site via the cytosol-facing channel, (Fig. 4) which was recently supported by evaluation of the free energy of passage of metabolite from the active site by several channels with metadynamics MD simulations [149]. The role of membrane on function of P450 enzyme in drug biotransformation was recently overviewed by Backes et al. [150].

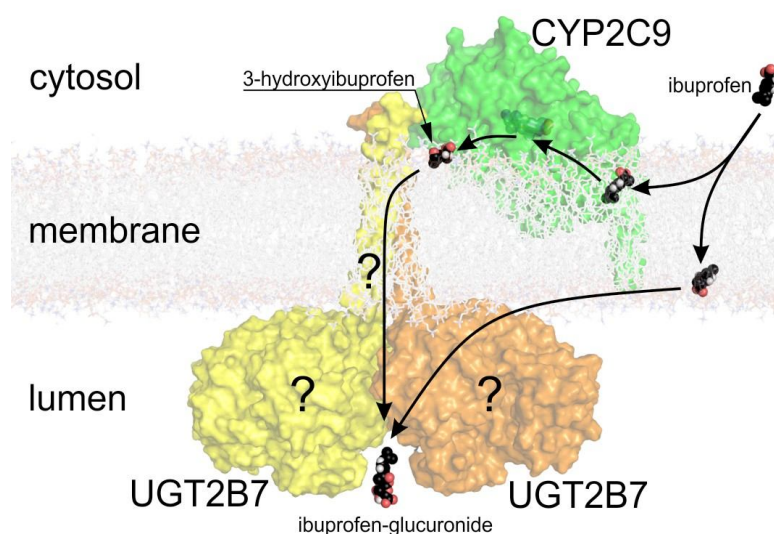


Fig. 4. Scheme of biotransformation of ibuprofen with membrane-bound CYP2C9 and UGT2B7 enzymes. Ibuprofen is transformed by cytochromes P450 (CYP2C9, CYP2C8, CYP2C19, CYP3A4) or UDP-glucuronosyltransferases (UGT2B7, UGT2B4, UGT1A1, UGT1A3, UGT1A9) [151] to hydroxyibuprofens or ibuprofen-glucuronides, respectively. CYP2C9 model was modelled in DOPC membrane according to Berka et al. [52]. UGT2B7 was modeled according to Laakonen et al. [152] from UGT2B7 CTD domain [153] using I-TASSER server [154] and Modeller 9.14 software [155]. Membrane topology and proposed dimeric organization of UGT2B7 are depicted as an arbitrary illustration of known experimental data from Ref. [156]. Also the transfer route of glucuronidation of hydroxyibuprofens is unknown. Ibuprofen biotransformation pathway was taken from Drugbank (www.drugbank.ca) [157]. CYP structure was modelled according to Ref. [52]

Metabolites from CYP biotransformations are usually more polar than the parent substrates. A statistical analysis carried out over the phase I metabolites showed that CYP products of hydroxylation and dealkylation reactions prevail. As a result, phase I products tend to have lower average molecular weight by 20–25 Da and tend to reduce lipophilicity; only a minority of metabolites (4 – 8%) being more lipophilic than their parents due to some dealkylation reactions [158]. It was indeed shown by theoretical calculations that those metabolites are not as deeply immersed in lipid bilayer as their parent compounds. Moreover, affinity of metabolites towards lipid bilayer is lower whereas the barriers for passive membrane crossing are higher than for substrates [140,159].

The most important enzymes catalyzing phase II reactions are UGTs, glutathione S-transferases (GSTs), N-acetyltransferases (NATs), and sulfotransferases (SULTs) [160]. Of those, the major drug metabolizing enzymes are from UGT1 and UGT2 subfamilies. UGT enzymes transfer a glucuronic acid to the drug forming a glycosidic bond [161,162]. The complete human UGT crystal structure is not available, but the crystal structure of the UGT2B7 C-terminal domain was published [153]. This structure together with templates for the missing N-terminal domain from various

sources (plant UGT enzymes, bacterial glycosyltransferases and macrolide transferases) have served for construction of several atomistic UGT models [152,160,163–165]. Albeit none of the models was built as cast in a membrane, they were used to identify the effects of amino acids in UGT1A1, whose mutations are known to play a role in the Crigler-Najjar type I or II syndromes or the Gilbert syndrome [152], or to assess substrate specificity between UGT1A9 and UGT1A10 [164]. The full atomistic membrane model of UGTs is however still missing.

Statistical analysis over the phase II metabolites showed rather systematic modifications of the physicochemical properties of biotransformed drugs and drug-like molecules. Conversely to phase I reactions, phase II conjugation reactions lead to a substantial gain in molecular weight (145 amu on average). Furthermore, phase II reactions lower $\log P$ values of drugs by 1.4 log units on average [158]. This agrees with previous analysis of membrane positioning of quercetin metabolites by means of MD simulations [166]. The conjugated substituent groups pulled quercetin moiety toward membrane surface. Overall, biotransformation reactions usually weaken drug-membrane interactions, leading to the excretion of drug in a final phase.

6. Efflux transport toward drug resistance

Drug extrusion (efflux) mainly occurs through membrane protein transporters. To the best of our knowledge, human efflux transporters are from the SLC and ATP-binding cassette (ABC) families.

MFS are a major class of SLC transporters in drug disposition. As said above (Section 4.2) they work following the "clamp-and-switch" mechanism that is actually not a unidirectional process; it means that this process can drive both influx (see Section 4.2) or efflux (*e.g.*, GpT transporter [121,167–169]). MD simulations may however support some discriminations between both processes, *e.g.*, highlighting

asymmetry in the influx or efflux substrate binding cavity that is likely to modulate drug transport specificity [170].⁵ A particular attention should also be paid to the MATE (multi-antimicrobial extrusion protein) transporter, which represents the only efflux SLC-type transporters considered of emerging clinical importance by the International Transporter Consortium [101]. Although a few theoretical investigations have been achieved [171], they can hardly be transposed to the human homolog functions (MATE-1 and MATE-K). This is complicated by the fact that no X-ray crystallographic structure is available for these human transporters so far. The rest of this section will review the computational efforts made to rationalize the main efflux process, namely through the ABC transporters.

Human ABC transporters are active exporters [172–174] that share a common architecture including two transmembrane domains (TMDs) and two cytoplasmic nucleotide-binding domains (NBDs, see Fig. 5A). TMDs are mainly responsible for binding of drugs and their release into the periplasmic (extracellular) compartment. NBDs bind ATP molecules and catalyze their hydrolysis. As observed for MFS transporters (Section 4.2), ABC-transporters were also crystallized in both their IF and OF-states.

5

It must be stressed that drug-protein binding affinities can be assessed by Molecular Mechanics / Poisson-Boltzmann or Generalized Born Surface Area (MM/PBSA or MM/GBSA); however these methods are not described here as drug-protein binding is out of the scope of this review.

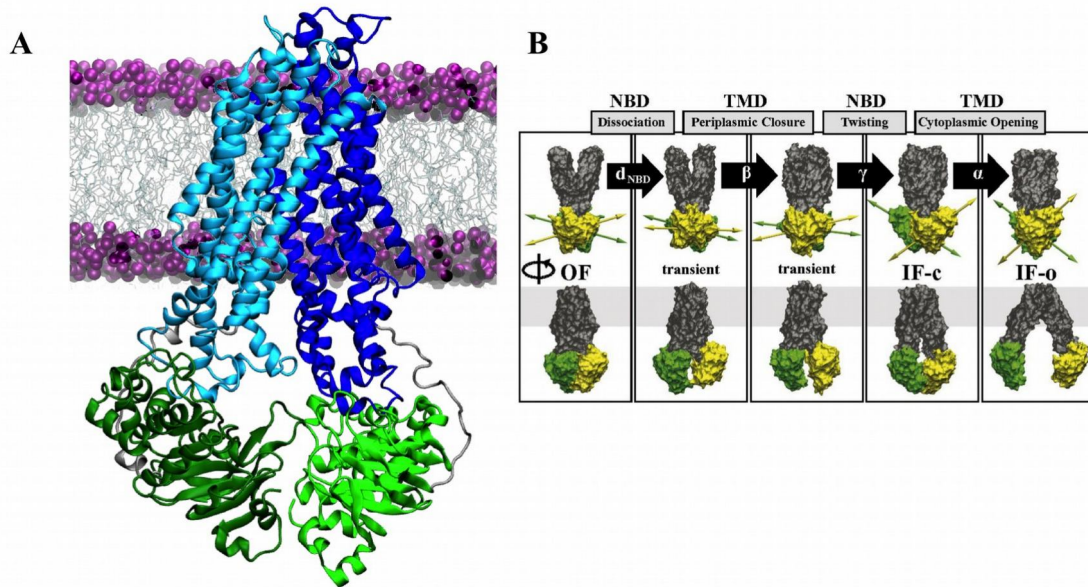


Fig. 5. (A) X-ray structure of a ABC-transporter (PDB-ID: 3G5U, P-glycoprotein [175]). TMDs and NBDs are depicted in bluish and greenish colors, respectively. (B) Proposed sequential OF-to-IF pathway of the MsbA transporter (reproduced from Ref. [176] ©2013 by National Academy of Sciences)

The IF-to-OF transition is the actual drug efflux mechanism; it has also been theoretically studied to reach a comprehensive atomic-scale understanding. NBDs have been suggested to be more than a simple energy provider (ATP hydrolysis). Starting from IF-conformation, the two NBDs proceed to a rigid body motion that keeps the TMDs' alignment [177]. This leads to the NBD-NBD noncovalent dimerization [109,178], which was predicted to trigger the further large-scale conformational changes [179]. The computational picture of the NBD-NBD supramolecular assembly shows the major role of dispersive and electrostatic interactions [180,181]. The further steps lead to OF-state, which are still a computational challenge due to coupling to the ATP-hydrolysis reaction. This would ideally require highly demanding computational effort, *e.g.*, hybrid QM/MM calculations to accurately describe kinetics of ATP-hydrolysis. Another approach (MD-based only) to describe the impact of ATP-hydrolysis is to simulate a two-step

mechanism: (i) ATP binding; then (ii) replace ATP by ADP and prolong the simulation [182,183]. Nevertheless, the complete supramolecular movement of both the protein and the membrane has not been described yet.

A relevant example of the computational contribution to the understanding of overall large-scale OF-to-IF transitions has recently been achieved on a bacterial ABC lipid flippase model (Msba) by biased-MD simulations [176,184]. In this very case (*i.e.*, OF-to-IF transition), no ATP hydrolysis is required, making the use of MD simulations particularly adapted as only conformational changes have to be figured out. A plausible sequential pathway has been proposed: i) increase of the inter- NBD-NBD distance; ii) TMD β -opening; iii) NBD γ -twisting; and iv) TMD α -opening (see Fig. 5B, for definition of α , β , γ angles). The key role of NBDs was thus pointed out since their dissociation was predicted to trigger the OF-to-IF transition. Also the third step (NBD γ -twisting), so-called the "doorknob" model, requires a careful description. It increases electrostatic repulsive interactions at the NBD-NBD interface leading to the NBD dissociation by opening TMD (α -opening), required to reach the IF-state [176].

MD simulations have also described some other key features of ABC-transporters. The high flexibility of the TMD within the IF-state has been suggested to allow drug inclusion into the transporter binding site directly from the inner membrane [185]. The MD framework is also currently the only tool capable of describing the role of atomic lipid-protein interactions as also shown for SLC transporters. Even though much work remains to be done, lipids have been shown to allow the reorientation of aromatic side chains and stabilize the protein in the membrane [185–187].

7. Membrane composition

The composition of cells and organelles' membranes is much more complex than simple bilayers made of a single phospholipid type; its composition and the related structure are pharmacologically crucial. It has been shown both experimentally [188] and theoretically [94,189,190] that the composition and especially lipid phase significantly affect drug membrane permeability or partitioning. The permeability through a fluid membrane is significantly higher than the permeability through an ordered membrane [188]. MD simulations can provide a correct description of the lipid bilayer phases, reproducing the phase transition temperature (T_m) [191,192], as well as order parameters obtained by NMR static splitting quadrupole [193]. Further, the lipid membrane composition was shown to affect the activity [194] or the orientation [195] of the membrane proteins.

Cholesterol is a particularly determinant ingredient; in animal cells it represents up to 20-50% of the bilayer and may control *e.g.*, fluidity, rigidity. Theoretical chemistry studies have extensively investigated its role. MD simulations enable some general conclusions to be drawn, *i.e.*, cholesterol addition: i) increases both thickness and rigidity of bilayers and decreases fluctuations [191,196,197]; ii) modify lateral packing [197,198]; iii) increases the order of initially disordered phase, whereas it is known to decrease order of ordered phases [199,200]; iv) decreases area per lipid [198,201]; v) drives, together with temperature, the formation of the liquid ordered (L_o) phase [198]; vi) induces phase separation [191] and the formation of (nano)-domains of lipids [202], also as suggested by lateral pressure heterogeneities [196,197]. It is unclear whether cholesterol is homogeneously distributed in the membranes, but it partitions better in between saturated lipids because the double bond precludes tight packing due to curved shape of lipids. There is no influence of cholesterol in the middle of the membrane. The lateral organization of cholesterol

molecules is driven by repulsive interactions between them, which are of entropic origin mainly (as enthalpy decreases when packing increases) [203]. Packing that is related to free volumes and van der Waals contact can elegantly and efficiently be described by V_{tail} [189], *i.e.*, the potential interaction energy between the lipid atoms in the lipid tail region (Lennard-Jones and short-range Coulomb potentials between all pairs of atoms). In the presence of cholesterol, V_{tail} decreases, thus increasing van der Waals contacts and packing [189].

Cholesterol is usually described to reduce the permeability. However, a thorough understanding at the atomic-level has appeared crucial. When cholesterol concentration increases, the energetic barriers increase in the lipid tail region [189], due to an increase in van der Waals contacts between lipid tails and cholesterol molecules. In other words, inside the bilayer, cholesterol increases packing, so it decreases both the amount of free volumes and area per lipid. It means that those van der Waals contacts must be broken to enable penetration of a given drug, which leads to a permeability decrease in this region [203,204]; the effect is even stronger for large solutes. Conversely, in the head group region, cholesterol addition increases distances between polar head groups, thus facilitating deeper insertion (increase permeation). These opposite effects of cholesterol in the different regions of the bilayer (bell-shape of the permeability-dependence according to the region of the bilayer) make that cholesterol influence depends on drug polarity, *i.e.*, it may facilitate permeation for compounds for which the barrier is localized in the head group region [204]. In other words, cholesterol addition induces: i) permeability decrease for polar compounds; and conversely ii) permeability increase for hydrophobic compounds. The size of the head group is also important (*i.e.*, permeability is more sensitive to cholesterol addition to lipid bilayers with small head groups) [189].

Small molecules and drugs are also known to affect membrane lateral organization, thus reshaping membrane domains. Even though no general trend based on chemical-physical properties has been elucidated so far, it has been recently shown in DPPC / dilinoeoyl-phosphatidylcholine (DLiPC) / cholesterol membrane with simple hydrophobic compounds that: i) aromaticity of compounds significantly affects membrane organization and cholesterol repartition; and ii) remodeling depend neither on size nor on cyclic nature of compounds [205]. Such observations agree with the crucial role of van der Waals interactions (*e.g.*, π - π dispersive interactions) on the shape of membrane domains.

Sphingolipids (including sphingomyelin) are also important ingredients of lipid bilayers. Sphingomyelin/cholesterol mixtures appeared to be more packed than DOPC/cholesterol [197]. In ternary lipid mixtures (DPPC/DLPC/cholesterol) containing saturated and polyunsaturated lipids, the coexistence of L_o/L_d phases was observed below T_m [201]. As expected, L_o and L_d domains were composed of saturated lipids / cholesterol and unsaturated lipids, respectively. In this case, cholesterol appeared to drive the lateral separation of the lipid phase domains [201]. Inhomogeneity in L_o regions was theoretically confirmed in other lipid ternary mixtures, in which the sub-structures were composed of saturated lipid chains, oriented parallel to the lipid bilayer normal with locally hexagonal order [206]. Saturated acyl chain indeed showed more ordering and less flexibility with respect to unsaturated chains [207].

To access larger systems and longer time scales, biased-MD and CG simulations can be used, in particular to better rationalize phase separation and coexistence of L_o/L_d but also gel/ L_o or phases. By doing so, a micro-emulsion-type state (formed with nanometer-sized L_o domains in an L_d environment) was shown to be probable

[208]. Domains could be stabilized by the mismatch of curvatures between both L_o and L_d phase monolayers, generating elastic tensions that decrease the line tension between the two phases. In CG simulations, symmetric leaflets of ternary mixtures exhibited L_o/L_d phase separation [209]. The inter-leaflet association of nano-domains was investigated by CG simulations, and key intermolecular interactions were identified [184,186,191,192]. In order to model realistic membranes, symmetric and asymmetric bilayer models were constructed using CG simulations. These models consisted of seven different lipids including GM3 glycolipids in the outer leaflet and an anionic lipid (PIP2) in the inner leaflet [211]. In the outer leaflet, GM3 glycolipids were strongly arranged together, leading to order clustering and nano-domain formation. The lateral distribution of lipids in the inner leaflet appeared more random with small domains composed of PIP2. A slow (lateral) diffusion was observed for most lipids, especially for GM3, together with flip-flops of cholesterol. A study of the glycosphingolipid GM1 and the palmitoyl sphingomyelin PSM in ternary and quaternary lipid bilayers also showed spontaneous phase separation (Fig. 6) [212]. Umbrella sampling simulations and CG simulations also predicted that cholesterol flip-flop was faster in polyunsaturated than in saturated bilayers [213]. Lipid composition and the degree of unsaturation of the lipids indeed modified local membrane curvature [214,215]. Finally, salt concentrations (NaCl) and water showed a significant impact on dynamic and structural properties of binary mixtures and stabilization of nano-domains [211,216].

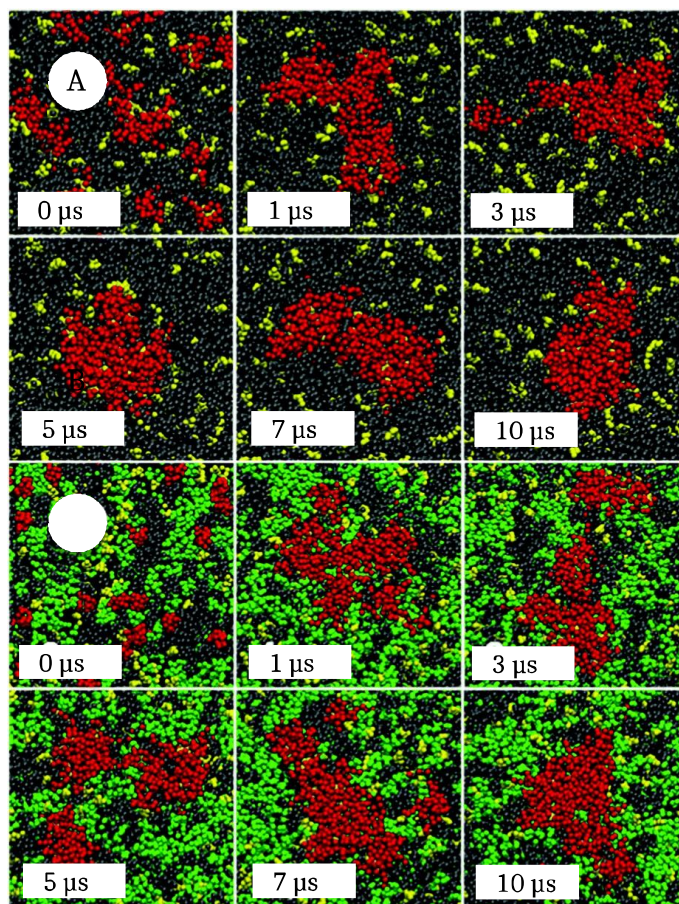


Fig. 6: Formation of nano-domains in (A) ternary and (B) quaternary mixtures. GM1, POPC, PSM and cholesterol are represented in red, grey, green and yellow, respectively. Adapted from Ref. [212].

8. Conclusion

In conclusion, standard atomic-level, biased and CG-MD simulations are sets of theoretical tools that are now capable of predicting drug passages through (increasingly realistic) biological membranes. The recent developments and achievements have paved the way towards *in silico* pharmacology. Although, benchmarking and comparison to experiments are still mandatory to reach a predictive usage in real-life applications (*i.e.*, to support clinical decisions), this is no longer science fiction. The pharmacological processes are described in an increasingly realistic way. Moreover, atomic-level MD simulations are building a picture of

insertion, interaction, crossing, inhomogeneities with an atomic resolution, which usually allows identification of forces driving the processes with a remarkable accuracy. The reader should bear in mind the computational resources required for the different simulations, which can be exemplified by providing estimation of computational time for a series of representative systems (Table 1).

Table 1: Simulation time (in ns) for two representative molecular systems with three types of force field with regular computational facilities (8 CPUs) achievable within a day.

	Lipid bilayer made of 128 POPC + box of water	Protein (ca. 65 kDa) embedded in lipid bilayer + box of water
All-atom MD simulations	10	1
United-atom MD simulations	20	2
CG simulations	2000	200

Still membrane organization vs. lipid composition has to be improved from the point of view of intermolecular interactions. Up to now, only CG simulation succeeded in visualizing phase separation or lipid segregation. However, the use of CG beads naturally overestimates some specific intermolecular interactions (*e.g.*, between lipids, with solvent), most probably lowering some enthalpic contributions with respect to entropic contribution. In this context, joint CG and all-atom MD approaches has appeared promising.

Also, the atomic-scale description of large conformational changes is still a major challenge. This includes description of membrane curvature, which can be partially caught by CG simulations, which, *e.g.*, can simulate the spontaneous endocytosis and provide crucial information of nanoparticle shape and size that enable an efficient wrapping by membrane [217–219]. Other

large conformational changes in pharmacological processes are those occurring in membrane proteins, for which biased MD simulations are highly promising techniques.

Acknowledgements: The authors thank Region Limousin, CALI, Czech Science Foundation (P208/12/G016), Ministry of Education, Youth and Sports of the Czech Republic (project LO1305), Operational Program Education for Competitiveness-European Social Fund (project CZ.1.07/2.3.00/20.0058 of the Ministry of Education, Youth and Sports of the Czech Republic), Marie Curie Research Training Network CHEBANA, FP7 ITN 2010-264772.

References

- [1] Wiley: Drug-Membrane Interactions: Analysis, Drug Distribution, Modeling, Volume 15 - Joachim K. Seydel, Michael Wiese, Raimund Mannhold, et al, (n.d.).<http://eu.wiley.com/WileyCDA/WileyTitle/productCd-3527616497.html>.
- [2] S. Balaz, Modeling Kinetics of Subcellular Disposition of Chemicals, *Chem. Rev.* 109 (2009) 1793–1899. doi:10.1021/cr030440j.
- [3] G.M. Cooper, *The Cell*, 2nd edition. A Molecular Approach, 2nd ed., Sinauer Associates, Sunderland, MA, USA, 2000.
- [4] S.J. Singer, G.L. Nicolson, The fluid mosaic model of the structure of cell membranes., *Science.* 175 (1972) 720–31.
- [5] I. Iwai, H. Han, L. den Hollander, S. Svensson, L.-G. Ofverstedt, J. Anwar, J. Brewer, M. Bloksgaard, A. Laloef, D. Nosek, S. Masich, L. a Bagatolli, U. Skoglund, L. Norlén, L. Den Hollander, S. Svensson, L.-G. Ofverstedt, J. Anwar, J. Brewer, M. Bloksgaard, A. Laloef, D. Nosek, S. Masich, L. a Bagatolli, U. Skoglund, L. Norlén, The Human Skin Barrier Is Organized as Stacked Bilayers of Fully Extended Ceramides with Cholesterol Molecules Associated with the Ceramide Sphingoid Moiety., *J. Invest. Dermatol.* 132 (2012) 2215–2225. doi:10.1038/jid.2012.43.
- [6] Y. Arinaminpathy, E. Khurana, D.M. Engelman, M.B. Gerstein, Computational analysis of membrane proteins: the largest class of drug targets., *Drug Discov. Today.* 14 (2009) 1130–5. doi:10.1016/j.drudis.2009.08.006.
- [7] J.P. Overington, B. Al-Lazikani, A.L. Hopkins, How many drug targets are there?, *Nat. Rev. Drug Discov.* 5 (2006) 993–996. doi:10.1038/nrd2199.
- [8] F.R. Salsbury, Molecular Dynamics Simulations of Protein Dynamics and their relevance to drug discovery, *Curr. Opin. Pharmacol.* 10 (2010) 738–744. doi:10.1016/j.coph.2010.09.016.
- [9] S. Nagar, K. Korzekwa, Commentary: Nonspecific Protein Binding versus Membrane Partitioning: It Is Not Just Semantics, *Drug Metab. Dispos.* 40 (2012) 1649–1652. doi:10.1124/dmd.112.046599.
- [10] S. Endo, B.I. Escher, K.-U. Goss, Capacities of Membrane Lipids to Accumulate Neutral Organic Chemicals, *Environ. Sci. Technol.* 45 (2011) 5912–5921. doi:10.1021/es200855w.
- [11] D. Smith, P. Artursson, A. Avdeef, L. Di, G.F. Ecker, B. Faller, J.B. Houston, M. Kansy, E.H. Kerns, S.D. Krämer, H. Lennernäs, H. van de Waterbeemd, K. Sugano, B. Testa, Passive Lipoidal Diffusion and Carrier-Mediated Cell Uptake Are Both Important Mechanisms of Membrane Permeation in Drug Disposition, *Mol. Pharm.* 11 (2014) 1727–1738. doi:10.1021/mp400713v.
- [12] D. Bassolino-Klimas, H.E. Alper, T.R. Stouch, Solute diffusion in lipid bilayer membranes: An atomic level study by molecular dynamics simulation, *Biochemistry (Mosc.)*. 32 (1993) 12624–12637. doi:10.1021/bi00210a010.
- [13] D. Bassolino-Klimas, H.E. Alper, T.R. Stouch, Mechanism of Solute Diffusion through Lipid Bilayer Membranes by Molecular Dynamics Simulation, *J. Am. Chem. Soc.* 117 (1995) 4118–4129. doi:10.1021/ja00119a028.
- [14] S.J. Marrink, H.J.C. Berendsen, Permeation Process of Small Molecules across Lipid Membranes Studied by Molecular Dynamics Simulations, *J. Phys. Chem.* 100 (1996) 16729–16738. doi:10.1021/jp952956f.
- [15] R.O. Dror, R.M. Dirks, J.P. Grossman, H. Xu, D.E. Shaw, Biomolecular Simulation: A Computational Microscope for Molecular Biology, *Annu. Rev. Biophys.* 41 (2012) 429–452. doi:10.1146/annurev-biophys-042910-155245.

- [16] M. Karplus, J.A. McCammon, Molecular dynamics simulations of biomolecules, *Nat. Struct. Mol. Biol.* 9 (2002) 646–652. doi:10.1038/nsb0902-646.
- [17] M. Karplus, J. Kuriyan, Molecular dynamics and protein function, *Proc. Natl. Acad. Sci. U. S. A.* 102 (2005) 6679–6685. doi:10.1073/pnas.0408930102.
- [18] W. Kopeć, J. Telenius, H. Khandelia, Molecular dynamics simulations of the interactions of medicinal plant extracts and drugs with lipid bilayer membranes, *FEBS J.* 280 (2013) 2785–2805. doi:10.1111/febs.12286.
- [19] D.A. Smith, Discovery and ADMET: Where are We Now, *Curr. Top. Med. Chem.* 11 (2011) 467–481.
- [20] J.-M. Alakoskela, P. Vitovic, P.K.J. Kinnunen, Screening for the drug-phospholipid interaction: correlation to phospholipidosis., *ChemMedChem.* 4 (2009) 1224–51. doi:10.1002/cmdc.200900052.
- [21] S. Natesan, V. Lukacova, M. Peng, R. Subramaniam, S. Lynch, Z. Wang, R. Tandlich, S. Balaz, Structure-Based Prediction of Drug Distribution Across the Headgroup and Core Strata of a Phospholipid Bilayer Using Surrogate Phases, *Mol. Pharm.* 11 (2014) 3577–3595. doi:10.1021/mp5003366.
- [22] S. Amjad-Iranagh, A. Yousefpour, P. Haghghi, H. Modarress, Effects of protein binding on a lipid bilayer containing local anesthetic articaine, and the potential of mean force calculation: a molecular dynamics simulation approach, *J. Mol. Model.* 19 (2013) 3831–3842. doi:10.1007/s00894-013-1917-6.
- [23] R.C. Bernardi, D.E.B. Gomes, R. Gobato, C.A. Taft, A.T. Ota, P.G. Pascutti, Molecular dynamics study of biomembrane/local anesthetics interactions, *Mol. Phys.* 107 (2009) 1437–1443. doi:10.1080/00268970902926238.
- [24] J.J.L. Cascales, S.D.O. Costa, R.D. Porasso, Thermodynamic study of benzocaine insertion into different lipid bilayers, *J. Chem. Phys.* 135 (2011) 135103. doi:10.1063/1.3643496.
- [25] C.-J. Högberg, A. Maliniak, A.P. Lyubartsev, Dynamical and structural properties of charged and uncharged lidocaine in a lipid bilayer, *Biophys. Chem.* 125 (2007) 416–424. doi:10.1016/j.bpc.2006.10.005.
- [26] L.J. Martin, R. Chao, B. Corry, Molecular dynamics simulation of the partitioning of benzocaine and phenytoin into a lipid bilayer, *Biophys. Chem.* 185 (2014) 98–107. doi:10.1016/j.bpc.2013.12.003.
- [27] M.F. Martini, M. Pickholz, Molecular dynamics study of uncharged bupivacaine enantiomers in phospholipid bilayers, *Int. J. Quantum Chem.* 112 (2012) 3341–3345. doi:10.1002/qua.24208.
- [28] M. Pickholz, L. Fernandes Fraceto, E. de Paula, Distribution of neutral prilocaine in a phospholipid bilayer: Insights from molecular dynamics simulations, *Int. J. Quantum Chem.* 108 (2008) 2386–2391. doi:10.1002/qua.21767.
- [29] R.D. Porasso, W.F. Drew Bennett, S.D. Oliveira-Costa, J.J. López Cascales, Study of the Benzocaine Transfer from Aqueous Solution to the Interior of a Biological Membrane, *J. Phys. Chem. B.* 113 (2009) 9988–9994. doi:10.1021/jp902931s.
- [30] Å.A. Skjevik, B.E. Haug, H. Lygre, K. Teigen, Intramolecular hydrogen bonding in articaine can be related to superior bone tissue penetration: A molecular dynamics study, *Biophys. Chem.* 154 (2011) 18–25. doi:10.1016/j.bpc.2010.12.002.

- [31] P. a Zapata-Morin, F.J. Sierra-Valdez, J.C. Ruiz-Suárez, The interaction of local anesthetics with lipid membranes., *J. Mol. Graph. Model.* 53C (2014) 200–205. doi:10.1016/j.jmgm.2014.08.001.
- [32] E.H. Mojumdar, A.P. Lyubartsev, Molecular dynamics simulations of local anesthetic articaine in a lipid bilayer, *Biophys. Chem.* 153 (2010) 27–35. doi:10.1016/j.bpc.2010.10.001.
- [33] D.S. Ragsdale, J.C. McPhee, T. Scheuer, W.A. Catterall, Molecular determinants of state-dependent block of Na⁺ channels by local anesthetics, *Science*. 265 (1994) 1724–1728.
- [34] G.M. Lipkind, H.A. Fozzard, Molecular Modeling of Local Anesthetic Drug Binding by Voltage-Gated Sodium Channels, *Mol. Pharmacol.* 68 (2005) 1611–1622. doi:10.1124/mol.105.014803.
- [35] M.F. Sheets, D.A. Hanck, Molecular Action of Lidocaine on the Voltage Sensors of Sodium Channels, *J. Gen. Physiol.* 121 (2003) 163–175. doi:10.1085/jgp.20028651.
- [36] P.-L. Chau, New insights into the molecular mechanisms of general anaesthetics, *Br. J. Pharmacol.* 161 (2010) 288–307. doi:10.1111/j.1476-5381.2010.00891.x.
- [37] H. Jerabek, G. Pabst, M. Rappolt, T. Stockner, Membrane-mediated effect on ion channels induced by the anesthetic drug ketamine., *J. Am. Chem. Soc.* 132 (2010) 7990–7997. doi:10.1021/ja910843d.
- [38] E. Yamamoto, T. Akimoto, H. Shimizu, Y. Hirano, M. Yasui, K. Yasuoka, Diffusive Nature of Xenon Anesthetic Changes Properties of a Lipid Bilayer: Molecular Dynamics Simulations, *J. Phys. Chem. B.* 116 (2012) 8989–8995. doi:10.1021/jp303330c.
- [39] B. Fábíán, M. Darvas, S. Picaud, M. Segá, P. Jedlovský, The effect of anaesthetics on the properties of a lipid membrane in the biologically relevant phase: a computer simulation study, *Phys. Chem. Chem. Phys.* 17 (2015) 14750–14760. doi:10.1039/C5CP00851D.
- [40] P.-L. Chau, K.M. Tu, K.K. Liang, I.T. Todorov, S.J. Roser, R. Barker, N. Matubayasi, The effect of pressure on halothane binding to hydrated DMPC bilayers, *Mol. Phys.* 110 (2012) 1461–1467. doi:10.1080/00268976.2012.659682.
- [41] K.M. Tu, N. Matubayasi, K.K. Liang, I.T. Todorov, S.L. Chan, P.-L. Chau, A possible molecular mechanism for the pressure reversal of general anaesthetics: Aggregation of halothane in POPC bilayers at high pressure, *Chem. Phys. Lett.* 543 (2012) 148–154. doi:10.1016/j.cplett.2012.06.044.
- [42] J. V. Levy, Myocardial and local anesthetic actions of β -adrenergic receptor blocking drugs: Relationship to physicochemical properties, *Eur. J. Pharmacol.* 2 (1968) 250–257. doi:10.1016/0014-2999(68)90074-5.
- [43] A.D. Auerbach, L. Goldman, beta-Blockers and reduction of cardiac events in noncardiac surgery: scientific review, *JAMA*. 287 (2002) 1435–1444.
- [44] M. Mizogami, K. Takakura, H. Tsuchiya, The interactivities with lipid membranes differentially characterize selective and nonselective β 1-blockers, *Eur. J. Anaesthesiol.* 27 (2010) 829–834. doi:10.1097/EJA.0b013e32833bf5e4.
- [45] G. Först, L. Cwiklik, P. Jurkiewicz, R. Schubert, M. Hof, Interactions of beta-blockers with model lipid membranes: Molecular view of the interaction of acebutolol, oxprenolol, and propranolol with phosphatidylcholine vesicles by time-dependent fluorescence shift and molecular dynamics simulations, *Eur. J. Pharm. Biopharm.* 87 (2014) 559–569. doi:10.1016/j.ejpb.2014.03.013.

- [46] L.M. Lichtenberger, Where is the evidence that cyclooxygenase inhibition is the primary cause of nonsteroidal anti-inflammatory drug (NSAID)-induced gastrointestinal injury?: Topical injury revisited, *Biochem. Pharmacol.* 61 (2001) 631–637. doi:10.1016/S0006-2952(00)00576-1.
- [47] L.M. Lichtenberger, Y. Zhou, V. Jayaraman, J.R. Doyen, R.G. O’Neil, E.J. Dial, D.E. Volk, D.G. Gorenstein, M.B. Boggara, R. Krishnamoorti, Insight into NSAID-induced membrane alterations, pathogenesis and therapeutics: characterization of interaction of NSAIDs with phosphatidylcholine., *Biochim. Biophys. Acta.* 1821 (2012) 994–1002. doi:10.1016/j.bbali.2012.04.002.
- [48] M.B. Boggara, M. Mihailescu, R. Krishnamoorti, Structural Association of Nonsteroidal Anti-Inflammatory Drugs with Lipid Membranes, *J. Am. Chem. Soc.* 134 (2012) 19669–19676. doi:10.1021/ja3064342.
- [49] H. Khandelia, S. Witzke, O.G. Mouritsen, Interaction of Salicylate and a Terpenoid Plant Extract with Model Membranes: Reconciling Experiments and Simulations, *Biophys. J.* 99 (2010) 3887–3894. doi:10.1016/j.bpj.2010.11.009.
- [50] C.B. Fox, R.A. Horton, J.M. Harris, Detection of Drug–Membrane Interactions in Individual Phospholipid Vesicles by Confocal Raman Microscopy, *Anal. Chem.* 78 (2006) 4918–4924. doi:10.1021/ac0605290.
- [51] M.B. Boggara, R. Krishnamoorti, Partitioning of nonsteroidal antiinflammatory drugs in lipid membranes: a molecular dynamics simulation study., *Biophys J.* 98 (2010) 586–95. doi:10.1016/j.bpj.2009.10.046.
- [52] K. Berka, T. Hendrychová, P. Anzenbacher, M. Otyepka, Membrane Position of Ibuprofen Agrees with Suggested Access Path Entrance to Cytochrome P450 2C9 Active Site, *J. Phys. Chem. A.* 115 (2011) 11248–11255. doi:10.1021/jp204488j.
- [53] D. Morin, T. Hauet, M. Spedding, J. Tillement, Mitochondria as target for antiischemic drugs, *Adv. Drug Deliv. Rev.* 49 (2001) 151–174.
- [54] R. Thuillier, G. Allain, S. Giraud, T. Saintyves, P.O. Delpuch, P. Couturier, C. Billault, E. Marchand, L. Vaahtera, J. Parkkinen, T. Hauet, Cyclodextrin curcumin formulation improves outcome in a preclinical pig model of marginal kidney transplantation, *Am. J. Transplant. Off. J. Am. Soc. Transplant. Am. Soc. Transpl. Surg.* 14 (2014) 1073–1083. doi:10.1111/ajt.12661.
- [55] K. Ioku, T. Tsushida, Y. Takei, N. Nakatani, J. Terao, Antioxidative activity of quercetin and quercetin monoglucosides in solution and phospholipid bilayers, *Biochim. Biophys. Acta BBA - Biomembr.* 1234 (1995) 99–104. doi:10.1016/0005-2736(94)00262-N.
- [56] L. Movileanu, I. Neagoe, M.L. Flonta, Interaction of the antioxidant flavonoid quercetin with planar lipid bilayers, *Int. J. Pharm.* 205 (2000) 135–146. doi:10.1016/S0378-5173(00)00503-2.
- [57] A. Arora, M.G. Nair, G.M. Strasburg, Structure–Activity Relationships for Antioxidant Activities of a Series of Flavonoids in a Liposomal System, *Free Radic. Biol. Med.* 24 (1998) 1355–1363. doi:10.1016/S0891-5849(97)00458-9.
- [58] J. Terao, M. Piskula, Q. Yao, Protective effect of epicatechin, epicatechin gallate, and quercetin on lipid peroxidation in phospholipid bilayers, *Arch. Biochem. Biophys.* 308 (1994) 278–284. doi:10.1006/abbi.1994.1039.
- [59] G. Fabre, A. Hänchen, C.-A. Calliste, K. Berka, S. Banala, M. Otyepka, R.D. Süßmuth, P. Trouillas, Lipocarbazole, an efficient lipid peroxidation inhibitor anchored in the membrane, *Bioorg. Med. Chem.* 23 (2015) 4866–4870. doi:10.1016/j.bmc.2015.05.031.

- [60] P. Podloucká, K. Berka, G. Fabre, M. Paloncýová, J.-L. Duroux, M. Otyepka, P. Trouillas, Lipid Bilayer Membrane Affinity Rationalizes Inhibition of Lipid Peroxidation by a Natural Lignan Antioxidant, *J. Phys. Chem. B.* 117 (2013) 5043–5049. doi:10.1021/jp3127829.
- [61] T.W. Sirk, E.F. Brown, A.K. Sum, M. Friedman, Molecular Dynamics Study on the Biophysical Interactions of Seven Green Tea Catechins with Lipid Bilayers of Cell Membranes, *J. Agric. Food Chem.* 56 (2008) 7750–7758. doi:10.1021/jf8013298.
- [62] T.W. Sirk, E.F. Brown, M. Friedman, A.K. Sum, Molecular Binding of Catechins to Biomembranes: Relationship to Biological Activity, *J. Agric. Food Chem.* 57 (2009) 6720–6728. doi:10.1021/jf900951w.
- [63] G. Fabre, I. Bayach, K. Berka, M. Paloncýová, M. Starok, C. Rossi, J.-L. Duroux, M. Otyepka, P. Trouillas, Synergism of antioxidant action of vitamins E, C and quercetin is related to formation of molecular associations in biomembranes, *Chem. Commun.* 51 (2015) 7713–7716. doi:10.1039/C5CC00636H.
- [64] J. Atkinson, T. Harroun, S.R. Wassall, W. Stillwell, J. Katsaras, The location and behavior of α -tocopherol in membranes, *Mol. Nutr. Food Res.* 54 (2010) 641–651. doi:10.1002/mnfr.200900439.
- [65] D. Marquardt, J.A. Williams, N. Kučerka, J. Atkinson, S.R. Wassall, J. Katsaras, T.A. Harroun, Tocopherol activity correlates with its location in a membrane: a new perspective on the antioxidant vitamin E, *J. Am. Chem. Soc.* 135 (2013) 7523–7533. doi:10.1021/ja312665r.
- [66] D. Marquardt, J.A. Williams, J.J. Kinnun, N. Kučerka, J. Atkinson, S.R. Wassall, J. Katsaras, T.A. Harroun, Dimyristoyl phosphatidylcholine: a remarkable exception to α -tocopherol's membrane presence, *J. Am. Chem. Soc.* 136 (2014) 203–210. doi:10.1021/ja408288f.
- [67] P. Lambelet, F. Saucy, J. Löliger, Chemical evidence for interactions between vitamins E and C, *Experientia.* 41 (1985) 1384–1388.
- [68] A. Nègre-Salvayre, A. Affany, C. Hariton, R. Salvayre, Additional antilipoperoxidant activities of alpha-tocopherol and ascorbic acid on membrane-like systems are potentiated by rutin, *Pharmacology.* 42 (1991) 262–272.
- [69] L.H. Pinto, L.J. Holsinger, R.A. Lamb, Influenza virus M2 protein has ion channel activity, *Cell.* 69 (1992) 517–528.
- [70] C.F. Chew, A. Guy, P.C. Biggin, Distribution and dynamics of adamantanes in a lipid bilayer., *Biophys. J.* 95 (2008) 5627–5636. doi:10.1529/biophysj.108.139477.
- [71] C. Li, M. Yi, J. Hu, H.-X. Zhou, T.A. Cross, Solid-State NMR and MD Simulations of the Antiviral Drug Amantadine Solubilized in DMPC Bilayers, *Biophys. J.* 94 (2008) 1295–1302. doi:10.1529/biophysj.107.112482.
- [72] E.S.E. Eriksson, L.A. Eriksson, The influence of cholesterol on the properties and permeability of hypericin derivatives in lipid membranes, *J. Chem. Theory Comput.* 7 (2011) 560–574. doi:10.1021/ct100528u.
- [73] E.S.E. Eriksson, D.J.V.A. dos Santos, R.C. Guedes, L.A. Eriksson, Properties and Permeability of Hypericin and Brominated Hypericin in Lipid Membranes, *J. Chem. Theory Comput.* 5 (2009) 3139–3149. doi:10.1021/ct9002702.
- [74] V. Galiano, J. Villalaín, Oleuropein aglycone in lipid bilayer membranes. A molecular dynamics study, *Biochim. Biophys. Acta BBA - Biomembr.* 1848 (2015) 2849–2858. doi:10.1016/j.bbamem.2015.08.007.

- [75] A.A. Bahar, D. Ren, Antimicrobial Peptides, *Pharmaceuticals*. 6 (2013) 1543–1575. doi:10.3390/ph6121543.
- [76] K.V.R. Reddy, R.D. Yedery, C. Aranha, Antimicrobial peptides: premises and promises, *Int. J. Antimicrob. Agents*. 24 (2004) 536–547. doi:10.1016/j.ijantimicag.2004.09.005.
- [77] K.A. Brogden, Antimicrobial peptides: pore formers or metabolic inhibitors in bacteria?, *Nat. Rev. Microbiol.* 3 (2005) 238–250. doi:10.1038/nrmicro1098.
- [78] P.K. Kyriakou, B. Ekblad, P.E. Kristiansen, Y.N. Kaznessis, Interactions of a class IIb bacteriocin with a model lipid bilayer, investigated through molecular dynamics simulations, *Biochim. Biophys. Acta BBA - Biomembr.* (2016). doi:10.1016/j.bbamem.2016.01.005.
- [79] Y. Wang, D.E. Schlamadinger, J.E. Kim, J.A. McCammon, Comparative Molecular Dynamics Simulations of the Antimicrobial Peptide CM15 in Model Lipid Bilayers, *Biochim. Biophys. Acta*. 1818 (2012) 1402–1409. doi:10.1016/j.bbamem.2012.02.017.
- [80] C. Appelt, F. Eisenmenger, R. Kühne, P. Schmieder, J.A. Söderhäll, Interaction of the Antimicrobial Peptide Cyclo(RRWRF) with Membranes by Molecular Dynamics Simulations, *Biophys. J.* 89 (2005) 2296–2306. doi:10.1529/biophysj.105.063040.
- [81] B.S. Perrin, Y. Tian, R. Fu, C.V. Grant, E.Y. Chekmenev, W.E. Wieczorek, A.E. Dao, R.M. Hayden, C.M. Burzynski, R.M. Venable, M. Sharma, S.J. Opella, R.W. Pastor, M.L. Cotten, High-Resolution Structures and Orientations of Antimicrobial Peptides Piscidin 1 and Piscidin 3 in Fluid Bilayers Reveal Tilting, Kinking, and Bilayer Immersion, *J. Am. Chem. Soc.* 136 (2014) 3491–3504. doi:10.1021/ja411119m.
- [82] T. Yuan, X. Zhang, Z. Hu, F. Wang, M. Lei, Molecular dynamics studies of the antimicrobial peptides piscidin 1 and its mutants with a DOPC lipid bilayer, *Biopolymers*. 97 (2012) 998–1009. doi:10.1002/bip.22116.
- [83] E. Han, H. Lee, Structural effects of tachyplesin I and its linear derivative on their aggregation and mobility in lipid bilayers, *J. Mol. Graph. Model.* 59 (2015) 123–128. doi:10.1016/j.jmgm.2015.04.007.
- [84] J.S. Hub, F.K. Winkler, M. Merrick, B.L. de Groot, Potentials of Mean Force and Permeabilities for Carbon Dioxide, Ammonia, and Water Flux across a Rhesus Protein Channel and Lipid Membranes, *J. Am. Chem. Soc.* 132 (2010) 13251–13263. doi:10.1021/ja102133x.
- [85] M. Orsi, J.W. Essex, Permeability of drugs and hormones through a lipid bilayer: insights from dual-resolution molecular dynamics, *Soft Matter*. 6 (2010) 3797–3808. doi:10.1039/C0SM00136H.
- [86] D. Bochicchio, E. Panizon, R. Ferrando, L. Monticelli, G. Rossi, Calculating the free energy of transfer of small solutes into a model lipid membrane: Comparison between metadynamics and umbrella sampling, *J. Chem. Phys.* 143 (2015) 144108. doi:10.1063/1.4932159.
- [87] S.-J. Marrink, H.J. Berendsen, Simulation of water transport through a lipid membrane, *J. Phys. Chem.* 98 (1994) 4155–4168.
- [88] D. Bemporad, J.W. Essex, C. Luttmann, Permeation of Small Molecules through a Lipid Bilayer: A Computer Simulation Study, *J. Phys. Chem. B*. 108 (2004) 4875–4884. doi:10.1021/jp035260s.
- [89] M. Orsi, J.W. Essex, Chapter 4:Passive Permeation Across Lipid Bilayers: a Literature Review, in: Chapter 4Passive Permeat. *Lipid Bilayers Lit. Rev.*,

- 2010: pp. 76–90. <http://pubs.rsc.org/en/content/chapter/bk9780854041893-00076/978-0-85404-189-3>.
- [90] H.E. Alper, T.R. Stouch, Orientation and Diffusion of a Drug Analog in Biomembranes: Molecular Dynamics Simulations, *J. Phys. Chem.* 99 (1995) 5724–5731. doi:10.1021/j100015a065.
- [91] J. Ulander, A.D.J. Haymet, Permeation Across Hydrated DPPC Lipid Bilayers: Simulation of the Titrable Amphiphilic Drug Valproic Acid, *Biophys. J.* 85 (2003) 3475–3484. doi:10.1016/S0006-3495(03)74768-7.
- [92] D. Bemporad, C. Luttmann, J.W. Essex, Behaviour of small solutes and large drugs in a lipid bilayer from computer simulations, *Biochim. Biophys. Acta BBA - Biomembr.* 1718 (2005) 1–21. doi:10.1016/j.bbamem.2005.07.009.
- [93] D.J.V.A. dos Santos, L.A. Eriksson, Permeability of Psoralen Derivatives in Lipid Membranes, *Biophys. J.* 91 (2006) 2464–2474. doi:10.1529/biophysj.105.077156.
- [94] E.S.E. Eriksson, L.A. Eriksson, The Influence of Cholesterol on the Properties and Permeability of Hypericin Derivatives in Lipid Membranes, *J. Chem. Theory Comput.* 7 (2011) 560–574. doi:10.1021/ct100528u.
- [95] M. Paloncýová, K. Vávrová, Ž. Sovová, R. DeVane, M. Otyepka, K. Berka, Structural Changes in Ceramide Bilayers Rationalize Increased Permeation through Stratum Corneum Models with Shorter Acyl Tails, *J. Phys. Chem. B.* 119 (2015) 9811–9819. doi:10.1021/acs.jpcc.5b05522.
- [96] M. Orsi, W.E. Sanderson, J.W. Essex, Permeability of Small Molecules through a Lipid Bilayer: A Multiscale Simulation Study, *J. Phys. Chem. B.* 113 (2009) 12019–12029. doi:10.1021/jp903248s.
- [97] D. Bemporad, J.W. Essex, C. Luttmann, Permeation of Small Molecules through a Lipid Bilayer: A Computer Simulation Study, *J. Phys. Chem. B.* 108 (2004) 4875–4884. doi:10.1021/jp035260s.
- [98] M. Orsi, J.W. Essex, Permeability of drugs and hormones through a lipid bilayer: insights from dual-resolution molecular dynamics, *Soft Matter.* 6 (2010) 3797. doi:10.1039/c0sm00136h.
- [99] Z. Ghaemi, M. Minozzi, P. Carloni, A. Laio, A Novel Approach to the Investigation of Passive Molecular Permeation through Lipid Bilayers from Atomistic Simulations, *J. Phys. Chem. B.* 116 (2012) 8714–8721. doi:10.1021/jp301083h.
- [100] K.M. Giacomini, S.-M. Huang, Transporters in Drug Development and Clinical Pharmacology, *Clin. Pharmacol. Ther.* 94 (2013) 3–9. doi:10.1038/clpt.2013.86.
- [101] K.M. Giacomini, S.-M. Huang, D.J. Tweedie, L.Z. Benet, K.L.R. Brouwer, X. Chu, A. Dahlin, R. Evers, V. Fischer, K.M. Hillgren, K.A. Hoffmaster, T. Ishikawa, D. Keppler, R.B. Kim, C.A. Lee, M. Niemi, J.W. Polli, Y. Sugiyama, P.W. Swaan, J.A. Ware, S.H. Wright, S.W. Yee, M.J. Zamek-Gliszczyński, L. Zhang, Membrane transporters in drug development, *Nat. Rev. Drug Discov.* 9 (2010) 215–236. doi:10.1038/nrd3028.
- [102] M.H. Saier, C.V. Tran, R.D. Barabote, TCDB: the Transporter Classification Database for membrane transport protein analyses and information, *Nucleic Acids Res.* 34 (2006) D181–D186. doi:10.1093/nar/gkj001.
- [103] M.H. Saier, V.S. Reddy, D.G. Tamang, Å. Västermark, The Transporter Classification Database, *Nucleic Acids Res.* 42 (2014) D251–D258. doi:10.1093/nar/gkt1097.

- [104] A. Schlessinger, S.W. Yee, A. Sali, K.M. Giacomini, SLC classification: an update, *Clin. Pharmacol. Ther.* 94 (2013) 19–23. doi:10.1038/clpt.2013.73.
- [105] A. Schlessinger, P. Matsson, J.E. Shima, U. Pieper, S.W. Yee, L. Kelly, L. Apeltsin, R.M. Stroud, T.E. Ferrin, K.M. Giacomini, A. Sali, Comparison of human solute carriers, *Protein Sci. Publ. Protein Soc.* 19 (2010) 412–428. doi:10.1002/pro.320.
- [106] A. Schlessinger, N. Khuri, K.M. Giacomini, A. Sali, Molecular modeling and ligand docking for solute carrier (SLC) transporters, *Curr. Top. Med. Chem.* 13 (2013) 843–856.
- [107] M.A. Hediger, B. Clémenton, R.E. Burrier, E.A. Bruford, The ABCs of membrane transporters in health and disease (SLC series): introduction, *Mol. Aspects Med.* 34 (2013) 95–107. doi:10.1016/j.mam.2012.12.009.
- [108] S.-M. Huang, L. Zhang, K.M. Giacomini, The International Transporter Consortium: A Collaborative Group of Scientists From Academia, Industry, and the FDA, *Clin. Pharmacol. Ther.* 87 (2010) 32–36. doi:10.1038/clpt.2009.236.
- [109] J. Li, P.-C. Wen, M. Moradi, E. Tajkhorshid, Computational characterization of structural dynamics underlying function in active membrane transporters, *Curr. Opin. Struct. Biol.* 31 (2015) 96–105. doi:10.1016/j.sbi.2015.04.001.
- [110] D. Dwyer, Molecular Modeling and Molecular Dynamics Simulations of Membrane Transporter Proteins, in: Q. Yan, Q.Y. MD (Eds.), *Membr. Transp.*, Humana Press, 2003: pp. 335–350. <http://dx.doi.org/10.1385/1-59259-387-9%3A335>.
- [111] F. Khalili-Araghi, J. Gumbart, P.-C. Wen, M. Sotomayor, E. Tajkhorshid, K. Schulten, Molecular dynamics simulations of membrane channels and transporters, *Curr. Opin. Struct. Biol.* 19 (2009) 128–137. doi:10.1016/j.sbi.2009.02.011.
- [112] E.M. Quistgaard, C. Löw, F. Guettou, P. Nordlund, Understanding transport by the major facilitator superfamily (MFS): structures pave the way, *Nat. Rev. Mol. Cell Biol.* 17 (2016) 123–132. doi:10.1038/nrm.2015.25.
- [113] E.M. Quistgaard, C. Löw, P. Moberg, L. Trésaugues, P. Nordlund, Structural basis for substrate transport in the GLUT-homology family of monosaccharide transporters, *Nat. Struct. Mol. Biol.* 20 (2013) 766–768. doi:10.1038/nsmb.2569.
- [114] L. Sun, X. Zeng, C. Yan, X. Sun, X. Gong, Y. Rao, N. Yan, Crystal structure of a bacterial homologue of glucose transporters GLUT1-4, *Nature.* 490 (2012) 361–366. doi:10.1038/nature11524.
- [115] G. Wisedchaisri, M.-S. Park, M.G. Iadanza, H. Zheng, T. Gonen, Proton-coupled sugar transport in the prototypical major facilitator superfamily protein XylE, *Nat. Commun.* 5 (2014) 4521. doi:10.1038/ncomms5521.
- [116] D. Deng, C. Xu, P. Sun, J. Wu, C. Yan, M. Hu, N. Yan, Crystal structure of the human glucose transporter GLUT1, *Nature.* 510 (2014) 121–125. doi:10.1038/nature13306.
- [117] M.-S. Park, Molecular Dynamics Simulations of the Human Glucose Transporter GLUT1, *PLoS ONE.* 10 (2015) e0125361. doi:10.1371/journal.pone.0125361.
- [118] M.Ø. Jensen, Y. Yin, E. Tajkhorshid, K. Schulten, Sugar transport across lactose permease probed by steered molecular dynamics, *Biophys. J.* 93 (2007) 92–102. doi:10.1529/biophysj.107.103994.

- [119] Y. Yin, M.Ø. Jensen, E. Tajkhorshid, K. Schulten, Sugar binding and protein conformational changes in lactose permease, *Biophys. J.* 91 (2006) 3972–3985. doi:10.1529/biophysj.106.085993.
- [120] M. Andersson, A.-N. Bondar, J.A. Freites, D.J. Tobias, H.R. Kaback, S.H. White, Proton-coupled dynamics in lactose permease, *Struct. Lond. Engl.* 1993. 20 (2012) 1893–1904. doi:10.1016/j.str.2012.08.021.
- [121] M. Moradi, G. Enkavi, E. Tajkhorshid, Atomic-level characterization of transport cycle thermodynamics in the glycerol-3-phosphate:phosphate antiporter, *Nat. Commun.* 6 (2015) 8393. doi:10.1038/ncomms9393.
- [122] D. Deng, P. Sun, C. Yan, M. Ke, X. Jiang, L. Xiong, W. Ren, K. Hirata, M. Yamamoto, S. Fan, N. Yan, Molecular basis of ligand recognition and transport by glucose transporters, *Nature.* 526 (2015) 391–396. doi:10.1038/nature14655.
- [123] J. Holyoake, M.S.P. Sansom, Conformational change in an MFS protein: MD simulations of LacY, *Struct. Lond. Engl.* 1993. 15 (2007) 873–884. doi:10.1016/j.str.2007.06.004.
- [124] D. Wang, G.A. Voth, Proton Transport Pathway in the ClC Cl⁻/H⁺ Antiporter, *Biophys. J.* 97 (2009) 121–131. doi:10.1016/j.bpj.2009.04.038.
- [125] A.-N. Bondar, C. del Val, S.H. White, Rhomboid protease dynamics and lipid interactions, *Struct. Lond. Engl.* 1993. 17 (2009) 395–405. doi:10.1016/j.str.2008.12.017.
- [126] F. Gruswitz, S. Chaudhary, J.D. Ho, A. Schlessinger, B. Pezeshki, C.-M. Ho, A. Sali, C.M. Westhoff, R.M. Stroud, Function of human Rh based on structure of RhCG at 2.1 Å, *Proc. Natl. Acad. Sci.* 107 (2010) 9638–9643. doi:10.1073/pnas.1003587107.
- [127] S. Doki, H.E. Kato, N. Solcan, M. Iwaki, M. Koyama, M. Hattori, N. Iwase, T. Tsukazaki, Y. Sugita, H. Kandori, S. Newstead, R. Ishitani, O. Nureki, Structural basis for dynamic mechanism of proton-coupled symport by the peptide transporter POT, *Proc. Natl. Acad. Sci.* 110 (2013) 11343–11348. doi:10.1073/pnas.1301079110.
- [128] I.F. Tsigelny, D. Kovalskyy, V.L. Kouznetsova, O. Balinskyi, Y. Sharikov, V. Bhatnagar, S.K. Nigam, Conformational Changes of the Multispecific Transporter Organic Anion Transporter 1 (OAT1/SLC22A6) Suggests a Molecular Mechanism for Initial Stages of Drug and Metabolite Transport, *Cell Biochem. Biophys.* 61 (2011) 251–259. doi:10.1007/s12013-011-9191-7.
- [129] D. Meredith, R.A. Price, Molecular Modeling of PepT1 — Towards a Structure, *J. Membr. Biol.* 213 (2007) 79–88. doi:10.1007/s00232-006-0876-6.
- [130] P. Anzenbacher, U.M. Zanger, *Metabolism of Drugs and Other Xenobiotics*, Wiley-VCH Verlag GmbH & Co. KGaA, Weinheim, Germany, 2012. doi:10.1002/9783527630905.
- [131] F.P. Guengerich, Human Cytochrome P450 Enzymes, in: *Cytochrome P450*, 2005: pp. 377–530.
- [132] D.R. Nelson, Cytochrome P450 Nomenclature, 2004, in: I.R. Phillips, E.A. Shephard (Eds.), *Methods Mol. Biol. Vol 320 Cytochrome P450 Protoc.* Second Ed., Humana Press Inc., Totowa, NJ, n.d.
- [133] M. Seliskar, D. Rozman, Mammalian cytochromes P450—importance of tissue specificity., *Biochim. Biophys. Acta.* 1770 (2007) 458–66. doi:10.1016/j.bbagen.2006.09.016.
- [134] V. Cojocar, K. Balali-Mood, M.S.P. Sansom, R.C. Wade, Structure and dynamics of the membrane-bound cytochrome P450 2C9., *PLoS Comput. Biol.* 7 (2011) e1002152. doi:10.1371/journal.pcbi.1002152.

- [135] M.R. Wester, J.K. Yano, G. Schoch, C. Yang, K.J. Griffin, C.D. Stout, E.F. Johnson, The structure of human cytochrome P450 2C9 complexed with flurbiprofen at 2.0-Å resolution., *J. Biol. Chem.* 279 (2004) 35630–35637. doi:10.1074/jbc.M405427200.
- [136] P.A. Williams, J. Cosme, A. Ward, H.C. Angove, D. Matak Vinković, H. Jhoti, Crystal structure of human cytochrome P450 2C9 with bound warfarin., *Nature*. 424 (2003) 464–8. doi:10.1038/nature01862.
- [137] C.A. Brown, S.D. Black, Membrane topology of mammalian cytochromes P-450 from liver endoplasmic reticulum. Determination by trypsinolysis of phenobarbital-treated microsomes., *J. Biol. Chem.* 264 (1989) 4442–9.
- [138] E. Szczesna-Skorupa, B. Mallah, B. Kemper, Fluorescence resonance energy transfer analysis of cytochromes P450 2C2 and 2E1 molecular interactions in living cells., *J. Biol. Chem.* 278 (2003) 31269–31276. doi:10.1074/jbc.M301489200.
- [139] G.A. Schoch, J.K. Yano, M.R. Wester, K.J. Griffin, C.D. Stout, E.F. Johnson, Structure of Human Microsomal Cytochrome P450 2C8, *J. Biol. Chem.* 279 (2004) 9497–9503. doi:10.1074/jbc.M312516200.
- [140] K. Berka, M. Paloncýová, P. Anzenbacher, M. Otyepka, Behavior of Human Cytochromes P450 on Lipid Membranes., *J. Phys. Chem. B*. 117 (2013) 11556–11564. doi:10.1021/jp4059559.
- [141] J.L. Baylon, I.L. Lenov, S.G. Sligar, E. Tajkhorshid, Characterizing the Membrane-Bound State of Cytochrome P450 3A4: Structure, Depth of Insertion and Orientation, *J. Am. Chem. Soc.* 135 (2013) 8542–8551. doi:10.1021/ja4003525.
- [142] I.G. Denisov, A.Y. Shih, S.G. Sligar, Structural differences between soluble and membrane bound cytochrome P450s, *J. Inorg. Biochem.* 108 (2012) 150–158. doi:10.1016/j.jinorgbio.2011.11.026.
- [143] Y.-L. Cui, Q. Xue, Q.-C. Zheng, J.-L. Zhang, C.-P. Kong, J.-R. Fan, H.-X. Zhang, Structural features and dynamic investigations of the membrane-bound cytochrome P450 17A1, *Biochim. Biophys. Acta BBA - Biomembr.* 1848 (2015) 2013–2021. doi:10.1016/j.bbamem.2015.05.017.
- [144] J. Park, L. Czaplá, R.E. Amaro, Molecular simulations of aromatase reveal new insights into the mechanism of ligand binding., *J. Chem. Inf. Model.* 53 (2013) 2047–56. doi:10.1021/ci400225w.
- [145] J. Sgrignani, A. Magistrato, Influence of the membrane lipophilic environment on the structure and on the substrate access/egress routes of the human aromatase enzyme. A computational study., *J. Chem. Inf. Model.* 52 (2012) 1595–1606. doi:10.1021/ci300151h.
- [146] D.R. McDougle, J.L. Baylon, D.D. Meling, A. Kambalyal, Y. V. Grinkova, J. Hammernik, E. Tajkhorshid, A. Das, Incorporation of charged residues in the CYP2J2 F-G loop disrupts CYP2J2–lipid bilayer interactions, *Biochim. Biophys. Acta BBA - Biomembr.* 1848 (2015) 2460–2470. doi:10.1016/j.bbamem.2015.07.015.
- [147] B.C. Monk, T.M. Tomasiak, M. V. Keniya, F.U. Huschmann, J.D.A. Tyndall, J.D. O’Connell, R.D. Cannon, J.G. McDonald, A. Rodriguez, J.S. Finer-Moore, R.M. Stroud, Architecture of a single membrane spanning cytochrome P450 suggests constraints that orient the catalytic domain relative to a bilayer, *Proc. Natl. Acad. Sci.* 111 (2014) 3865–3870. doi:10.1073/pnas.1324245111.
- [148] A.A. Sagatova, M. V. Keniya, R.K. Wilson, B.C. Monk, J.D.A. Tyndall, Structural Insights into Binding of the Antifungal Drug Fluconazole to

- Saccharomyces cerevisiae* Lanosterol 14 α -Demethylase, *Antimicrob. Agents Chemother.* 59 (2015) 4982–4989. doi:10.1128/AAC.00925-15.
- [149] M. Paloncýová, V. Navrátilová, K. Berka, A. Laio, M. Otyepka, Role of Enzyme Flexibility in Ligand Access and Egress to Active Site: Bias-Exchange Metadynamics Study of 1,3,7-Trimethyluric Acid in Cytochrome P450 3A4, *J. Chem. Theory Comput.* 12 (2016) 2101–2109. doi:10.1021/acs.jctc.6b00075.
- [150] E.E. Scott, C.R. Wolf, M. Otyepka, S.C. Humphreys, J.R. Reed, C.J. Henderson, L.A. McLaughlin, M. Paloncýová, V. Navrátilová, K. Berka, P. Anzenbacher, U.P. Dahal, C. Barnaba, J.A. Brozik, J.P. Jones, F. Estrada, J.S. Laurence, J.W. Park, W.L. Backes, The Role of Protein-Protein and Protein-Membrane Interactions on P450 Function, *Drug Metab. Dispos.* (2016) dmd.115.068569. doi:10.1124/dmd.115.068569.
- [151] S.-F. Zhou, Z.-W. Zhou, L.-P. Yang, J.-P. Cai, Substrates, inducers, inhibitors and structure-activity relationships of human Cytochrome P450 2C9 and implications in drug development, *Curr. Med. Chem.* 16 (2009) 3480–3675.
- [152] L. Laakkonen, M. Finel, A Molecular Model of the Human UDP-Glucuronosyltransferase 1A1, Its Membrane Orientation, and the Interactions between Different Parts of the Enzyme, *Mol. Pharmacol.* 77 (2010) 931–939. doi:10.1124/mol.109.063289.
- [153] M.J. Miley, A.K. Zielinska, J.E. Keenan, S.M. Bratton, A. Radomska-Pandya, M.R. Redinbo, Crystal Structure of the Cofactor-Binding Domain of the Human Phase II Drug-Metabolism Enzyme UDP-Glucuronosyltransferase 2B7, *J. Mol. Biol.* 369 (2007) 498–511. doi:10.1016/j.jmb.2007.03.066.
- [154] A. Roy, A. Kucukural, Y. Zhang, I-TASSER: a unified platform for automated protein structure and function prediction, *Nat. Protoc.* 5 (2010) 725–738. doi:10.1038/nprot.2010.5.
- [155] N. Eswar, B. Webb, M.A. Marti-Renom, M. s. Madhusudhan, D. Eramian, M. Shen, U. Pieper, A. Sali, Comparative Protein Structure Modeling Using MODELLER, in: *Curr. Protoc. Protein Sci.*, John Wiley & Sons, Inc., 2001. <http://onlinelibrary.wiley.com/doi/10.1002/0471140864.ps0209s50/abstract>.
- [156] K.W. Bock, C. Köhle, Topological aspects of oligomeric UDP-glucuronosyltransferases in endoplasmic reticulum membranes: Advances and open questions, *Biochem. Pharmacol.* 77 (2009) 1458–1465. doi:10.1016/j.bcp.2008.12.004.
- [157] D.S. Wishart, C. Knox, A.C. Guo, S. Shrivastava, M. Hassanali, P. Stothard, Z. Chang, J. Woolsey, DrugBank: a comprehensive resource for in silico drug discovery and exploration, *Nucleic Acids Res.* 34 (2006) D668–D672. doi:10.1093/nar/gkj067.
- [158] J. Kirchmair, A. Howlett, J.E. Peironcelly, D.S. Murrell, M.J. Williamson, S.E. Adams, T. Hankemeier, L. Van Buren, G. Duchateau, W. Klaffke, R.C. Glen, How do metabolites differ from their parent molecules and how are they excreted?, *J. Chem. Inf. Model.* 53 (2013) 354–367. doi:10.1021/ci300487z.
- [159] M. Paloncýová, K. Berka, M. Otyepka, Molecular Insight into Affinities of Drugs and Their Metabolites to Lipid Bilayers., *J. Phys. Chem. B.* 117 (2013) 2403–10. doi:10.1021/jp311802x.
- [160] S.P. Tripathi, A. Bhadauriya, A. Patil, A.T. Sangamwar, Substrate selectivity of human intestinal UDP-glucuronosyltransferases (UGTs): in silico and in vitro insights., *Drug Metab. Rev.* 45 (2013) 231–52. doi:10.3109/03602532.2013.767345.

- [161] P.I. Mackenzie, K. Walter Bock, B. Burchell, C. Guillemette, S. Ikushiro, T. Iyanagi, J.O. Miners, I.S. Owens, D.W. Nebert, Nomenclature update for the mammalian UDP glycosyltransferase (UGT) gene superfamily, *Pharmacogenet. Genomics*. 15 (2005) 677–685. doi:10.1097/01.fpc.0000173483.13689.56.
- [162] Y. Ishii, A. Nurrochmad, H. Yamada, Modulation of UDP-Glucuronosyltransferase Activity by Endogenous Compounds, *Drug Metab. Pharmacokinet.* 25 (2010) 134–148. doi:10.2133/dmpk.25.134.
- [163] F. R., M. Nakajima, T. Yamamoto, H. Nagao, T. Yokoi, In silico and in vitro Approaches to Elucidate the Thermal Stability of Human UDP-glucuronosyltransferase UGT 1A9, *Drug Metab. Pharmacokinet.* 24 (2009) 235–244. doi:10.2133/dmpk.24.235.
- [164] S.P. Tripathi, R. Prajapati, N. Verma, A.T. Sangamwar, Predicting substrate selectivity between UGT1A9 and UGT1A10 using molecular modelling and molecular dynamics approach, *Mol. Simul.* 00 (2015) 1–19. doi:10.1080/08927022.2015.1044451.
- [165] C.W. Locuson, T.S. Tracy, Comparative modelling of the human UDP-glucuronosyltransferases: insights into structure and mechanism., *Xenobiotica Fate Foreign Compd. Biol. Syst.* 37 (2007) 155–168. doi:10.1080/00498250601129109.
- [166] P. Košinová, K. Berka, M. Wykes, M. Otyepka, P. Trouillas, P. Kosinova, P. Ko, Positioning of antioxidant quercetin and its metabolites in lipid bilayer membranes: implication for their lipid-peroxidation inhibition., *J Phys Chem B*. 116 (2012) 1309–18. doi:10.1021/jp208731g.
- [167] Y. Huang, M.J. Lemieux, J. Song, M. Auer, D.-N. Wang, Structure and Mechanism of the Glycerol-3-Phosphate Transporter from *Escherichia coli*, *Science*. 301 (2003) 616–620. doi:10.1126/science.1087619.
- [168] G. Enkavi, E. Tajkhorshid, Simulation of spontaneous substrate binding revealing the binding pathway and mechanism and initial conformational response of GlpT, *Biochemistry (Mosc.)*. 49 (2010) 1105–1114. doi:10.1021/bi901412a.
- [169] C.J. Law, G. Enkavi, D.-N. Wang, E. Tajkhorshid, Structural Basis of Substrate Selectivity in the Glycerol-3-Phosphate: Phosphate Antiporter GlpT, *Biophys. J.* 97 (2009) 1346–1353. doi:10.1016/j.bpj.2009.06.026.
- [170] J. Baker, S.H. Wright, F. Tama, Simulations of substrate transport in the multidrug transporter EmrD, *Proteins Struct. Funct. Bioinforma.* 80 (2012) 1620–1632. doi:10.1002/prot.24056.
- [171] Y.M. Leung, D.A. Holdbrook, T.J. Piggot, S. Khalid, The NorM MATE transporter from *N. gonorrhoeae*: insights into drug and ion binding from atomistic molecular dynamics simulations, *Biophys. J.* 107 (2014) 460–468. doi:10.1016/j.bpj.2014.06.005.
- [172] D.C. Rees, E. Johnson, O. Lewinson, ABC transporters: the power to change, *Nat. Rev. Mol. Cell Biol.* 10 (2009) 218–227. doi:10.1038/nrm2646.
- [173] J. ter Beek, A. Guskov, D.J. Slotboom, Structural diversity of ABC transporters, *J. Gen. Physiol.* 143 (2014) 419–435. doi:10.1085/jgp.201411164.
- [174] I.B. Holland, M.A. Blight, ABC-ATPases, adaptable energy generators fuelling transmembrane movement of a variety of molecules in organisms from bacteria to humans, *J. Mol. Biol.* 293 (1999) 381–399. doi:10.1006/jmbi.1999.2993.
- [175] S.G. Aller, J. Yu, A. Ward, Y. Weng, S. Chittaboina, R. Zhuo, P.M. Harrell, Y.T. Trinh, Q. Zhang, I.L. Urbatsch, G. Chang, Structure of P-glycoprotein reveals a

- molecular basis for poly-specific drug binding, *Science*. 323 (2009) 1718–1722. doi:10.1126/science.1168750.
- [176] M. Moradi, E. Tajkhorshid, Mechanistic picture for conformational transition of a membrane transporter at atomic resolution, *Proc. Natl. Acad. Sci.* 110 (2013) 18916–18921. doi:10.1073/pnas.1313202110.
- [177] S.-Y. Chang, F.-F. Liu, X.-Y. Dong, Y. Sun, Molecular insight into conformational transmission of human P-glycoprotein, *J. Chem. Phys.* 139 (2013) 225102. doi:10.1063/1.4832740.
- [178] H. Liu, D. Li, Y. Li, T. Hou, Atomistic molecular dynamics simulations of ATP-binding cassette transporters, *Wiley Interdiscip. Rev. Comput. Mol. Sci.* (2016) n/a–n/a. doi:10.1002/wcms.1247.
- [179] B.J. Grant, A.A. Gorfe, J.A. McCammon, Large conformational changes in proteins: signaling and other functions, *Curr. Opin. Struct. Biol.* 20 (2010) 142–147. doi:10.1016/j.sbi.2009.12.004.
- [180] C.F. Higgins, K.J. Linton, The ATP switch model for ABC transporters, *Nat. Struct. Mol. Biol.* 11 (2004) 918–926. doi:10.1038/nsmb836.
- [181] P.M. Jones, A.M. George, Opening of the ADP-bound active site in the ABC transporter ATPase dimer: evidence for a constant contact, alternating sites model for the catalytic cycle, *Proteins*. 75 (2009) 387–396. doi:10.1002/prot.22250.
- [182] G. Gyimesi, S. Ramachandran, P. Kota, N.V. Dokholyan, B. Sarkadi, T. Hegedűs, ATP hydrolysis at one of the two sites in ABC transporters initiates transport related conformational transitions, *Biochim. Biophys. Acta BBA - Biomembr.* 1808 (2011) 2954–2964. doi:10.1016/j.bbamem.2011.07.038.
- [183] G. Gyimesi, S. Ramachandran, P. Kota, N.V. Dokholyan, B. Sarkadi, T. Hegedűs, Corrigendum to “ATP hydrolysis at one of the two sites in ABC transporters initiates transport related conformational transitions” [*Biochim. Biophys. Acta* 1808 (2011) 2954–2964], *Biochim. Biophys. Acta BBA - Biomembr.* 1818 (2012) 1435. doi:10.1016/j.bbamem.2012.01.004.
- [184] M. Moradi, E. Tajkhorshid, Computational Recipe for Efficient Description of Large-Scale Conformational Changes in Biomolecular Systems, *J. Chem. Theory Comput.* 10 (2014) 2866–2880. doi:10.1021/ct5002285.
- [185] P.-C. Wen, B. Verhalen, S. Wilkens, H.S. Mchaourab, E. Tajkhorshid, On the origin of large flexibility of P-glycoprotein in the inward-facing state., *J. Biol. Chem.* 288 (2013) 19211–20. doi:10.1074/jbc.M113.450114.
- [186] J.-F. St-Pierre, A. Bunker, T. Róg, M. Karttunen, N. Mousseau, Molecular dynamics simulations of the bacterial ABC transporter SAV1866 in the closed form, *J. Phys. Chem. B*. 116 (2012) 2934–2942. doi:10.1021/jp209126c.
- [187] M.L. O’Mara, A.E. Mark, The Effect of Environment on the Structure of a Membrane Protein: P-Glycoprotein under Physiological Conditions, *J. Chem. Theory Comput.* 8 (2012) 3964–3976. doi:10.1021/ct300254y.
- [188] T.X. Xiang, B.D. Anderson, Permeability of acetic acid across gel and liquid-crystalline lipid bilayers conforms to free-surface-area theory, *Biophys. J.* 72 (1997) 223–237. doi:10.1016/S0006-3495(97)78661-2.
- [189] C.L. Wennberg, D. van der Spoel, J.S. Hub, Large Influence of Cholesterol on Solute Partitioning into Lipid Membranes, *J. Am. Chem. Soc.* 134 (2012) 5351–5361. doi:10.1021/ja211929h.
- [190] M. Paloncýová, R.H. DeVane, B.P. Murch, K. Berka, M. Otyepka, Rationalization of Reduced Penetration of Drugs through Ceramide Gel Phase Membrane, *Langmuir*. 30 (2014) 13942–13948. doi:10.1021/la503289v.

- [191] W.F.D. Bennett, D.P. Tieleman, Computer simulations of lipid membrane domains, *Biochim. Biophys. Acta.* 1828 (2013) 1765–1776. doi:10.1016/j.bbamem.2013.03.004.
- [192] R.N.A.H.L. Todd P. W. McMullen, Cholesterol–phospholipid interactions, the liquid-ordered phase and lipid rafts in model and biological membranes, *Curr. Opin. Colloid Amp Interface Sci.* 8 (2004) 459–468. doi:10.1016/j.cocis.2004.01.007.
- [193] A. Botan, F. Favela-Rosales, P.F.J. Fuchs, M. Javanainen, M. Kanduč, W. Kulig, A. Lamberg, C. Loison, A. Lyubartsev, M.S. Miettinen, L. Monticelli, J. Määttä, O.H.S. Ollila, M. Retegan, T. Róg, H. Santuz, J. Tynkkynen, Toward Atomistic Resolution Structure of Phosphatidylcholine Headgroup and Glycerol Backbone at Different Ambient Conditions, *J. Phys. Chem. B.* 119 (2015) 15075–15088. doi:10.1021/acs.jpcc.5b04878.
- [194] A.G. Lee, How lipids affect the activities of integral membrane proteins, *Biochim. Biophys. Acta.* 1666 (2004) 62–87. doi:10.1016/j.bbamem.2004.05.012.
- [195] V. Navrátilová, M. Paloncýová, M. Kajšová, K. Berka, M. Otyepka, Effect of Cholesterol on the Structure of Membrane-Attached Cytochrome P450 3A4, *J. Chem. Inf. Model.* 55 (2015) 628–635. doi:10.1021/ci500645k.
- [196] P.S. Niemelä, S. Ollila, M.T. Hyvönen, M. Karttunen, I. Vattulainen, Assessing the Nature of Lipid Raft Membranes, *PLoS Comput Biol.* 3 (2007) e34. doi:10.1371/journal.pcbi.0030034.
- [197] P.S. Niemelä, M.T. Hyvönen, I. Vattulainen, Atom-scale molecular interactions in lipid raft mixtures, *Biochim. Biophys. Acta.* 1788 (2009) 122–135. doi:10.1016/j.bbamem.2008.08.018.
- [198] Y. Zhang, A. Lervik, J. Seddon, F. Bresme, A coarse-grained molecular dynamics investigation of the phase behavior of DPPC/cholesterol mixtures, *Chem. Phys. Lipids.* 185 (2015) 88–98. doi:10.1016/j.chemphyslip.2014.07.011.
- [199] H. Ohvo-Rekilä, B. Ramstedt, P. Leppimäki, J.P. Slotte, Cholesterol interactions with phospholipids in membranes, *Prog. Lipid Res.* 41 (2002) 66–97.
- [200] T. Róg, M. Pasenkiewicz-Gierula, I. Vattulainen, M. Karttunen, Ordering effects of cholesterol and its analogues, *Biochim. Biophys. Acta.* 1788 (2009) 97–121. doi:10.1016/j.bbamem.2008.08.022.
- [201] H.J. Risselada, S.J. Marrink, The molecular face of lipid rafts in model membranes, *Proc. Natl. Acad. Sci.* 105 (2008) 17367–17372. doi:10.1073/pnas.0807527105.
- [202] M.L. Berkowitz, Detailed molecular dynamics simulations of model biological membranes containing cholesterol, *Biochim. Biophys. Acta BBA - Biomembr.* 1788 (2009) 86–96. doi:10.1016/j.bbamem.2008.09.009.
- [203] C. Díaz-Tejada, I. Ariz-Extreme, N. Awasthi, J.S. Hub, Quantifying Lateral Inhomogeneity of Cholesterol-Containing Membranes, *J. Phys. Chem. Lett.* 6 (2015) 4799–4803. doi:10.1021/acs.jpcclett.5b02414.
- [204] F. Zocher, D. van der Spoel, P. Pohl, J.S. Hub, Local Partition Coefficients Govern Solute Permeability of Cholesterol-Containing Membranes, *Biophys. J.* 105 (2013) 2760–2770. doi:10.1016/j.bpj.2013.11.003.
- [205] J. Barnoud, G. Rossi, S.J. Marrink, L. Monticelli, Hydrophobic Compounds Reshape Membrane Domains, *PLoS Comput Biol.* 10 (2014) e1003873. doi:10.1371/journal.pcbi.1003873.

- [206] A.J. Sodt, M.L. Sandar, K. Gawrisch, R.W. Pastor, E. Lyman, The Molecular Structure of the Liquid-Ordered Phase of Lipid Bilayers, *J. Am. Chem. Soc.* 136 (2014) 725–732. doi:10.1021/ja4105667.
- [207] S. Capponi, J.A. Freites, D.J. Tobias, S.H. White, Interleaflet mixing and coupling in liquid-disordered phospholipid bilayers, *Biochim. Biophys. Acta BBA - Biomembr.* 1858 (2016) 354–362. doi:10.1016/j.bbamem.2015.11.024.
- [208] S. Meinhardt, R.L.C. Vink, F. Schmid, Monolayer curvature stabilizes nanoscale raft domains in mixed lipid bilayers, *Proc. Natl. Acad. Sci.* 110 (2013) 4476–4481. doi:10.1073/pnas.1221075110.
- [209] J.D. Perlmutter, J.N. Sachs, Interleaflet Interaction and Asymmetry in Phase Separated Lipid Bilayers: Molecular Dynamics Simulations, *J. Am. Chem. Soc.* 133 (2011) 6563–6577. doi:10.1021/ja106626r.
- [210] T. Róg, A. Orłowski, A. Llorente, T. Skotland, T. Sylvänne, D. Kauhanen, K. Ekroos, K. Sandvig, I. Vattulainen, Interdigitation of long-chain sphingomyelin induces coupling of membrane leaflets in a cholesterol dependent manner, *Biochim. Biophys. Acta BBA - Biomembr.* 1858 (2016) 281–288. doi:10.1016/j.bbamem.2015.12.003.
- [211] H. Koldsø, D. Shorthouse, J. Hélie, M.S.P. Sansom, Lipid Clustering Correlates with Membrane Curvature as Revealed by Molecular Simulations of Complex Lipid Bilayers, *PLoS Comput Biol.* 10 (2014) e1003911. doi:10.1371/journal.pcbi.1003911.
- [212] I. Basu, C. Mukhopadhyay, In silico phase separation in the presence of GM1 in ternary and quaternary lipid bilayers, *Phys. Chem. Chem. Phys.* 17 (2015) 17130–17139. doi:10.1039/C5CP01970B.
- [213] S. Jo, H. Rui, J.B. Lim, J.B. Klauda, W. Im, Cholesterol Flip-Flop: Insights from Free Energy Simulation Studies, *J. Phys. Chem. B.* 114 (2010) 13342–13348. doi:10.1021/jp108166k.
- [214] W.F.D. Bennett, J.L. MacCallum, M.J. Hinner, S.J. Marrink, D.P. Tieleman, Molecular View of Cholesterol Flip-Flop and Chemical Potential in Different Membrane Environments, *J. Am. Chem. Soc.* 131 (2009) 12714–12720. doi:10.1021/ja903529f.
- [215] G. Parisio, A. Ferrarini, M.M. Sperotto, Model studies of lipid flip-flop in membranes, *Int. J. Adv. Eng. Sci. Appl. Math.* (2016) 1–13. doi:10.1007/s12572-015-0155-9.
- [216] C. Hong, D.P. Tieleman, Y. Wang, Microsecond Molecular Dynamics Simulations of Lipid Mixing, *Langmuir.* 30 (2014) 11993–12001. doi:10.1021/la502363b.
- [217] H. Ding, Y. Ma, Theoretical and Computational Investigations of Nanoparticle–Biomembrane Interactions in Cellular Delivery, *Small.* 11 (2015) 1055–1071. doi:10.1002/smll.201401943.
- [218] R. Vácha, F.J. Martinez-Veracoechea, D. Frenkel, Receptor-Mediated Endocytosis of Nanoparticles of Various Shapes, *Nano Lett.* 11 (2011) 5391–5395. doi:10.1021/nl2030213.
- [219] R. Vácha, F.J. Martinez-Veracoechea, D. Frenkel, Intracellular Release of Endocytosed Nanoparticles Upon a Change of Ligand–Receptor Interaction, *ACS Nano.* 6 (2012) 10598–10605. doi:10.1021/nn303508c.